

NASA CR-174625

R81AEG282
February 1981



National Aeronautics and
Space Administration

SUBSONIC/TRANSONIC STALL FLUTTER INVESTIGATION OF A ROTATING RIG

FINAL REPORT

by

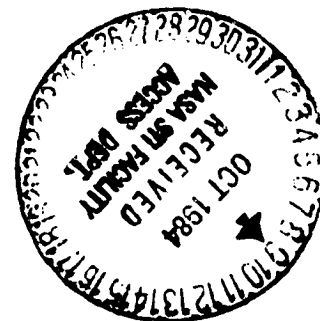
R.R. Jutras

R.B. Fost

R.M. Chi

B.F. Beacher

General Electric Company
Aircraft Engine Business Group
Advanced Technology Programs Department
Cincinnati, Ohio 45215



Prepared For

National Aeronautics and Space Administration
Lewis Research Center
21000 Brookpark Road
Cleveland, Ohio 44135

(NASA-CR-174625) SUBSONIC/TRANSONIC STALL
FLUTTER INVESTIGATION OF A ROTATING RIG
Final Report (General Electric Co.) 319 p
HC A14/MF A01 CSCL 01C

N84-33417

Unclass
G3/08 23945

Contract
NAS3-20605

1 Report No. NASA CR 174625		2 Government Accession No.		3 Recipient's Catalog No.	
4 Title and Subtitle SUBSONIC/TRANSONIC STALL FLUTTER INVESTIGATION OF A ROTATING RIG				5 Report Date 28 February 1981	
				6 Performing Organization Code	
7 Author(s) R.R. Jutras, R.B. Fost, R.M. Chi, B.F. Beacher				8 Performing Organization Report No. R81AEG282	
9 Performing Organization Name and Address General Electric Company Aircraft Engine Business Group Cincinnati, Ohio 45215				10 Work Unit No.	
				11 Contract or Grant No. NAS3-20605	
				13 Type of Report and Period Covered Final Report	
12 Sponsoring Agency Name and Address NASA-Lewis Research Center 21000 Brookpark Road Cleveland, Ohio 44135				14 Sponsoring Agency Code	
15 Supplementary Notes					
16 Abstract <p>The objective of this test research program was to investigate stall flutter by obtaining detailed quantitative steady and unsteady aerodynamic and aeromechanical measurements in a typical fan rotor. The experimental investigation was made with a 31.3 percent scale model of the Quiet Engine Program Fan C rotor system. Both subsonic/transonic (torsional mode) flutter and supersonic (flexural) flutter were investigated. Extensive steady and unsteady data on the blade deformations and aerodynamic properties surrounding the rotor were acquired while it was operating in both the steady and flutter modes. Analysis of this data showed that while there may be more than one traveling wave present during flutter, they are all forward traveling waves. The compilation of this data will be useful in the future development and extension of stall flutter prediction techniques.</p>					
17 Key Words (Suggested by Author(s)) Stall Flutter Aeroelasticity Traveling Waves Unsteady Measurements					
19 Security Classif. (of this report) Unclassified		20 Security Classif. (of this page) Unclassified		21 No. of Pages 297	22 Price*

FOREWORD

The test research program reported herein was conducted by the General Electric Company under National Aeronautics and Space Administration, Lewis Research Center, Contract NAS3-20605 and conducted under the cognizance of W. Stevans and J. Adamczyk of the Lewis Research Center.

This test research program was conducted to investigate stall flutter by providing detailed quantitative steady and unsteady aerodynamic and aeromechanical measurements in a typical fan rotor. Both subsonic/transonic (torsional mode) flutter and supersonic (flexural mode) flutter were investigated. The tests were conducted in two builds: Build 1 tested during November, 1978; Build 2, Tests 1 and 2 during March, 1979; and Build 2, Test 3 during January, 1980. This report documents the results of this program.

The authors would like to acknowledge the valuable assistance of L.W. Kruger and Mike Chalfin in the FFT acquisition and analysis of the test data, of R.J. Klapproth in analyzing the test data, and of T.A. Dodd in preparing data presented in this report.

TABLE OF CONTENTS

<u>Section</u>	<u>Page</u>
1.0 INTRODUCTION	1
1.1 Program Description	2
2.0 TEST VEHICLE DESCRIPTION	6
2.1 Aerodynamic Design	9
2.2 Mechanical Design	9
3.0 TEST FACILITY	12
3.1 General	12
3.2 Data Acquisition	12
3.2.1 Aerodynamic Performance Data	12
3.2.2 Aeromechanical Data	15
4.0 INSTRUMENTATION	16
4.1 General	16
4.2 Steady-State Aerodynamic Performance Instrumentation	16
4.3 Unsteady Aerodynamic Instrumentation	16
4.3.1 Blade-Mounted Kulite Sensor Calibration	29
4.4 Aeromechanical Instrumentation	29
4.4.1 Blade Deformation Instrumentation	29
4.4.2 Dynamic Strain Gages	33
4.5 Rotor Position Instrumentation	33
5.0 DATA ANALYSIS PROCEDURES	37
5.1 Steady Aerodynamic Performance Data	37
5.1.1 Calculations of Overall Fan Performance	37
5.1.2 Calculations of Blade Element Data	38
5.2 Strain Gages	39
5.2.1 Vibratory Response	39
5.2.2 Interblade Phase Angle	39
5.2.3 Phasing of Rotating Instrumentation Signals	41
5.2.4 Phasing of Stationary Instrumentation Signals	41
5.3 Blade Displacement Data	45
5.3.1 Steady-State Deformation	46
5.3.2 Unsteady Deformation	47
5.4 Blade-Mounted Sensors	47
5.4.1 Kulites	48
5.5 Casing-Mounted Kulites	48
5.5.1 Transformation to Rotating Reference System	49
5.6 Traversable Probes	55
5.7 Structural Response Predictions	56
5.8 Blade Work Per Mode Calculation	56
6.0 TEST RESULTS	60
6.1 Steady Aerodynamic Performance	60
6.1.1 Overall Fan Performance	60

TABLE OF CONTENTS (Continued)

<u>Section</u>	<u>Page</u>
6.1.2 Fan Rotor Blade Element Data	64
6.2 Blade Dynamic Strain Gage Data	72
6.2.1 Bench Test Frequencies	72
6.2.2 Flutter Frequency Response	72
6.2.3 Flutter Vibratory Stress Amplitude	72
6.2.4 Interblade Phase Angles	78
6.3 Blade Displacement Data	90
6.3.1 Steady-State Deformation	93
6.3.2 Unsteady Deformation	101
6.4 Blade-Mounted Sensors	110
6.4.1 Blade-Mounted Kulite Time Histories	110
6.4.2 Airfoil Unsteady Pressure	118
6.4.3 Unsteady Pressure Phase Angle	128
6.5 Blade Tip Static Pressure Field	128
6.5.1 Static Pressure Distribution	128
6.5.2 Analysis of Unsteady Casing Kulite Data	145
6.5.3 Traveling Wave Analysis	145
6.6 Rotor Exit Total Pressure	163
6.6.1 Circumferentially Averaged Total Pressur	163
6.6.2 Total Pressure Radial Distribution	168
6.6.3 Analysis of Unsteady Exit Total Pressure	168
6.6.4 Traveling Wave Contents	179
6.7 Inlet and Exit Flow Data	179
6.7.1 Absolute Velocity and Flow Angle Radial Distributions	187
6.7.2 Circumferential Variation of Absolute Velocity and Angle	192
6.7.3 Analysis of Unsteady Absolute Velocity	204
6.7.4 Traveling Wave Contents	204
6.8 Blade Work Per Mode	204
7.0 SUMMARY, CONCLUSIONS, AND RECOMMENDATIONS	223
7.1 Summary	223
7.2 Conclusions	225
7.3 Recommendations	226
APPENDIX A - BLADE ELEMENT DATA	227
APPENDIX B - BLADE COORDINATES	249
APPENDIX C - BLADE/MOUNTED-KULITE TIME HISTORIES	256
APPENDIX D - EXAMPLES OF UNSTEADY DATA COMPUTER PROCESSING	262
APPENDIX E - X-ARRAY - PROBE CONTOUR PLOTS AT NON-FLUTTER POINTS	273

LIST OF ILLUSTRATIONS

<u>Figure</u>		<u>Page</u>
1.	Comparison of Rotating Rig Fan Blade with Full Scale Fan C Blade.	3
2.	NASA Rotating Rig Performance Map, Build 2.	5
3.	Rotating Rig Assembly.	8
4.	Scale Model Fan/Compressor Test Facility.	13
5.	Air Turbine Schematic Flow Diagram.	14
6.	Rotating Rig Instrumentation.	18
7.	Blade Mounted Kulite Sensor Locations.	24
8.	Blade Mounted Hot Film Sensor Locations.	25
9.	Casing-Mounted Kulite Geometry.	27
10.	Blade-Mounted Pressure Sensor Installation.	30
11.	Schematic Representation of Light Probe Locations.	32
12.	Rotor Blade Strain Gage Location.	34
13.	Rotating Rig, Build 2, Configuration.	35
14.	Total Pressure and Total Temperature/Radial Profiles, 95% Speed.	36
15.	Comparison of Fixed Instrumentation and Traverse Probe Blade Element Data, 70 Percent Speed.	40.
16.	Data Acquisition for One Revolution.	42
17.	Ensemble Average of Time Frames.	43
18.	Stationary to Rotating Reference Transformation.	44
19.	Averaged Casing Kulite Time Histories, 70 Percent Speed Flutter.	50
20.	Average Casing Kulite Time Histories, 95% Speed Flutter.	51
21.	Reference Coordinate Systems.	53
22.	Finite Element Model of Rotating Rig Blade.	57
23.	NASA Rotating Rig Fan Rotor Bypass Performance Map.	61
24.	NASA Rotating Rig Fan Rotor Hub Performance Map.	65
25.	NASA Fan Stage Performance Map.	66
26.	NASA Rotating Rig Speed-Flow Characteristics.	67
27.	Bypass Flow Deviation Angle Versus Untwisted Incidence.	68
28.	Bypass Flow Diffusion Factor Versus Untwisted Incidence.	69
29.	Bypass Flow Loss Coefficient Versus Untwisted Incidence.	70

LIST OF ILLUSTRATIONS (Continued)

<u>Figure</u>		<u>Page</u>
30.	Bypass Flow Loss Parameter Versus Diffusion Factor.	71
31.	Blade Bench Test Frequency Variation Around the Rotor-Build 2.	75
32.	Rotating Rig Campbell Diagram.	76
33.	Blade Torsional Response Frequencies.	77
34.	Blade Flexural Response Frequencies.	77
35.	Overall and Filtered Strain Gage Signals During Torsional Flutter at 65 Percent Speed.	79
36.	Overall and Filtered Strain Gage Signals During Transient to Torsional Flutter at 70 Percent Speed.	80
37.	Overall and Filtered Strain Gage Signals During Flexural Flutter at 90 Percent Speed.	81
38.	Overall and Filtered Strain Gage Signals During Flexural Flutter at 95 Percent Speed.	82
39.	Circumferential Variations of Blade Stress at 65 Percent Speed.	83
40.	Circumferential Variation of Blade Stress at 70 Percent Speed.	84
41.	Circumferential Variation of Blade Stress at 90 Percent Speed.	85
42.	Circumferential Variation of Blade Stress at 95 Percent Speed.	86
43.	Phasemeter Strain Gage Phasing.	87
44.	FFT Cross Spectral Analysis at 70 Percent Speed Flutter.	88
45.	FFT Cross Spectral Analysis at 90 Percent Speed Flutter.	89
46.	Strain Gage Phase Data, 65 Percent Speed Torsional Flutter.	91
47.	Strain Gage Phase Data, 70 Percent Speed Torsional Flutter.	91
48.	Rotating Rig Blade Phase Data 90 Percent Speed, Flexural Flutter.	92
49.	Rotating Rig Blade Phase Data 95 Percent Speed, Flexural Flutter.	92
50.	Blade Tip Absolute Tangential Displacement Versus Chord.	94
51.	Absolute Tangential Displacement Versus Chord, 78.9 Percent Span.	95

LIST OF ILLUSTRATIONS (Continued)

<u>Figure</u>		<u>Page</u>
52.	Absolute Tangential Displacement Versus Chord, 57.2 Percent Span.	95
53.	Tip Tangential Deflection Versus Chord, Nominal Operating Line.	96
54.	Tip Tangential Displacement Versus Chord, Intermediate Operating Line.	97
55.	Tip Tangential Displacement Versus Chord, Flutter.	98
56.	Tip Untwist Versus Speed.	99
57.	Untwist Versus Speed at Intermediate Span Locations.	100
58.	Untwist Versus Span at 65 Percent Speed.	102
59.	Untwist Versus Span at 70 Percent Speed.	102
60.	Untwist Versus Span at 90 Percent Speed.	102
61.	Untwist Versus Span at 95 Percent Speed.	102
62.	Total Blade Camber Change with Speed and Operating Line.	103
63.	Blade Stress and Deflection in Torsional Flutter at 65 Percent Speed.	104
64.	Blade Stress and Deflection in Torsional Flutter at 70 Percent Speed.	105
65.	Blade Stress and Deflection in Flexural Flutter at 95 Percent Speed.	106
66.	Blade Phase Data at 70 Percent Speed Torsional Flutter.	111
67.	Blade Phase Data at 95 Percent Speed Flexural Flutter.	112
68.	Blade-Mounted Kulite Time Histories, 65 Percent Speed Flutter.	115
69.	Blade-Mounted Kulite Time Histories, 70 Percent Speed Flutter.	116
70.	Blade-Mounted Kulite Time Histories, 95 Percent Speed Flutter.	117
71.	Blade-Mounted Kulite Auto Spectra, 65 Percent Speed Flutter.	119
71.	Blade-Mounted Kulite Auto Spectra, 65 Percent Speed Flutter (Continued).	120
71.	Blade-Mounted Kulite Auto Spectra, 65 Percent Speed Flutter (Concluded).	121
72.	Blade-Mounted Kulite Auto Spectra, 70 Percent Speed Flutter.	122

LIST OF ILLUSTRATIONS (Continued)

<u>Figure</u>		<u>Page</u>
73.	Blade-Mounted Kulite Auto Spectra, 95 Percent Speed Flutter.	123
73.	Blade-Mounted Kulite Auto Spectra, 95 Percent Speed Flutter (Concluded).	124
74.	Blade-Mounted Kulite Measured Pressure, 65 Percent Speed.	125
75.	Blade-Mounted Kulite Measured Pressure, 70 Percent Speed.	126
76.	Blade-Mounted Kulite Measured Pressure, 95 Percent Speed.	127
77.	Blade-Mounted Kulite Cross Spectrum, 65 Percent Speed Flutter.	129
78.	Blade-Mounted Kulite Cross Spectrum, 65 Percent Speed Flutter.	130
79.	Blade-Mounted Kulite Phase Data.	131
80.	Dynamic Part of the Instantaneous Static Pressure, 65 and 70 Percent Speed Flutter.	132
81.	Dynamic Part of the Instantaneous Static Pressure, 90 and 95 Percent Speed Flutter.	133
82.	Casing Kulite Contour Plot, 65 Percent Speed Flutter.	134
83.	Casing Kulite Contour Plot, 70 Percent Speed Flutter.	135
84.	Casing Kulite Contour Plot, 90 Percent Speed Flutter.	136
85.	Casing Kulite Contour Plot, 95 Percent Speed Flutter.	137
86.	Casing Kulite Contour Plot, 65 Percent Speed Intermediate Operating Line.	139
87.	Casing Kulite Contour Plot, 70 Percent Speed Nominal Operating Line.	140
88.	Casing Kulite Contour Plot, 70 Percent Speed Intermediate Operating Line.	141
89.	Casing Kulite Contour Plot, 90 Percent Speed Nominal Operating Line.	142
90.	Casing Kulite Contour Plot, 90 Percent Speed Intermediate Operating Line.	143
91.	Casing Kulite Contour Plot, 95 Percent Speed Intermediate Operating Line.	144
92.	Casing Kulite Cross Spectra, 70 Percent Speed Flutter.	146
93.	Circumferential Variation of Blade Tip Unsteady Pressure and Relative Phase at 70 Percent Speed Flutter, CK705.	147
94.	Circumferential Variation of Blade Tip Unsteady Pressure and Relative Phase at 70 Percent Speed Flutter, CK707.	148

LIST OF ILLUSTRATIONS (Continued)

<u>Figure</u>		<u>Page</u>
95.	Circumferential Variation of Blade Tip Unsteady Pressure and Relative Phase at 70 Percent Speed Flutter, CK709.	149
96.	Casing Kulite (Number 702) Spectrum, 70 Percent Speed Flutter.	151
97.	Casing Kulite (Number 704) Spectrum, 70 Percent Speed Flutter.	152
98.	Casing Kulite (Number 706) Spectrum, 70 Percent Speed Flutter.	153
99.	Casing Kulite (Number 708) Spectrum, 70 Percent Speed Flutter.	154
100.	Casing Kulite (Number 710) Spectrum, 70 Percent Speed Flutter.	155
101.	Casing Kulite (Number 702) Spectrum, 95 Percent Speed Flutter.	156
102.	Casing Kulite (Number 704) Spectrum, 95 Percent Speed Flutter.	157
103.	Casing Kulite (Number 706) Spectrum, 95 Percent Speed Flutter.	158
104.	Casing Kulite (Number 708) Spectrum, 95 Percent Speed Flutter.	159
105.	Casing Kulite (Number 712) Spectrum, 95 Percent Speed Flutter.	160
106.	Circumferential Variation of Blade Tip Unsteady Pressure and Phase at 70 Percent Speed Flutter.	164
107.	Circumferential Variation of Blade Tip Unsteady Pressure and Phase at 95 Percent Speed Flutter.	165
108.	Radial Distribution of Steady Total Pressure, 65 and 70 Percent Speed Flutter.	166
109.	Radial Distribution of Steady Total Pressure, 90 and 95 Percent Speed Flutter.	167
110.	Dynamic Part of Instantaneous Total Pressure, 70 Percent Speed Flutter.	169
111.	Dynamic Part of Instantaneous Total Pressure, 95 Percent Speed Flutter.	170
112.	Total Pressure Contour Plot, 65 Percent Speed Flutter.	171
113.	Total Pressure Contour Plot, 70 Percent Speed Flutter.	172
114.	Total Pressure Contour Plot, 90 Percent Speed Flutter.	173
115.	Total Pressure Contour Plot, 95 Percent Speed Flutter.	174

LIST OF ILLUSTRATIONS (Continued)

<u>Figure</u>		<u>Page</u>
116.	Total Pressure Contour Plot, 70 Percent Speed IOL.	175
117.	Total Pressure Contour Plot, 90 Percent Speed NOL.	176
118.	Total Pressure Contour Plot, 90 Percent Speed IOL.	177
119.	Total Pressure Cross Spectra, Percent Speed Flutter.	178
120.	Circumferential Variation of Unsteady Total Pressure, 70 Percent Speed Flutter.	180
121.	Circumferential Phase Variation of Total Pressure, 70 Percent Speed Flutter.	181
122.	Total Pressure Spectrum, 14.5 Percent Immersion, 70 Percent Speed Flutter.	182
123.	Total Pressure Spectrum, 42.2 Percent Immersion, 70 Percent Speed Flutter.	183
124.	Total Pressure Spectrum, 82 Percent Immersion, 70 Percent Speed Flutter.	184
125.	Total Pressure Spectrum, 14.5 Percent Immersion, 95 Percent Speed Flutter.	185
126.	Total Pressure Spectrum, 42.2 Percent Immersion, 95 Percent Speed Flutter.	186
127.	Radial Distribution of Inlet Absolute Velocity, 65 Percent Speed.	188
128.	Radial Distribution of Inlet Flow Angle, 65 Percent Speed.	188
129.	Radial Distribution of Exit Absolute Velocity, 65 Percent Speed.	188
130.	Radial Distribution of Exit Flow Angle, 65 Percent Speed.	188
131.	Radial Distribution of Inlet Absolute Velocity, 70 Percent Speed.	189
132.	Radial Distribution of Inlet Flow Angle, 70 Percent Speed.	189
133.	Radial Distribution of Exit Absolute Velocity, 70 Percent Speed.	189
134.	Radial Distribution of Exit Flow Angle, 70 Percent Speed.	189
135.	Radial Distribution of Inlet Absolute Velocity, 90 Percent Speed.	190
136.	Radial Distribution of Inlet Flow Angle, 90 Percent Speed.	190

LIST OF ILLUSTRATIONS (Continued)

<u>Figure</u>		<u>Page</u>
137.	Radial Distribution of Exit Absolute Velocity, 90 Percent Speed.	190
138.	Radial Distribution of Exit Flow Angle, 90 Percent Speed.	190
139.	Radial Distribution of Inlet Flow Velocity, 95 Percent Speed.	191
140.	Radial Distribution of Inlet Flow Angle, 95 Percent Speed.	191
141.	Radial Distribution of Exit Flow Velocity, 95 Percent Speed.	191
142.	Radial Distribution of Exit Flow Angle, 95 Percent Speed.	191
143.	Circumferential Variation of Inlet Absolute Velocity and Flow Angle, 70 Percent Speed Flutter.	193
144.	Circumferential Variation of Exit Absolute Velocity and Flow Angle, 70 Percent Speed Flutter.	194
145.	Circumferential Variation of Inlet Absolute Velocity and Flow Angle, 95 Percent Speed Flutter.	195
146.	Circumferential Variation of Exit Absolute Velocity and Flow Angle, 95 Percent Speed Flutter.	196
147.	Inlet Absolute Velocity Contour Plot, 65 Percent Speed Flutter.	197
148.	Inlet Flow Angle Contour Plot, 65 Percent Speed Flutter.	197
149.	Exit Absolute Velocity Contour Plot, 65 Percent Speed Flutter.	198
150.	Exit Flow Angle Contour Plot, 65 Percent Speed Flutter.	198
151.	Inlet Absolute Velocity Contour Plot, 70 Percent Speed Flutter.	199
152.	Inlet Flow Angle Contour Plot, 70 Percent Speed Flutter.	199
153.	Exit Absolute Velocity Contour Plot, 70 Percent Speed Flutter.	200
154.	Exit Flow Angle Contour Plot, 70 Percent Speed Flutter.	200
155.	Inlet Absolute Velocity Contour Plot, 90 Percent Speed Flutter.	201
156.	Inlet Flow Angle Contour Plot, 90 Percent Speed Flutter	201
157.	Exit Absolute Velocity Contour Plot, 90 Percent Speed Flutter.	202

LIST OF ILLUSTRATIONS (Continued)

<u>Figure</u>		<u>Page</u>
158.	Exit Flow Angle Contour Plot, 90 Percent Speed Flutter.	202
159.	Inlet Absolute Velocity Contour Plot, 95 Percent Speed Flutter.	203
160.	Inlet Flow Angle Contour Plot, 90 Percent Speed Flutter.	203
161.	Inlet X-Array Aliased Spectral Analysis (8.4 Percent Immersion), 70 Percent Speed Flutter.	205
162.	Circumferential Variation of Unsteady Inlet Velocity, 70 Percent Speed Flutter.	206
163.	Circumferential Phase Variation of Unsteady Inlet Velocity, 70 Percent Speed Flutter.	207
164.	Inlet Velocity Spectrum, 8.4 Percent Immersion, 70 Percent Speed Flutter.	208
165.	Inlet Velocity Spectrum, 28.5 Percent Immersion, 70 Percent Speed Flutter.	209
166.	Inlet Velocity Spectrum, 58.2 Percent Immersion, 70 Percent Speed Flutter.	210
167.	Exit Velocity Spectrum, 14.5 Percent Immersion, 70 Percent Speed Flutter.	211
168.	Exit Velocity Spectrum, 42.2 Percent Immersion, 70 Percent Speed Flutter.	212
169.	Exit Velocity Spectrum, 82 Percent Immersion, 70 Percent Speed Flutter.	213
170.	Inlet Velocity Spectrum, 8.4 Percent Immersion, 95 Percent Speed Flutter.	214
171.	Inlet Velocity Spectrum, 28.5 Percent Immersion, 95 Percent Speed Flutter.	215
172.	Inlet Velocity Spectrum, 58.2 Percent Immersion, 95 Percent Speed Flutter.	216
173.	Exit Velocity Spectrum, 14.5 Percent Immersion, 95 Percent Speed Flutter.	217
174.	Exit Velocity Spectrum, 42.2 Percent Immersion, 95 Percent Speed Flutter.	218
175.	Exit Velocity Spectrum, 82 Percent Immersion, 95 Percent Speed Flutter.	219
B-1.	Airfoil Geometry Definitions for Manufacturing Coordinates.	249
C-1.	Blade-Mounted Kulite Time Histories, 65 Percent Speed Intermediate Operating Line.	256
C-2.	Blade-Mounted Kulite Time Histories, 70 Percent Speed Nominal Operating Line.	257

LIST OF ILLUSTRATIONS (Continued)

<u>Figure</u>		<u>Page</u>
C-3.	Blade-Mounted Kulite Time Histories, 70 Percent Speed Intermediate Operating Line.	258
C-4.	Blade-Mounted Kulite Time Histories, 90 Percent Speed Nominal Operating Line.	259
C-5.	Blade-Mounted Kulite Time Histories, 90 Percent Speed Intermediate Operating Line.	260
C-6.	Blade-Mounted Kulite Time Histories, 95 Percent Speed Intermediate Operating Line.	261
D-1.	Once Per Revolution Sampling of Casing Kulite.	264
D-2.	Once Per Revolution Sampling of Strain Gage.	264
D-3.	Once Per Revolution Sampling of P _T Yaw Probe.	266
D-4.	Once Per Revolution Sampling of Strain Gage.	266
E-1.	Inlet Flow Angle Contour Plot, 65 Percent Speed Intermediate Operating Line.	273
E-2.	Inlet Absolute Velocity Contour Plot, 65 Percent Speed Intermediate Operating Line.	274
E-3.	Exit Flow Angle Contour Plot, 65 Percent Speed Intermediate Operating Line.	275
E-4.	Exit Absolute Velocity Contour Plot, 65 Percent Speed Intermediate Operating Line.	276
E-5.	Inlet Flow Angle Contour Plot, 70 Percent Speed Nominal Operating Line.	277
E-6.	Inlet Absolute Velocity Contour Plot, 70 Percent Speed Nominal Operating Line.	278
E-7.	Exit Flow Angle Contour Plot, 70 Percent Speed Nominal Operating Line.	279
E-8.	Exit Absolute Velocity Contour Plot, 70 Percent Speed Nominal Operating Line.	280
E-9.	Inlet Flow Angle Contour Plot, 70 Percent Speed Intermediate Operating Line.	
E-10.	Inlet Absolute Velocity Contour Plot, 70 Percent Speed Intermediate Operating Line.	282
E-11.	Exit Flow Angle Contour Plot, 70 Percent Speed Intermediate Operating Line.	283
E-12.	Exit Absolute Velocity Contour Plot, 70 Percent Speed Intermediate Operating Line.	284
E-13.	Inlet Flow Angle Contour Plot, 90 Percent Speed Nominal Operating Line.	285

LIST OF ILLUSTRATIONS (Concluded)

<u>Figure</u>		<u>Page</u>
E-14.	Inlet Absolute Velocity Contour Plot, 90 Percent Speed Nominal Operating Line.	286
E-15.	Exit Flow Angle Contour Plot, 90 Percent Speed Nominal Operating Line.	287
E-16.	Exit Absolute Velocity Contour Plot, 90 Percent Speed Nominal Operating Line.	288
E-17.	Inlet Flow Angle Contour Plot, 90 Percent Speed Intermediate Operating Line.	289
E-18.	Inlet Absolute Velocity Contour Plot, 90 Percent Speed Intermediate Operating Line.	290
E-19.	Exit Flow Angle Contour Plot, 90 Percent Speed Intermediate Operating Line.	291
E-20.	Exit Absolute Velocity Contour Plot, 90 Percent Speed Intermediate Operating Line.	292
E-21.	Inlet Flow Angle Contour Plot, 95 Percent Speed Intermediate Operating Line.	293
E-22.	Inlet Absolute Velocity Contour Plot, 95 Percent Speed Intermediate Operating Line.	294
E-23.	Exit Flow Angle Contour Plot, 95 Percent Speed Intermediate Operating Line.	295
E-24.	Exit Absolute Velocity Contour Plot, 95 Percent Speed Intermediate Operating Line.	296

LIST OF TABLES

<u>Table</u>		<u>Page</u>
I.	Full Fan C Aerodynamic Design Features.	4
II.	Rotating Rig Design Characteristics.	7
III.	Fan Blade Mechanical Summary.	11
IV.	Rotating Rig Instrumentation.	17
V.	Steady-State Aerodynamic Instrumentation Locations.	19
VI.	Static Pressure Tap Locations.	20
VII.	Pitot Static Inlet Rake Immersions.	21
VIII.	Steady-State Traverse Probe and Rake Locations.	22
IX.	Casing-Mounted Kulite Locations.	26
X.	Dynamic Traverse Probes.	28
XI.	Results of Blade-Mounted Kulite Laboratory Calibrations.	31
XII.	One Per Rev Sampling Rates and Instability Frequencies.	45
XIII.	NASA Rotating Rig Fan Rotor Performance Data.	62
XIII.	NASA Rotating Rig Fan Rotor Performance Data. (Concluded)	63
XIV.	NASA Rotating Rig Data Point Summary.	73
XV.	Blade Vibratory Stress and Phase Lag Summary for the Four Flutter Points.	74
XVI.	Tangential Maximum Deflection Excursions (Mils-DA) at 10802 rpm.	107
XVII.	Tangential Maximum Deflection Excursions (Mils-DA) at 11630 rpm.	108
XVIII.	Tangential Maximum Deflection Excursions (Mils-DA) at 15743 rpm.	109
XIX.	Unsteady Tip Displacement Phase Lag (In Degrees) at 70 Percent Speed Flutter	113
XX.	Unsteady Tip Displacement Phase Lag (In Degrees) at 95 Percent Speed Flutter.	114
XXI.	Traveling Wave Amplitudes and Phases, 70 Percent Speed Torsional Flutter.	161
XXII.	Traveling Wave Amplitudes and Phases, 95 Percent Speed Flexural Flutter.	162
XXIII.	Damping Data at 70 Percent Speed Torsional Flutter.	220
XXIV.	Damping Data at 95 Percent Speed Flexural Flutter.	221
A-1.	Design Point (Predicted) Blade Element Data.	229

LIST OF TABLES (Continued)

<u>Table</u>		<u>Page</u>
A-1.	Design Point (Predicted) Blade Element Data (Concluded).	230
A-2.	Blade Element Data from Fixed Instrumentation, Intermediate O.L., 65% Speed, Reading 158.	231
A-3.	Blade Element Data from Fixed Instrumentation, Near Stall Flutter, 65% Speed, Reading 54.	32
A-4.	Blade Element Data from Fixed Instrumentation, Stall Flutter, 65% Speed, Reading 79.	233
A-5.	Blade Element Data from Fixed Instrumentation, Near Peak Efficiency, 70% Speed, Reading 105.	234
A-6.	Blade Element Data from Fixed Instrumentation, Low Operating Line, 75% Speed, Reading 154.	235
A-7.	Blade Element Data from Fixed Instrumentation, Intermediate O.L., 70% Speed, Reading 179.	236
A-8.	Blade Element Data from Fixed Instrumentation, Near Stall Flutter, 70% Speed, Reading 56.	237
A-9.	Blade Element Data from Fixed Instrumentation, At Stall Flutter, 70% Speed, Reading 89.	238
A-10.	Blade Element Data from Fixed Instrumentation, Near Stall Flutter, 75% Speed, Reading 57.	239
A-11.	Blade Element Data from Fixed Instrumentation, Near Stall Flutter, 85% Speed, Reading 61.	240
A-12.	Blade Element Data from Fixed Instrumentation, Low Operating Line, 90% Speed, Reading 172.	241
A-13.	Blade Element Data from Fixed Instrumentation, Intermediate O.L., 90% Speed, Reading 176.	242
A-14.	Blade Element Data from Fixed Instrumentation, At Stall Flutter, 90% Speed, Reading 169.	243
A-15.	Blade Element Data from Fixed Instrumentation, Below Peak Efficiency, 95% Speed, Reading 110.	244
A-16.	Blade Element Data from Fixed Instrumentation, Below Peak Efficiency, 95% Speed, Reading 117.	245
A-17.	Blade Element Data from Fixed Instrumentation, Intermediate O.L., 95% Speed, Reading 151.	246
A-18.	Blade Element Data from Fixed Instrumentation, Near Stall Flutter, 95% Speed, Reading 63.	247
A-19.	Blade Element Data from Fixed Instrumentation, At Stall Flutter, 95% Speed, Reading 148.	248

LIST OF TABLES (Concluded)

<u>Table</u>		<u>Page</u>
B-1.	Section A	250
B-2.	Section B	250
B-3.	Section C	251
B-4.	Section D	251
B-5.	Section E	252
B-6.	Section F	252
B-7.	Section G	253
B-8.	Section H	253
B-9.	Section J	254
B-10.	Section K	254
B-11.	Section L	255
D-1.	Casing Kulite Ensemble Average for 200 Points.	262
D-2.	Cross Spectral Analysis of Casing Kulite and Reference Strain Gage for Phasing.	263
D-3.	P _T Yaw Probe Ensemble Average for 200 Points.	265
D-4.	Cross Spectral Analysis of P _T Yaw Probe and Reference Strain Gage for Phasing.	267
D-5.	X-Array Probe Ensemble Average for 200 Points.	268
D-5.	X-Array Probe Ensemble Average for 200 Points (Concluded).	269
D-6.	Once Per Revolution Sampling of X-Array Probe.	270
D-6.	Once Per Revolution Sampling of X-Array Probe (Concluded)	271
D-7.	Cross Spectral Analysis of X-Array Probe and Reference Strain Gage for Phasing.	272

NOMENCLATURE

<u>Symbol</u>	<u>Definition</u>
A_i	Maximum tangential tip displacement of i th blade
A_{mn}	Amplitude of m th harmonic wave
AC	Alternating current, unsteady component
<u>ALF</u>	Aft looking forward
<u>BK</u>	Blade-mounted Kulite
<u>BPR</u>	Bypass ratio
<u>BTW</u>	Backward traveling wave
CC	Concave face
<u>CK</u>	Casing-mounted Kulite
<u>CW</u>	Clockwise
<u>CX</u>	Convex face
c	Chord
DC	Direct current, steady component
DFT	Direct Fourier transform
da	Double amplitude
E_n	Average kinetic energy per cycle
FFT	Fast Fourier transform
FTW	Forward traveling wave
IFT	Inverse Fourier transform
IOL	Intermediate operating line
k_i	Blade index
k_{mn}	wave number
LE	Leading edge

<u>Symbol</u>	<u>Definition</u>
LP	Light probe
M	Modal mass
m	Wave harmonic number
N, N_f	Rotor speed
N_b	Number of blades
ND	Nodal diameter
NOL	Nominal operating line
n	Travelling wave number (number of nodal diameters)
<u>OGV</u>	Outlet guide vane
O/L	Overall level
P_s	Static pressure
P_t	Total pressure
p	Total unsteady pressure in rotating system
$\underline{p_{mn}}$	Complex amplitude of p_n
P_n	Unsteady pressure for nth nodal diameter wave
ΔP_n	Pressure difference across the airfoil from nth nodal diameter
QEP	Quiet Engine Program
R_h, R_t	Radius of hub, tip
rpm	Revolutions per minute
S	Span
SG, S/G	Strain gage
S/N	Serial number
TE	Trailing edge
TWBL	TWISTED BLADE computer program
t	Time

<u>Symbol</u>	<u>Definition</u>
t_m/c	Maximum thickness to chord ratio
V_Z, V_θ	Axial, tangential flow velocity
W_n	Aerodynamic work done per cycle
x, Z	Axial location
1F, 1T	First flexural, torsional vibratory mode
1/rev	Once per revolution
26/rev	26 per revolution, once per blade, blade passing frequency

Greek Nomenclature

β	Angle between rotating reference and inertial reference at $t = 0$
δ	Inlet total pressure divided by standard day pressure, 10.13 N/cm ² (14.7 psia)
δ_{aero}	Aerodynamic logarithmic decrement
δ_i	Normal deflection of i th blade tip
δ_n	Normal deflection of blade tip in the n th nodal diameter mode
$\dot{\delta}_n$	$d\delta_n/dt$, time derivative of δ_n
η	Efficiency
θ	Angular position in rotating system; Absolute flow angle; Angular position on rotor; Total temperature divided by standard day temperature, 288.1° K (518.6° R)
λ	Blade stagger angle
ρ	Air mass density
τ_i	Time shift
ϕ	Phase angle; Phase lag; Absolute phase angle
ϕ_i	Interblade phase angle
Ω	Rotor speed; Direction of rotation

SymbolDefinition

ω	Flutter frequency in rotating system
ω_{mn}	Flutter frequency in stationary system

Subscripts

<u>AC</u>	Unsteady component
<u>DC</u>	Steady component
o	Value of quantity at $t = 0$
i, j	Indices
<u>LE</u>	Leading edge
S	Static
T	Total
<u>SA</u>	Stacking axis
1	Leading edge
2	Trailing edge
14	Bypass OGV inlet plane
20	Core OGV inlet plane

1.0 INTRODUCTION

An important limiting factor in the development of gas turbine engines is blade instability or flutter of fan and compressor airfoils. Flutter invariably produces intolerable vibration levels that exceed the airfoil's allowable fatigue strength, severely affecting engine life. Whenever flutter is present within the operational range of an airfoil, extensive design modifications are necessary for production engines.

Avoiding blade flutter in gas turbines is always a primary goal for gas turbine designers. Unfortunately, flutter prediction has not kept pace with the overall advances and new requirements of turbomachinery design. This has been true because of the complexity of flutter phenomena, which can be characterized as a combination of aerodynamic and structural interactions within a feedback system. As a result, the detailed flow mechanism in stall flutter, to cite one example, remains ill-defined, a fact which has prevented the development of a valid analytical model. In fact, present technical achievements in the theoretical analysis of flutter problems are all the more remarkable in view of the complexity of the problem involved.

Blade flutter, as it occurs in rotors, is a predominantly non-integral per-rev blade response at one of the blade's natural frequencies, generally in first flexural or first torsional modes. Usually, the amplitude of a blade's vibratory response is fairly constant with fixed flow conditions when flutter occurs alone, not in combination with other forms of blade excitation. Due to the complexity of the unsteady aerodynamics, however, the exact details of how aerodynamic forces generated by the blade motion do work on the blade system over a given vibratory cycle have not been adequately determined.

Because there is no valid analytical method for predicting flutter boundaries, the industry has used various semi-empirical methods. These methods vary in detail but are often similar in concept: the flutter boundary is experimentally determined on each of several experimental rotors in terms of basic rotor parameters. This composite is then used to predict the flutter boundary for the new designs. Although this method has been relatively successful for parameters within the range of experience, it does not provide a basic understanding of the flutter mechanisms.

Semi-empirical techniques depend on the analytical models of the flutter mechanism to establish the "primary" parameters against which flutter experience is interpreted. Therefore, these techniques can be influenced by the same inherent limitations of the analytical model on which they are based. Obviously, an improved analytical representation would result in better semi-empirical techniques and should lead to direct analytical methods with potential for developing design criteria for preventing flutter.

The specific objectives of this program were to obtain detailed measurements of both the steady and unsteady flowfields surrounding the rotor, and to determine the mechanical state of the rotor while it was operating in both the

steady and flutter modes. This data could then be used to formulate empirical and semiempirical correlations for predicting the onset of stall flutter in high-speed axial flow rotors.

1.1 PROGRAM DESCRIPTION

This flutter research program was initiated to investigate stall flutter by providing detailed quantitative steady and unsteady aerodynamic and aeromechanical measurements of a typical fan rotor. Both subsonic/transonic torsional mode flutter and supersonic flexural mode flutter were investigated.

The rotor configuration chosen for this program is a 31.3 percent geometric scale model of the Quiet Engine Program (QEP) Fan C, Build 3 design (Reference 1). Figure 1 provides a comparison of the scale model rotating rig fan blade with the full scale Fan C blade. The model blade is an exact geometrical scale of the original fan, the major aerodynamic design features of which are shown in Table I. The scaled fan blade resulted in a 54.35 cm (21.4 inch) tip diameter with a design pressure ratio of 1.61 and a corrected airflow of 40.8 kg/sec (89.9 lb/sec). The test facility in which this rotor was tested is described in Section 3.0.

Both conventional and innovative instrumentation methods were used to measure the steady and unsteady flowfields and the mechanical state in and around the test rotor. The instrumentation details are described in Section 4.0.

The testing in this program was handled in a total of three tests using two separate Builds. This approach was taken in order to meet all the objectives outlined for the program and to acquire all the necessary data from the instrumentation.

Build 1 consisted of two tests:

1. The first was a mechanical checkout. The vehicle's soundness was determined by monitoring vibrations in the blade system throughout the speed and throttle ranges defined for the test program.
2. The second was an aerodynamic performance test which completely defined stall and flutter boundaries.

Build 2 was the special instrumentation test. The program's fundamental research activities were conducted during this phase of the program. All of the aerodynamic and mechanical unsteady data were obtained during the testing of Build 2. The original plan called for the investigation of fifteen data points during this phase - three data points (for three levels of flutter penetration) on each of five different speed lines. However, the plans were changed when flutter penetration caused the blade's vibratory stresses to increase rapidly until the blades were in jeopardy of failure. The data points where unsteady data were obtained are shown on the rotor performance map in Figure 2.

ORIGINAL PHOTOGRAPH
OF POOR QUALITY

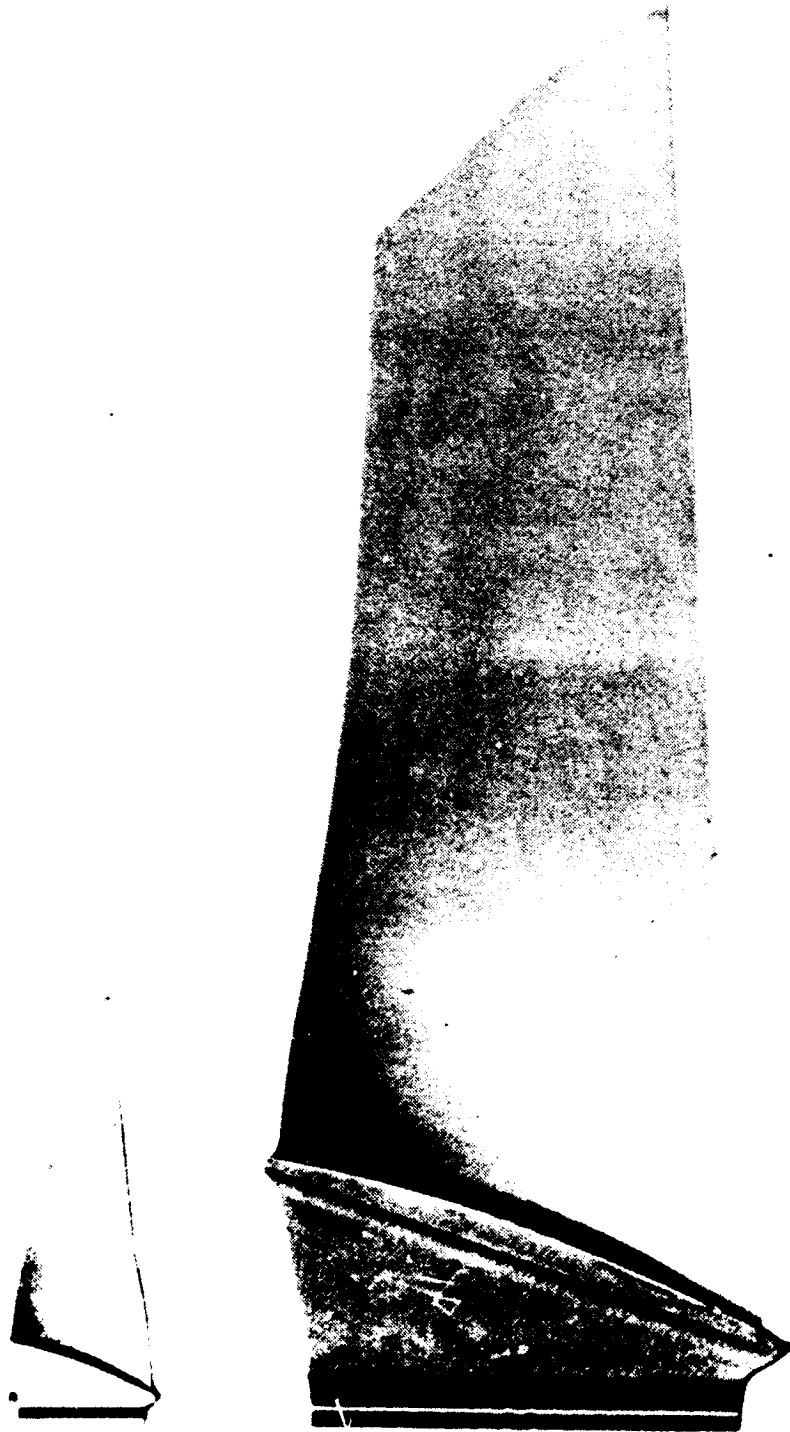


Figure 1. Comparison of Rotating Rig Fan Blade with Full Scale Fan C Blade.

Table I. Full Fan C Aerodynamic Design Features.

Corrected rotor tip speed	472.4 m/sec (1550 ft/sec)
Inlet hub-tip radius ratio	0.36
Rotor inlet tip diameter	1.73 m (68.30 in)
Corrected airflow	415 kg/sec (915 lbm/sec)
Inlet corrected flow/annulus area	201.6 kg/sec-m ² (41.3 lbm/sec-ft ²)
Bypass ratio	5.0
Bypass stream total-pressure ratio	1.60
Core stream total-pressure ratio	1.49
Rotor aspect ratio	2.09
Rotor solidity, tip	1.40
Rotor solidity, hub	2.45
Number of rotor blades	26
Rotor tip diffusion factor	0.325
Number of bypass stream OGV's	60
Number of core stream OGV's (tandem airfoil)	60
Design relative tip Mach number	1.52
Design speed, rpm	5200

OF FLOW

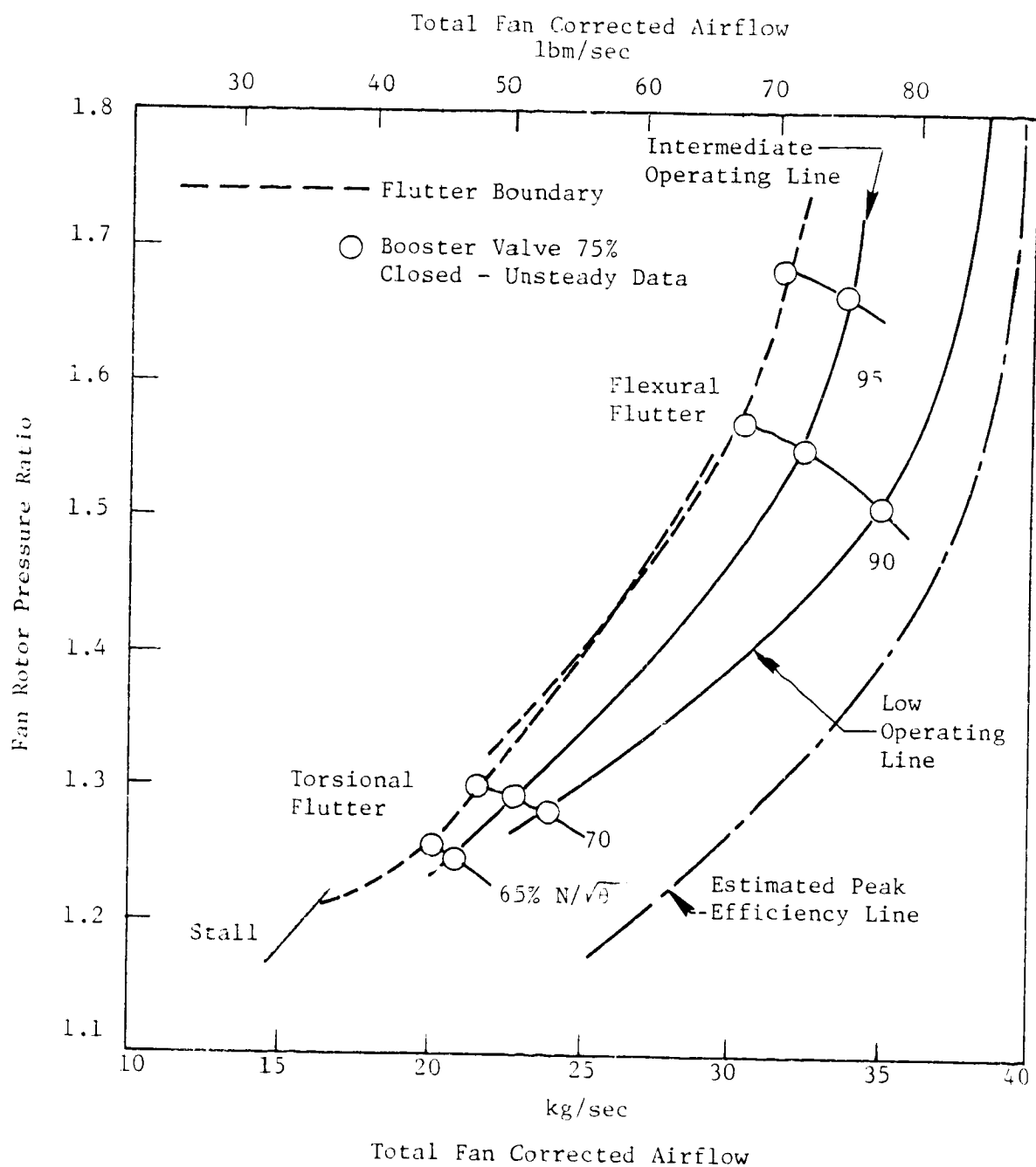


Figure 2. NASA Rotating Rig Performance Map, Build 2.

2.0 TEST VEHICLE DESCRIPTION

The rotor stage selected for this experimental research program was Fan C from the NASA Quiet Engine Program (QEP), Reference 1. The fan rotor tested on this program was a 31.3 percent scale of the full scale single stage fan. The design characteristics for the scale model fan are summarized in Table II.

The rotating rig test vehicle included a cantilevered, single-stage fan rotor system with a split discharge flowpath configuration, see Figure 3. Major control features included (1) a variable discharge vane row in the bypass duct to control the vehicle bypass ratio and, further downstream, (2) a facility discharge valve to throttle the fan above the design operating line to stall and flutter.

The overall test arrangement was comprised of the following features (see Figure 3):

- an inlet screen and a bellmouth cylindrical inlet,
- a fan module, flow splitter, fan bypass discharge valve, and fan discharge frame,
- a sump and drive shaft system, and
- a facility discharge mechanism.

The fan module was an exact scale of the Fan C system including the rotor blade-disk system, the core and bypass outer guide vanes (OGV's), the flow-path casings, and the rotating spinner.

The fan stationary components were mounted on the forward end of the fan discharge frame, a boilerplate structure which provided primary support for the test vehicle. The inlet bellmouth and flow measurement section were supported separately. They were mechanically decoupled as a unit from the basic vehicle by a silicone rubber O-ring. For easy access to the rotor, the fan rotor casing was a split casing consisting of two 180° segments jointed by axial flanges at the horizontal centerline.

The rotor contained 26 titanium blades with integrally machined platforms, a straight shank, and a single tang dovetail. The pressure faces of the dovetails were protected from fretting by an application of copper-nickel-indium coating. The blades were retained in position by an aft ring which locks the blades in the disk.

Table II. Rotating Rig Design Characteristics.

Corrected rotor tip speed	472.4 m/sec (1550 ft/sec)
Inlet hub-tip radius ratio inlet	0.36
Rotor inlet tip diameter	53.80 cm (21.18 in)
Corrected airflow	40.74 kg/sec (89.81 lbm/sec)
Inlet corrected flow/annulus area	201.6 kg/sec-m ² (41.3 lbm/sec-ft ²)
Bypass ratio	5.0
Bypass stream total-pressure ratio	1.60
Core stream total-pressure ratio	1.49
Rotor aspect ratio	2.09
Rotor solidity, tip	1.40
Rotor solidity, hub	2.45
Number of rotor blades	26
Rotor tip diffusion factor	0.325
Number of bypass stream OGV's	60
Number of core stream OGV's	60
Design relative tip Mach number	1.52
Design speed, rpm	16597

ORIGINAL
OF POKK 100-11

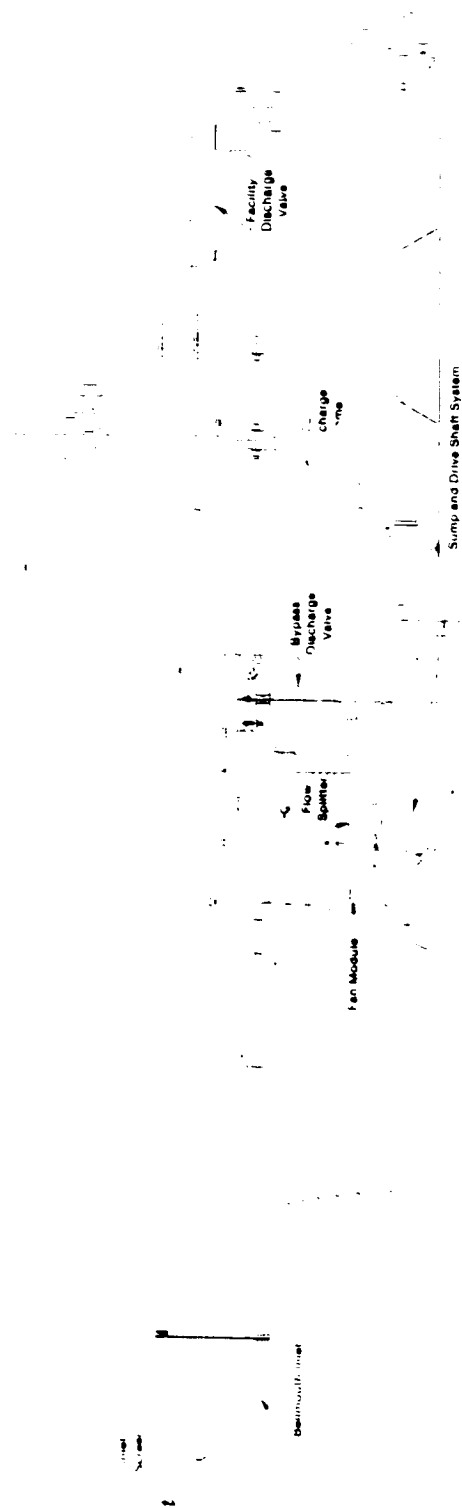


Figure 3. Rotating Rig Assembly.

2.1 AERODYNAMIC DESIGN

The scale model fan rotor tested in the rotating rig vehicle was an exact geometric scale of the NASA Quiet Engine Program Fan C Build 3 single-stage fan. The scaling factor was determined as a ratio of the tip diameters ($21.4/68.3 = 0.3133$). Fan C was designed as a high speed, lightly loaded, high bypass ratio fan with a low hub-to-tip radius ratio and large axial spacing between the rotor and bypass OGV's to reduce noise. In the Build 3 configuration, the part-span shrouds were removed and the blades were twisted closed, resulting in improved aerodynamic performance. However, significant stall flutter was encountered below the aerodynamic stall line. Full details of the Fan C test program are given in Reference 1.

The aerodynamic design point for the scale model test vehicle was chosen to match a measured operating point at 100 percent corrected speed taken during the full scale Fan C Build 3 component test. At this point, the measured flow conditions were nearly equivalent to the Fan C design objectives. The scaled total fan flow was 40.8 kg/sec (89.9 lbm/sec), and the bypass stream stage pressure ratio was 1.61 with a stage adiabatic efficiency of 83.9 percent (slightly less than the measured peak efficiency at speed). The core flow stage pressure ratio was 1.500. The vector diagrams obtained by an axisymmetric modeling of the full scale fan's measured flow properties were duplicated in the scale model rotating rig from the fan rotor inlet to downstream of the flow splitter in the vicinity of the outlet guide vanes. Design stream-surfaces were established through the rotor along which flow area distributions were determined for use in subsequent blade element data analyses.

Although the bypass and core OGV's were not exact scales of the Fan C geometry, they were designed to perform similarly so as to preserve the rotor aerodynamics while transitioning the flow smoothly into the test facility discharge valves. The Scale Model Compressor Test Facility, as discussed in Section 3.0, incorporated a single discharge valve rather than the separate discharge valves used by Fan C for both bypass and core streams. In order to set the bypass ratio, a ring of moveable vanes was installed behind the bypass OGV's to be used as a trimmer adjustment to the bypass flow rate. The main discharge valve was used to set the overall operating line; see Figure 3.

The major aerodynamic factor that cannot be scaled exactly except by testing the model at impractical inlet pressures is the Reynolds number. The effects of Reynolds number on efficiency and stall margin are known to be quite small if the absolute level of the scale model's Reynolds number is greater than 3×10^5 . Reynolds numbers for the scale model fan are 7×10^5 at 60 percent speed and 11×10^5 at 100 percent speed, high enough to assure aerodynamic performance similarity.

2.2 MECHANICAL DESIGN

The rotor for this program was a 31.3 percent scale of the NASA QEP Fan C Build 3. The aerodynamic design was maintained by incorporating an exact geometrical scale of the airfoil shape, including tolerances, surface finish, and

tip clearance. The mechanical design of the rotor blades consisted of the same material (Ti 6-6-2) and exact scales of platforms, shank and dovetail configurations, airfoil to shank offset, etc. The rotor disk was sized to provide the exact scale of overall rotor stiffness and was made of the same material, D6AC steel.

The aeroelastic parameters were also scaled from the original rotor. Their Campbell diagrams are identical since frequency and speed scale by the same factor. Therefore, resonant crossovers occur at identical percent speeds for both fan sizes. Likewise, reduced velocities are consistent as a function of speed, Mach number, and incidence angle. Blade untwist due to centrifugal loads and air loads are directly scalable effects. Table III summarizes the airfoil mechanical parameters.

Table III. Fan Blade Mechanical Summary.

No. of Stages	1
Blade Type	Cantilever
Material	Ti 6-6-2
N_b	26
Dia_{Tip}	53.14 cm (20.92 in)
L_{SA}	15.49 cm (6.099 in)
$(R_h/R_t)_{LE}$	0.36
Chord: Root	6.46 cm (2.544 in)
Tip	8.92 cm (3.510 in)
Aspect Ratio (Root)	2.40
t_m/c : Root	0.114
Tip	0.027
Stagger: Root	6.47 deg
Tip	71.11 deg
Camber: Root	91.098 deg
Tip	-1.664 deg
Solidity: Root	2.414
Tip	1.389

3.0 TEST FACILITY

3.1 GENERAL

The stall flutter test program was conducted at the General Electric Co. (Evendale, Ohio) in Cell A9 of the Component Test Facility, located in Building 303. The equipment room and test tanks are located on the first floor of the two-story structure, while the control room and data recording center are located on the second floor. The test facility consists of three tanks, each 3.05m (10 ft.) in diameter by 8.23m (27 ft.) long, which are mounted horizontally and interconnected as shown in Figure 4. The two outside tanks, East and West, are the test chambers, serving as the inlet plenum chamber and housing the test compressor unit, the facility throttle valve, and the test compressor after-coolers. This flutter investigation test program was conducted in the West tank. The center tank, called the booster tank, houses the booster compressor, booster compressor after-coolers, booster bypass valve, and flow measuring sections (four calibrated venturies).

The facility's power is supplied by a 3.356 M Watt (4500 HP) electric motor operated in parallel with a 61 cm (24 in.) diameter single stage "non-constant work" high-pressure turbine to provide up to 6.338 M Watt (8500 HP) at 20,000 rpm.

This test program was conducted in the open cycle (ambient condition) mode. In this mode, cooling air was provided to the West tank by diverting the high pressure turbine discharge air into the test chamber, as shown in Figure 5, to maintain a constant inlet temperature of 15.6° C (60° F).

An inlet filter system was incorporated to minimize erosion and contamination of the instrumentation systems.

3.2 DATA ACQUISITION

On this program, data was acquired with analog and digital data recording systems, and with on-line photographic equipment.

3.2.1 Aerodynamic Performance Data

The Digital Recording System, which is part of the overall system for acquiring performance data, was used to obtain steady-state performance measurements. On-line processing of performance data was provided by a data transmission link between the test cell digital system and the computer (GE 635) in the Instrumentation Data Room. Prior to performance calculations, all data was averaged, converted to engineering units, error-tested for pre-defined limit tolerances, and then printed and stored in a data bank system.

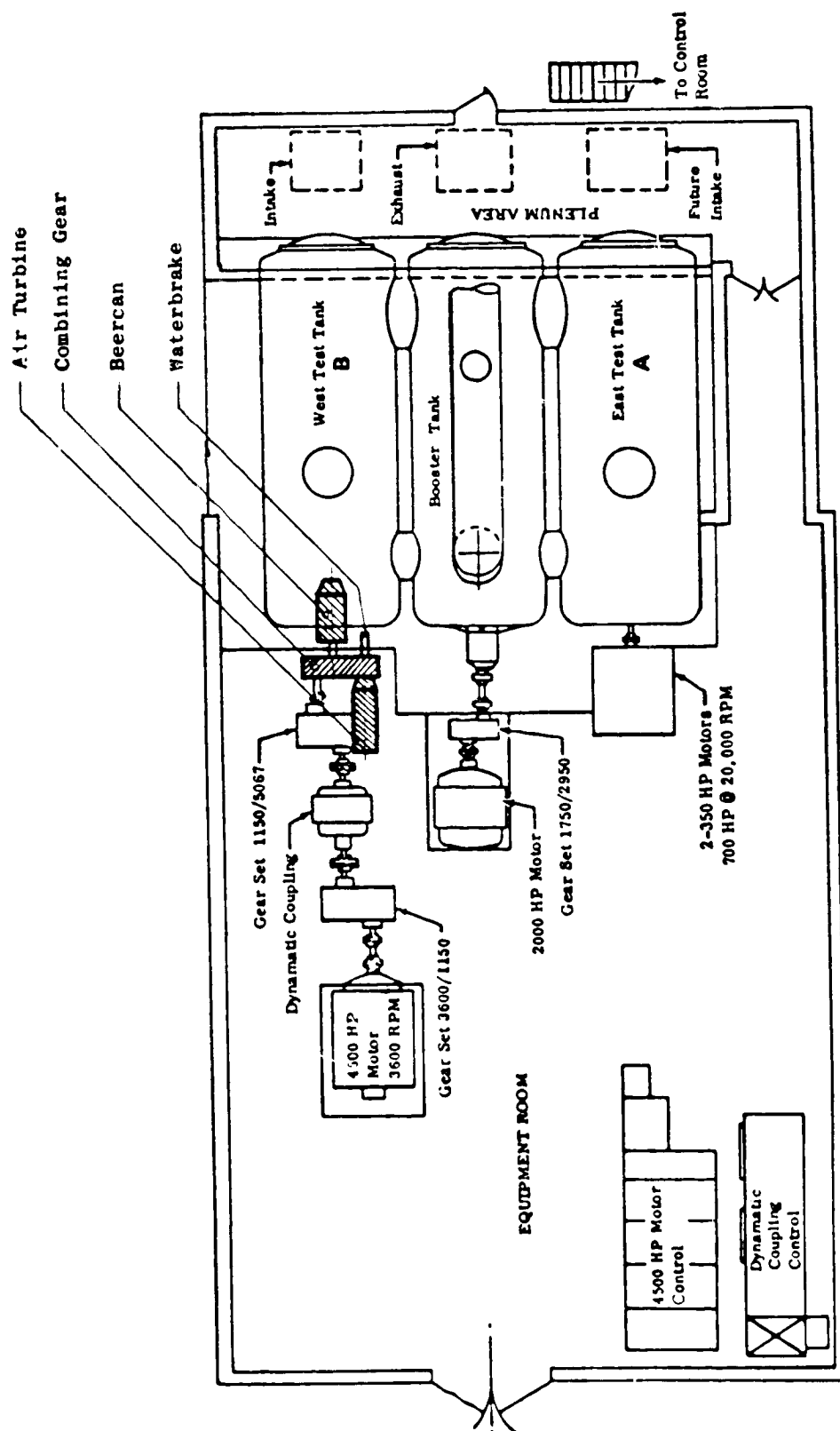


Figure 4. Scale Model Fan/Compressor Test Facility.

ORIGINAL FILED IN
OF POOR QUALITY

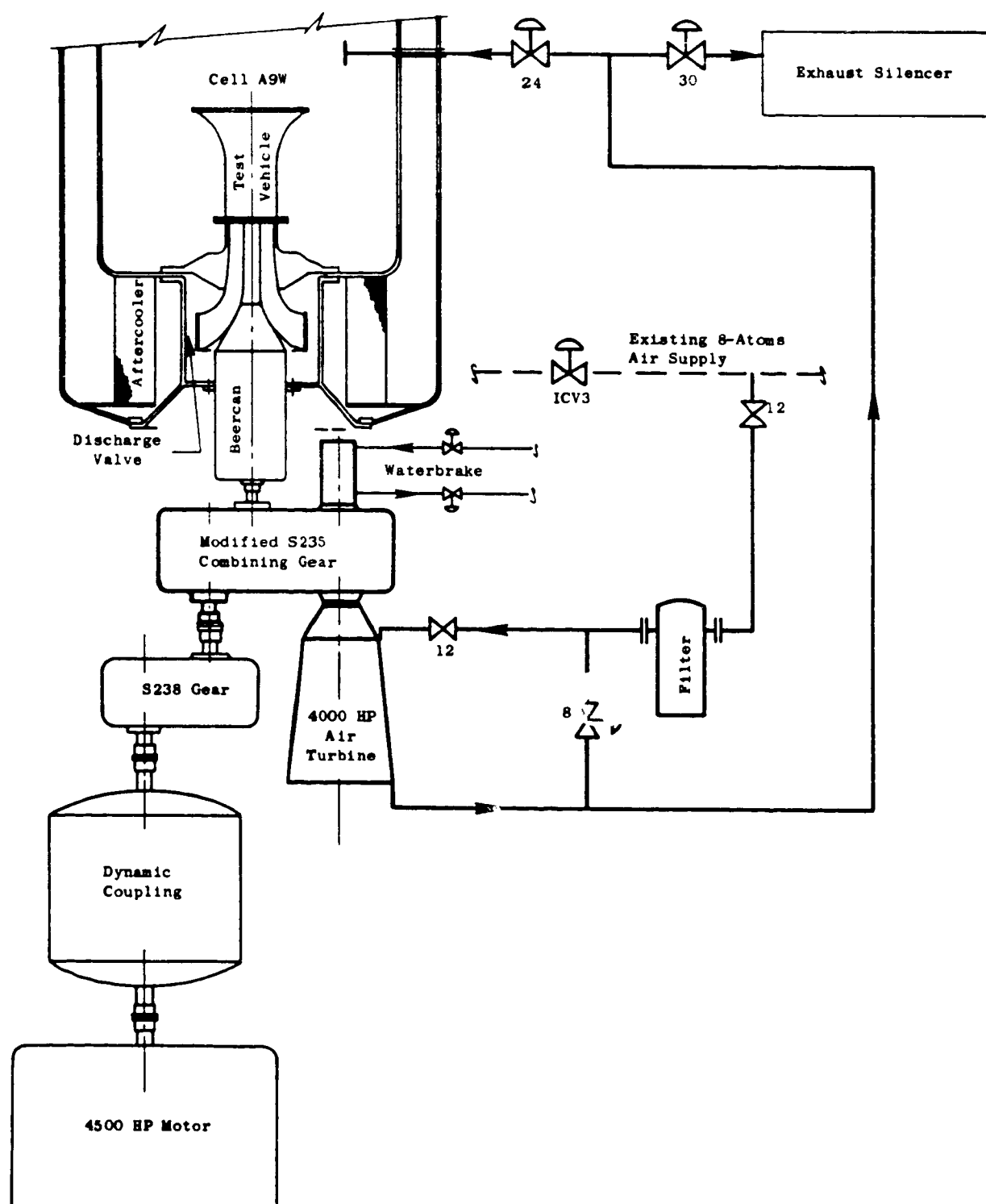


Figure 5. Air Turbine Schematic Flow Diagram.

A Burr-Brown Analog Computer system was primarily used to provide on-line computations and monitoring of weight flow and pressure ratio. These real-time parameters were especially valuable in setting desired test conditions.

Sanborn recorders were used to provide a permanent chart of transient data. In addition to aerodynamic parameters, the Sanborn system was also used to monitor system vibration accelerometers for vehicle safety.

Unsteady data from stationary instrumentation was recorded on analog magnetic tape operated at 152.4 cm (60 in) per second to obtain the high frequency content of the signals.

3.2.2 Aeromechanical Data

The data acquisition system for dynamic stress signals consists of a 28-channel tape recorder with a selector switch providing either AM or FM playback, plus signal conditioning pre-amplifiers, oscilloscopes, and spectrum analyzers.

To record all the instrumentation measurements, four complete systems were used on this program:

1. Data from rotating instrumentation, such as strain gages and blade-mounted hot films and kulites, was analog recorded at 76.2 cm (30 in) per second.
2. This data was also digitized via the FFT/computer system and stored on disk for post-test analysis. The FFT/computer system has two on-line modes of operation: the gapped data mode which provides continuous real-time processing and display of data, and the continuous data mode which allows the data to be digitized and written to computer disk. Some of the data was processed on-line in real time, but to minimize expensive test time, all of the data was digitized and stored on disk.
3. Blade deformation data was monitored on-line and recorded on analog magnetic tape.
4. The steady deformations were recorded primarily by photographs, and the unsteady deformations were digitized and stored on disk for post-test processing.

4.0 INSTRUMENTATION

4.1 GENERAL

Instrumentation was an important element of this stall flutter program. The steady and unsteady instrumentation described in this section was used to determine the steady and unsteady aerodynamic and aeromechanical characteristics of a rotor blade operating in both subsonic and supersonic stall flutter and in stable conditions.

Table IV summarizes the aerodynamic and aeromechanical instrumentation used. This summary defines the types and quantities of instrumentation used on each test and what parameters were measured. Basic positioning of this instrumentation within the test vehicle is shown in Figure 6.

4.2 STEADY-STATE AERODYNAMIC PERFORMANCE INSTRUMENTATION

The aerodynamic instrumentation measured the overall performance of the rotor and blades under steady-state clean inlet flow operating conditions. Measurements of total pressure, static pressure and total temperature were obtained from both fixed and traversable rakes located forward and aft of the rotor. The traversable rakes were also used to measure flow angle aft of the rotor.

Traverse data was taken only on Build 1, because a comparison of the fixed and traversable rake data showed them to be in good agreement. As a result, only fixed rake data was taken on subsequent builds without compromising the data accuracy.

A summary of the locations of the steady state instrumentation is provided in Table V, for the static pressure taps in Table VI, for the static inlet rake immersions in Table VII, and for the steady-state traverse probes and rake immersions in Table VIII. These locations are also shown in the instrumentation drawing of Figure 6.

4.3 UNSTEADY AERODYNAMIC INSTRUMENTATION

Aerodynamic unsteady or time-varying characteristics forward and aft of the rotor, on the airfoil surface, and on the casing over the blade tip were measured with blade-mounted sensors, casing-mounted sensors, and traversable dynamic probes.

High response dynamic pressure transducers (Kulites) and heated thin film anemometers were applied to the rotor blades to define regions of flow separation and to obtain the chordwise instantaneous dynamic pressure distribution (PT)AC around the airfoil. The heated thin film anemometers also provided additional qualitative chordwise unsteady flow characteristics - flow separation on the airfoil and velocity variations within a blade passage.

Table IV. Rotating Rig Instrumentation. *

Location	Type	Quantity	Measures	User for Tests 1 2 3
Inlet Screen	Thermocouples	28	Total Temperature	X X X
Inlet Duct	Pressure Taps	14	Static Pressure	X X X
	6-Element Pressure Radial Rakes	4	Total-Pressure/Static Pressure	X X X
Rotor Inlet	Kulites, Casing-Mounted	3	Dynamic Pressure	- - -
	Pressure Taps	9	Static Pressure	X X X
	2-Element Traversable Hot-Wire Probes	1	Axial & Tangential Mass Flow	- - -
	Wedge Traverse Probe	1	Static Pressure	- - -
	Laser Light Probe	2	Radial Untwist & Edge Bending	- - -
	10-Element Boundary Layer Rake	1	Total Pressure	X
Rotor Tip	Kulites, Casing-Mounted	8	Dynamic Pressures	X
	Light Probes	8	Steady-State Airfoil Orientation and Deflection	- - -
	Pressure Taps	8	Static Pressure	- - -
	Axial Deformation Light Probe	1	Blade Axial Deflection	- - -
Rotor Exit	Kulite, Casing-Mounted	1	Dynamic Pressure	- - -
Bypass Stream	Pressure Taps	18	Static Pressure	X X X
	**X P _y Yaw 3-Element Traverse Kulite Probe	1	Dynamic Pressure & Vector Directed	- - -
	COBRA Traverse Probe	1	Total-Pressure and Flow Angle	- X -
	2-Element Traversable Hot-Wire Probe	1	Axial and Tangential Mass Flow	- - -
	Wedge Probe	1	Static Pressure & Flow Angle	- - -
	Laser Light Probe	2	Radial Untwist & Edge Bending	- - -
Rotor Exit - Core Stream	Pressure Taps (Splitter Inner Flowpath)	6	Static Pressure	X X X
	Pressure Taps (Hub)	6	Static Pressure	X X X
	4-Element Radial Rakes	3	Total-Pressure/Total Temp.	X X X
OCV Blade Row	7-Element Radial Rakes	3	Total-Pressure/Total Temp.	X X X
	Pressure Taps (Outer)	3	Static Pressure	X X X
Bypass (OCV) Exit	Pressure Taps (Inner)	3	Static Pressure	X X X
Core (OCV) Exit	Pressure Taps (Splitter Inner Flowpath)	6	Static Pressure	X X X
	Pressure Taps (Hub)	6	Static Pressure	X X X
	4-Element Radial Rake	1	Total Pressure	X X X
Bladed-Mounted	Hot-Film	11	Flow Velocity	X - -
	Kulites	16	Dynamic Pressure	- - -
	Strain Gages:			
	Blades	26	Dynamic Strain	X X X
	Bypass (OCV)	4	Dynamic Strain	X X X
	Core (OCV)	3	Dynamic Strain	X X X
	Discharge Vane	4	Dynamic Strain	X X X

*See Figure 6 for locations.

**This probe was replaced by a blue ball dynamic pressure probe after Kulite failure.

18

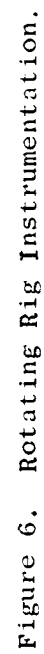


Figure 6. Rotating Rig Instrumentation.

Table V. Steady-State Aerodynamic Instrumentation Locations.

	Description	Z** Axial Location		Circumferential Location, ALF-CW*
		cm	(in)	
Fwd of Rotor	6 Element Radial Rakes	-57.15	(-22.5)	70°, 160°, 250°, 340°
	10 Element Boundary Layer Rake	-8.38	(-22.5)	230°
	Traverse Wedge Probe	-1.27	(-0.50)	330°
Aft of Rotor Bypass Duct	Traverse Wedge Probe	10.665	(4.199)	310°
	Traverse Cobra Probe	10.665	(4.199)	70°
OGV Plane Bypass Duct	7 Element Radial Rake	22.621	(8.906)	0°, 180°, 270°
Aft of OGV in Bypass Duct	Traverse Wake Rake (Opt.)	28.09	(11.06)	306°
Core Inlet	4 Element Radial Rake	12.576	(4.951)	0°, 160°, 250°
Core Exit	4 Element Radial Rake	32.26	(12.70)	45°

*ALF-CW = Aft Looking Forward, Clockwise

**Z is axial station relative to rotor blade leading edge root.

Table VI. Static Pressure Tap Locations.

	Z Axial Location cm (in)		Circumferential Location, ALF-CW
Inlet Duct	-61.0	(-24.0)	55°
	-57.2	(-22.5)	55°, 115°, 175°, 235°, 295°, 355°
	-38.1	(-15.0)	30°
	-25.4	(-10.0)	30°
	-8.4	(-3.3)	55°
	-11.95	(-4.704)	0°
	-7.48	(-2.945)	0°
	-4.85	(-1.911)	0°
	-2.23	(-0.877)	0°
Fan Inlet	-1.27	(-0.50)	0°, 72°, 144°, 216°, 288°
	0.00	(0.00)	0°
	0.64	(0.25)	0°
	1.47	(0.58)	0°
Above Rotor	1.83	(0.72)	0°
	2.21	(0.87)	0°
	2.59	(1.02)	0°
	2.97	(1.17)	0°
	3.35	(1.32)	0°
	3.73	(1.47)	0°
	4.11	(1.62)	0°
Fan Exit Bypass Duct O.D.	4.88	(1.92)	0°
	10.67	(4.199)	15°, 105°, 195°, 285°
	22.62	(8.906)	40°, 100°, 160°, 220°, 280°, 340°
Bypass OGV Exit O.D.	26.42	(10.40)	99°, 219°, 339°
Fan Exit Bypass Duct I.D.	10.67	(4.199)	105°, 300°
	22.62	(8.906)	40°, 100°, 160°, 220°, 280°, 340°
Bypass OGV Exit I.D.	26.67	(10.50)	99°, 219°, 339°
Fan Exit Core Duct O.D.	12.58	(4.951)	30°, 90°, 150°, 210°, 270°, 330°
Core OGV Exit O.D.	18.03	(7.10)	105°, 225°, 345°
Core Exit O.D.	32.26	(12.70)	105°, 225°, 345°
Fan Exit Core Duct I.D.	12.58	(4.951)	30°, 90°, 150°, 210°, 270°, 330°
Core OGV Exit I.D.	18.03	(7.10)	105°, 225°, 345°
Core Exit I.D.	32.26	(12.70)	105°, 225°, 345°

Table VII. Pitot Static Inlet Rake Immersions.

Immersion	Radius		Percent* Immersion	Z Axial Location	
	cm	(in)		cm	(in)
A	25.631	(10.091)	4.27	-57.150	(-22.500)
B	23.193	(9.131)	13.38	-56.672	(-22.312)
C	20.447	(8.050)	23.63	-56.195	(-22.124)
D	17.275	(6.801)	35.48	-55.717	(-21.936)
E	13.388	(5.271)	50.00	-55.240	(-21.748)
F	7.724	(3.041)	71.15	-54.762	(-21.560)

*From the outer casing

Table VIII. Steady-State Traverse Probe and Rake Locations.

Rotor Exit Plane $\phi Z = 6.764 \text{ cm (2.663 in)}$ Z Immersion ^a	Rotor Inlet (1) Traverse Plane $\phi Z = -1.270 \text{ cm (-0.500 in)}$ Z Immersion ^a		Rotor Exit Bypass (2) Traverse Plane $\phi Z = 10.665 \text{ cm (4.199 in)}$ Z Immersion ^a		Bypass Rotor Exit Fixed Rake $\phi Z = 22.621 \text{ cm (8.906 in)}$ Z Immersion ^a	
	cm	Radius (in)	cm	Radius (in)	cm	Radius (in)
5	4.2	26.518 (10.440)	7.5	25.293 (9.958)	7.0	25.352 (9.981)
10	8.4	25.827 (10.168)	14.5	24.698 (9.688)	13.6	24.714 (9.730)
15	14.0	24.737 (9.739)	24.0	23.678 (9.322)	20.2	24.079 (9.480)
30	28.5	22.103 (8.707)	42.2	21.900 (8.622)	40.1	22.162 (8.725)
50	48.0	18.560 (7.307)	68.5	19.329 (7.610)	66.1	19.657 (7.739)
60	58.2	16.708 (6.578)	82.0	18.011 (7.091)	79.7	18.349 (7.224)
70	67.5	15.016 (5.912)	94.0	16.838 (6.629)	93.0	17.066 (6.719)
Core Stream						
80 85 90 95	Rotor Exit Fixed Rake $\phi Z = 12.576 \text{ cm (4.951 in)}$ Z Immersion ^a		Core Duct Exit Fixed Rake $\phi Z = 32.258 \text{ cm (12.700 in)}$ Z Immersion ^a		Core Duct Exit Fixed Rake $\phi Z = 32.258 \text{ cm (12.700 in)}$ Z Immersion ^a	
	cm	Radius (in)	cm	Radius (in)	cm	Radius (in)
	78.0	13.109 (5.161)	19.5	14.854 (5.848)	Ref. 0	17.783 (7.001)
	82.8	12.238 (4.818)	39.2	14.178 (5.582)		17.374 (6.840)
	88.0	11.293 (4.446)	58.8	13.505 (5.317)		16.787 (6.609)
	93.5	10.295 (4.053)	79.2	12.807 (5.042)		16.180 (6.370)
						15.550 (6.122)
					Ref. 100	15.077 (5.936)
						115.225 (5.994) Eff

^a From the outer casing based on full rotor exit annulus height^{aa} From the inner diameter of the flow splitter^{aaa} The immersions are based on centers of equal "Effective" area (10% blockage assumption) and measured from the inner diameter of the flow splitter.

(1) Applies for the wedge probe at the rotor inlet

(2) Applies for the wedge and cobra probes at the rotor exit

The blade-mounted Kulites were positioned to survey two radial stations, 87.5 and 75 percent span, with four Kulites on each of four blades. The instrumented blades were paired so as to measure data on the adjacent suction (convex) and pressure (concave) airfoil surfaces facing one common flowstream. Figure 7 shows chordwise locations of the blade-mounted Kulites along with the circumferential positions of the four Kulite instrumented blades.

Problems were encountered with these Kulites due to the technique used to mount them on the blade. Consequently, a development program was conducted to alter the blade mounting technique for the Kulites to improve their response by reducing their induced strain sensitivity and to maintain more adequate sensor life in a centrifugal field. This new mounting technique is discussed in Section 4.3.1.

Blade-mounted heated thin film sensors were applied at one radial position, 87.5 percent span, on two blades facing the same flowstream. Figure 8 shows how the sensors were distributed. One sensor on each blade had a common chordwise location (at the leading edge) and the remaining sensors were alternately spaced as a function of percent chord from the leading edge. Figure 8 also depicts the circumferential location of the hot film blades.

Twelve casing-mounted high frequency dynamic pressure transducers (Kulites) located above the rotor blade tip were installed on two axial lines staggered as specified in Table IX and depicted in Figure 9 relative to the cold blade tip position. These Kulites were used to investigate the shock structures and their effects on the local boundary layer. Of the twelve casing-mounted Kulites used, three were located at the fan inlet, eight over the blade tip, and one directly aft of the fan rotor.

A static pressure tap was installed at the same axial station as each Kulite to provide a reference level of the DC component of static pressure for each Kulite.

A 3-element traversable Kulite probe (P_T yaw) was used to measure the magnitude of instantaneous total unsteady pressure behind the rotating stage. In addition, steady (DC) transducers provided parallel measurements some distance along the total pressure tube from the element inlet. The DC outer elements were used to set the orientation angle of the probe for each radial immersion, which is held at a constant DC value. The location of this probe is shown in Figure 6 and in Table X along with the seven radial immersions. A Blue Ball (P_T) dynamic pressure probe was used as a replacement for the P_T yaw probe when the Kulite elements failed. The Blue Ball probe has no yaw capability but is relatively insensitive to flow angle variations. This probe was installed at the same location as the P_T yaw probe.

Two x-array, traversable, heated thin-film anemometer probes were used to obtain two-dimensional fluid flow information. These probes measured the mass flux in the axial (ρV_z) and in the circumferential (tangential) direction (ρV_θ) at the seven radial immersions given in Table X. One x-array probe was located forward and one aft of the rotor as shown in Figure 6 and Table X. The

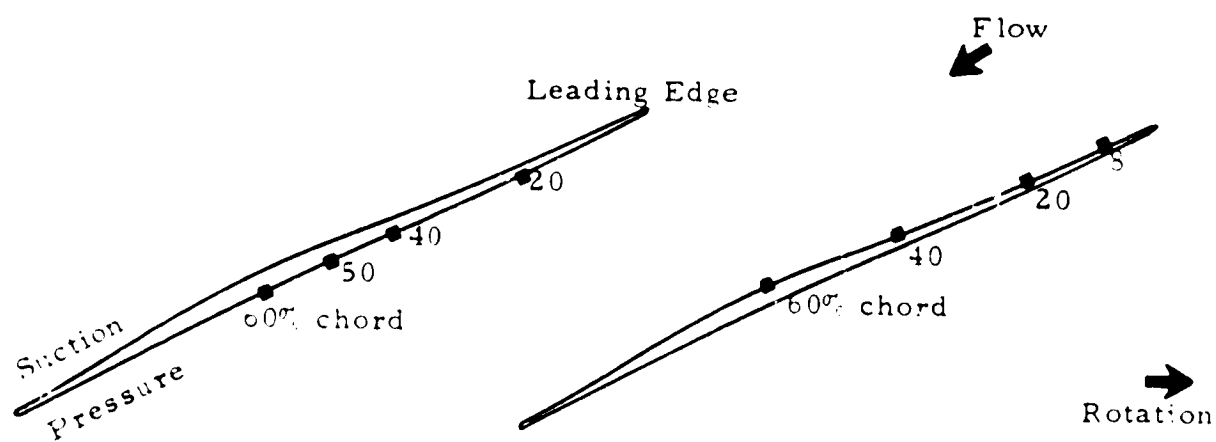
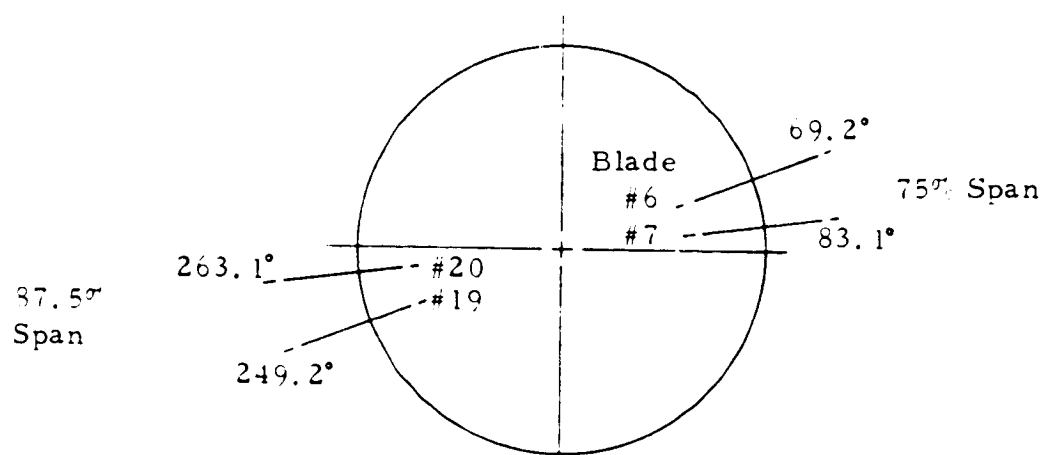
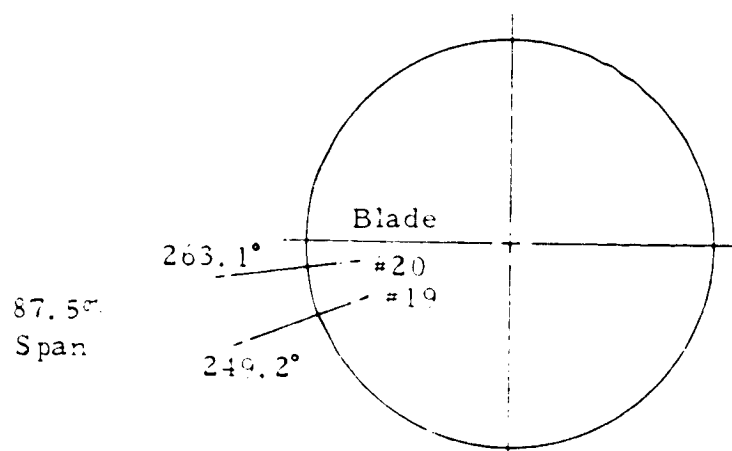


Figure 1. Blade-Mounted Kulite Sensor Locations.



Aft Looking Forward

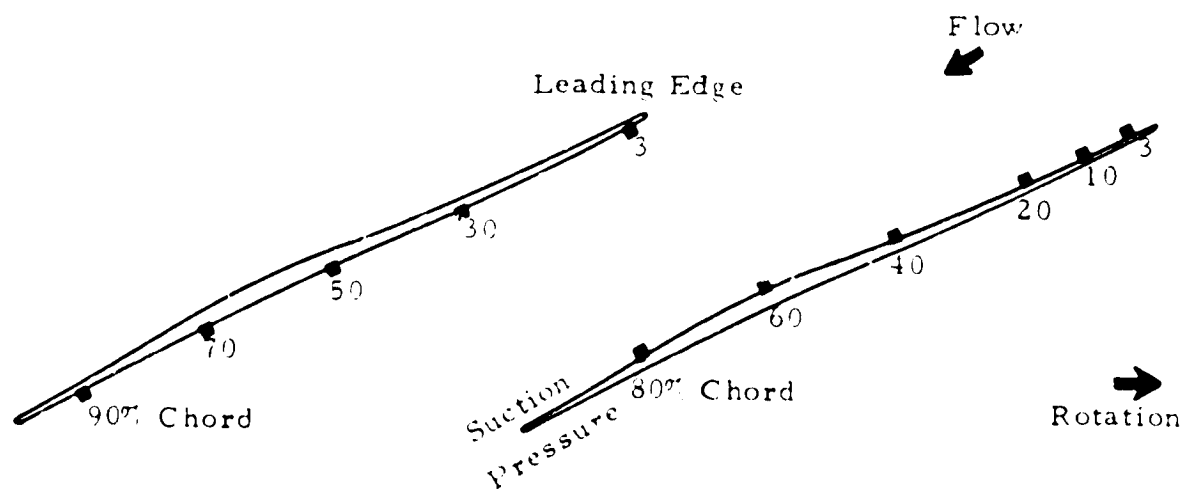
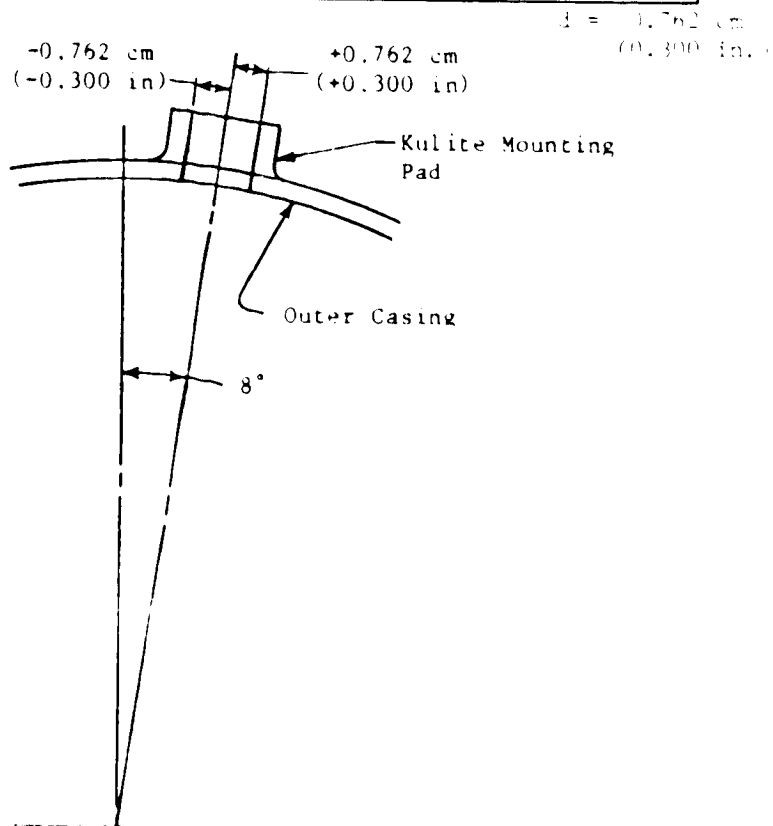


Figure 8. Blade-Mounted Hot Film Sensor Locations.

OF P...

Table IX. Casing-Mounted Kulite Locations.

	Z Axial, Location		Circumferential Location, ALF - CW
	cm	(in)	
Fan Inlet	0.00	(0.0)	$8^\circ + d$
	0.64	(0.25)	$8^\circ - d$
	1.47	(0.58)	$8^\circ + d$
Above Rotor	1.83	(0.72)	$8^\circ + d$
	2.21	(0.87)	$8^\circ - d$
	2.59	(1.02)	$8^\circ + d$
	2.97	(1.17)	$8^\circ - d$
	3.35	(1.32)	$8^\circ + d$
	3.73	(1.47)	$8^\circ - d$
	4.11	(1.62)	$8^\circ + d$
Fan Exit Bypass Duct	4.50	(1.77)	$8^\circ - d$
	4.88	(1.92)	$8^\circ + d$



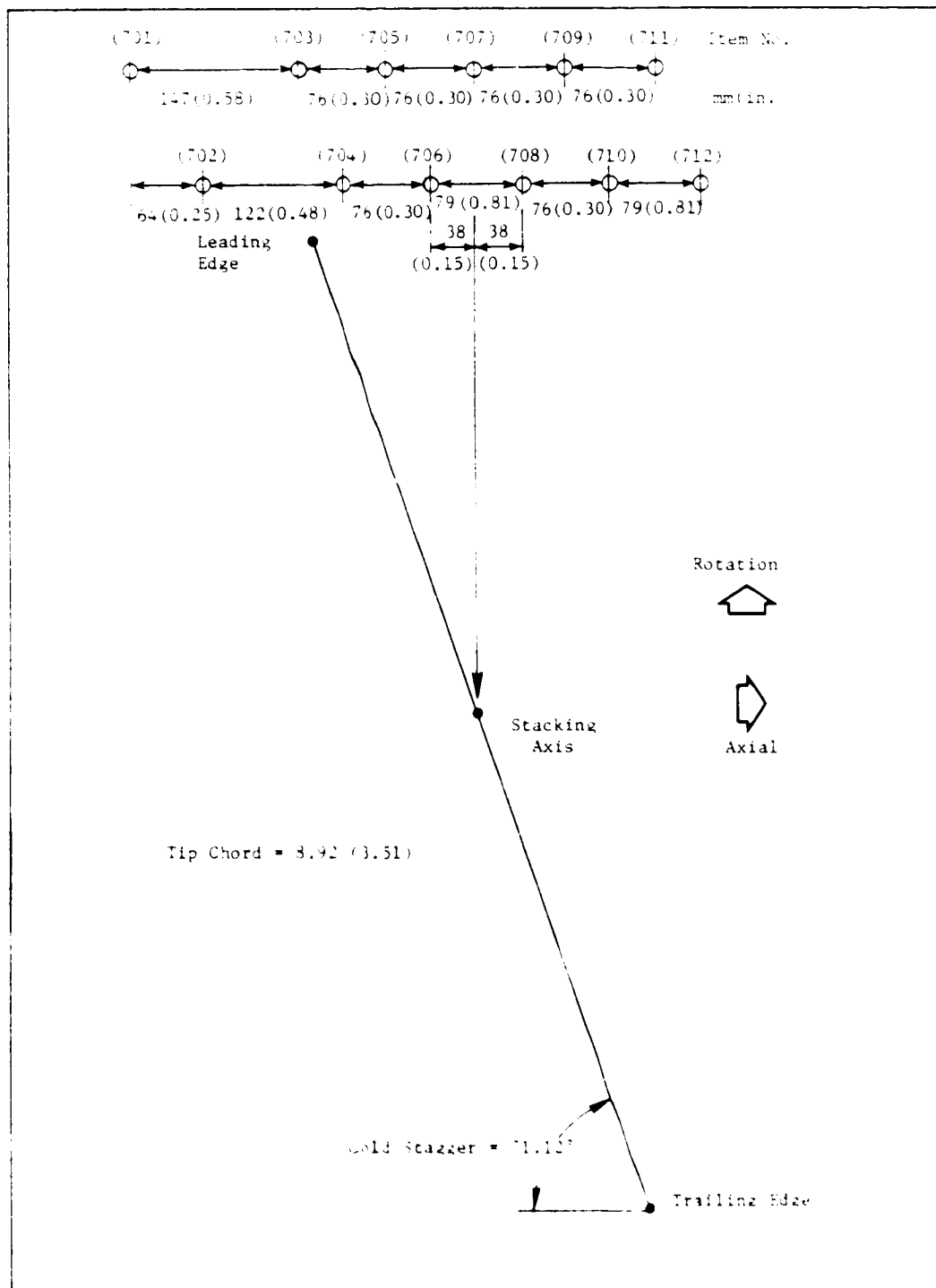


Figure 9. Casing-Mounted Kulite Geometry.

Table X. Dynamic Traverse Probes.

Location		Description	Z		Circumferential Location ALF - CW
Locations			Axial cm	Location (in)	
Fwd of Rotor:		2-Element Heated Thin Film Probe	-1.27	(-0.50)	110°
Aft of Rotor:		3-Element Heated Thin Film Probe	10.665	(4.199)	340°
		3-Element Dynamic Pressure Probe	10.665	(4.199)	40°
Immersion					
Rotor Exit Plane (@ Z = 6.764 cm (2.663 in) % Immersion*		Rotor Inlet (1) Traverse Plane (@ Z = -1.270 cm (-0.500 in)		Rotor Exit (2) Traverse Plane (@ Z = 10.665 cm (4.199 in)	
		% Immersion	Radius		% Immersion
			cm	(in)	
5		4.2	26.518	(10.440)	7.5
10		8.4	25.827	(10.168)	14.5
15		14.0	24.737	(9.739)	24.0
30		28.5	22.103	(8.702)	42.2
50		48.0	18.560	(7.307)	68.5
60		58.2	16.708	(6.578)	82.0
70		67.5	15.016	(5.912)	94.0
					25.293 (9.958)
					24.608 (9.688)
					23.678 (9.322)
					21.900 (8.622)
					19.329 (7.610)
					18.011 (7.091)
					16.838 (6.629)

(1) Applies for the 2-element heated thin film probe at the rotor inlet

(2) Applies for the 3-element Kulite probe and the 2-element heated thin film probe at the rotor exit

*From the outer casing based on full rotor exit annular height

probe's output is an instantaneous analog voltage level as measured by the two orthogonal wires of the probe. From these measurements, steady time-averaged values of mass flux were obtained and unsteady values determined from the perturbation about the steady values.

4.3.1 Blade-Mounted Kulite Sensor Calibration

During initial testing with the rotating rig, the Kulites were simply epoxied into countersunk holes in the blades. Unfortunately, this application technique made the Kulites extremely sensitive to mechanical strain induced by blade vibration.

In response to this problem, an improved technique for installing Kulite sensors was developed. The Kulite transducer is attached with epoxy to a glass tube which is isolated from the blade with RTV as shown in Figure 10. About 10 percent of the glass tube is epoxied to the blade, which maintains reasonable operating reliability in a centrifugal field while minimizing the influence of the blade strain. Table XI lists the bench test calibration results with this new application along with those of the original application method. Strain sensitivity in the first flexural mode was reduced to within the measurement accuracy obtainable in the laboratory. But for the first torsional mode, the strain sensitivity remains significant - even after consideration of transverse g-loading effects which are much greater in torsion than in flexure due to the higher vibratory frequency. Moreover, the sensors were oriented in the airfoil to minimize strain sensitivity in the flexural modes. This may be the major factor contributing to the high torsional strain sensitivity.

In summary, the new installation technique for the blade-mounted Kulite sensors successfully reduced their sensitivity to mechanical strain induced by the blade's flexural vibration. It worked somewhat less successfully in the first torsional mode.

4.4 AEROMECHANICAL INSTRUMENTATION

4.4.1 Blade Deformation Instrumentation

The primary objective of the blade deformation measurements made during this program was to determine the time-averaged (steady) and unsteady changes in stagger (untwist) and camber (chordwise bending) of the test stage while it operated at the onset of instability and while it was in instability. These measurements were made with bifurcated fiber optic scanners (light probes) mounted in the casing. A total of 14 sensors of three different types were utilized to obtain complete airfoil deformations. The locations of these light probes are shown in Figure 6 and schematically depicted in Figure 11.

Eight of the light probes were located on the casing over the blade tip section and aligned with the calculated 100 percent speed blade tip stagger

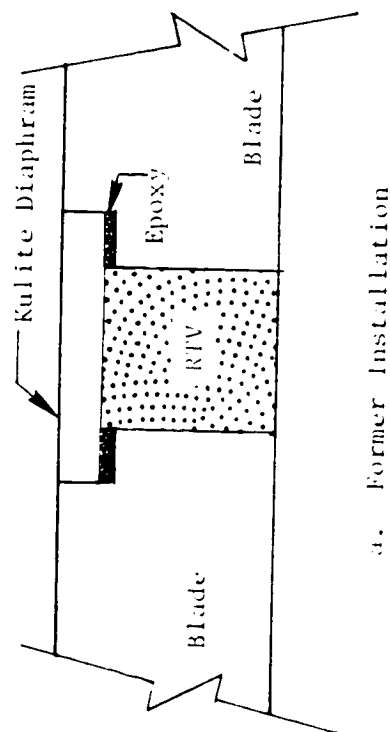
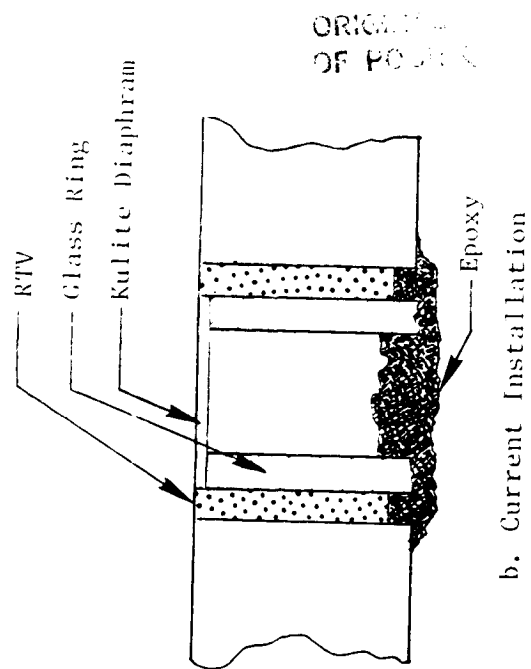


Figure 10. Blade-Mounted Pressure Sensor Installation.

Table XI. Results of Blade-Mounted Kulite Laboratory Calibrations.

Blade No.	Spanwise Location (Surface)	Mode	Freq. (Hz)	Kulite						
				CC	-	A	B	C	D	
				CX	A	B	C	-	D	
				% c	8%	20%	40%	50%	60%	
a. Former Installation Technique										
2	75% S (CX)	1F	120		0.052	0.052	0.110	-	0.178	Ion Plated Leads
		2F	394		0.545	0.391	0.616	-	1.00	
		1T	878		0.256	0.216	0.216	-	0.360	
3	75% S (CC)	1F	124		-	0.188	0.009	0.014	0.058	
		2F	402		-	0.571	0.072	0.008	0.284	
		1T	890		-	0.506	0.101	0.245	0.182	
1	87.5% S (CX)	1F	122		0.061	-	0.024	-	0.220	
		2F	400		0.784	-	0.158	-	0.761	
		1T	910		0.354	-	0.179	-	0.514	
4	87.5% S (CC)	1F	120		-	0.038	0.007	0.056	0.013	
		2F	384		-	0.008	0.055	0.077	0.133	
		1T	874		-	0.050	0.204	0.071	0.146	
b. Current Installation Technique										
2	75% S (CX)	1F	120		<0.02	<0.02	<0.02	-	<0.02	Standard Leads
		1T	880		0.226	0.062	0.064	-	0.072	
3	75% S (CC)	1F	122		-	<0.02	<0.02	<0.02	<0.02	
		1T	888		-	0.113	0.02	0.032	0.084	
1	87.5% S (CX)	1F	118		<0.02	<0.02	<0.02	-	<0.02	
		1T	900		0.191	0.164	0.062	-	0.062	
4	87.5% S (CC)	1F	116		-	<0.02	<0.02	0.023	<0.02	
		1T	874		-	0.065	0.050	0.024	0.050	
Note: Kulite response normalized to 6.894 N/cm ² (10.0 psi)										

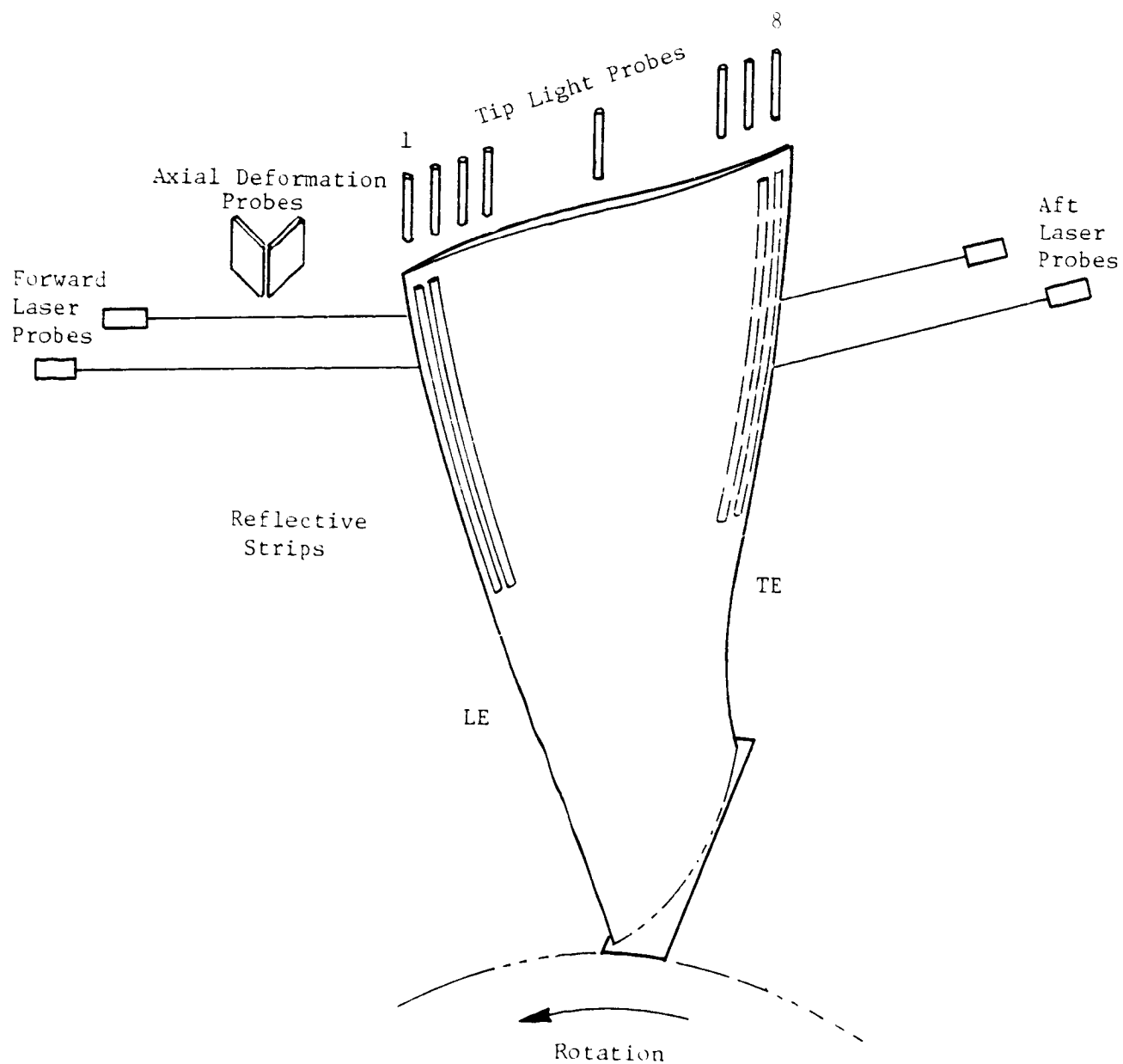


Figure 11. Schematic Representation of Light Probe Locations.

angle. This allowed for the measurement of blade tangential displacement from which the blade tip untwist and chordwise bending could be calculated. Two axial deformation light probes were incorporated in the casing over the blade tip leading edge to measure the time averaged axial location of the rotor blade tip leading edge. Two laser light probes were located on the casing forward of the rotor to measure the leading edge deformations at 60 and 87.5 percent span locations with two 16 mm (0.0625 in) reflective targets strips located on the blade convex (suction) side. Two laser light probes were also located on the casing aft of the rotor to measure the trailing edge deformations at 60 and 87.5 percent span locations with two similar reflective targets strips located on the concave (pressure) side of the blades. The laser light probe systems were incorporated to measure blade untwist at the selected spanwise locations. Posttest measurements showed the lasers to intersect the blades at 57.2 and 78.9 percent span.

4.4.2 Dynamic Strain Gages

The rotor was instrumented with 26 dynamic strain gages, one on each blade at the same location - near the leading edge at about 15 percent span from the blade root on the pressure (concave) side, as shown in Figure 12. For reference, Figure 13 shows the circumferential location of each blade identified by their serial number, strain gage item number, and rotor slot location.

The gages were located to be sensitive to the first three modes of vibration most representative of flutter. These gages were used for safety monitoring as well as for measuring such blade dynamic characteristics as frequency, vibratory stress amplitude, rotor modal content, and phase angle at selected operating conditions. Blade-to-blade phasing was obtained while operating at the onset of and within instability for selected data points. Strain gage signals were continuously monitored and recorded throughout each test.

The strain gages were used as the fundamental basis of identifying flutter, making general diagnoses, establishing a reference for comparison of other mechanical and aerodynamic data, and for immediate interpretations allowing control of test conduct and test safety.

4.5 ROTOR POSITION INSTRUMENTATION

An accurate rotor position signal is required for timing and data correlation purposes for the analysis of the data obtained from the aforementioned special instrumentation. The timing signal (1/rev) was obtained from one of the four magnetic pickups located at the rotor hub seal as shown in Figure 6. Figure 14 shows their circumferential locations. The 1/rev signal was then transmitted to an electronic shaft angle encoder which can generate any user-selectable number of pulses (between 1 and 99,999) in the time interval between successive 1/rev pulses. Here the shaft encoder was used to generate the 26/rev, or 1/blade, signals.

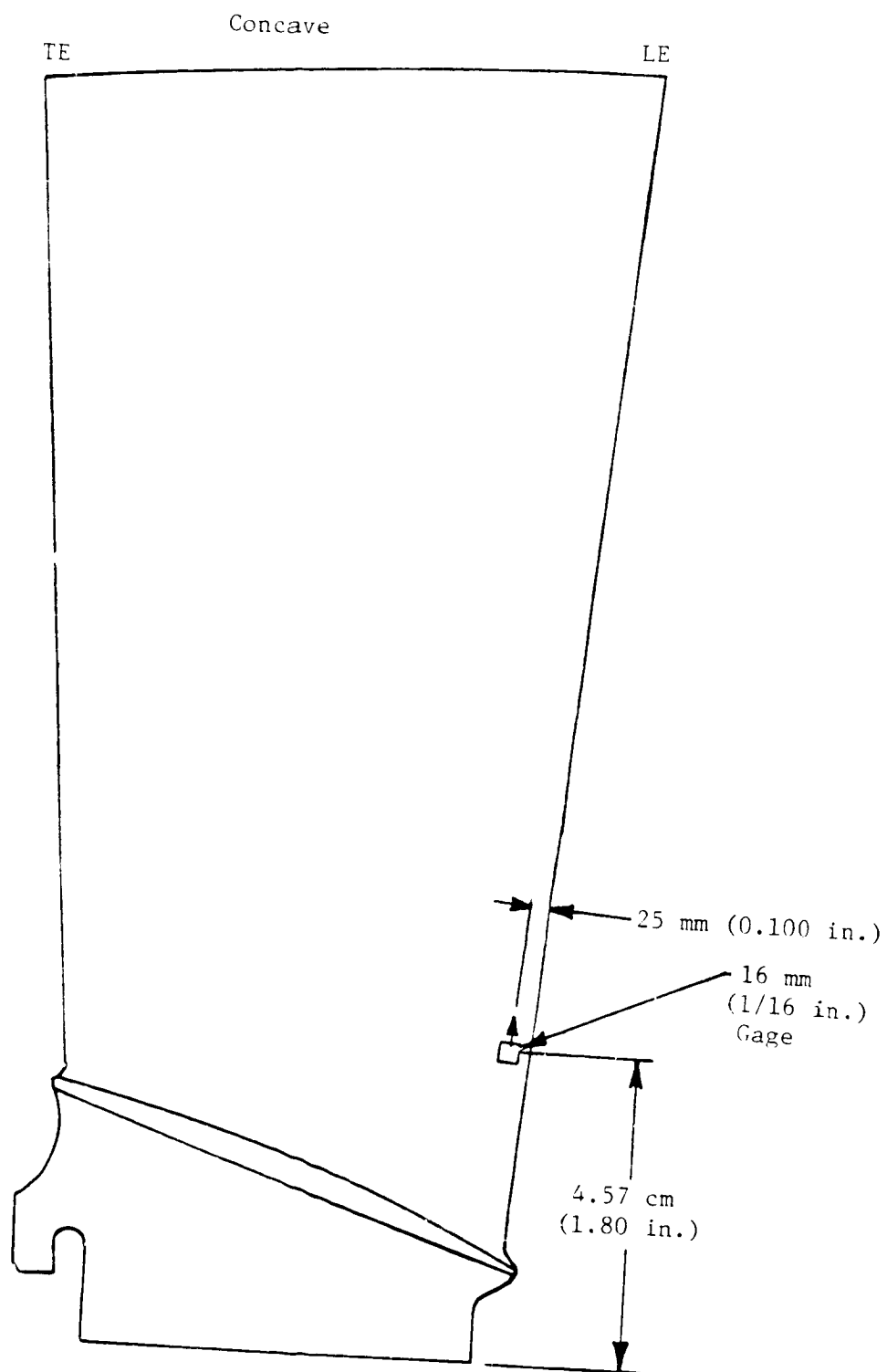
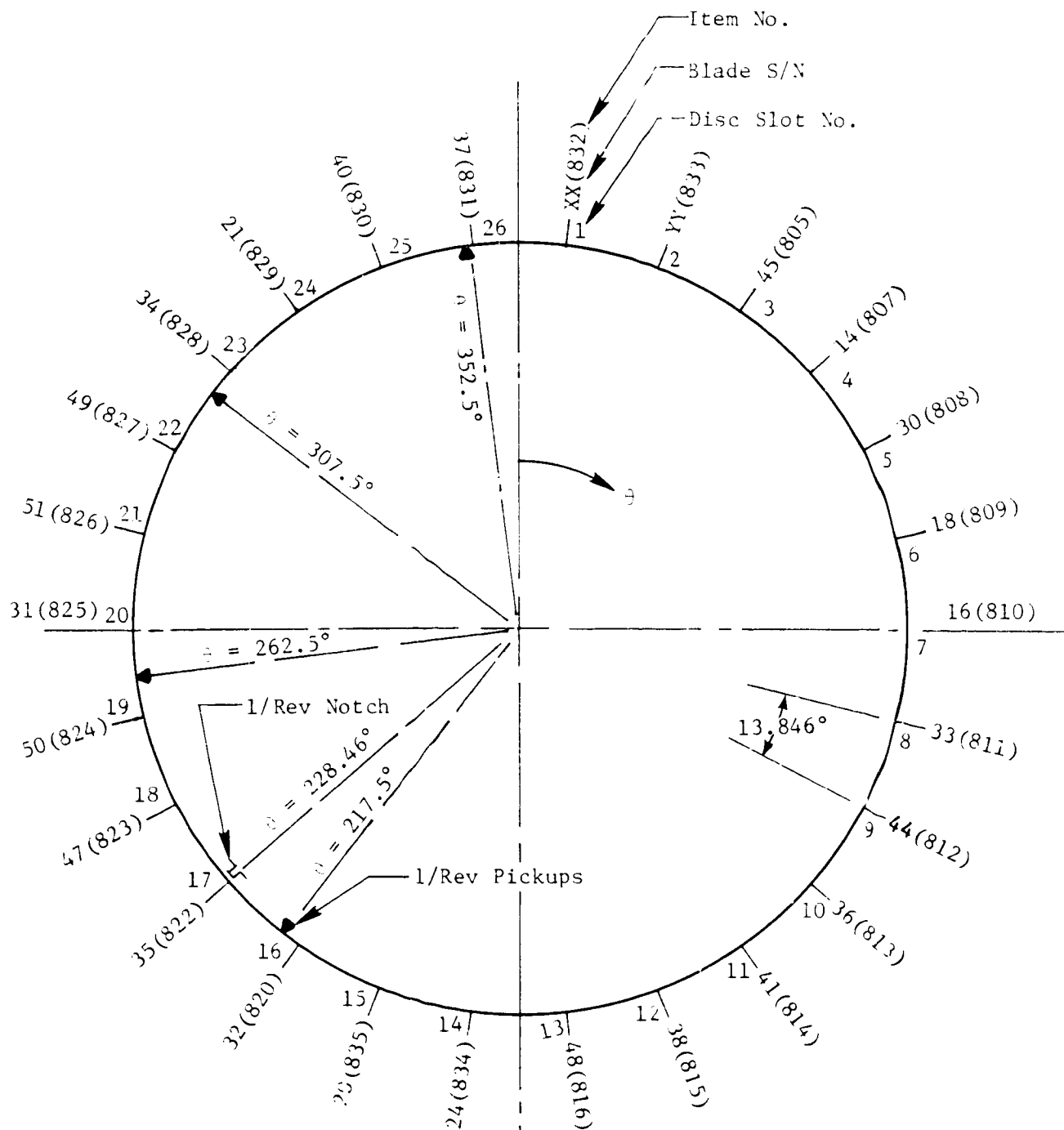


Figure 12. Rotor Blade Strain Gage Location.



Aft Looking Forward, Clockwise

Rotating Rig

Build 2

Figure 13. Rotating Rig, Build 2, Configuration.

ON THE EFFECTS OF POOR QUALITY

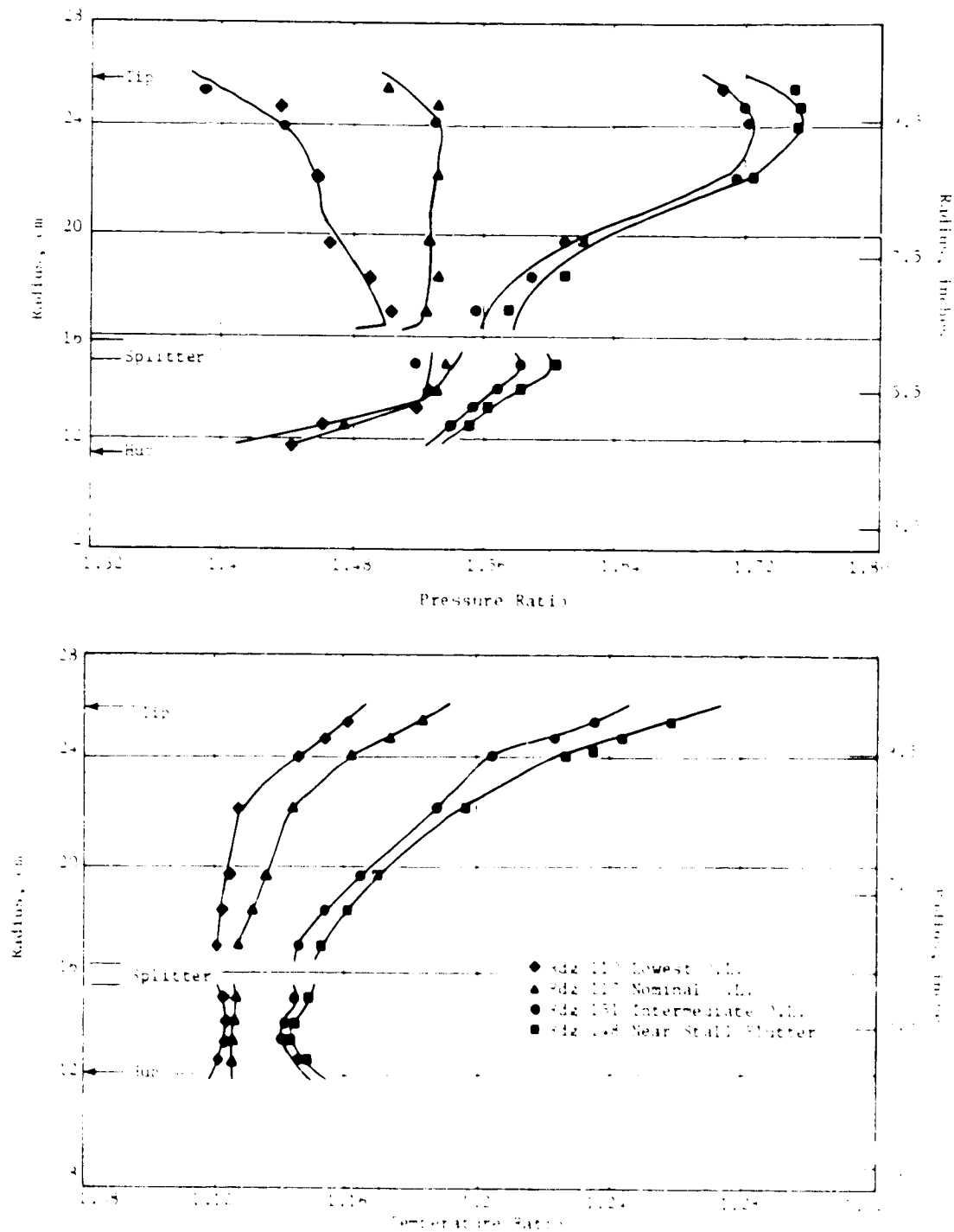


Figure 14. Total Pressure and Total Temperature Radial Profiles, 95% Speed.

5.6 DATA ANALYSIS PROCEDURES

This section discusses the data acquisition and analysis procedures used to obtain quantitative data for both (1) the steady and unsteady flowfield surrounding the fan rotor and (2) the rotor's mechanical state in both the steady and flutter modes of operation.

The principal data analysis tool used for this program was the FFT/computer system. In addition to on-line analog-to-digital conversion and disk storage of test data for post-test processing, the FFT/computer system provided spectral analyses of the data using the well known fast Fourier transform (FFT). The spectral analyses include generating the direct Fourier transform (DFT), the inverse Fourier transform (IFT), the power or auto spectrum, and the cross spectrum. (It should be noted that the term "linear spectrum", used throughout this report, refers to the square root of the auto spectrum.)

5.1 STEADY AERODYNAMIC PERFORMANCE DATA

Measured data needed to calculate the overall performance and blade element data of the scaled Fan C rotor were obtained from the fixed and traversable instrumentation described in Section 4.0.

5.1.1 Calculations of Overall Fan Performance

Performance data for the bypass stream were obtained by measuring total pressure and total temperature with instruments located in the inlet duct and with three 7-element radial rakes located on the leading edge of the bypass OGV's (see Figure 6). Performance data for the core stream were obtained by measuring total pressure and total temperature with the inlet duct instruments and with three 4-element radial rakes located in front of the core OGV's (see Figure 6).

Fan stage bypass performance was estimated for the Rotating Rig. Instrumentation was not used behind the bypass OGV to measure flow losses. As a result, a representative radial distribution was assumed for the value of the bypass OGV loss coefficient. This distribution corresponded to Fan C measured values in the intermediate operating range between peak efficiency and stall flutter.

Inlet properties were determined from measurements of total temperature, total pressure, static pressure, and water-air ratio. Total temperature was defined by the arithmetic average of readings from the inlet screen thermocouples, corrected for static-wire calibration factors. Total and static pressures were defined by the arithmetic average of the readings from the four 6-element radial inlet rakes. Thermodynamic relationships and real gas properties were used to compute stagnation enthalpy, inlet phi-function, and inlet flow.

Rotor exit properties at discrete immersions were determined from measurements of total temperature, total pressure, and flowpath surface static pressures. The total temperature and total pressure were defined by the arithmetic average of the readings from the three rake elements at each immersion. The static pressure was based on a radial linear interpolation between arithmetically averaged hub and casing static tap readings. Corrections were made to the average temperatures for static-wire factors and Mach number effects. Thermodynamic relationships and real gas properties were used to find values of stagnation enthalpy (actual and ideal), exit phi-functions, velocity, and density at each immersion. The local mass flow associated with each immersion was calculated with an effective flow area consistent with the static pressure level.

Rotor exit properties were mass-averaged using the local immersion values. Specifically, the following properties were computed in both the bypass and core streams: actual stagnation enthalpy, ideal stagnation enthalpy, and exit phi-function. From these properties the rotor performance parameters of adiabatic efficiency and rotor total pressure ratio were calculated.

Flow was determined by summing the local immersion flows at each of the three calculation planes. Core stream flow was also computed at the core duct exit from the arithmetic average values of pressure and temperature. Total fan flow was independently measured by the facility venturi flowmeters.

Bypass ratio was calculated from the core duct exit flow and the integrated inlet rake flow.

5.1.2 Calculations of Blade Element Data

Blade element data were computed in basically the same manner as done in the NASA/GE ATT Fan Program, Reference 2. Blade element sections were chosen parallel to the calculation stream surfaces of the scale model design point at 100 percent corrected speed. These sections passed through specified immersions defined as a percentage of the average blade height. For the bypass stream, the selected immersions were 5, 10, 15, 30, 50, 60, and 70 percent annulus from the blade tip, and for the core stream, the immersions were 80, 85, 90, and 95 percent.

Rotor blade element data were calculated using an axisymmetric streamline analysis procedure. This method used the measured radial distributions of total temperature and total pressure obtained from the fixed rakes, both forward and aft of the rotor, plus some wall static pressure measurements, to calculate all other fluid properties and vector diagram parameters on axisymmetric stream surfaces. The analysis iteratively selected streamline slope, curvature, and streamline radial position at each calculation station to satisfy the equations of continuity, energy, and radial equilibrium. The assumed axial distributions of effective-area coefficients (or blockages) needed by the analysis were initially chosen individually to match the wall static pressure data of each reading. When no substantial differences in these distributions were found among the first eighteen readings, a constant

set of values was used. The assumed duct losses in total pressure known to exist between the blade edges and the measurement planes were confined to the fluid near the flowpath walls, and the values were based on limited data from the boundary layer rake and cobra traverse probe. Chordwise distributions of relative total pressure loss and work input through the fan rotor were selected by matching the measured axial static pressure distribution at the fan tip, and transitioning into quarter-sine wave distributions across the subsonic hub sections. Fluid properties at the rotor trailing edge were made continuous across the splitter streamline, so smooth blending was required between bypass stream data and core stream data. Figure 14 illustrates how the analysis modeled the measured data, showing radial profiles of total pressure and temperature for the four data points analyzed along the 95 percent speed line. The profiles are not continuous between bypass and core streams because the plotted values come from the measurement planes, which are separated by the splitter. The effects of throttling, which are more pronounced in the fan tip region, are apparent.

A second method of calculating blade element data was used for the five data points of Build 1 for which traverse probe measurements of flow angle and static pressure were obtained. This method had sufficient data available to determine all fluid properties and vector diagram parameters at the measurement planes without a streamline analysis, hence, it was used to verify the results of the first method. The data was translated from measurement planes to blade edges by applying continuity, conservation of energy, and conservation of moment of tangential momentum along stream surfaces similar to those used in the streamline analysis. The results obtained with both methods are compared in Figure 15 for a sample reading, the near-flutter point at 70 percent corrected speed. At all bypass immersions, adequate agreement between incidence and deviation angles, diffusion factors and loss coefficients confirmed the validity of the streamline analysis method. Based on these results, subsequent testing used fixed rake measurements only.

5.2 STRAIN GAGES

5.2.1 Vibratory Response

Each blade was instrumented with one dynamic strain gage located so it would respond to the blade's first three vibratory modes, as shown in Figure 12. The flutter response was obtained from the tape-recorded strain gage signals in terms of stress amplitude, frequency, and interblade phase angle. The stress amplitude for each blade was obtained from playback of the strain gage signals in terms of overall stress levels and stress levels filtered at the flutter frequency. The blade vibratory response frequency was determined on-line and verified with the tape-recorded data.

5.2.2 Interblade Phase Angle

Interblade phase angles were determined from the strain gage data by two principal data analysis methods: (1) analog phasemeter time history analysis

COMPARISON OF OF POOR QUALITY

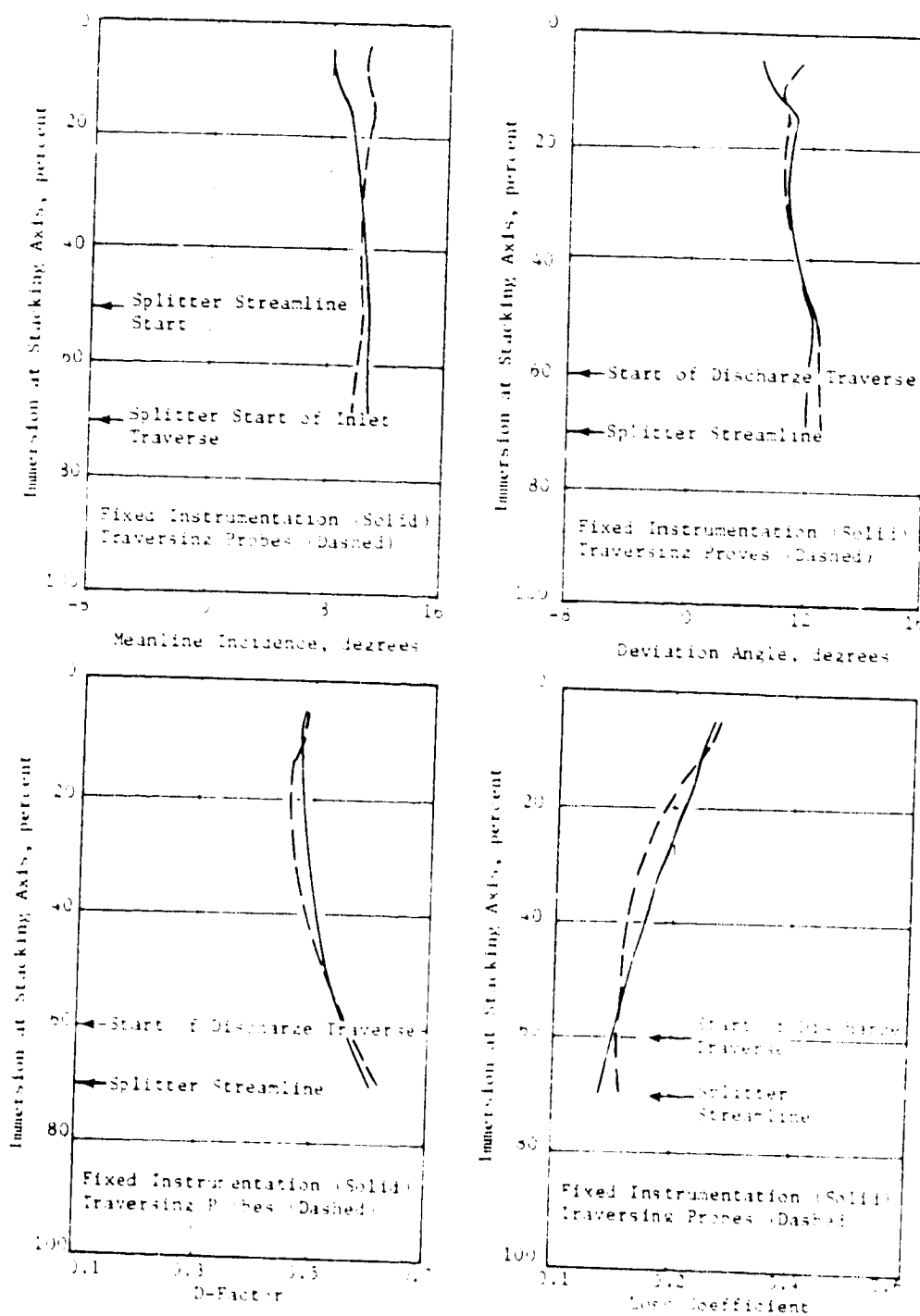


Figure 15. Comparison of Fixed Instrumentation and Traverse Probe Blade Element Data, 70 Percent Speed.

and (2) FFT cross spectral analysis. Further verification was also obtained by on-line phasing analysis and by phasing of individual waveforms from tape playback.

5.2.3 Phasing of Rotating Instrumentation Signals

Phasing between a reference strain gage signal (different reference strain gages were used at different speeds) and the rotating blade-mounted Kulite and hot film signals was obtained with the FFT cross spectral analysis using the continuous time histories.

5.2.4 Phasing of Stationary Instrumentation Signals

The true, unsteady amplitudes and phase data were determined using the digitized time records corresponding to instantaneous measurements for the selected sector of blades (200 consecutive data points, see Figure 16) acquired over 128 rotor revolutions. However, in this case, the time frames were not ensemble averaged (Figure 17) as they were for steady data - instead the perturbations at selected discrete time points (discrete circumferential locations) were used to establish the unsteady characteristics. Figure 18 illustrates the approach used to assemble frames of unsteady data that correspond to different discrete circumferential locations in the rotor coordinate system. Similar frames of data were assembled for the reference strain gage signal to provide a common reference for phase calculations.

As a result of this approach, the unsteady component of the signal obtained from the stationary sensor was sampled for a specific rotor circumferential location at a sampling rate equal to the rotor speed, i.e., a rate of one sample per revolution. Hence, sample points were obtained at a fixed spatial location relative to the rotor coordinate system, thereby achieving the same result that would be realized if the stationary sensor were rotating with the rotor. Therefore, a coordinate transformation from the stationary coordinate system to the rotor coordinate system was achieved for the fixed sensor by the 1/rev sampling. The timing of the extracted data was controlled to be constant by reference to the 1/rev clocking signal.

Comparing the 1/rev sampling frequencies with the corresponding instability frequencies in Table XII, shows that the former were clearly not high enough to meet the Shannon sampling criterion, which specifies that the sampling rate must be at least twice as high as the highest frequency of interest in the signal. The only recourse was to employ deliberate aliasing to translate the frequencies of interest, namely the flutter frequency and its components, into the Fourier analysis range. The time histories constructed by this 1/rev sampling at discrete circumferential locations in the rotating coordinate systems, and the resulting FFT aliasing of the frequencies, are referred to throughout this report as "aliased time histories."

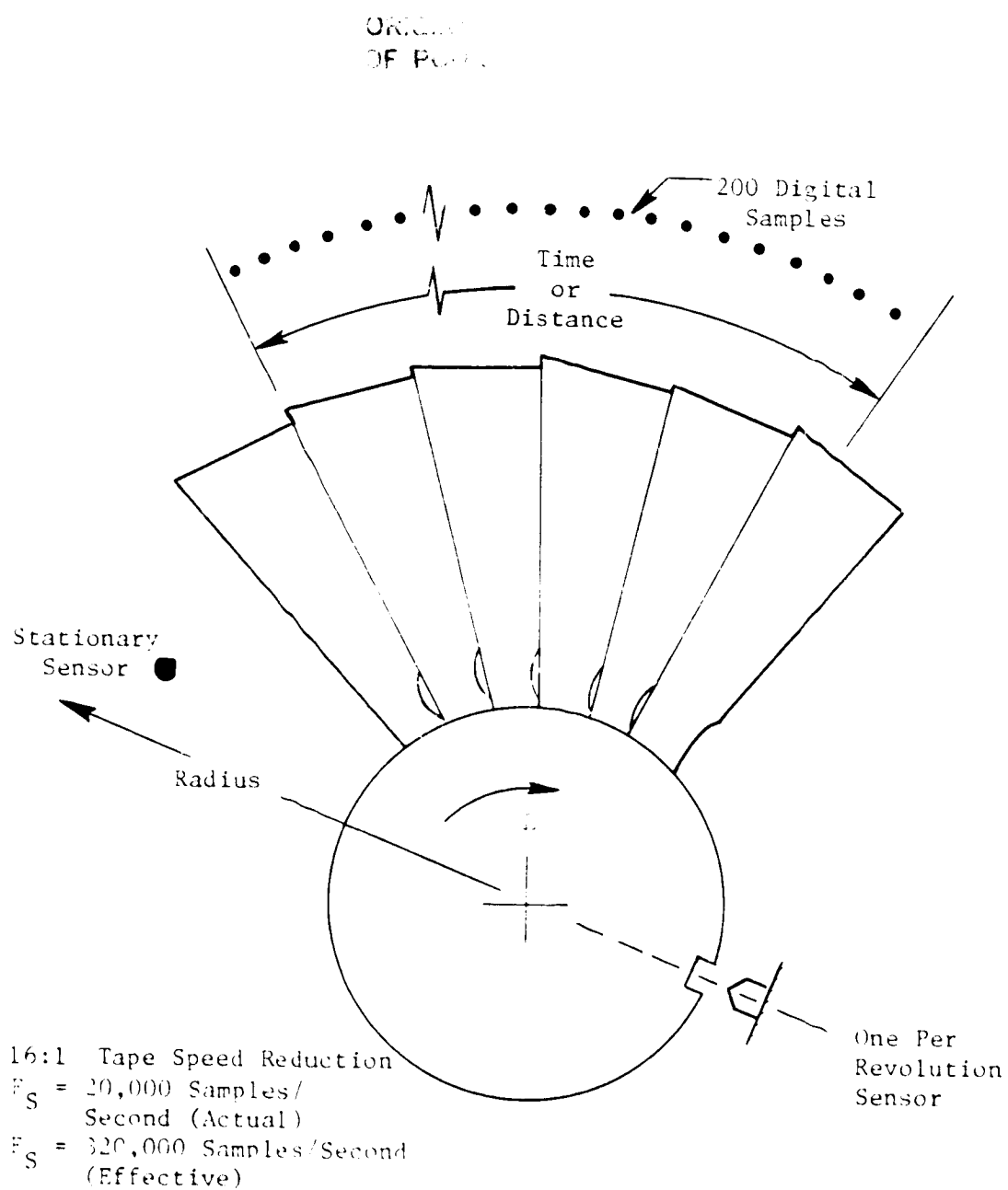


Figure 16. Data Acquisition for One Revolution.

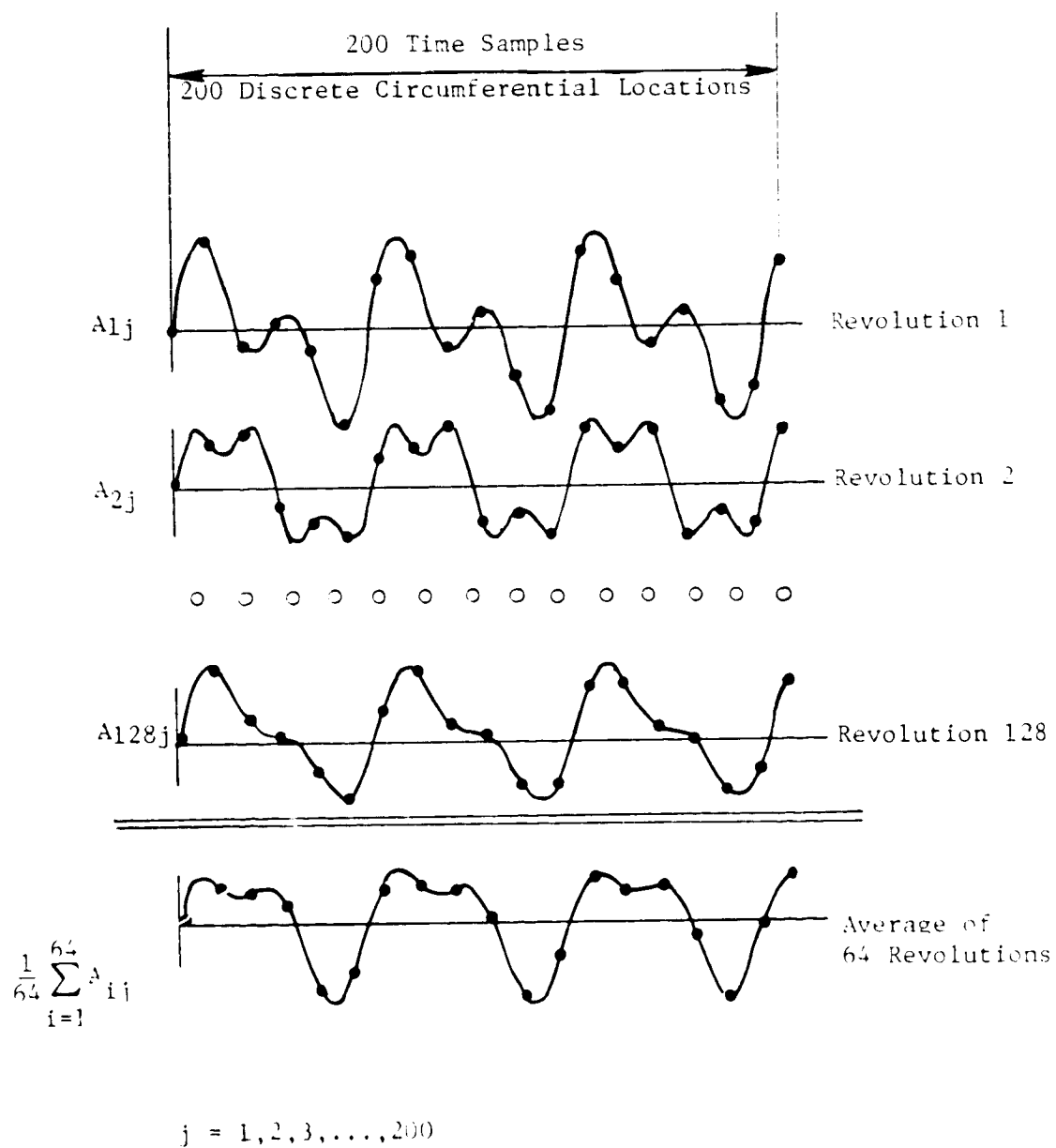


Figure 17. Ensemble Average of Time Frames.

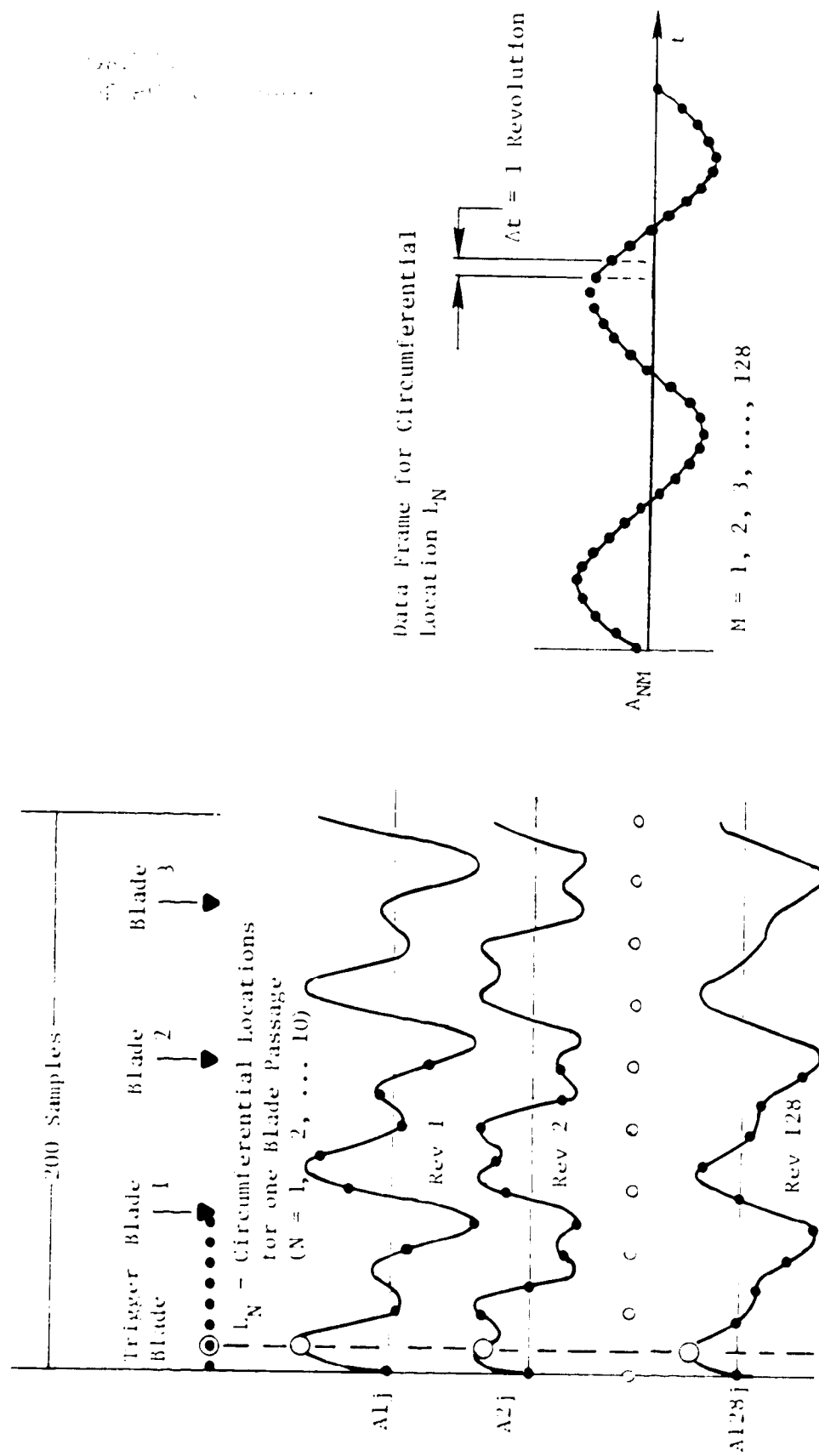


Figure 18. Stationary to Rotating Reference Transformation.

Table XII. One Per Rev Sampling Rates and Instability Frequencies.

Mode	Percent Speed (16597 = 100%)	1/Rev Sampling Rate (Hz)	Flutter Freq. (Hz)
1T	65	179.8	896
	70	193.7	896
1F	90	249.0	320
	95	262.8	336

Actually, two different techniques were used to obtain phase information. One was to alias all the flutter frequency components in the total stationary sensor signal (the stationary sensors see the instability at many frequencies). The other technique was to extract individual spectral components from the direct Fourier transform linear spectra of the time history sample, then perform an inverse Fourier transform on these components to obtain the corresponding time history. This results in a time history for a single nodal diameter plus its harmonics, which are at multiples of the blade passing frequency. Proper 1/rev sampling of this nodal diameter's time histories (128 of them) permits the phasing analysis with the reference strain gage signal similarly sampled. This second technique was used only for the casing-mounted Kulites.

Now, when the relative phase between point A in the flowstream and point B on the reference blade is determined and the relative phase between point C in the flowstream and point B on the reference blade is determined, then the relative phase between points A and C in the flowstream can be obtained from the difference between the two relative flowstream/blade phase angles.

5.3 BLADE DISPLACEMENT DATA

As discussed in Section 4.4.1, three different light probe systems were used to measure blade deformations. However, problems were encountered with the axial and spanwise deformation measurement systems. The axial deformation light probe system was inadvertently mounted on the casing so that, when operating at speed, the blade tip leading edge was forward of the light probes. Thus no useful axial deformation data was obtained. During Test 3 the laser light probes did not work properly when oil became embedded in blade-mounted reflective strips because of a facility oil leak during flutter testing. Hence, most of the blade displacement data was obtained from the casing-mounted blade tip light probe system.

5.3.1 Steady-State Deformation

5.3.1.1 Tangential Deflections

The steady tangential deflections were determined from on-line Polaroid photographs taken of a four-channel oscilloscope multiple sweep display (the signal displayed in these photographs shows the passing of a single blade over several revolutions). The triggering of the oscilloscope could be controlled to delay the display to show subsequent blades, one at a time. Thus, separate records were obtained for individual selected airfoils. The scope display allows graphical measurement of the elapsed time between the electronically generated 26/rev clocking signal and the blade light probe signal. This elapsed time was converted to time averaged displacement using the scope sweep time and the measured rotor speed.

The low reflectivity of the oil embedded reflective strips mentioned above made the photographs of the laser light probes very blurred. Photo enhancement techniques were considered, but the only practical "enhancement" for the on-line photographs was to enlarge them and either manually measure the enlargements or digitize them. It was felt that sufficient accuracy could be obtained by carefully measuring the on-line photographs, exercising engineering judgment regarding the blurred light probe traces.

To extract absolute displacement, the measured blade displacement relative to the 26/rev signal at the speed point of interest must be compared to that at "zero" speed. The "zero" speed reference used here was 2000 rpm, where the blade displacements were assumed to be negligibly small. In addition to the two relative displacements mentioned above, it is necessary to know the location of the 26/rev relative to the 1/rev signal at both the speed point and at "zero" speed. The only special instrumentation data points where the above data was obtained so that absolute displacements could be determined were the 65 percent speed torsional flutter point, the 70 percent speed intermediate operating line (IOL) point, and the 90 percent speed flexural flutter point.

5.3.1.2 Blade Untwist

Knowing the tangential tip deflections at the leading edge and the aftmost chordwise location where light probe data is available, one can calculate the blade tip untwist angle experienced by the blades at various operating conditions. This determination requires only the relative tangential displacements.

5.3.1.3 Chordwise Bending

The relative tangential displacement data at the blade leading edge, mid-chord, and trailing edge were used to estimate the chord-wise bending during various operating conditions. The change in the angle formed by the line from the leading edge to the mid-chord and the line from the mid-chord

to the trailing edge was used to indicate the amount of chord-wise bending at the blade tip.

5.3.2 Unsteady Deformation

5.3.2.1 Tangential Deflections

In parallel with the time averaged steady deflections, the unsteady deformation amplitudes of the blades were digitally acquired on-line by the FFT/computer system. Data from the eight light probes was not recorded simultaneously. Due to buffer storage limitations (4096 samples per buffer), the FFT/computer software was designed to acquire the 128 revolutions of data from one light probe at a time. If more than 4096 samples were recorded, more than one buffer would be required, causing some delay due to writing the buffer to disk. This delay could result in gapped data and/or shifting of the data within the buffer causing problems in determining which sample went with which blade.

The data acquired is the final voltage level of a ramp signal generated by external electronic hardware and terminated by the occurrence of a light probe signal. Each of the 26 ramp peaks (one ramp is generated per blade) were recorded for 128 revolutions. Then, for each blade, the 128 samples had the minimum voltage subtracted so that, knowing the ramp slope, the double-amplitude vibratory displacement was calculated.

5.3.2.2 Deflection Phase Angles

The interblade phase angle data was obtained by the FFT cross spectrum analysis of the blade deflection aliased time histories. (As discussed in Section 5.2.4, 1/rev sampling results in aliasing of the flutter frequency: hence the term "aliased time histories.") The time shift of the recorded data due to the light probe sequential sampling of the blades is accounted for in the phase data.

5.4 BLADE-MOUNTED SENSORS

Quantitative and qualitative measurements of the flowfield within a blade passage were made with two kinds of blade-mounted sensors: dynamic pressure transducers (Kulites) and heated thin-film anemometers (hot-film sensors). Problems were encountered with both of these sensors, primarily the mounting technique for the Kulites (see the discussion in Section 4.3.1), the temperature compensation for the hot-films, and the induced strain sensitivity for both.

The rotating bridge for the hot-film sensors was mounted in the rotor shaft to eliminate slipping noise from the hot film signal. The temperature environment in the shaft was not accurately known. During the vehicle check-out, the hot-film signal sensitivity appeared adequate but gradually diminished

to low or zero output as the testing continued. System modifications were made, but despite these changes, the hot-film data recorded was unusable for analyses in this program. Therefore, hot-film data is not presented in this report.

5.4.1 Kulites

The blade-mounted Kulites were positioned to survey the unsteady pressure at two radial stations, one each on two pairs of blades (see Section 4.3). The data was measured on adjacent suction (convex) and pressure (concave) blade surfaces facing one common flowstream. Amplitudes were determined from the tape recorded data playback in the form of overall levels and waveforms.

FFT analyses of the blade-mounted Kulite data were performed using 20 samples averaged in the frequency domain. Averaging in the frequency domain was accomplished by acquiring successive sample time histories -- each initiated with the 1/rev trigger, obtaining the Fourier transform of each sample, adding the transforms together, and dividing by the number of samples. Frequency averaging was done because it preserves the non-synchronous response whereas time averaging does not.

Cross spectral analyses were used for phasing the pressure signals relative to a reference strain gage signal.

5.5 CASING-MOUNTED KULITES

Since stationary sensors see the flutter response in terms of multiple traveling waves plus their harmonics, all casing Kulite data was recorded at 1.52 mps (60 ips) on magnetic tape for post-test processing at a reduced tape speed to recover the high frequency content. The FFT/computer system was used for all casing Kulite data reduction and for the evaluation of the unsteady pressure characteristics of each circumferential point relative to the rotor coordinate system.

The casing Kulites measured the dynamic component $(P_s)_{AC}$ of the static pressure at 12 points above the blade tip (see Section 4.3). The corresponding DC component was measured with conventional casing-mounted static taps so that the instantaneous static pressure was obtained by algebraically adding $(P_s)_{AC}$ and $(P_s)_{DC}$.

The casing kulite data were used to provide:

- The circumferential variation, over a few blade passages, of the unsteady component $(P_s)_{AC}$ of the static pressure
- Contour plots of the total static pressure distribution over the rotor blade tips during stable operation and during flutter

- Aliased time histories of the unsteady pressure, corresponding to different discrete circumferential locations in the rotor coordinate system, for relative amplitude and phasing information
- Analysis of the traveling wave content present during flutter.

The circumferential variation of the unsteady pressure was obtained from the ensemble average of 64 samples, as shown in Figure 17. These 200 data point time histories covered about three blade passages at 65 and 70 percent speed and four passages at 90 and 95 percent speed.

The contour plots of the pressure distribution over the blade tips were obtained from time histories comprised of the ensemble average of five instantaneous unsteady pressure time histories taken in consecutive rotor revolutions plus the DC portion of the static pressure measured by the static taps. (Recall, from Section 4.3, a static tap was provided for each Kulite at the same axial location.) Examples of these time histories are shown in Figures 19 and 20 for flutter at 70 and 95 percent speed, respectively. The time histories for the odd-numbered Kulites were shifted so that the contour plots were made as if all 12 Kulites were at the same circumferential position. This set of 12 static pressure time histories was then input into a contour plotting program which linearly interpolated between the Kulites for the specified pressure levels.

The procedure for obtaining the aliased time histories of both the unsteady pressures and the strain gage signals was described in Section 5.2.4 (see Figure 18). This was done for enough equally spaced points on the rotor circumference to insure that there were at least 10 points in the flowstream between two blades.

The traveling wave content, as observed in the stationary reference frame, of the rotor response during flutter was determined from linear spectra obtained through Fourier analysis of the casing Kulite signals. Typically, the linear spectra were the result of 256 samples, each 12.8 seconds long, averaged in the frequency domain with a bandwidth of 20 Hz.

5.5.1 Transformation to Rotating Reference System

With careful handling, casing Kulite data can produce accurate information on the amplitude and phase of all significant traveling waves from which, through linear superposition, one can calculate the unsteady static pressure due to blade vibrations which would be observed in the rotating reference system. The unsteady static pressure in the rotating reference system is the key physical quantity that all unsteady aerodynamic theories are developed to predict.

To translate the unsteady pressure data, measured by the stationary casing Kulites, into the rotating coordinate system, the harmonic components for each nodal diameter traveling wave were summed vectorially.

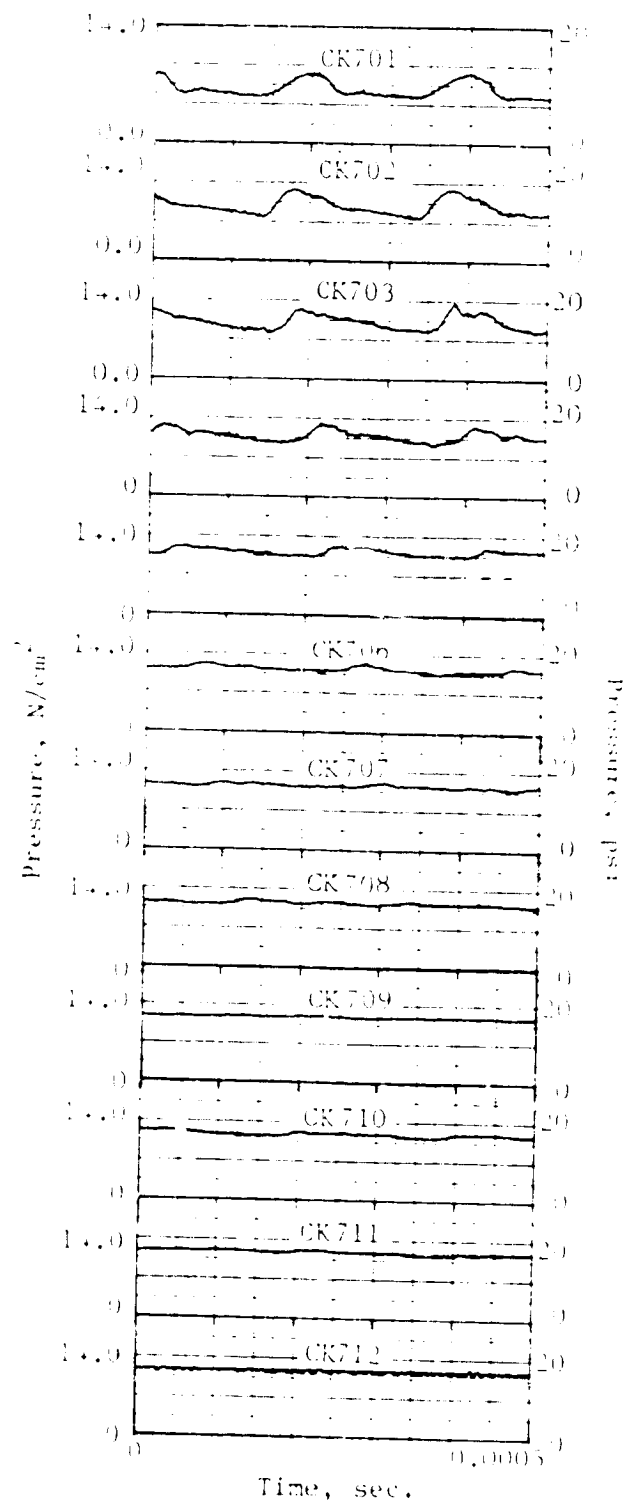


Figure 19. Averaged Casing Kilite Time Histories, 70° Speed Flutter.

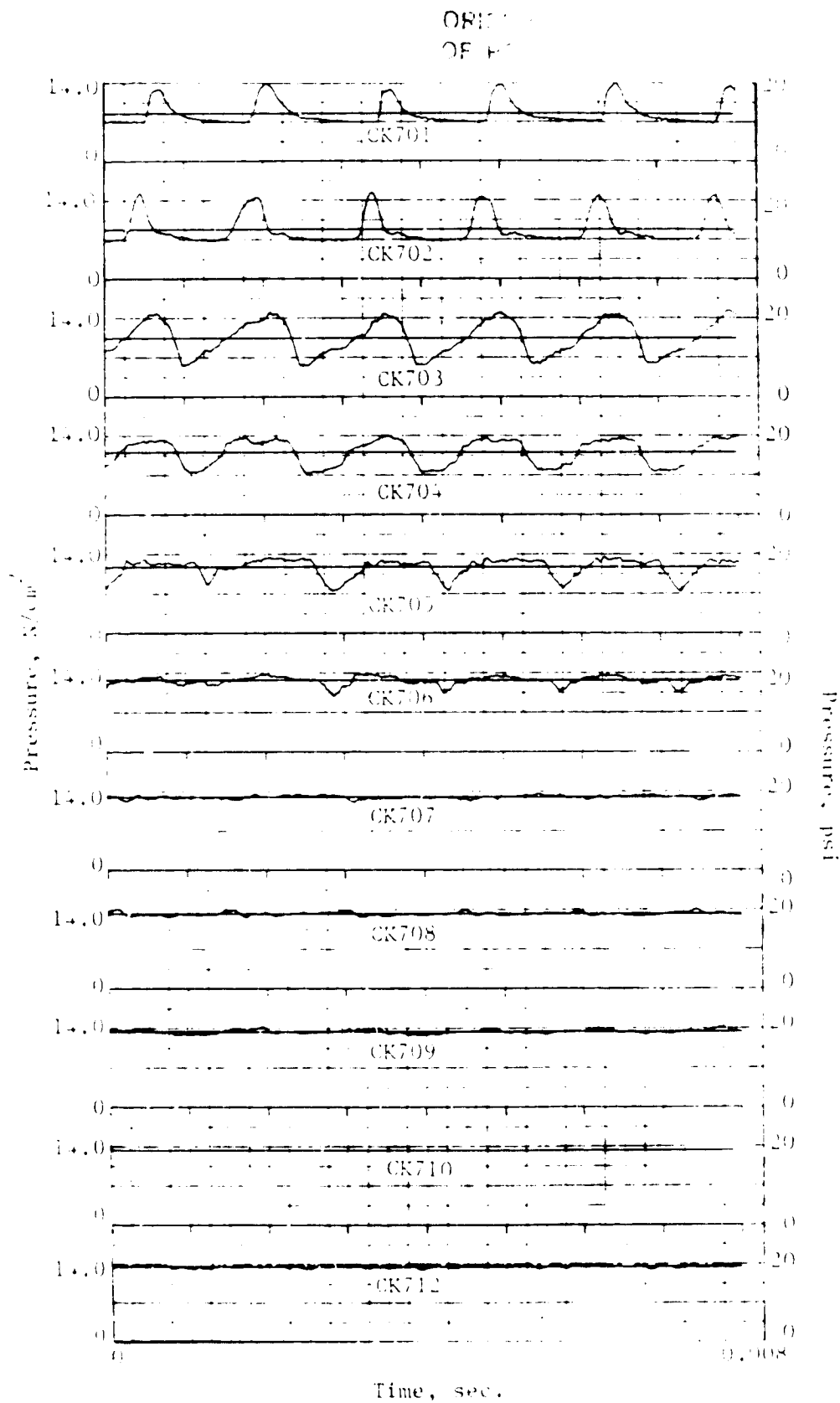


Figure 20. Averaged Casing Kullite Time Histories, 95% Speed Flutter.

Consider the reference coordinate systems shown in Figure 21: for a traveling wave of nodal diameter, n , the unsteady pressure, p_n , at a given axial location, x , is a periodic function of the rotating circumferential coordinate, θ , with a period of $2\pi/N_b$ at time, t , and can be expressed in terms of its harmonics in the Fourier series:

$$p_n(x, \theta, t) = \sum_{m=-\infty}^{\infty} A_{mn} e^{i[\omega t + (n + mN_b)\theta]} \quad (1)$$

where

- A_{mn} = amplitude of m th harmonic wave
- ω = flutter frequency in rotating system
- m = wave harmonic number
- n = traveling wave number (number of nodal diameters)
- N_b = number of blades (26 for the rotating rig)
- θ = angular position in rotating system, measured positive opposing rotor rotation

and where the sign of n indicates a forward traveling wave (FTW) when positive and a backward traveling wave (BTW) when negative. The number of symmetrical components is equal to $N_b/2 = 13$; hence the highest number of nodal diameters is equal to $26/2 = 13$.

Equation (1) is the most general expression for the unsteady pressure traveling wave of nodal diameter n in the rotating system. To transform it into the stationary system, the following coordinate transformation was used (see Figure 21).

$$\theta = \theta_0 + \omega t - \beta \quad (2)$$

where ω is the rotor speed (rev/sec), θ_0 is the absolute angular coordinate measured in inertial space positive opposing rotor rotation, and β is the angle between the inertial reference and the rotating reference at $t=0$. For this study, the inertial reference was taken as the Kulite location and the rotating reference was the slipring 1/rev trigger. Substituting Equation (2) into Equation (1) yields the general form of pressure waveform in the stationary system:

$$p_n(x, \theta_0, t) = \sum_{m=-\infty}^{\infty} p_{mn}(x) e^{i(\omega_{mn} t + k_{mn} \theta_0)} \quad (3)$$

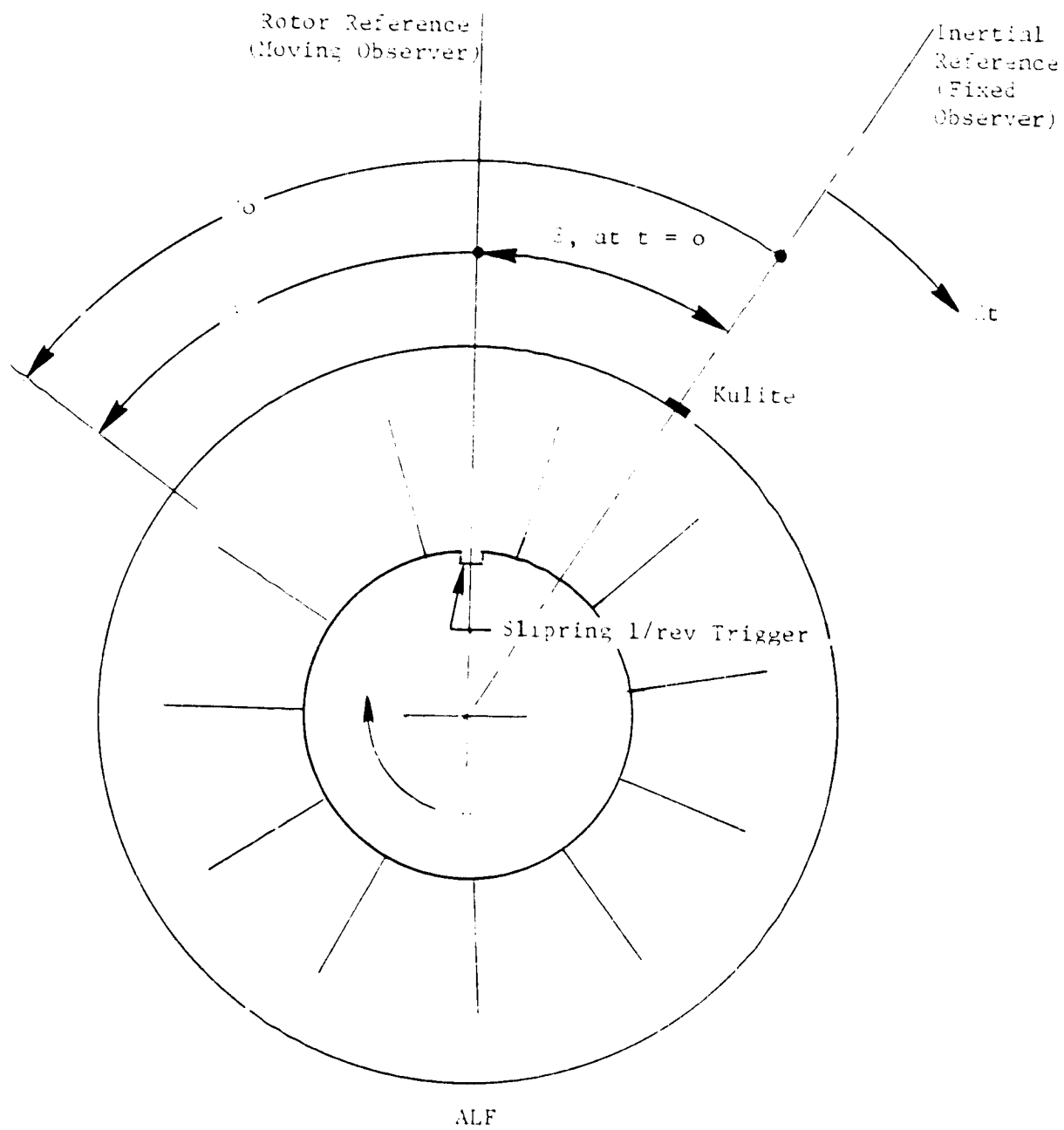


Figure 21. Reference Coordinate Systems.

where

$$p_{mn}(x) = A_{mn}(x) e^{ik_{mn}x} \quad (4)$$

= complex amplitude

$$\omega_{mn} = \omega + k_{mn}\Omega \quad (5)$$

= flutter frequency perceived in station system

$$k_{mn} = n + mN_b \quad (6)$$

= wave number

From Equation (5) it is easy to see that the single flutter frequency, ω , observed in the rotating system becomes a spectrum of many frequencies when observed in the stationary system.

The complex amplitude, Equation (4), can be written as

$$p_{mn}(x) = |p_{mn}(x)| e^{i\phi_{mn}(x)} \quad (7)$$

where the amplitude, $|p_{mn}(x)|$, and the phase, $\phi_{mn}(x)$, can be extracted from the casing Kulite data. This being done, one can calculate the amplitude, $A_{mn}(x)$, for the rotating system wave form, Equation (1), from the following:

$$A_{mn}(x) = |p_{mn}(x)| e^{i[\phi_{mn}(x) + k_{mn}\beta]} \quad (8)$$

Now, substituting Equation (8) into Equation (1) gives the general form of the unsteady pressure traveling wave of nodal diameter n in the rotating system:

$$p_n(x, \theta, t) = \sum_{m=-\infty}^{\infty} |p_{mn}(x)| e^{i[\omega t + \phi_{mn}(x) + k_{mn}(\theta + \beta)]} \quad (9)$$

from which one can calculate the amplitude and phase of the pressure wave at each circumferential location θ . Careful measurement of the angle θ results in a good estimate of the unsteady pressure information on both the pressure side and the suction side of the blade tip.

An alternate form of Equation (9) is

$$p_n(x, \theta, t) = \left\{ \sum_{m=-\infty}^{\infty} |p_{mn}(x)| e^{i[\phi_{mn}(x) + mN_b\theta + k_{mn}\beta]} \right\} e^{i(\omega t + n\theta)} \quad (10)$$

The quantity inside the brackets $\{ \}$ is a periodic function of θ with period $2\pi/N_b$, i.e., it is invariant for geometrically similar points in each blade passage - points separated by one blade pitch. From this invariance property, the net pressure, p_n , will exhibit a constant interblade phase angle of $360 n/N_b$ degrees because of the exponential factor $e^{in\theta}$ outside the bracket.

To obtain the total flutter unsteady pressure signal in the rotating system, the pressure, P_n , was summed over all significant nodal diameters, i.e.,

$$p(x, \theta, t) = \sum_{n = -N_b/2}^{N_b/2} p_n(x, \theta, t) \quad (11)$$

To make a reasonable estimate of the phase (in relation to a fixed initial time) several samples of the casing Kulite data should be initiated at the same phase point (the same point in the cycle) and averaged for the particular frequency of interest. Because the flutter traveling wave frequencies, ω_{mn} , differ from the system flutter frequency, ω , by integral multiples of the rotor speed, Ω , the proper integral number of rotor revolutions separating two consecutive samples to achieve the same phase start for the fundamental system flutter frequency applies to all other traveling wave frequencies as well. The slip ring 1/rev signal was chosen as the initial time to which all phases are referenced.

Calculations indicated that 50 rotor revolutions separating consecutive sample initiations should, in principle, produce approximately the same phase start for casing Kulite data at the 70 and 95 percent speed flutter points. The sampling rate used was 128,000 samples per second with a sample length of 0.064 seconds. Thirty-two samples were taken and averaged in the time domain. An aliasing filter with a roll-off rate of 48 dB per octave was used. The cutoff frequency was 50 kHz.

Having obtained the averaged time history of the Kulite data, the normalized Fourier transform of the averaged data was generated. Box-car windowing was used in the digital Fourier transform procedures. Because of the leakage effect of the digital Fourier transform, the obtained phase angles of the Fourier transforms were interpolated to obtain a better estimate of the true pressure phases. The phase interpolation formula, Reference 3, uses the phase at the frequency of the locally largest response corrected according to the ratio between the locally largest magnitude and the next largest magnitude at the frequency which is one bandwidth apart from the largest response frequency.

5.6 TRAVERSABLE PROBES

The radial distribution of the free stream total pressure was measured at the exit traverse plane, as described in Section 4.3, with a traversable Kulite probe. Also described in Section 4.3 are the two x-array, traversable, heated thin-film anemometer probes used to obtain two-dimensional fluid flow information (absolute flow velocity and flow angle) forward and aft of the rotor. These probes were used to obtain ensemble average time histories, circumferentially averaged radial distributions, contour plots of the radial distributions, circumferential amplitude variation and corresponding phase relative to a reference strain gage, and traveling wave content. All of this

information was obtained using the same reduction techniques used for the casing Kulite data, explained in the preceding section.

The contour plots were an exception, however. Contour plots for the Kulite probe used the ensemble average of 64 samples (200 points each) of the unsteady total pressure (P_T)_{AC} plus the circumferentially averaged steady total pressure (P_T)_{DC}. Contour plots from the x-array probes were obtained with the ensemble average of 64 samples (200 points each) of the absolute flow velocity and of the flow angle.

As was done for the casing Kulites, all traversable probe data was recorded at 1.52 mps (60 ips) on magnetic tape for post-test processing at a reduced tape speed to recover the high frequencies of the traveling wave harmonics.

5.7 STRUCTURAL RESPONSE PREDICTIONS

Static and vibratory analyses of the Rotating Rig blading were made with General Electric's TWISTED BLADE (TWBL) computer program. This program provides a beam solution with numerical integration performed on a tenth-order differential equation set with provisions for including general boundary conditions. The coupling of bending and torsion is included for both static and vibratory analyses.

The TWBL program was also executed as a component within General Electric's COUPLED BLADE-DISC program which considers the complete system of disk and blades to analyze the traveling wave problem.

For the blade work calculations, blade vibratory analyses were made with General Electric's TAMP finite element program using eight-noded brick elements to model the blade as shown in Figure 22. The brick element is a 3-D isoparametric solid element with 33 degrees-of-freedom: 24 corresponding to the three motions at each of the eight nodes, and nine internal degrees-of-freedom which are eliminated to minimize the strain energy. The stiffening effects of rotation are included in TAMP. Output from this program are the stresses, static deformations, frequencies, mode shapes, modal masses, and mode shape slopes.

5.8 BLADE WORK PER MODE CALCULATION

Using the rotor blade data obtained during this experimental flutter investigation, the rotor system's stability can be evaluated by means of the aerodynamic logarithmic decrement, δ_{aero} , for the predominant traveling waves (Reference 4). Aerodynamic damping is present for each traveling wave response and is defined by the familiar logarithmic decrement, which is proportional to the ratio of the aerodynamic work done per vibratory cycle on one blade to the blade's average kinetic energy per cycle.

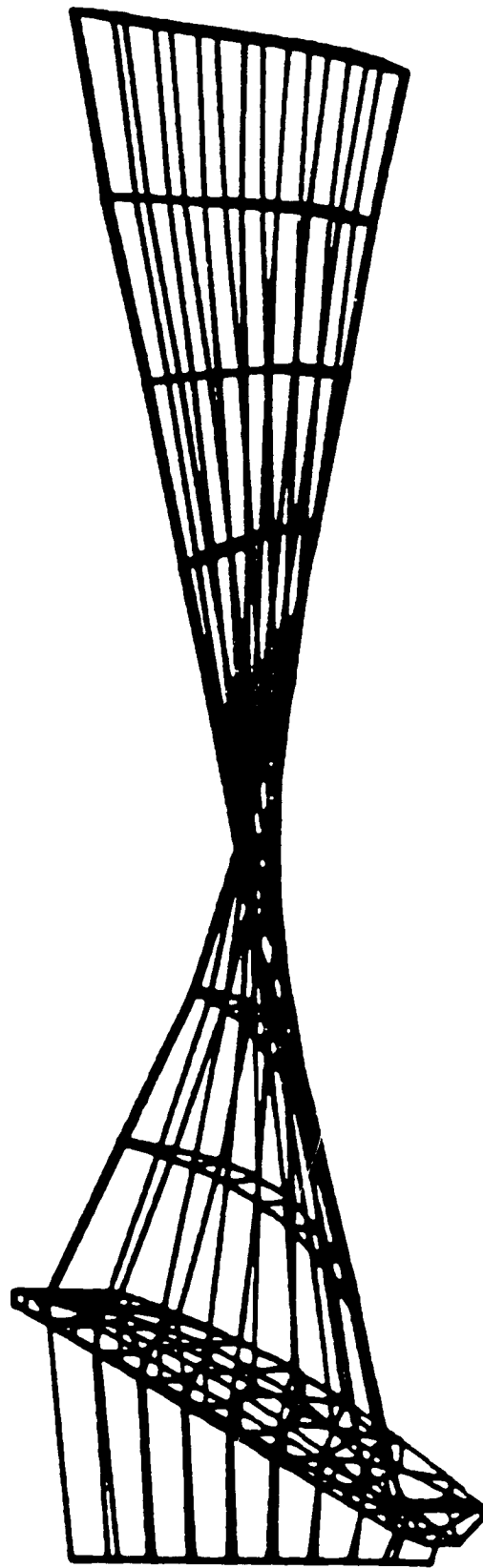


Figure 22. Finite Element Model of Rotating Rig Blade.

$$\delta_{\text{aero}} = - \frac{W_n}{4E_n} \quad (12)$$

Stability is indicated when $\delta_{\text{aero}} > 0$; instability, on the other hand, is indicated when $\delta_{\text{aero}} < 0$. In other words, when $W_n < 0$, energy is dissipated by the airfoil and the system is stable, but when $W_n > 0$, energy is gained by the airfoil and it is unstable.

The aerodynamic work done per cycle from the n th nodal diameter traveling wave was determined by the expression.

$$W_n = \int_0^c \int_0^{\frac{2\pi}{\omega}} \Delta p_n \dot{\delta}_n dt dc \quad (13)$$

where:

Δp_n = pressure difference across the airfoil from the n th nodal diameter

δ_n = normal deflection of blade tip in the n th nodal mode

$\dot{\delta}_n$ = $d \delta_n / dt$

t = time

ω = flutter frequency

c = chord

Equation (9) or its equivalent, Equation (10), was used before to obtain the pressure amplitude and phase. But this phase is the "absolute" phase angle which is relative to the $t = 0$ starting time of the data sample. The problem here for the work/cycle/mode was to obtain the phasing between the blade tip displacement and the blade tip pressure differential. Given the relative phase between the deflection and a reference strain gage, and between the pressure differential and the same strain gage, the relative phase between the displacement and the pressure differential can be determined.

For the work/cycle/mode then, the casing Kulite pressure signals were processed as follows: the Fourier transform of the overall signal was taken, the traveling wave was extracted along with its harmonics, and the inverse Fourier transform (IFT) produced the time history for the selected traveling wave. This traveling wave time history was then 1/rev sampled, along with that of the reference strain gage, to construct aliased time histories for stress and pressure on each side of the blade. The desired phasing information was then obtained with cross-spectral analyses.

The unsteady blade tip deformation data obtained from the light probes, discussed in Section 5.3.2 and presented in Section 6.3.3, were used for the work/cycle/mode calculations. The measured tip deflections and interblade phase angles were used in the following expression for each rotor blade

$$\delta_i(t) = A_i \sin [\omega(t - \tau_i) - \phi_i] \cos \lambda \quad (14)$$

where

$\delta_i(t)$ = normal deflection of the i th blade tip

A_i = measured maximum tangential tip displacement of the i th blade

$\tau_i = \frac{k_i}{N_b \pi} =$ time shift to account for sequential sampling of the blades

k_i = blade index

N_b = number of blades in the rotor ($N_b = 26$)

ϕ_i = measured interblade phase angle

λ = stagger angle

Equation (14) was evaluated for each blade at the same instant to obtain the instantaneous circumferential distribution of the blade tip normal displacement. This circumferential distribution was then Fourier decomposed spatially to determine the amplitude, δ_n , of each nodal diameter traveling wave present.

Simultaneous 1/rev sampling of the light probes and a strain gage was not done. The relative phase between the tip displacement and a reference strain gage was determined from the blade finite element vibratory analysis described in Section 5.7.

For a single blade, the average kinetic energy per cycle of the n th nodal diameter traveling wave was determined from

$$E_n = \frac{1}{2} \int_0^c \omega^2 M \delta_n^2 dc \quad (15)$$

where:

M = modal mass, from TAMP (see Section 5.7)

It should be noted that since there was no data from the axial deformation light probe system (see Section 5.3), engineering judgment was used to locate the casing kulites and the light probes relative to the blade tip chord.

6.0 TEST RESULTS

The overall objectives of this program were to obtain detailed measurements of (1) the steady and unsteady flowfield surrounding the fan rotor and (2) the mechanical state of the rotor while operating in both the steady and flutter modes. The data from each of the individual measurements is discussed in detail below.

6.1 STEADY AERODYNAMIC PERFORMANCE

Overall performance and blade element data for the scaled Fan C Rotor were calculated by the methods described in Section 5.1. The measured data that was needed for the calculations was obtained from both the fixed and traversable instrumentation described in Section 4.0. Fan rotor performance is presented as a separate performance map for both the bypass flow and core flow streams. A limited comparison of scale model rotor performance is made with the full scale fan to verify that similar performance characteristics were achieved. Blade element data are presented for the five steady traverse data points of Build 1, for the ten unsteady traverse data points of Build 2, and for three additional data points which extend the results over a wider range of operation.

6.1.1 Overall Fan Performance

In the rotor bypass stream performance map, Figure 23, the mass-averaged values of pressure ratio and adiabatic efficiency are plotted against the corrected fan inlet flow for all data points obtained during the test program. The performance map shows lines of constant speed plus several "operating" lines which are indicative of various degrees of throttling between peak efficiency and stall flutter. These operating lines were established by using the data having consistent bypass ratios and facility valve settings. The low or nominal operating line was established by setting the main discharge valve at its most open setting, and the intermediate operating line was defined at a valve setting approximately midway between its most open and its stall flutter settings. At a few of the speeds tested, further unthrottling below the nominal operating line was achieved by opening an auxiliary (booster bypass) valve downstream of the test vehicle. In this manner, peak efficiency at high speeds was identified, as shown in Figure 23. The eighteen readings for which blade element data were generated are identified on the map with solid symbols. The aerodynamic design point is shown for reference. Data scatter observed among the remaining data points was caused by the variations that occurred in bypass ratio, corrected speed, and facility discharge valve settings. A tabulation of the significant overall performance parameters for all the readings taken is given in Table XIII.

Table XIII. NASA Rotating Rig Fan Rotor Performance Data.

Build 1 - Mechanical Checkout and Steady Aerodynamic Test										Build 2 - Special Instrumentation Measurements Test									
Reading	$2\pi r/\delta$	$\frac{W_1/\delta_1}{\delta_1}$	P_{14}/P_1	η_{14}	P_{20}/P_1	BPR	Operating Point	Reading	$2\pi r/\delta$	$\frac{W_1/\delta_1}{\delta_1}$	P_{14}/P_1	η_{14}	P_{20}/P_1	BPR	Operating Point				
14	70.1	55.97	1.272	0.837	1.292	5.4		71	69.9	57.64	1.262	0.867	1.289	4.9	Near Flutter				
15	70.2	55.36	1.277	0.834	1.295	5.2		72	69.7	49.24	1.298	0.793	1.297	4.9	Near Flutter				
16	80.7	65.81	1.396	0.853	1.392	5.8		73	69.4	49.42	1.294	0.795	1.294	4.8	Near Flutter				
17	80.7	64.67	1.406	0.847	1.400	5.3		74	69.5	60.47	1.232	0.885	1.279	3.9	Near Flutter				
18	88.9	73.39	1.536	0.860	1.486	6.0		75	85.5	77.39	1.343	0.853	1.413	4.3					
19	89.9	74.63	1.557	0.850	1.499	6.0		76	85.8	64.58	1.500	0.799	1.470	4.4	Near Flutter				
20	89.9	73.67	1.567	0.843	1.508	5.5		77	100.6	88.45	1.476	0.836	1.542	4.7					
21	100.5	85.02	1.809	0.857	1.625	6.9		78	65.2	45.61	1.256	0.785	1.260	4.8	In Flutter				
22	100.4	82.59	1.678	0.856	1.663	5.8		79	65.3	45.50	1.257	0.791	1.259	4.8	In Flutter				
23	105.2	87.34	1.998	0.858	1.732	6.1		80	65.3	45.37	1.257	0.796	1.260	4.7	In Flutter				
24	110.2	91.65	2.113	0.851	1.804	6.4		81	95.0	71.89	1.704	0.816	1.601	3.8	Near Flutter				
25	69.8	48.31	1.305	0.784	1.303	5.7	Near Flutter	82	95.2	70.83	1.688	0.819	1.589	4.6	Near Flutter				
26	80.0	60.47	1.414	0.809	1.398	5.8	Near Flutter	84	70.2	61.35	1.275	0.881	1.280	4.2	Near Flutter				
27	90.0	70.95	1.579	0.827	1.516	5.8	Near Flutter	86	70.3	56.95	1.263	0.845	1.292	4.4					
28	94.8	40.31	1.159	0.824	1.174	5.4		87	70.3	54.48	1.279	0.830	1.296	4.7					
29	94.6	34.00	1.174	0.764	1.161	12.6	Rotating stall	89	70.2	48.28	1.394	0.792	1.305	5.0	In Flutter				
30	74.5	58.99	1.317	0.829	1.326	5.9		90	70.2	48.07	1.307	0.781	1.302	5.1	In Flutter				
31	69.7	53.94	1.275	0.825	1.291	5.4		91	76.8	68.77	1.275	0.910	1.333	4.4					
32	69.6	48.71	1.299	0.792	1.297	5.8	Near Flutter	92	70.0	61.07	1.223	0.856	1.273	4.0					
33	57.1	35.55	1.192	0.754	1.173	13.2	Near Stall	93	69.7	57.91	1.257	0.857	1.285	3.5					
34	59.6	15.37	1.217	0.738	1.202	10.0		94	69.8	48.29	1.305	0.772	1.300	3.7	Near Flutter				
35	64.6	44.40	1.252	0.786	1.252	5.6	Near Flutter	95	65.6	49.18	1.295	0.787	1.293	4.5	Near Flutter				
36	74.9	57.21	1.339	0.824	1.339	5.3		96	85.1	75.65	1.356	0.868	1.412	4.1					
37	74.7	54.11	1.348	0.784	1.339	5.8		97	83.8	66.83	1.460	0.883	1.438	3.8	Near Flutter				
38	74.7	57.81	1.333	0.817	1.337	5.2		99	85.0	65.84	1.477	0.849	1.442	4.7	Near Flutter				
39	79.2	62.66	1.394	0.835	1.386	5.4		100	100.0	87.17	1.500	0.828	1.548	4.4					
40	89.4	59.41	1.408	0.802	1.388	6.0	Near Flutter	101	95.0	84.21	1.458	0.848	1.505	4.3	Near Flutter				
41	89.4	72.01	1.557	0.838	1.498	5.5		103	94.9	71.78	1.674	0.822	1.568	5.4	Near Flutter				
42	89.2	68.97	1.563	0.819	1.498	5.8	Nar Flutter	104	94.9	70.42	1.673	0.813	1.566	5.5	In Flutter				
43	94.8	76.58	1.699	0.835	1.576	5.3		105	70.1	60.94	1.238	0.907	1.281	4.0					
44	94.8	72.76	1.693	0.804	1.579	5.4	Near Flutter	106	69.8	60.77	1.234	0.885	1.279	4.0					
45	100.2	82.81	1.843	0.839	1.642	6.0		107	70.0	60.64	1.236	0.887	1.280	4.1					
46	100.4	75.26	1.837	0.783	1.666	6.1	Near Flutter	108	85.1	75.67	1.360	0.860	1.416	4.1					
47	100.6	81.82	1.863	0.831	1.656	6.2		109	85.3	63.46	1.496	0.809	1.457	4.4	Near Flutter				
48	64.6	47.72	1.237	0.809	1.246	5.0		110	95.0	84.26	1.456	0.842	1.504	4.3	Near Flutter				
49	64.6	45.10	1.251	0.799	1.250	5.5	Near Flutter	111	95.1	70.12	1.681	0.813	1.572	5.6	Near Flutter				
50	64.6	44.67	1.253	0.791	1.253	5.6	Near Flutter	112	95.5	84.41	1.480	0.851	1.511	4.3					
51	64.7	44.49	1.253	0.778	1.252	5.6	Near Flutter	113	95.4	70.68	1.714	0.796	1.606	3.6	Near Flutter				
52	64.7	44.92	1.251	0.788	1.251	5.6	Near Flutter	114	84.9	74.92	1.375	0.863	1.414	4.1					
53	69.7	49.00	1.297	0.780	1.293	5.6	Near Flutter	115	85.1	63.41	1.493	0.801	1.456	4.4	Near Flutter				
54	69.7	48.95	1.298	0.784	1.292	5.8	Near Flutter	116	95.5	70.73	1.688	0.803	1.584	5.5	In Flutter				
55	74.8	54.43	1.346	0.789	1.339	5.8	Near Flutter	117	95.5	83.85	1.525	0.860	1.514	4.5	Near Flutter				
56	84.6	64.36	1.469	0.813	1.439	5.2		118	95.3	70.70	1.681	0.797	1.581	5.4	Near Flutter				
57	84.9	65.46	1.481	0.810	1.444	5.4	Near Flutter	119	85.3	73.79	1.409	0.873	1.425	4.4					
58	85.0	65.21	1.476	0.805	1.441	5.4	Near Flutter	120	85.2	63.57	1.495	0.802	1.457	4.3	Near Flutter				
59	95.3	75.69	1.708	0.818	1.584	5.0	Near Flutter	121	85.1	69.26	1.466	0.843	1.435	5.0					
60	95.3	71.90	1.700	0.795	1.586	5.0	Near Flutter	122	85.2	63.10	1.495	0.793	1.458	4.4	Near Flutter				
61	94.8	71.55	1.698	0.791	1.580	5.0	Near Flutter	123	95.1	79.96	1.600	0.855	1.535	5.9					
62	100.4	81.45	1.854	0.834	1.648	5.6		124	95.3	70.32	1.678	0.792	1.580	5.4	Near Flutter				
63	100.6	79.42	1.874	0.830	1.661	5.8		125	90.3	67.08	1.580	0.798	1.521	4.7	Near Flutter				
64	85.3	65.71	1.483	0.806	1.447	5.5	Near Flutter	126	90.3	67.23	1.580	0.804	1.520	4.7	Near Flutter				
65	74.6	55.04	1.340	0.788	1.336	5.6	Near Stall	127											
66	59.7	36.10	1.217	0.746	1.210	6.7	Near Stall	128	90.2	66.98	1.581	0.804	1.519	4.8	Near Flutter				
67	59.7	37.38	1.221	0.763	1.215	5.7	Near Stall												

Table XIII. NASA Rotating Rig Fan Rotor Performance Data. (Concluded)

Build 2 - Special Instrumentation Measurements Test							
Reading	$\%N/\sqrt{\theta}$	$\frac{W_1\sqrt{\theta_1}}{\delta_1}$	P_{14}/P_1	η_{14}	P_{20}/P_1	BPR	Operating Point
141	94.8	82.32	1.594	0.882	1.546	4.1	
142	94.9	81.04	1.630	0.878	1.552	4.1	
144	95.0	70.11	1.685	0.798	1.579	4.8	In Flutter
147	95.0	70.06	1.686	0.804	1.577	4.8	In Flutter
148	94.9	69.97	1.685	0.806	1.577	4.9	In Flutter
149	95.0	75.90	1.651	0.840	1.555	5.7	Intermediate O.L.
150	94.9	74.70	1.667	0.832	1.563	5.2	Intermediate O.L.
151	94.9	74.63	1.665	0.834	1.562	5.2	Intermediate O.L.
152	94.9	74.72	1.667	0.834	1.563	5.2	Intermediate O.L.
153	70.0	52.76	1.281	0.826	1.292	4.7	Low O.L.
154	70.0	52.71	1.280	0.813	1.291	4.7	Low O.L.
155	69.9	52.67	1.280	0.812	1.291	4.7	Low O.L.
156	70.0	47.68	1.300	0.774	1.294	6.1	Near Flutter
157	64.9	46.06	1.248	0.797	1.253	4.7	Intermediate O.L.
158	65.1	45.95	1.250	0.797	1.254	4.6	Intermediate O.L.
159	65.0	45.96	1.249	0.794	1.253	4.7	Intermediate O.L.
160	65.0	44.51	1.255	0.785	1.254	5.0	In Flutter
161	75.1	52.87	1.354	0.783	1.345	5.4	In Flutter
162	84.9	61.43	1.479	0.791	1.438	6.4	In Flutter
164	90.6	77.55	1.510	0.862	1.480	5.0	Low O.L.
165	90.5	66.74	1.581	0.794	1.515	5.5	In Flutter
167	89.9	65.39	1.574	0.800	1.502	5.9	In Flutter
168	89.8	67.16	1.577	0.818	1.504	4.8	In Flutter
169	89.8	67.23	1.575	0.811	1.506	4.8	In Flutter
170	89.6	67.13	1.572	0.810	1.506	4.8	In Flutter
171	89.7	76.14	1.503	0.869	1.471	5.3	Low O.L.
172	89.6	76.30	1.498	0.858	1.471	5.2	Low O.L.
173	89.6	76.32	1.497	0.847	1.472	5.1	Low O.L.
174	89.8	76.50	1.501	0.859	1.473	5.2	Low O.L.
175	89.9	71.66	1.552	0.828	1.500	4.9	Intermediate O.L.
176	89.8	71.44	1.550	0.825	1.499	4.9	Intermediate O.L.
177	89.7	71.31	1.550	0.829	1.497	4.9	Intermediate O.L.
178	70.0	50.24	1.292	0.802	1.292	5.2	Intermediate O.L.
179	70.1	50.37	1.293	0.806	1.293	5.2	Intermediate O.L.
180	69.9	50.27	1.292	0.805	1.292	5.1	Intermediate O.L.
184	99.2	87.24	1.495	0.834	1.536	4.5	Lowest O.L.
185	102.4	86.90	1.763	0.864	1.609	6.1	
186	103.1	89.13	1.707	0.863	1.606	5.0	
187	102.8	88.59	1.704	0.865	1.599	5.0	
188	102.0	88.59	1.617	0.844	1.578	4.6	
190	102.6	88.82	1.567	0.823	1.576	4.5	
191	102.4	88.80	1.517	0.805	1.566	4.5	
192	94.7	75.49	1.690	0.832	1.581	4.2	
193	94.8	75.33	1.698	0.838	1.581	4.2	

In the core stream rotor performance map, Figure 24, a similar procedure was used: mass-averaged value of pressure ratio was plotted against the corrected fan inlet flow. The nominal bypass ratio was 5, although there was some scatter in the actual values recorded during the test, so the core stream airflow was approximately one-sixth of the total fan flow shown in Figure 24. Core stream efficiency values were unrealistically high, and there were inconsistencies observed between the Plane 20 and Plane 25 total temperature measurements. Because no core region traverse data were available to help resolve temperature measurements, the core stream efficiency is not reported.

Superimposed on the full scale Fan C bypass stage performance map, Figure 25, is the Rotating Rig Build 1 data modified by the loss assumption based on the full scale data. The comparison shows good agreement in terms of speed line characteristics and stage efficiency. Most important, the scale model vehicle exhibited rotating stall and stall flutter of the same type and at similar aerodynamic conditions as Fan C. The flow-speed relationships plotted in Figure 26 provide further evidence that the two vehicles are aerodynamically similar. The Rotating Rig Build 2 data compares favorably with Fan C in terms of flow versus speed along an operating line passing near peak efficiency. Considering the difficulties involved in defining a distinct flutter boundary, the flow-speed comparison at the stress limit is also in very good agreement.

6.1.2 Fan Rotor Blade Element Data

Rotor blade element data were calculated for the eighteen readings shown on the performance map, Figure 23, using an axisymmetric streamline analysis procedure discussed in Section 5.1.2. The rotor blade element data are presented in Figures 27 through 29 as plots of total pressure loss coefficient, diffusion factor, and deviation angle versus the meanline incidence angle. A complete tabulation of these parameters, plus the radial distributions of the flow properties at the blade edges, is given separately for each of the eighteen readings in Appendix A. The plots present the data in a standard NASA format which groups data from all speeds according to a given immersion. Only the bypass immersions are shown, since the inconsistencies observed in the core stream measurements resulted in some unrealistic values. In addition to the 10 data points at which unsteady data are reported, three steady-state readings (two at 95 percent speed, and one at 70 percent speed) are included to extend the range of the blade element data to flow conditions near peak efficiency operation. The incidence angle used for this presentation is based upon the design value of the blade leading edge angle; a more accurate value would account for the variations in measured blade untwist that occur at lower-than-design speeds. The true incidence angle, however, would not significantly improve the scatter of the blade element data observed in Figures 27 through 29. A more meaningful display of the loss data is shown in Figure 30, where the total pressure loss parameter for the rotor blade is plotted as a function of blade diffusion factor. The result is a better correlation, indicating that the rotor blade performance is more closely related to diffusion levels than to variations in speed or incidence angle variations.

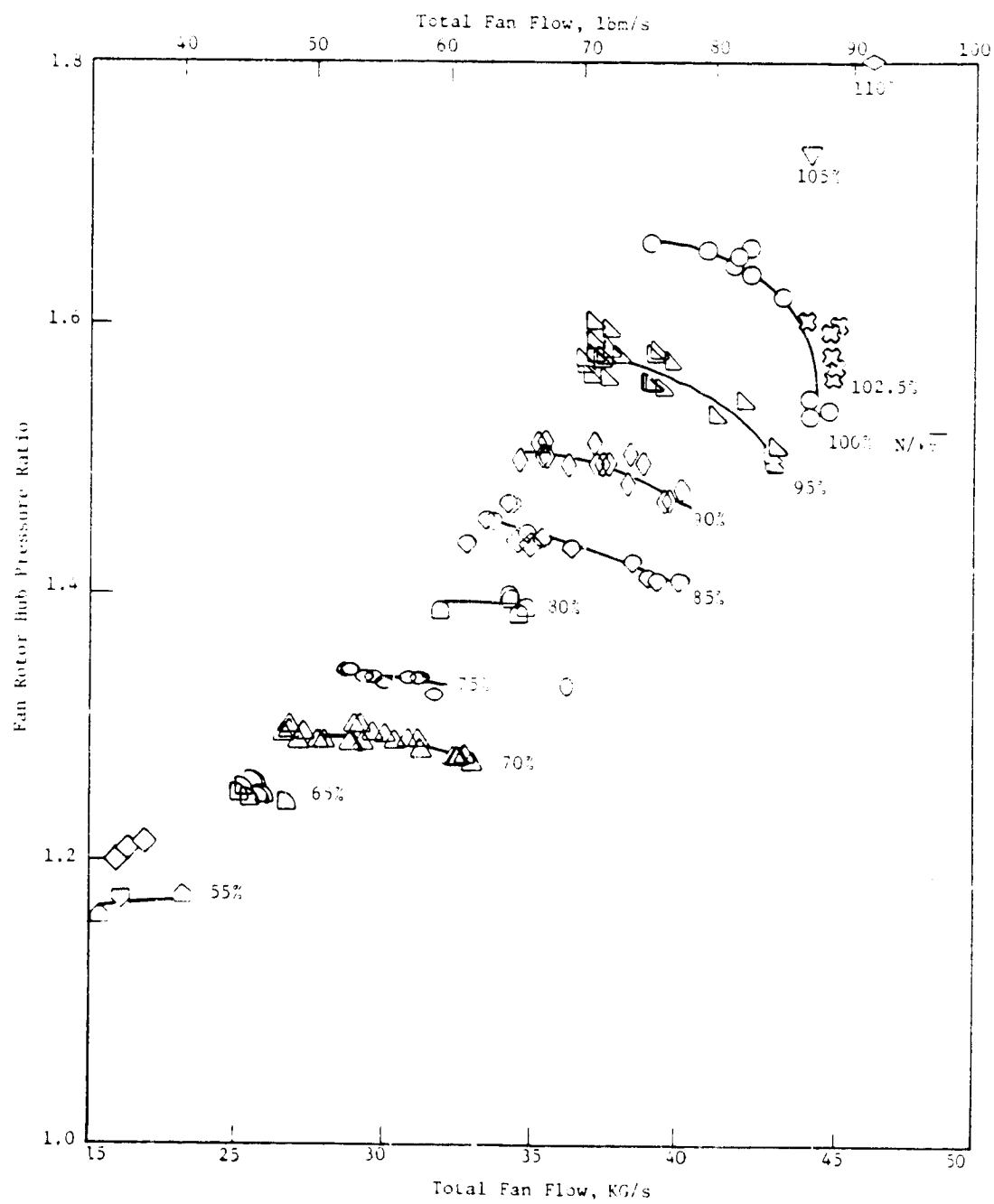


Figure 24. NASA Rotating Rig Fan Rotor Hub Performance Map.

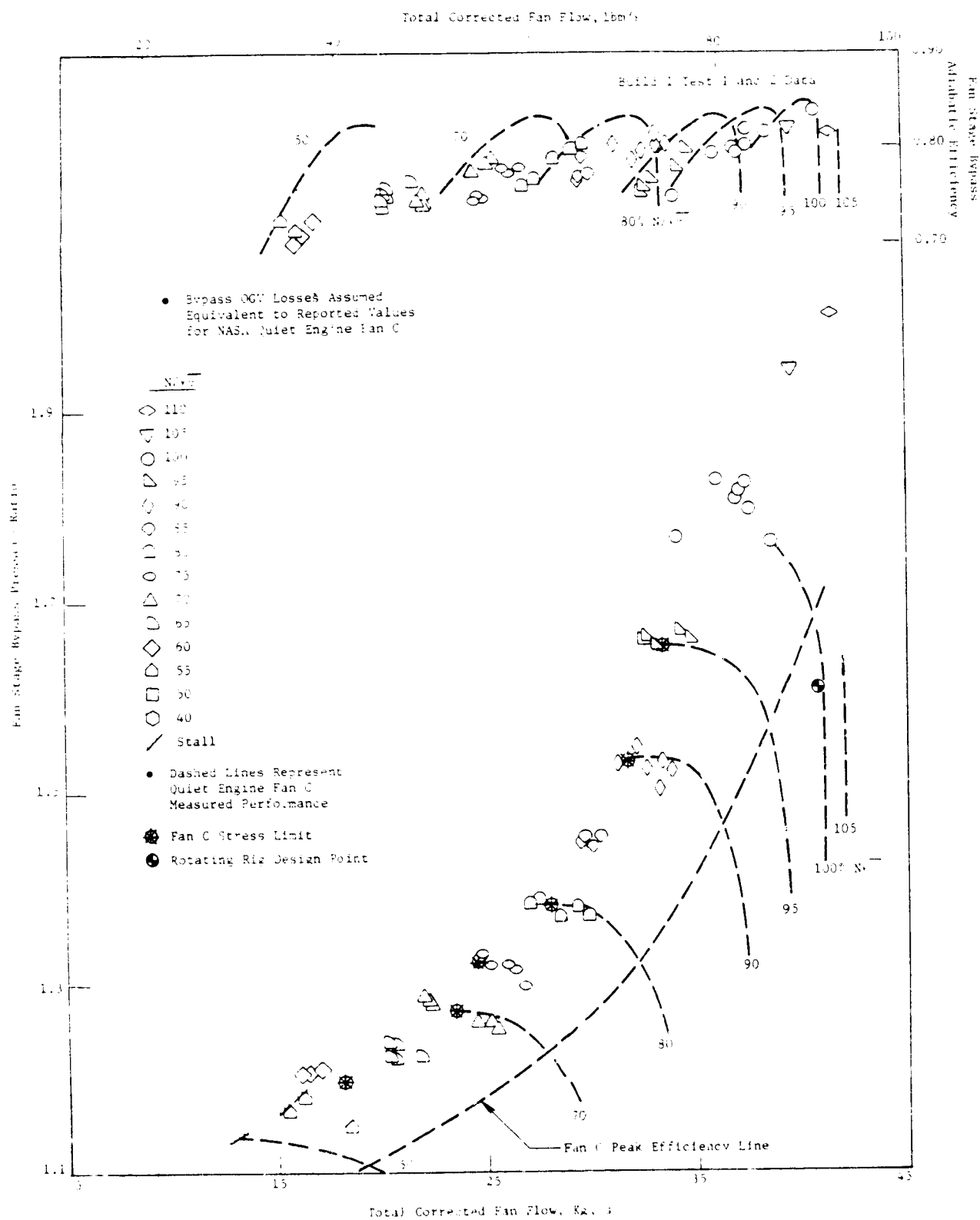


Figure 25. NASA Fan Stage Performance Map.

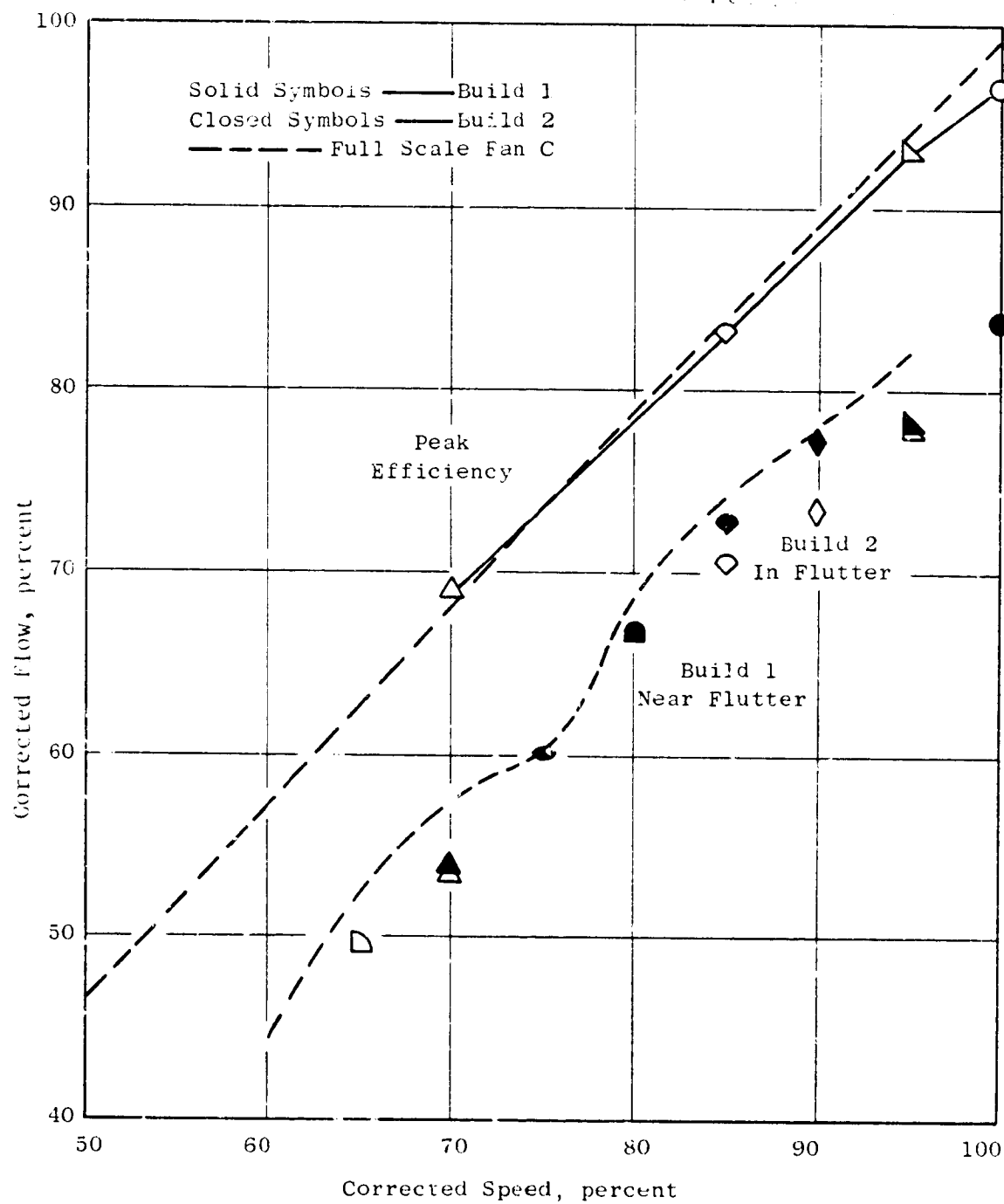


Figure 26. NASA Rotating Rig Speed-Flow Characteristics.

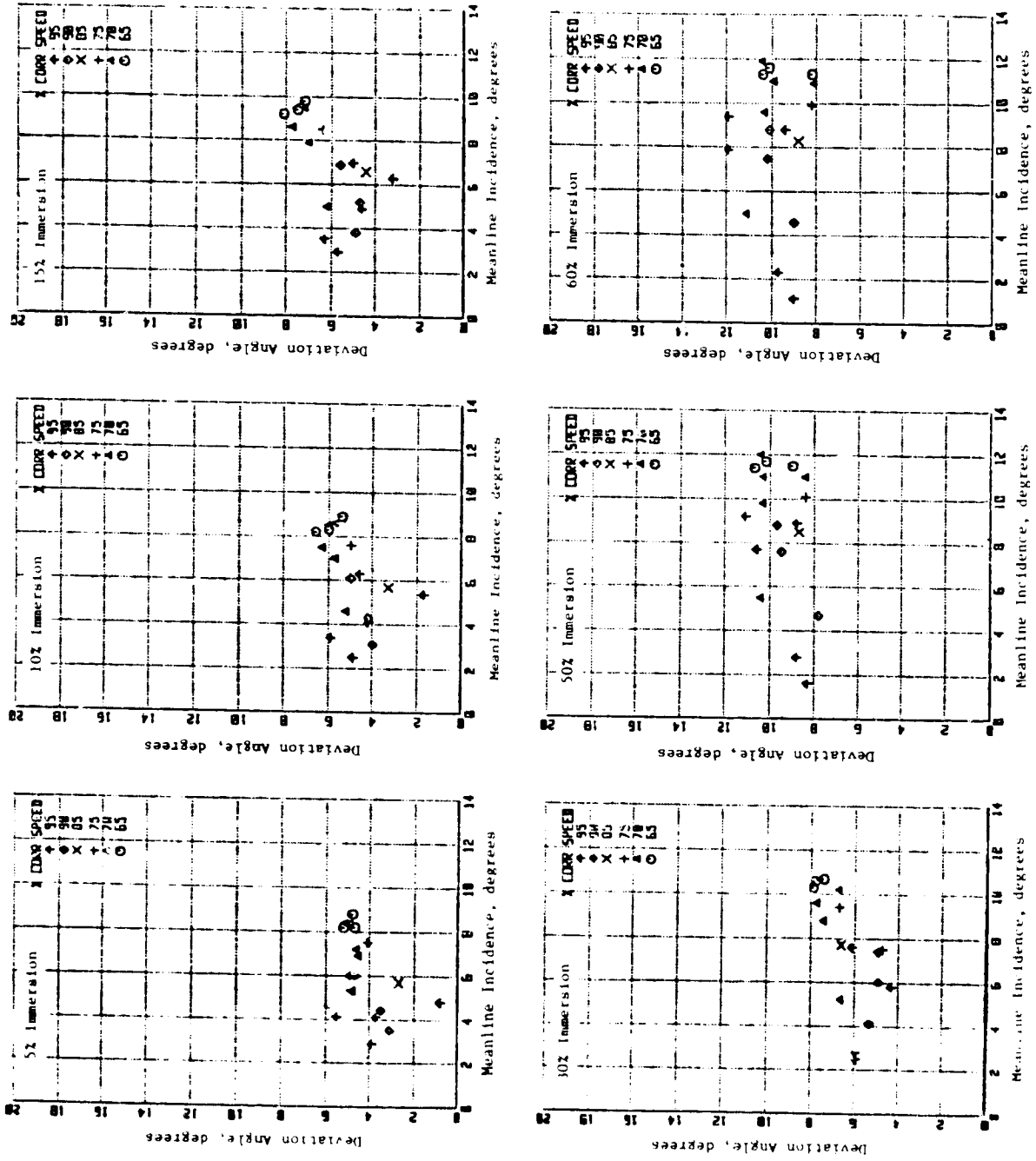


Figure 27. Bypass Flow Deviation Angle Versus Untwisted Incidence.

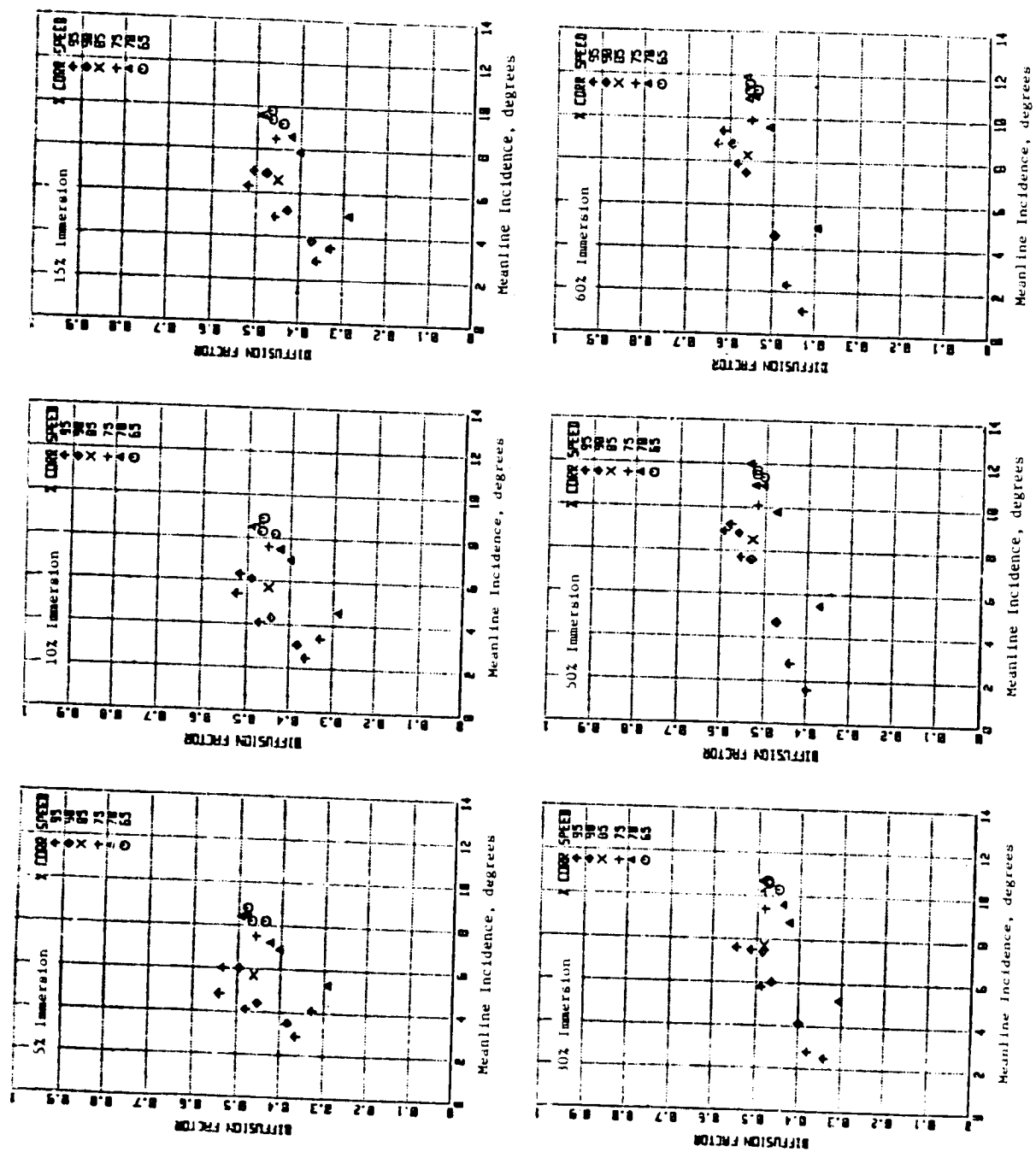


Figure 28. Bypass Flow Diffusion Factor Versus Untwisted Incidence.

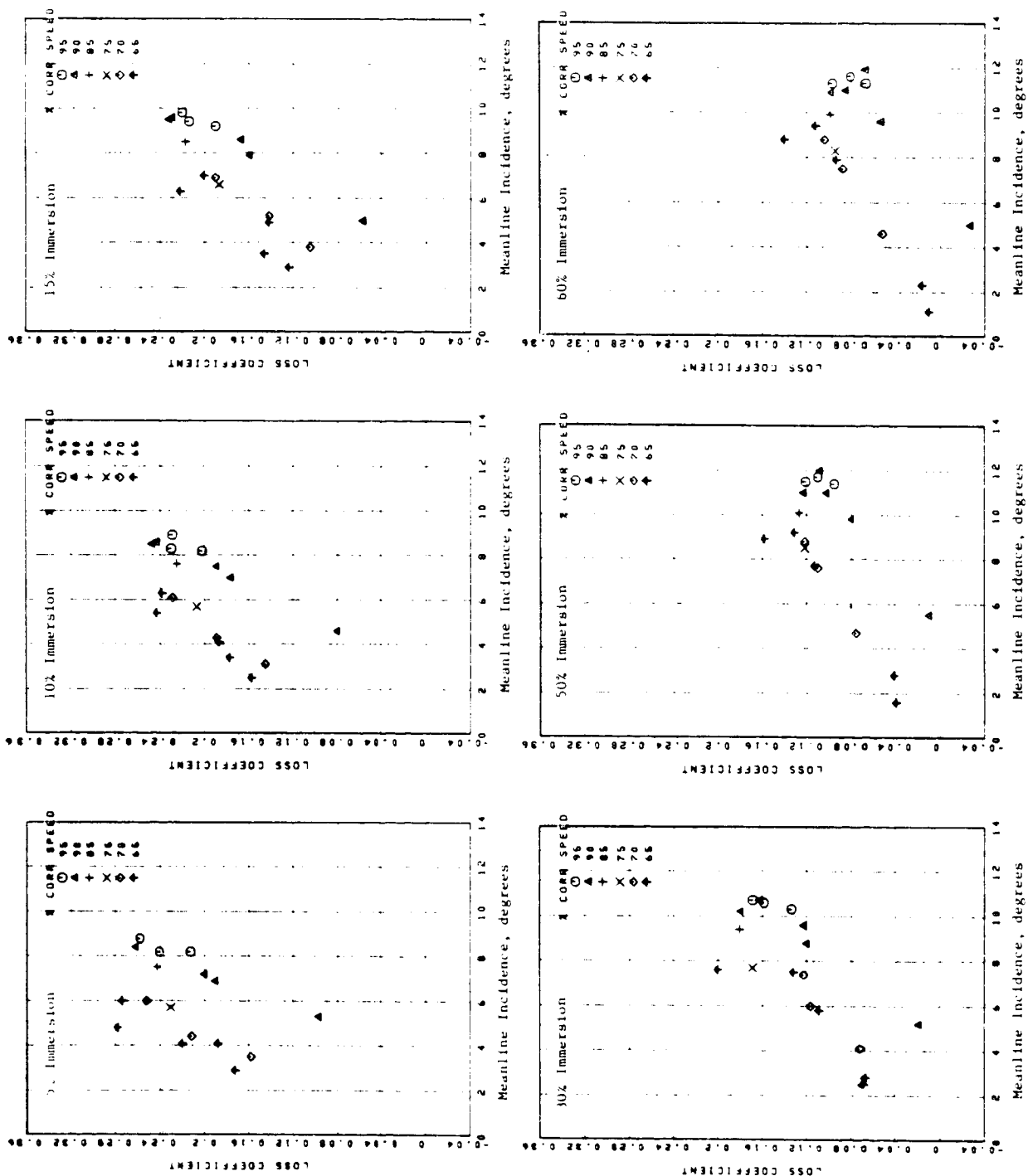


Figure 29. Bypass Flow Loss Coefficient Versus Untwisted Incidence.

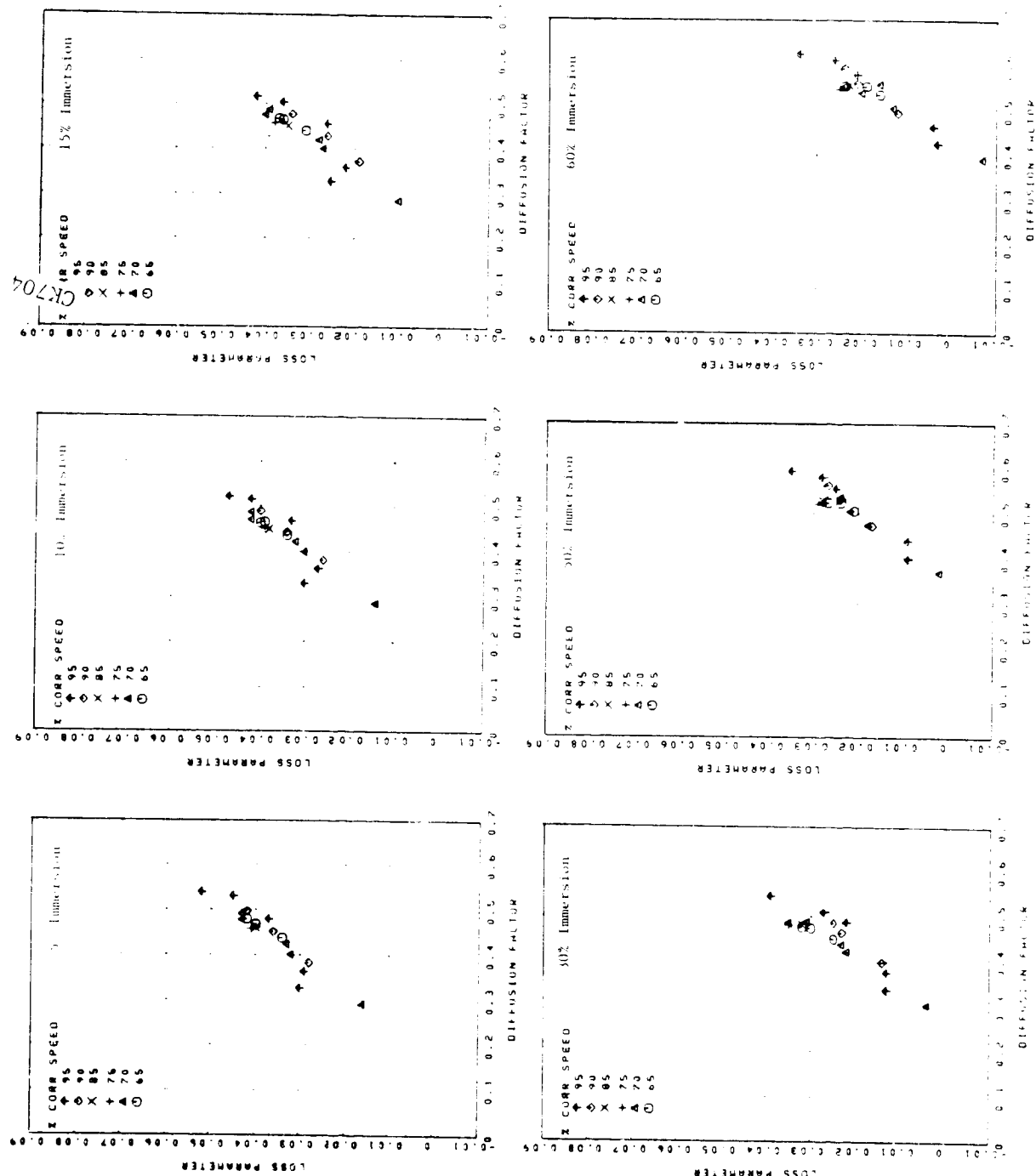


Figure 30. Bypass Flow Loss Parameter Versus Diffusion Factor.

6.2 BLADE DYNAMIC STRAIN GAGE DATA

The ten aerodynamic operational conditions at which steady and unsteady measurements were taken are shown in Figure 2. The operating parameters are summarized in Table XIV. All 26 blades in the rotor were instrumented with dynamic strain gages, although not all gages could be monitored and recorded for each test. Blade mounted hot films and kulites limited leadout capabilities through the 100 point slip ring. Usually, twelve to nineteen gages were monitored during the three tests, excluding failed gages. The data obtained, on a continuous basis, from blade strain gages include vibratory stresses, frequencies, and interblade phase angles.

6.2.1 Bench Test Frequencies

Figure 31 shows the bench (laboratory, zero speed) test blade frequencies and their disposition around the rotor as tested in Build 2. Since all blade bench test frequencies were within 2 percent of the average measured flexural frequency and within 2 percent of the average measured torsional frequency, no effort was made to selectively arrange the blades in the rotor.

6.2.2 Flutter Frequency Response

At the nominal and intermediate operating lines (NOL and IOL), as defined in Section 6.1.1 (Figure 23), the rotor blades responded predominantly at their individual natural blade frequencies. These frequencies varied from blade-to-blade. A typical Campbell diagram is shown in Figure 32 for a nominal operating line accel from 2000 rpm to 18500 rpm. As can be seen, the vibratory stress amplitudes were very low throughout the speed range with the maximum response at the second flexural mode - 3/rev cross-over where stresses reached about 5.5 kN/cm²-da (8 ksi-da). As the fan was throttled from the nominal to the intermediate operating line at 70 percent and 90 percent speeds. Some of the airfoils experienced a slight frequency shift while other airfoils did not experience any frequency change at all. Shifting of the natural frequency seems to be independent of the mode as shown in Figures 33 and 34.

Throttling further to the flutter boundary, aerodynamic coupling appears to drive all the blades at a common flutter frequency. This is shown in Figure 33 for the torsional flutter mode at 65 and 70 percent speeds and in Figure 34 for the flexural flutter mode at 90 and 95 percent speeds. A significant increase in the flutter frequency between 90 to 95 percent speed is observed due to the centrifugal stiffening effect on the bending mode, see Figure 32. As expected, centrifugal stiffening did not have a significant effect on the torsional mode.

6.2.3 Flutter Vibratory Stress Amplitude

In this program, flutter was identified primarily by strain gage response which provided flutter frequencies and vibratory stress amplitudes. Data points, at which steady and unsteady flutter measurements were made, were

Table XIV. NASA Rotating Rig Data Point Summary.

Reading	Speed		Pressure Ratio	Bypass Ratio	Corrected Flow		Operating Line
	%	rpm			(kg/sec)	(lbm/sec)	
159	65	10793	1.249	4.65	20.85	(45.96)	Int
80	65	10836	1.257	5.14	20.58	(45.37)	F
155	70	11601	1.280	4.71	23.87	(52.62)	Nom
180	70	11601	1.292	5.12	22.80	(50.27)	Int
89	70	11654	1.308	5.03	21.90	(48.28)	F
174	90	14906	1.501	5.16	34.70	(76.50)	Nom
175	90	14919	1.552	4.88	32.50	(71.66)	Int
168	90	14892	1.577	4.85	30.46	(67.16)	F
152	95	15751	1.667	5.15	33.89	(74.72)	Int
148	95	15769	1.685	4.86	31.74	(69.97)	F

Table XV. Blade Vibratory Stress and Phase Lag Summary
for the Four Flutter Points.

Slot No.	Item No.	Percent Speed							
		65		70		90		95	
		Stress	ϕ (deg)	Stress	ϕ (deg)	Stress	ϕ (deg)	Stress	ϕ (deg)
1	832	0.055	0	0.070	187				
2	833	0.065	306	0.070	212	0.116	274	0.063	127
3	805			0.100	0	0.175	311	0.072	207
4	807								
5	808								
6	809			0.200	140				
7	810			0.245	191	0.221	114	0.093	103
8	811			0.215	130	0.162	132	0.110	100
9	812								
10	813			0.190	90				
11	814								
12	815	0.195	54					0.337	---
13	816					0.194	214	0.275	169
14	834	0.110	312			0.213	271	0.321	235
15	835	0.058	274	0.073	68				
16	820	0.120	238	0.145	68	0.360	331	0.570	311
17	822			0.130	72	0.359	0	0.512	0
18	823			0.145	144				
19	824								
20	825	0.050	162	0.067	216	0.240	304	0.331	335
21	826	0.060	180	0.071	209	0.187	159	0.025	188
22	827	0.135	256	0.055	83	0.215	196	0.246	228
23	828	0.115	259	0.110	86	0.202	222	0.223	252
24	829			0.150	115	0.151	243	0.145	280
25	830			0.065	148	0.118	256	0.089	276
26	831	0.100	252	0.085	194	0.079	281	0.061	340

Note: ϕ = Phase Lag

• Stress normalized to 68.94 kN/cm² (100.0 ksi)

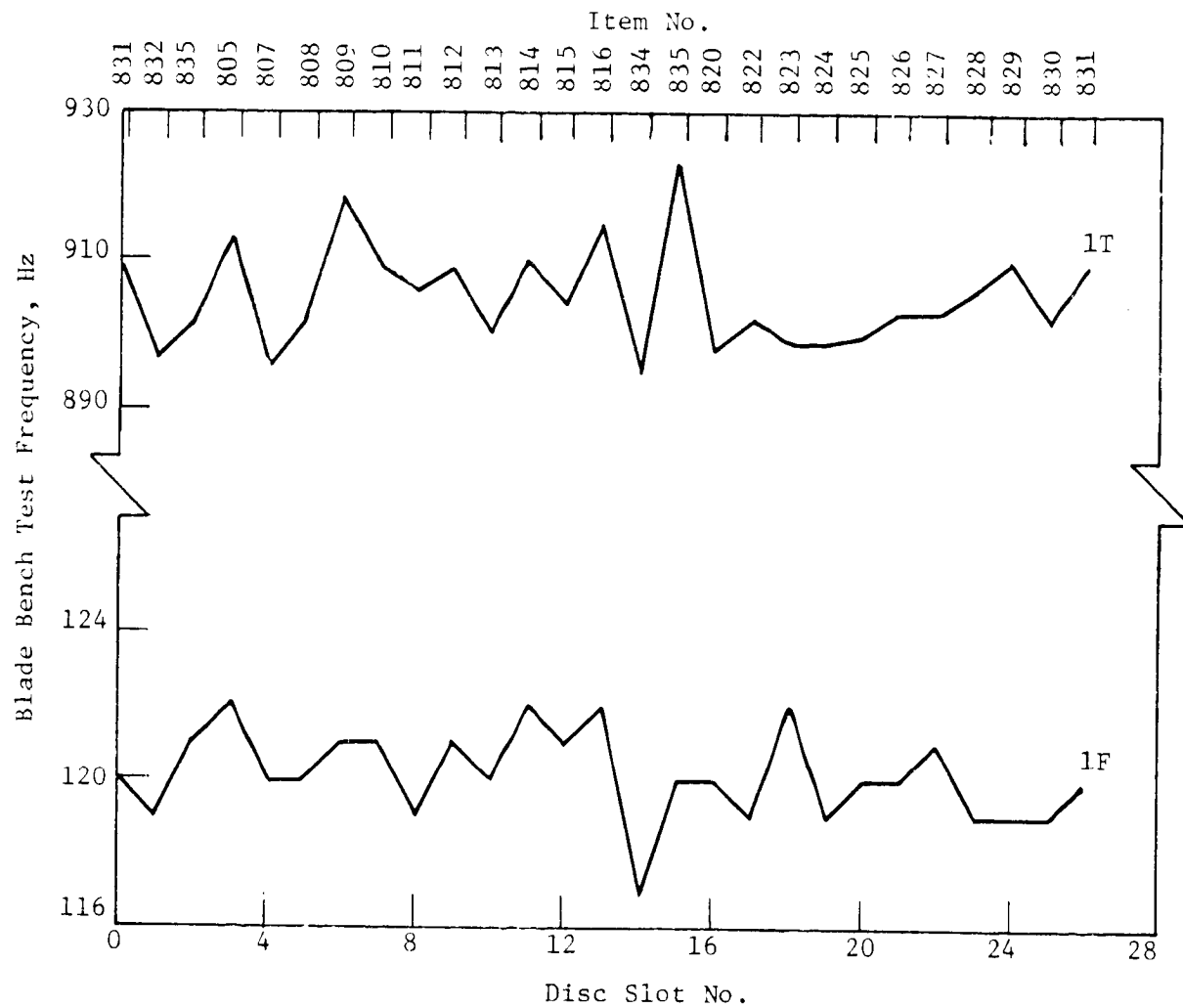


Figure 31. Blade Bench Test Frequency Variation Around the Rotor - Build 2.

ORIGINAL PAGE IS
OF POOR QUALITY

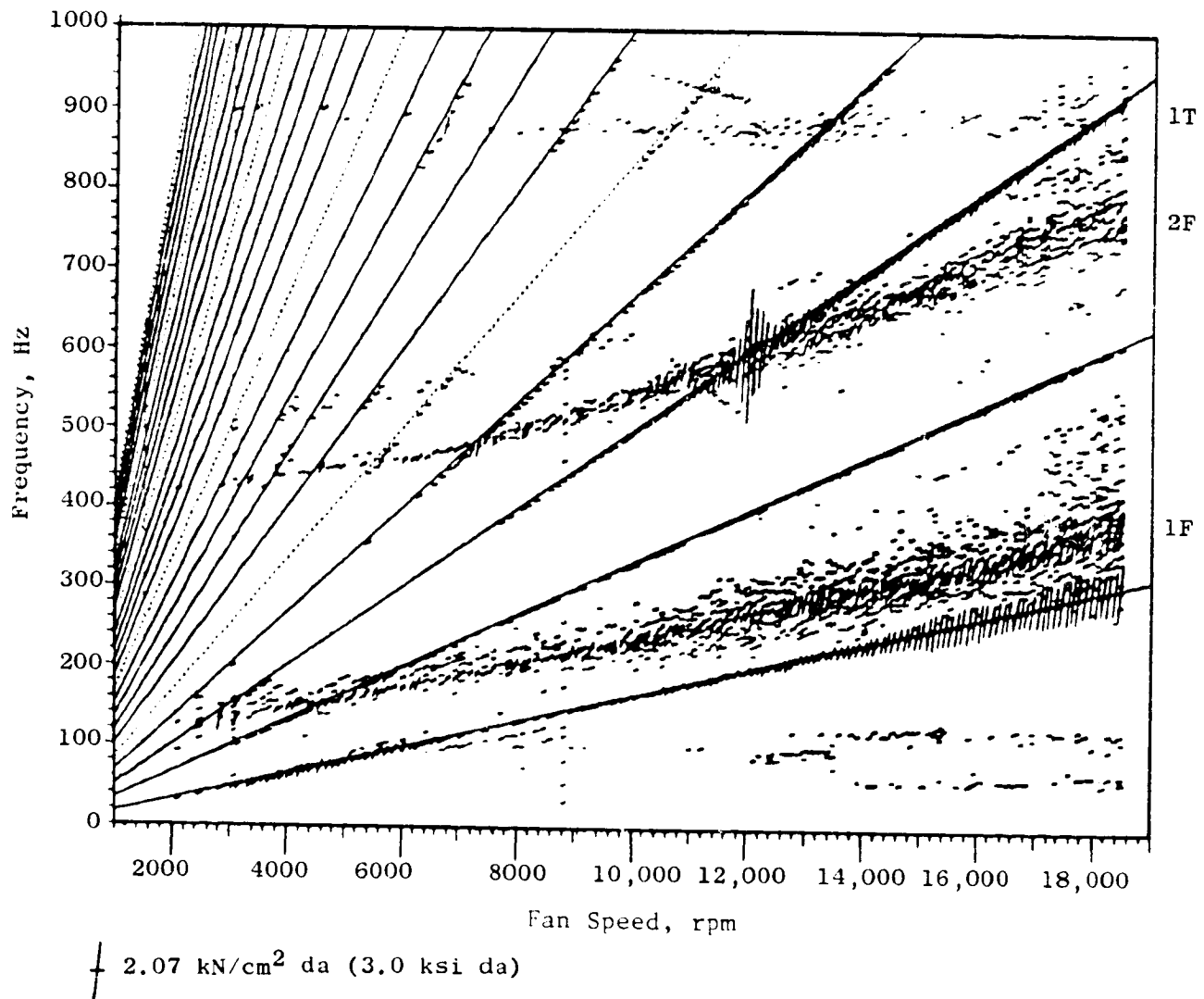


Figure 32. Rotating Rig Campbell Diagram.

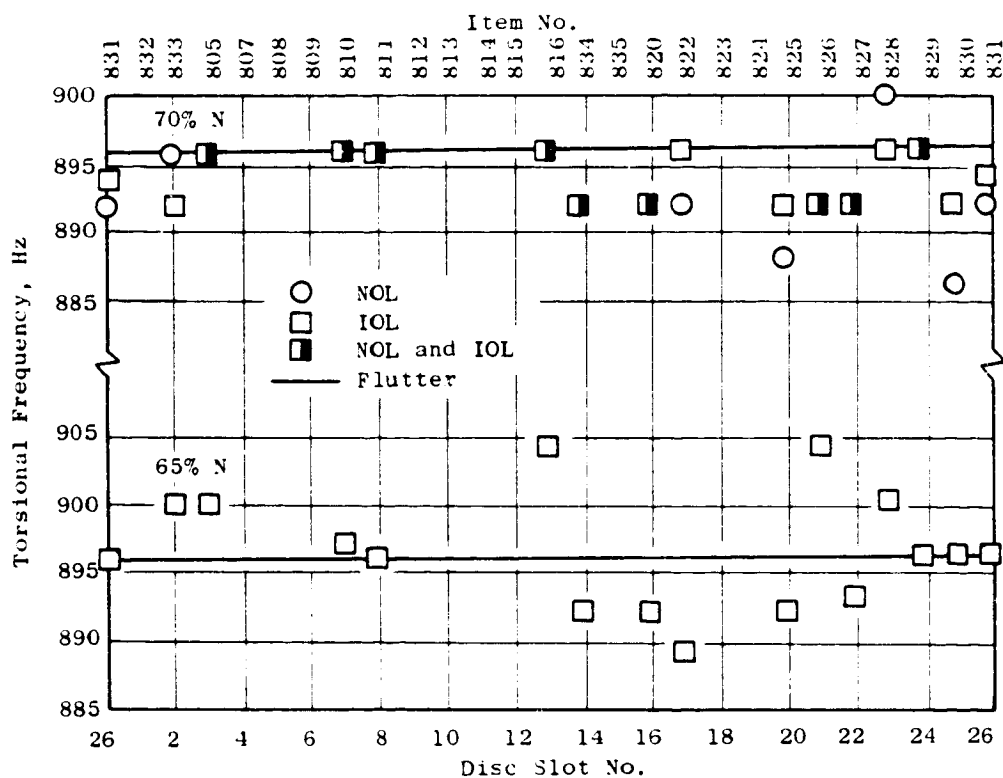


Figure 33. Blade Torsional Response Frequencies.

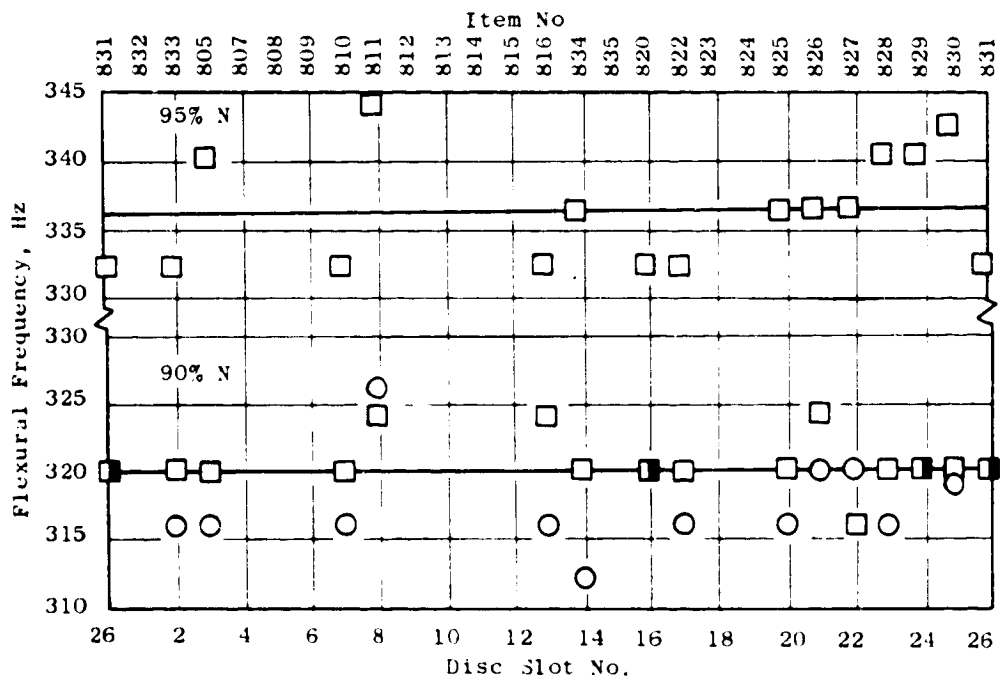


Figure 34. Blade Flexural Response Frequencies.

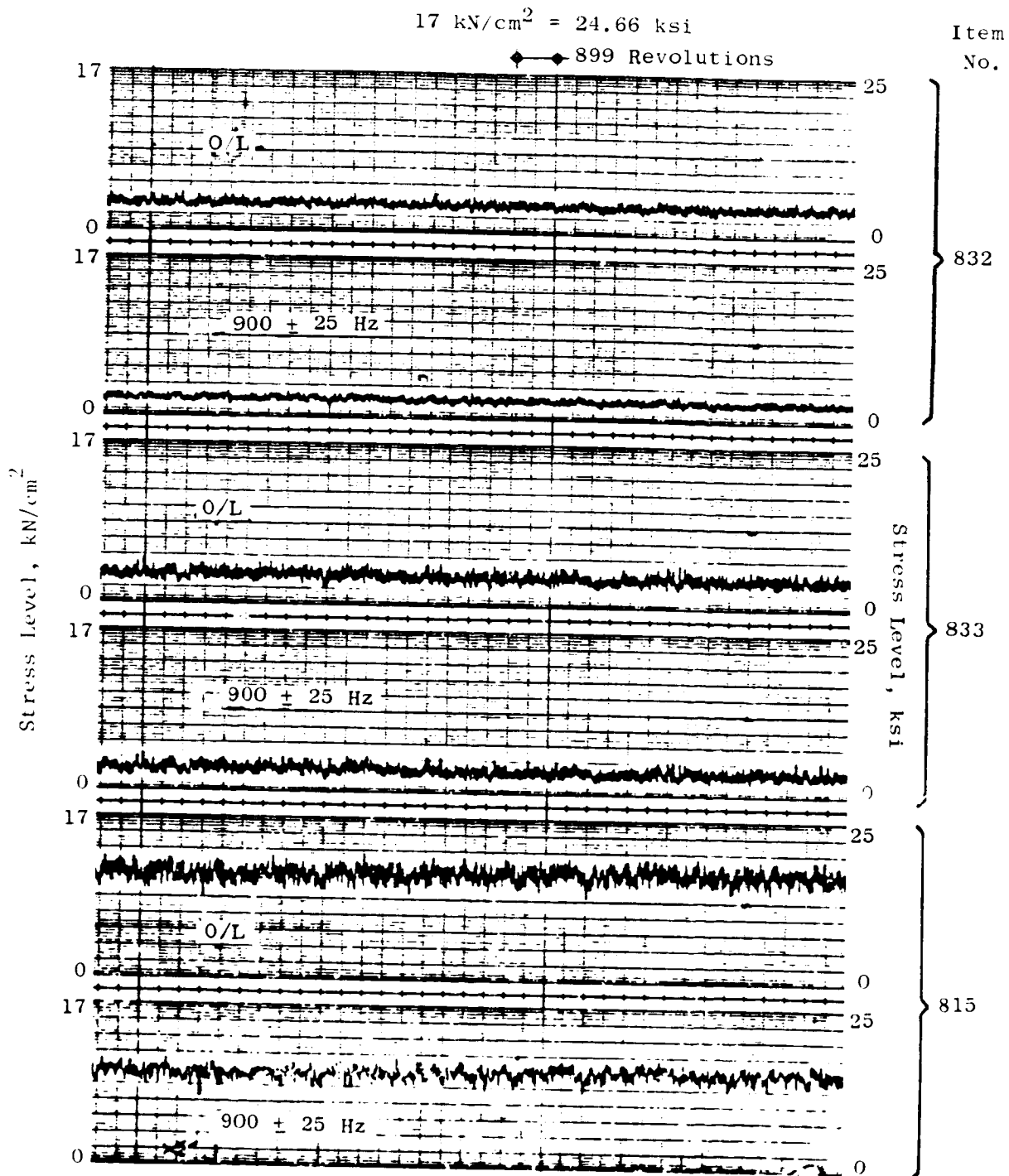
determined by the stress amplitudes at the flutter frequency. The intent was to have all the blades responding at relatively high amplitudes in flutter, but without exceeding the established fatigue limits. Figures 35 through 38 show the time histories of the overall peak-to-peak stress amplitudes and filtered peak-to-peak amplitudes at their respective flutter frequencies. Filtered flutter frequencies are 900 ± 25 Hz for the 65 and 70 percent speeds (Figures 35 and 36) and 320 ± 10 Hz at 90 and 95 percent speeds (Figures 37 and 38). These time histories show that most of the overall signal is at the flutter frequency. As Figures 35 through 38 show, the stress amplitudes increased quite rapidly at flutter onset, indicating a rapid decrease in the system's aerodynamic damping. At 65 percent speed, Figure 35, the amplitudes are relatively constant and the overall signal does contain some second flex/3 per rev resonance response as shown in Figure 32 at about 11,600 rpm. At 70 percent speed, Figure 36, the stress amplitudes fluctuate considerably as the onset of torsional flutter is reached, becoming less erratic after a few seconds of stabilization. For bending flutter, Figures 37 and 38, the vibratory stress amplitudes of most of the rotor blades fluctuate drastically as a function of time. This variation in amplitude with time was initiated at flutter onset and continued until the operating condition was changed, i.e., until the discharge valve was opened to lower the operating line. Separated flow vibration was essentially nonexistent on this fan even at conditions close to flutter onset. Occasionally, the blades were driven in and out of flutter, especially at 90 percent speed (Figure 37). Throttling the fan further into flutter was impractical since the blade stresses were fluctuating up to the blade's fatigue limits.

From the time histories, amplitude variations of overall and filtered levels around the rotor were obtained at a specific time for each of the four speed lines at the ten special data points. (See Figures 39 through 42.) Stress amplitudes on the nominal and intermediate operating lines were relatively low, with some blade-to-blade variation. At the flutter conditions, whether bending or torsion, the stress amplitudes were relatively high, with some blades reaching fatigue limits. Also, a large variation in blade-to-blade stress amplitudes was observed with the maximum response blade being different for each speed. This shows that it could be dangerous to test a fan or any blade row with only a few strain gaged blades. The instrumented blade could be a low response blade while other nonstrain gaged blades in the rotor could be responding at stress levels above fatigue limits.

The blade-to-blade stress amplitude variation in flutter, for the four speeds tested, is an indication of the existence of more than one traveling wave in the rotor which is probably due to the effects of mistuning.

6.2.4 Interblade Phase Angles

Interblade phase angles relative to a reference blade were determined for all the available strain gage data with two data analysis methods: analog phasemeter and cross spectral analysis. Examples of each are shown in Figures 43 through 45. Figure 43 illustrates that a constant phase angle exists



$$17 \text{ kN/cm}^2 = 24.66 \text{ ksi}$$

Item
No.

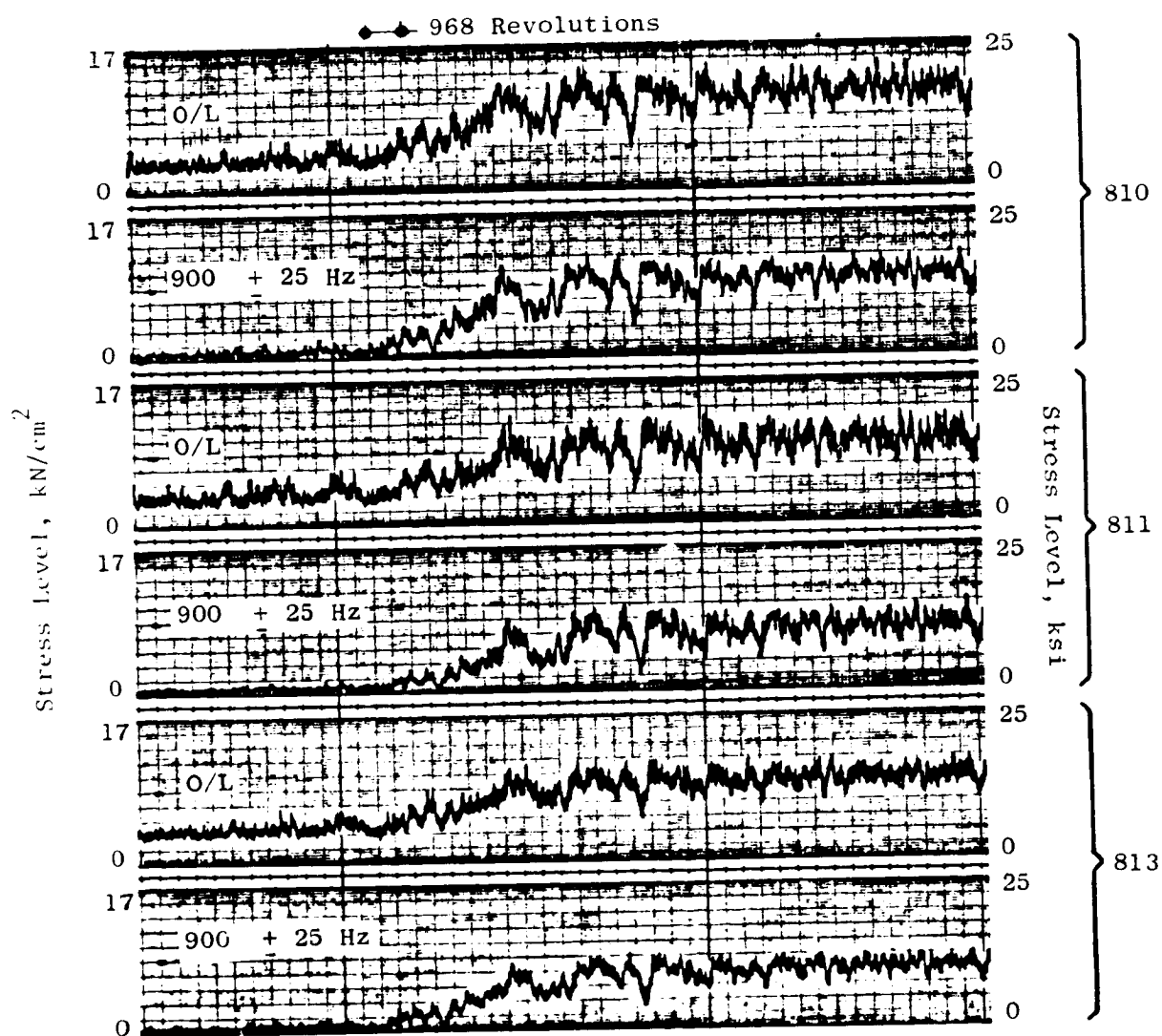


Figure 36. Overall and Filtered Strain Gage Signals During Transient to Torsional Flutter at 70 Percent Speed.

$$49 \text{ kN/cm}^2 = 49.32 \text{ ksi}$$

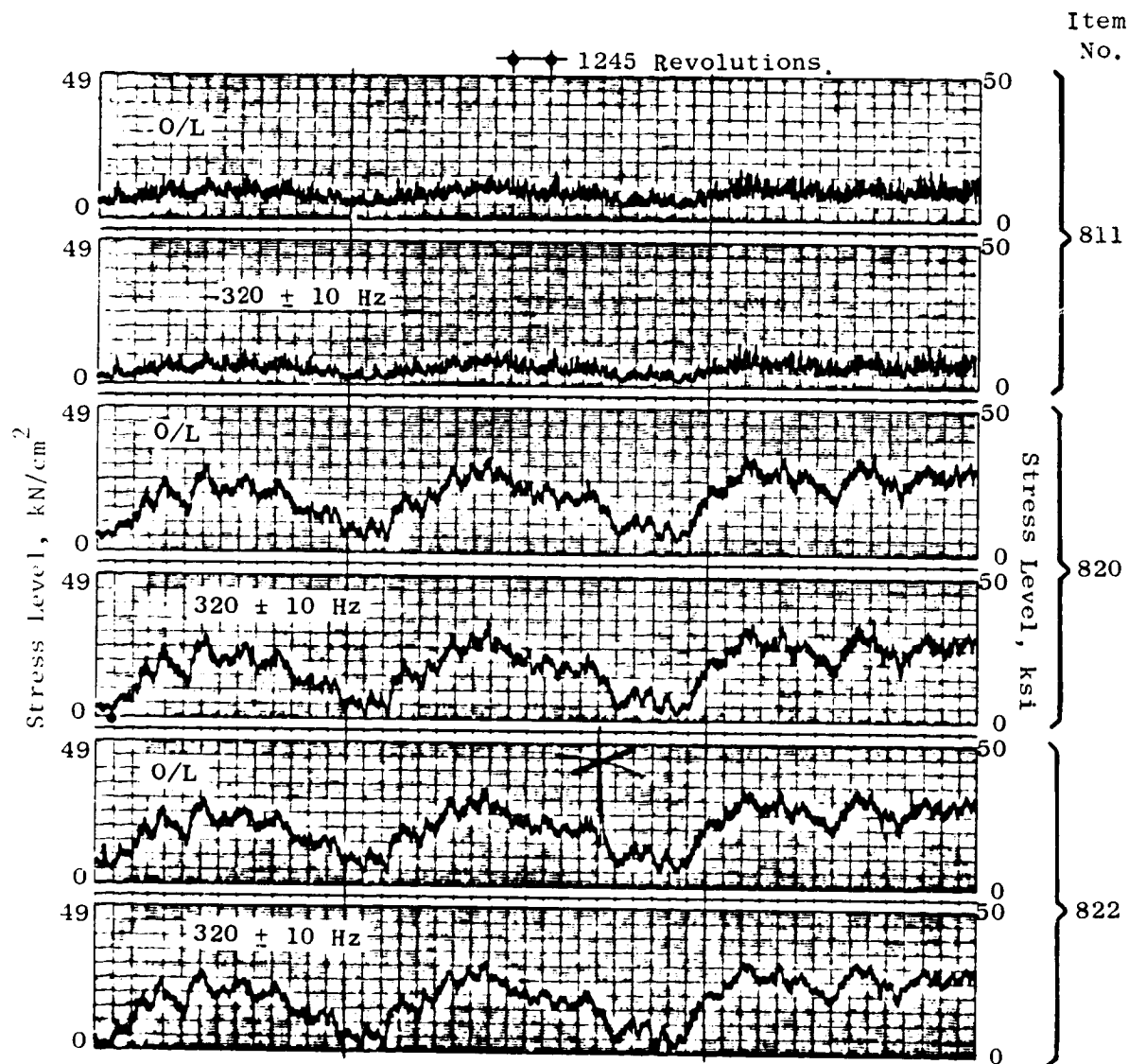


Figure 37. Overall and Filtered Strain Gage Signals During Flexural Flutter at 90 Percent Speed.

49 kN/cm² = 49.32 ksi

Item
No.

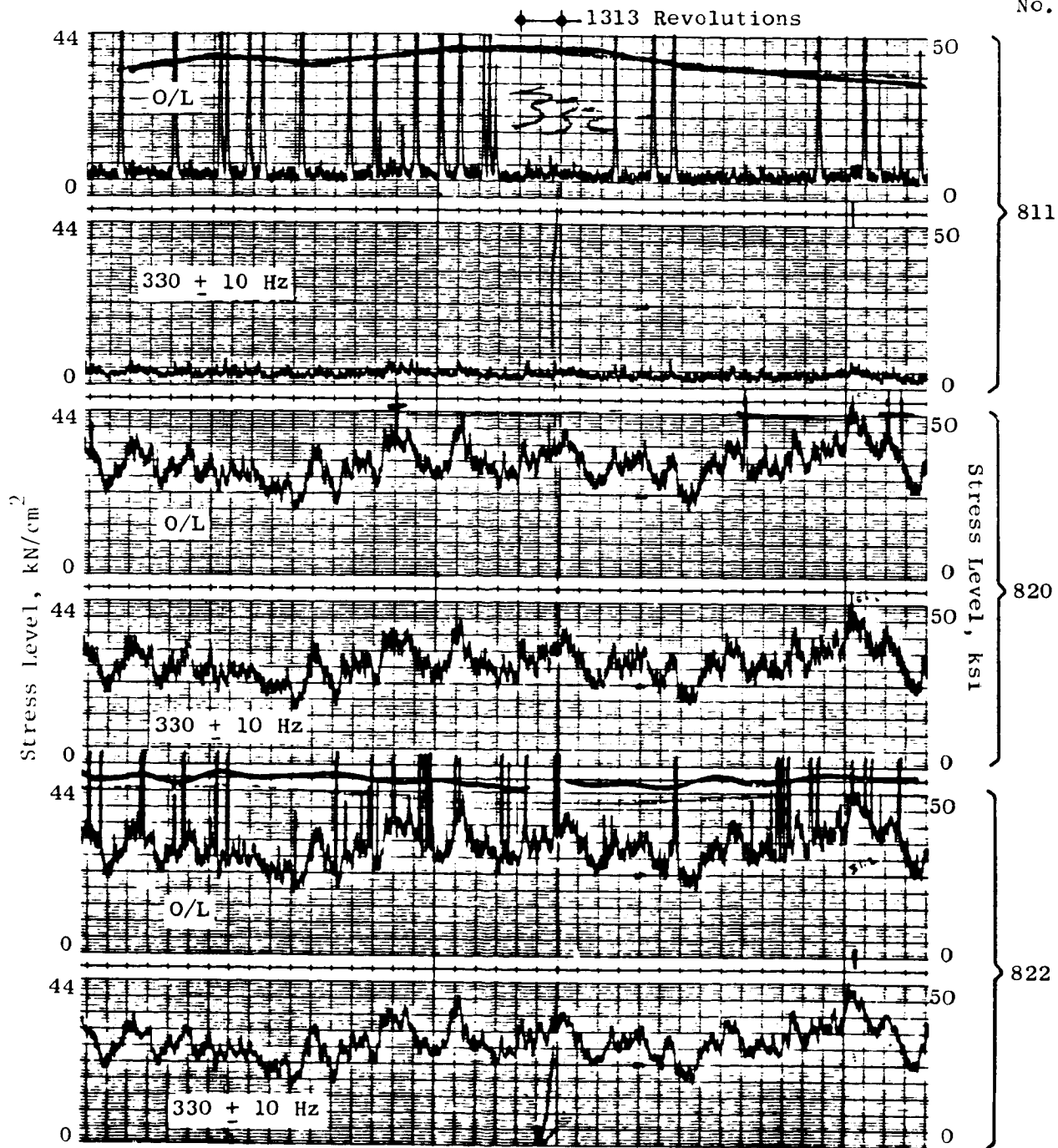


Figure 38. Overall and Filtered Strain Gage Signals During Flexural Flutter at 95 Percent Speed.

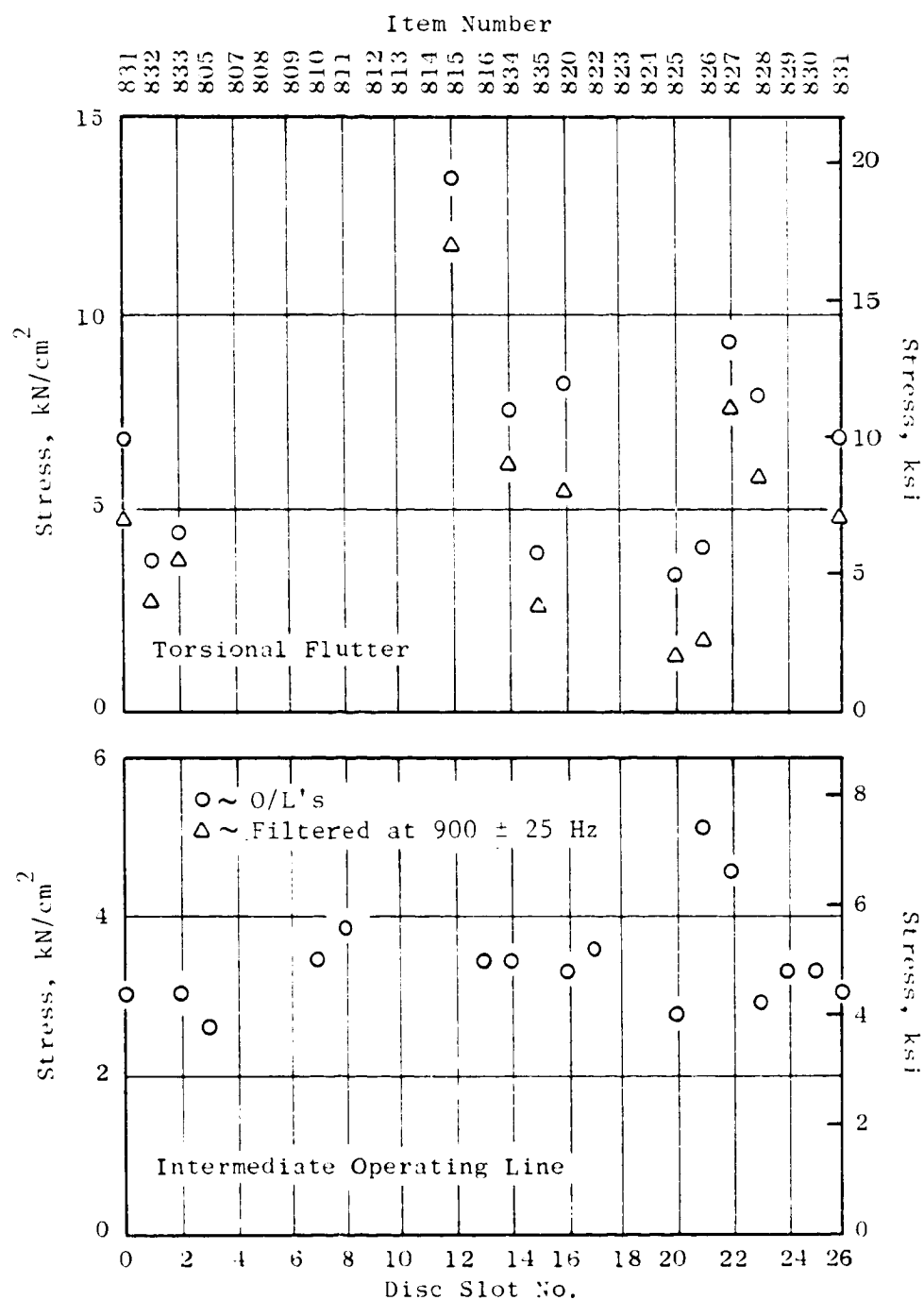


Figure 39. Circumferential Variations of Blade Stress at 65 Percent Speed.

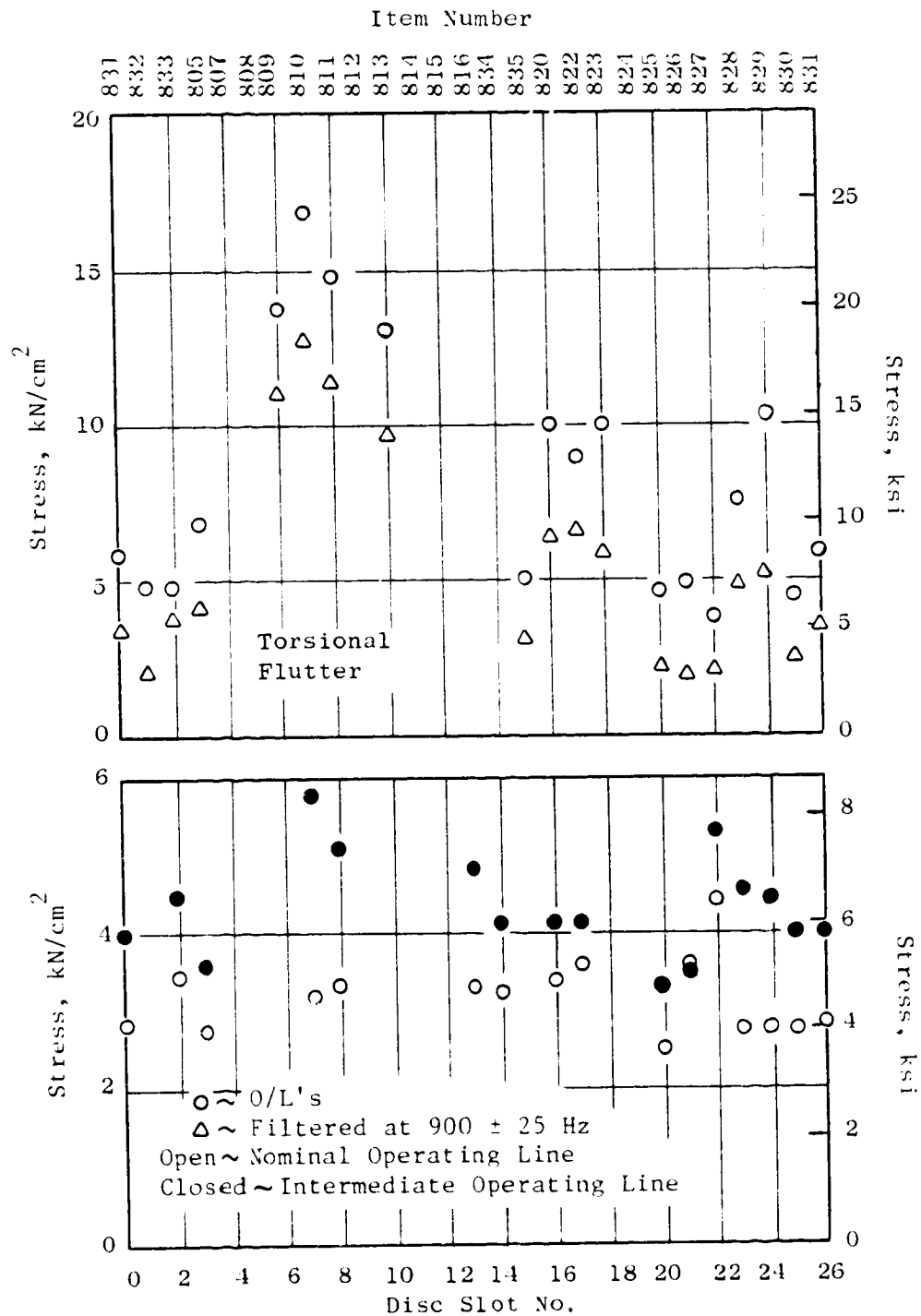


Figure 40. Circumferential Variation of Blade Stress at 70 Percent Speed

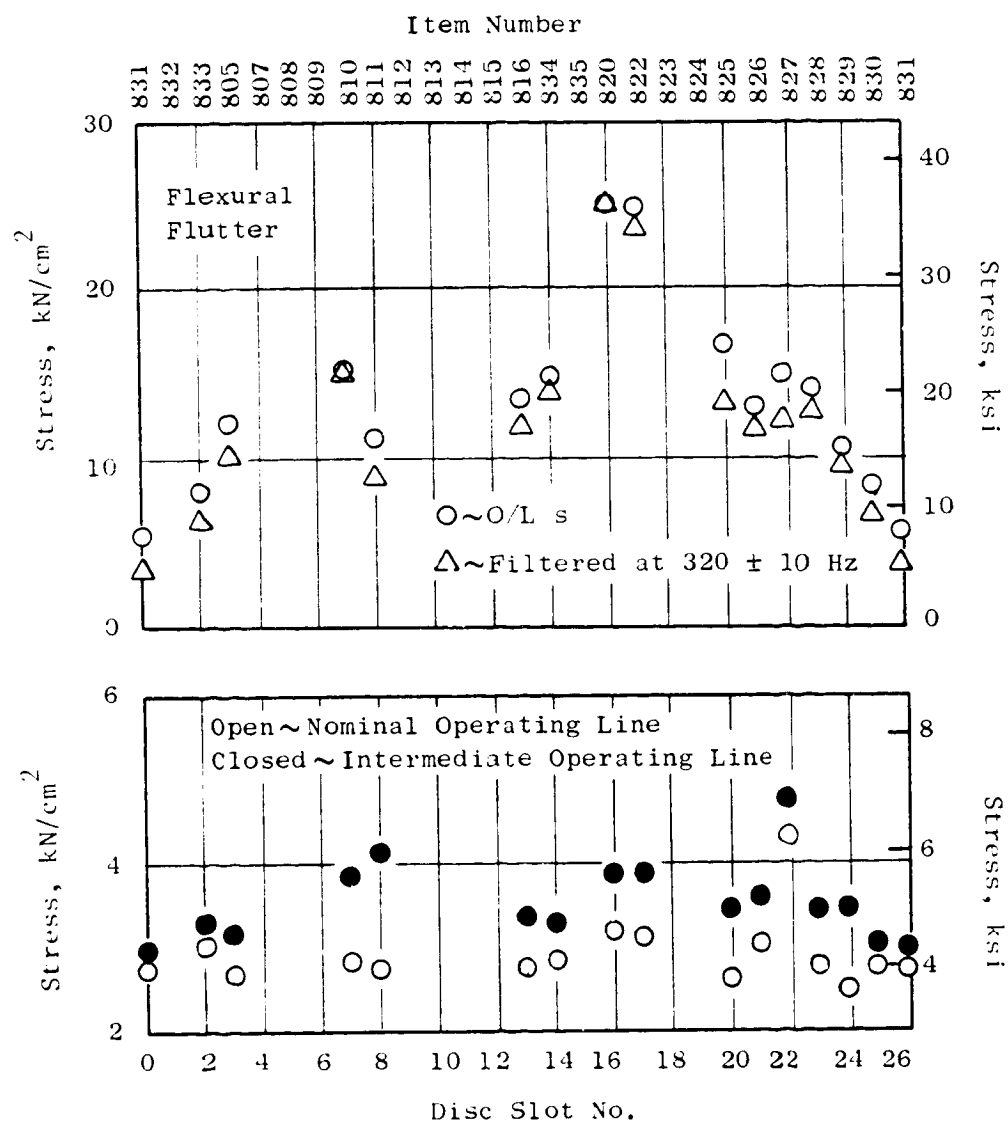


Figure 41. Circumferential Variation of Blade Stress at 90 Percent Speed.

CHINA OF PEOPLE'S

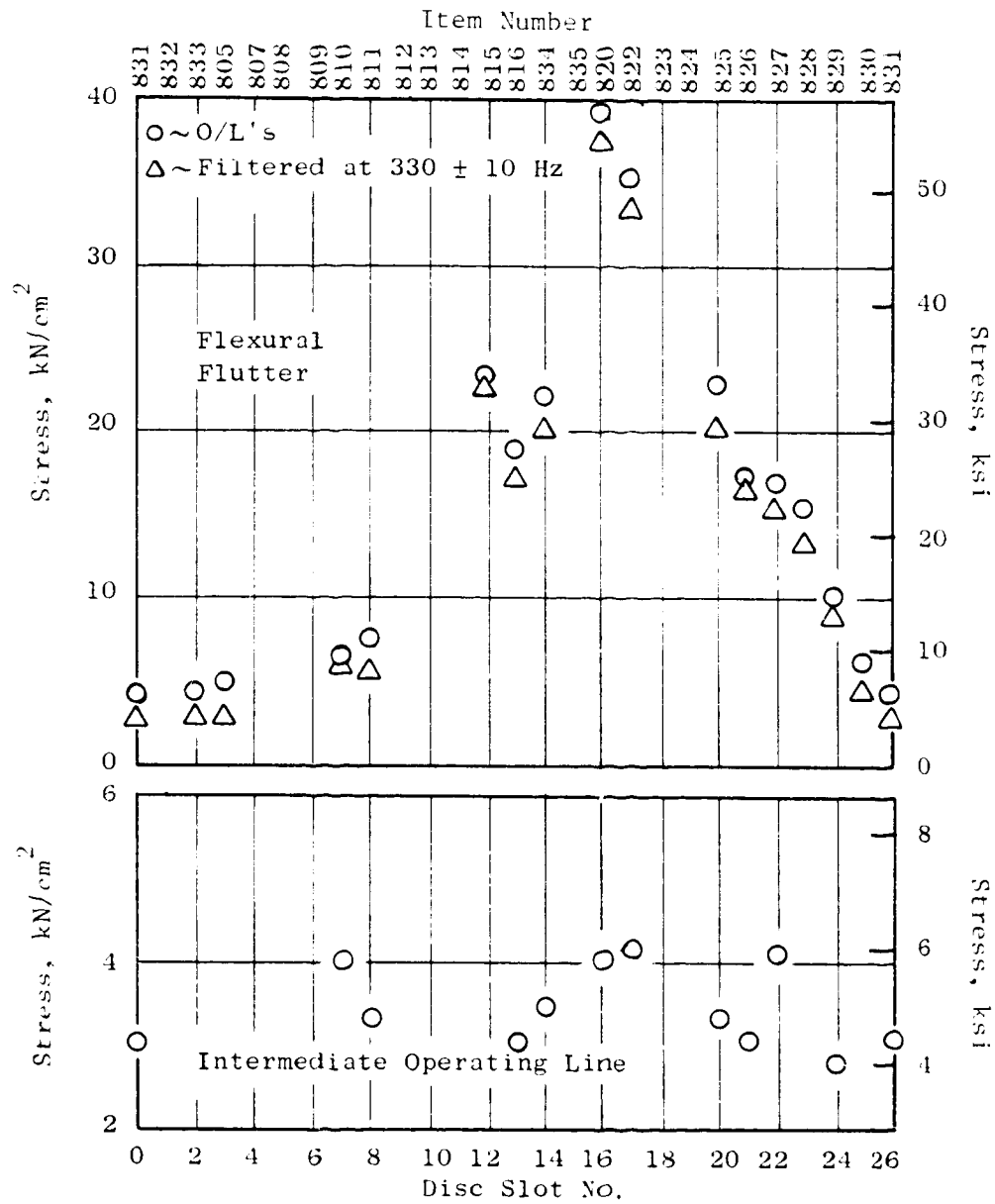


Figure 42. Circumferential Variation of Blade Stress at 95 Percent Speed.

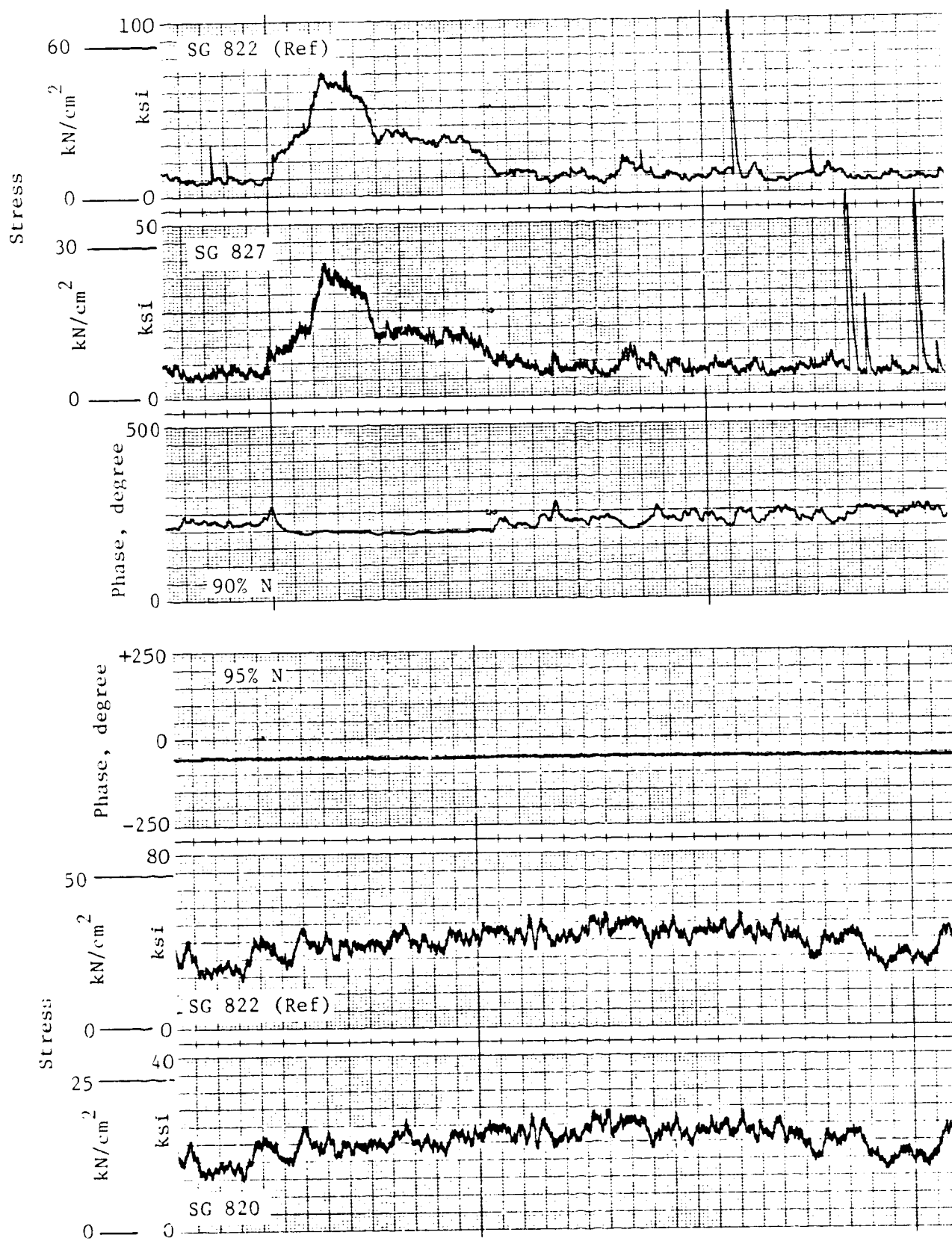


Figure 43. Phasemeter Strain Gage Phasing.

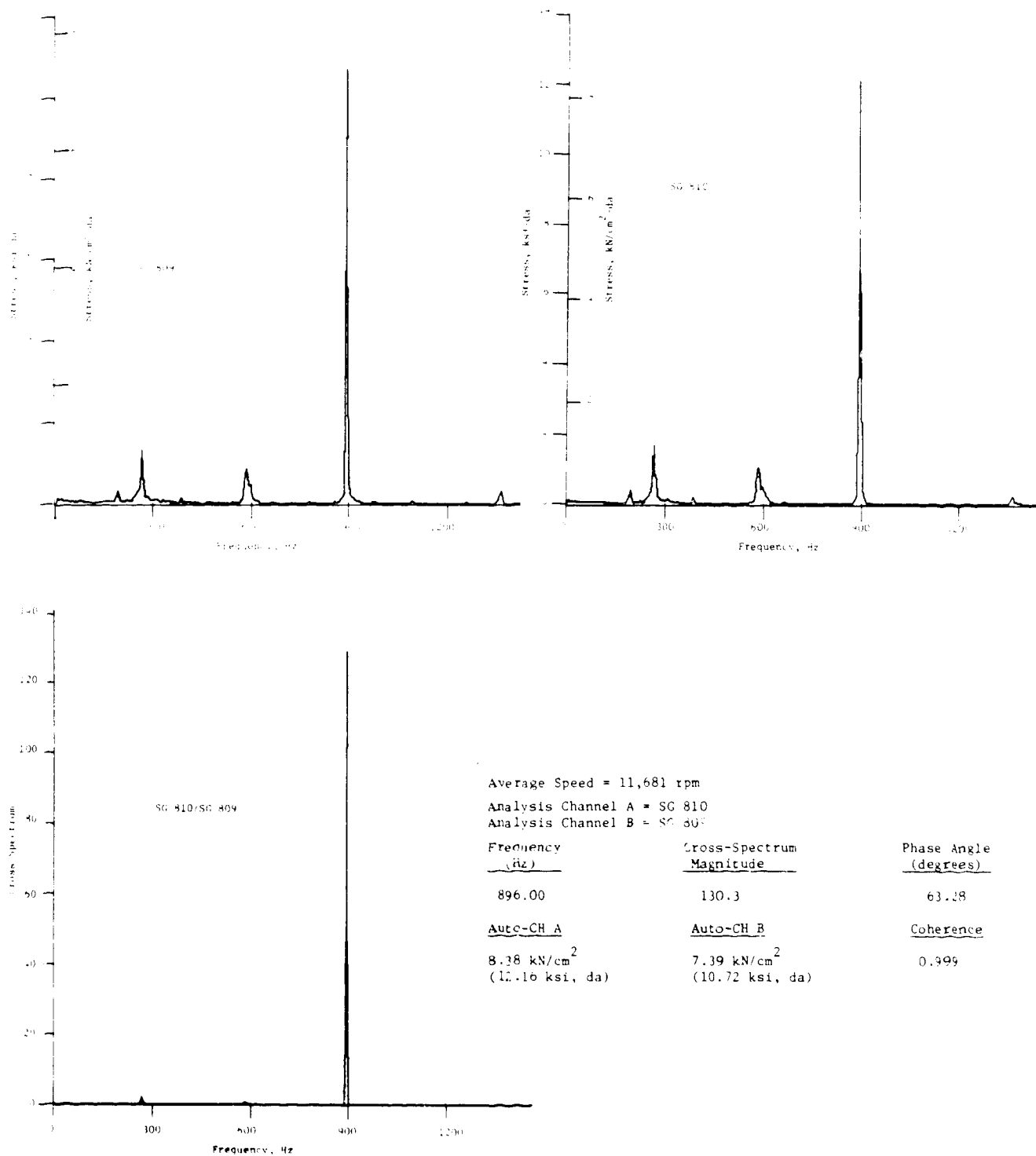


Figure 44. FFT Cross Spectral Analysis at 70 Percent Speed Flutter.

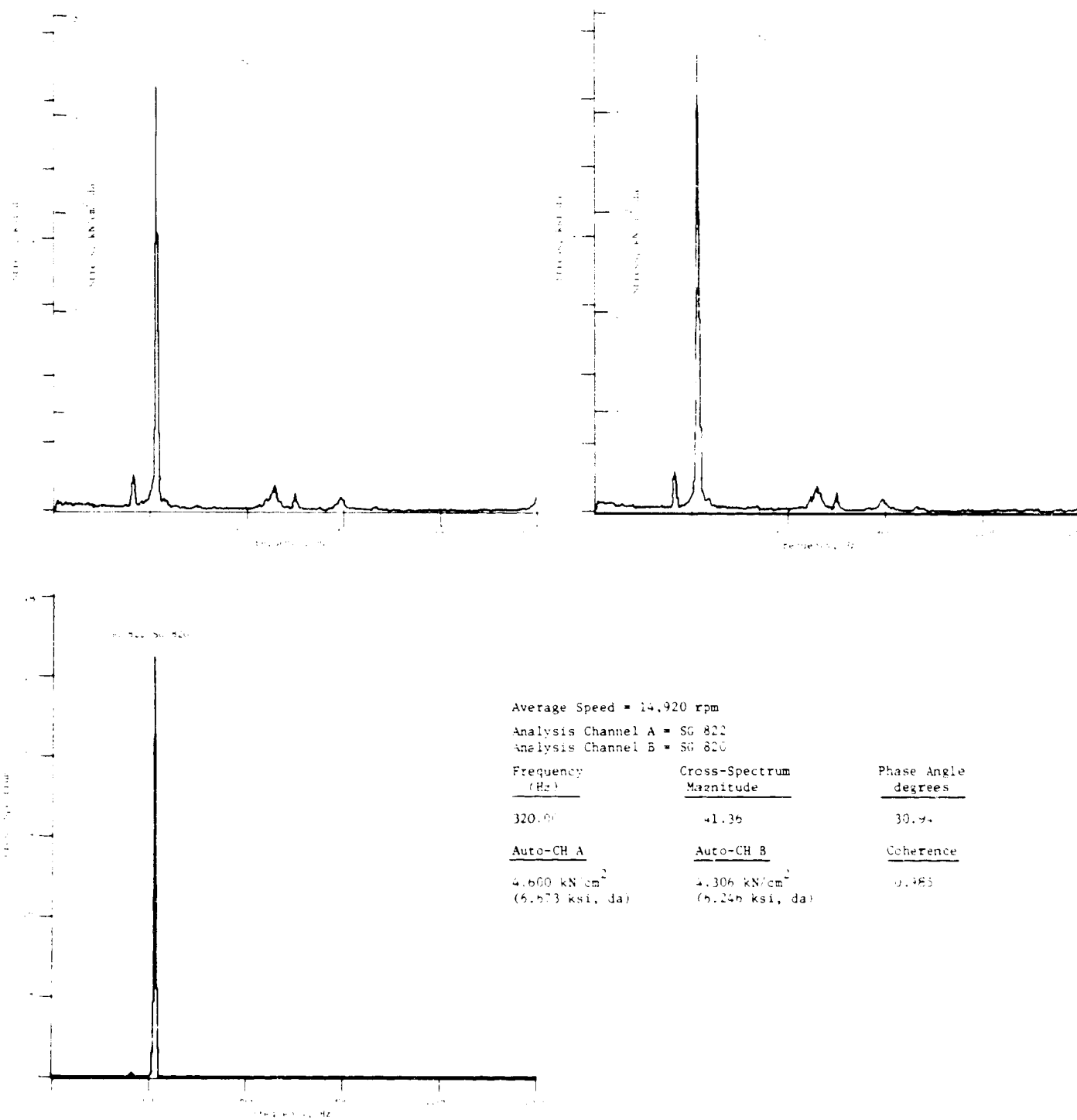


Figure 45. FFT Cross Spectral Analysis at 90 Percent Speed Flutter.

between two blades as a function of time for 90 and 95 percent speeds. At 90 percent speed, the blades were oscillating in and out of flutter; the phase angle is shown to be constant while they are in flutter and to vary considerably when they are not in flutter. Similar data was analyzed at the same operating condition a few hours later and the results were the same, that is, the identical phase angle existed between the same two airfoils.

The strain gage responses were also analyzed with the FFT/computer. Typical linear spectra and cross spectra of strain gage data are shown in Figure 44 for 70 percent torsional flutter and in Figure 45 for 90 percent flexural flutter. The predominant spike is apparent at each of the flutter frequencies, although the stress amplitudes are average values and do not represent the maximum response. The cross spectra yield the relative phase between the two linear spectra. These phase angles were in good agreement with the phasemeter data. Averaging in this case proved to be inconsequential since the phase angle between two blades was constant as shown in Figure 43.

The phase angles of the flutter stress signals were plotted on system mode wave diagrams in Figures 46 through 49 to determine the traveling wave nodal diameter and its direction. For torsional flutter at 65 percent speed, the data shows either a two or six nodal diameter forward traveling wave. At 70 percent speed torsional flutter, both four and six nodal diameter forward traveling waves are evident. For flexural flutter at 90 and 95 percent speeds, there are two and three nodal diameter forward traveling waves respectively. Precise wave decomposition was encumbered by the lack of stress data on many blades (recall that not all blades could be monitored). However, the missing interblade phase information from the blade stress can be supplemented by the interblade phase data from measured blade tip displacement as discussed in Section 6.3.2.2. It is noteworthy that only forward traveling waves were observed in both flutter modes.

A summary of the measured peak-to-peak stress amplitudes and the phase angles is provided in Table XV for the four flutter points. The phase angles are shown in terms of phase lag relative to the reference blade. The reference blade is indicated by a zero phase angle at each speed. Note that different reference blades were used.

6.3 BLADE DISPLACEMENT DATA

One objective of this flutter research program was the direct measurement of blade deformation. The steady deformation of the rotor blades can change the aerodynamic flow within the blade row due to the change in flow channel profiles. A blade stagger change (untwist) directly varies the flow incidence angle, a controlling parameter for stall flutter. Similarly, chordwise bending of the blades may alter the aerodynamic characteristics of the flow for blades of low or medium aspect ratio especially at transonic air speeds. Although steady deformations are of greater concern at flutter onset conditions, data was obtained at all special instrumentation data points.

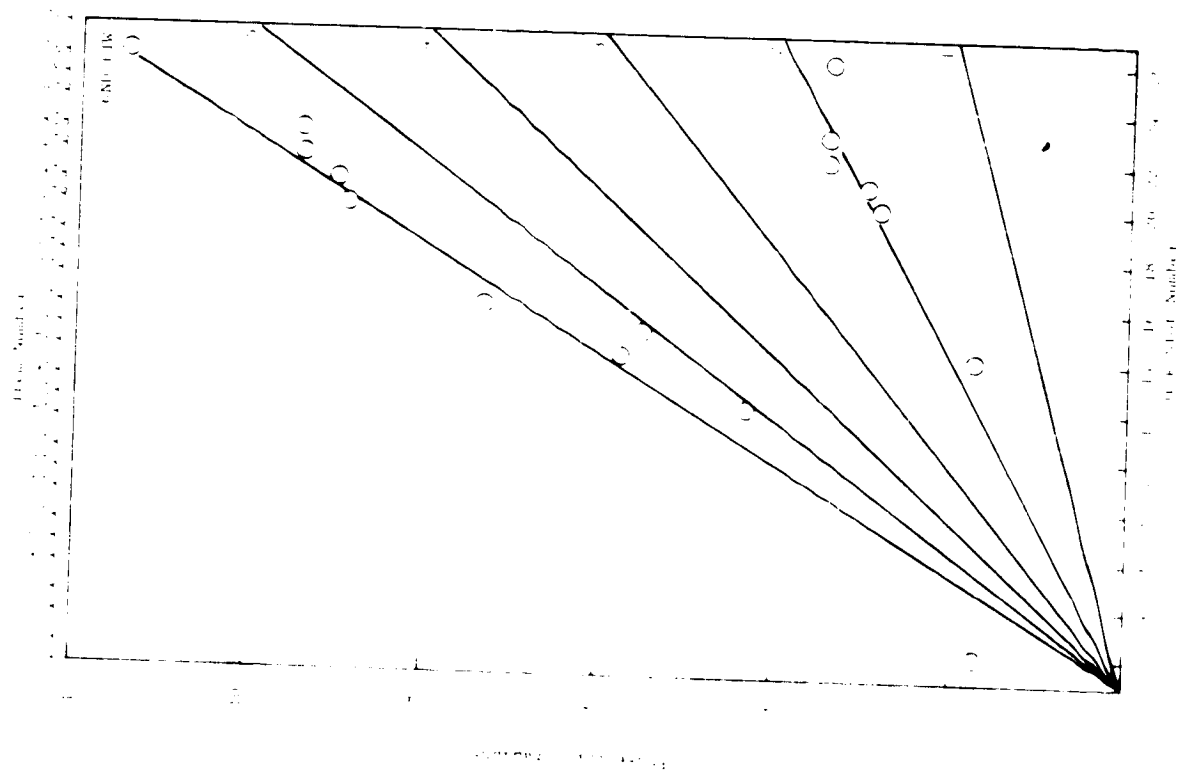


Figure 46. Strain Gage Phase Data,
65 Percent Speed Torsional
Flutter.

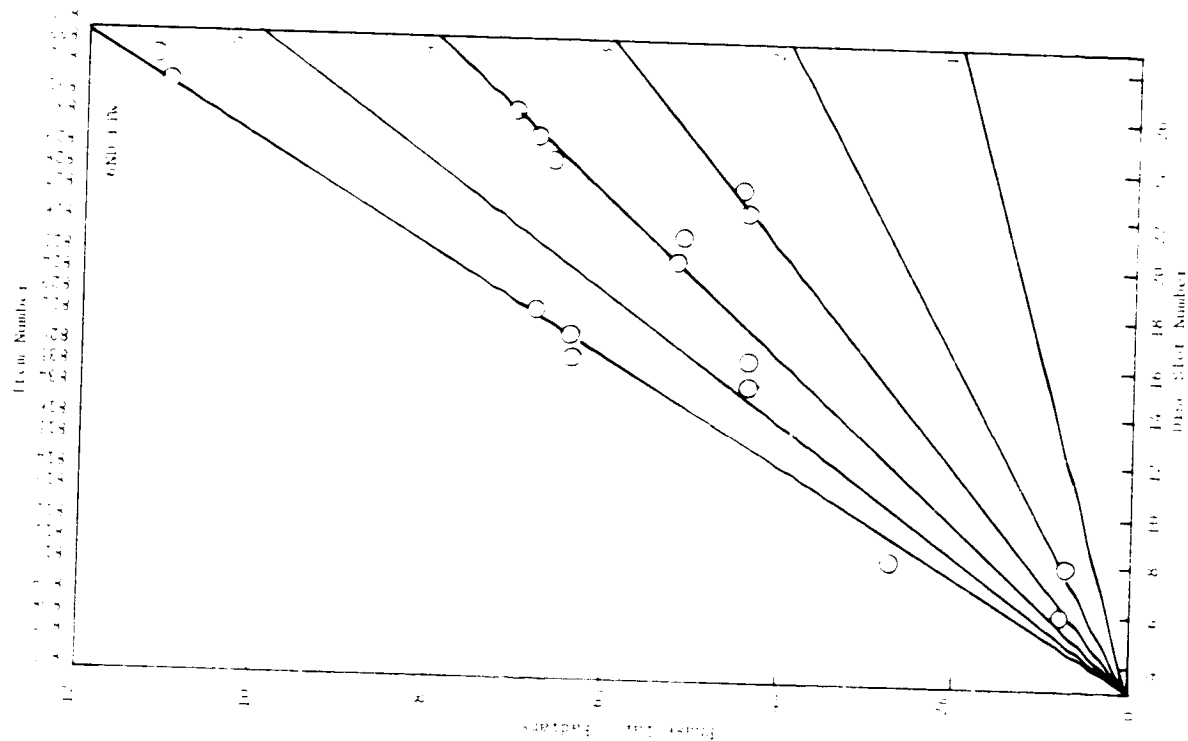


Figure 47. Strain Gage Phase Data,
70 Percent Speed Torsional
Flutter.

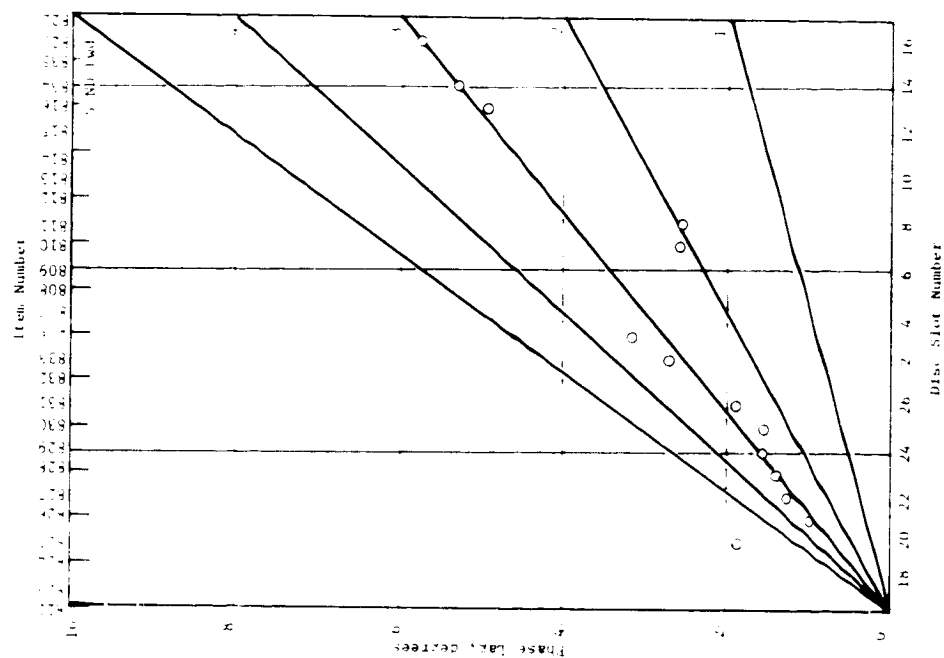


Figure 49. Rotating Rig Blade Phase Data 95% Speed, Flexural Flutter.

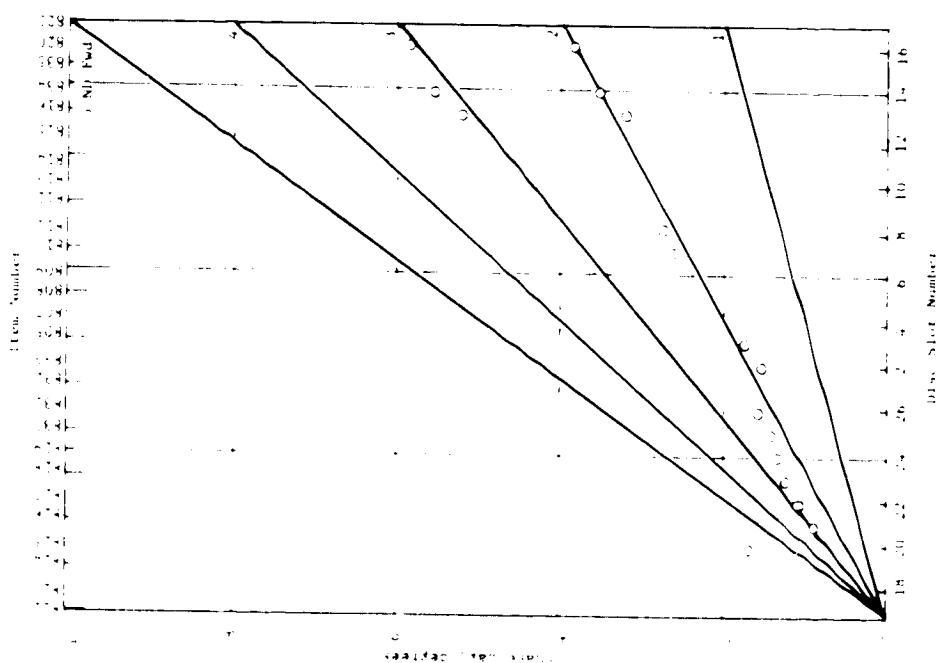


Figure 48. Rotating Rig Blade Phase Data 90% Speed, Flexural Flutter.

Along with the time-averaged steady deflections, the unsteady deformations of the blades were also acquired to determine the blade flutter mode shapes and interblade phase angles.

6.3.1 Steady-State Deformation

6.3.1.1 Tangential Deflections

The available (see Section 5.3.1.1) absolute steady tangential blade tip displacements are shown in Figures 50 through 52. The test data shows that the steady aerodynamic loading and the centrifugal loading on the blades caused the front portion of the blade tip section to deflect against the direction of rotor rotation and the rear portion of the blade tip section to deform in the direction of rotor rotation; in other words, the blade untwists.

For the intermediate spanwise locations, Figures 51 and 52 show the available absolute steady tangential deflection data for 78.9 and 57.2 percent span respectively. Toward the end of the tests, the 57.2 percent span trailing edge laser light probe signals were blurred due to oil contamination and were not recorded - hence the lack of 57.2 percent span trailing edge data for the 70 percent speed IOL and 90 percent speed flutter points. As expected, less untwist is indicated at these spanwise locations than is shown at the tip for the 70 percent speed IOL and the 90 percent speed flutter points. The data at the 65 percent speed flutter point is questionable since it indicates the blade twists, which is not consistent with all other data.

The relative steady tangential deflections at the blade tip for various blade tip chord locations obtained from light probe measurements are shown in Figures 53 through 55 for the points on the NOL, the IOL, and the flutter boundary respectively. In these figures, the measurement corresponding to the aft-most chord position, where light probe data is available, has been taken as the reference point as indicated by zero relative tangential displacement. For a given operating line, higher speed operations always produced large tangential deflections between the blade leading edge and 55 percent chord location, with the possible exception of torsional flutter at 65 and 70 percent speeds.

6.3.1.2 Blade Tip Untwist

Figure 56 shows the steady component of the blade tip untwist at the four rotor speeds tested. The steady untwist increased approximately 2° as the rotor speed was increased from 65 to 95 percent design speed. The test results agree well with the TWBL (nominal operating line) analysis. The higher blade loading due to throttling produces slightly larger untwist values than that of lower operating line conditions.

The blade untwist at the intermediate span locations, calculated from the laser light probe data, is compared with predictions in Figure 57. The scatter

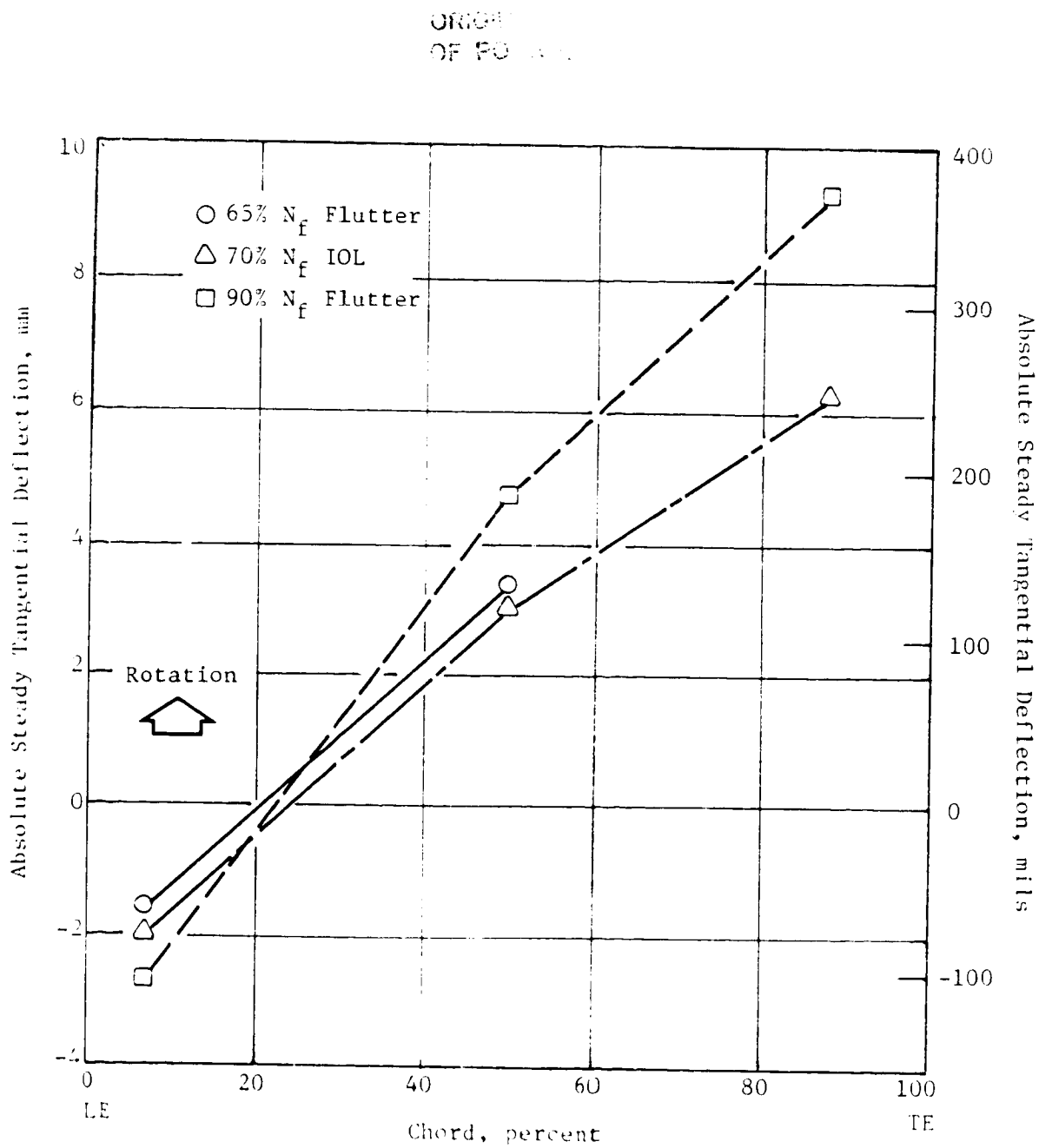


Figure 50. Blade Tip Absolute Tangential Displacement Versus Chord.

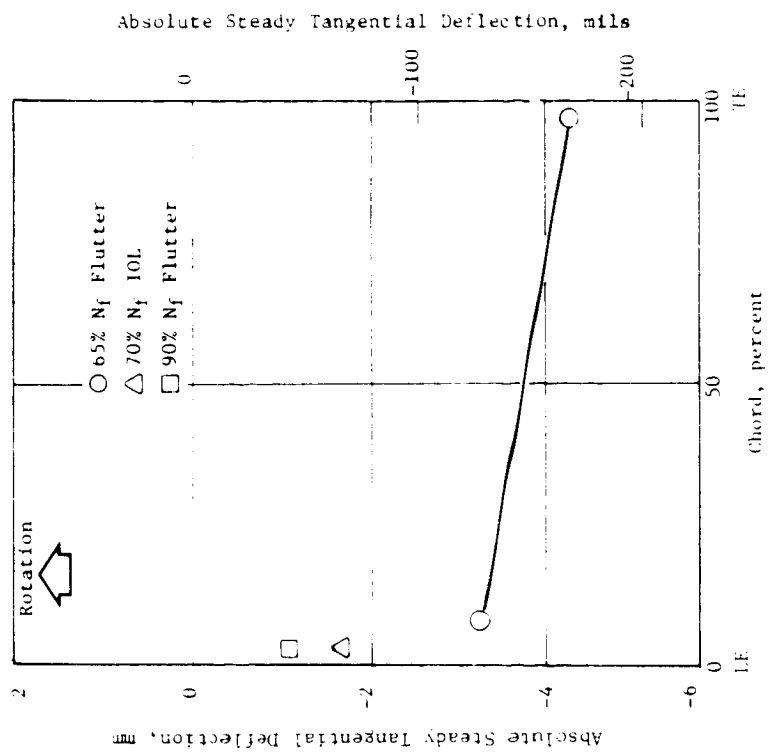


Figure 51. Absolute Tangential Displacement Versus Chord, 57.2 Percent Span.

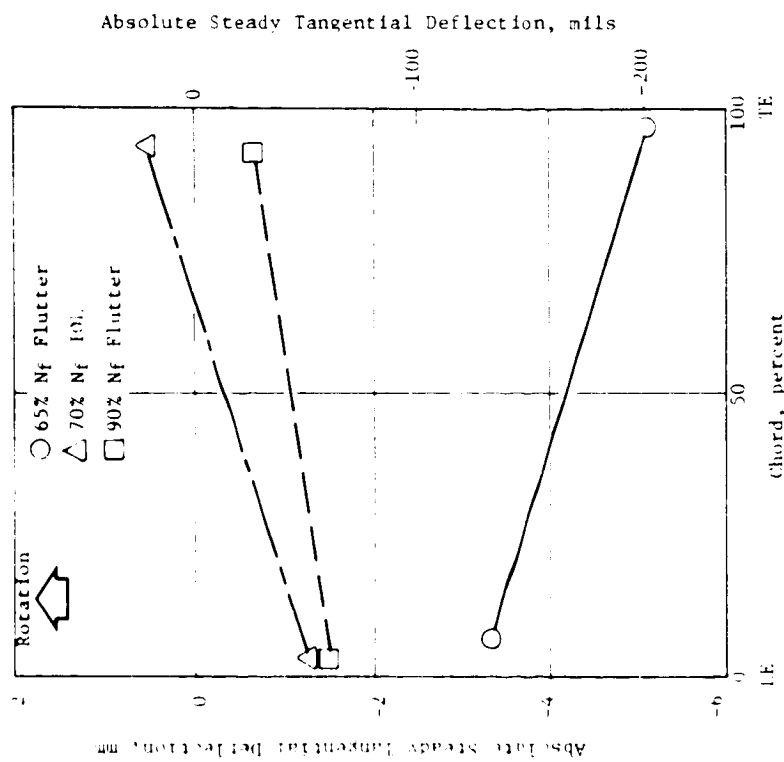


Figure 52. Absolute Tangential Displacement Versus Chord, 78.9 Percent Span.

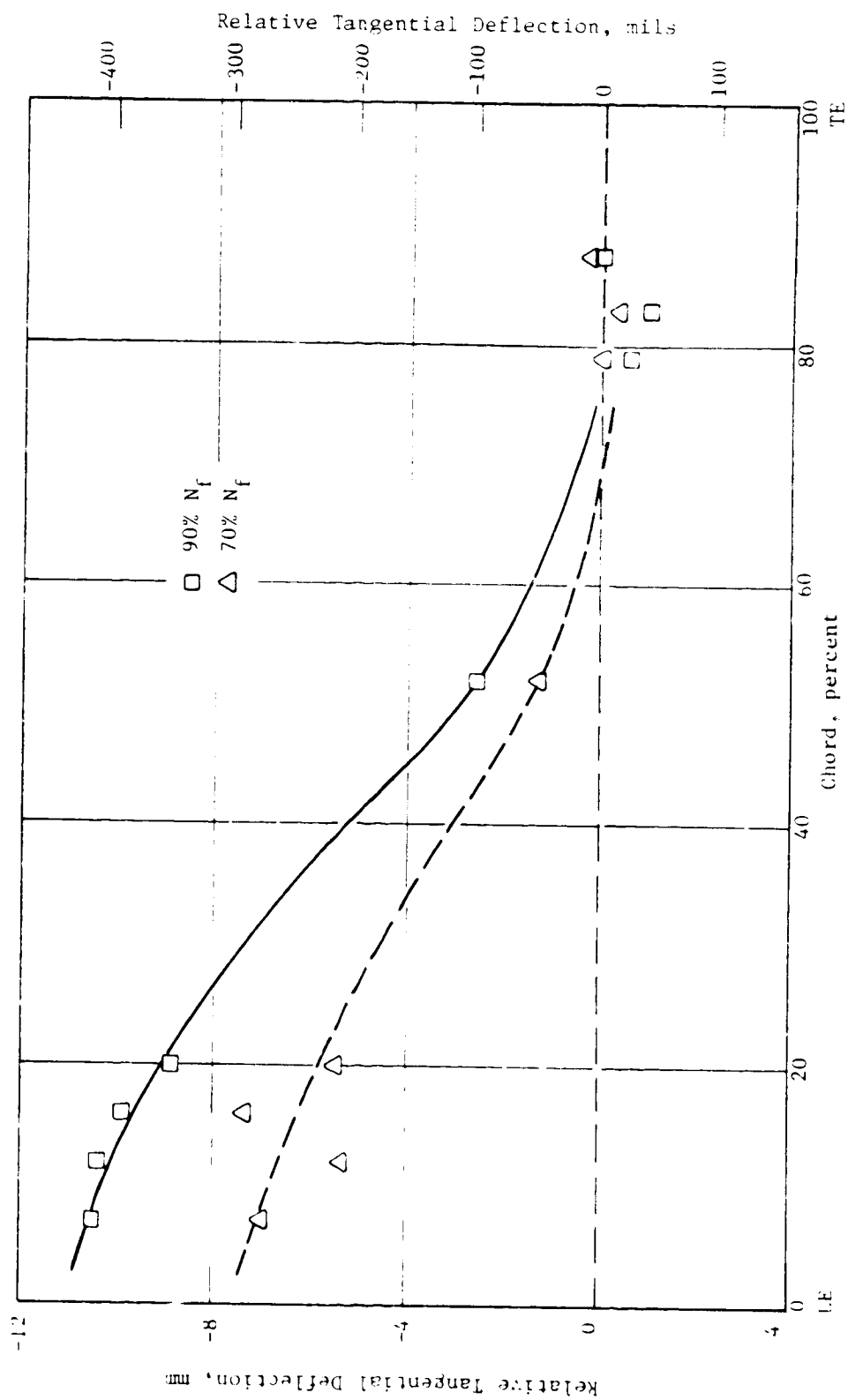


Figure 53. Tip Tangential Deflection Versus Chord, Nominal Operating Line.

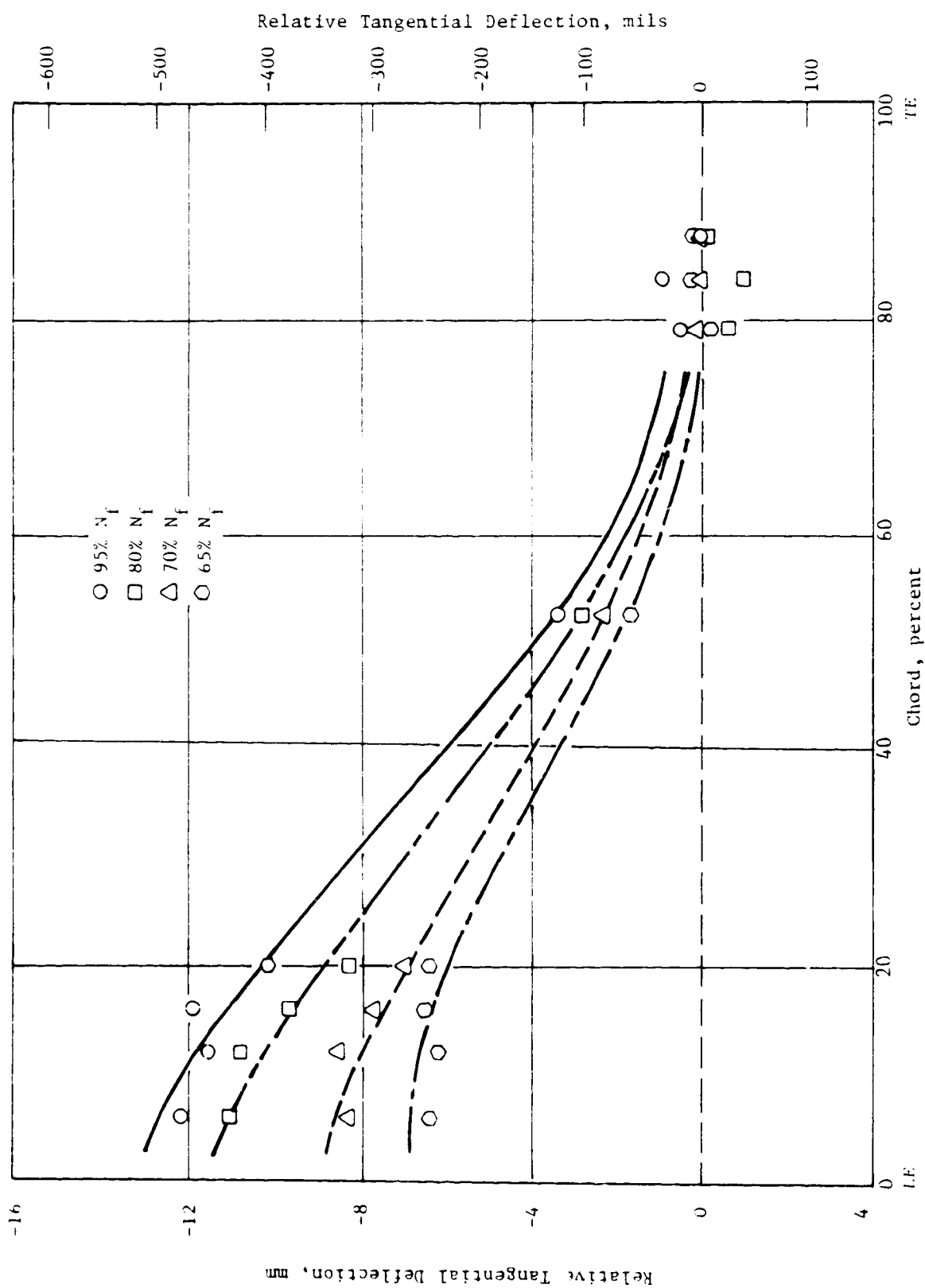


Figure 54. Tip Tangential Displacement Versus Chord, Intermediate Operating Line.

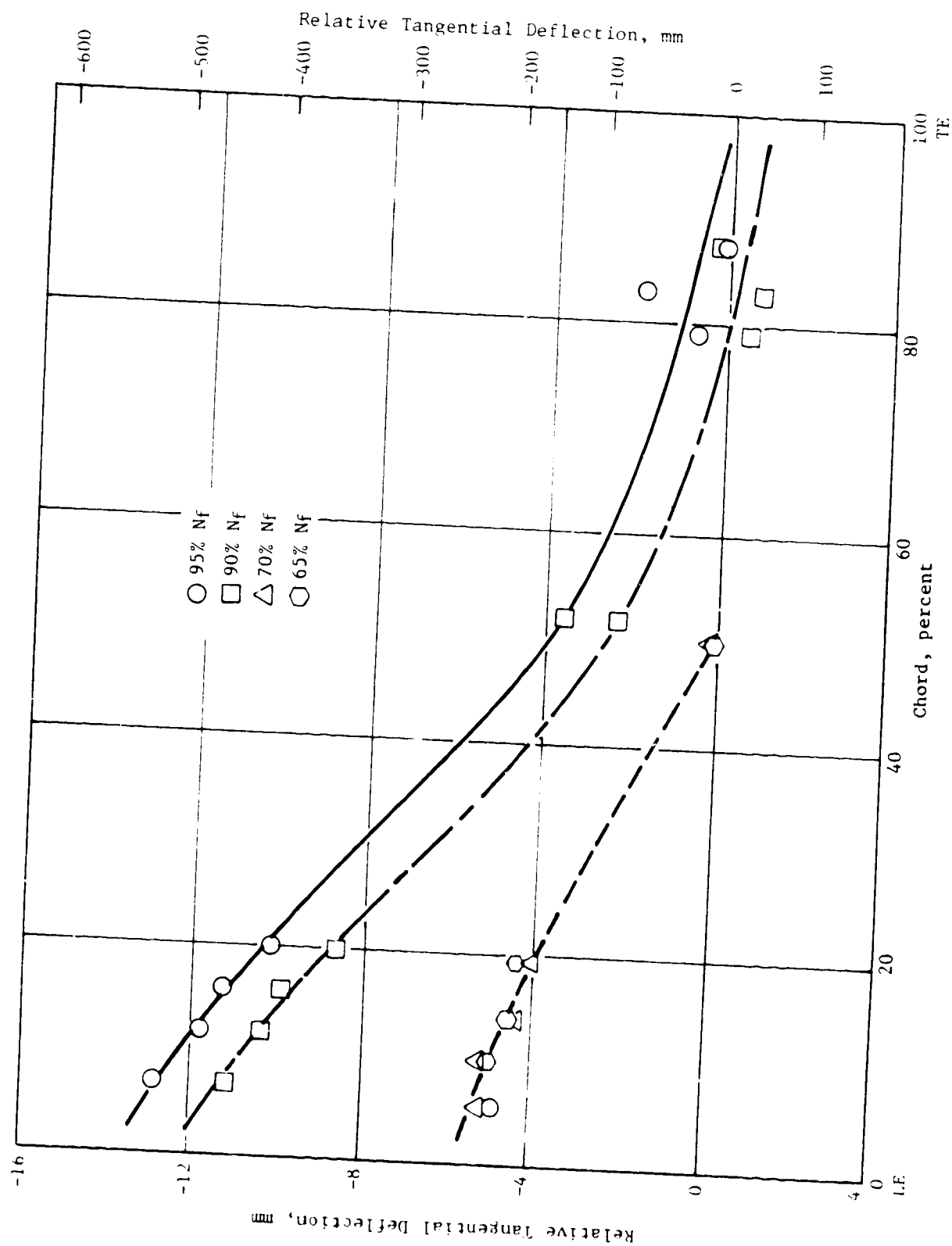


Figure 55. Tip Tangential Displacement Versus Chord, Flutter.

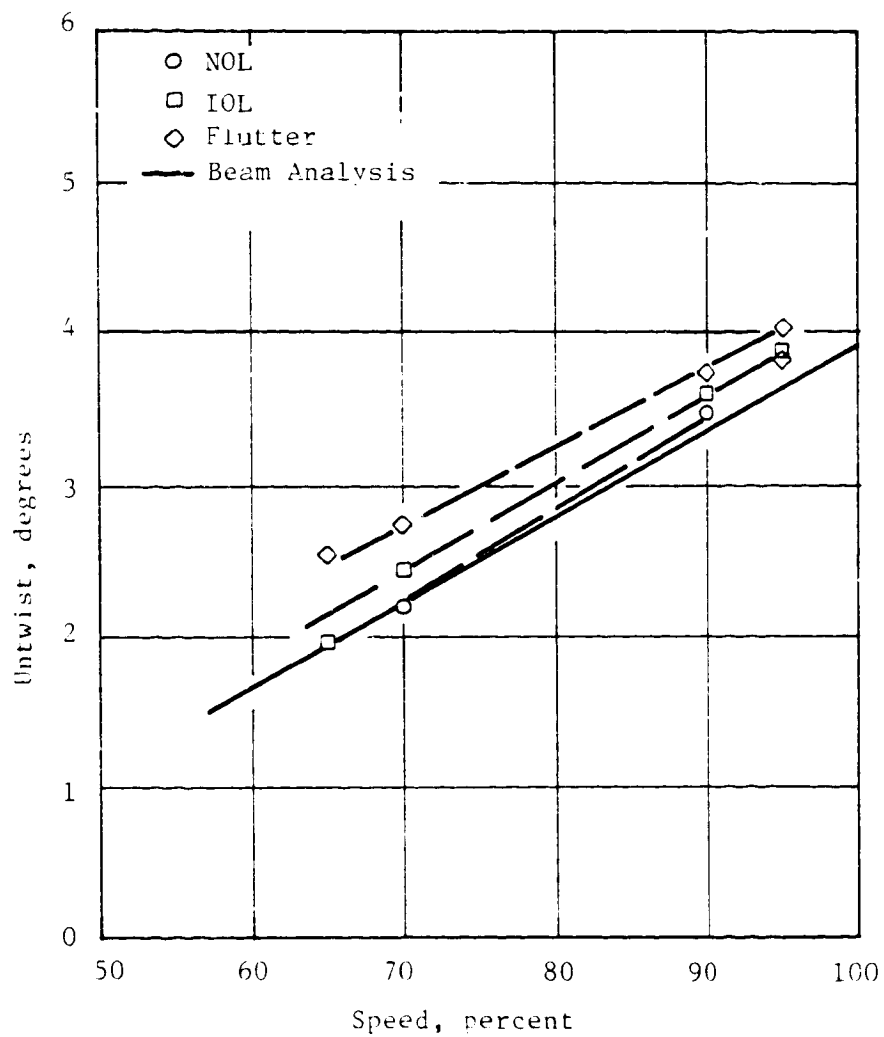


Figure 56. Tip Untwist Versus Speed.

OF PEEK Q...

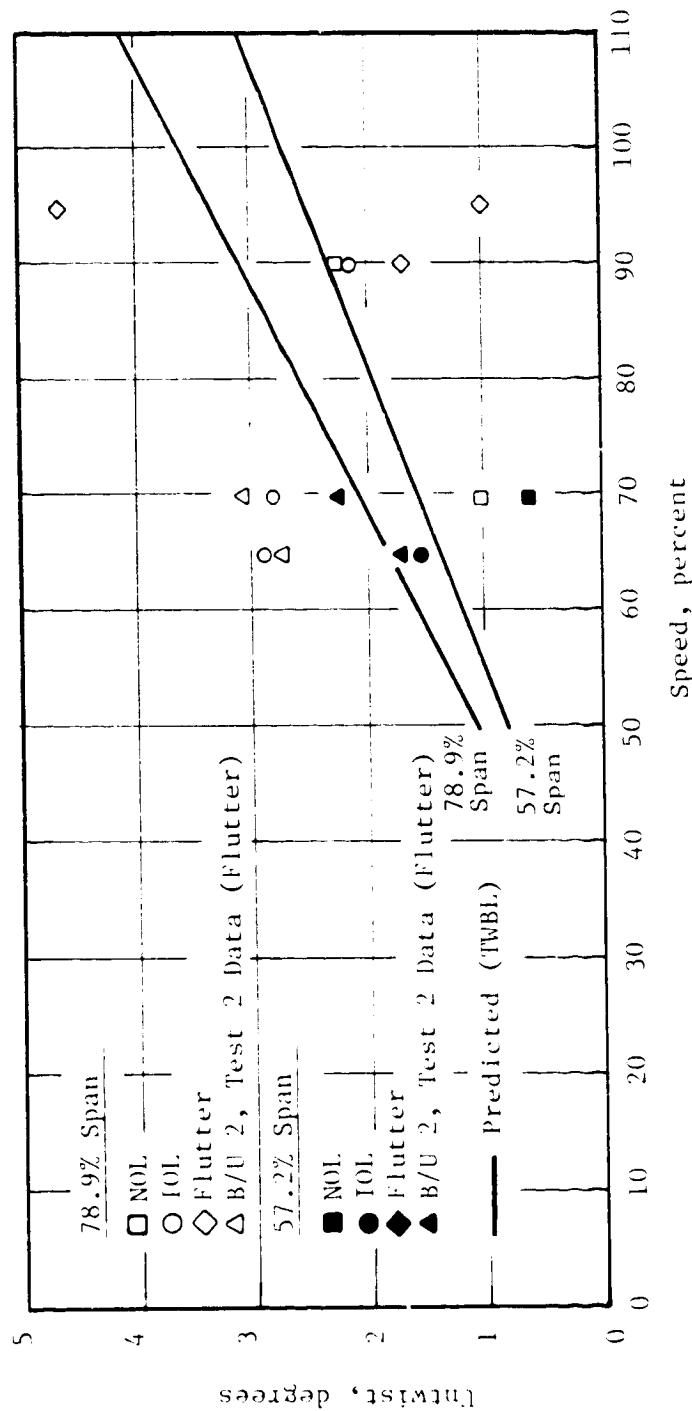


Figure 57. Untwist Versus Speed at Intermediate Span Locations.

observed is due to the poor quality of the data from test 3. In test 2, the laser data obtained at the 65 and 70 percent speed torsional flutter points was more definitive, and indicates that the measurement accuracy of this system (compared with the TWBL predictions) is within $\pm 1^\circ$ of untwist.

The blade untwist is plotted versus blade span for 65, 70, 90, and 95 percent speeds in Figures 58 through 61, respectively. These plots show the tip light probe data to agree within 0.2° of the predictions. The previously mentioned scatter in the intermediate span data is also evident.

6.3.1.3 Chordwise Bending

The straight line relationships described in Section 5.3.1.3 were used to determine the chordwise bending at the blade tip. Figure 62 shows the total blade angle change for various speeds and operating conditions. It can be seen that the largest chordwise bending occurred at the flutter conditions, with the maximum at the 70 percent speed flutter point. This is due to the torsional mode response at the lower speeds.

6.3.2 Unsteady Deformation

6.3.2.1 Tangential Deflections

Figures 63 through 65 show the blade-to-blade variation of the maximum blade tip tangential deflections occurring during the 128 revolution data acquisition for 65, 70, and 95 percent speed at flutter conditions. Also shown are the corresponding maximum blade stress amplitudes. Data at 90 percent speed are omitted because of the intermittent flutter exhibited at that speed. These figures show deflection data from the leading edge light probe (#755) as it recorded large blade tip deflections in both flexure and torsion. In general, the deflection amplitude varies from blade to blade, as does the stress amplitude, with the maximum values occurring at about the same circumferential location on the rotor. The local discrepancies between the stress and deflection levels are due to the stress data being acquired at a different time than the deflection data. The large variations in the stresses and deflections around the rotor may originate from differences in blade frequencies commonly known as blade mistuning. (There is about 2 percent variation in the blade natural frequencies.)

The maximum measured blade tip deflections are tabulated in Tables XVI, XVII, and XVIII for the 65, 70, and 95 percent speed flutter points respectively. Blade deflection data were not available from the trailing edge light probes at the 65 and 70 percent speed torsional flutter points due to an inadvertent axial mislocation of the light probe pad. This was rectified for all other subsequent special instrumentation data points.

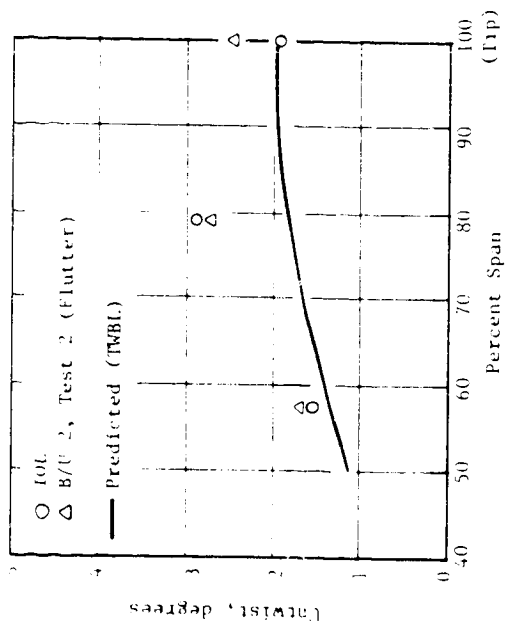


Figure 58. Untwist Versus Span at 65 Percent Speed.

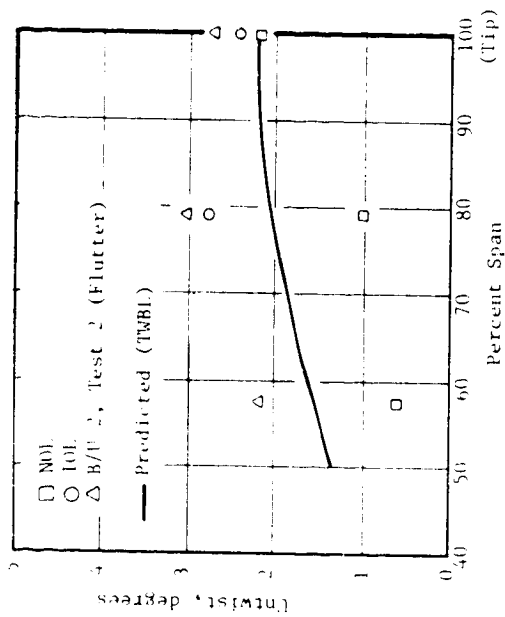


Figure 59. Untwist Versus Span at 70 Percent Speed.

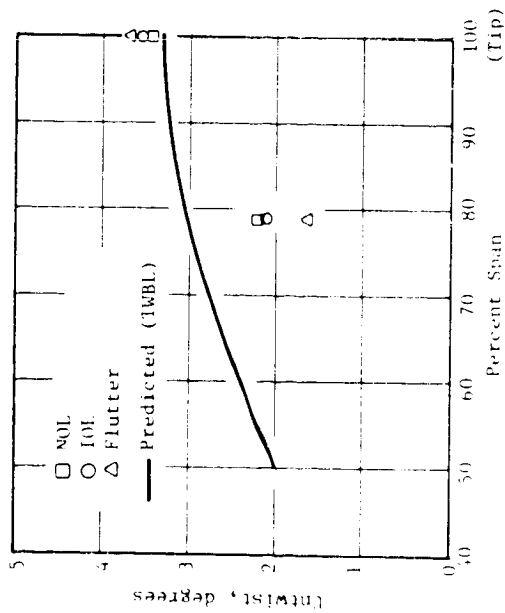


Figure 60. Untwist Versus Span at 90 Percent Speed.

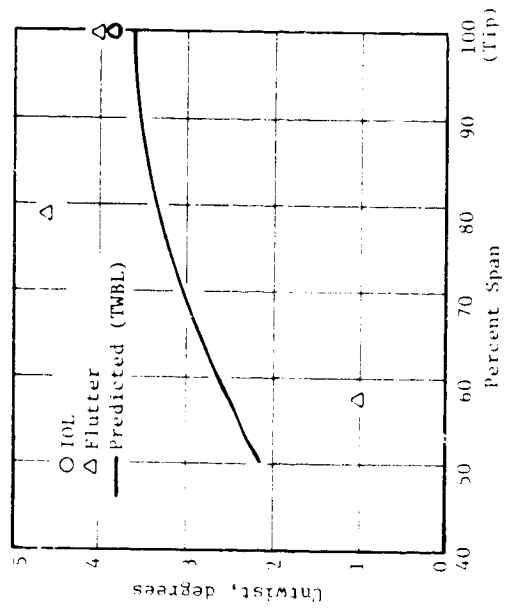


Figure 61. Untwist Versus Span at 95 Percent Speed.

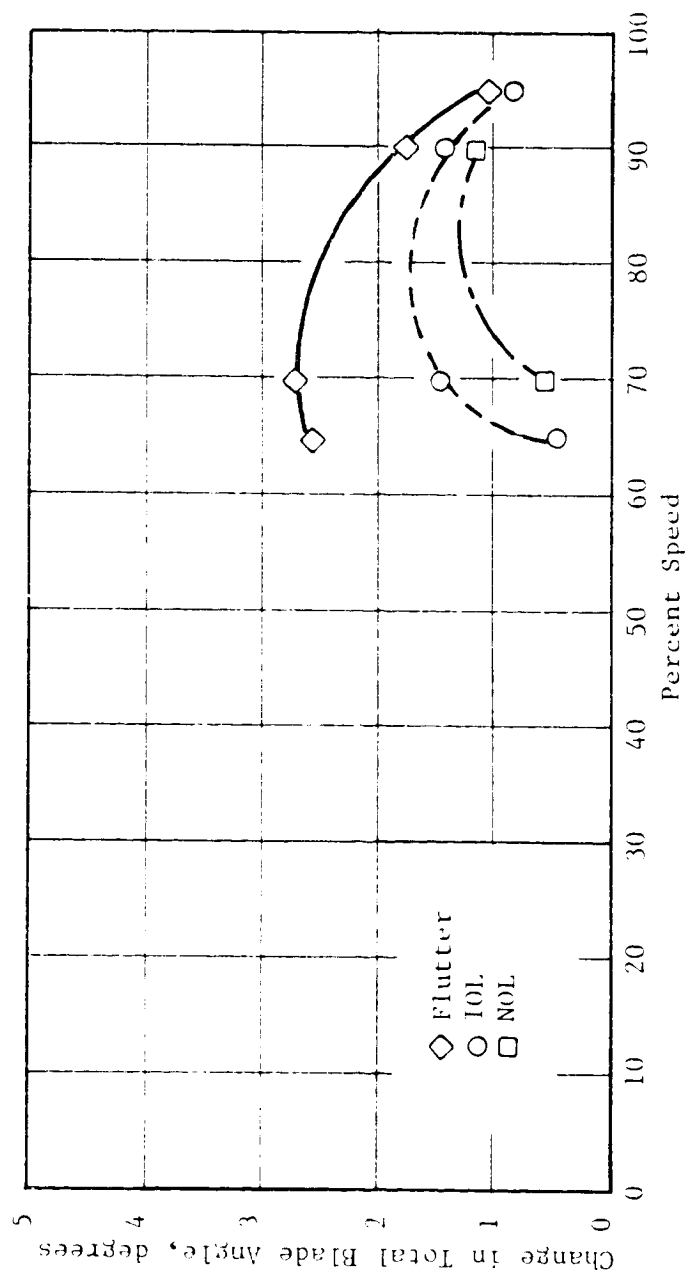


Figure 62. Total Blade Camber Change with Speed and Operating Line.

OF PAGES

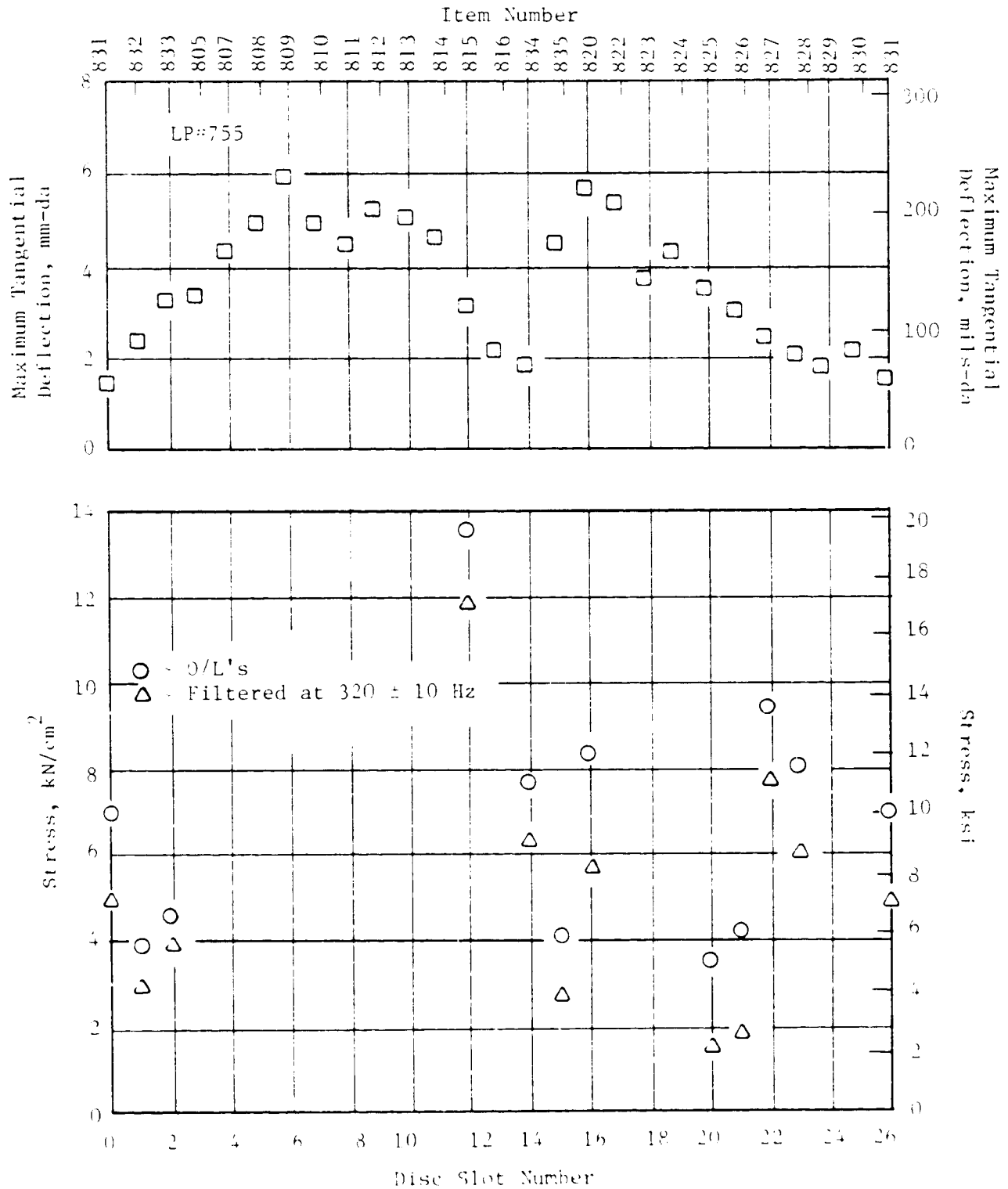


Figure 63. Blade Stress and Deflection in Torsional Flutter at 65 Percent Speed.

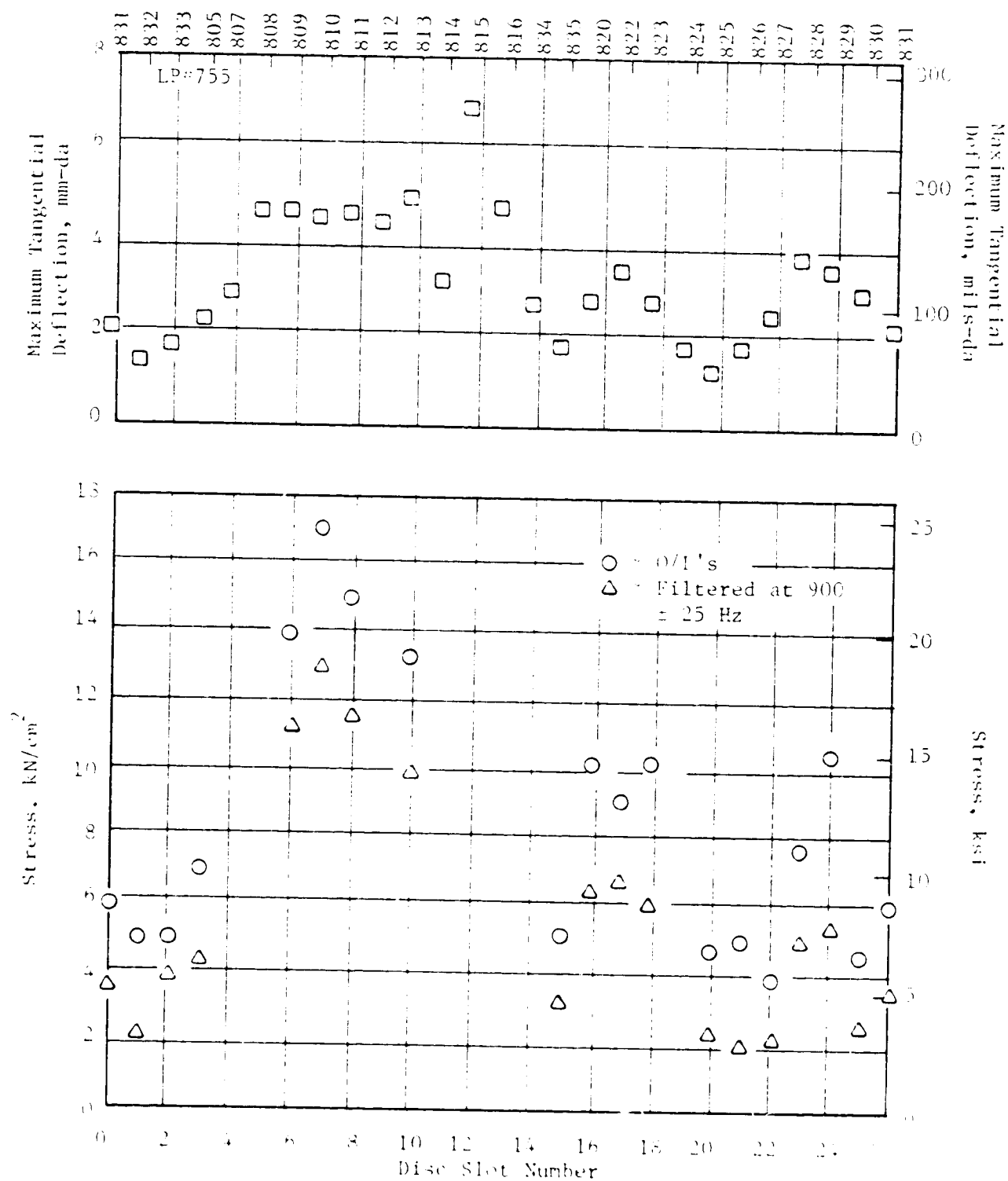


Figure 64. Blade Stress and Deflection in Torsional Vibration at 70 Percent Speed.

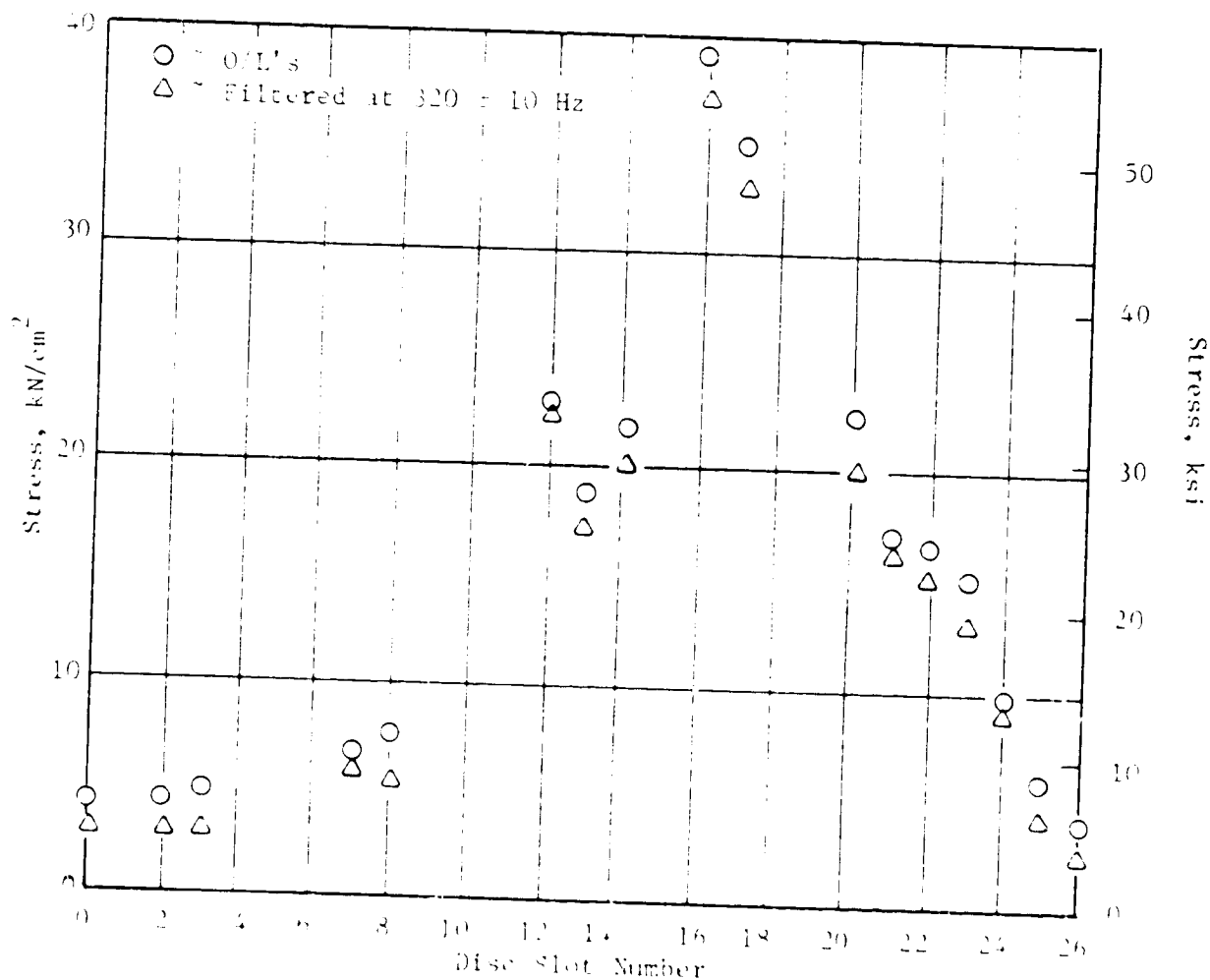
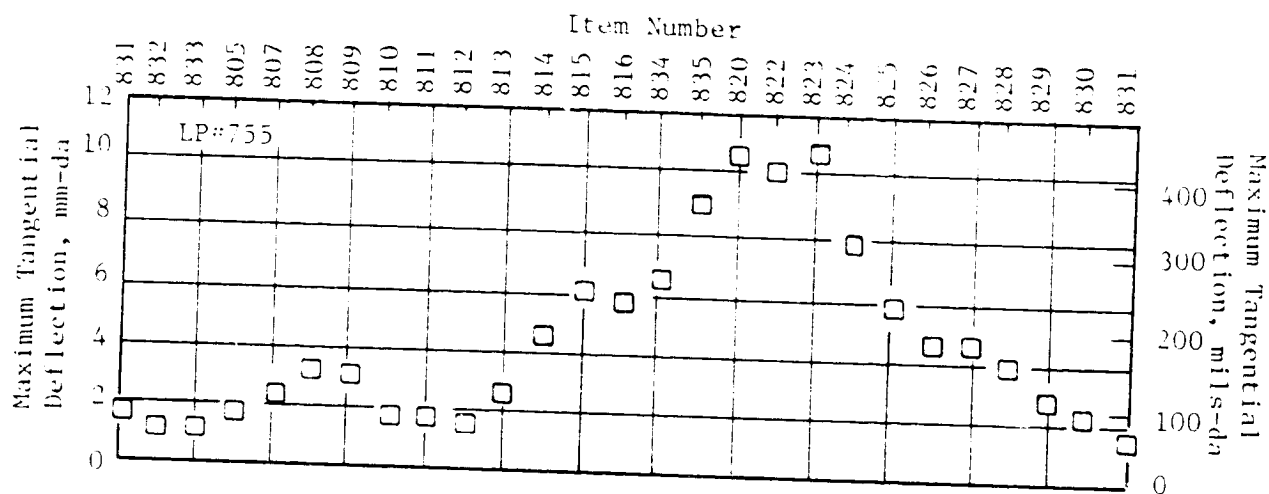


Figure 65. Blade Stress and Deflection in Flexural Flutter at 95 Percent Speed.

Table XVI. Tangential Maximum Deflection Excursions (Mils-DA) at 10802 rpm.

Disk Slot No.	LP #755	LP #756	LP #757	LP #758	LP #759
1	0.93013E+02	0.68437E+02	0.74885E+02	0.52069E+02	0.61429E+02
2	0.12694E+03	0.10646E+03	0.10823E+03	0.93022E+02	0.10472E+03
3	0.13104E+03	0.10002E+03	0.10297E+03	0.10004E+03	0.10882E+03
4	0.16731E+03	0.12401E+03	0.13456E+03	0.12461E+03	0.14334E+03
5	0.19085E+03	0.12635E+03	0.13163E+03	0.10414E+03	0.12227E+03
6	0.23075E+03	0.15518E+03	0.16323E+03	0.16440E+03	0.16849E+03
7	0.19363E+03	0.10880E+03	0.10999E+03	0.11174E+03	0.11174E+03
8	0.17374E+03	0.12225E+03	0.11116E+03	0.64940E+02	0.11759E+03
9	0.20241E+03	0.48549E+02	0.60844E+02	0.75470E+02	0.54994E+02
10	0.19773E+03	0.77211E+02	0.87171E+02	0.60844E+02	0.86001E+02
11	0.18018E+03	0.83645E+02	0.87171E+02	0.73715E+02	0.86001E+02
12	0.12109E+03	0.80136E+02	0.88926E+02	0.69035E+02	0.73130E+02
13	0.82483E+02	0.64928E+02	0.49143E+02	0.52654E+02	0.48558E+02
14	0.69613E+02	0.42115E+02	0.40368E+02	0.39783E+02	0.32762E+02
15	0.17433E+03	0.50304E+02	0.52069E+02	0.47973E+02	0.42123E+02
16	0.22113E+03	0.81891E+02	0.94777E+02	0.71960E+02	0.89511E+02
17	0.20884E+03	0.98854E+02	0.10472E+03	0.10414E+03	0.10589E+03
18	0.14215E+03	0.97684E+02	0.98872E+02	0.84246E+02	0.98287E+02
19	0.16789E+03	0.93004E+02	0.10765E+03	0.81906E+02	0.10648E+03
20	0.13572E+03	0.76626E+02	0.89511E+02	0.71960E+02	0.83076E+02
21	0.11817E+03	0.54984E+02	0.56164E+02	0.58504E+02	0.56749E+02
22	0.94768E+02	0.57323E+02	0.41538E+02	0.43878E+02	0.39783E+02
23	0.78973E+02	0.58493E+02	0.40953E+02	0.54409E+02	0.49729E+02
24	0.66689E+02	0.44455E+02	0.39783E+02	0.46218E+02	0.36858E+02
25	0.81313E+02	0.67267E+02	0.53824E+02	0.53239E+02	0.53239E+02
26	0.57329E+02	0.52644E+02	0.47973E+02	0.48558E+02	0.59089E+02

Table XVII. Tangential Maximum Deflection Excursions (Mils-DA) at 11630 rpm.

Disk Slot No.	LP #755	LP #756	LP #757	LP #758	LP #759
1	0.52276E+02	0.56045E+02	0.56680E+02	0.61718E+02	0.53526E+02
2	0.68021E+02	0.85012E+02	0.69275E+02	0.57309E+02	0.85642E+02
3	0.88806E+02	0.89420E+02	0.98245E+02	0.68016E+02	0.96347E+02
4	0.11211E+03	0.13035E+03	0.89428E+02	0.10706E+03	0.95717E+02
5	0.18013E+03	0.16562E+03	0.14170E+03	0.14107E+03	0.14547E+03
6	0.17887E+03	0.17758E+03	0.13981E+03	0.11588E+03	0.12783E+03
7	0.17320E+03	0.16688E+03	0.16878E+03	0.13855E+03	0.18136E+03
8	0.17572E+03	0.18136E+03	0.14548E+03	0.13288E+03	0.15617E+03
9	0.17005E+03	0.18640E+03	0.16248E+03	0.15052E+03	0.22796E+03
10	0.19021E+03	0.20592E+03	0.18767E+03	0.16941E+03	0.17254E+03
11	0.12093E+03	0.15932E+03	0.13792E+03	0.13036E+03	0.24118E+03
12	0.26642E+03	0.26070E+03	0.20405E+03	0.15115E+03	0.26133E+03
13	0.18391E+03	0.17632E+03	0.14107E+03	0.11903E+03	0.12468E+03
14	0.10203E+03	0.10831E+03	0.73684E+02	0.73054E+02	0.91939E+02
15	0.64872E+02	0.74937E+02	0.71164E+02	0.76832E+02	0.70529E+02
16	0.10455E+03	0.96347E+02	0.93836E+02	0.84390E+02	0.93828E+02
17	0.13037E+03	0.13224E+03	0.11525E+03	0.79981E+02	0.11461E+03
18	0.10266E+03	0.10013E+03	0.90687E+02	0.79351E+02	0.68639E+02
19	0.65502E+02	0.77456E+02	0.56680E+02	0.54790E+02	0.65491E+02
20	0.45348E+02	0.66121E+02	0.45344E+02	0.52901E+02	0.59823E+02
21	0.62353E+02	0.64231E+02	0.57309E+02	0.59828E+02	0.76196E+02
22	0.90695E+02	0.11146E+03	0.88168E+02	0.73684E+02	0.84382E+02
23	0.14234E+03	0.111776E+03	0.96985E+02	0.89428E+02	0.10516E+03
24	0.13226E+03	0.13161E+03	0.10769E+03	0.96355E+02	0.11524E+03
25	0.11211E+03	0.85642E+02	0.85019E+02	0.64867E+02	0.10579E+03
26	0.82507E+02	0.87531E+02	0.75573E+02	0.71794E+02	0.83753E+02

Table XVIII. Tangential Maximum Deflection Excursions (Mils-DA) at 15743 rpm.

Disk Slot No.	LP #755	LP #756	LP #757	LP #758	LP #759	LP #760	LP #761
1	0.47356E+02	0.71070E+02	0.66831E+02	0.72767E+02	0.83751E+02	0.38932E+02	0.69374E+02
2	0.45665E+02	0.86299E+02	0.82905E+02	0.98151E+02	0.98978E+02	0.49088E+02	0.53299E+02
3	0.65115E+02	0.83761E+02	0.94748E+02	0.97305E+02	0.11928E+03	0.60937E+02	0.56683E+02
4	0.90484E+02	0.12099E+03	0.14043E+03	0.14046E+03	0.13112E+03	0.51627E+02	0.85448E+02
5	0.12854E+03	0.12606E+03	0.14128E+03	0.15484E+03	0.16666E+03	0.77863E+02	0.11337E+03
6	0.12346E+03	0.91376E+02	0.80367E+02	0.90536E+02	0.13112E+03	0.76171E+02	0.72758E+02
7	0.64269E+02	0.10830E+03	0.10152E+03	0.10407E+03	0.95594E+02	0.66015E+02	0.76142E+02
8	0.65115E+02	0.19290E+03	0.16327E+03	0.17430E+03	0.18865E+03	0.66015E+02	0.12013E+03
9	0.59195E+02	0.23352E+03	0.19119E+03	0.17684E+03	0.23349E+03	0.51627E+02	0.14467E+03
10	0.10063E+03	0.36212E+03	0.28001E+03	0.27499E+03	0.26733E+03	0.85480E+02	0.19720E+03
11	0.17589E+03	0.44757E+03	0.37392E+03	0.35368E+03	0.43060E+03	0.19720E+03	0.29864E+03
12	0.23763E+03	0.46365E+03	0.37645E+03	0.40191E+03	0.36630E+03	0.25475E+03	0.24281E+03
13	0.22494E+03	0.29782E+03	0.25379E+03	0.26907E+03	0.29609E+03	0.19974E+03	0.20643E+03
14	0.25285E+03	0.42557E+03	0.39676E+03	0.37906E+03	0.40014E+03	0.21497E+03	0.27834E+03
15	0.36278E+03	0.64725E+03	0.54819E+03	0.49668E+03	0.51181E+03	0.32499E+03	0.41370E+03
16	0.42113E+03	0.66755E+03	0.62686E+03	0.63375E+03	0.57779E+03	0.36900E+03	0.45008E+03
17	0.40675E+03	0.72593E+03	0.68946E+03	0.62952E+03	0.62348E+03	0.35885E+03	0.48308E+03
18	0.43466E+03	0.54910E+03	0.47459E+03	0.48398E+03	0.45682E+03	0.36985E+03	0.29611E+03
19	0.31373E+03	0.34181E+03	0.29355E+03	0.27414E+03	0.27071E+03	0.25136E+03	0.22166E+03
20	0.23171E+03	0.31220E+03	0.31132E+03	0.30545E+03	0.30539E+03	0.19297E+03	0.20812E+03
21	0.18520E+03	0.28851E+03	0.28340E+03	0.24792E+03	0.22672E+03	0.17858E+03	0.17851E+03
22	0.18266E+03	0.28428E+03	0.23941E+03	0.24284E+03	0.28340E+03	0.15234E+03	0.20304E+03
23	0.16067E+03	0.20475E+03	0.17934E+03	0.13876E+03	0.14804E+03	0.14726E+03	0.11760E+03
24	0.11332E+03	0.14214E+03	0.13028E+03	0.13030E+03	0.13028E+03	0.10749E+03	0.10575E+03
25	0.92175E+02	0.74454E+02	0.80367E+02	0.74459E+02	0.93902E+02	0.77017E+02	0.54991E+02
26	0.60886E+02	0.70224E+02	0.76983E+02	0.65998E+02	0.81213E+02	0.48241E+02	0.58375E+02

6.3.2.2 Interblade Phase Angles

Typical interblade phase angles, in terms of phase lag, determined from the light probe measured tip displacements are shown in Figures 66 and 67 along with those from the strain gage signals for 70 percent speed torsional flutter and 95 percent speed flexural flutter respectively. It can be seen that there is good agreement between the strain gage phase data and the light probe phase data. The phase data do not fall along any one of the nodal diameter lines which indicates the possible existence of multiple traveling waves of different nodal diameters. Multiple system mode flutter response is possibly a consequence of the blade mistuning which was discussed in the preceding section as a possible cause of the blade-to-blade vibratory amplitude variations. These phase plots also show the presence of predominant forward traveling wave flutter response.

In Tables XIX and XX, the phase data for all blades from all light probes is tabulated for the 70 and 95 percent speed flutter points. These phase data were obtained through FFT cross spectrum analyses. Both the aliasing effect on the phase data due to 1/rev sampling and the time shift of the recorded data due to the light probe sequential sampling of all blades are taken into account in the phase data. It is interesting to note that, for each flutter point, all light probe measurements - and consequently all blade tip tangential displacements - have essentially the same blade-to-blade phase relationships.

6.4 BLADE-MOUNTED SENSORS

Flowfield measurements within a blade passage were made with blade-mounted sensors: dynamic pressure transducers (Kulites) and heated thin-film anemometers (hot-films). Because of hot-film temperature compensation problems, discussed in Section 5.4, meaningful data was not obtained from these sensors. The blade-mounted Kulite data recorded during this rotating rig test are in general unreliable, primarily because of the Kulite's known sensitivity to the blade mechanical strain (see Section 4.3.1). The strain sensitivity is especially severe for torsional mode which appeared during low speed flutter (65 and 70 percent speed). During high speed bending flutter (90 and 95 percent speed), the strain sensitivity is less; however, the higher speeds made the Kulite response more susceptible to stronger centrifugal effect and was probably the cause for Kulite failures.

6.4.1 Blade-Mounted Kulite Time Histories

Typical time histories of Kulite sensors at 65, 70, and 95 percent speed flutter points are shown in Figures 68 through 70 respectively.

During 65 percent speed flutter, at 75 percent span, the Kulite time histories in Figure 68 show noticeable flutter response at 20 and 60 percent chord on the pressure side and at only 20 percent chord on the suction side.

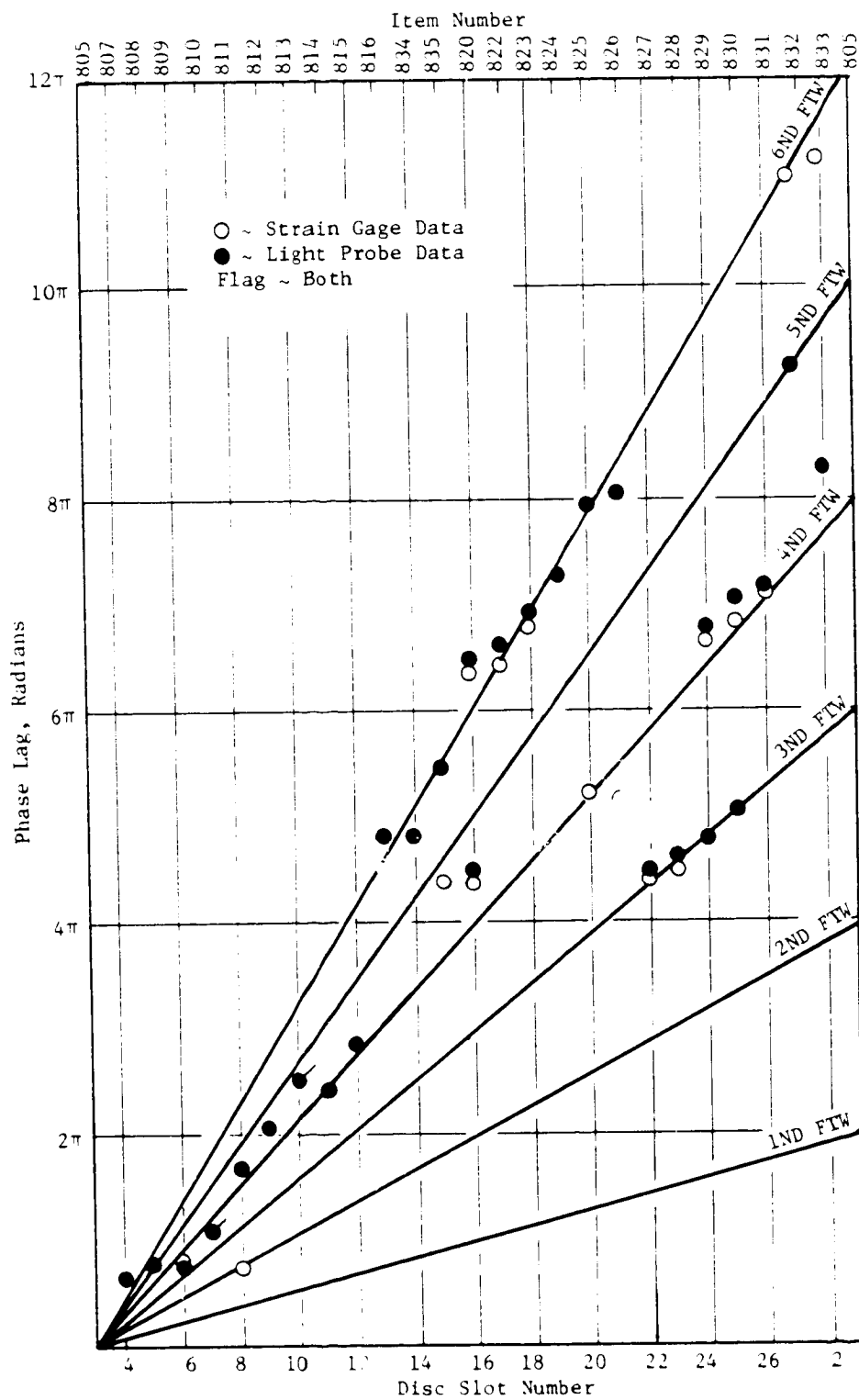


Figure 66. Blade Phase Data at 70 Percent Speed Torsional Flutter.

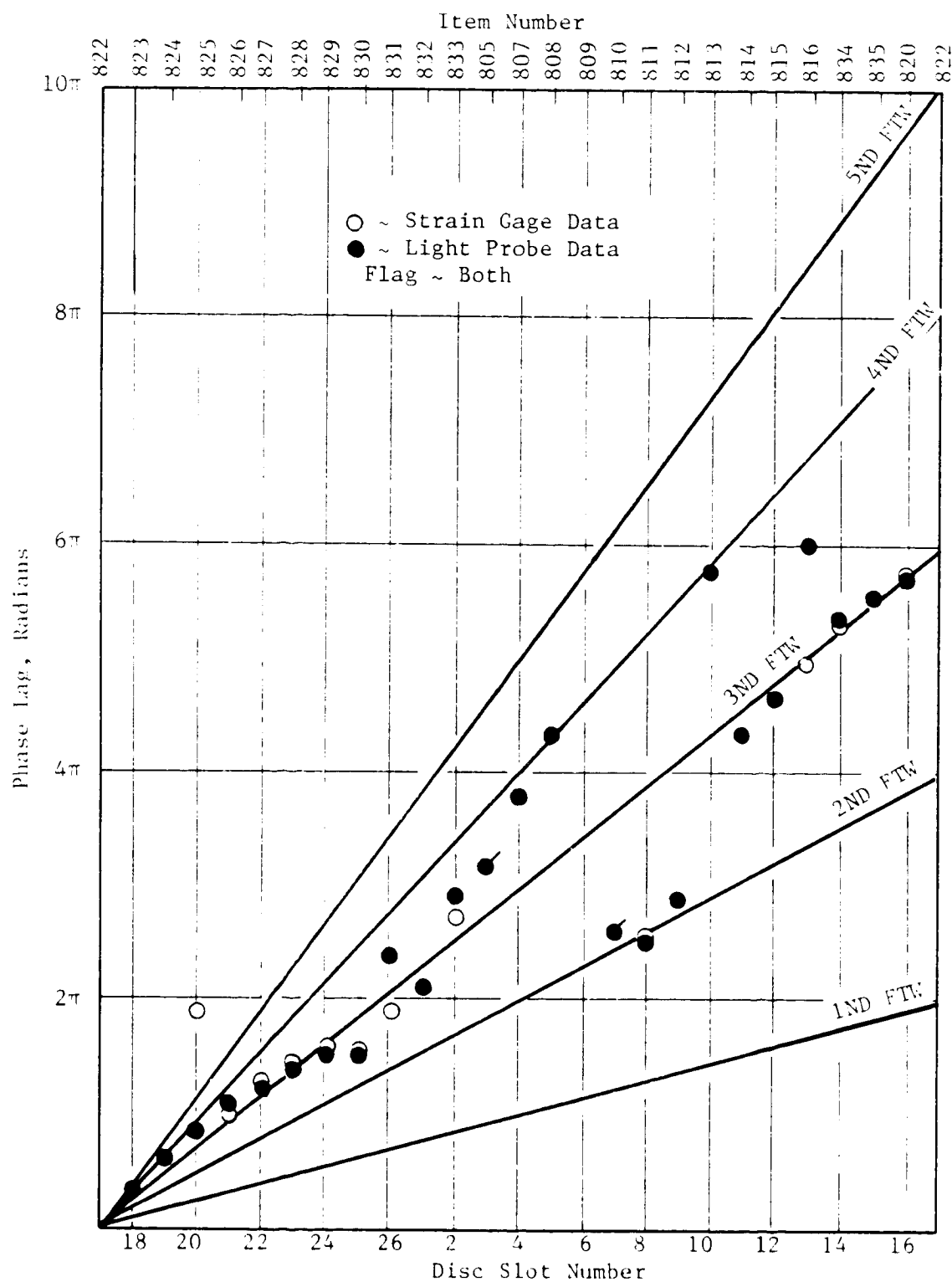


Figure 67. Blade Phase Data at 95 Percent Speed Flexural Flutter.

Table XIX. Unsteady Tip Displacement Phase Lag (In Degrees)
at 70 Percent Speed Flutter.

Disk Slot No.	Light Probe				
	#755	#756	#757	#758	#759
1	220	198	186	205	233
2	41	43	26	61	25
3	0	0	0	0	0
4	111	122	99	155	114
5	138	141	127	149	125
6	129	135	119	156	124
7	194	197	180	208	195
8	301	307	292	328	296
9	8	4	352	19	5
10	81	87	70	112	75
11	72	74	61	98	82
12	150	152	136	170	143
13	143	149	133	163	153
14	144	151	135	176	147
15	260	263	249	282	301
16	71	80	71	115	73
17	106	106	92	126	110
18	160	164	152	165	157
19	227	235	218	267	243
20	343	45	335	28	298
21	9	27	4	66	354
22	86	87	76	108	65
23	108	108	92	138	100
24	135	135	118	150	126
25	184	194	174	194	180
26	204	202	184	235	227

Note: Reference Blade in Disk Slot No. 3

Table XX. Unsteady Tip Displacement Phase Lag (In Degrees)
at 95 Percent Speed Flutter.

Disk Slot No.	Light Probe							
	#755	#756	#757	#758	#759	#760	#761	#762
1	14	79	61	46	24	10	38	18
2	160	163	130	118	113	140	88	156
3	208	310	251	226	252	192	303	296
4	319	36	9	345	15	338	354	81
5	55	89	43	53	1	73	56	357
6	110	109	87	103	79	121	94	95
7	104	29	356	355	305	108	8	301
8	91	100	80	91	77	102	90	70
9	155	240	224	236	219	162	232	207
10	313	356	341	353	340	313	352	329
11	57	57	51	58	63	58	68	50
12	114	118	111	117	121	114	124	125
13	355	190	176	136	181	175	182	185
14	238	222	209	217	224	239	226	213
15	274	254	247	250	253	274	252	261
16	310	298	295	293	290	311	296	277
17	0	0	0	0	0	0	0	0
18	54	55	56	56	55	55	58	68
19	106	104	99	104	101	109	97	71
20	148	127	126	127	128	151	134	138
21	183	166	172	170	165	184	168	169
22	220	198	198	199	194	221	198	210
23	245	244	234	238	238	247	239	240
24	268	258	216	225	225	274	235	236
25	268	313	259	288	307	281	297	355
26	65	73	38	32	27	86	31	331

Note: Reference blade in disk slot Number 17.

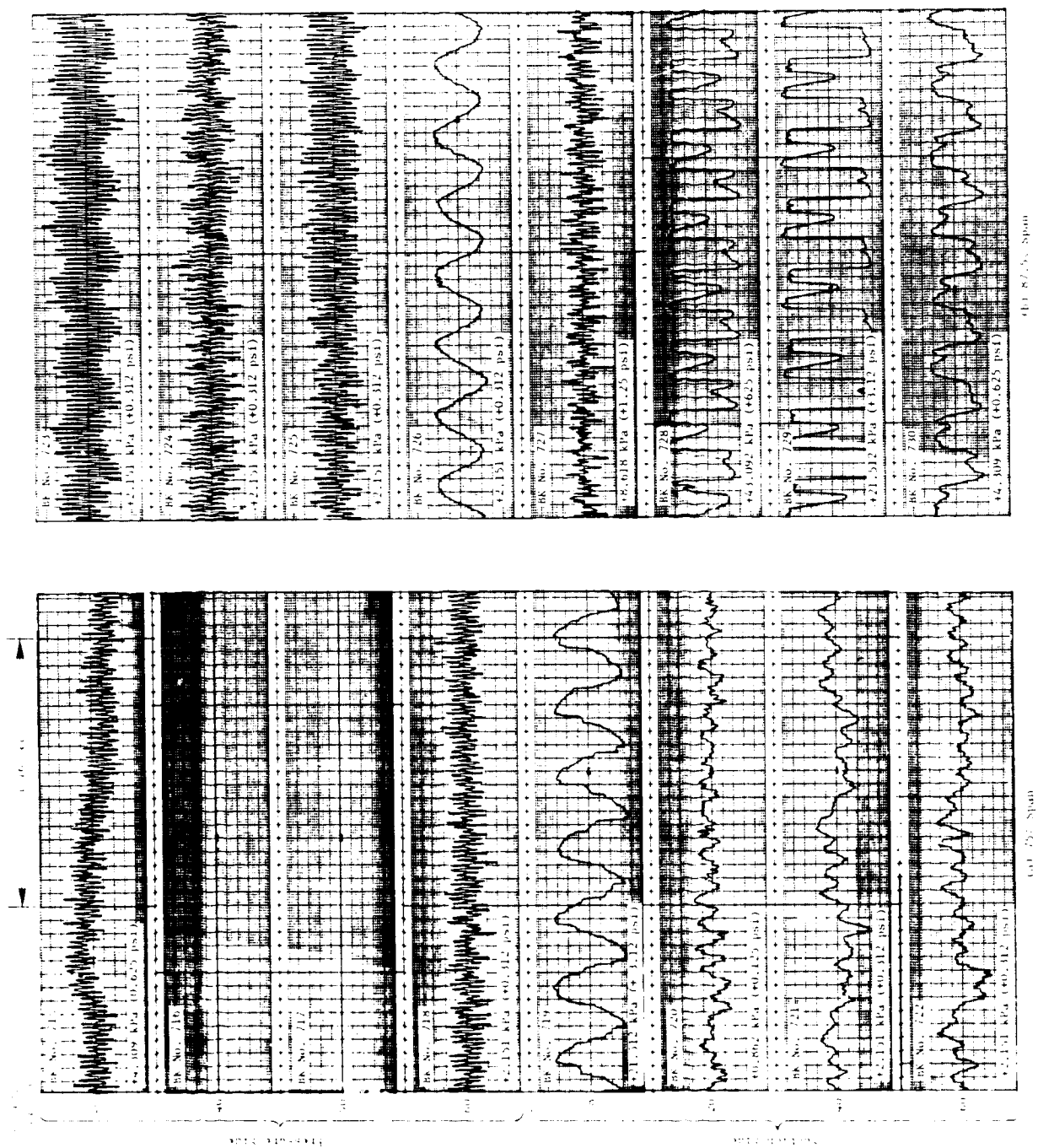
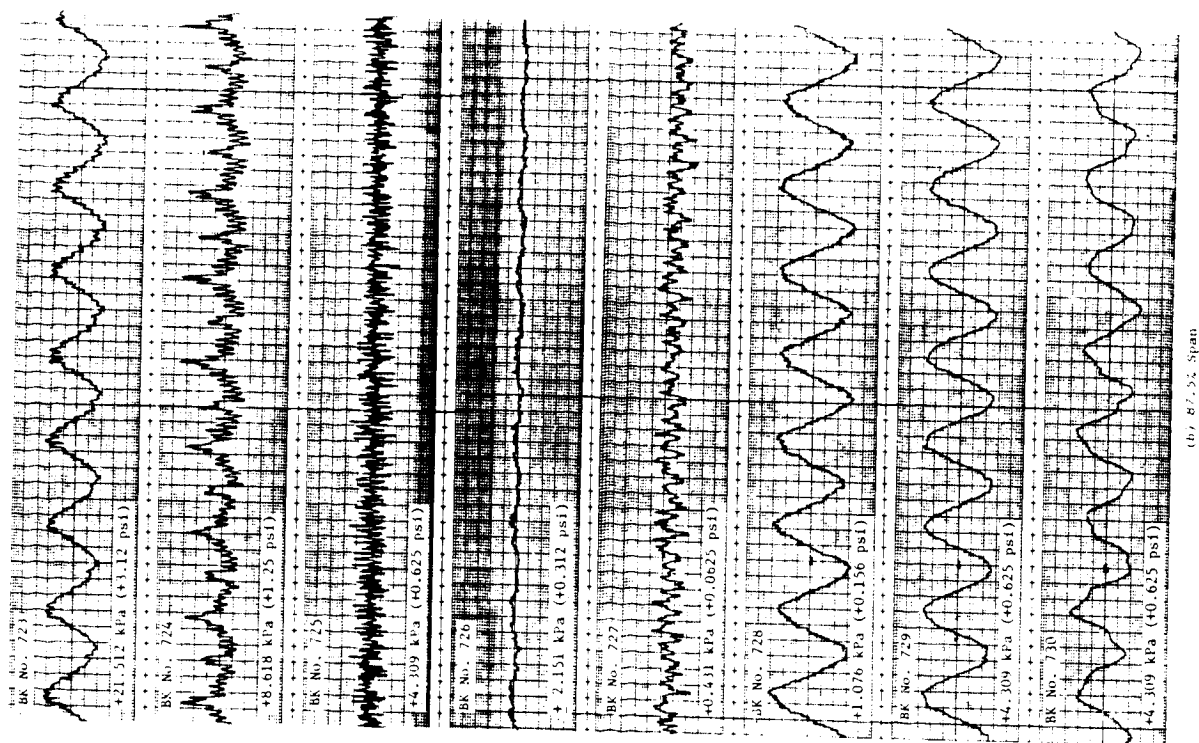
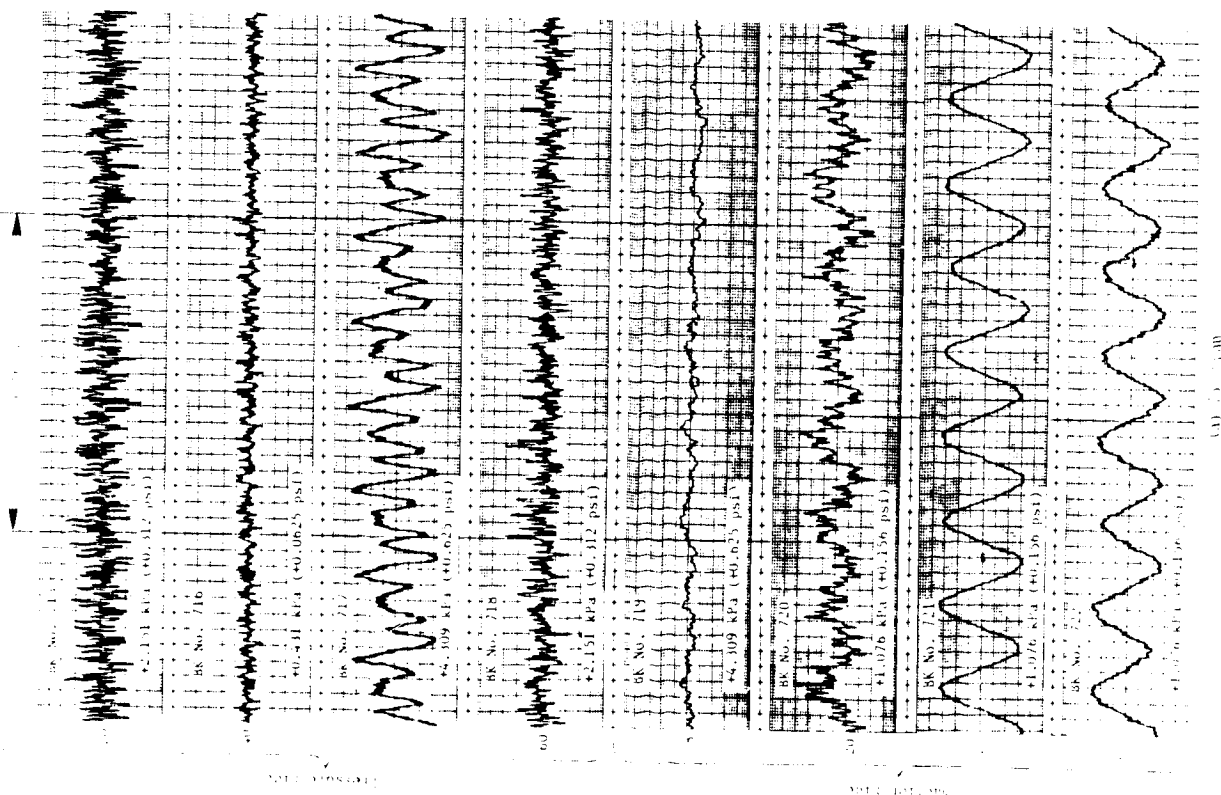


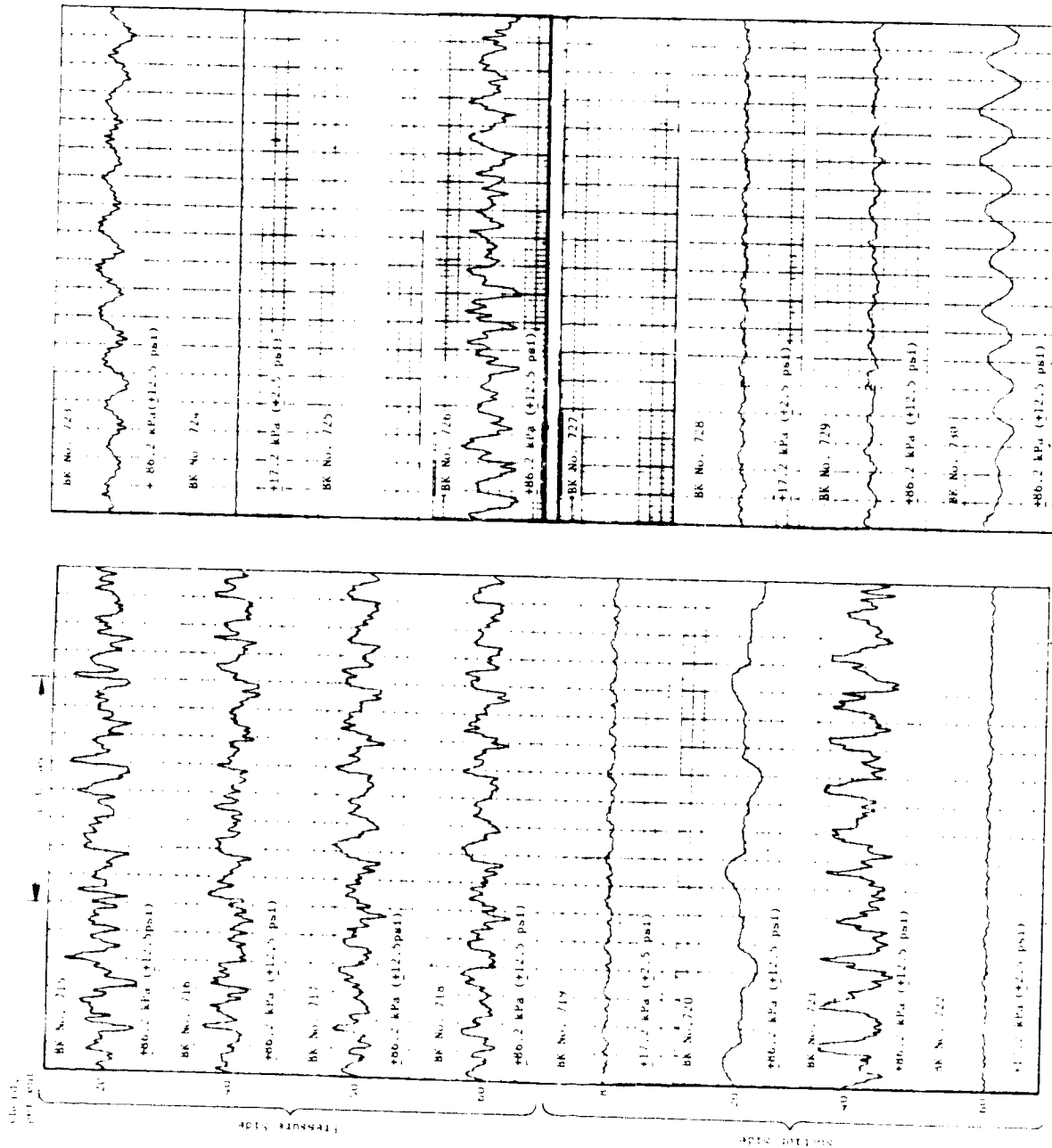
Figure 68. Blade-Mounted Kulite Time Histories, 65 Percent Speed Flutter.



ORIGINAL
OF POKK

Figure 69. Blade-Mounted Kulite Time Histories, 70 Percent Speed Flutter.

ORIGINAL
OF FOUR



Case 70-1000

(b) 87.5% Speed

Figure 70. Blade-Mounted Kulite Time Histories, 95 Percent Speed Flutter.

On the pressure side the response at 20 percent chord is approximately twice as large as the response at 60 percent chord. The suction side has much smaller responses than the pressure side. At 87.5 percent span more Kulites were operational at this speed and they responded at the flutter frequency. On the pressure side, flutter response is obvious at 20, 40, and 50 percent chord with the largest response at 20 percent chord. On the suction side, only the Kulite at 8 percent chord showed some flutter response. In the span-wise direction, the response at 20 percent chord on the pressure side is seen to be slightly larger at 75 percent span than at 87.5 percent span.

The time histories taken during 70 percent speed flutter, shown in Figure 69, are qualitatively very similar to those of 65 percent speed flutter except that the flutter responses at 70 percent speed are severely masked by noise and other nonflutter signals. Similar results obtained at the 95 percent speed flutter condition are shown in Figure 70. These figures provide for only a qualitative assessment of the response.

The Kulite time histories for intermediate and nominal operating conditions are provided in Appendix C for reference. The effects of throttling to the flutter boundary can be qualitatively examined using the appropriate time histories. The time histories for the operable blade-mounted Kulites at 65 and 70 percent speed indicate that the airfoil dynamic pressure tends to be less at the flutter boundary than at the non-flutter points. But at 95 percent speed, the airfoil dynamic pressures almost double at the flutter boundary. It may be the torsional strain sensitivity of the blade-mounted Kulites that makes the recorded pressure amplitudes at 65 and 70 percent speed behave contrary to intuition.

6.4.2 Airfoil Unsteady Pressure

Another observation of the unsteady pressure on the airfoil can be obtained from the linear spectra of the blade-mounted Kulite time histories. Figures 71 and 72 are the linear spectra of the operational blade-mounted Kulites during torsional flutter at 65 and 70 percent speed respectively. The portion of the Kulite response which is at the torsional flutter frequency of 896 Hz can be seen in these spectra. For 95 percent speed flutter, the linear spectra in Figure 73 show the Kulites to have a significant pressure component at the flexural frequency of 336 Hz.

Blade-mounted Kulite spectra for the nonflutter points show that the majority of the Kulites do not have an unsteady pressure component at the flutter frequency. This is illustrated in Figures 74 through 76 where the spectral amplitudes of the blade-mounted Kulite response are plotted for the flutter and nonflutter points at 65, 70, and 95 percent speed respectively. Obviously, the nearly sinusoidal response of the blades at the flutter boundary stimulate a blade-mounted Kulite pressure component at the flutter frequency.

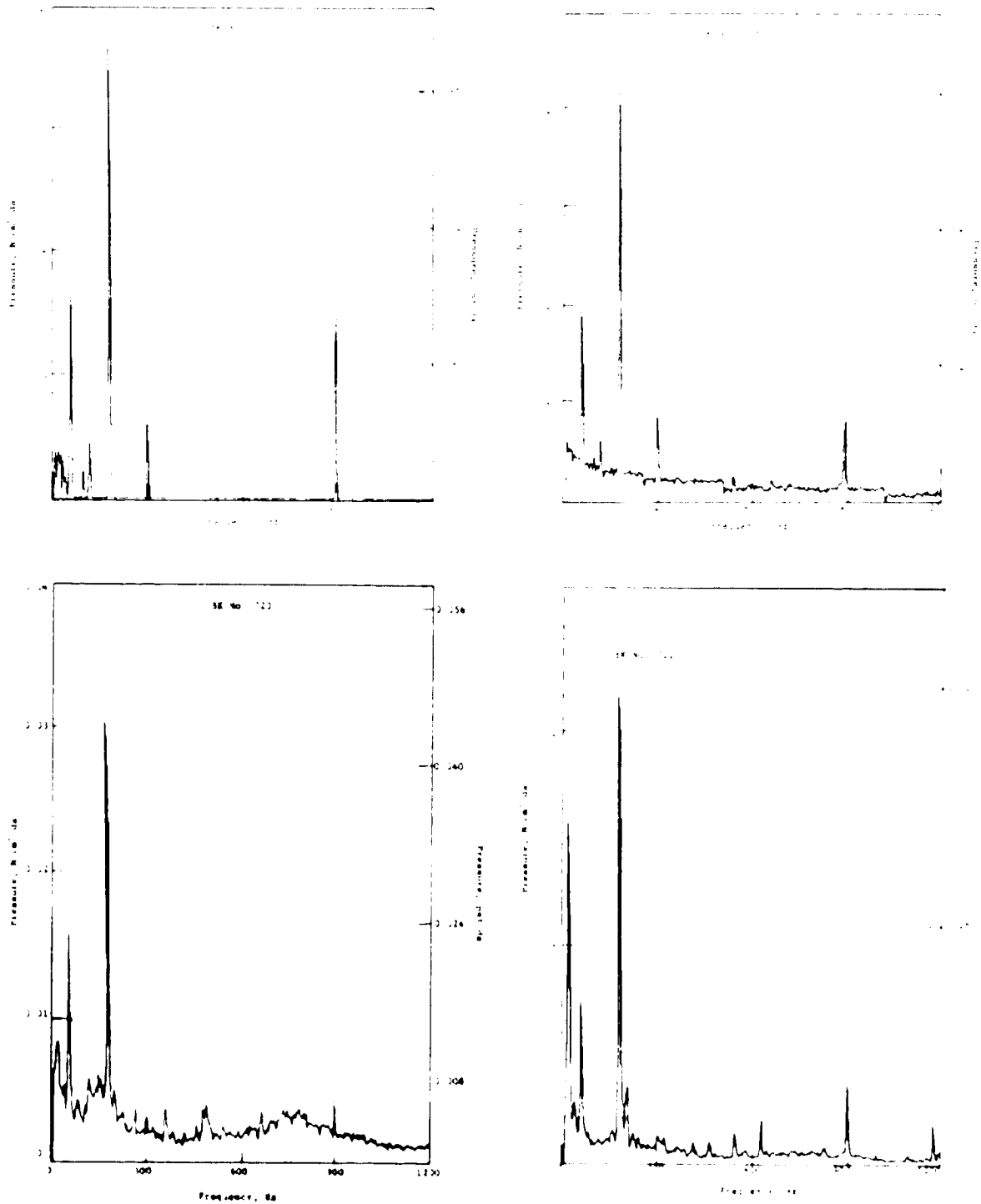


Figure 71. Blade-Mounted Kulite Auto Spectra, 65 Percent Speed Flutter.

ORIGINAL OF POOR QUALITY

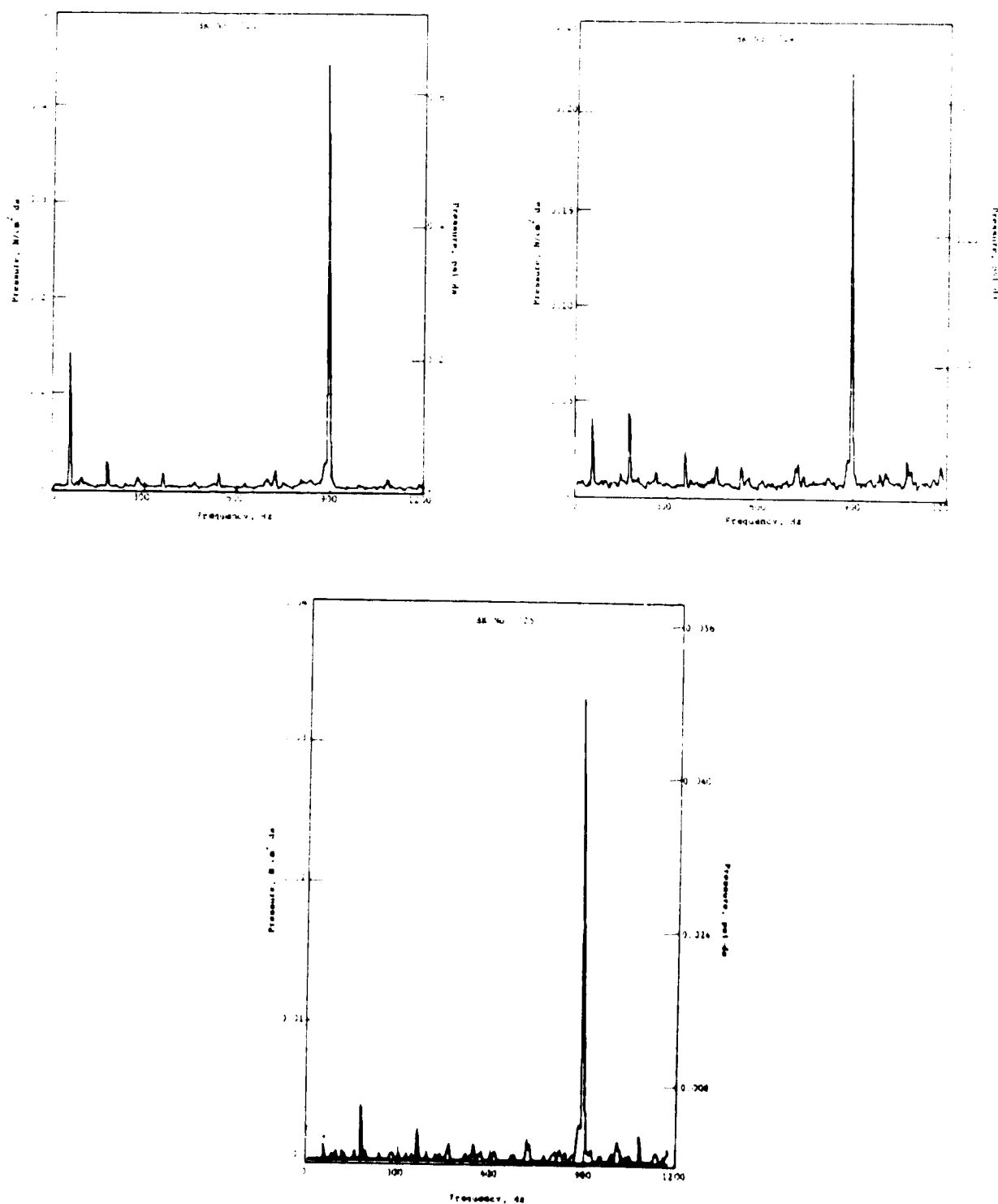


Figure 71. Blade-Mounted Kulite Auto Spectra, 65 Percent Speed Flutter (Continued).

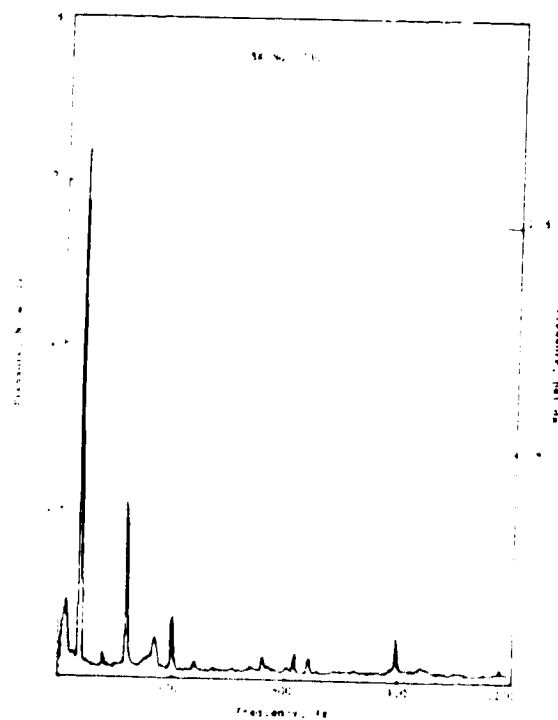
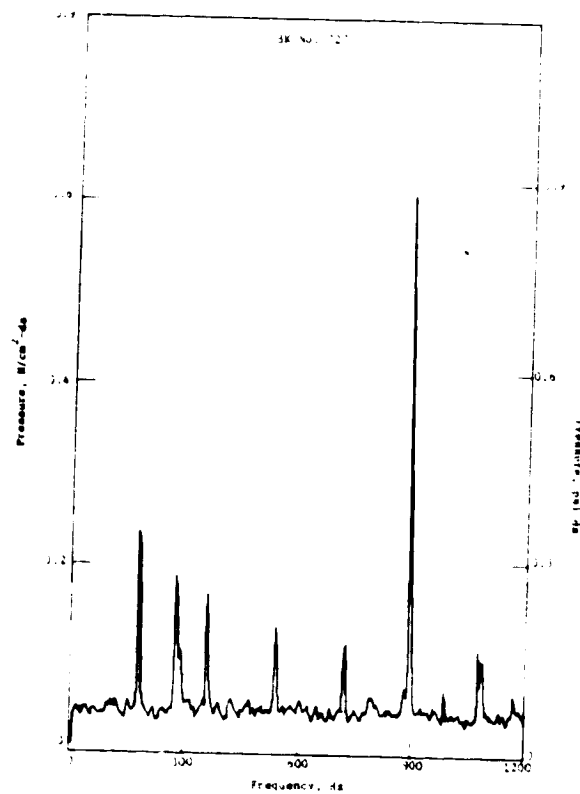


Figure 71. Blade-Mounted Kulite Auto Spectra, 65 Percent Speed Flutter (Concluded).

ORIGINAL COPY
OF POOR QUALITY

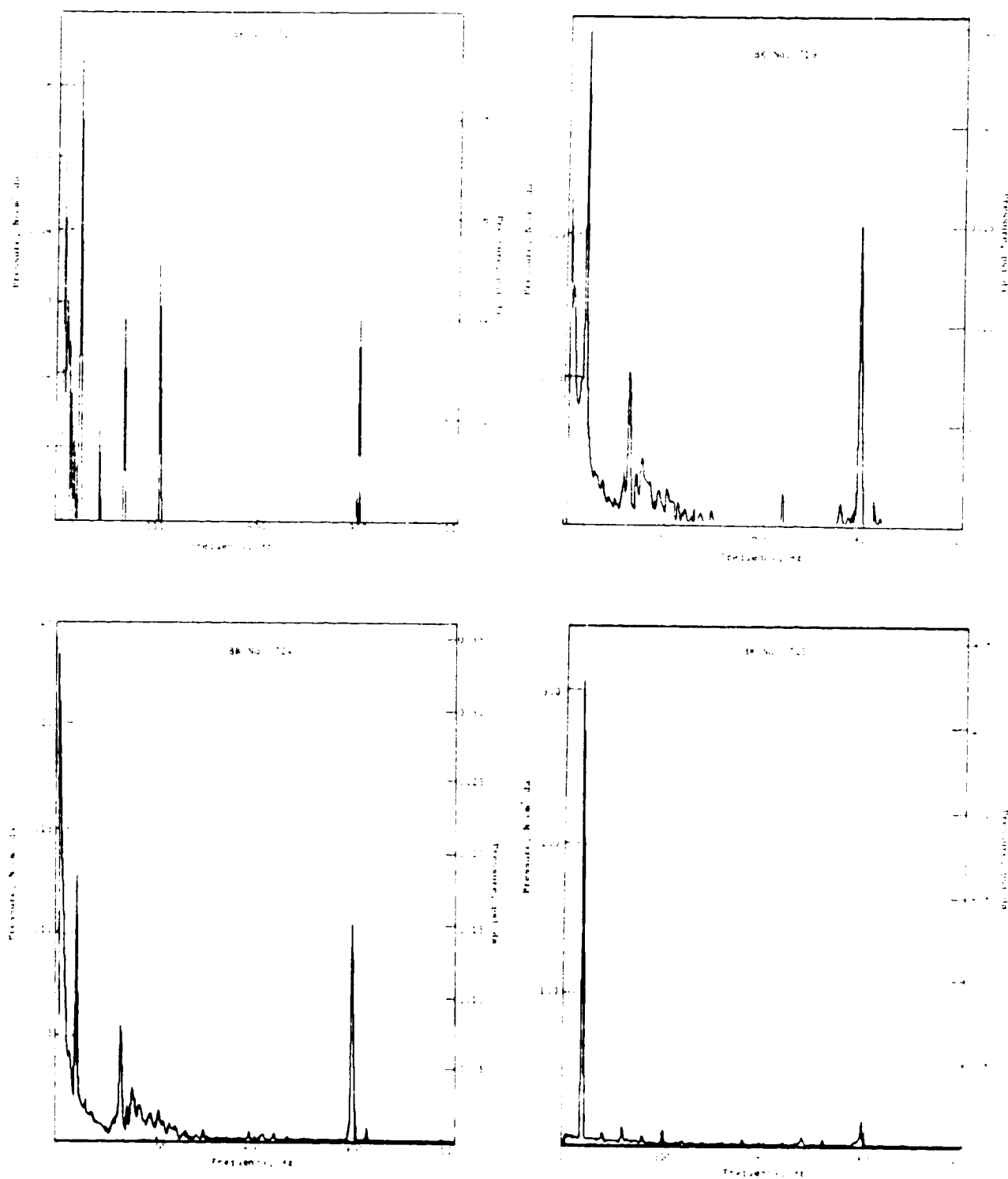


Figure 72. Blade-Mounted Kulite Auto Spectra, 70 Percent Speed Flutter.

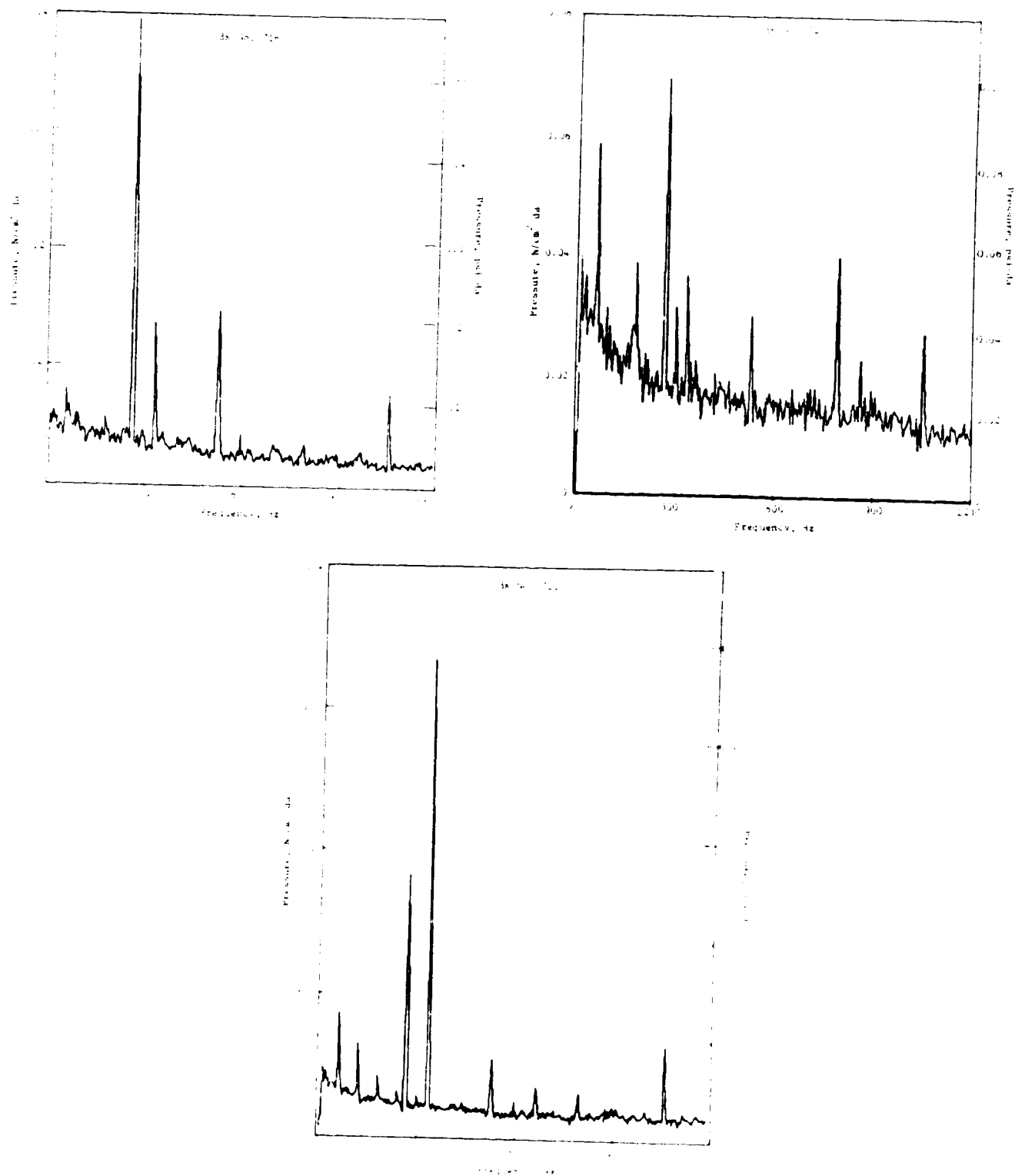


Figure 73. Blade-Mounted Kulite Auto Spectra, 95 Percent Speed Flutter.

ORIGINAL
OF POOR QUALITY

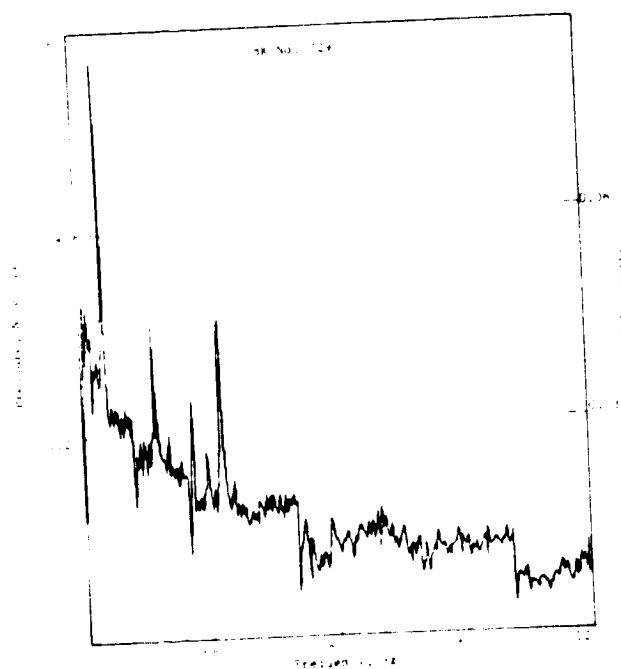
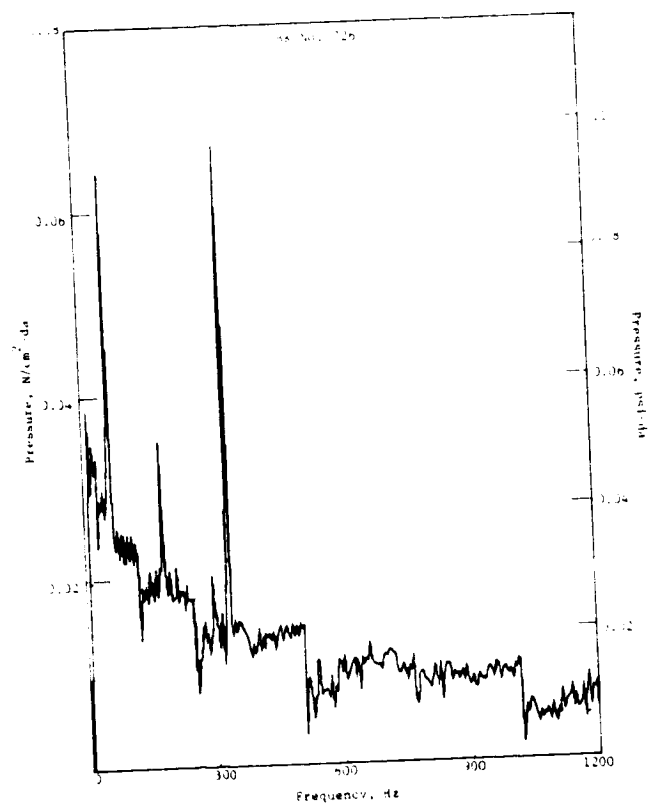


Figure 73. Blade-Mounted Kulite Auto Spectra,
95 Percent Speed Flutter (Concluded).

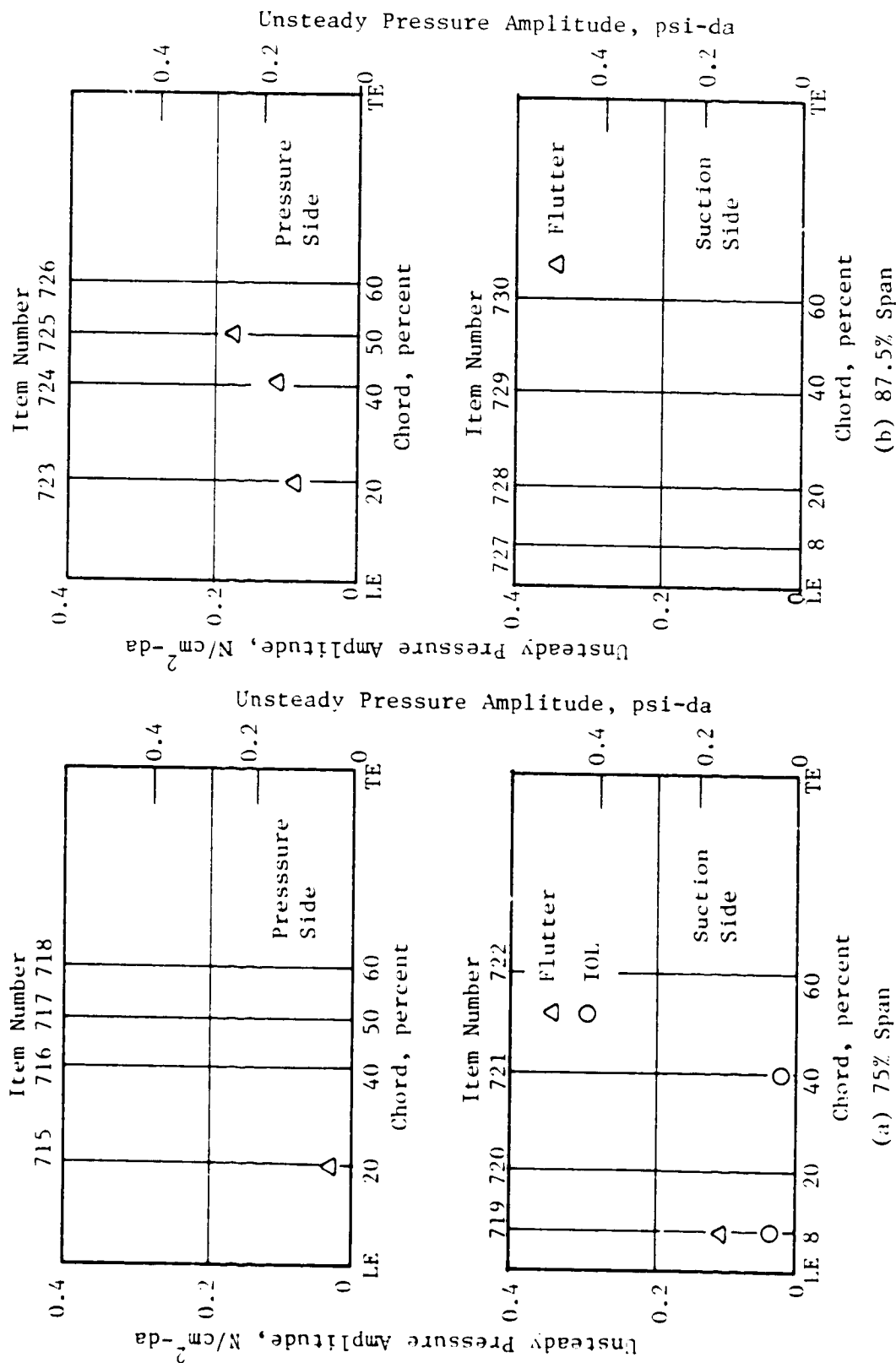
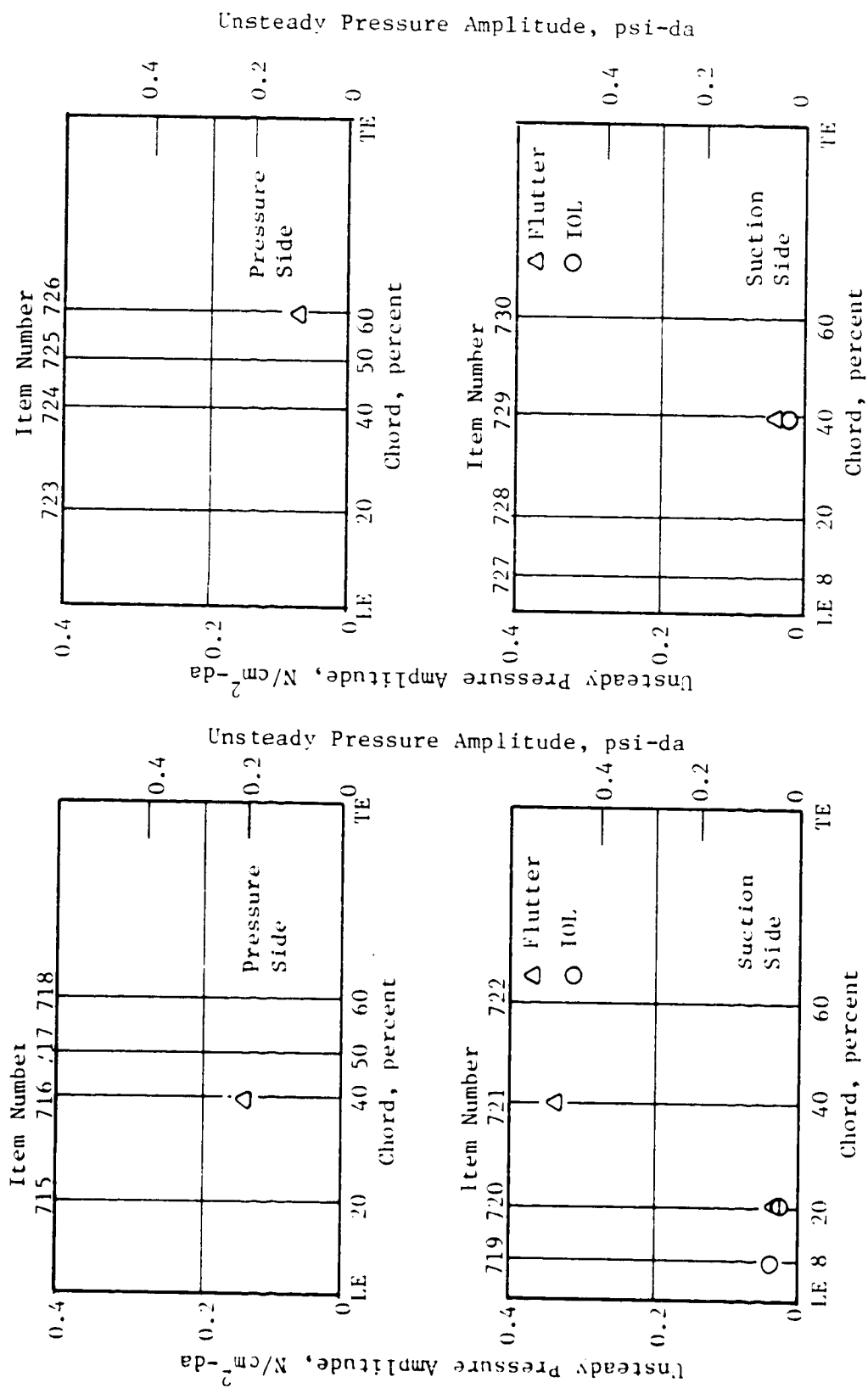


Figure 75. Blade-Mounted Kulite Measured Pressure, 70 Percent Speed.



(a) 75% Span

(b) 87.5% Span

Figure 76. Blade-Mounted Kulite Measured Pressure, 95 Percent Speed.

6.4.3 Unsteady Pressure Phase Angle

Cross spectral analyses were made to find the phase angle between the blade-mounted Kulite response and the reference strain gage response at the flutter frequency. Figures 77 and 78 are typical results for 65 and 70 percent speed flutter respectively. Note that different reference strain gages were used at different speeds. The phase angles generated from this analysis are shown in Figure 79. The phase data were very limited due to sensor failures.

6.5 BLADE TIP STATIC PRESSURE FIELD

Acquiring detailed measurements of steady and unsteady aerodynamics surrounding the rotor was a prime objective of this program. Measurements to obtain this data were made over the blade tip with casing-mounted Kulites and static taps. Here the objective was to establish the shock structure at the blade tip while operating at nonflutter and flutter conditions.

The flowfield static pressure distribution was generated between blade passages as would be observed in the rotating reference system. The characteristics of the static pressure distribution have a definite bearing on the perturbation pressure fluctuations due to blade vibration.

The unsteady part of the static pressure, $(P_s)_{AC}$, measured by the casing Kulites, was used to identify and analyze the traveling waves that existed in the flutter modes. The casing Kulite data can produce accurate information on the amplitude and phase of all significant traveling waves from which, with linear superposition, one can calculate the unsteady static pressure due to blade vibrations as would be observed in the rotating reference system. The unsteady static pressure in the rotating reference system is the key physical quantity that all unsteady aerodynamic theories are developed to predict.

6.5.1 Static Pressure Distribution

The 64-sample ensemble average (see Section 5.2.4) of the casing Kulite data gave the circumferential distribution of the dynamic part of the instantaneous static pressure. Typical results for the four flutter points tested are shown in Figures 80 and 81. These results show the apparent blade passing as identified by a rapid change in pressure. Also, the pressure patterns are cleaner at the blade leading edge. It can be seen that the peak unsteady static pressure amplitude decreases in going from the leading edge to the trailing edge.

Contour plots of the total static pressure, variation over the blade tips $(P_s)_{AC} + (P_s)_{DC}$, are presented in Figures 82 through 85 for the four flutter points. With each contour plot is the circumferential average of the steady static pressure, $(P_s)_{DC}$, as a function of axial position. These contour plots are presented with isobars superimposed on an unwrapped view of several adjacent blade passages.

ORIGINAL PAGE IS
OF POOR QUALITY

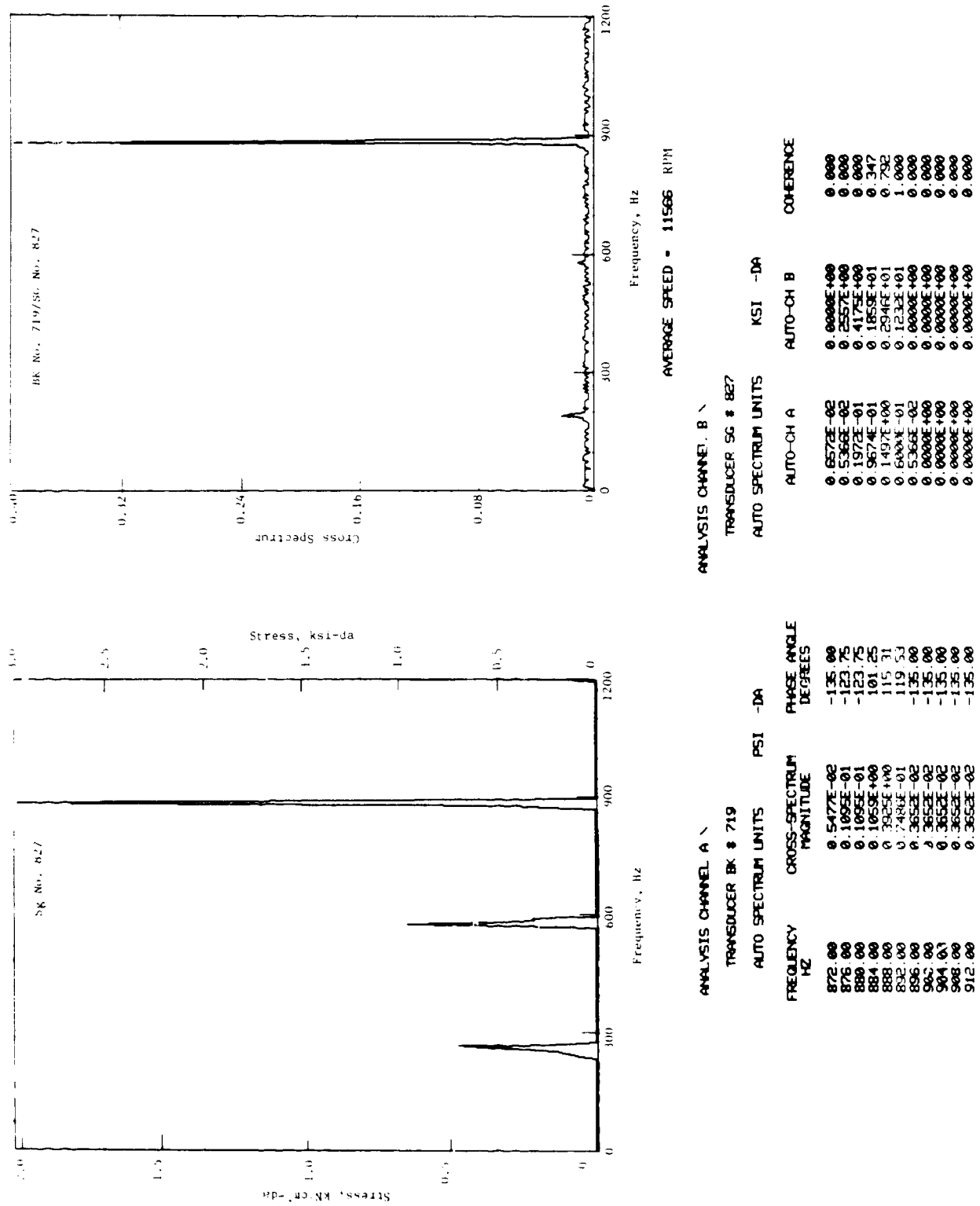
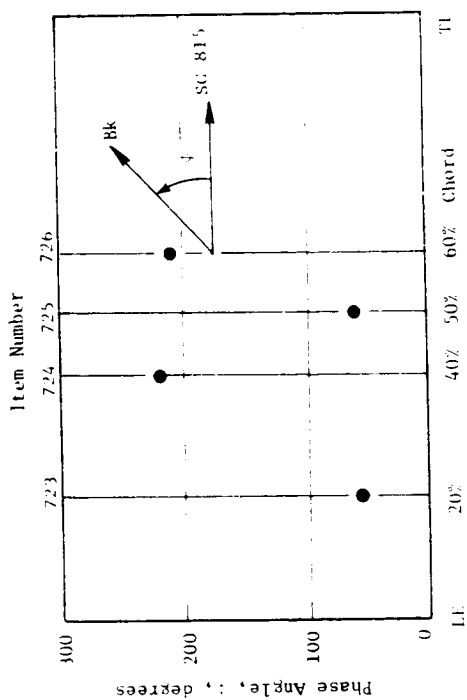
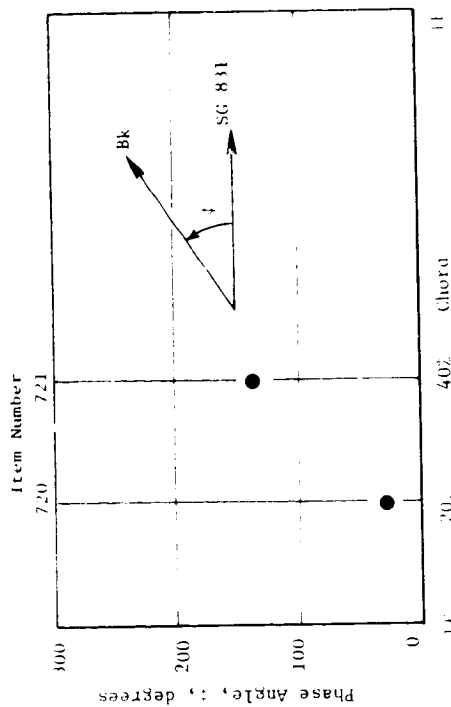


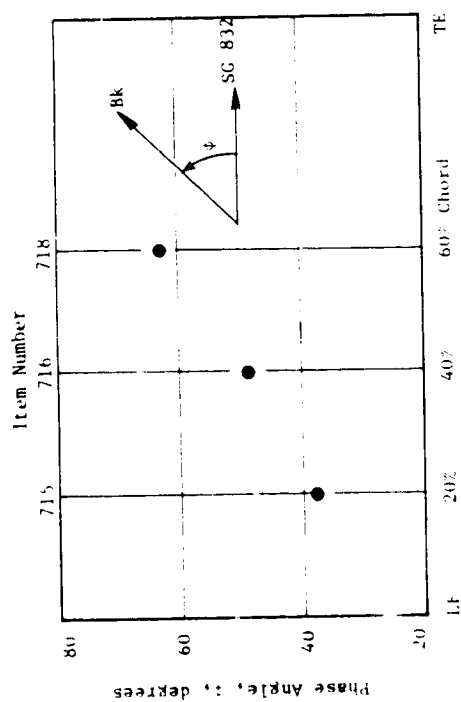
Figure 78. Blade-Mounted Kulite Cross Spectrum, 65 Percent Speed Flutter.



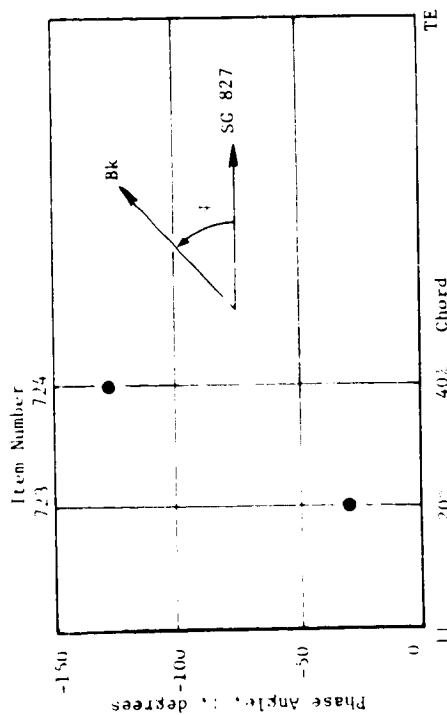
(b) 65% N Flutter, 87.5% Span, Pressure Side



(d) 95% Speed Flutter, 75% Span, Suction Side



(a) 65% N Flutter, 75% Span, Pressure Side



(c) 70% Speed Flutter, 87.5% Span, Pressure Side

Figure 79. Blade-Mounted Kulite Phase Data.

OF PCC

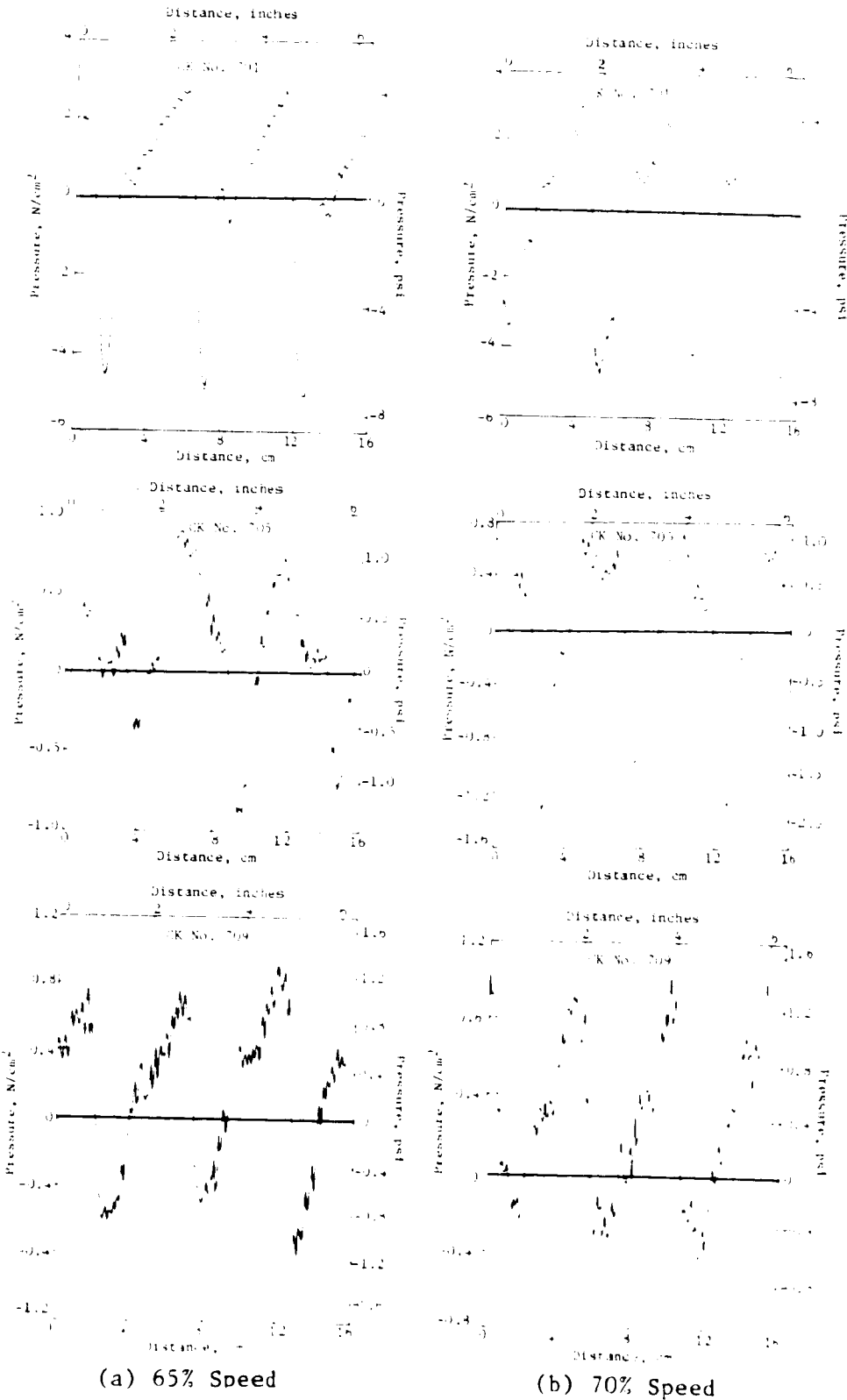
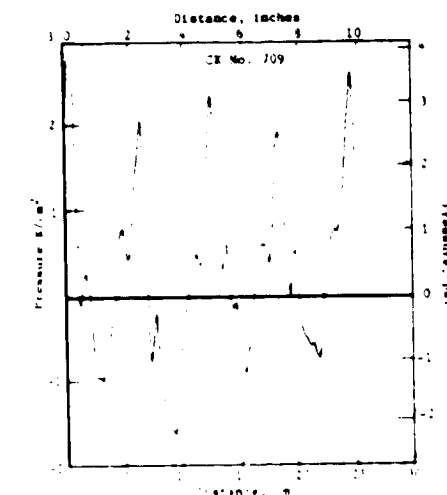
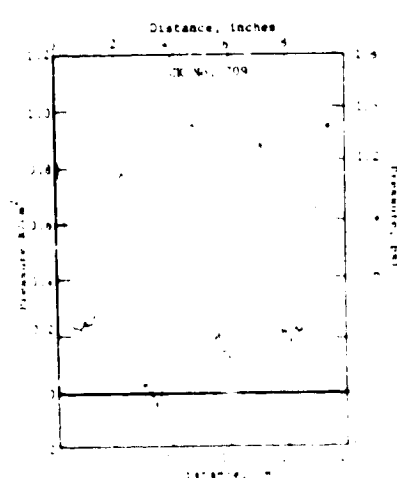
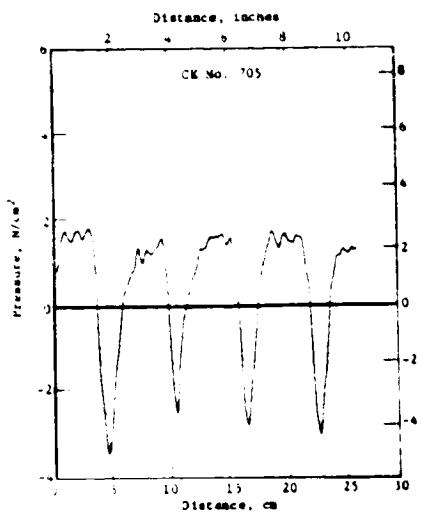
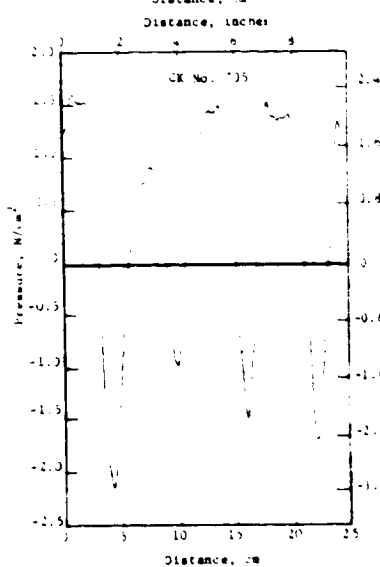
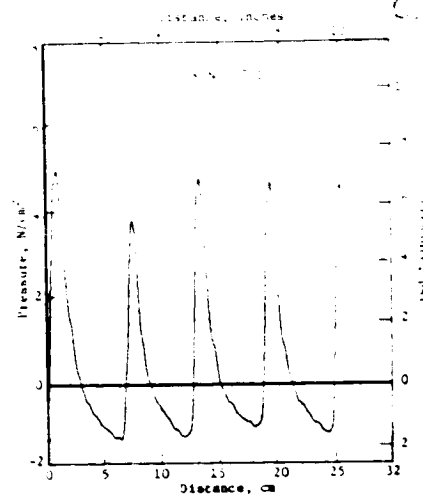
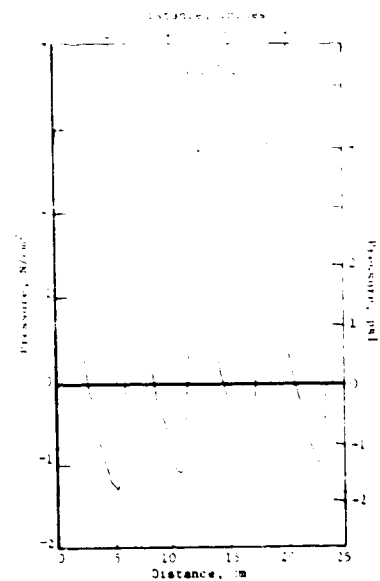


Figure 80. Dynamic Part of the Instantaneous Static Pressure, 65 and 70 Percent Speed Flutter.



(c) 90% Speed

(d) 95% Speed

Figure 81. Dynamic Part of the Instantaneous Static Pressure, 90 and 95 Percent Speed Flutter.

ORIGINAL
OF POCOR

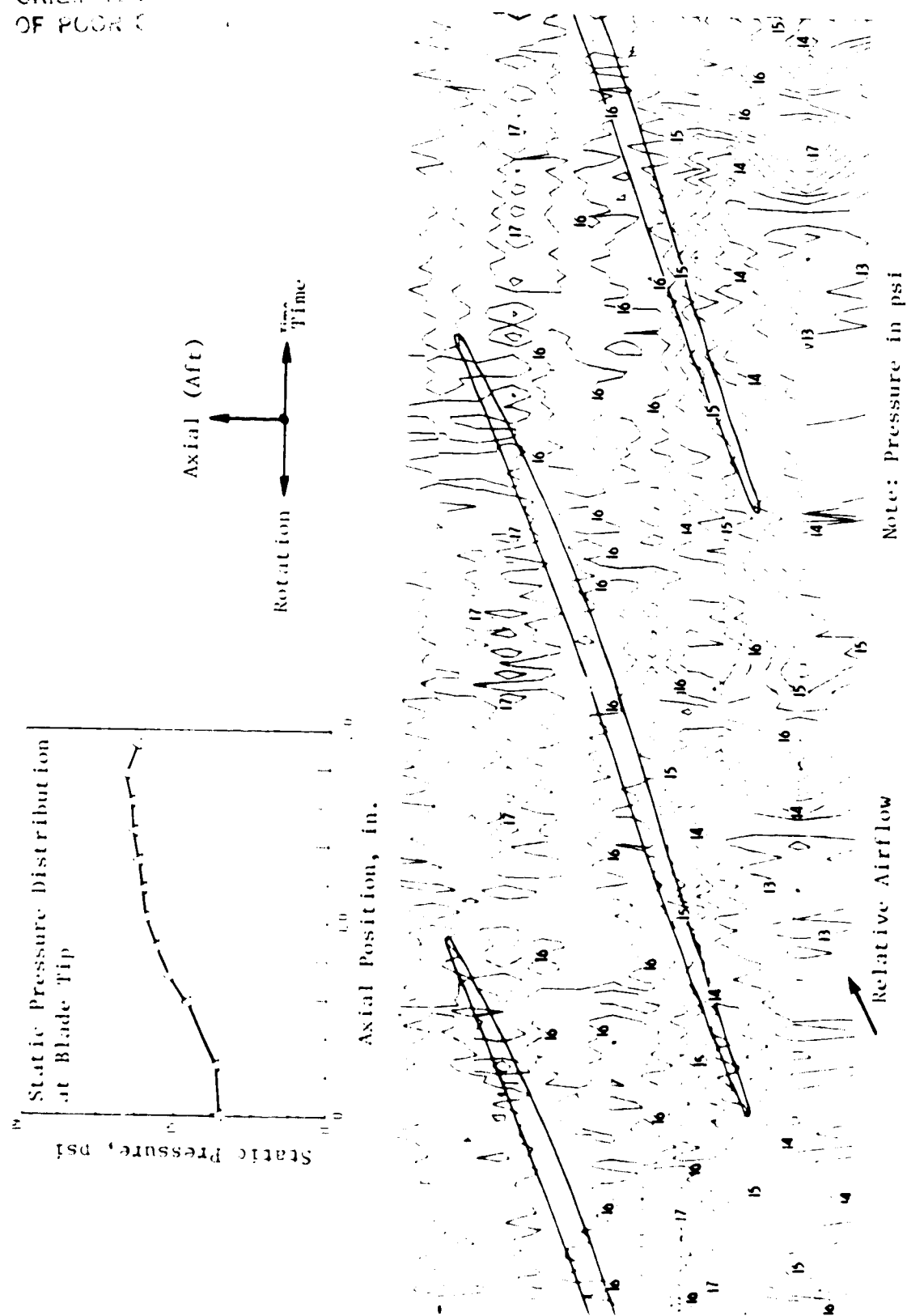


Figure 82. Casing Kulite Contour Plot, 65 Percent Speed Flutter.

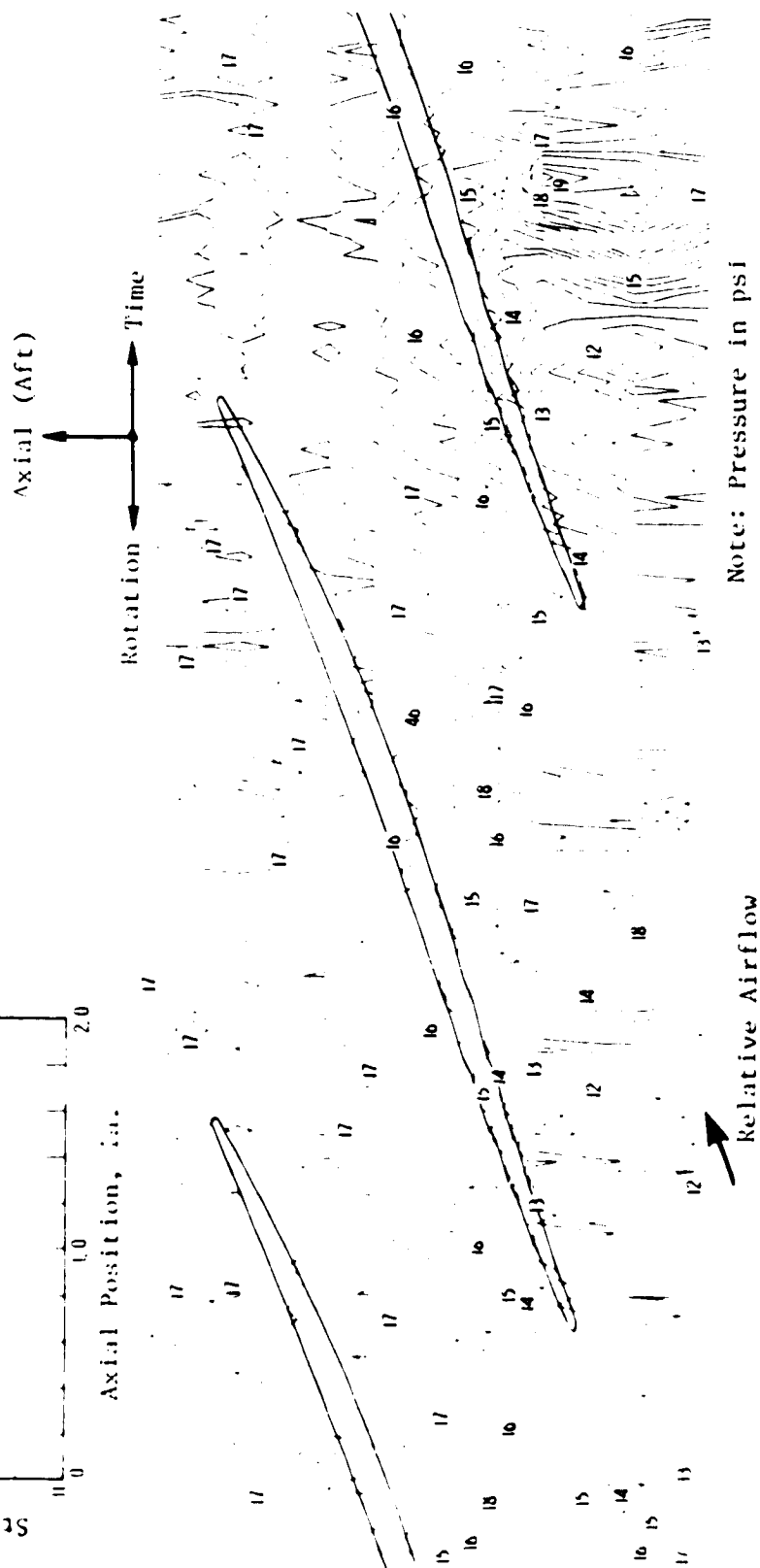
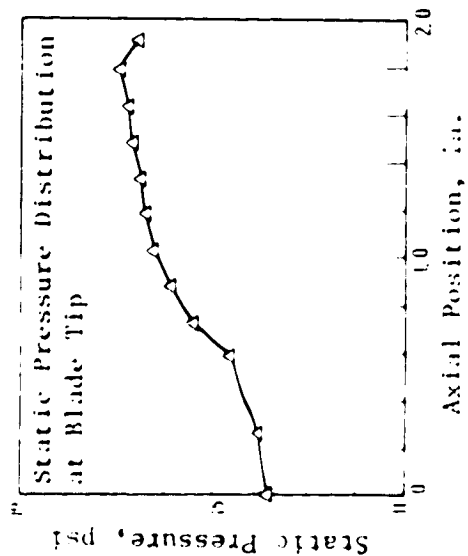
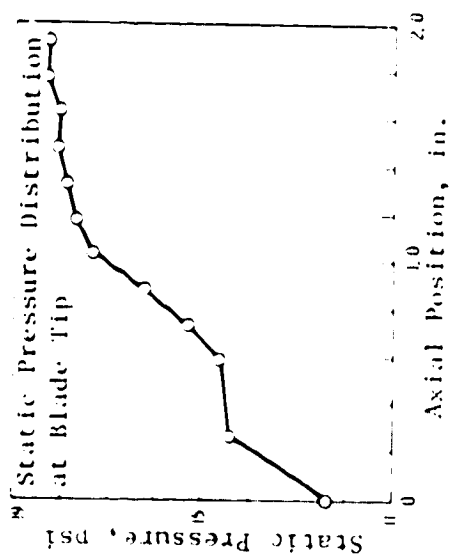


Figure 83. Casing Kelite Contour Plot, 70 Percent Speed Flutter.

ORIGIN
OF POOR QUALITY



Rotation → Axial (Aft) ↑ Time

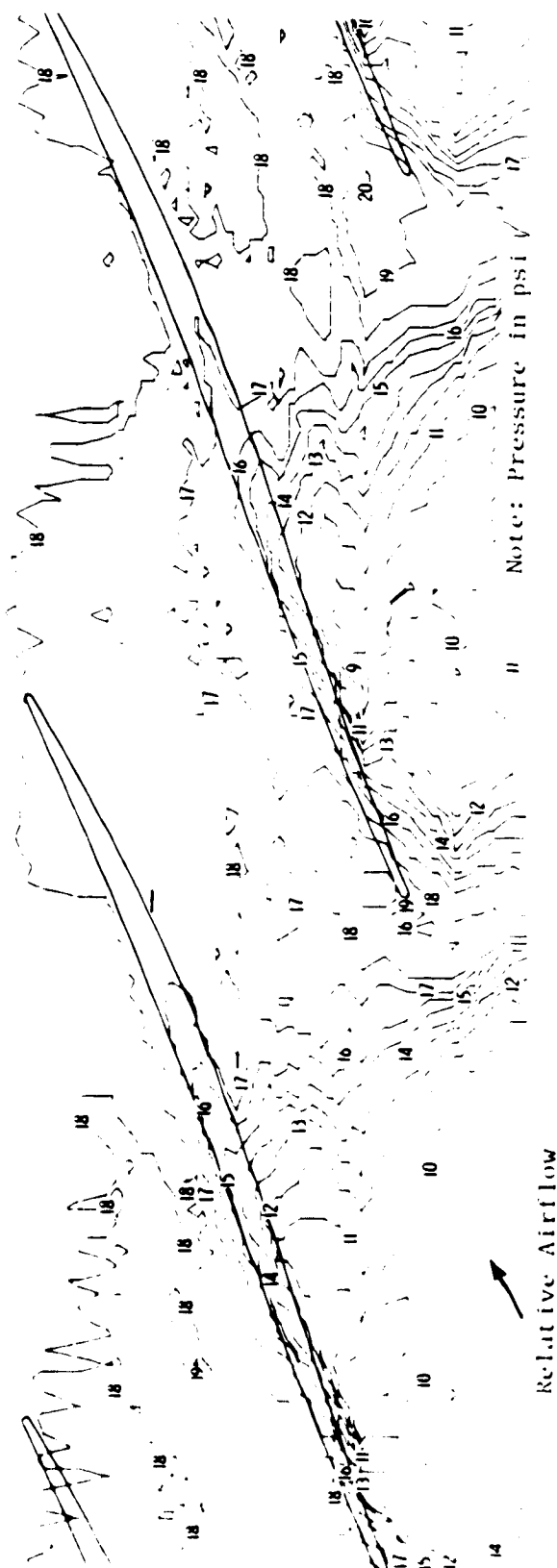


Figure 84. Casing Kulite Contour Plot, 90 Percent Speed Flutter.

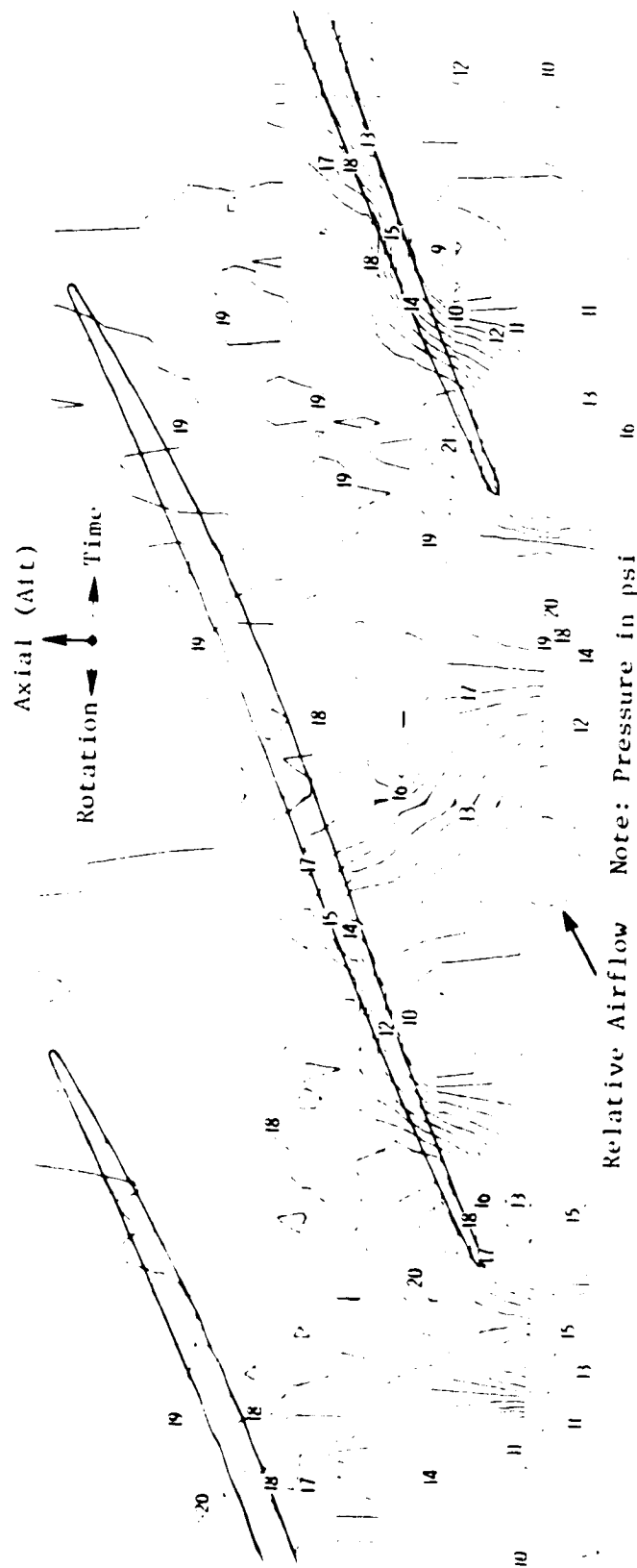
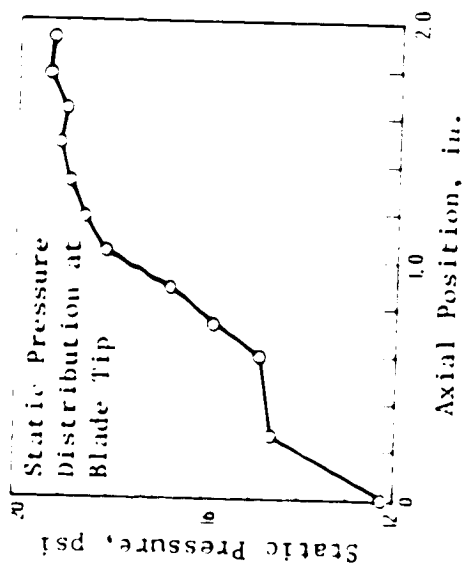


Figure 85. Casing Kulite Contour Plot, 95 Percent Speed Flutter.

Similar contour plots for the six nonflutter points, shown in Figures 86 through 91, are from the casing Kulite data acquired on the NOL at 70 and 90 percent speed and on an IOL at all four speeds tested. These total static pressure contour plots provide data to determine the changes in shock patterns with throttling and with stable versus flutter operating conditions.

At the 65 percent speed flutter point, it can be seen that the pressure field suggests a predominantly subsonic flow situation with only slight evidence of a bow shock (tip relative Mach number of 0.9 and a flow angle of 77 degrees). A detached bow shock wave is apparent at the 70 percent speed flutter point impinging on the suction surface normal to the flow direction (see also Reference 5). The flowfield behind the shock is subsonic at a nearly uniform pressure level.

At the 90 percent speed flutter point, the higher Mach numbers and overall pressure rise create a more complex pressure pattern. The relative inlet tip Mach number is 1.3 and the flow angle varies from 72 degrees at the low operating line point to 74 degrees at the flutter condition. The flow is noticeably accelerated along the suction surface at the leading edge to a Mach number of about 1.5. This is followed by a slight precompression which lowers the Mach number back to 1.3 before encountering the bow shock of the adjacent blade at approximately 60 percent of the chord length. As was the case at the low speeds, these data points are too throttled to allow the leading edge shock to assume a "started" position as an attached oblique shock. For each of the three 90 percent speed data points, the flow is subsonic behind the normal bow shock and then diffuses uniformly to the required pressure level at the trailing edge.

The inlet Mach number is 1.4 at flow angles of 72 and 73 degrees for the two 95 percent speed data points obtained. As observed at the lower speeds, the leading edge shock stands off normal to the relative flow direction in an "unstarted" position, and flow conditions behind the shock are subsonic.

At all speeds, the pressure contours are well defined through the forward half of the blade passage but are less distinct in the aft region. Pressure contours in this subsonic region that would be expected to be normal to the flow direction were often missed by the transducers. Similarly, the pressure gradients associated with the presence of the blade were well defined only in the leading edge region. In general, the location of the leading edge bow shock in the blade passage could be accurately determined, and its forward movement was observed as the rotor was throttled toward the stall flutter boundary.

The data, as expected, shows that throttling or increasing back pressure causes the shock to move forward towards the leading edge, especially at the high speed points. For 90 and 95 percent speeds, the leading edge bow shocks are observed to be swallowed into the blade passages more deeply at nonflutter conditions than at flutter conditions. In other words, the region of shock intersection on the blade suction surface is moved forward as the flutter boundary is approached. This forward movement of the shock intersection region seems to have a strong influence on the occurrence of high speed flexural flutter.

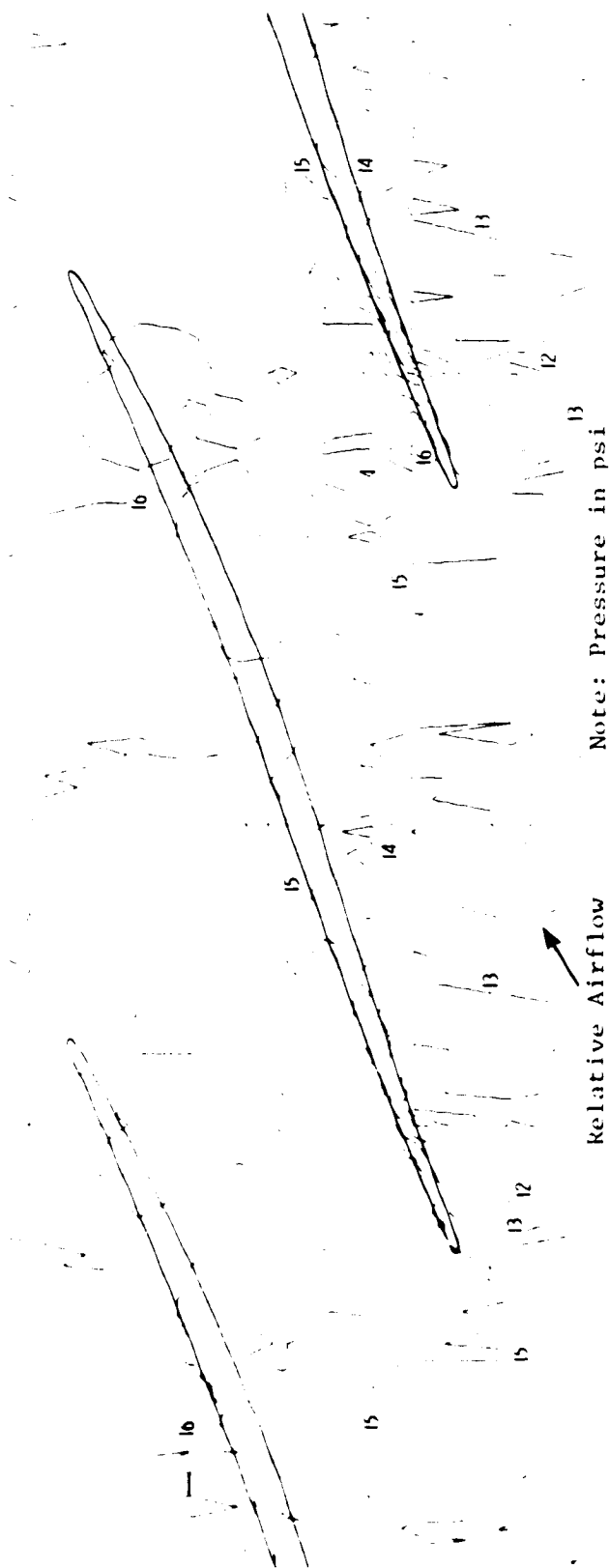
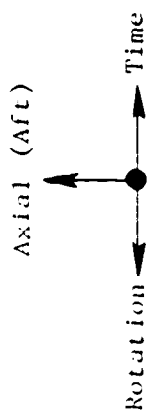
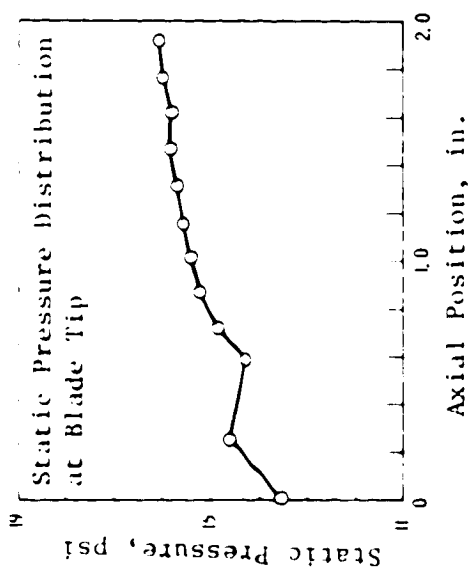


Figure 86. Casing Kulite Contour Plot, 65 Percent Speed Intermediate Operating Line.

ORIGINAL PHOTOGRAPH
OF POOR QUALITY

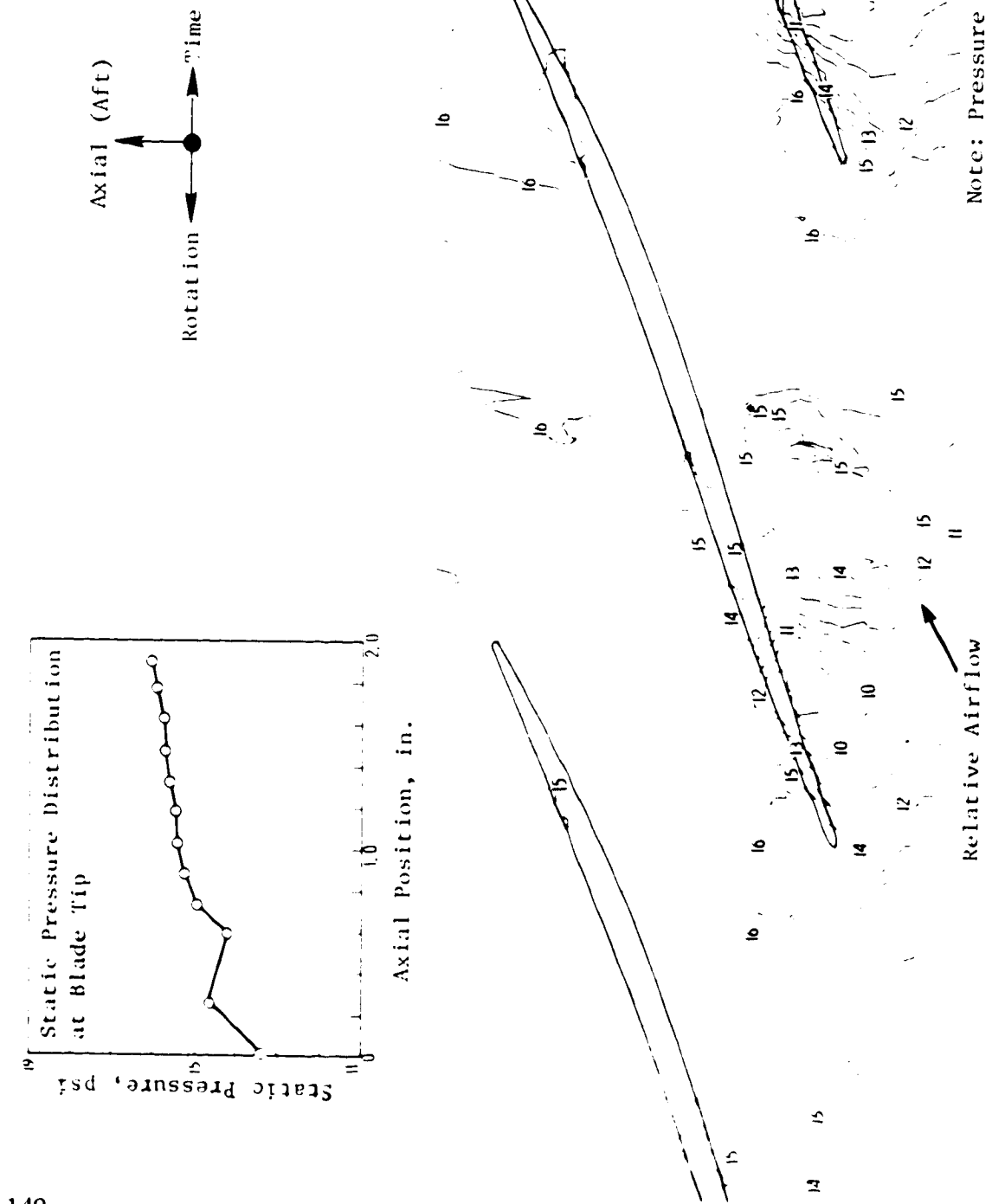
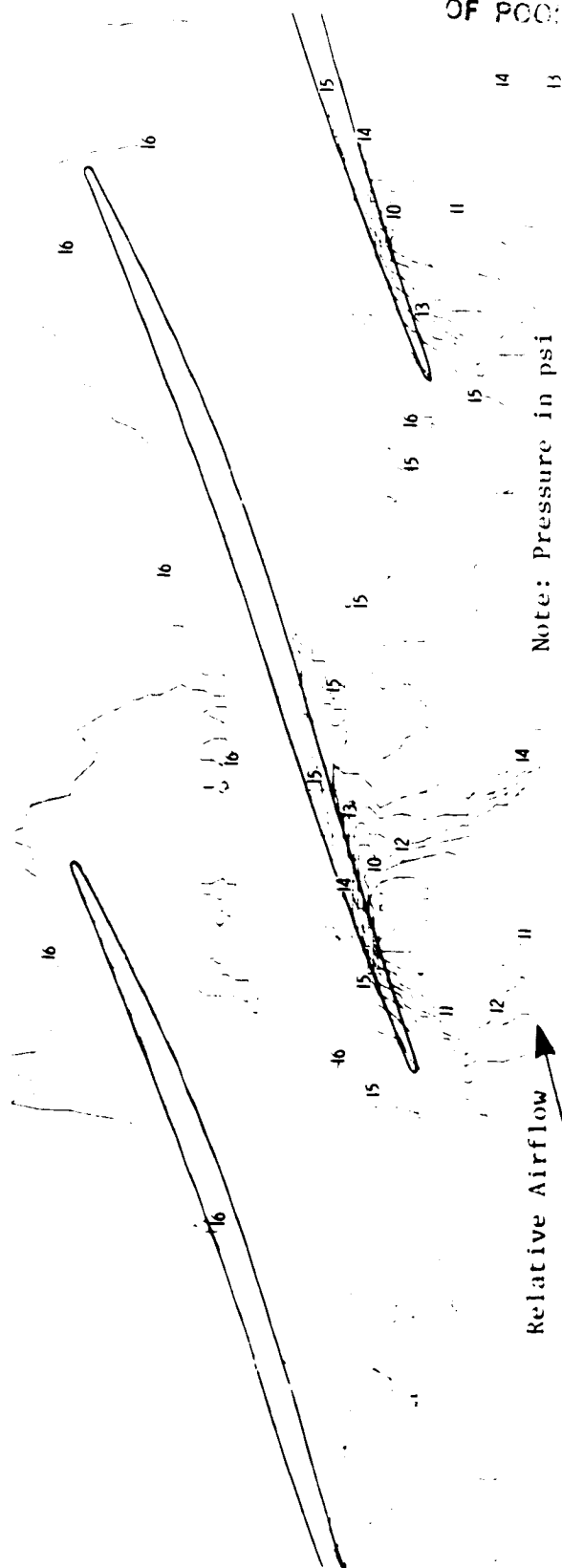
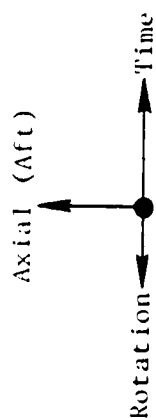
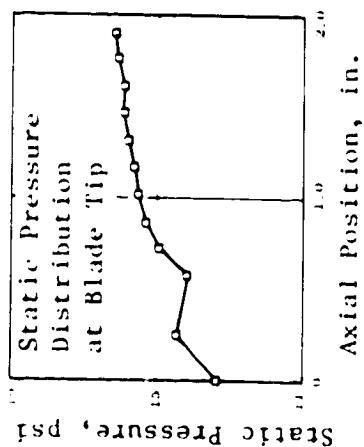


Figure 87. Casing Kulite Contour Plot, 70 Percent Speed Nominal Operating Line.



Note: Pressure in psi

Relative Airflow

ORIGINAL
OF POOR COPY

Figure 88. Casing Kulite Contour Plot, 70 Percent Speed Intermediate Operating Line.

ORIGINAL
OF RECORD

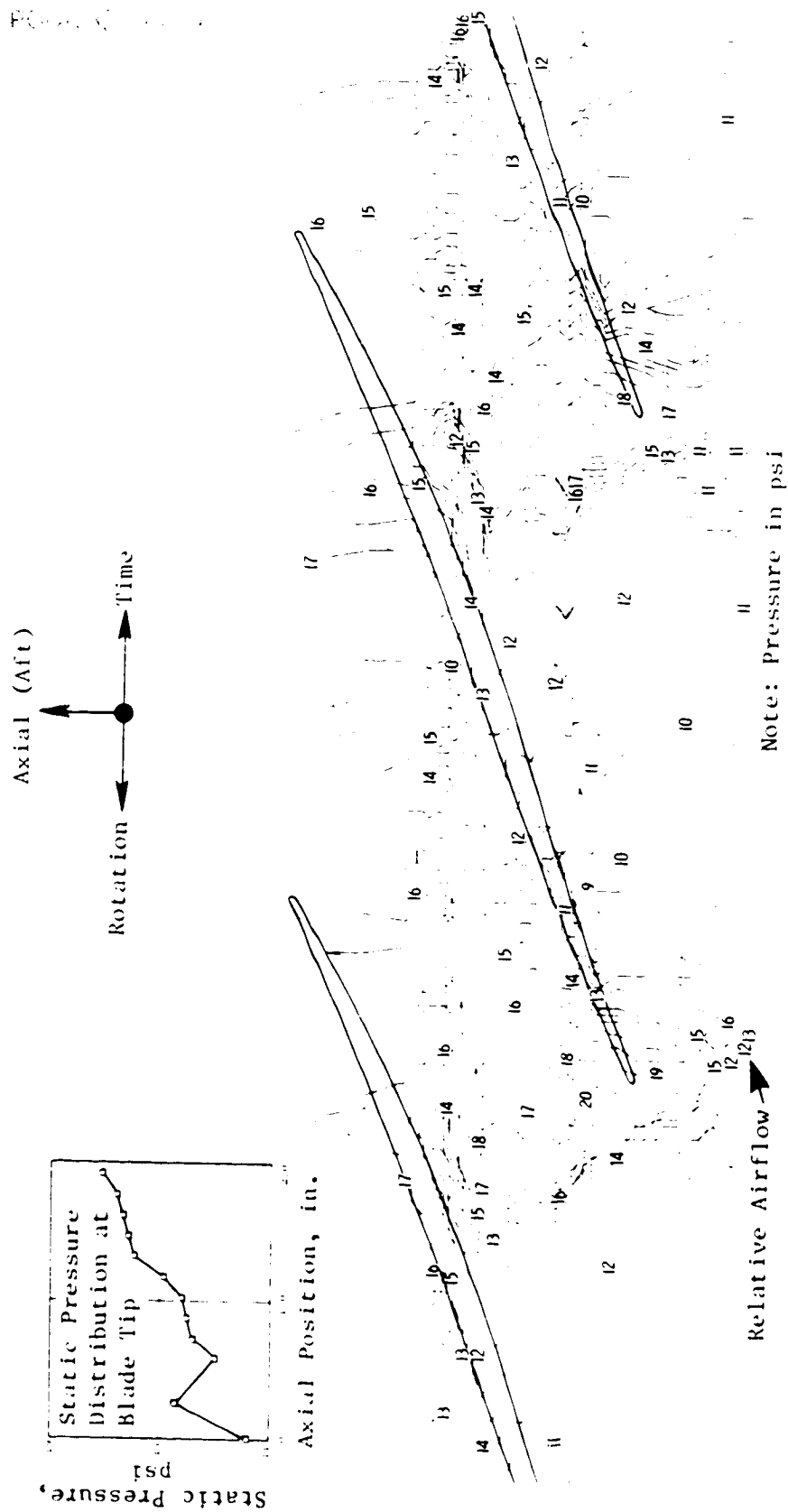


Figure 89. Casing Kulite Contour Plot, 90 Percent Speed Nominal Operating Line.

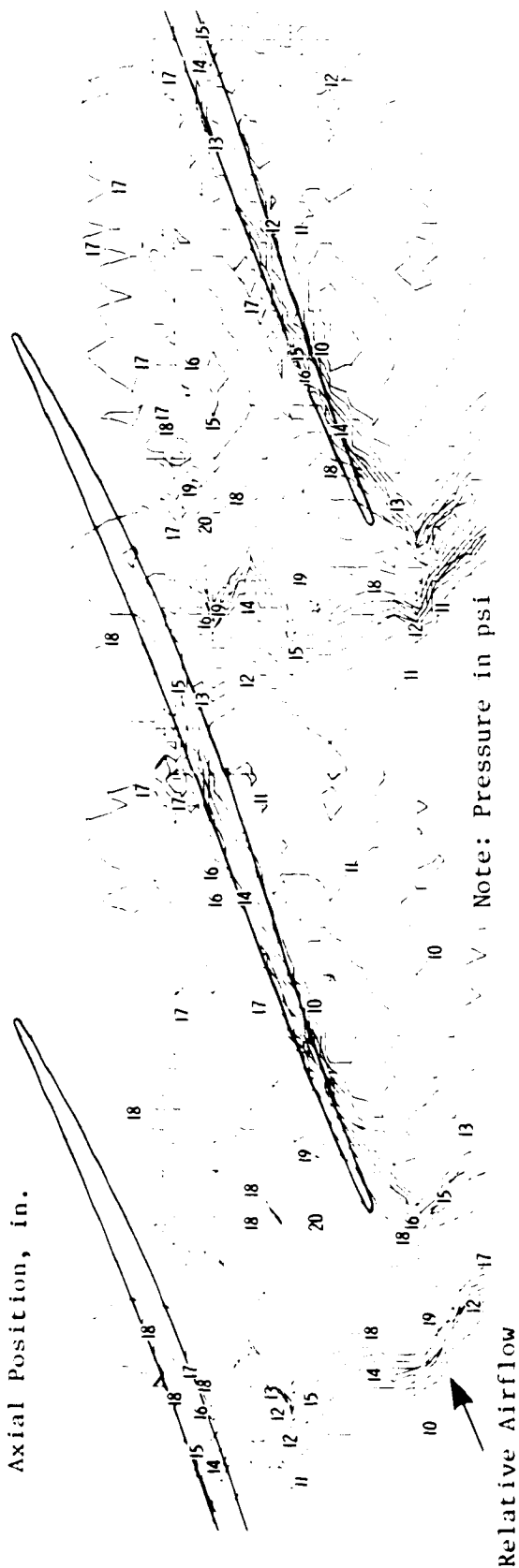
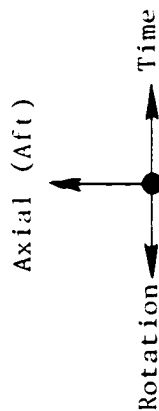
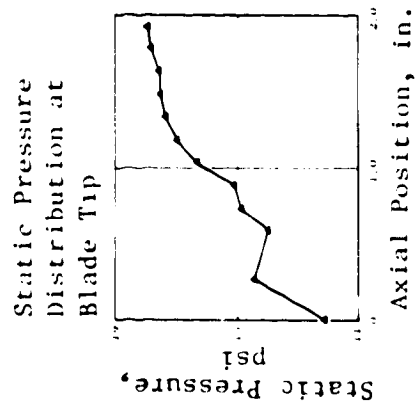


Figure 90. Casing Kulite Contour Plot, 90 Percent Speed Intermediate Operating Line.

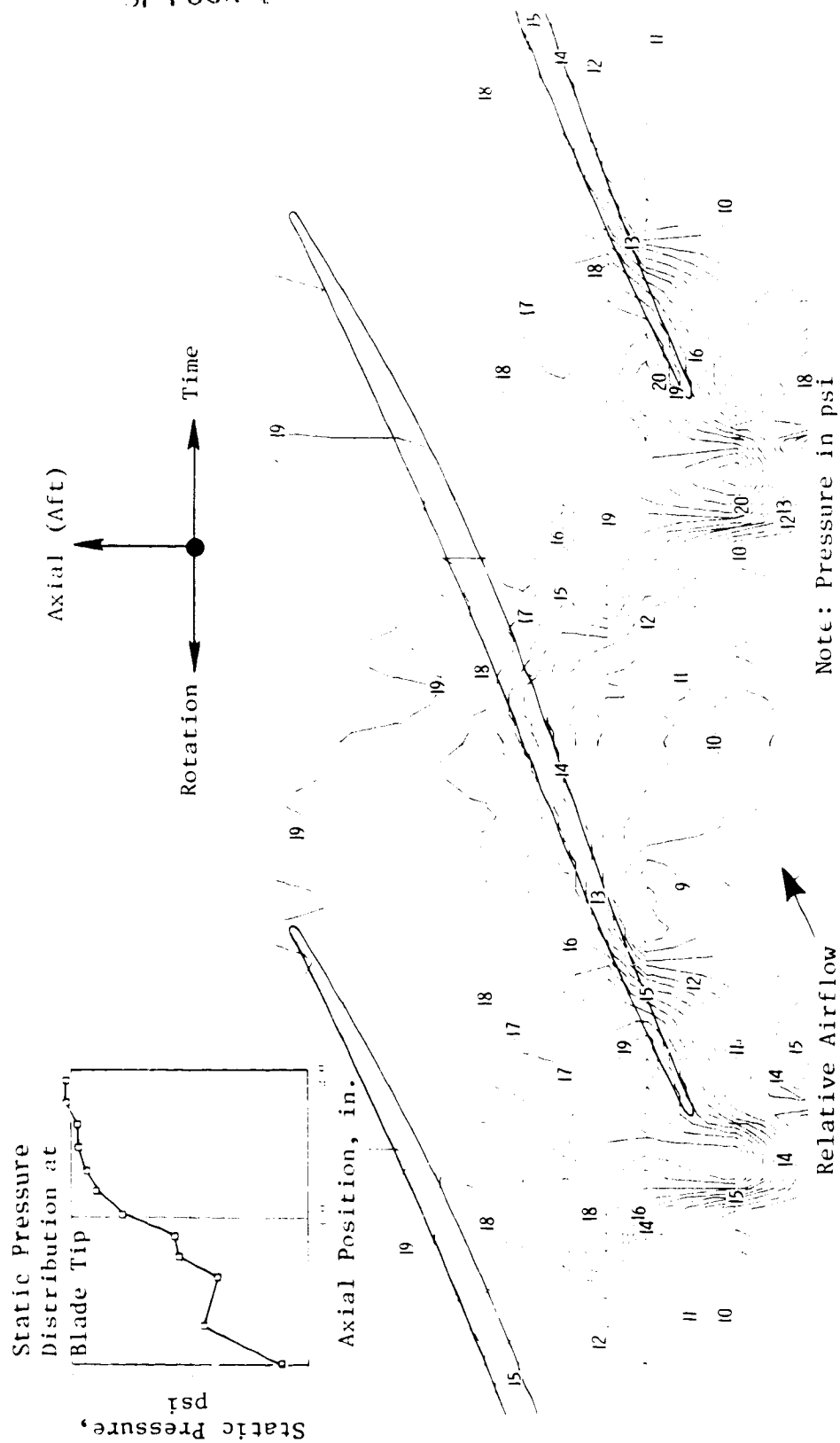


Figure 91. Casing Kulite Contour Plot, 95 Percent Speed Intermediate Operating Line.

6.5.2 Analysis of Unsteady Casing Kulite Data

Averaged digitized time histories corresponding to instantaneous pressure measurements for the selected sector of blades were used to determine the unsteady pressure amplitudes in the preceding section. In this analysis, however, the time histories were not averaged; the pressure perturbations at selected discrete time points (i.e., circumferential locations) were used to examine the unsteady characteristics. Aliased time histories were generated for 20 of the 200 digitized points from each of the 128 digitized time history samples acquired on-line. Since the aliased time histories are not an average but, rather, a collection of specific data points, the signal-to-noise ratio was rather low. This tended to mask the flutter frequency, pressure amplitude, and phase in the FFT analyses. Also, slight changes in the 1/rev triggering due to speed fluctuations during the 128 revolutions of data acquisition, or slight variations in the initializing time during data reprocessing, could cause a shift of the aliased frequencies in the resulting spectra.

Figure 92 shows a typical example of the aliased linear spectra for a Kulite and the reference strain gage, and the corresponding cross spectrum. The example corresponds to the casing Kulite located at approximately mid-chord (#705) for the 70 percent speed flutter condition. As can be seen on this figure, the flutter frequency is aliased to 80.6 Hz due to the sampling rate. The resultant unsteady pressure amplitude and phase relative to the strain gage data (SG #828) at the flutter frequency of 896 Hz are shown in Figure 93 for about two blade passages. Similar results for two other Kulite sensors (#707 and #709) are shown in Figures 94 and 95. One important observation from these data is that the flutter related unsteady pressure amplitude does not repeat itself from blade passage to blade passage. In fact, periodicity from blade passage to blade passage occurs if there is only one traveling wave in the flutter mode. In general, the periodic pattern simply disappears when several traveling waves exist simultaneously during flutter. In this program multiple traveling waves existed during both low speed torsional flutter and high speed bending flutter as will be seen in the next section.

6.5.3 Traveling Wave Analysis

The following discussion on traveling wave analysis applies only to the 70 percent speed torsional flutter point and the 95 percent speed flexural flutter point. At 65 percent speed flutter, the flutter frequency was within 8 Hz of the integral order response which made it difficult to distinguish. A narrowband (0.2 Hz) analysis was done on this data but the number of samples was very small and other equipment limitations were encountered. As previously mentioned for the 90 percent speed flutter point, the rotor system was oscillating in and out of flutter at the flutter point. As a result, a consistent set of data could not be obtained.

ORIGINAL OF POC

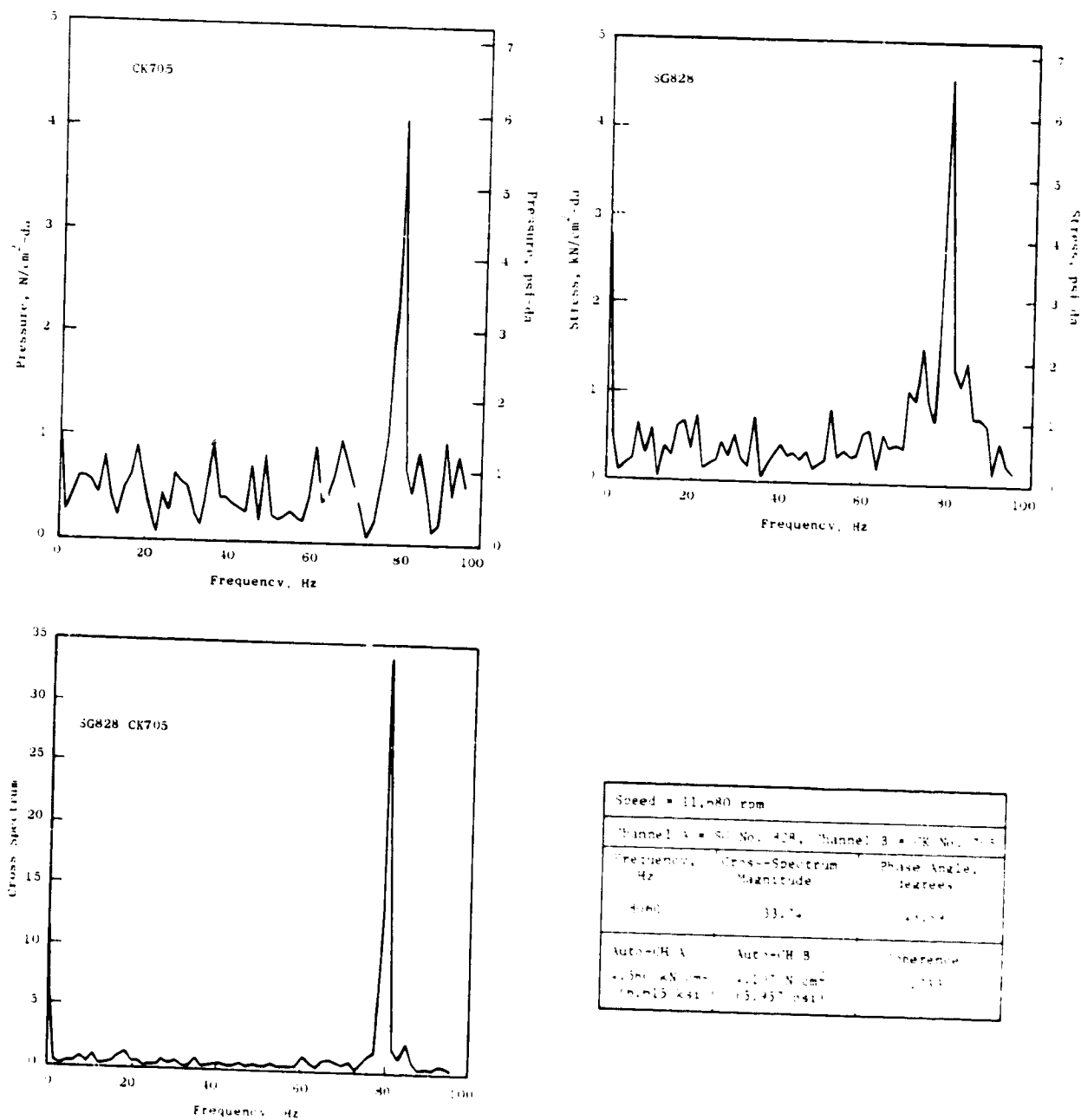


Figure 92. Casing Kulite Cross Spectra, 70 Percent Speed Flutter.

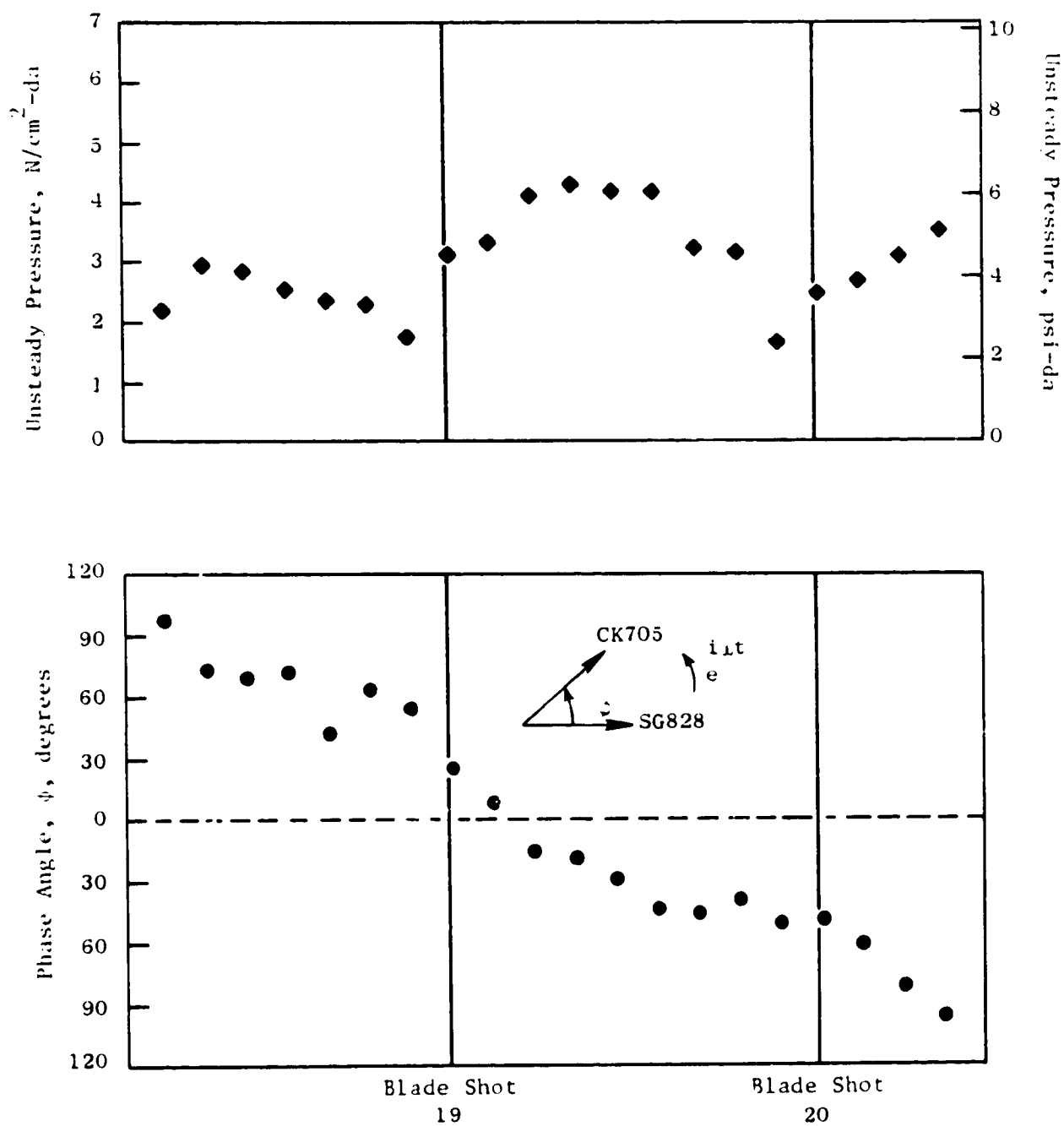


Figure 93. Circumferential Variation of Blade Tip Unsteady Pressure and Relative Phase at 70 Percent Speed Flutter, CK705.

ORIGINAL
OF POCN C-100-1

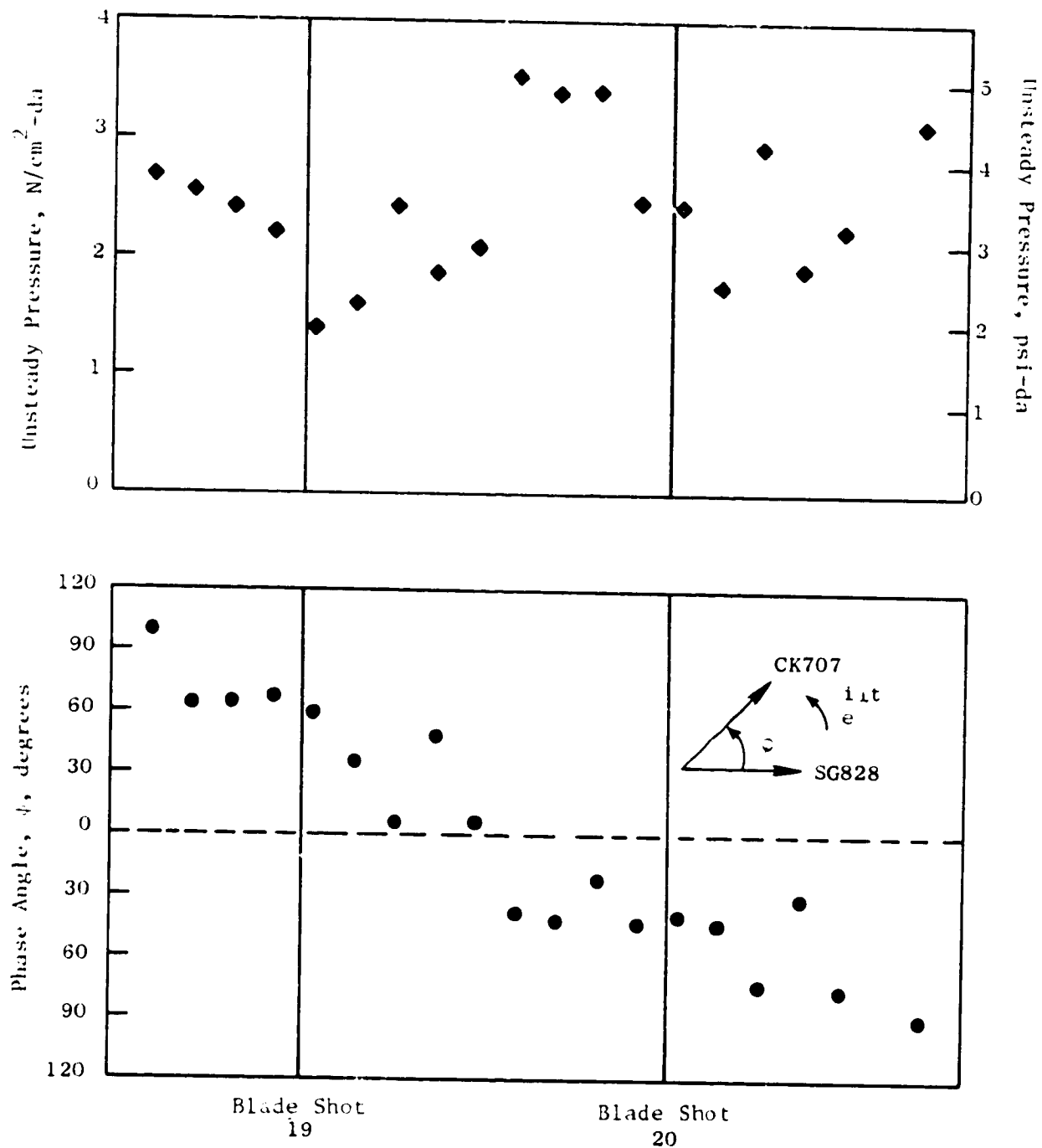


Figure 94. Circumferential Variation of Blade Tip Unsteady Pressure and Relative Phase at 70 Percent Speed Flutter, CK707.

OF

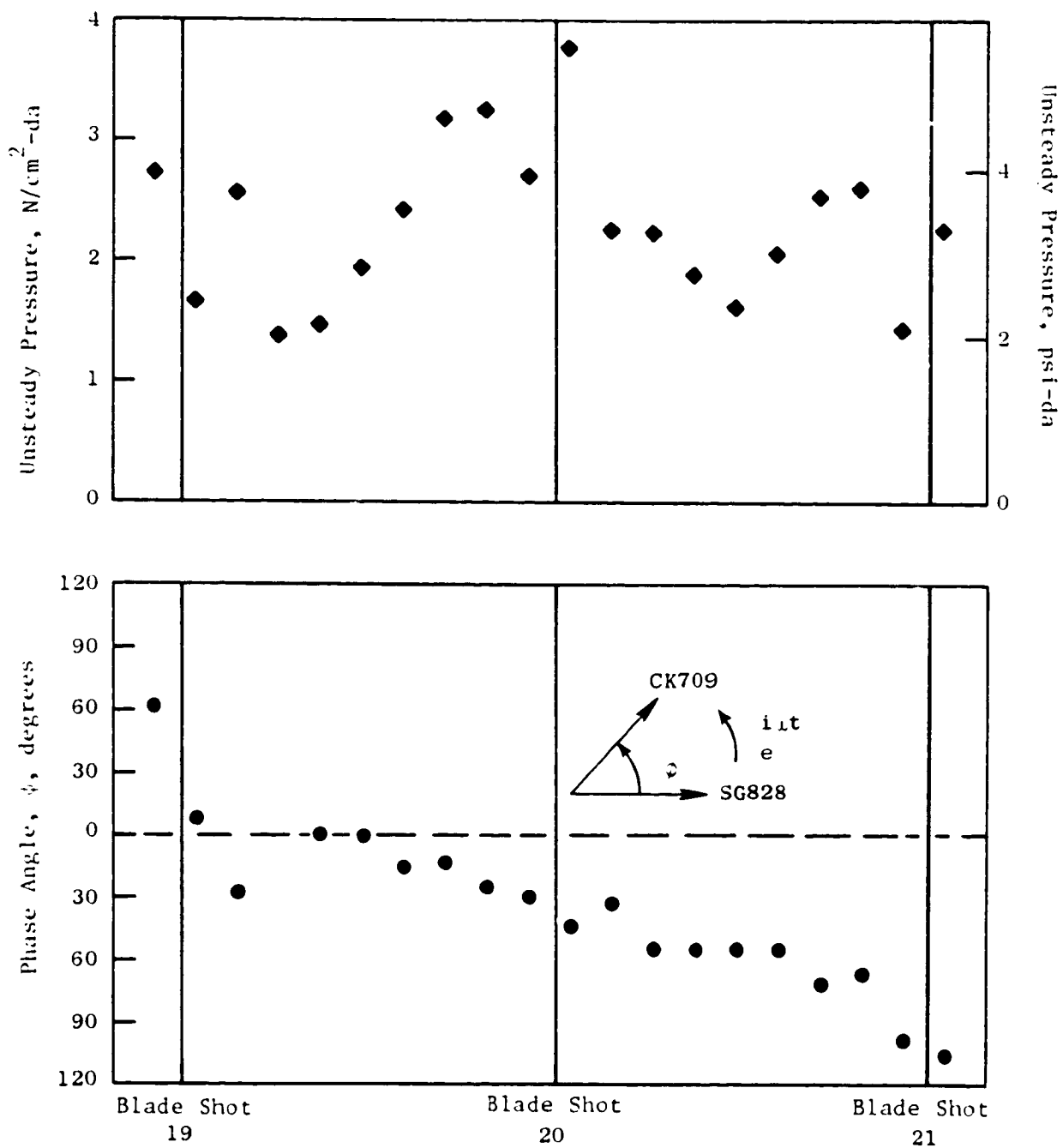


Figure 95. Circumferential Variation of Blade Tip Unsteady Pressure and Relative Phase at 70 Percent Speed Flutter, CK709.

6.5.3.1 Traveling Wave Identification

Figures 96 through 100 show the linear spectra of five representative casing Kulites for the 70 percent speed flutter point. These spectra indicate that the Kulite data over all of the blade tip chord have clearly discernable flutter signals composed primarily of forward traveling waves. At nonflutter conditions, these nonintegral responses disappear. Also seen in these spectra are the higher harmonics (see Section 5.5.1) of the traveling waves. The $m = 0$, $n = 0$ frequency is the flutter frequency observed on the rotor.

Another observation is that the amplitudes of some traveling waves and their harmonics, primarily $n = 3$ to 7, increase as a function of chord and peak at about 75 percent chord from the leading edge.

The unsteady pressure linear spectra for the 95 percent speed flutter point are shown in Figures 101 through 105. As at 70 percent speed, the predominantly forward traveling waves of nodal diameters from 2 to 9 are indicated, and the amplitudes of the higher harmonics are also significant. The 95 percent speed data indicate that the traveling wave amplitudes peak at a more forward position on the blade chord than that observed at 70 percent speed.

The spectra shown in Figures 96 through 105 cover the frequency range of 0 to 10 kHz. Linear spectra obtained up to 50 kHz indicated that the harmonics of the traveling waves, at 70 percent speed, were about eight to ten times smaller in amplitude than the dominant traveling waves below 10 kHz. At the 95 percent speed flutter point, however, significant traveling wave harmonics signals were observed at frequencies up to 40 kHz.

6.5.3.2 Traveling Wave Amplitude and Phase

The phase results, obtained as indicated in Section 5.5.2, of selected Kulite data are tabulated in Tables XXI and XXII with the corresponding pressure amplitude for 70 percent speed torsional flutter and 95 percent speed flexural flutter respectively. Only the results for frequencies below 10 kHz are tabulated because the accuracy of the phase data deteriorates dramatically for frequencies beyond 10 kHz. This results from magnetic tape skew during tape playback and the inherent 1/rev triggering inaccuracy. In fact, the phases for the traveling waves of frequencies up to 7 kHz are accurate to only within about ± 30 degrees. Note that the frequencies with the square brackets in Tables XXI and XXII are actually negative frequencies calculated from Equation (5). Their corresponding phases are the negative of standard FFT results because the FFT/computer only calculates positive frequencies.

In Table XXI, the phases (relative to slipring 1/rev signal) for the significant forward traveling waves of nodal diameters up to 13 are tabulated for 70 percent speed flutter. Also shown in the table are the unsteady pressure amplitudes of these traveling waves. Similar results of the 95 percent speed flutter point are tabulated in Table XXII for forward traveling waves of nodal diameters 2 through 5.

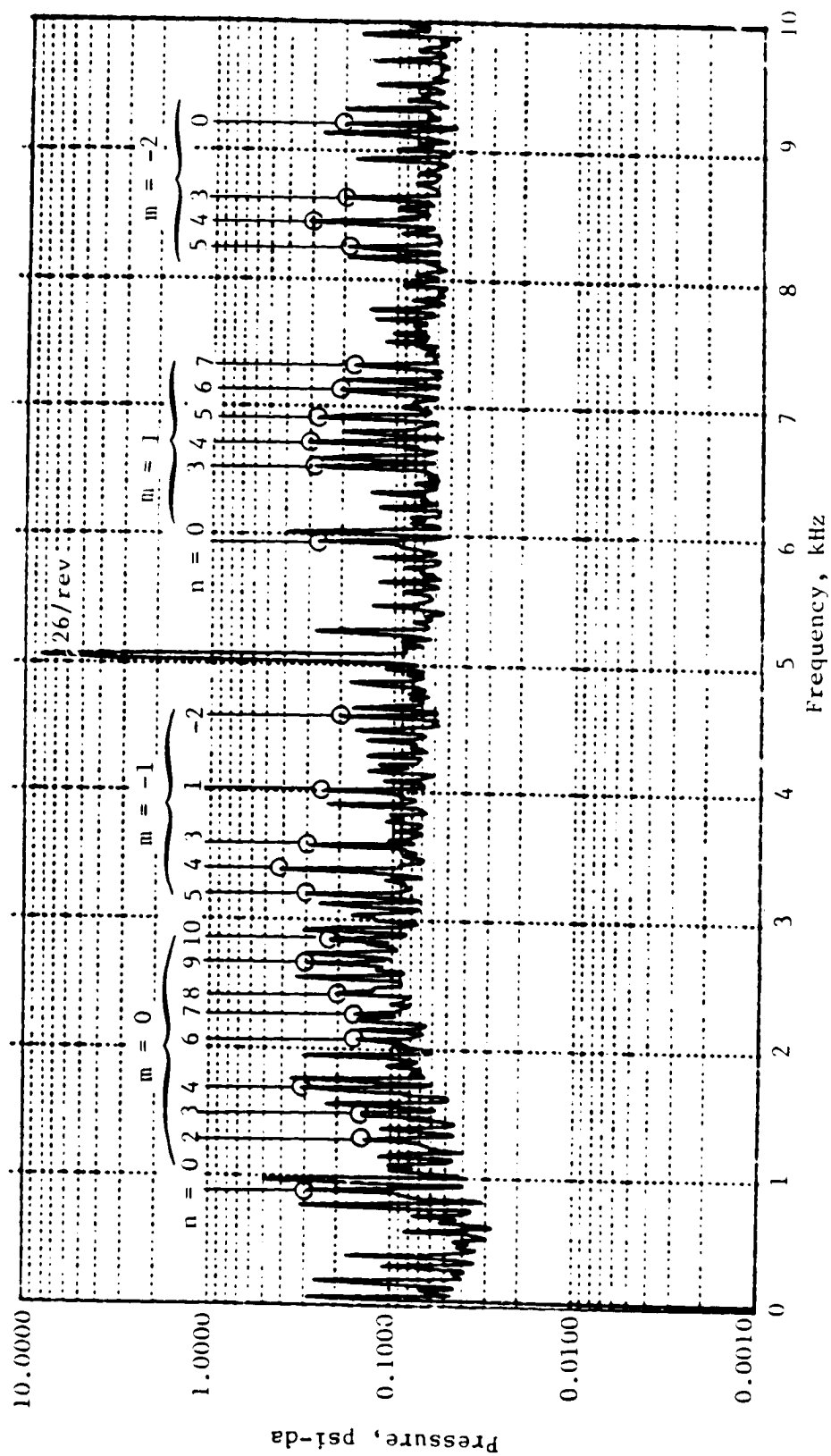


Figure 96. Casing Kulite (No. 702) Spectrum, 70 Percent Speed Flutter.

ORIGINAL DOCUMENT
OF POOR QUALITY

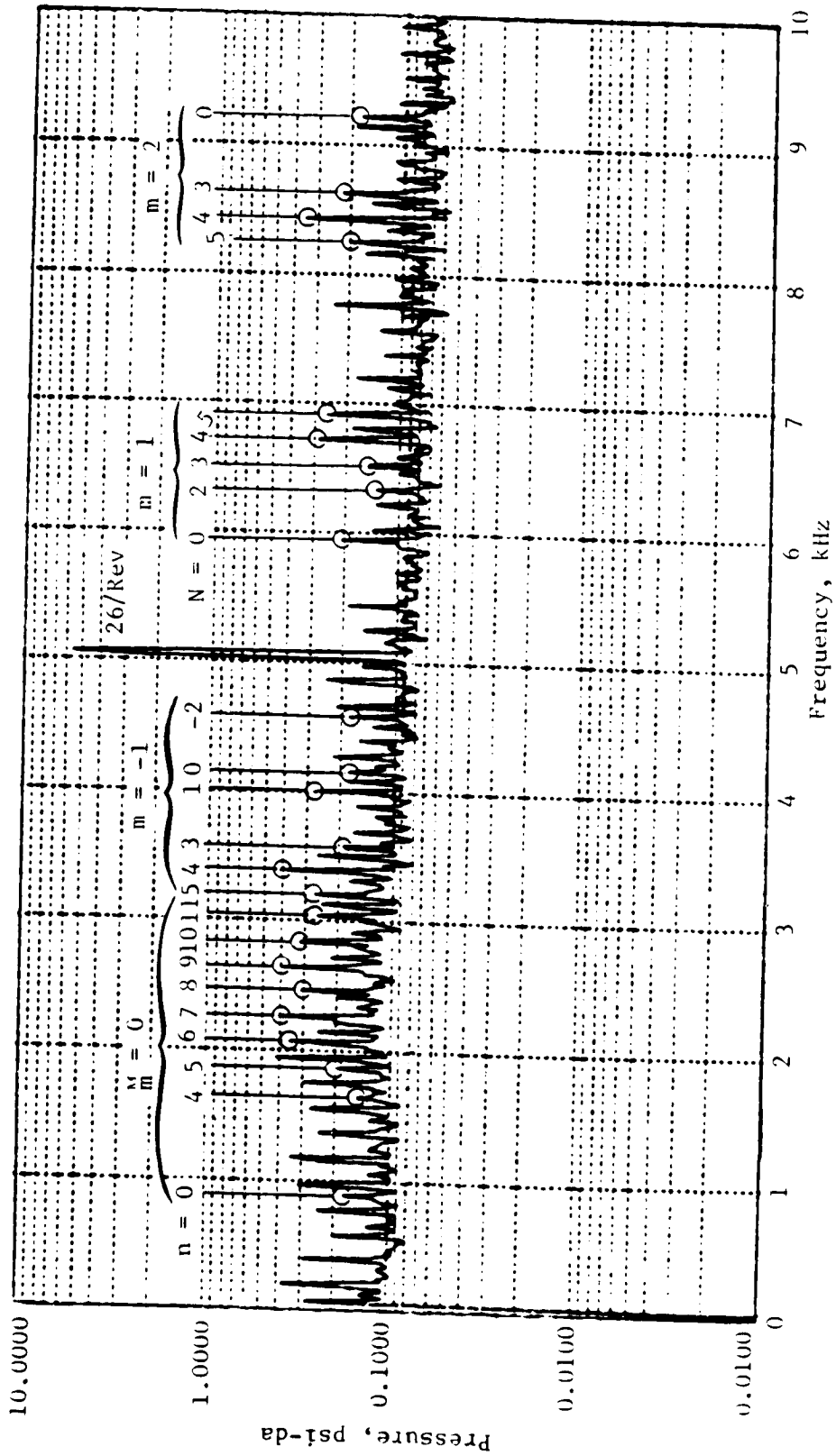


Figure 97. Casing Kulite (Number 704) Spectrum, 70 Percent Speed Flutter.

ORIGINAL
OF POOR QUALITY

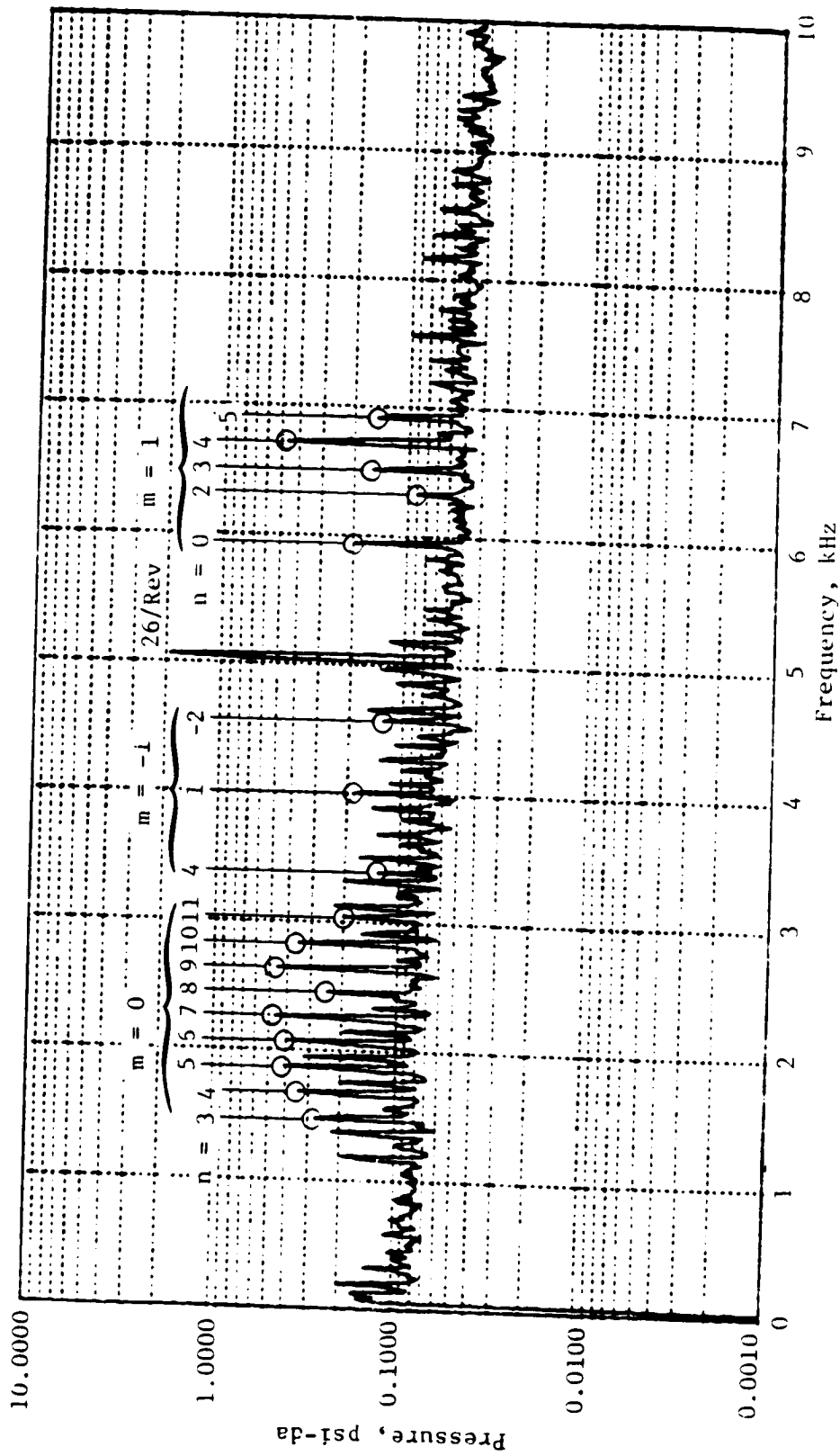


Figure 98. Casing Kulite (Number 706) Spectrum, 70 Percent Speed Flutter.

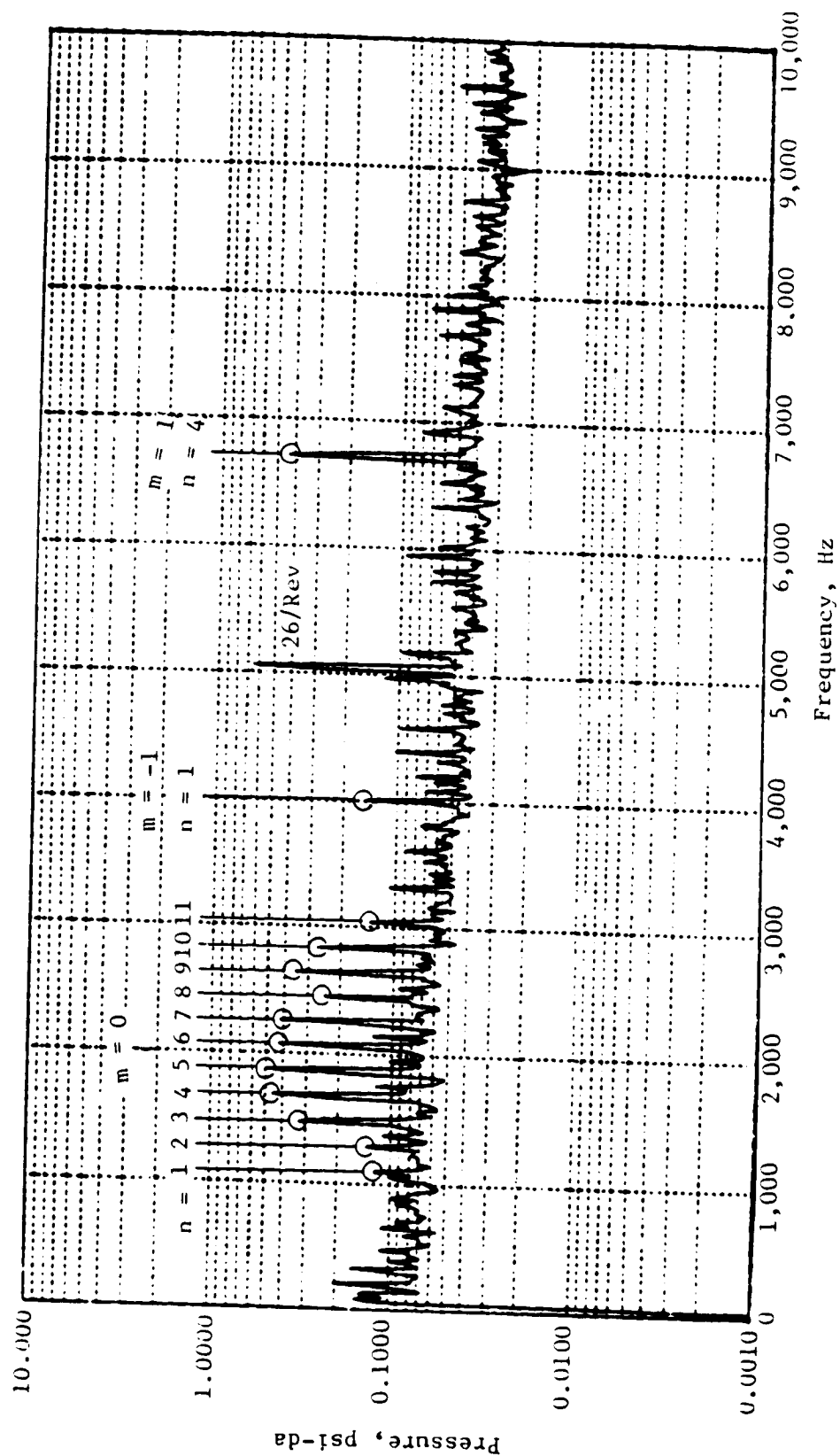


Figure 99. Casing Kulite (Number 708) Spectrum, 70 Percent Speed Flutter.

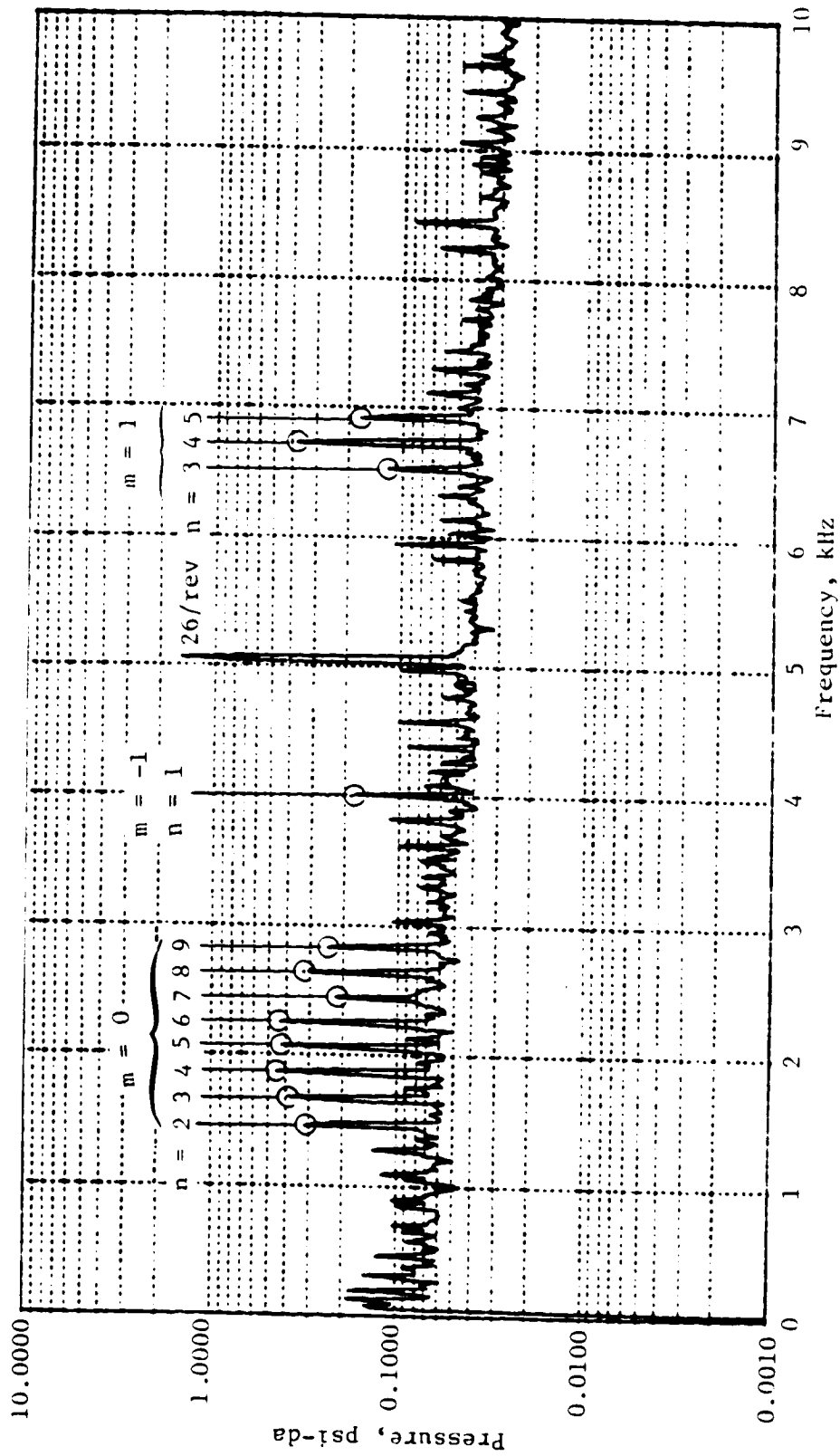


Figure 100. Casing Kulite (No. 710) Spectrum, 70 Percent Speed Flutter.

ORIGINAL
OF POOR QUALITY

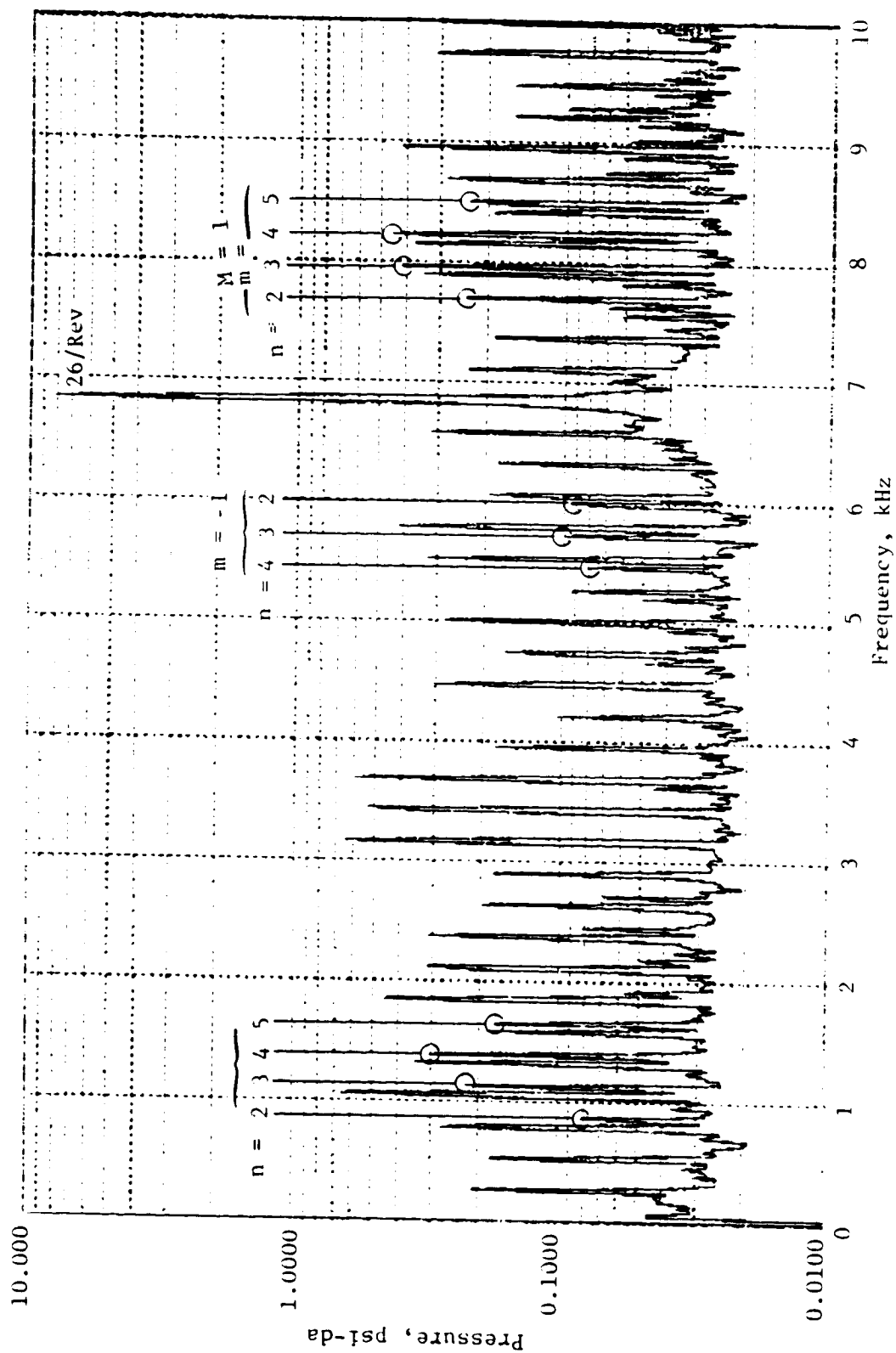


Figure 101. Casing Kulite (Number 702) Spectrum, 95 Percent Speed Flutter.

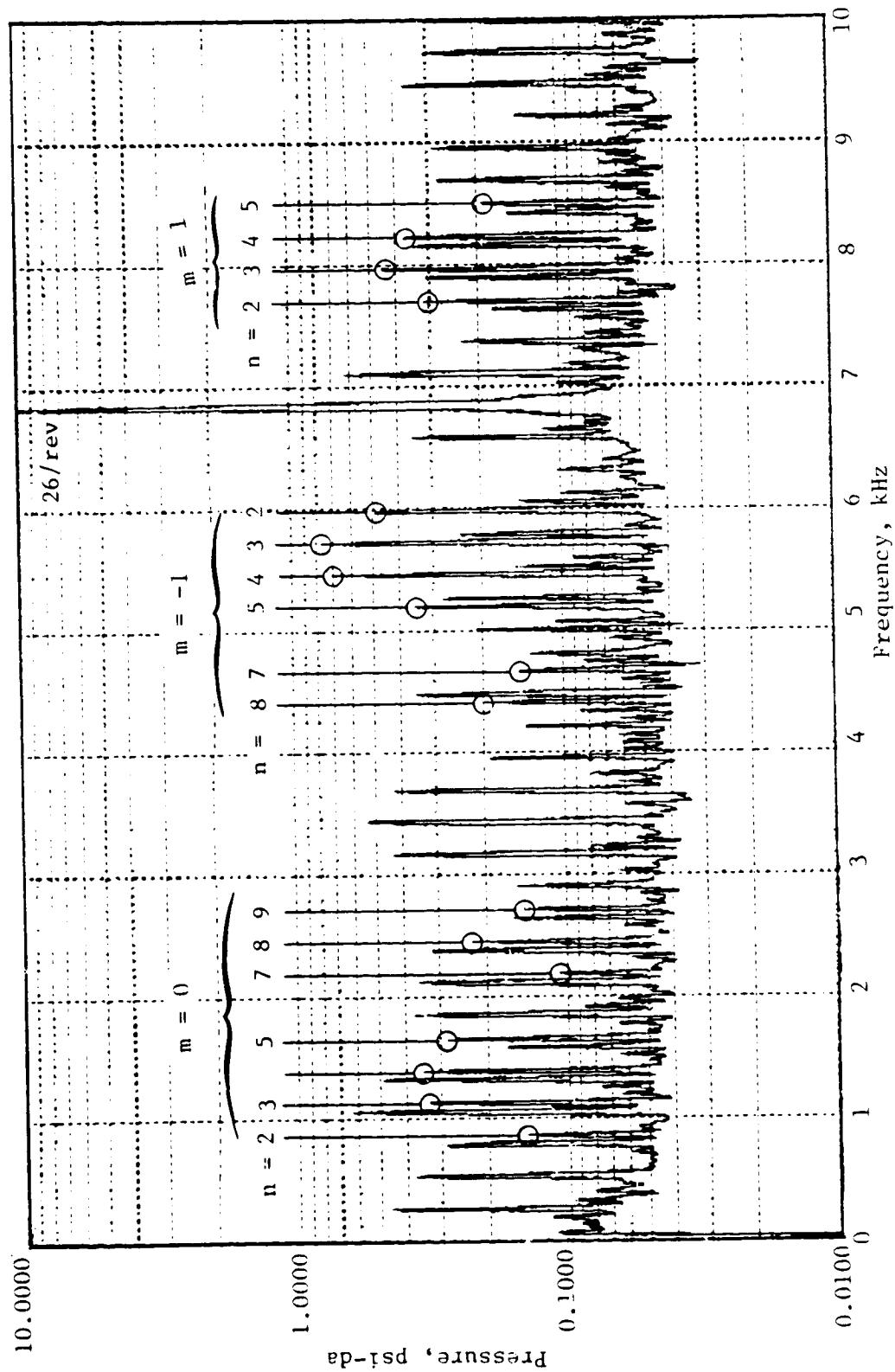


Figure 102. Casing Kulite (No. 704) Spectrum, 95 Percent Flutter.

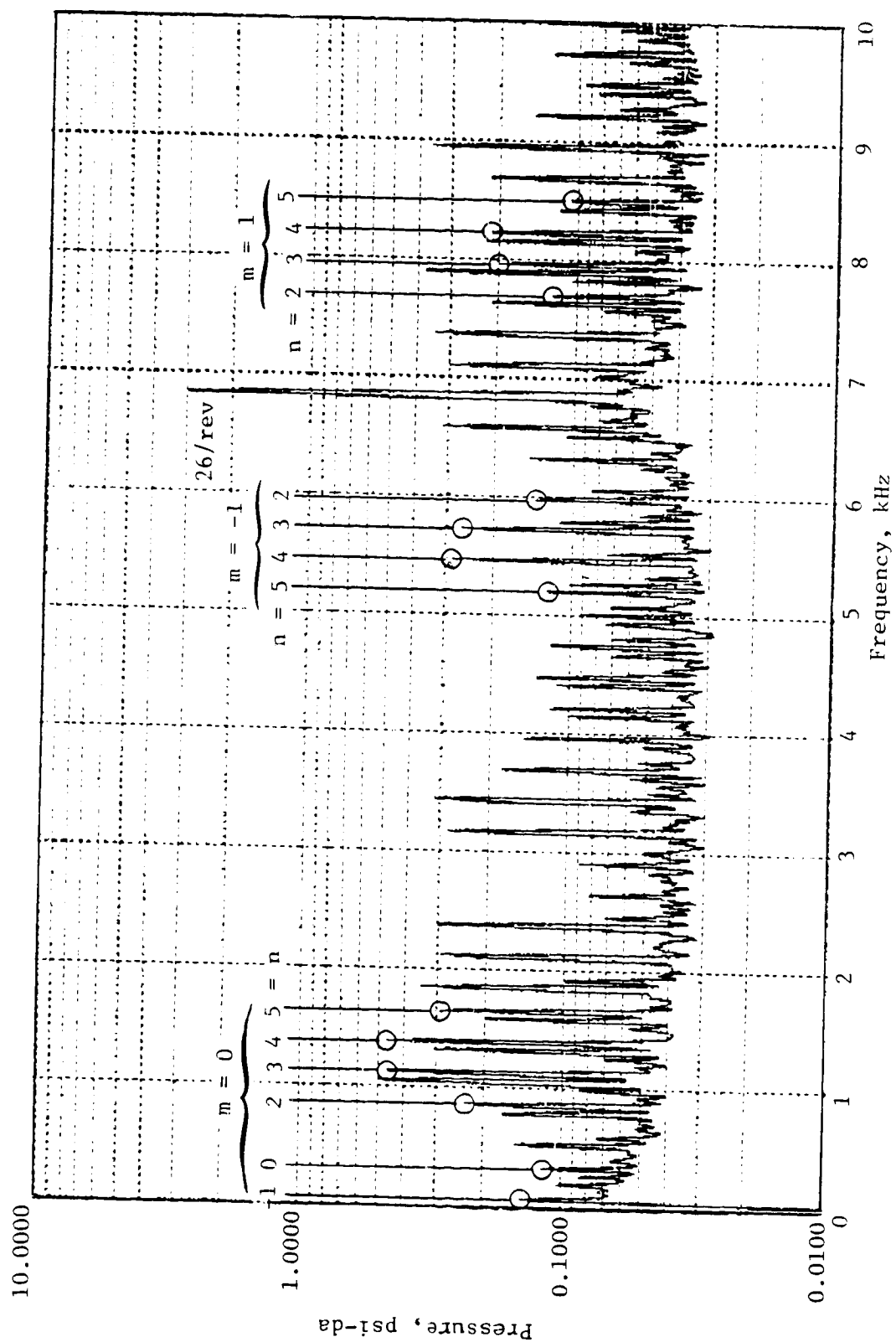


Figure 103. Casing Kulite (No. 706) Spectrum, 95 Percent Speed Flutter.

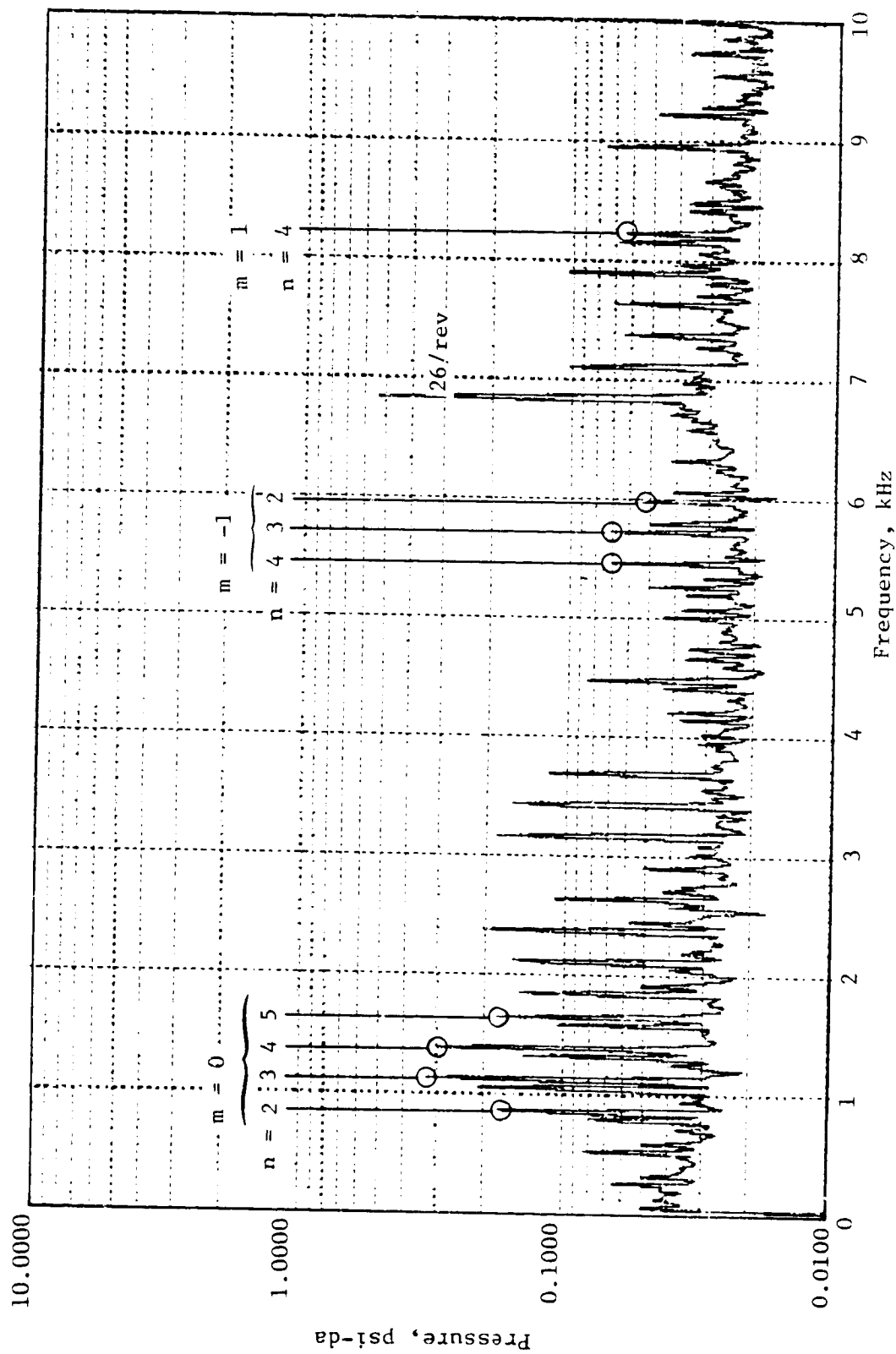


Figure 104. Casing Kulite (No. 708) Spectrum, 95 Percent Speed Flutter.

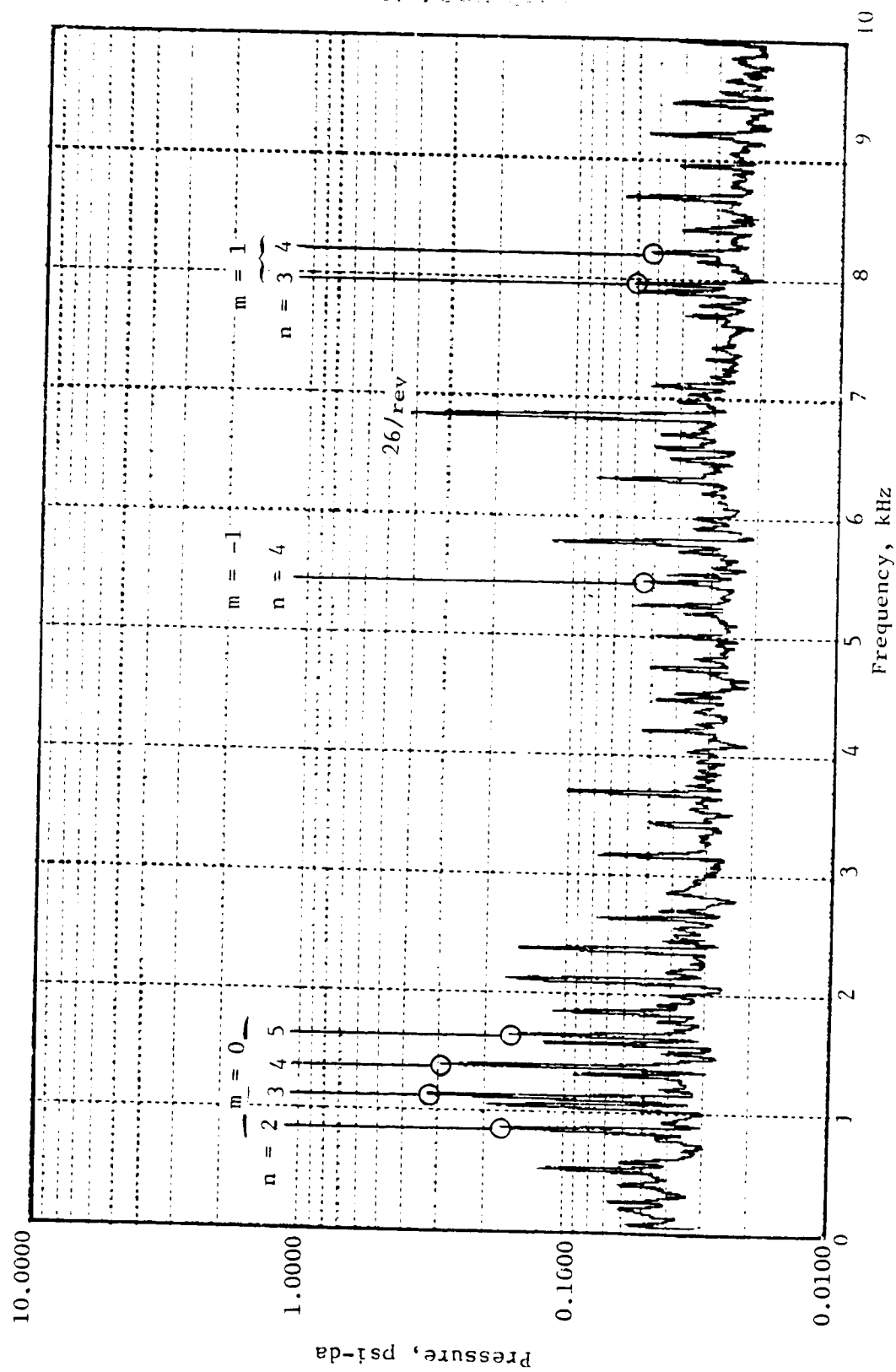


Figure 105. Casing Kulite (No. 712) Spectrum, 95 Percent Speed Flutter.

Table XXI. Traveling Wave Amplitudes and Phases, 70 Percent Speed Torsional Flutter.

n	m	f (hz)	CK 702		CK 704		CK 706		CK 708		CK 710	
			Pres.	φ (deg.)	Pres.	φ (deg.)	Pres.	φ (deg.)	Pres.	φ (deg.)	Pres.	φ (deg.)
0	-2	[9188]*			0.09	-125						
	0	900	0.16	-54	0.09	-147						
	1	5944	0.14	172	0.13	-132	0.23	102	0.24	38		
1	0	1094									0.13	156
2	0	1288									0.15	179
	1	6332			0.07	68	0.10	-8				
3	-2	[8606]			0.11	-129						
	-1	[3562]	0.15	-107								
	0	1482	0.11	-7			0.32	254	0.62	-145	0.36	-64
	1	6526	0.12	90	0.11	-74						
4	-2	[8412]			0.17	-184						
	-1	[3368]	0.22	-128			0.15	84			0.12	-204
	0	1676	0.14	-82			0.35	69	0.70	-28	0.39	-61
	1	6720	0.15	171	0.15	152	0.53	86	0.92	157	0.42	72
5	-2	[8218]			0.10	-16						
	-1	[3174]	0.14	34	0.16	-140	0.13	-132				
	0	1870	0.06	96	0.10	66	0.40	-12	0.84	-44	0.43	44
	1	6914	0.14	149	0.13	-10	0.23	165			0.18	-114
6	-1	[2980]			0.07	82						
	0	2064	0.09	102	0.17	-33	0.46	25	0.90	-94	0.47	112
	1	7108							0.14	-39		
7	0	2258	0.12	10	0.21	143	0.50	55	0.92	151	0.46	98
8	0	2452	0.13	14			0.28	122	0.45	104	0.22	-130
9	0	2646	0.14	7	0.19	58	0.41	134	0.57	58		
10	0	2840	0.15	166	0.20	-22	0.38	-112	0.45	-152	0.23	-68
11	0	3034			0.11	4	0.19	54	0.25	167	0.12	101
13	0	3422			0.22	56						

*Frequencies in brackets are negative frequencies as calculated by Equation 5.

Note: Pressure normalized to 0.689 N/cm² (1.00 psi)

Table XXII. Traveling Wave Amplitudes and Phases, 95 Percent Speed Flexural Flutter.

n	m	f (Hz)	CK 702		CK 704		CK 706		CK 708		CK 710	
			Pres.	ϕ (deg.)	Pres.	ϕ (deg.)	Pres.	ϕ (deg.)	Pres.	ϕ (deg.)	Pres.	ϕ (deg.)
2	-1	[5980]*										
	0	858	0.10	20	0.50	-134	0.20	-241	0.23	126	0.49	142
	1	7696	0.36	-69	0.37	-15	0.20	-165			0.14	-103
3	-1	[5717]	0.11	-171	0.86	-42	0.39	-87	0.11	-118	0.18	-205
	0	1121	0.26	56	0.34	22	0.74	24	0.48	-57	0.88	-51
	1	7959	0.61	-95	0.50	148	0.32	14	0.08	170	0.16	208
4	-1	[5454]			0.84	-169	0.42	70	0.11	-3	0.17	94
	0	1384	0.34	-138	0.37	130	0.76	-173	0.45	100	0.78	133
	1	8222	0.60	233	0.38	60	0.28	-47	0.07	-7	0.13	-66
5	-1	[5191]			0.35	80	0.18	-30	0.09	4		
	0	1647			0.27	-102	0.35	-42	0.22	-125	0.42	-89
	1	8485			0.17	182	0.15	67				

*Frequencies in brackets are negative frequencies as calculated by Equation 5.

Note: Pressure normalized to 0.689 N/cm² (1.00 psi)

6.5.3.3 Pressure in Rotating Reference System

The traveling wave information, amplitude and phase, from Tables XXI and XXII was used with Equation (10) in Equation (11) to generate the total unsteady pressure signal that would be perceived in the rotating reference system during flutter. The results, spanning one blade pitch, are shown in Figure 106 for 70 percent speed torsional flutter and in Figure 107 for 95 percent speed flexural flutter.

For 70 percent speed torsional flutter, Figure 106a shows the amplitudes of unsteady pressure distributions over an equivalent blade passage with the blade position at the center. Strong variation in the unsteady pressure magnitude is seen over an equivalent blade passage in both the circumferential and the axial direction. Figures 106b through 106f show the phase angle distributions through an equivalent blade passage for the even numbered casing Kulite sensors (Kulite #712 was out). The interesting point here is that near the blade position there is significant change in phase for Kulites #704 and #706. These correspond to about 23 and 49 percent chord position from the leading edge. Conversely, no dramatic change in phase are seen for other chordwise locations. This may suggest that flutter is caused primarily by the aerodynamic work input into the rotor blades over the front portion of the blades.

Similar results are shown for 95 percent speed bending flutter in Figure 107 (Kulite #710 was out). Again a significant change in phase is seen for Kulites #704 and #706 (or about 21 and 44 percent chord). Consequently, the front portion of the blades may again be playing a dominant role in the flutter occurrence. In addition, large phase variations occur near the midpoints of blade passages. This large phase variation is attributed to the existence of shock structure for this high speed flutter condition.

6.6 ROTOR EXIT TOTAL PRESSURE

As part of the effort to understand the blade wake characteristics while operating in flutter, the radial distribution (six immersions) of the free stream total pressure was measured at the exit traverse plane. These measurements were limited to the bypass stream where most active aerodynamic activity occurs. The data presentation will follow closely the format used in the casing Kulite static pressure discussions.

6.6.1 Circumferentially Averaged Total Pressure

The total pressure loss from the designated traverse plane to the downstream vane was shown to be minimal in Build 2 tests by comparing cobra probe data in the traverse plane and vane-rake data downstream of the rotor. For the special instrumentation data points, the circumferentially averaged steady total pressure distribution, $(P_T)_{DC}$, measured at different radial immersions, is shown in Figures 108 and 109 in terms of vane-rake data along with

ORIGINAL
OF POOR QUALITY

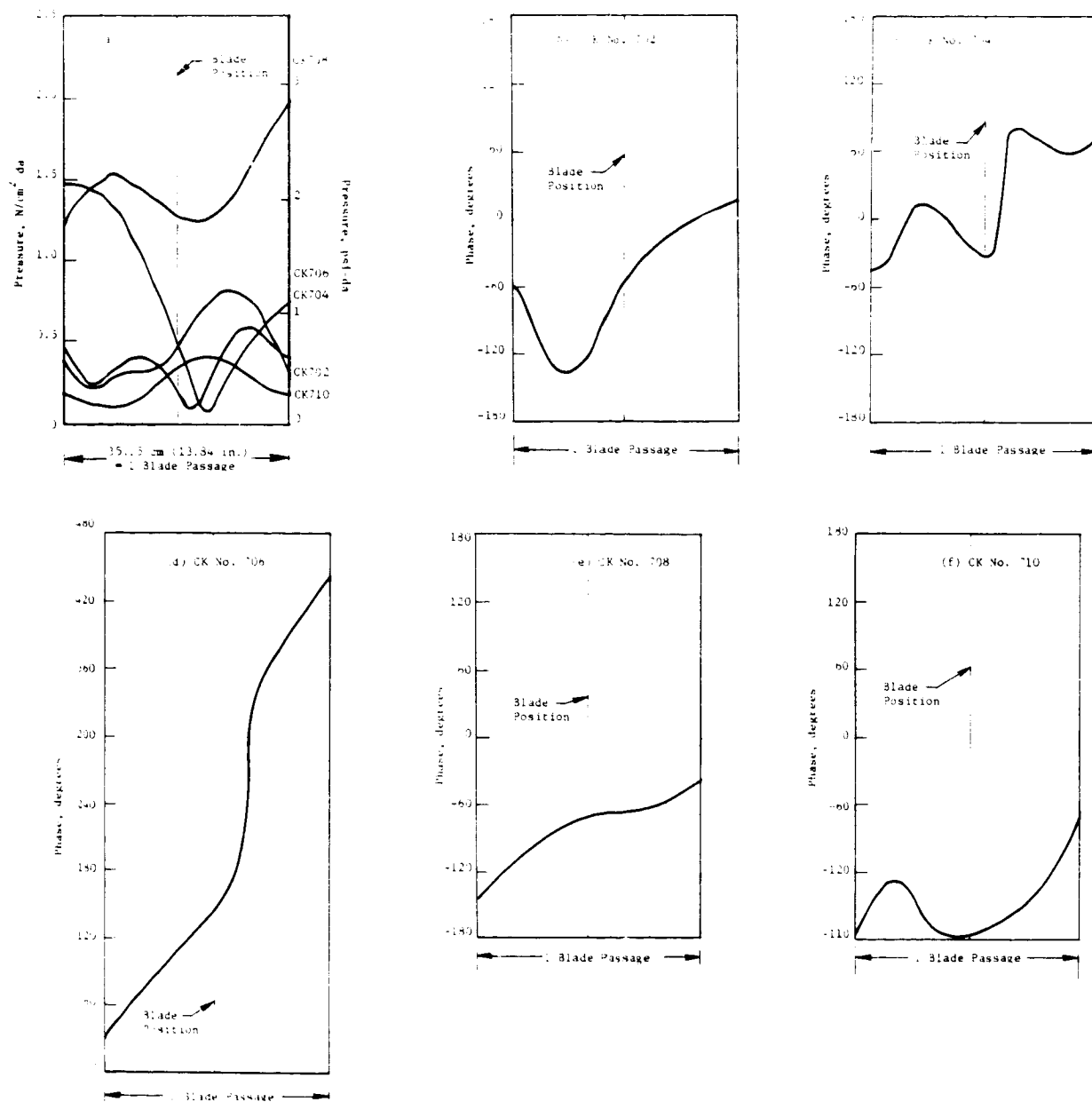


Figure 106. Circumferential Variation of Blade Tip Unsteady Pressure and Phase at 70 Percent Speed Flutter.

ORIGINAL OF POCR Q. 1. 1

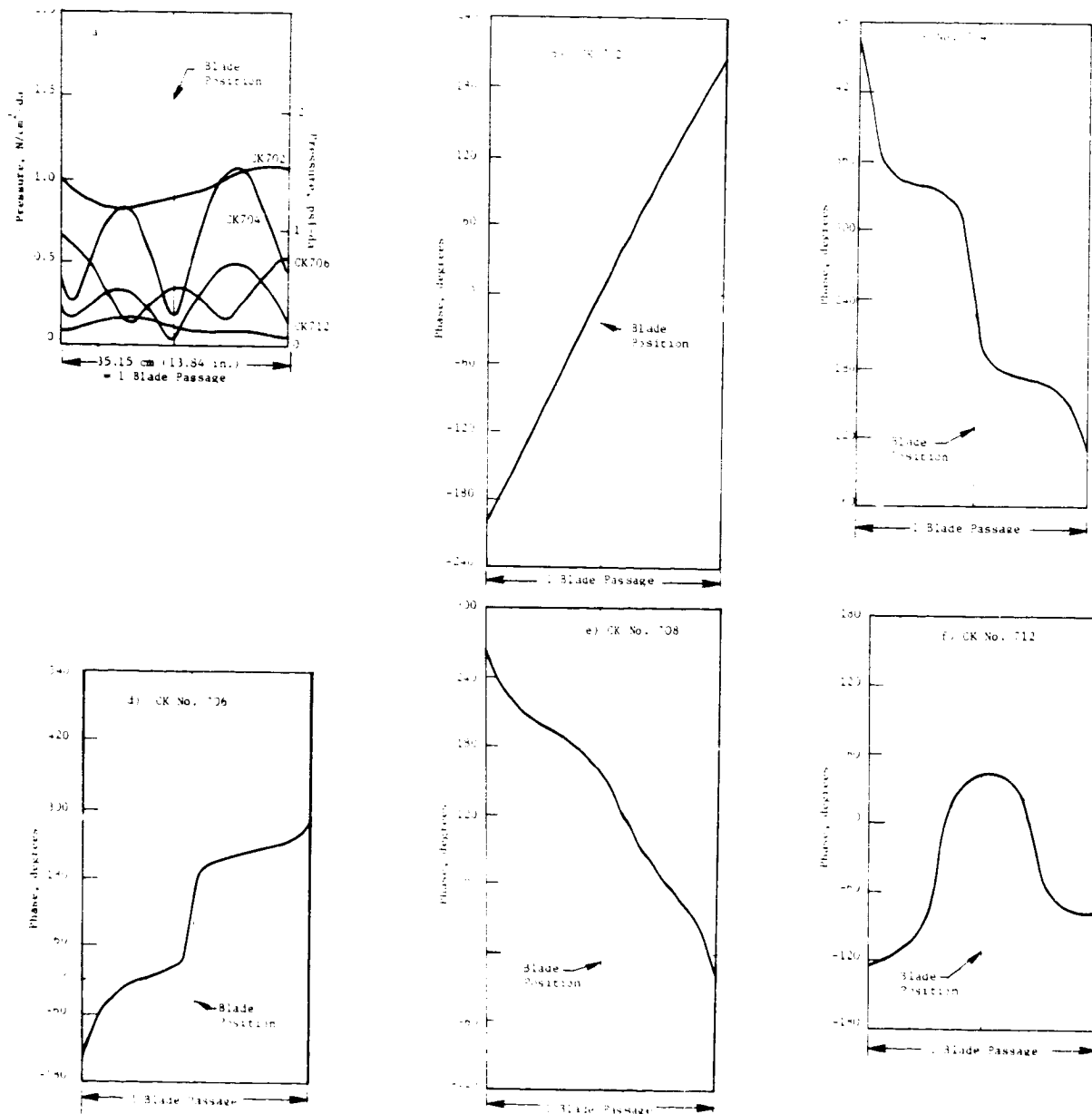


Figure 107. Circumferential Variation of Blade Tip Unsteady Pressure and Phase at 95 Percent Speed Flutter.

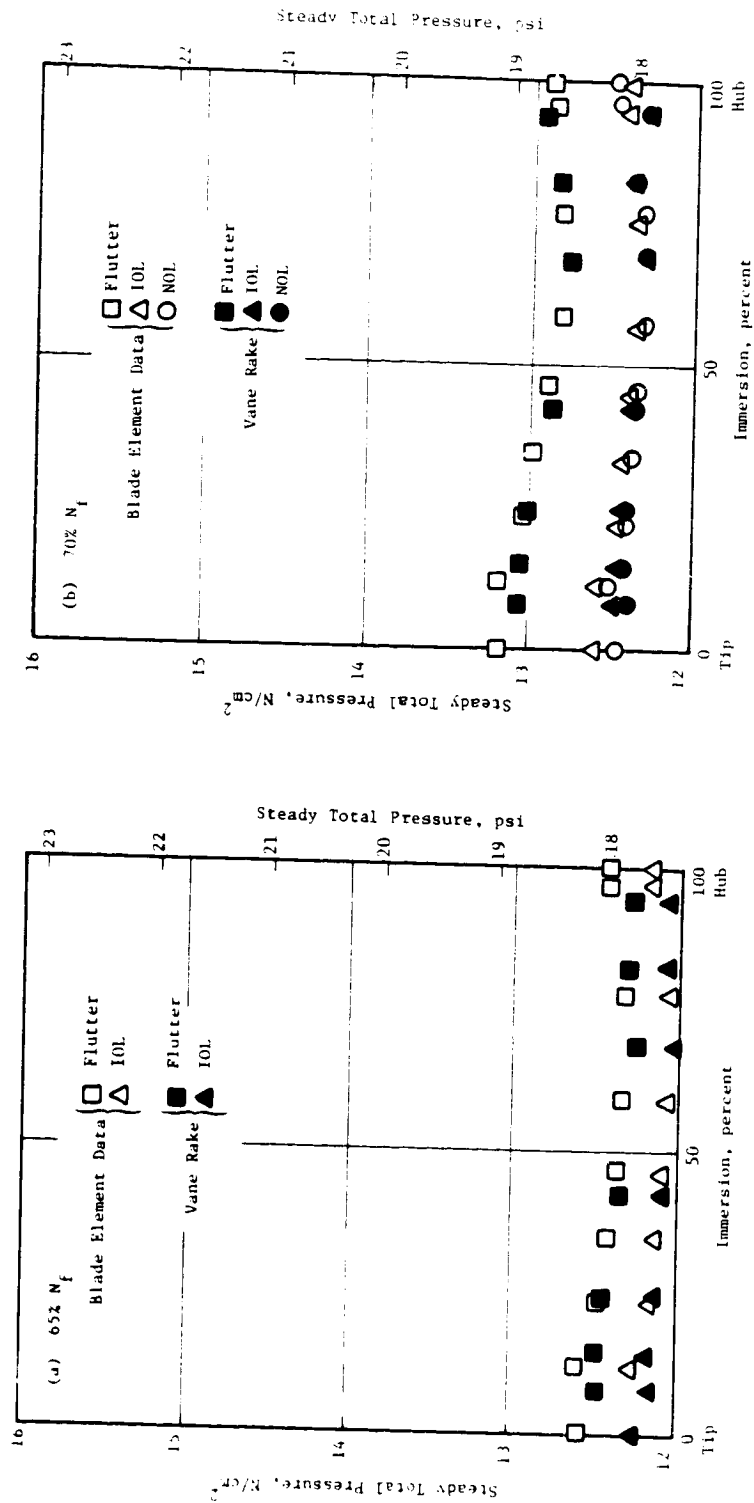


Figure 108. Radial Distribution of Steady Total Pressure, 65 and 70% Speed Flutter.

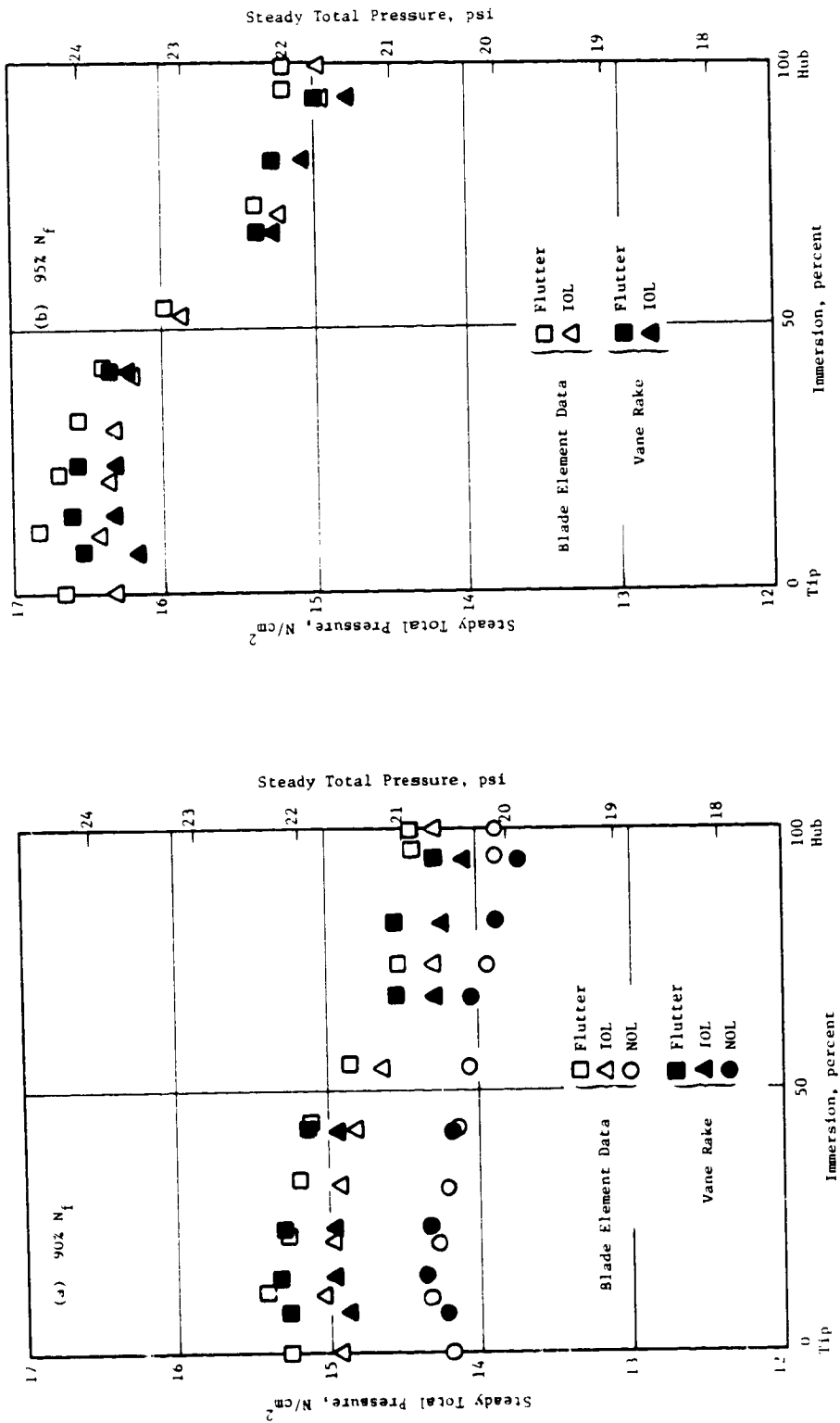


Figure 109. Radial Distribution of Steady Total Pressure, 90 and 95% Speed Flutter.

the calculated blade element data at the traverse plane. At all operating conditions, the flow near the casing always had the largest total pressure due to fan compression. Also apparent is the increase in total pressure for all immersions when throttling to flutter at constant rotor speed.

6.6.2 Total Pressure Radial Distribution

The total pressure probe data were ensemble averaged as shown in Section 5.2.4 to obtain the dynamic part of the instantaneous total pressure, $(P_T)_{AC}$. Typical ensemble averages are shown in Figures 110 and 111 for the 70 and 95 percent speed flutter points respectively.

To obtain the true instantaneous total pressure, the averaged unsteady total pressure, $(P_T)_{AC}$, was added to the circumferentially averaged steady total pressure, $(P_T)_{DC}$. Results of the true total pressure are presented as contour plots in Figures 112 through 115 for the four flutter points. These results are presented in terms of isobars superimposed on an unwrapped view of three adjacent blade trailing edges. Results at 65 and 70 percent speed, Figures 112 and 113 respectively, show the blade wakes and areas of boundary layer buildup next to the outer wall and at the splitter. A large pressure gradient exists near the outer casing indicating a relatively thick boundary layer and what appears to be significant vorticity distribution in that region. In the supersonic stall flutter region, at 90 and 95 percent speed, the blade wakes and the boundary layers are no longer apparent as seen in Figures 114 and 115.

Contour plots of instantaneous total pressures for nonflutter operating conditions are shown in Figures 116 through 118 for 70 and 90 percent speed. Blade wakes are not apparent at either speed on the intermediate operating line. This may be due to the small change in total pressure, amounting to less than 0.69 N/cm^2 (1.0 psi), across the three blade passages. A plot with a smaller increment in total pressure did not reveal the wakes or provide additional insight. At 90 percent speed on the nominal operating line, Figure 118, some evidence of blade wakes are observed.

6.6.3 Analysis of Unsteady Exit Total Pressure

The unsteady total pressures obtained from the dynamic traverse probe were determined, as with the casing Kulites, by a cross spectrum analysis of the 1/rev sampled time histories. Time histories constructed with 1/rev samples had the effect of decreasing the signal to noise ratio, and thereby possibly masking the flutter pressure amplitude and phase.

A typical example of linear spectra for both the pressure and the strain gage are shown in Figure 119. This data corresponds to the 7.5 percent immersion (from the outer wall) at the 70 percent speed flutter condition. As seen on this figure, the flutter frequency is aliased to 77.56 Hz for both the pressure and strain gage spectra. Also shown is a cross spectrum of these two signals and a summary of coherence and phase between the pressure and strain.

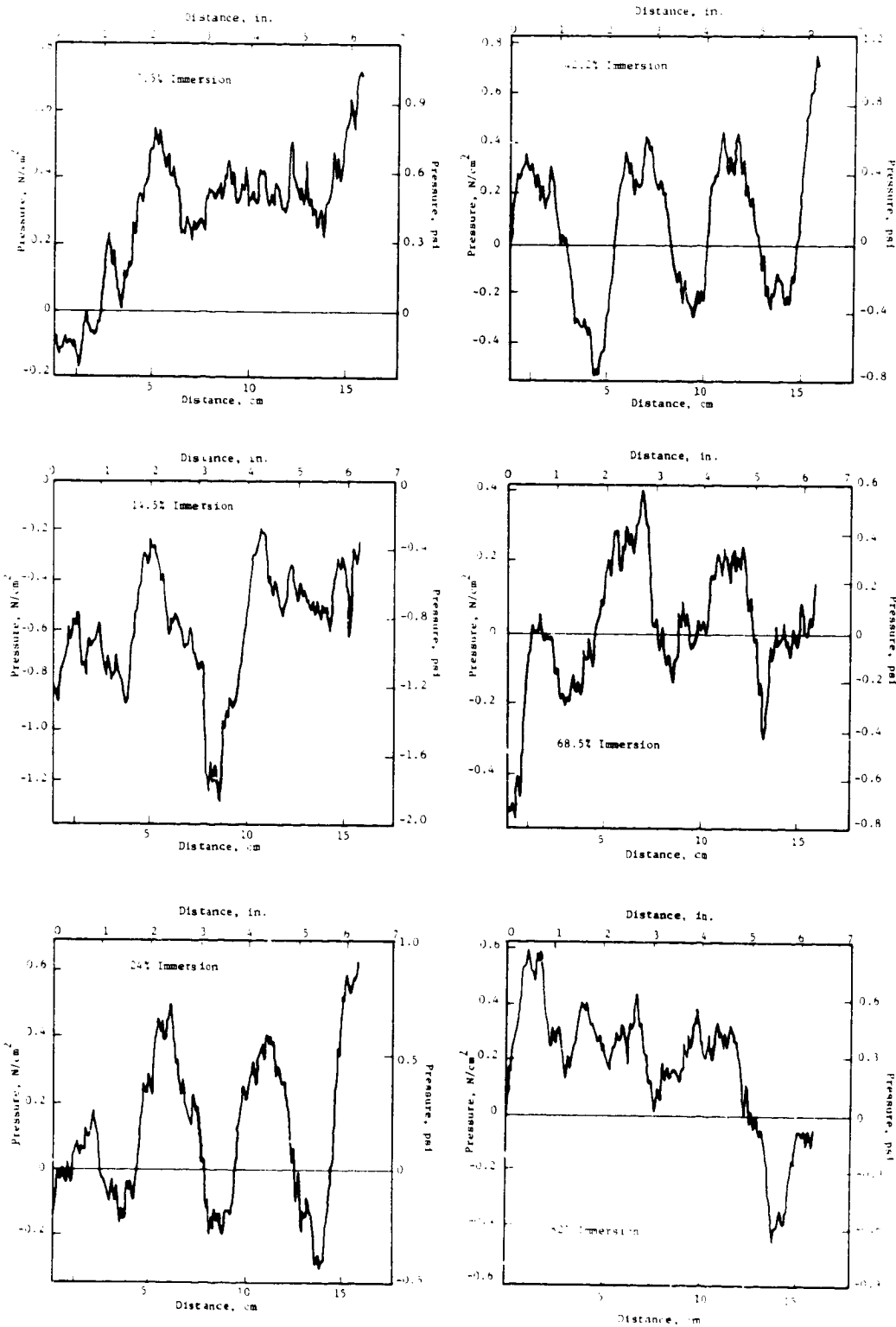


Figure 110. Dynamic Part of Instantaneous Total Pressure, 70% Speed Flutter.

ORIGINAL PAGE IS
OF POOR QUALITY

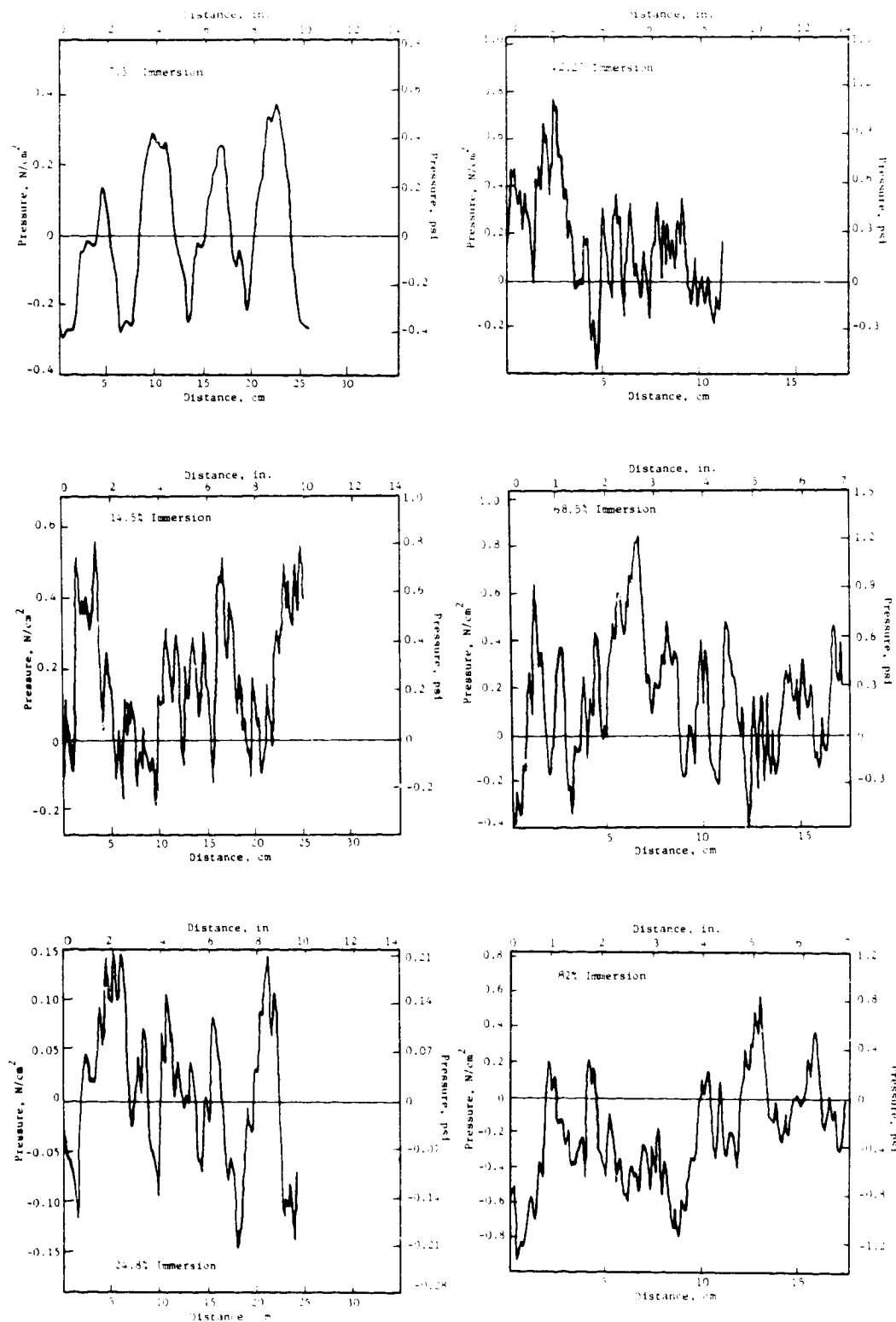


Figure 111. Dynamic Part of Instantaneous Total Pressure, 95% Speed Flutter.

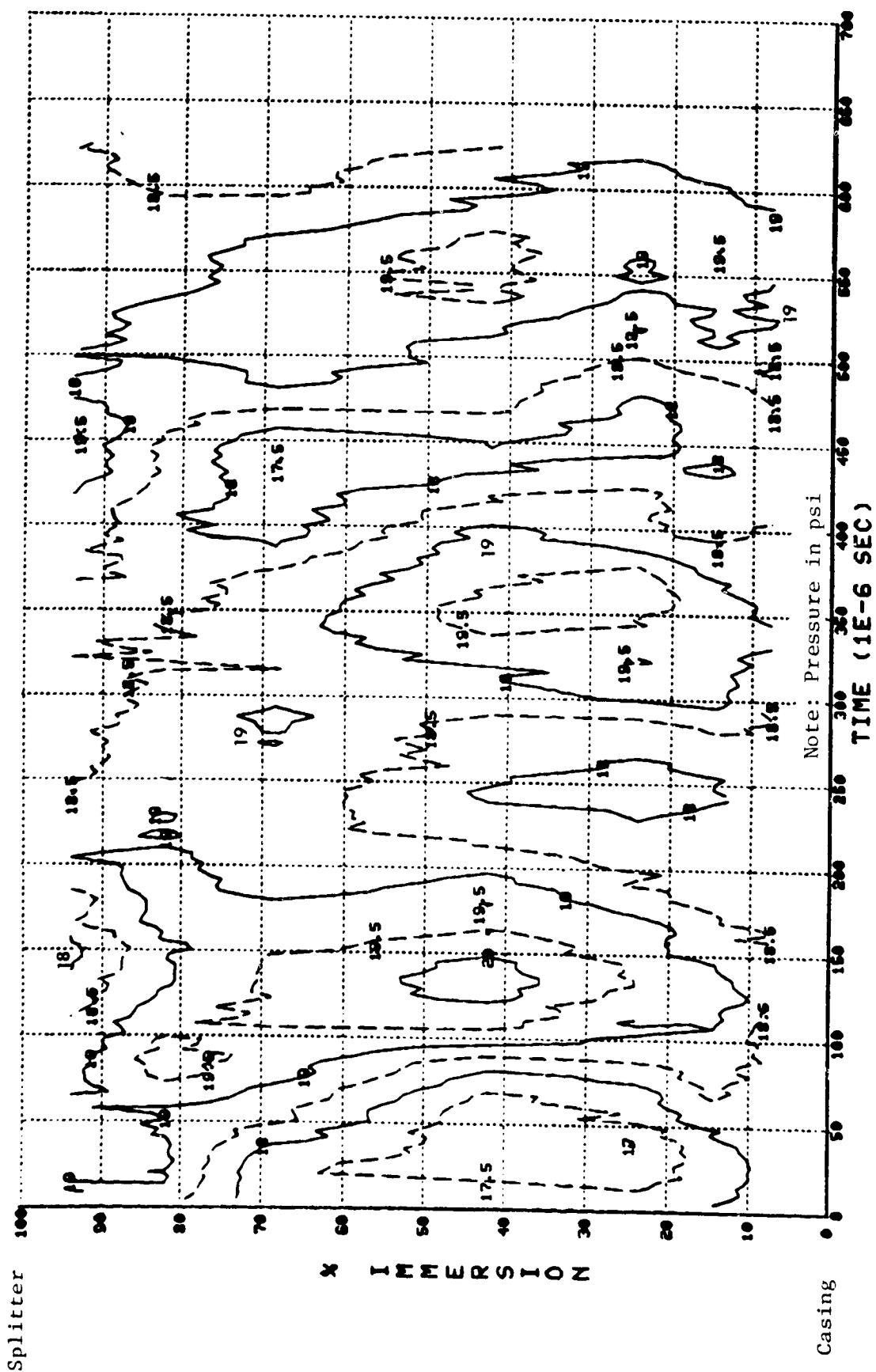


Figure 112. Total Pressure Contour Plot, 65% Speed Flutter.

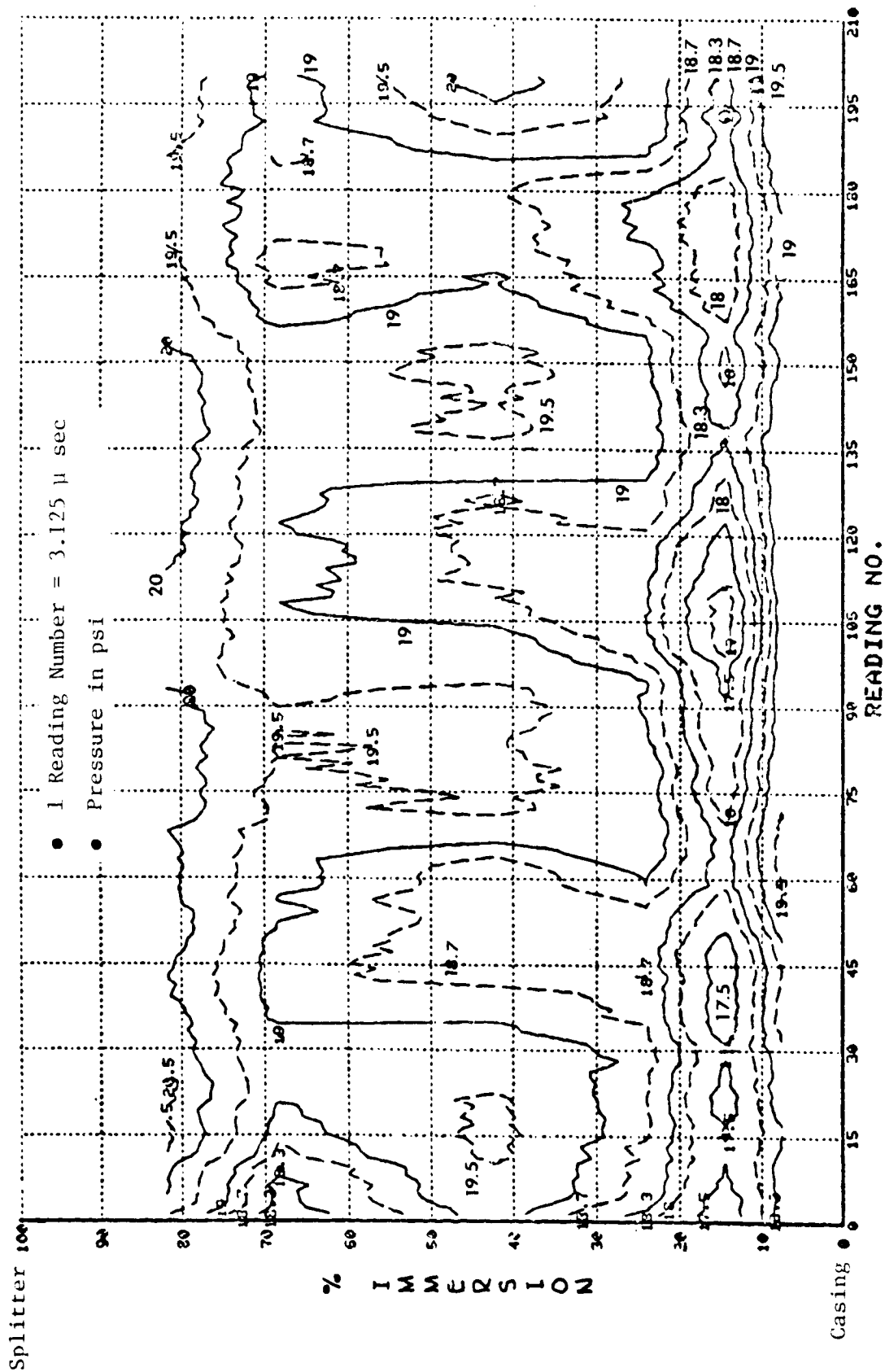


Figure 113. Total Pressure Contour Plot, 70% Speed Flutter.

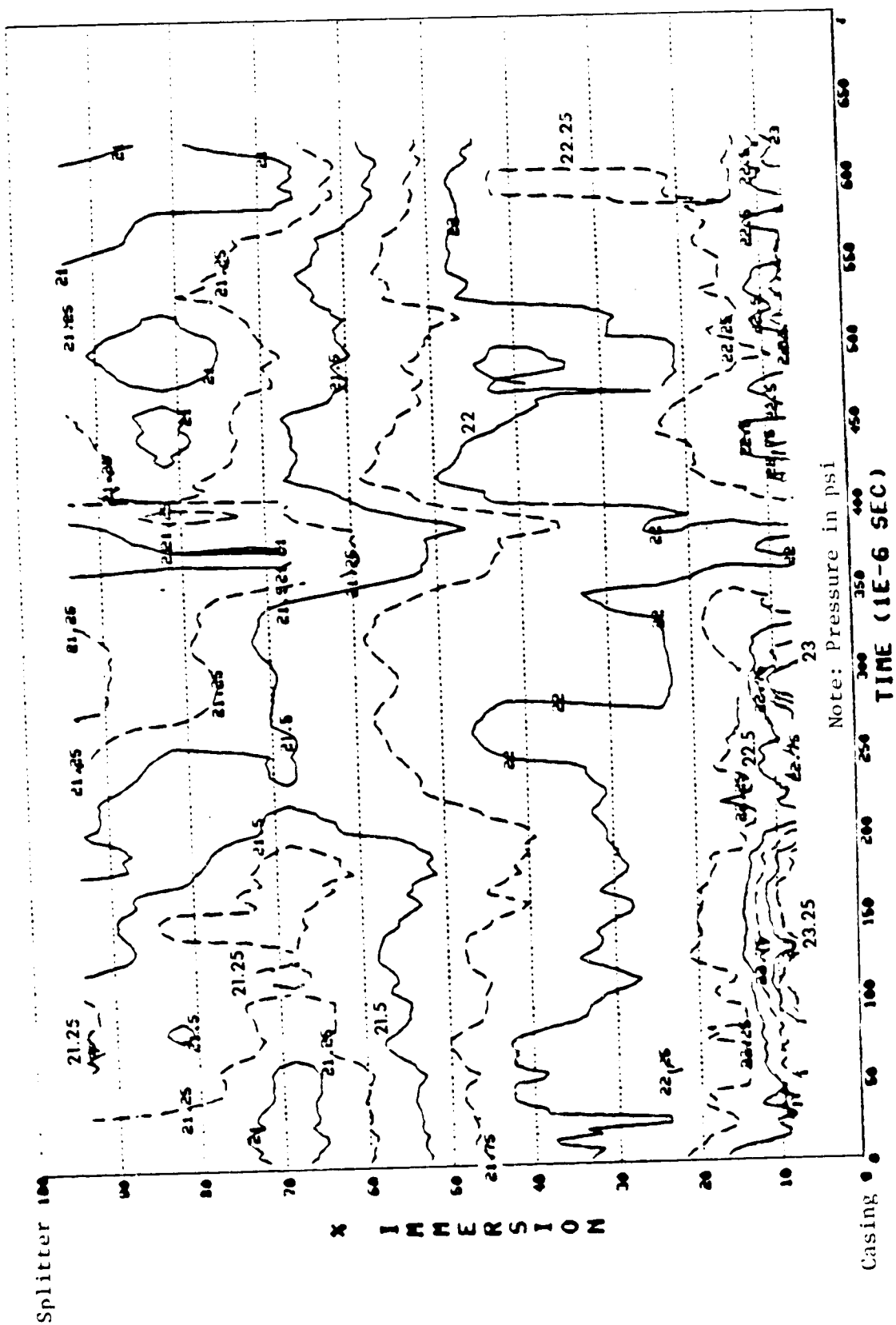


Figure 114. Total Pressure Contour Plot, 90% Speed Flutter.

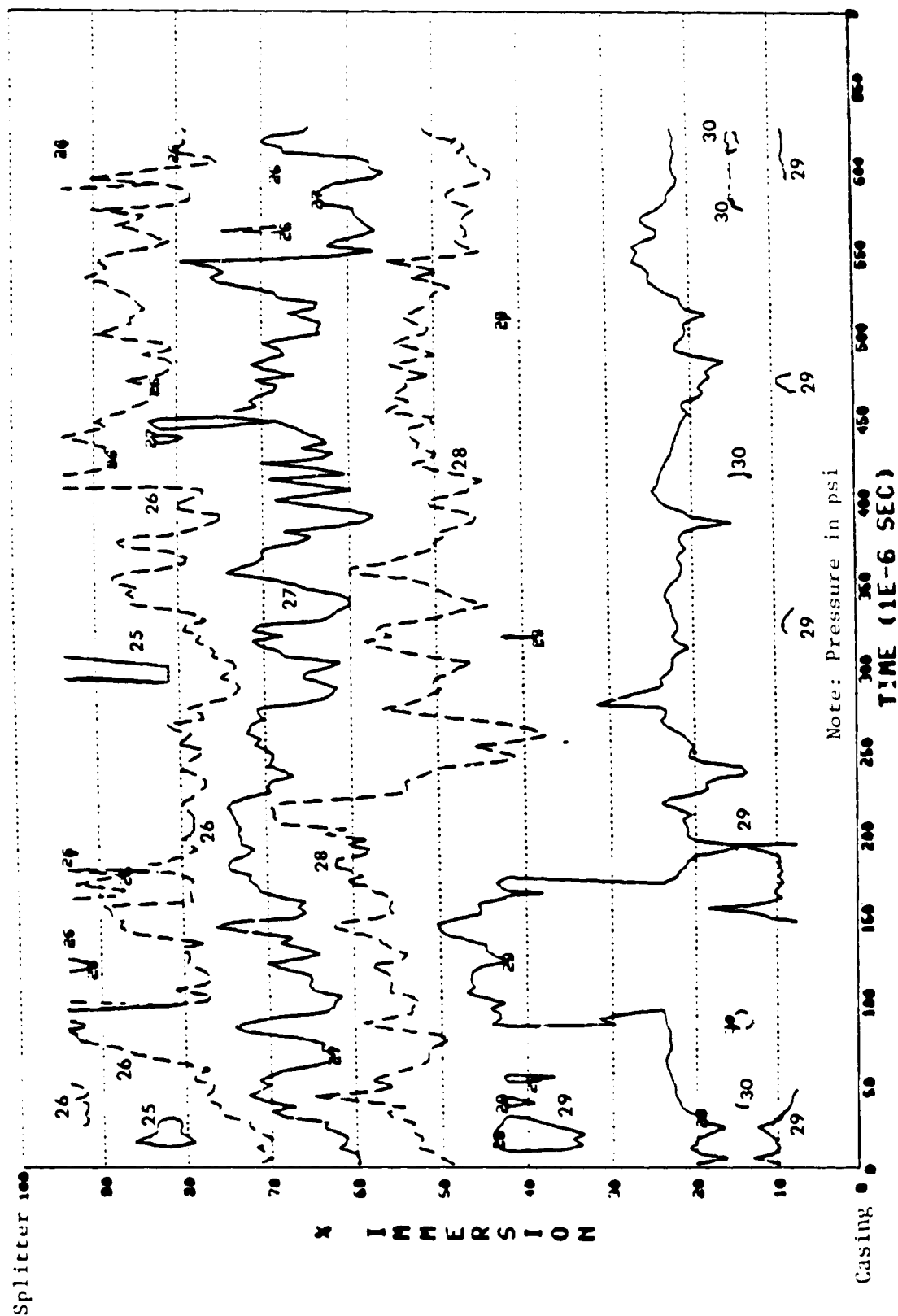


Figure 115. Total Pressure Contour Plot, 95% Speed Flutter.

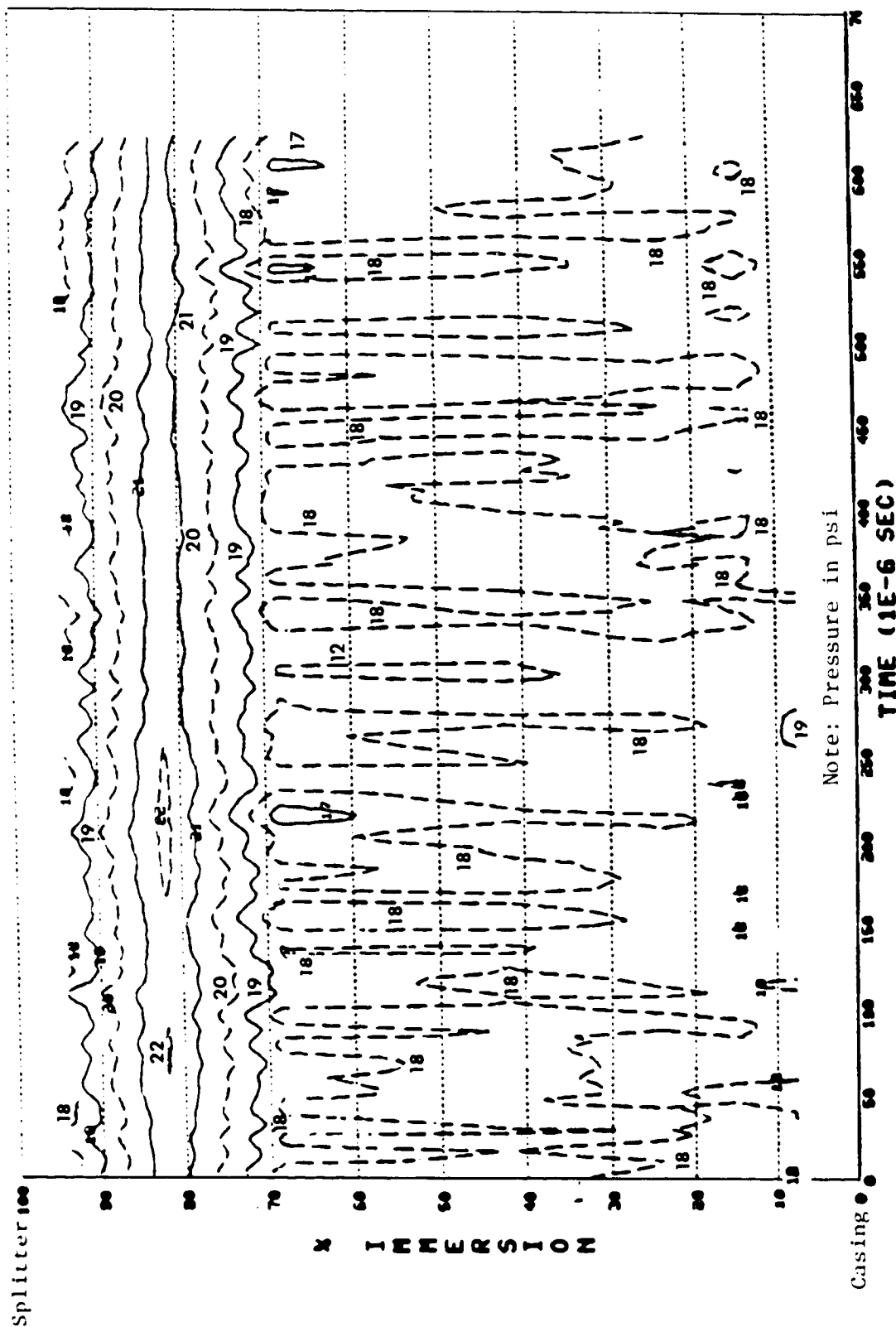
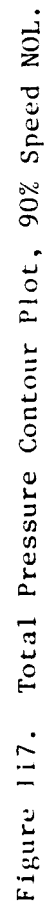


Figure 116. Total Pressure Contour Plot, 70% Speed IOL.



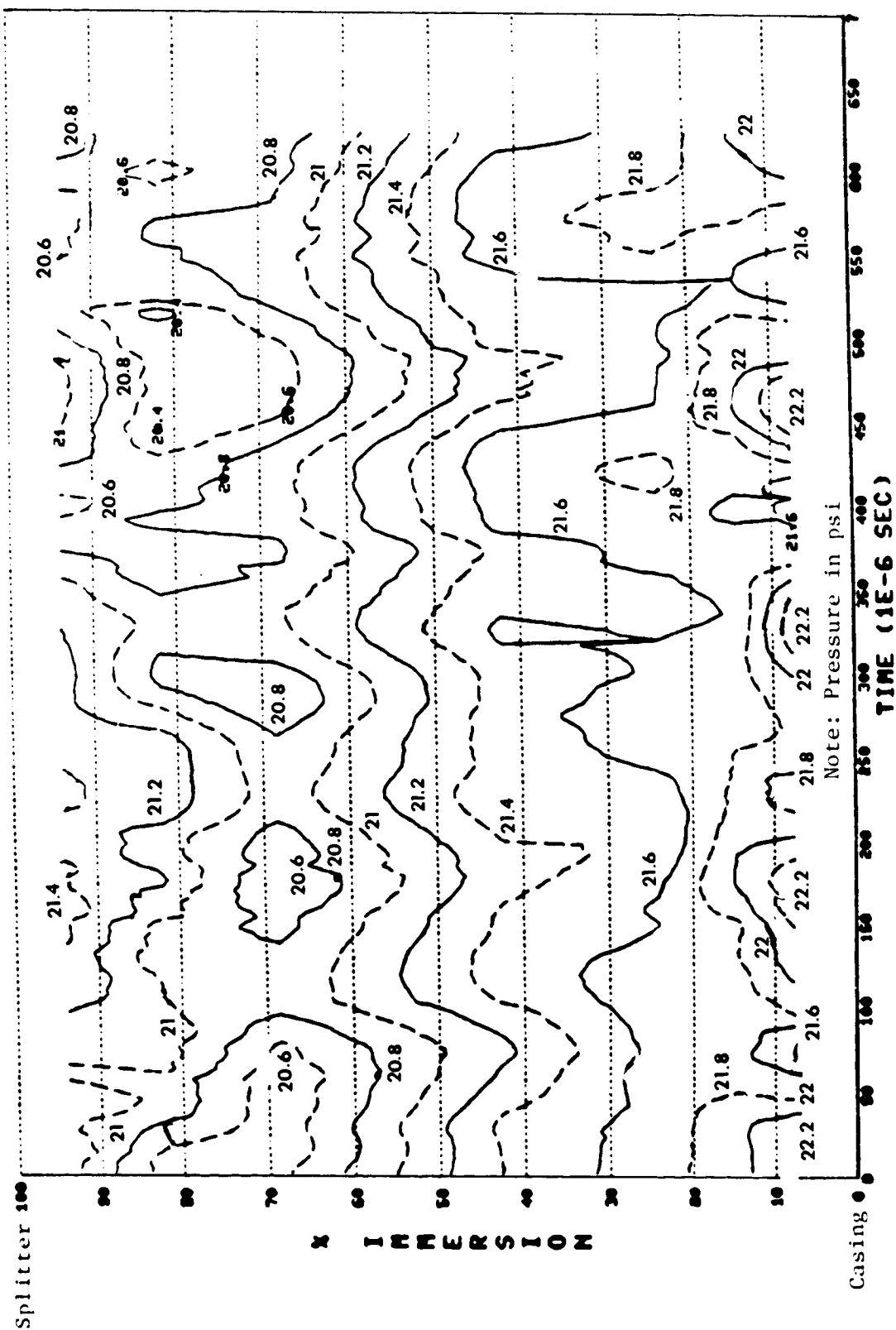


Figure 118. Total Pressure Contour Plot, 90% Speed IOL.

ORIGINAL FIGURE
OF POOR QUALITY

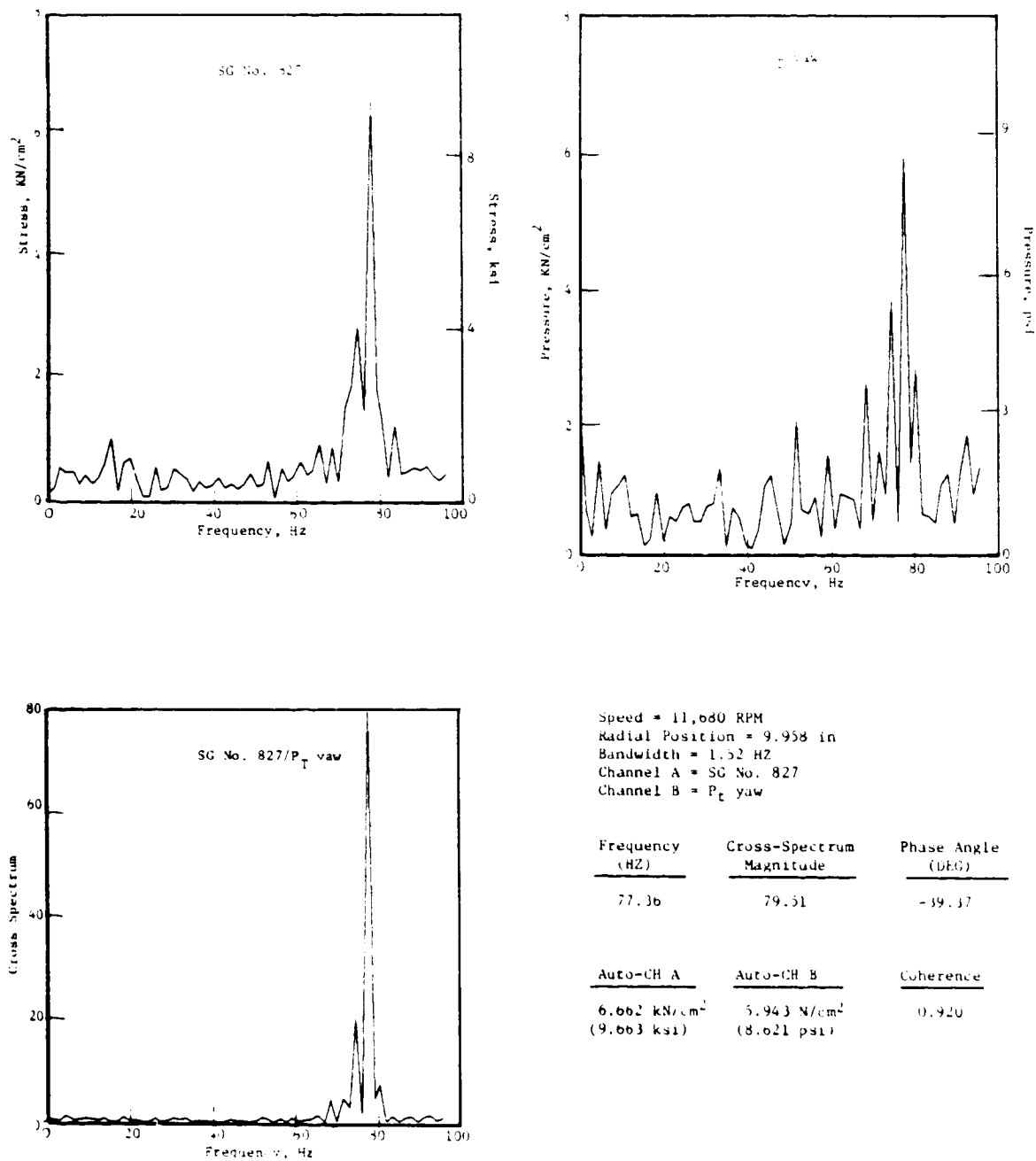


Figure 119. Total Pressure Cross Spectra, Percent Speed Flutter.

The circumferential variation of the total pressure at the six immersions is shown in terms of the unsteady pressures in Figure 120 and in terms of phase (relative to the strain gage signal) in Figure 121 for the 70 percent speed flutter point. The unsteady pressure variation for most immersions is shown to increase at mid-passage and decrease as the blade approaches the sensor. Also, the amplitudes are generally higher at the outer portion (tip) of the blade passage. The phase distribution suggests a forward traveling wave flutter mode, which will be seen more clearly from the linear spectra of the continuous unsteady total pressure responses discussed in the next section.

6.6.4 Traveling Wave Contents

The linear spectra of the unsteady total pressure measurement were generated to determine the traveling wave content in flutter at 70 and 95 percent speeds. The linear spectra for torsional flutter at 70 percent speed, Figures 122 through 124, show three predominant traveling waves - the 4, 5, and 6 nodal diameter waves - at all immersions, three of which are shown. The 2, 3, and 7 nodal diameter forward traveling waves were present but had significantly lower magnitudes. Beyond 2.5 kHz, traveling waves were either buried in the noise or were nonexistent. This would indicate that the unsteady total pressure did not vary in the circumferential direction as drastically as did the unsteady static pressure within blade passages and across the blade tips as seen in Section 6.5.

For flexural flutter at 95 percent speed, only data for 14.5 and 42.2 percent immersions, Figures 125 and 126 respectively, were successfully acquired due to Kulite failure. At 95 percent speed, the noise floor is considerably higher - by a factor of 10, than that at 70 percent speed. Forward traveling waves of 2, 3, and 4 nodal diameters, and a backward traveling wave of two nodal diameters, are seen at 14.5 percent immersion. No significant traveling waves are seen at the 42.2 percent immersion. This indicates that flutter activity was concentrated at the blade tip region during flexural flutter - as other blade vibration data and unsteady aerodynamic data have consistently indicated.

6.7 INLET AND EXIT FLOW DATA

Two x-array, traversable, heated thin-film anemometer probes were used to obtain two-dimensional fluid flow information (absolute flow velocity and flow angle) at each of seven radial immersions. One x-array probe was located forward, and the other one aft of the rotor (see Section 4.3).

The measured results are presented in terms of circumferentially averaged flow velocities and absolute flow angles, contour plots for absolute flow velocities and flow angles, and the traveling wave content from spectral analyses.

ORIGINAL FILED
OF POOR QUALITY

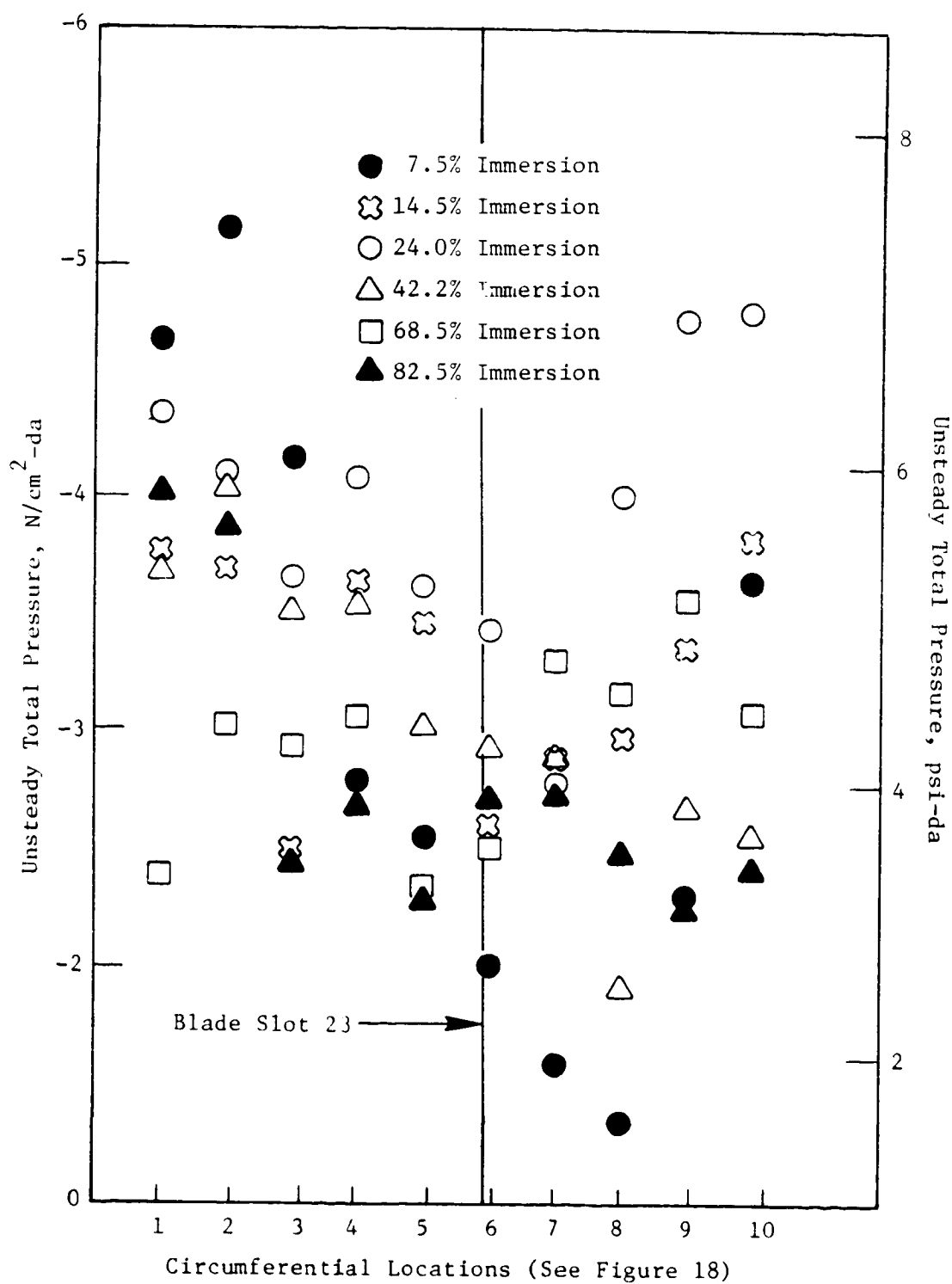


Figure 120. Circumferential Variation of Unsteady Total Pressure, 70 Percent Speed Flutter.

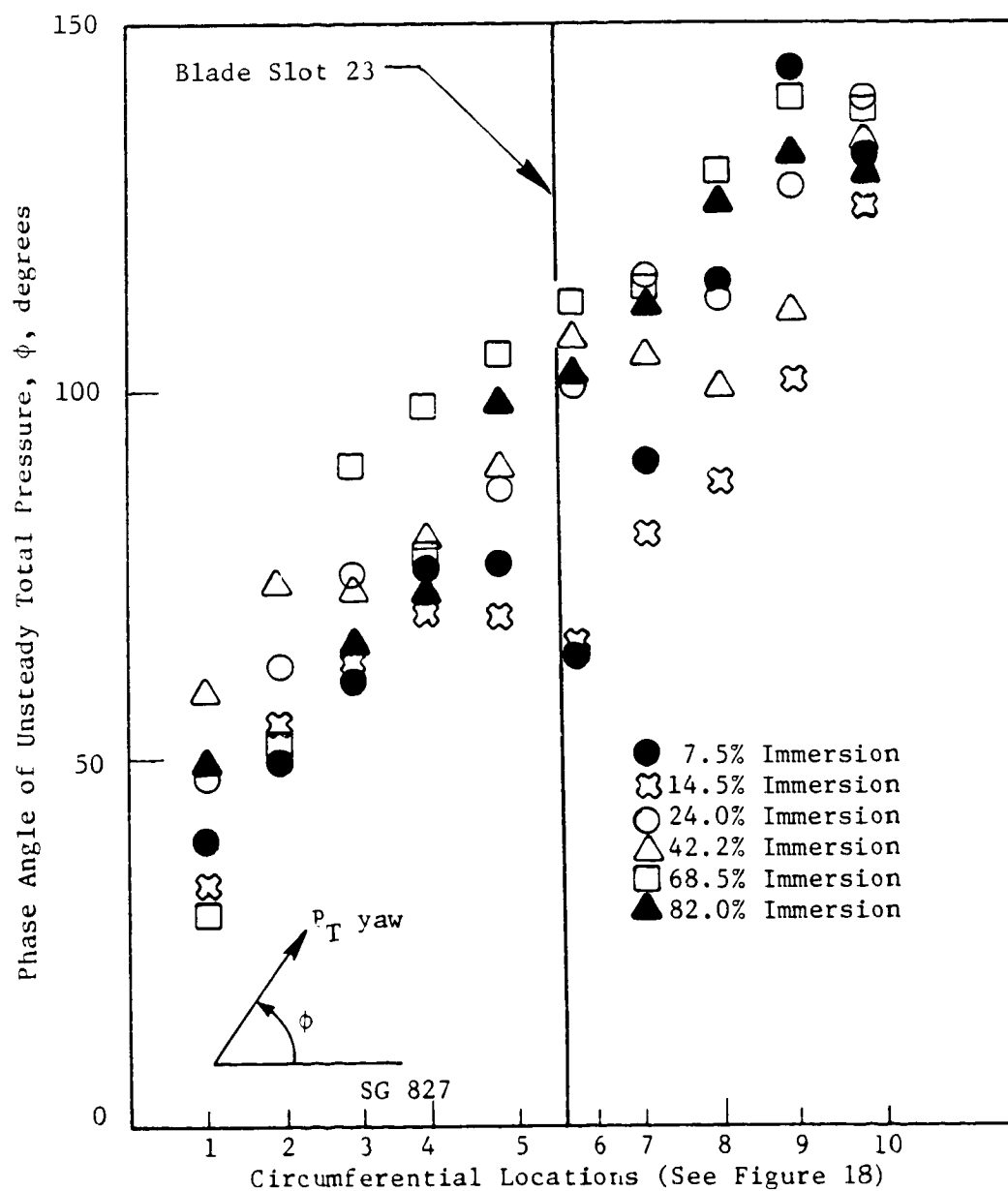


Figure 121. Circumferential Phase Variation of Total Pressure, 70 Percent Speed Flutter.

ORIGINAL 17.7
OF POOR QUALITY

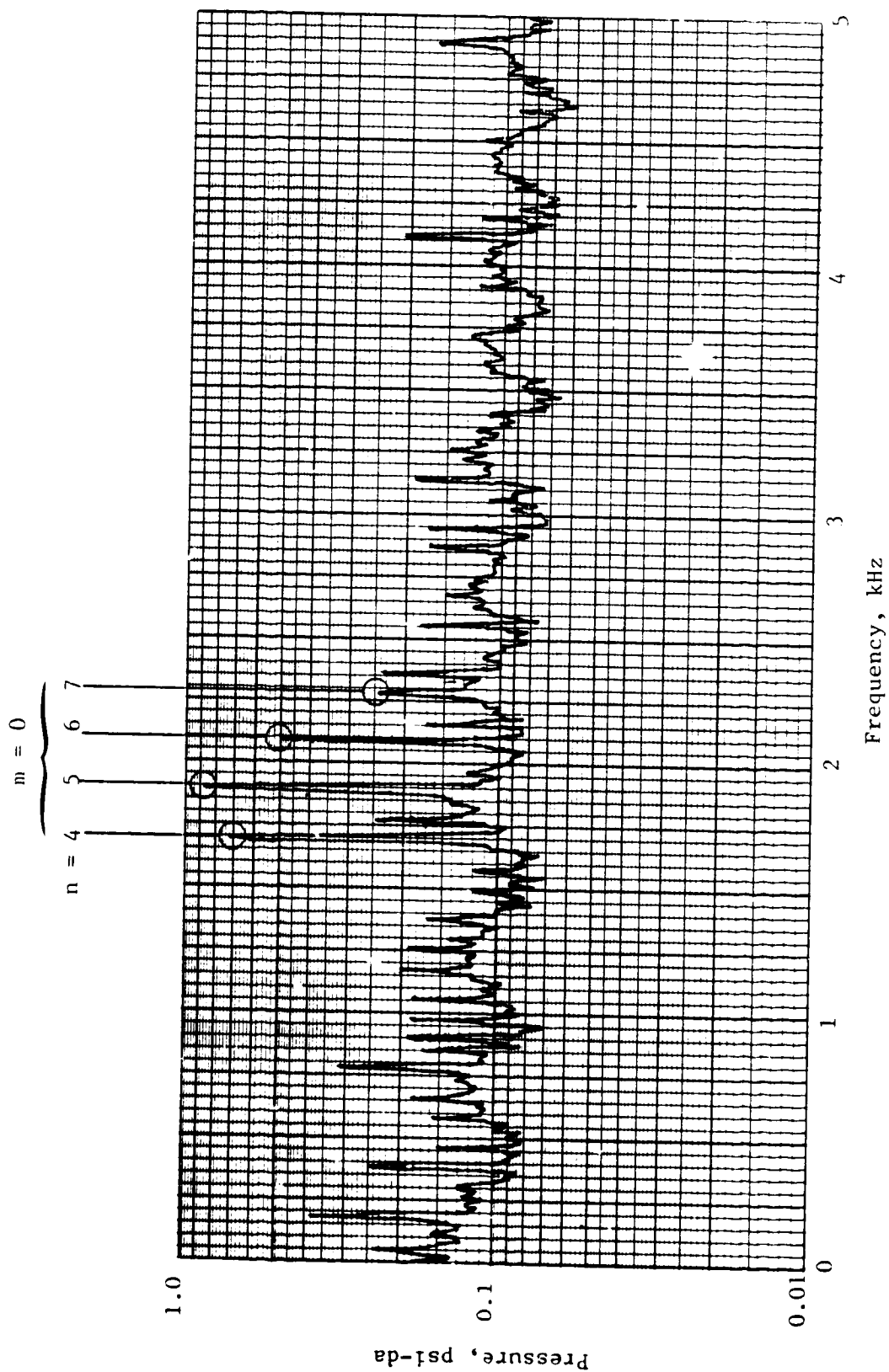


Figure 122. Total Pressure Spectrum, 14.5 Percent Immersion, 70 Percent Speed Flutter.

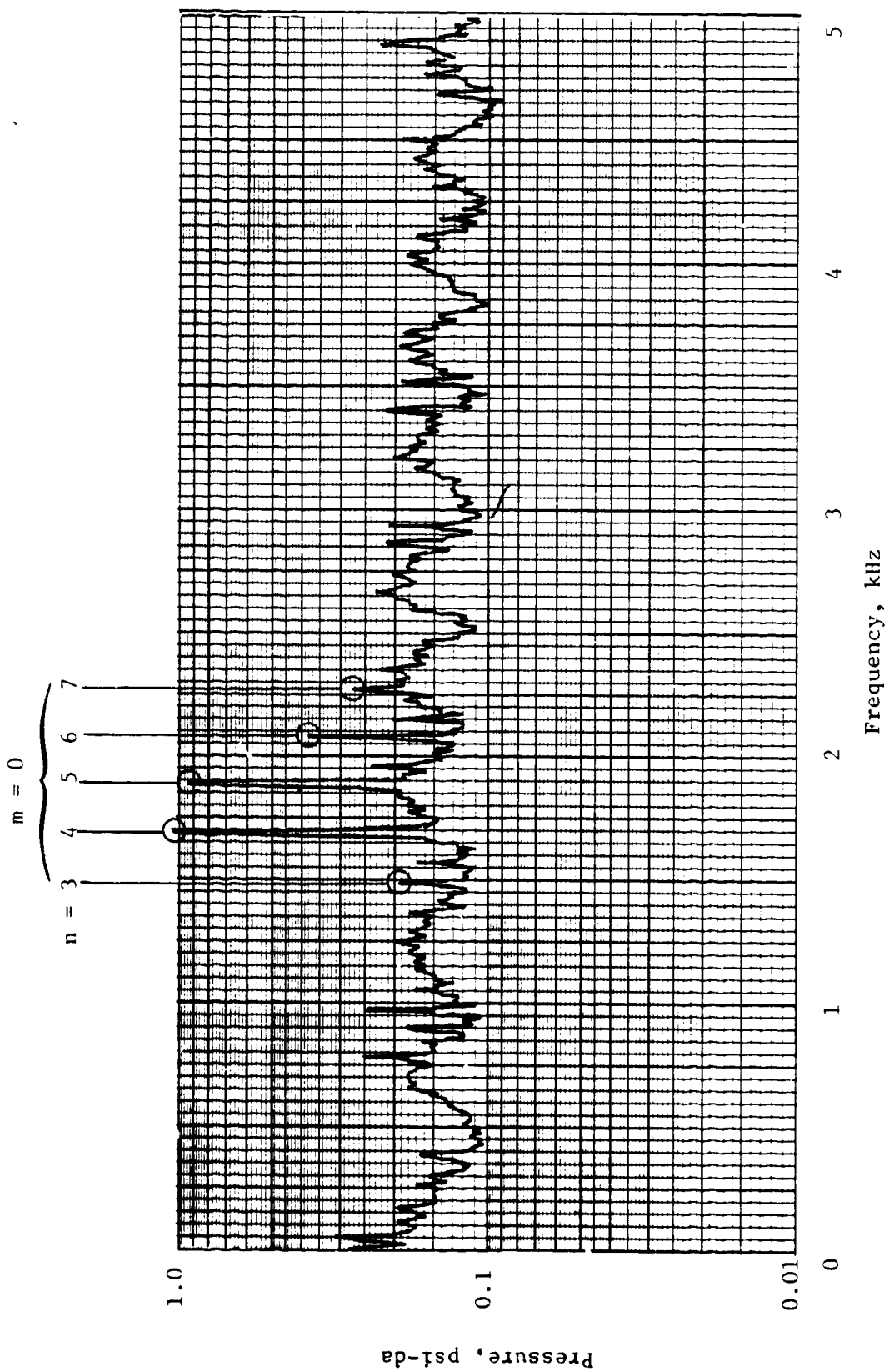


Figure 123. Total Pressure Spectrum, 42.2 Percent Immersion, 70% Speed Flutter.

ORIGINALLY FOR THE
OF POOR QUALITY

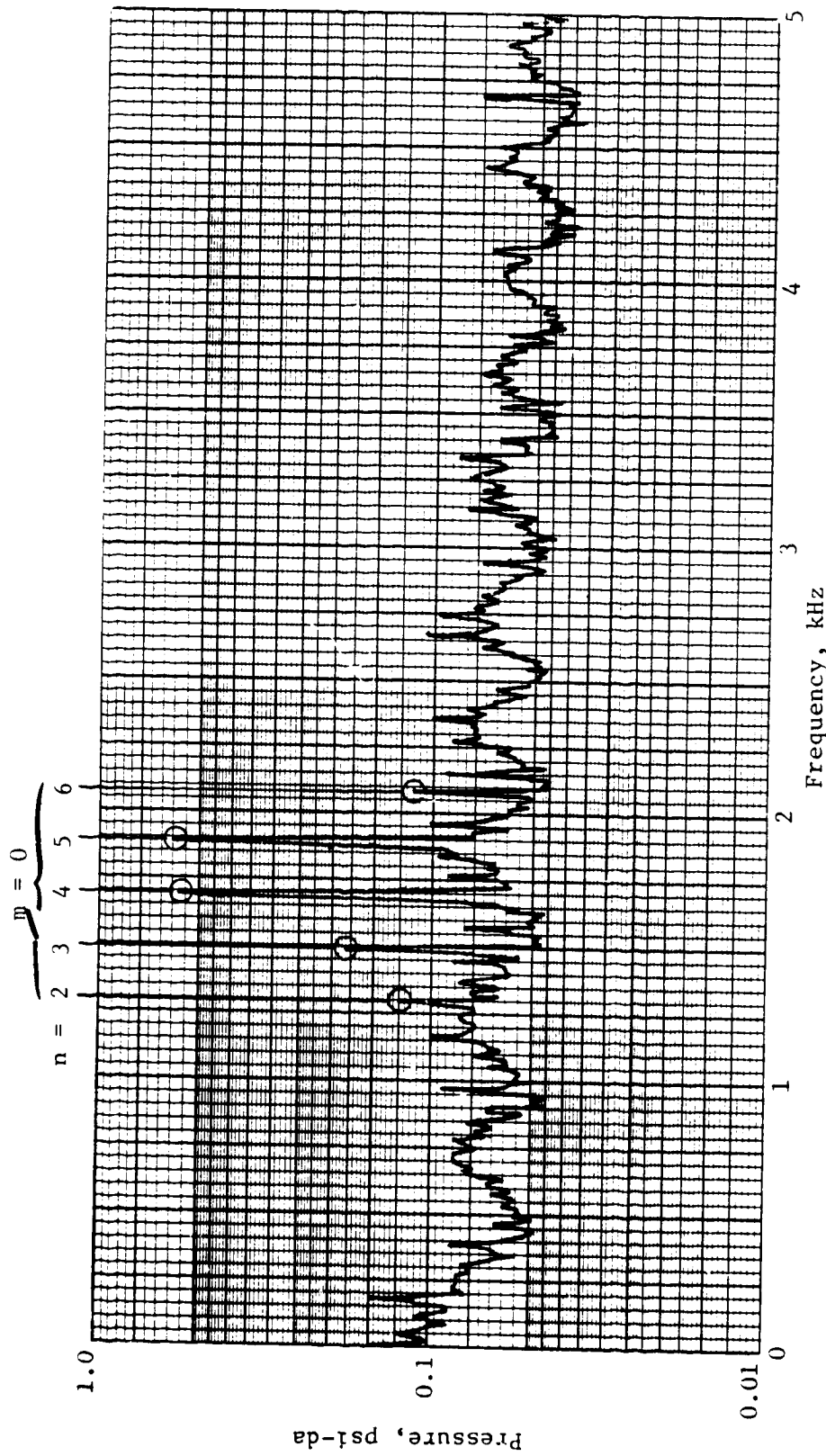


Figure 124. Total Pressure Spectrum, 82 Percent Immersion, 70 Percent Speed Flutter.

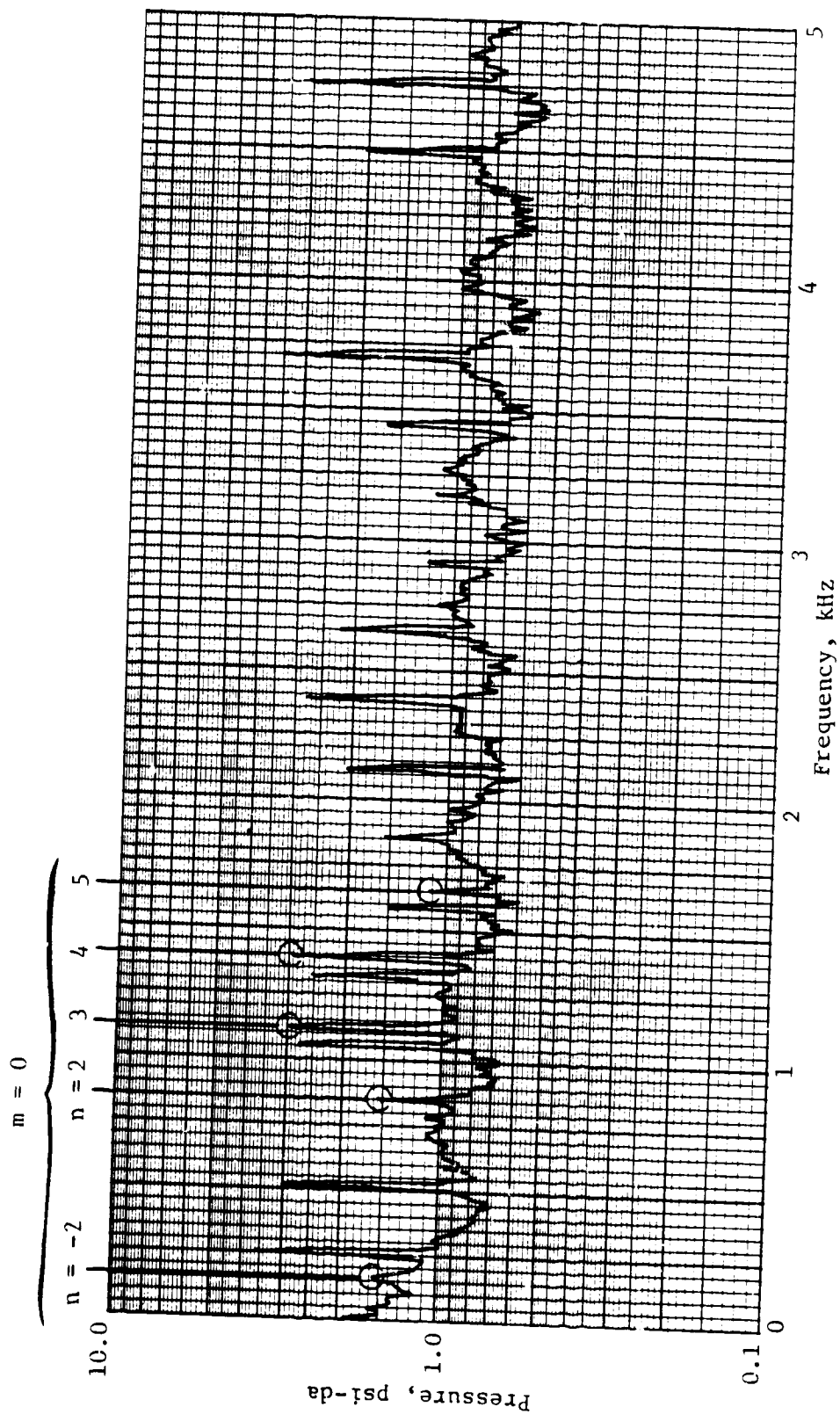


Figure 125. Total Pressure Spectrum, 14.5 Percent Immersion, 95 Percent Speed Flutter.

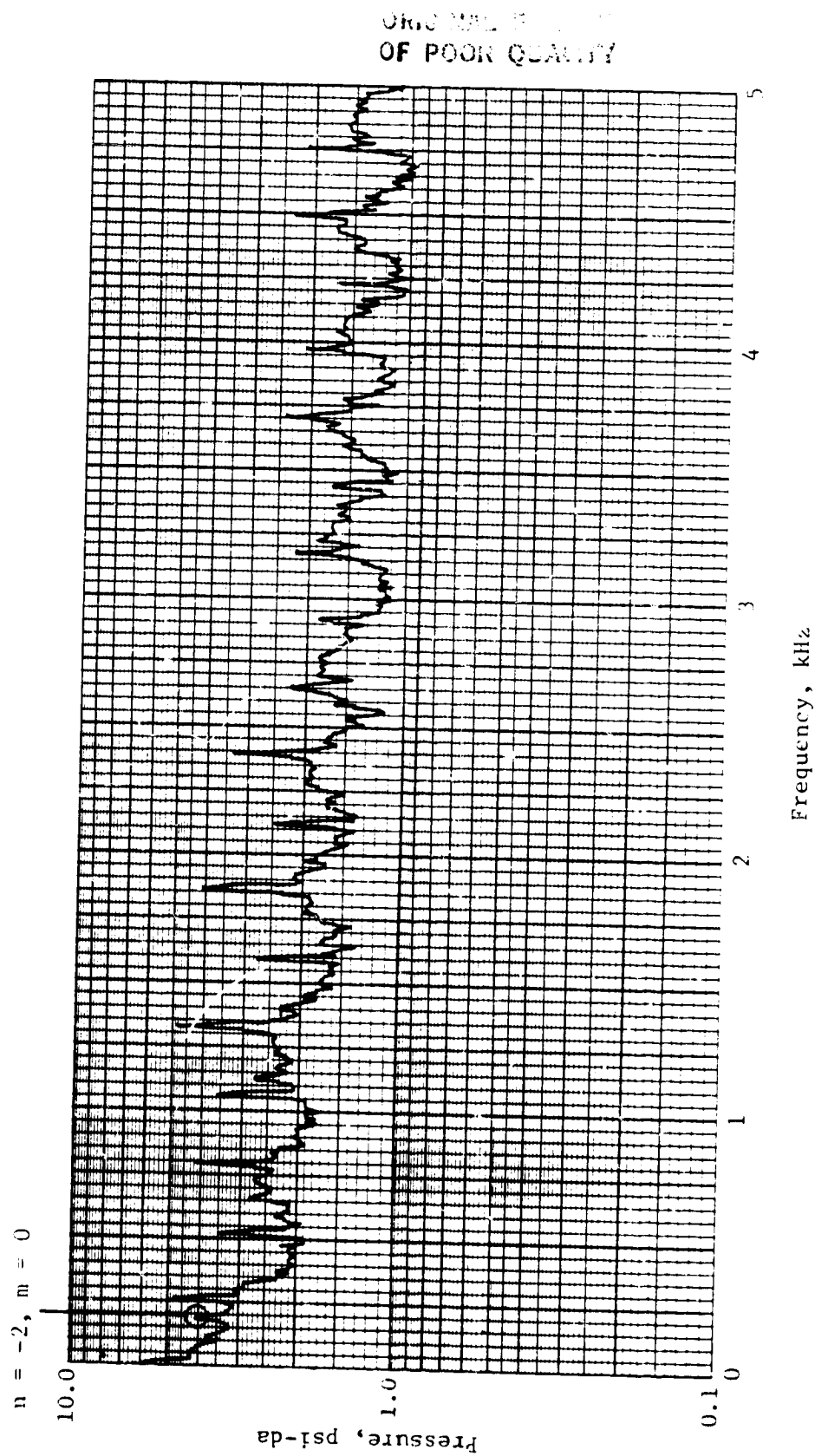


Figure 126. Total Pressure Spectrum, 42.2 Percent Immersion, 95 Percent Speed Flutter.

6.7.1 Absolute Velocity and Flow Angle Radial Distributions

Figures 127 through 130 show the radial distribution of the time averaged absolute flow velocities and flow angles at the inlet and exit traverse planes for the two 65 percent speed operating points. The inlet absolute flow velocity for flutter was generally lower than that for the IOL at all immersions as seen in Figure 127. This means that the relative incidence angle of the rotor blades was definitely higher over the whole span at the flutter condition, given the fact that the inlet flow angles were relatively small as shown in Figure 128. Also shown in Figure 127 is the calculated inlet absolute flow velocity based on inlet rake measurements at the flutter condition. Calculated results show the same radial distribution shape, although with lower inlet absolute flow velocity, as that of the x-array data. The calculation used an inviscid theory with an empirical correction for the casing boundary layer blockage effect to simulate the velocity defect near the casing. Also shown in Figure 128 is the inlet flow angle near the flutter condition measured by a wedge probe. It can be seen that there is good agreement between the wedge probe data and the x-array data at the flutter condition, while at the IOL unexplained discrepancies exist.

At the exit plane at 65 percent speed, Figure 129 shows lower absolute flow velocities at the flutter condition compared to those at the nonflutter condition, except near the splitter. Calculated data predict a lower exit absolute flow velocity at the flutter condition. The casing boundary layer in the exit plane was relatively thinner than that in the inlet plane discussed earlier. Larger exit flow angles were measured toward the blade tip region for both operating conditions, Figure 130, as a result of higher blade linear velocity and larger blade twist angle toward the blade tip region. Also shown in Figure 130 is the exit flow angle distributions measured by both a cobra probe and a wedge probe at a near flutter condition. The wedge probe data are in better overall agreement with the x-array data than are the cobra probe data.

Similar results for the three 70 percent speed operating points are shown in Figures 131 through 134. The general behavior of the inlet and exit absolute flow velocities and flow angles was very similar to that discussed above for 65 percent speed operating points.

The radial distribution of the same physical parameters are given in Figures 135 through 138 for the three 90 percent speed operating conditions. It is seen in these figures that the inlet and exit absolute flow velocities and flow angles at the flutter condition were not clearly separable from the corresponding data at the nonflutter conditions. During the test, the 90 percent speed flutter condition could not be steadily maintained as has been mentioned before. There is good agreement between calculated and measured data for the inlet absolute velocity and for the exit absolute velocity and flow angle over the inner halfspan of the blade.

For the two 95 percent speed operating points, Figures 139 through 142 show the same physical quantities for the seven immersions. Fair agreement is

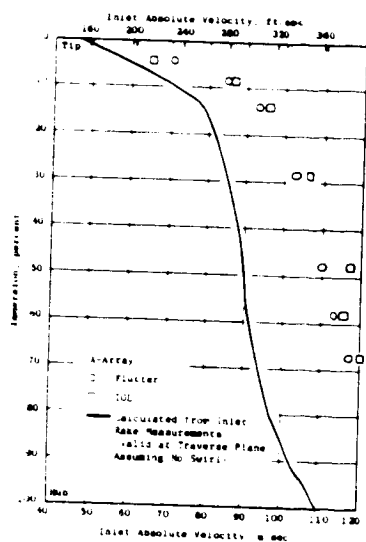


Figure 127. Radial Distribution of Inlet Absolute Velocity, 65 Percent Speed.

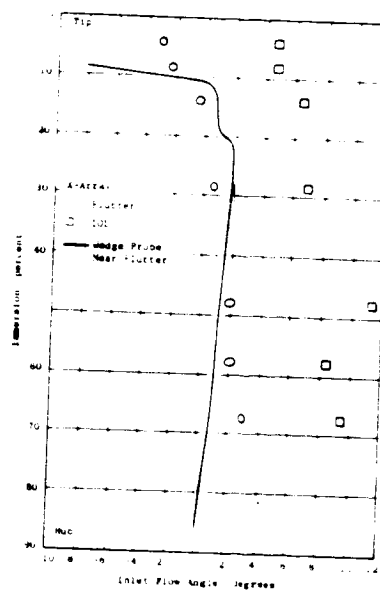


Figure 128. Radial Distribution of Inlet Flow Angle, 65 Percent Speed.

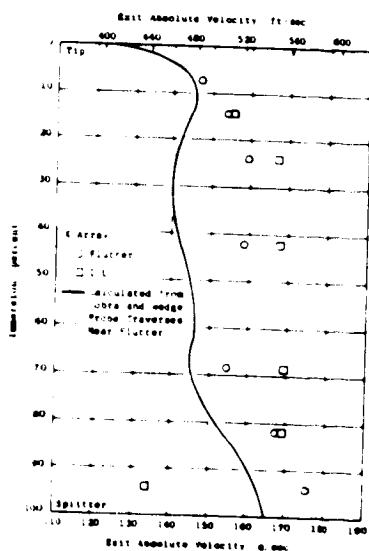


Figure 129. Radial Distribution of Exit Absolute Velocity, 65 Percent Speed.

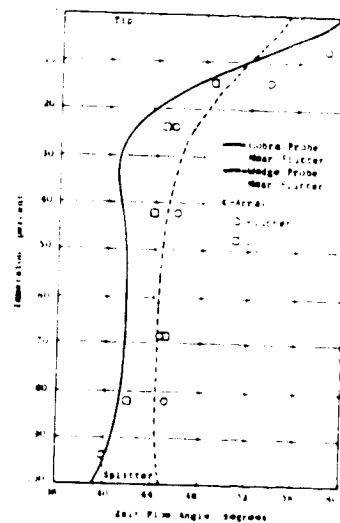


Figure 130. Radial Distribution of Exit Flow Angle, 65 Percent Speed.

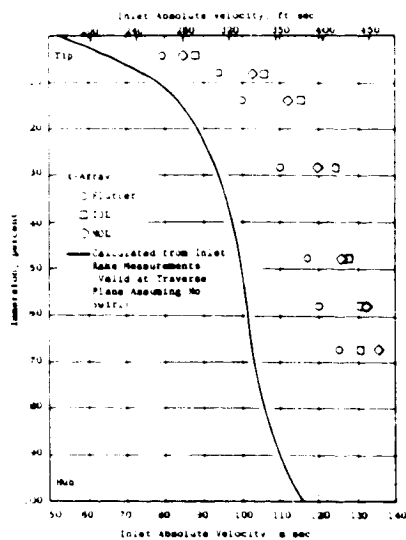


Figure 131. Radial Distribution of Inlet Absolute Velocity, 70 Percent Speed.

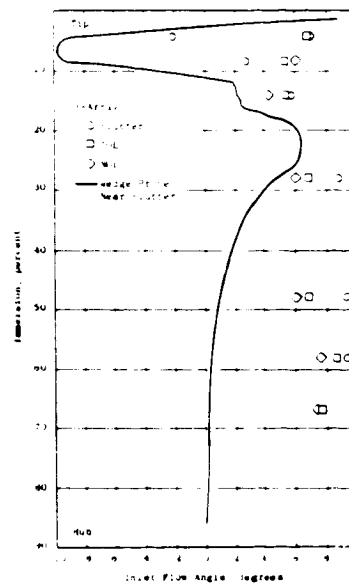


Figure 132. Radial Distribution of Inlet Flow Angle, 70 Percent Speed.

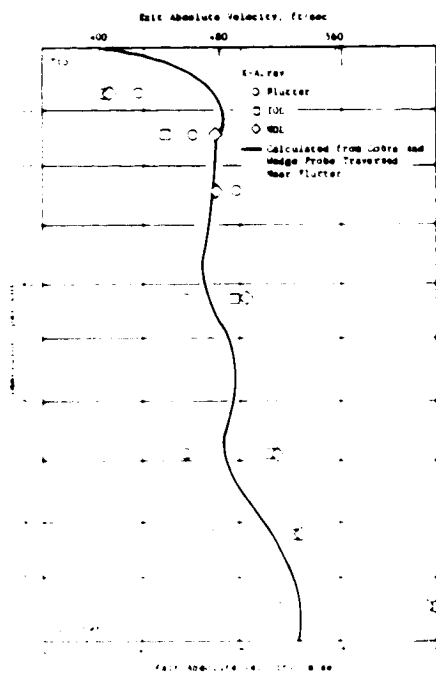


Figure 133. Radial Distribution of Exit Absolute Velocity, 70 Percent Speed.

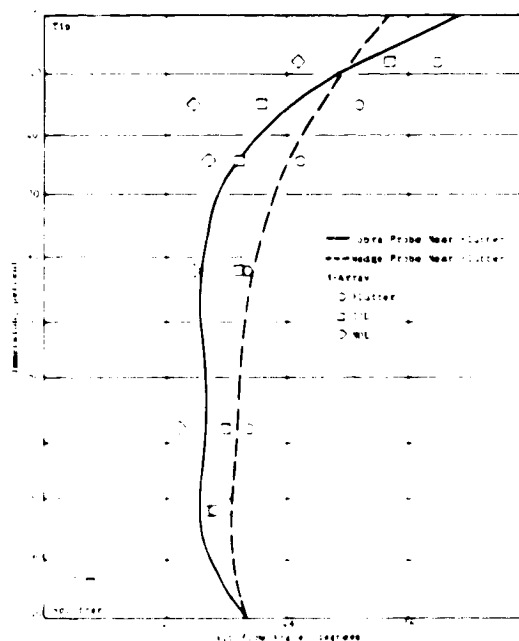


Figure 134. Radial Distribution of Exit Flow Angle, 70 Percent Speed.

ORIGINAL PAGE OF POOR QUALITY

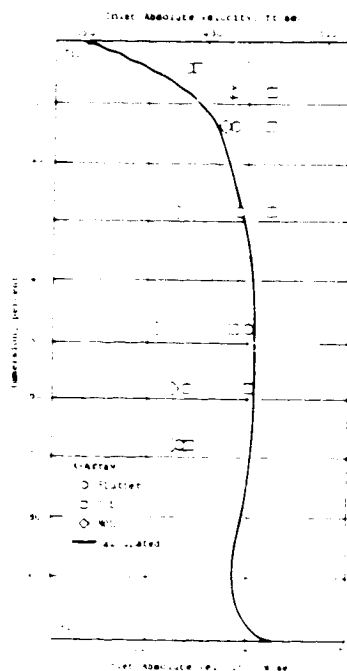


Figure 135. Radial Distribution of Inlet Absolute Velocity, 90 Percent Speed.

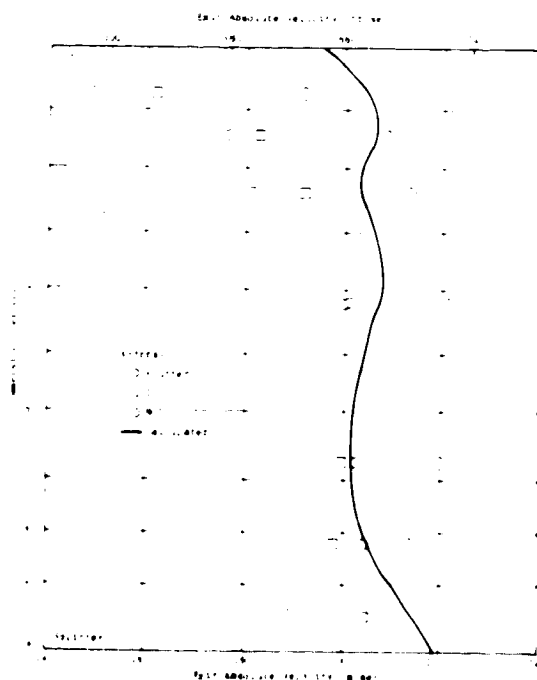


Figure 137. Radial Distribution of Exit Absolute Velocity, 90 Percent Speed.

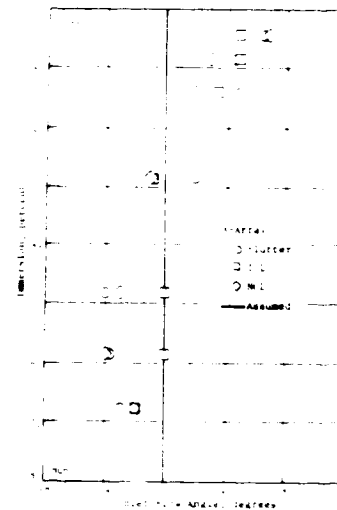


Figure 136. Radial Distribution of Inlet Flow Angle, 90 Percent Speed.

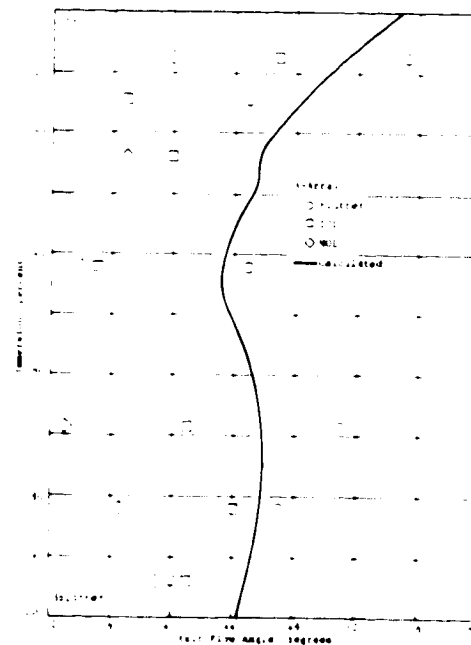


Figure 138. Radial Distribution of Exit Flow Angle, 90 Percent Speed.

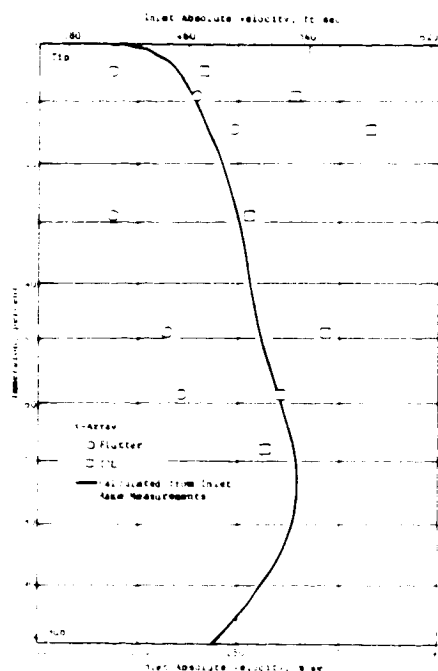


Figure 139. Radial Distribution of Inlet Flow Velocity, 95 Percent Speed.

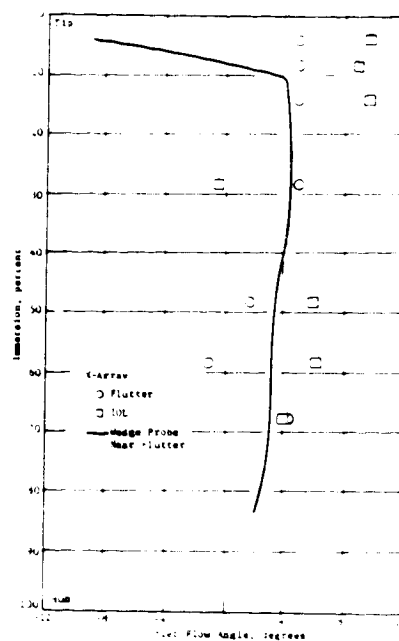


Figure 140. Radial Distribution of Inlet Flow Angle, 95 Percent Speed.

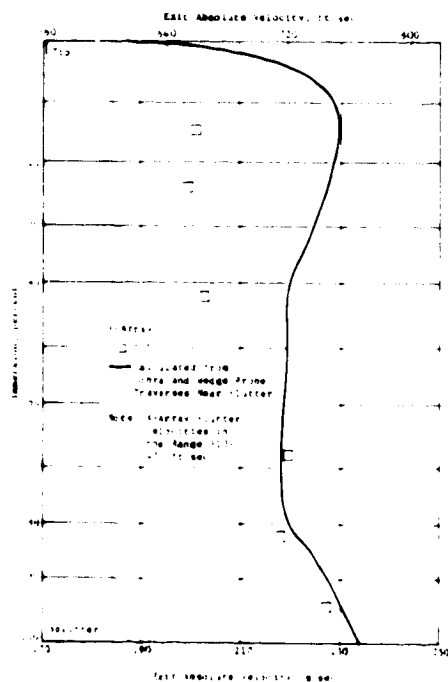


Figure 141. Radial Distribution of Exit Flow Velocity, 95 Percent Speed.

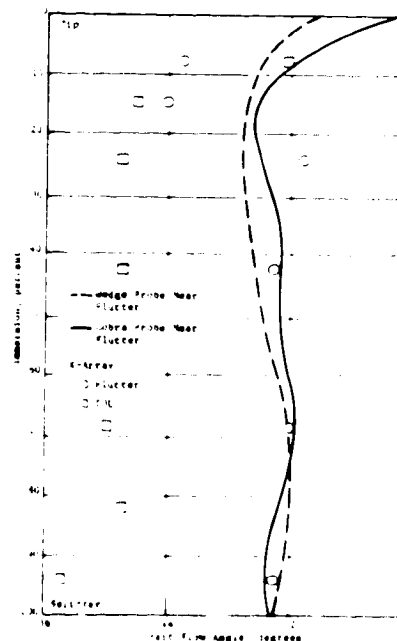


Figure 142. Radial Distribution of Exit Flow Angle, 95 Percent Speed.

shown between the calculated and measured inlet absolute velocity in Figure 139, but there is excellent agreement between the calculated and measured exit flow angle at the flutter condition as shown in Figure 142. Also, the inlet wedge probe measured flow angles agree well with the x-array data shown in Figure 140. For presently unknown reasons, the exit x-array measured extremely low flow velocities at the flutter point; these are not shown in Figure 141. However, based on the other three sets of flutter point data presented here, the flutter flow velocity should not be too far removed from that at the intermediate operating line, which agrees with the calculated data shown in Figure 141.

6.7.2 Circumferential Variation of Absolute Velocity and Angle

The ensemble averaged data measured by the x-array probes was used to calculate the absolute flow velocity and direction (angle). Figures 143 and 144 are plots of this data for the inlet and exit x-array probes respectively at the 70 percent speed flutter point, each at three representative immersions. Similar data is shown for the 95 percent speed flutter point in Figures 145 and 146 (the previously mentioned inexplicably low exit flow velocity can be seen in Figure 146). In Figures 143 and 144, the individual blade passages can be clearly seen for the 70 percent speed flutter point. However, at the higher flow velocities for the 95 percent speed flutter point, the blade passages are no longer discernable, as can be seen in Figures 145 and 146.

Contour plots of absolute flow velocity and flow angle as a function of the circumferential and radial coordinates were generated in the same fashion as was done for the casing Kulite data and the total pressure data. Figures 147 through 160 show these contour plots for all flutter conditions - except for the 95 percent flutter data in the exit plane because of the low measured velocities. These plots show the absolute flow velocity and flow angle distributions over about three (65 and 70 percent speeds) or four (90 and 95 percent speeds) blade passages, as one would observe in the rotor reference system in the absence of blade vibrations (they are time averaged).

For 65 and 70 percent speed flutter, the periodic wake pattern is seen in both the flow velocity and flow angle plots, though it is less obvious in the exit plane for 70 percent speed flutter. The existence of the inlet casing boundary layer is apparent in Figures 147 and 148, for 65 percent speed flutter, and in Figures 151 and 152 for 70 percent speed flutter, because of the large gradient in flow velocity and flow angle near the casing. Both the casing and the splitter boundary layers are apparent in the exit traverse plane as seen in Figures 149 and 150 for 65 percent speed flutter and in Figures 153 and 154 for 70 percent speed flutter.

For 90 and 95 percent speed flutter points, the resultant contour plots shown in Figures 155 through 160 indicate the variation in velocities and flow angles in the radial and circumferential direction.

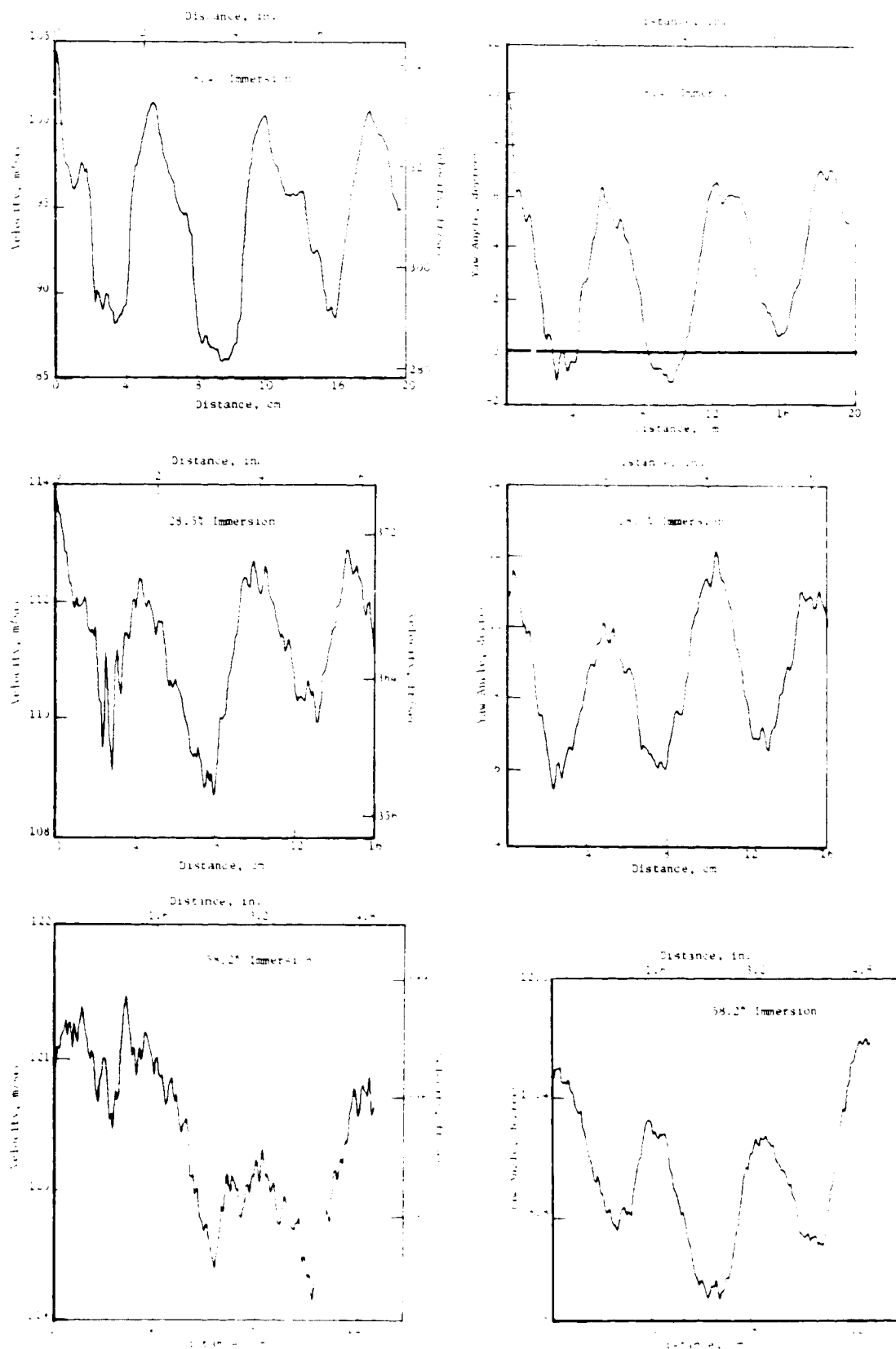


Figure 143. Circumferential Variation of Inlet Absolute Velocity and Flow Angle, 70 Percent Speed Flutter.

ORIGINAL OF PAPER 10-11-17

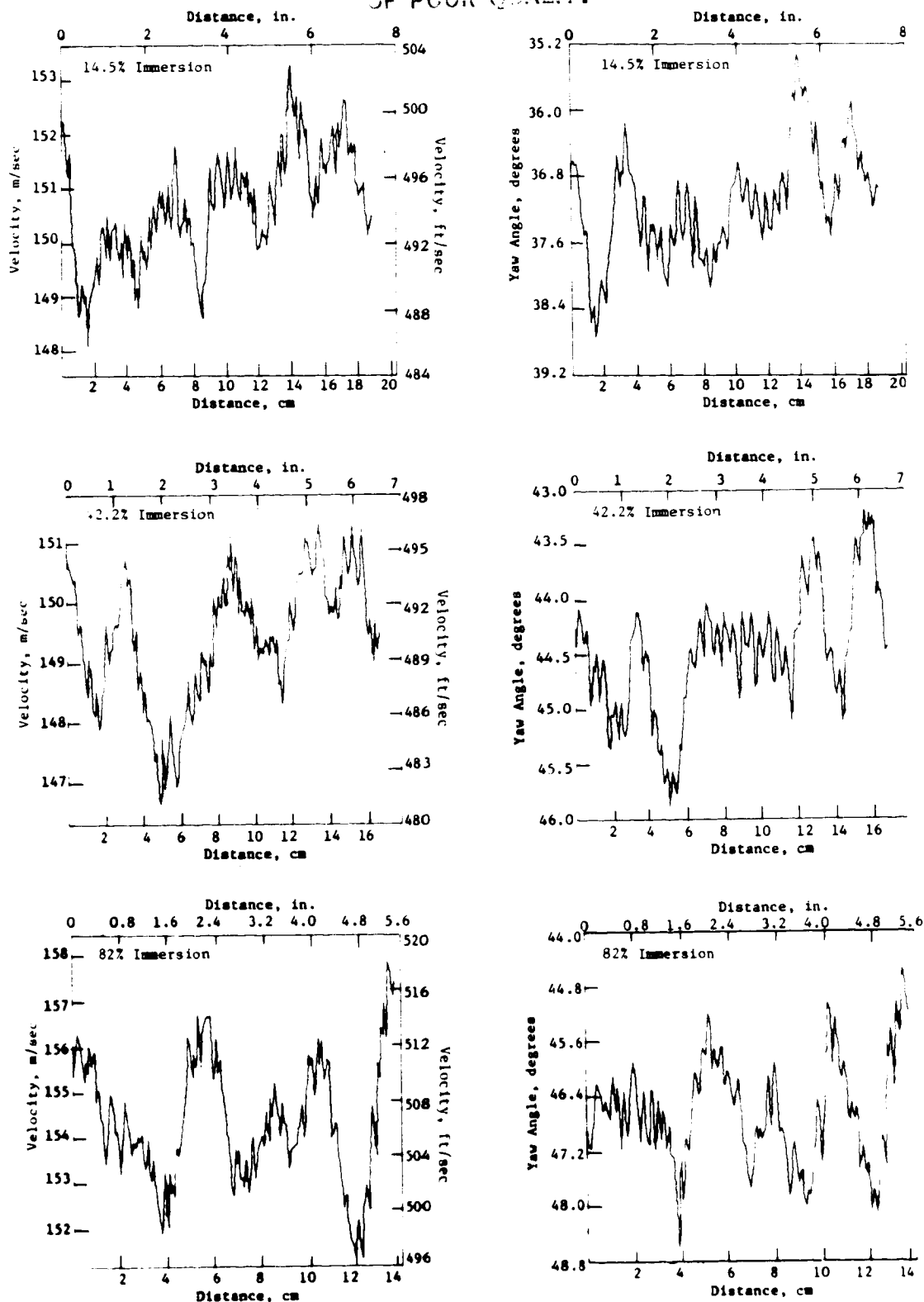


Figure 144. Circumferential Variation of Exit Absolute Velocity and Flow Angle, 70 Percent Speed Flutter.

OF FLOW

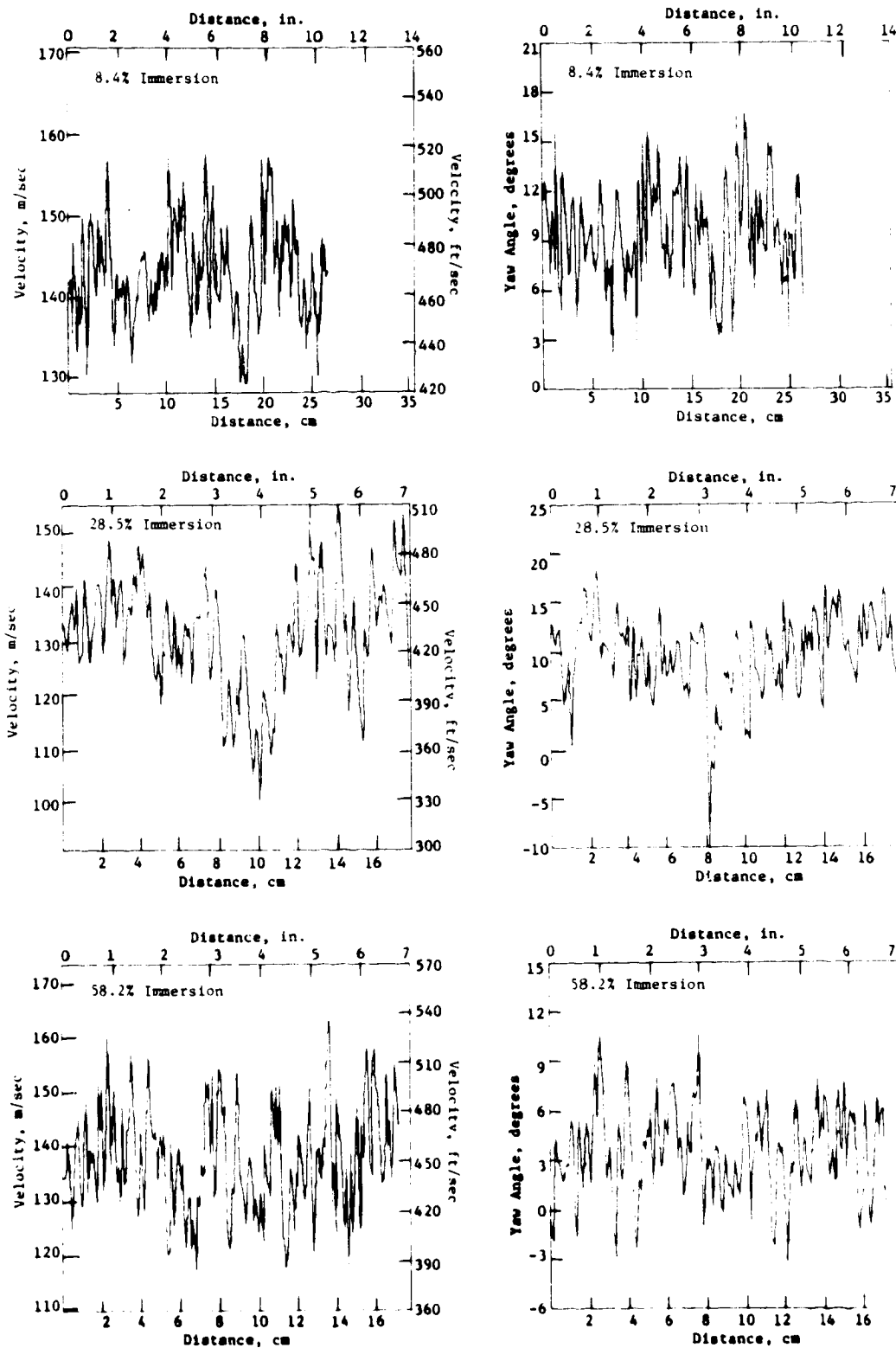


Figure 145. Circumferential Variation of Inlet Absolute Velocity and Flow Angle, 95 Percent Speed Flutter.

CHARACTERISTICS OF PITCH FLUTTER

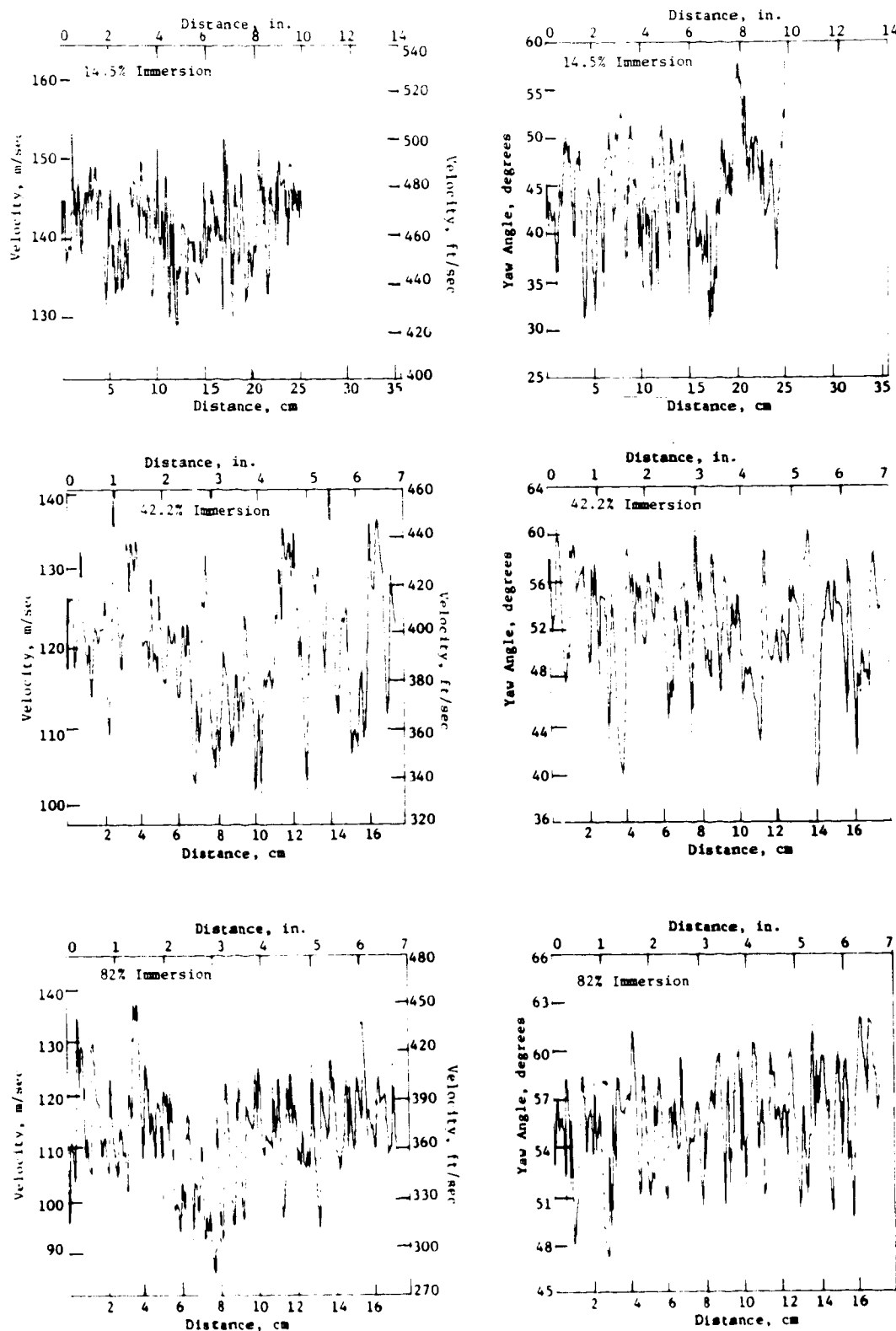


Figure 146. Circumferential Variation of Exit Absolute Velocity and Flow Angle, 95 Percent Speed Flutter.

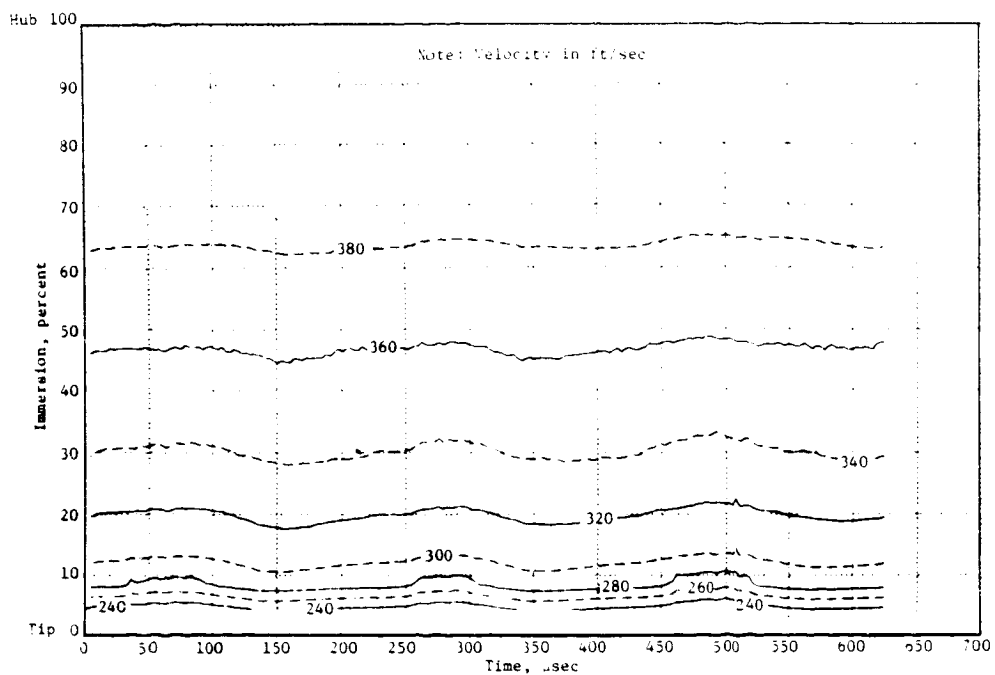


Figure 147. Inlet Absolute Velocity Contour Plot, 65 Percent Speed Flutter.

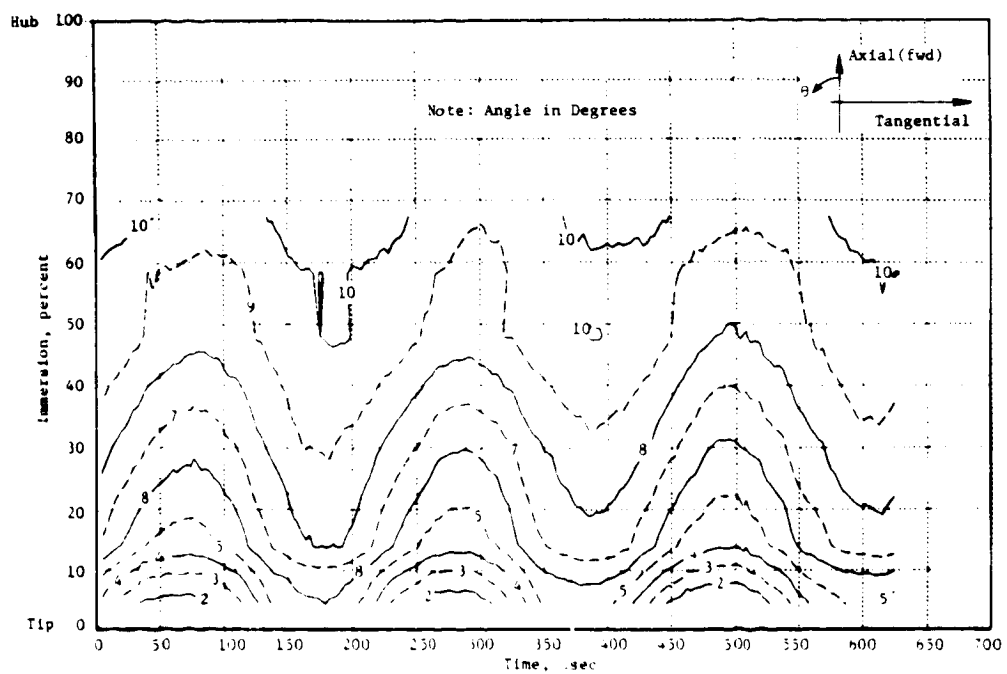


Figure 148. Inlet Flow Angle Contour Plot, 65 Percent Speed Flutter.

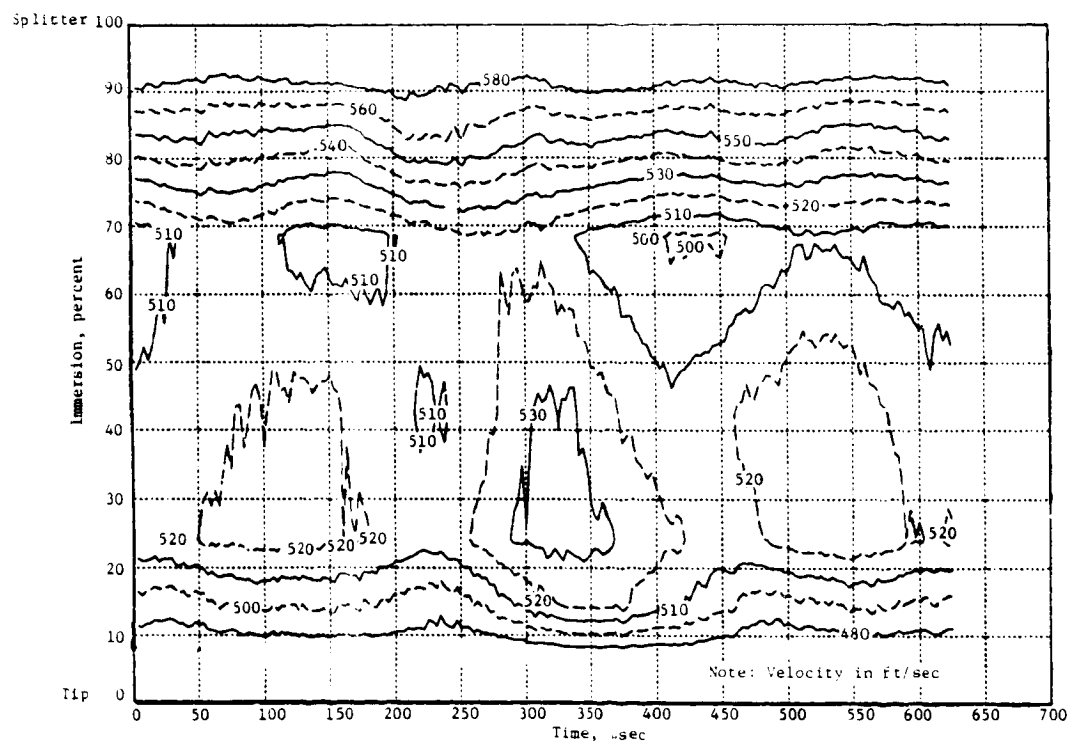


Figure 149. Exit Absolute Velocity Contour Plot, 65 Percent Speed Flutter.

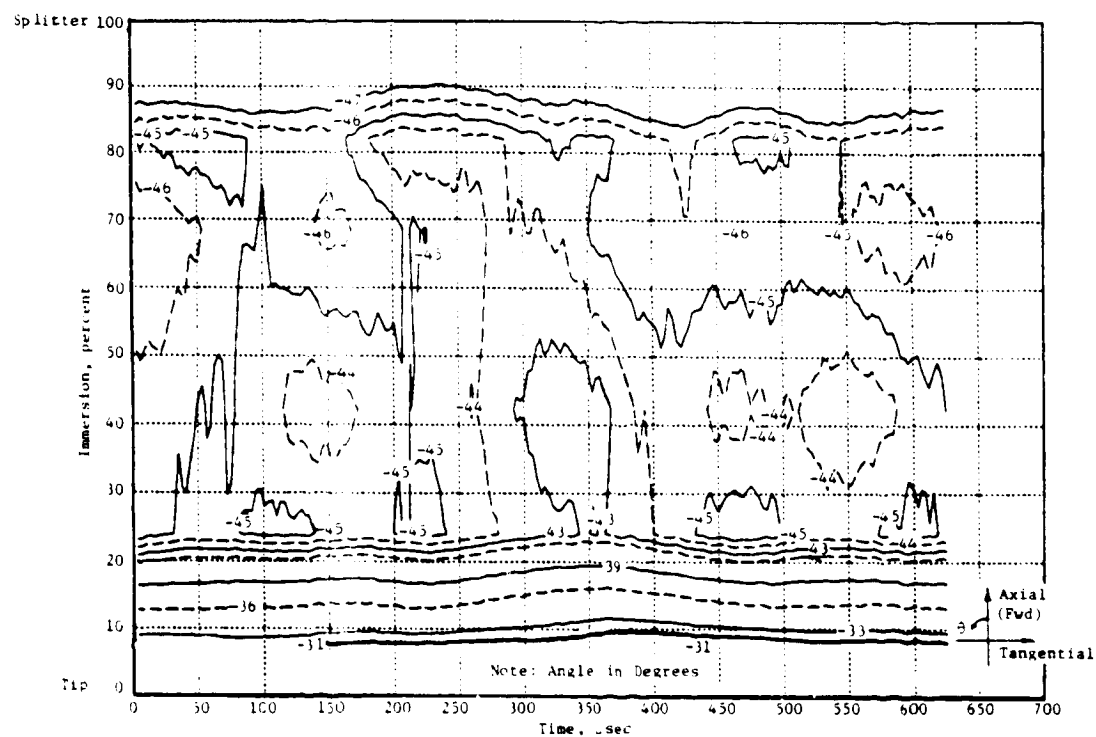


Figure 150. Exit Flow Angle Contour Plot, 65 Percent Speed Flutter.

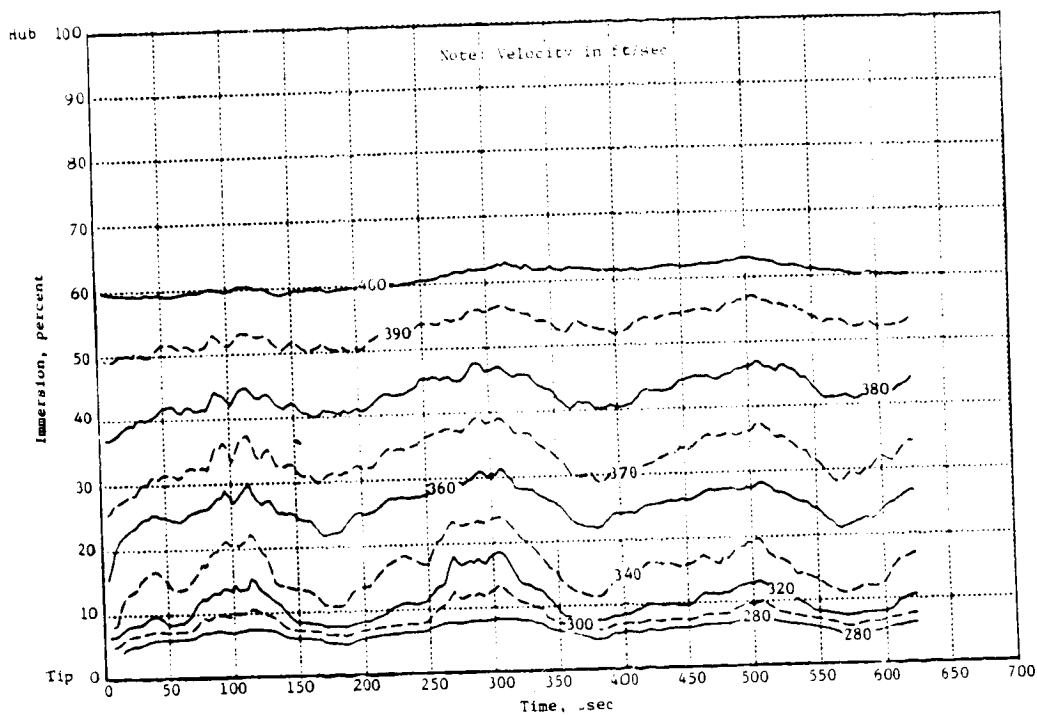


Figure 151. Inlet Absolute Velocity Contour Plot, 70 Percent Speed Flutter.

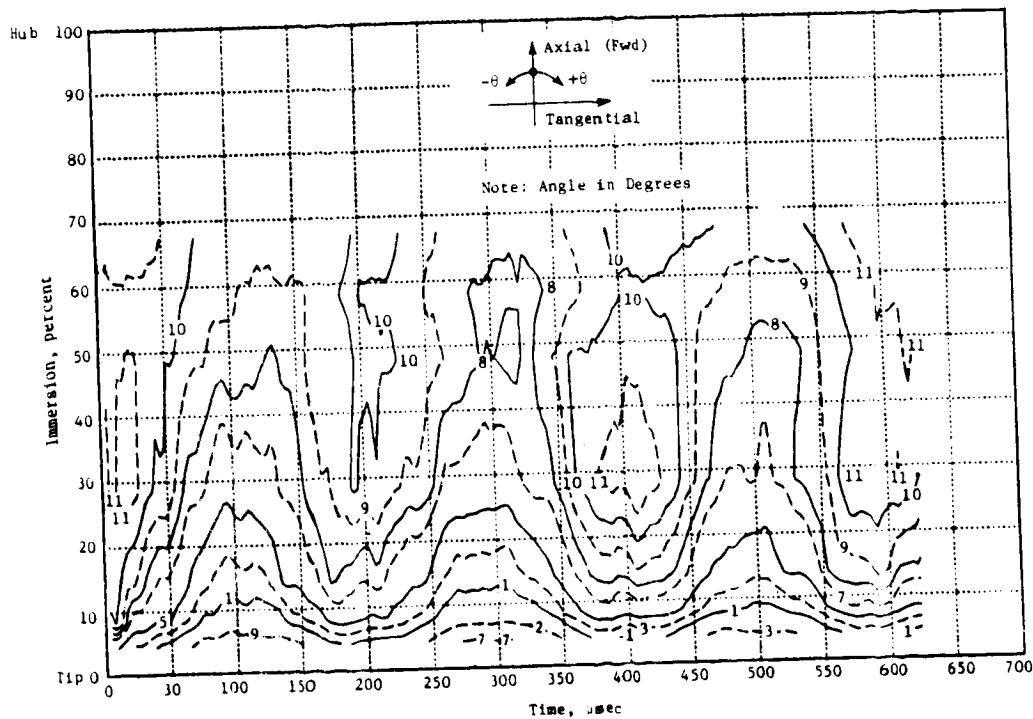


Figure 152. Inlet Flow Angle Contour Plot, 70 Percent Speed Flutter.

ORIGINAL OF PHOTOGRAPH

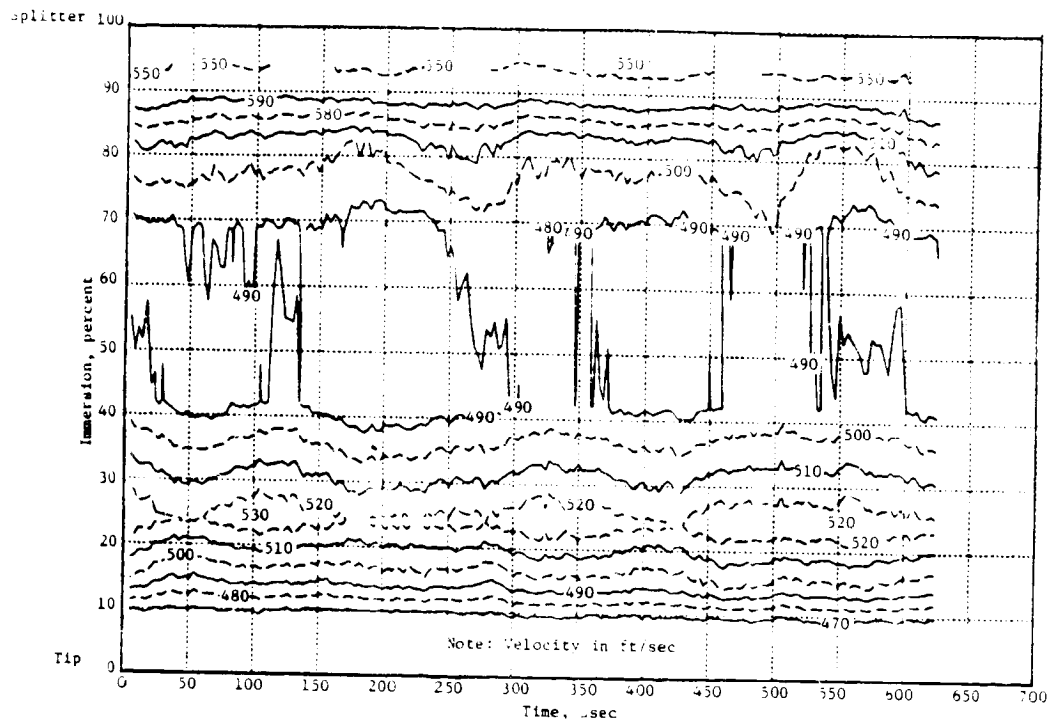


Figure 153. Exit Absolute Velocity Contour Plot, 70 Percent Speed Flutter.

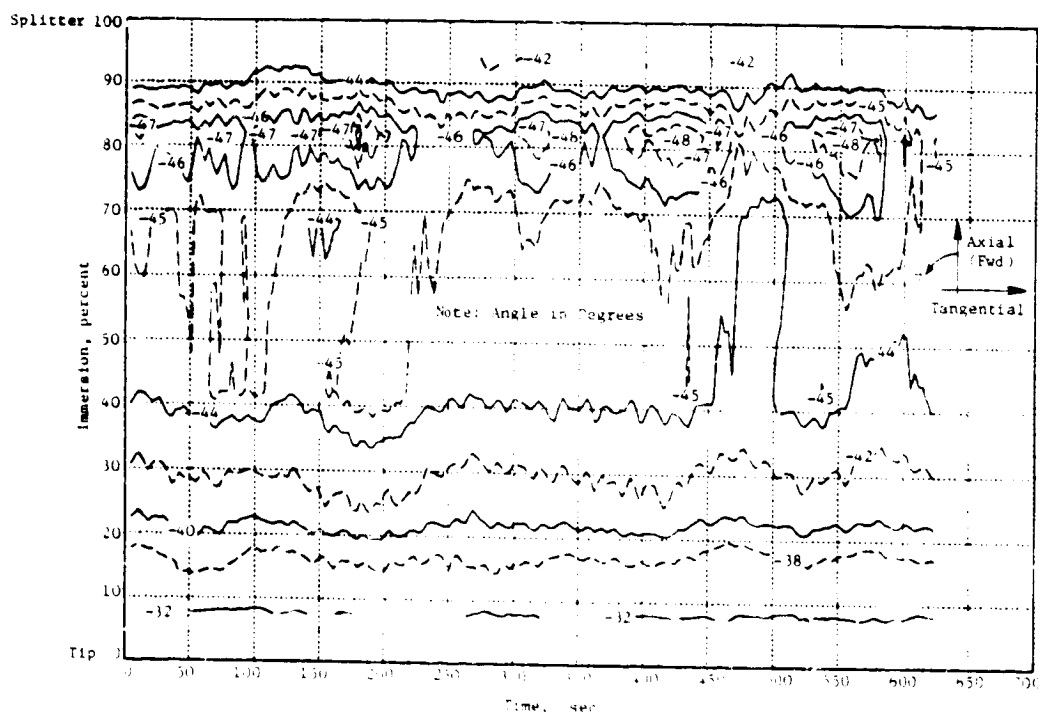


Figure 154. Exit Flow Angle Contour Plot, 70 Percent Speed Flutter.

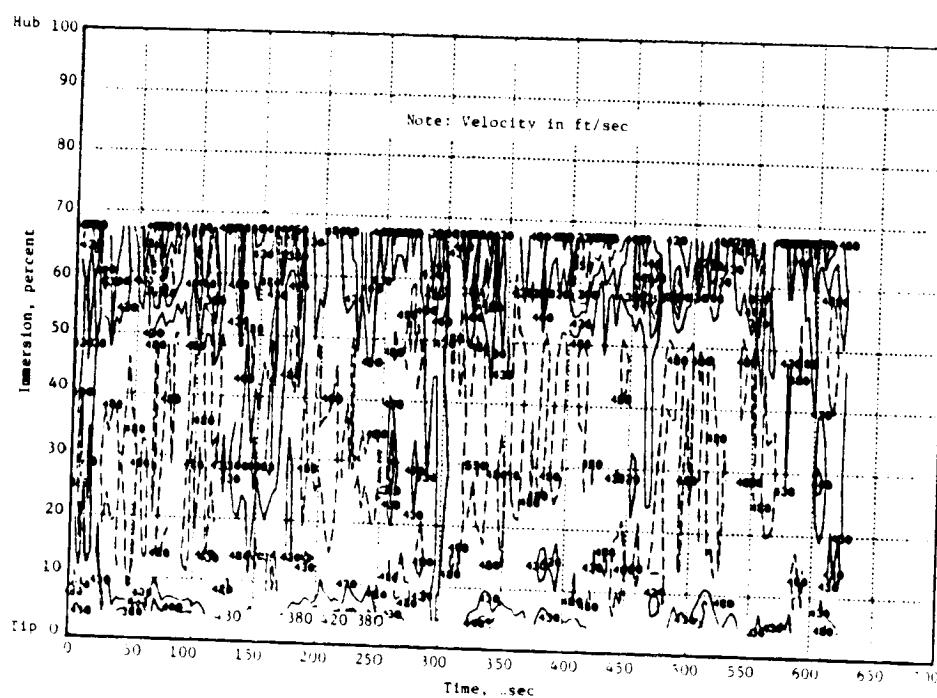


Figure 155. Inlet Absolute Velocity Contour Plot, 90 Percent Speed Flutter.

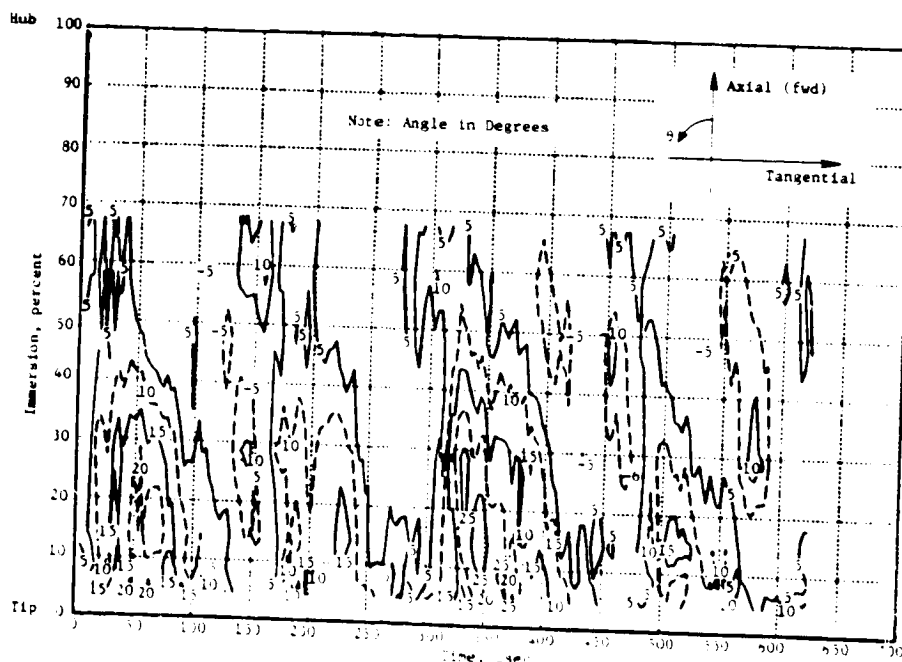


Figure 156. Inlet Flow Angle Contour Plot, 90 Percent Speed Flutter.

ORIGINAL PAGE IS
OF POOR QUALITY

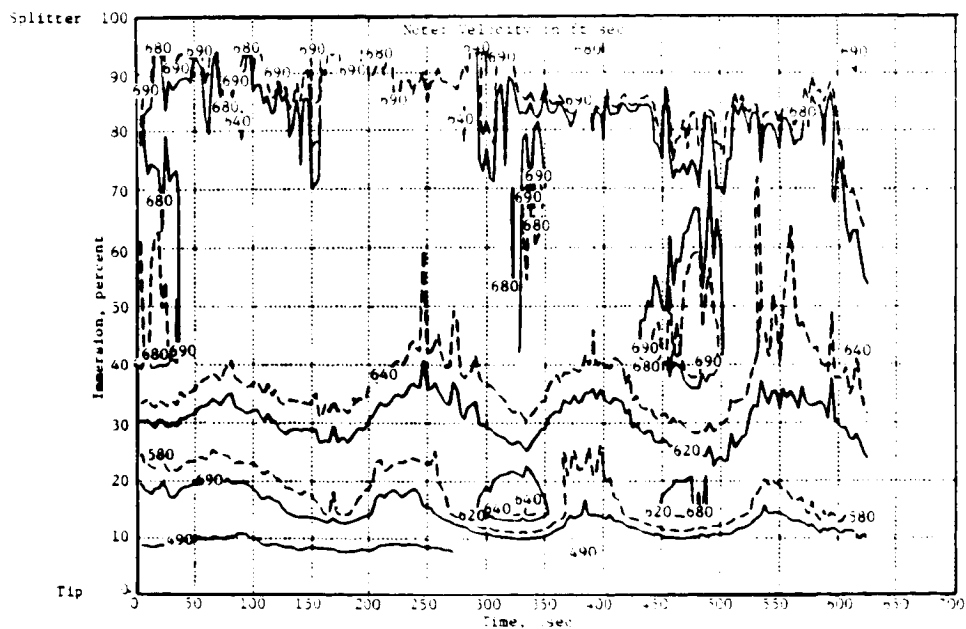


Figure 157. Exit Absolute Velocity Contour Plot, 90 Percent Speed Flutter.

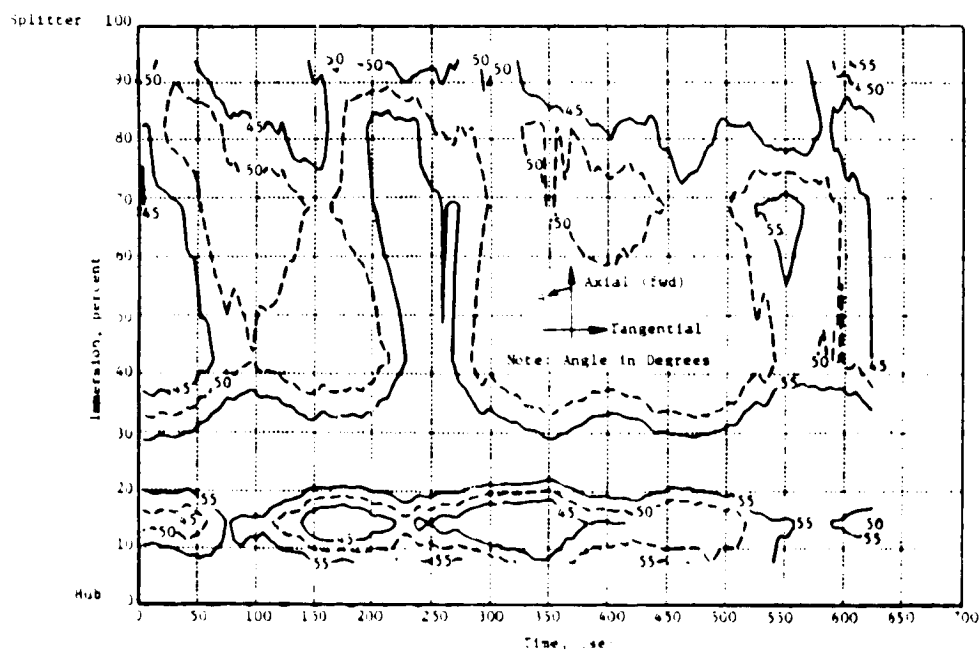


Figure 158. Exit Flow Angle Contour Plot, 90 Percent Speed Flutter.

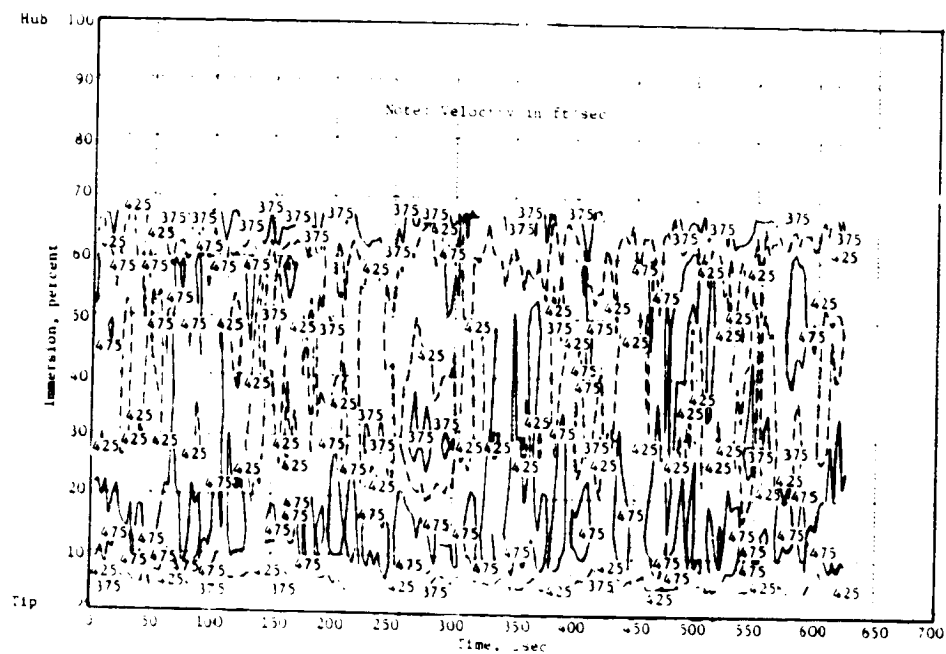


Figure 159. Inlet Absolute Velocity Contour Plot, 95 Percent Speed Flutter.

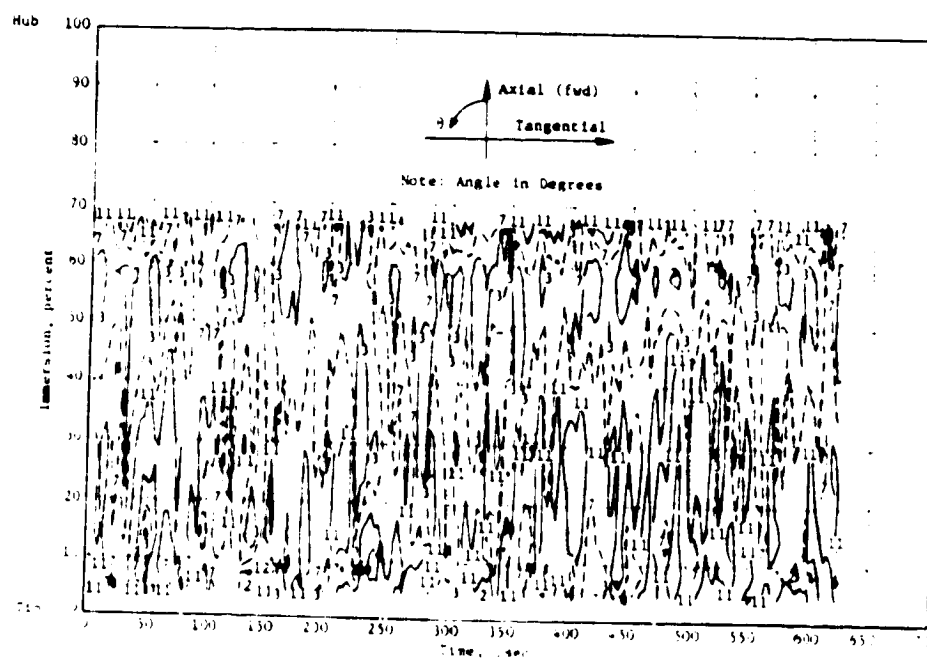


Figure 160. Inlet Flow Angle Contour Plot, 90 Percent Speed Flutter.

For the nonflutter conditions, reasonably good contour plots are provided in Appendix E for reference purposes.

6.7.3 Analysis of Unsteady Absolute Velocity

The aliased time history of the absolute flow velocity, along with that of the reference strain gage, were processed by the FFT/computer to obtain the linear and cross spectrum amplitudes, coherence, and relative phase for the selected intrablade points in the flowstream for each immersion. An example of the results of the spectral analyses of these aliased time histories are presented in Figure 161 for the 8.4 percent immersion, 70 percent speed flutter point. The spectral analysis results (the inlet absolute velocity amplitude and the phase relative to strain gage #828) for ten circumferential locations covering essentially one blade pitch are shown in Figures 162 and 163 respectively for the 70 percent speed flutter point. In Figure 162 a sudden drop in the unsteady inlet velocity between 14 and 8.4 percent immersion is seen on the pressure side of the blade leading edge (points 4, 5 and 6). This probably implies a significant effect of the viscous boundary on the unsteady inlet velocity due to blade flutter. The phase data in Figure 163 again indicate forward traveling wave type oscillations at 70 percent speed flutter as the casing Kulite data and total pressure data did earlier.

6.7.4 Traveling Wave Contents

The traveling wave contents in the unsteady velocity data are seen in the linear spectra selected at representative immersions and shown in Figures 164 through 169 for 70 percent speed flutter and in Figures 170 through 175 for 95 percent speed flutter. In general, forward traveling waves show up consistently in the inlet and exit velocity data as they did in the unsteady casing Kulite data and in the unsteady total pressure data. For 70 percent speed flutter, higher harmonic components of the dominant traveling waves appear in both inlet and exit unsteady velocity data although there are more of the higher harmonic components in the inlet traverse plane than in the exit traverse plane. At the 95 percent speed flutter condition, higher harmonic components appear in the inlet traverse plane but not in the exit traverse plane.

6.8 BLADE WORK PER MODE

The aerodynamic damping was calculated, as indicated in Section 5.8, for the 70 and 95 percent speed flutter points. The forward traveling wave nodal diameter patterns considered were those shown to be predominant in the casing Kulite data of Section 6.5.3: $n = 3$ through 7 for 70 percent speed torsional flutter, and $n = 2$ through 5 for 95 percent speed flexural flutter.

The results of these calculations are presented in Tables XXIII and XXIV in terms of the log decrement, δ_{aero} , negative values of which indicate

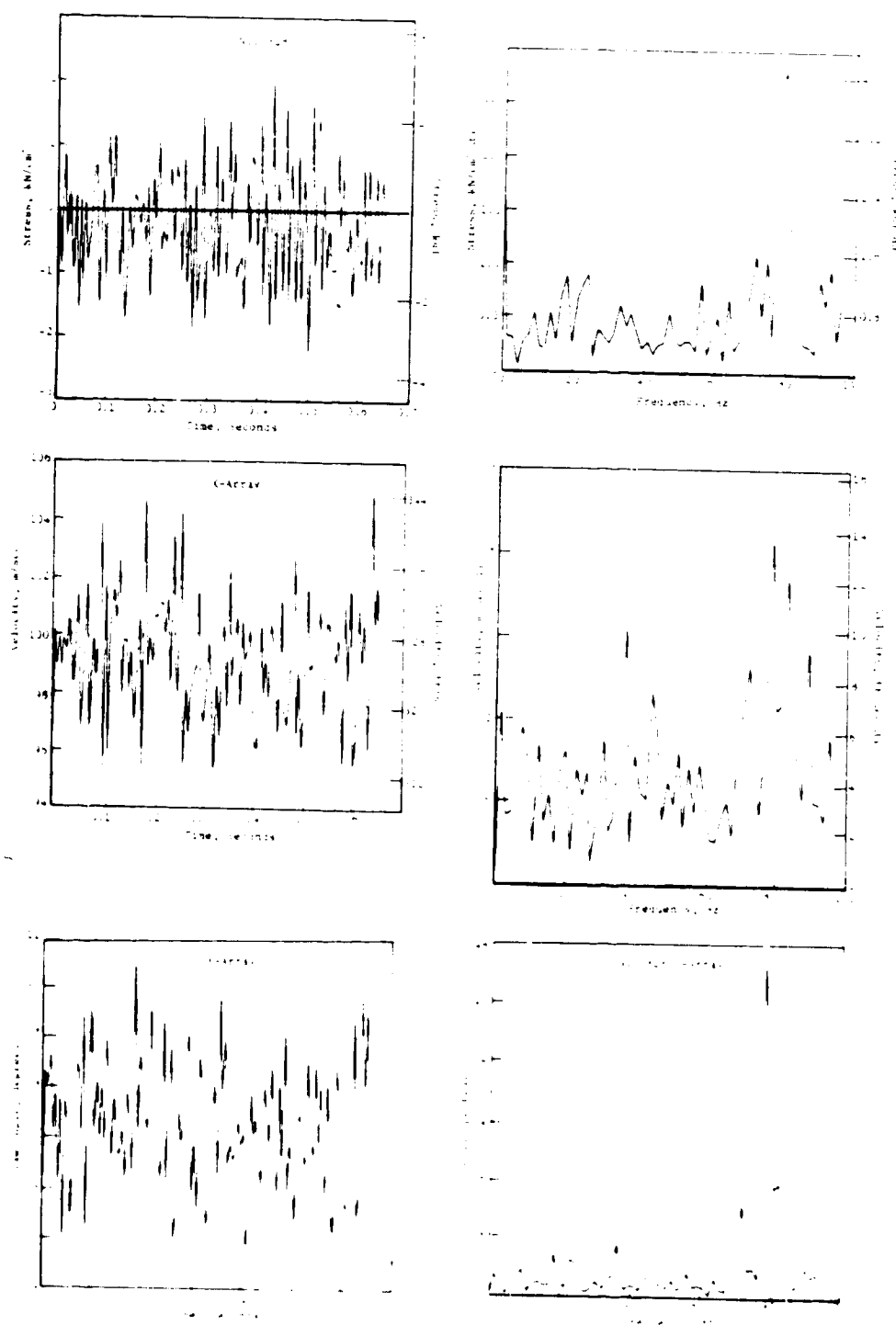


Figure 161. Inlet X-Array Aliased Spectral Analysis
(8.4% Immersion), 70% Speed Flutter.

ORIGINAL
OF POOR QUALITY

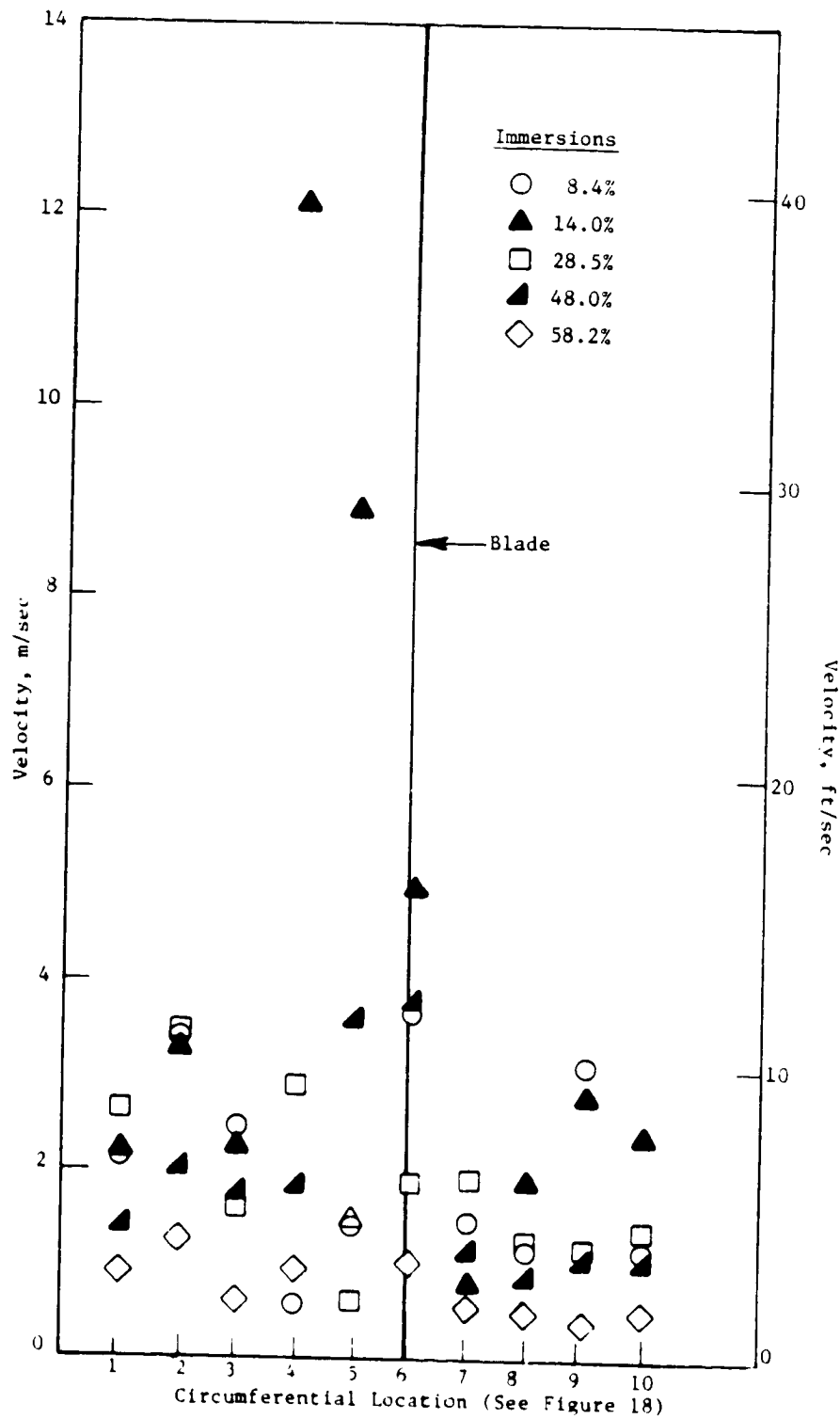


Figure 162. Circumferential Variation of Unsteady Inlet Velocity, 70 Percent Speed Flutter.

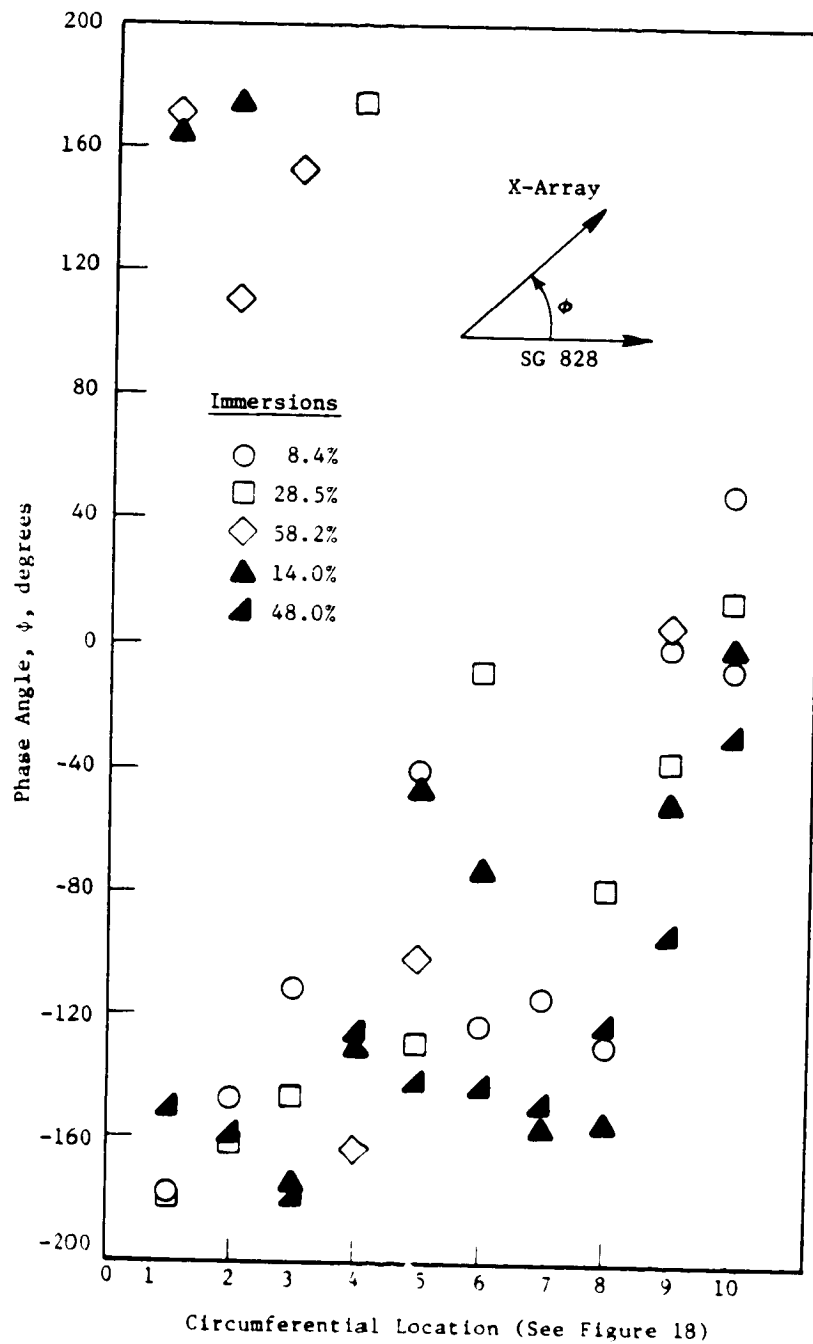


Figure 163. Circumferential Phase Variation of Unsteady Inlet Velocity, 70 Percent Speed Flutter.

ORIGINAL
OF POOR QUALITY

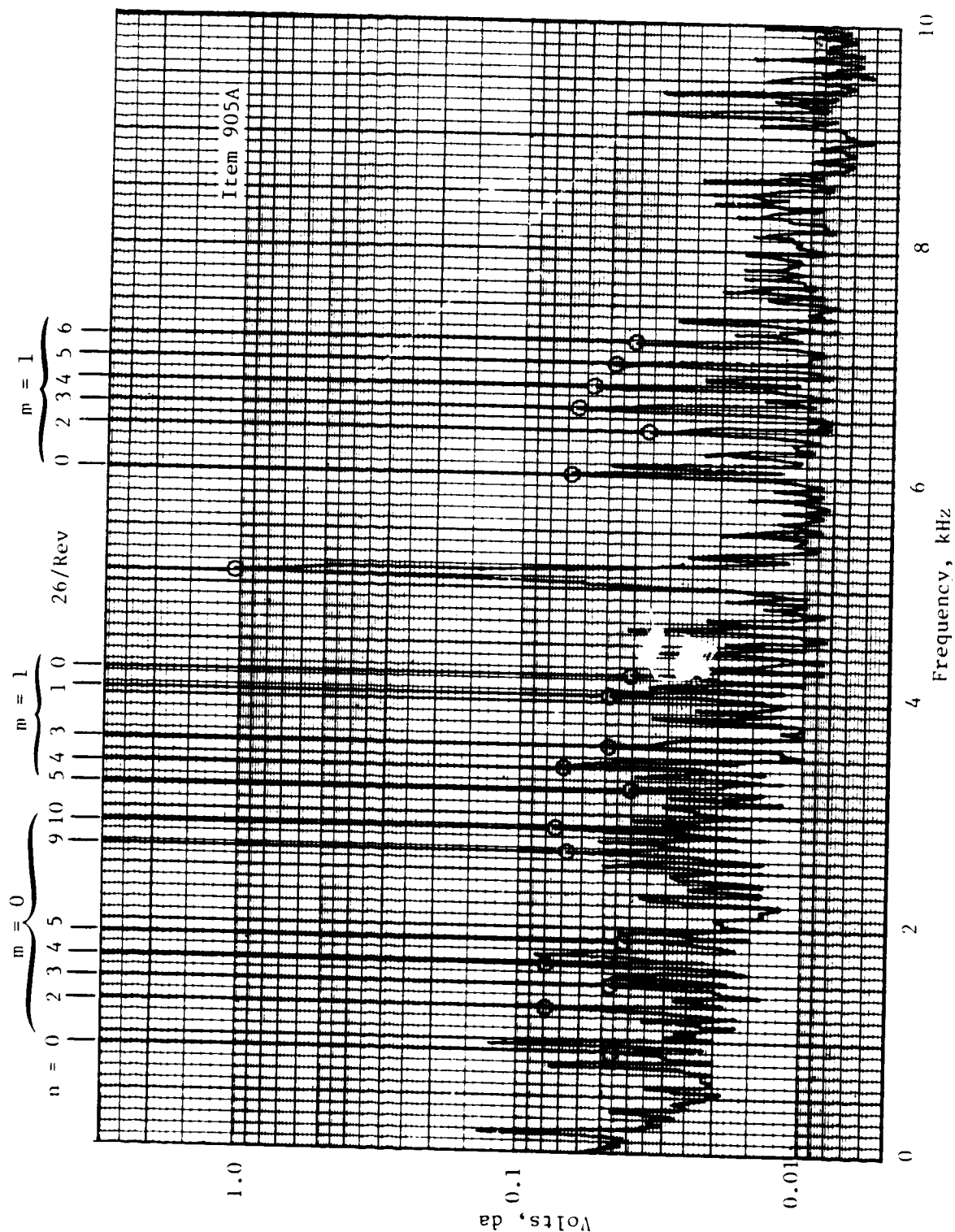


Figure 164. Inlet Velocity Spectrum, 8.4 Percent Immersion, 70 Percent Speed Flutter.

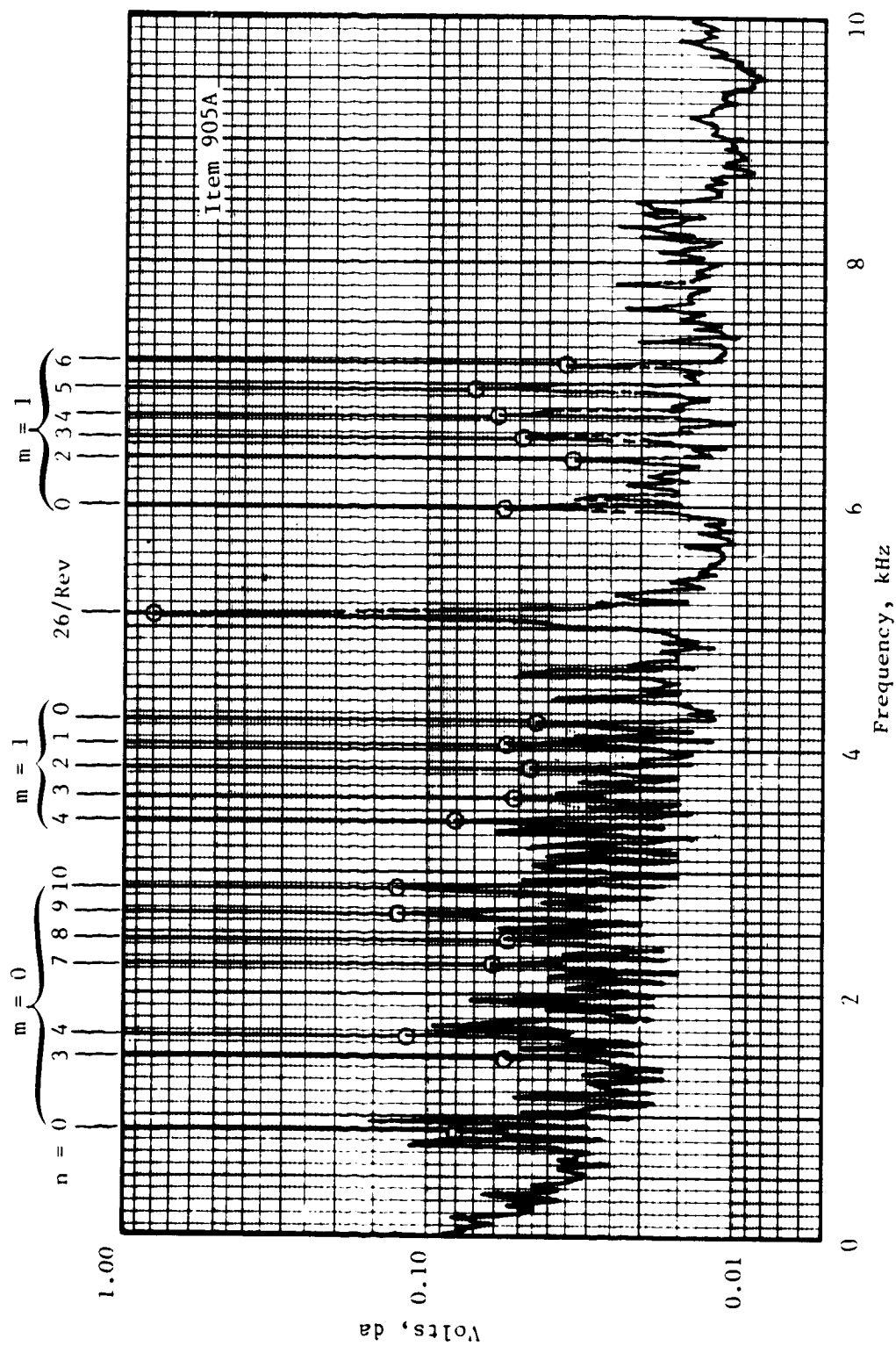


Figure 165. Inlet Velocity Spectrum, 28.5 Percent Immersion, 70 Percent Speed Flutter

ORIGINAL
OF POOR QUALITY

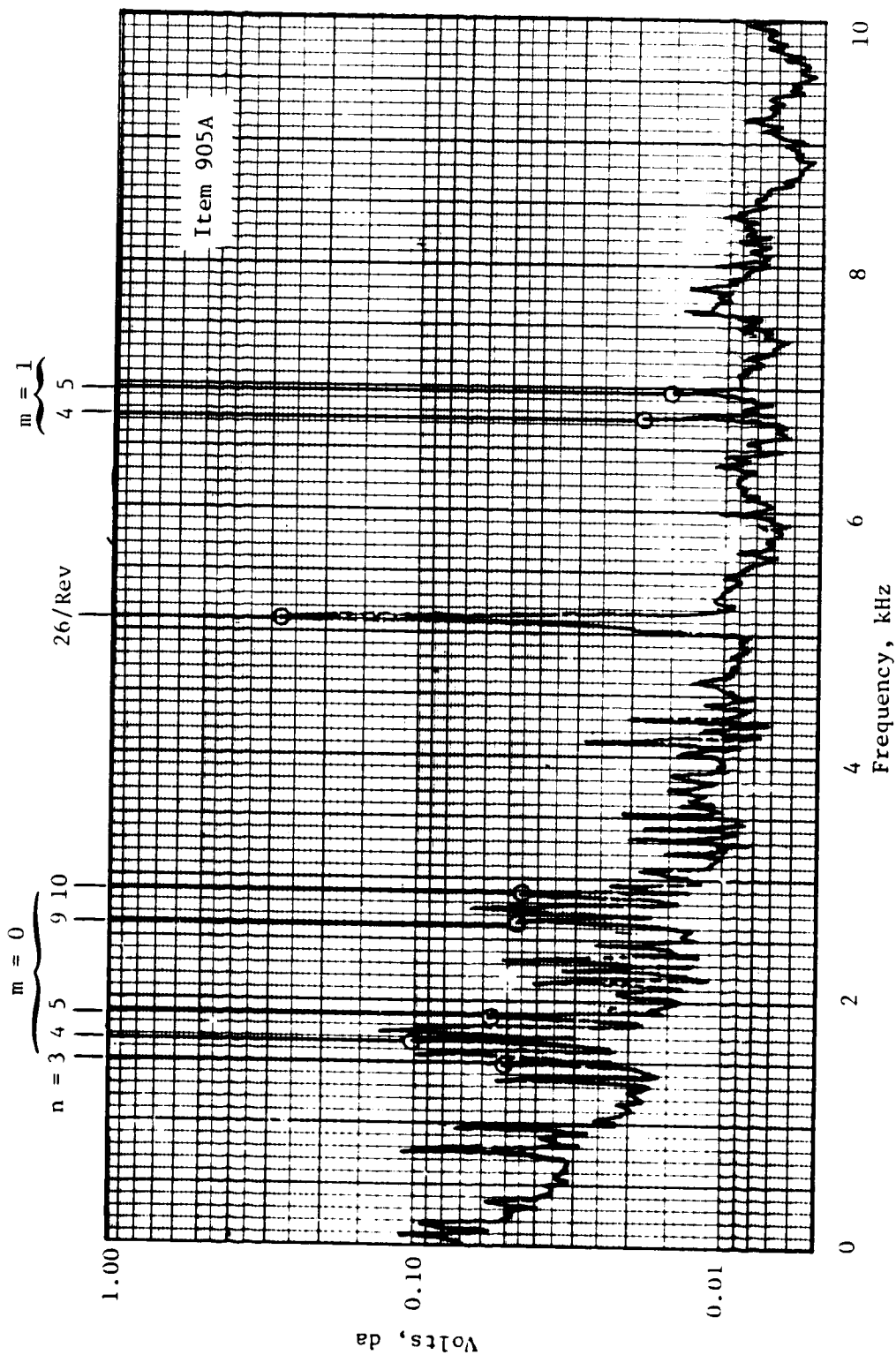


Figure 166. Inlet Velocity Spectrum, 58.2 Percent Immersion, 70 Percent Speed Flutter.

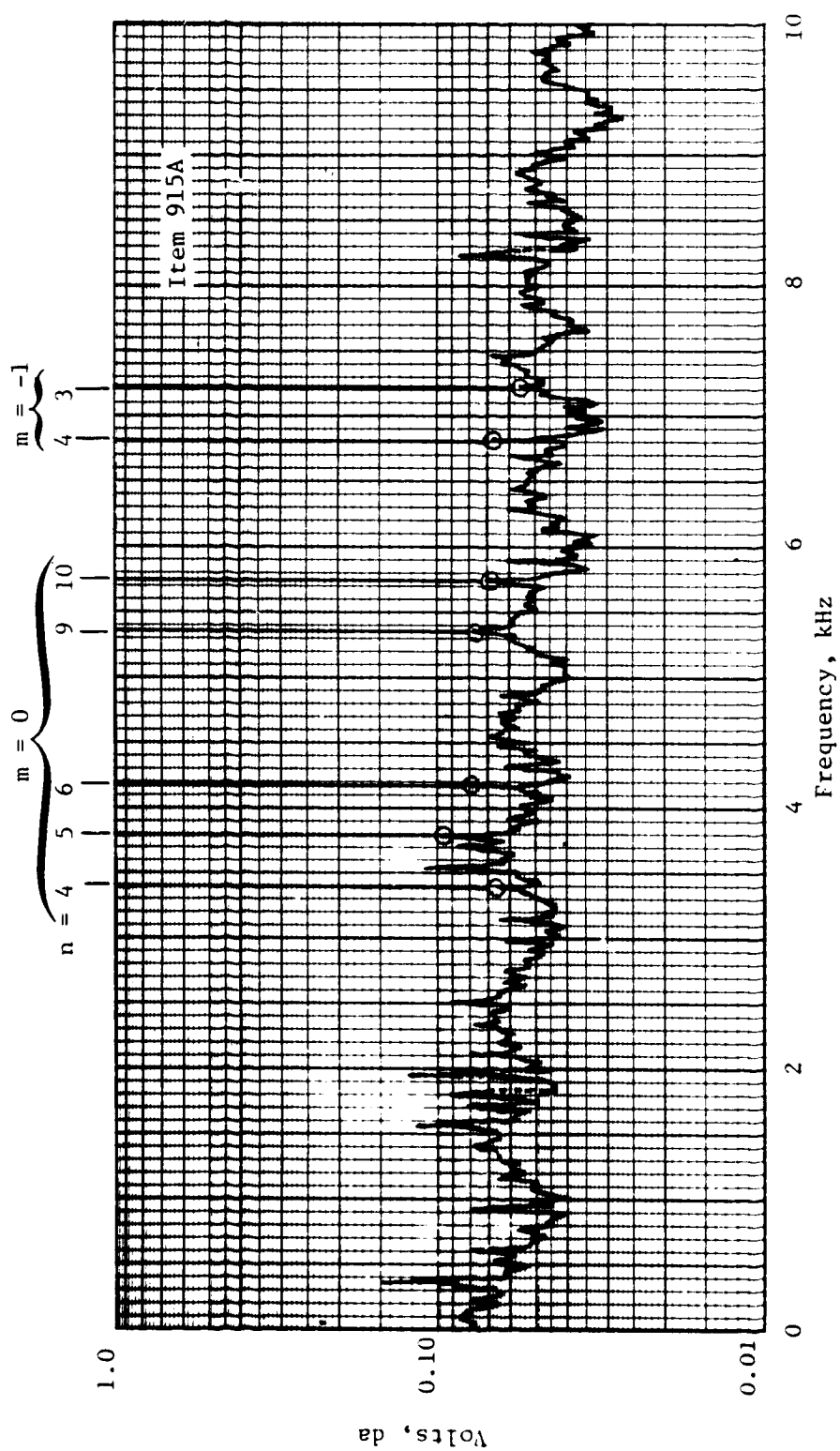


Figure 167. Exit Velocity Spectrum, 14.5 Percent Immersion, 70 Percent Speed Flutter.

ORIGINAL
OF POOR QUALITY

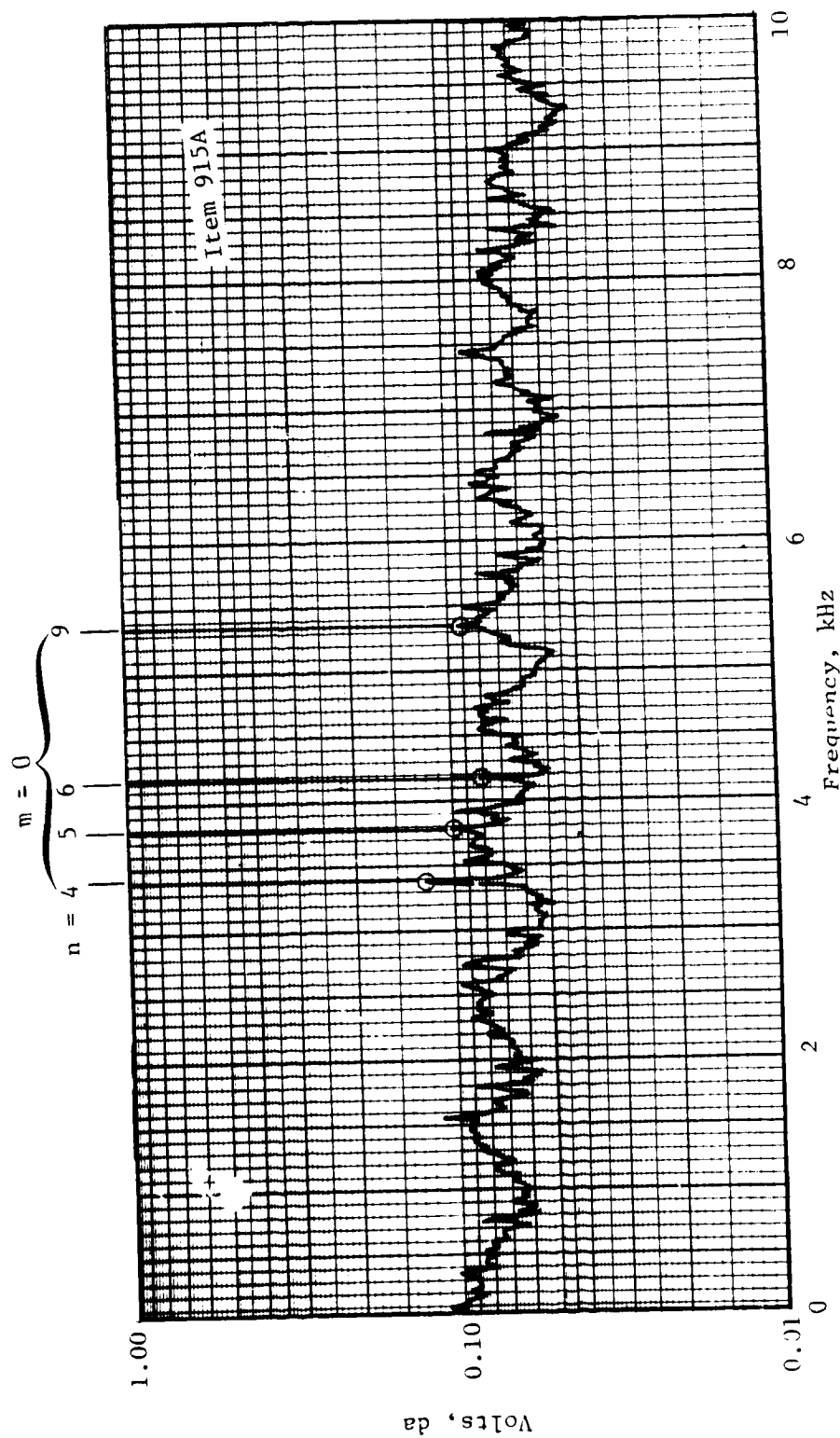


Figure 168. Exit Velocity Spectrum, 42.2 Percent Immersion, 70 Percent Speed Flutter.

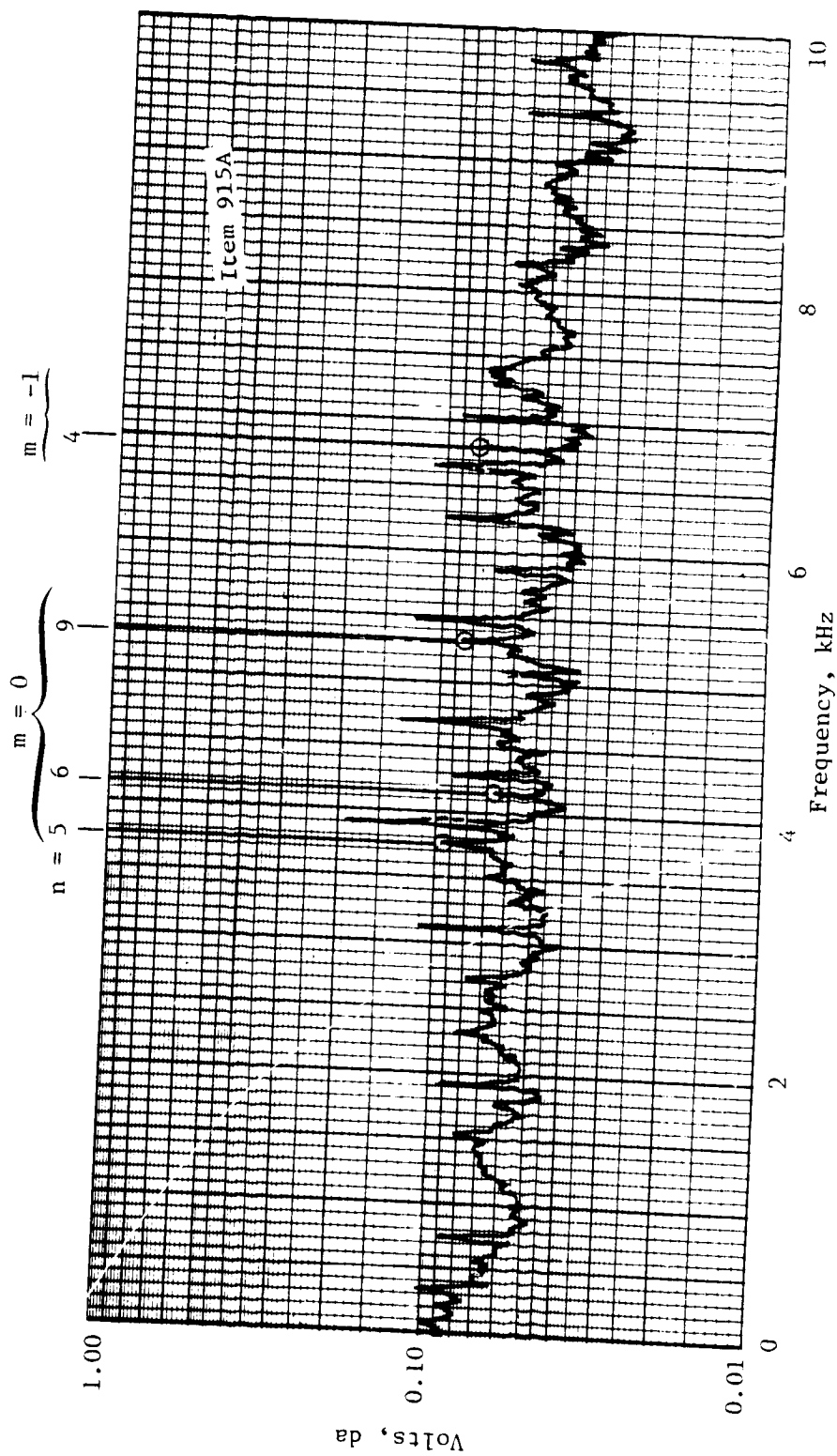


Figure 169. Exit Velocity Spectrum, 82 Percent Immersion, 70 Percent Speed Flutter.

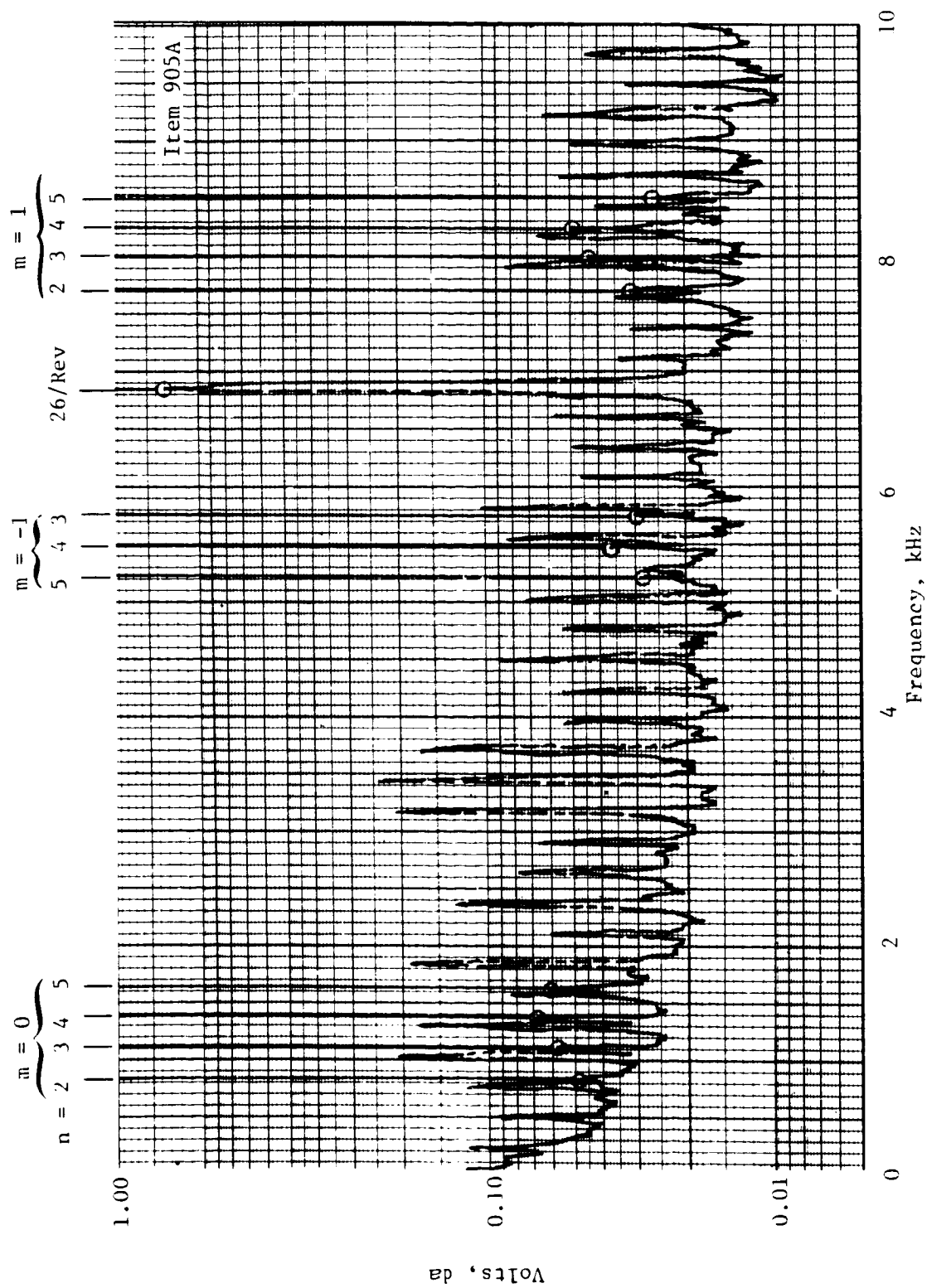


Figure 170. Inlet Velocity Spectrum, 8.4 Percent Immersion, 95 Percent Speed Flutter.

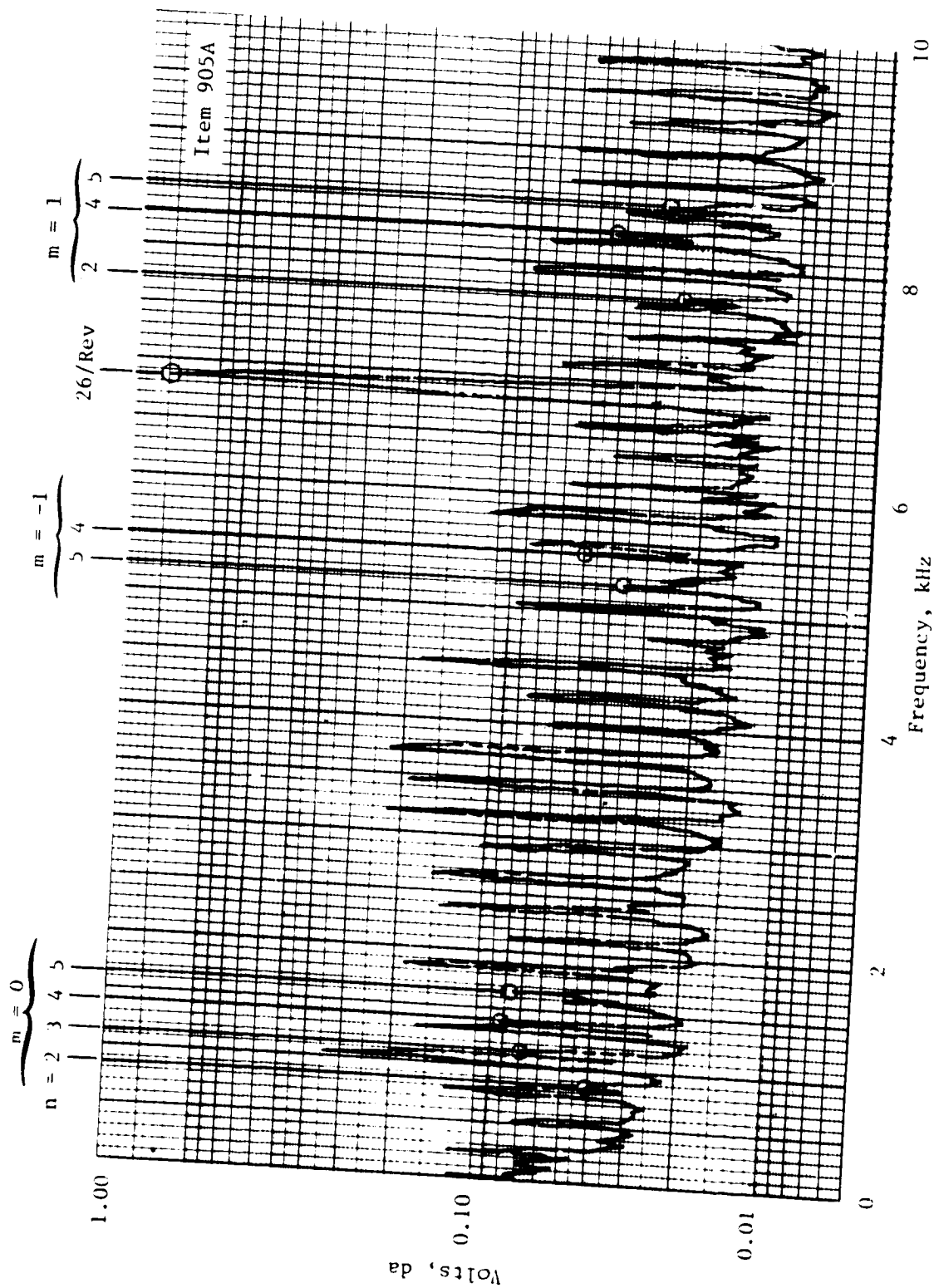


Figure 171. Inlet Velocity Spectrum, 28.5 Percent Immersion, 95 Percent Speed Flutter.

ORIGINAL
OF POOR QUALITY

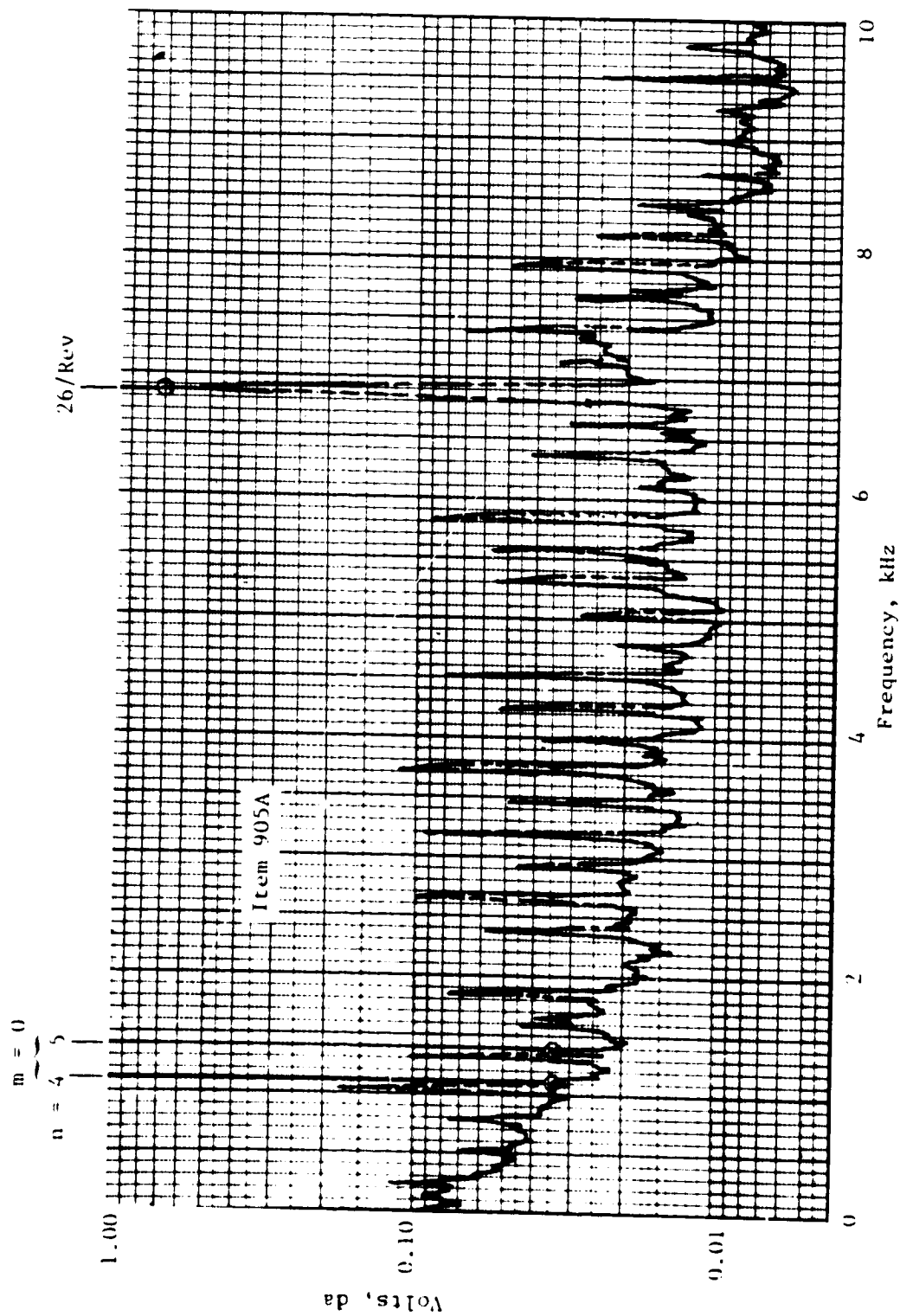


Figure 172. Inlet Velocity Spectrum, 58.2 Percent Immersion, 95 Percent Speed Flutter.

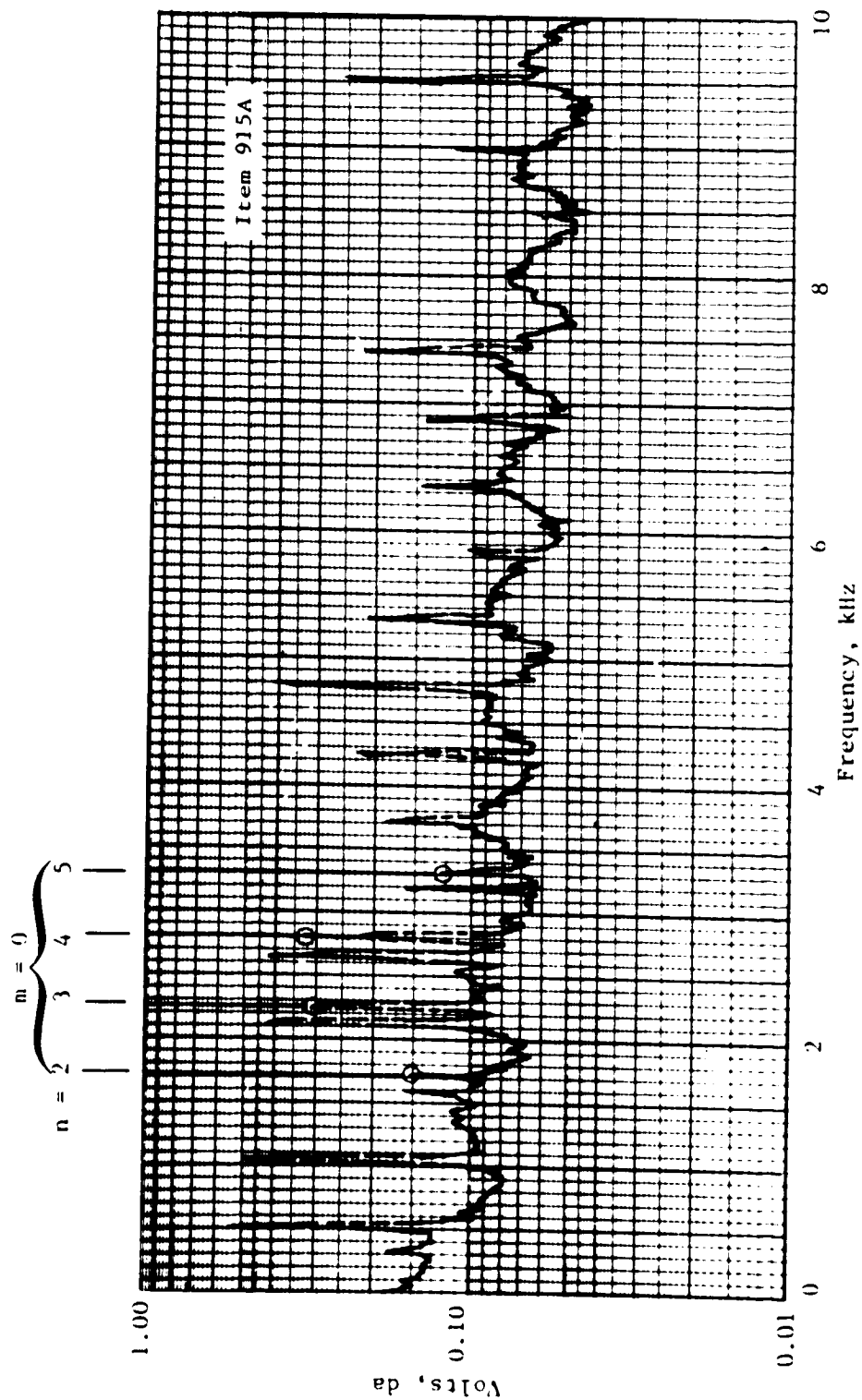


Figure 173. Exit Velocity Spectrum, 14.5 Percent Immersion, 95 Percent Speed Flutter.

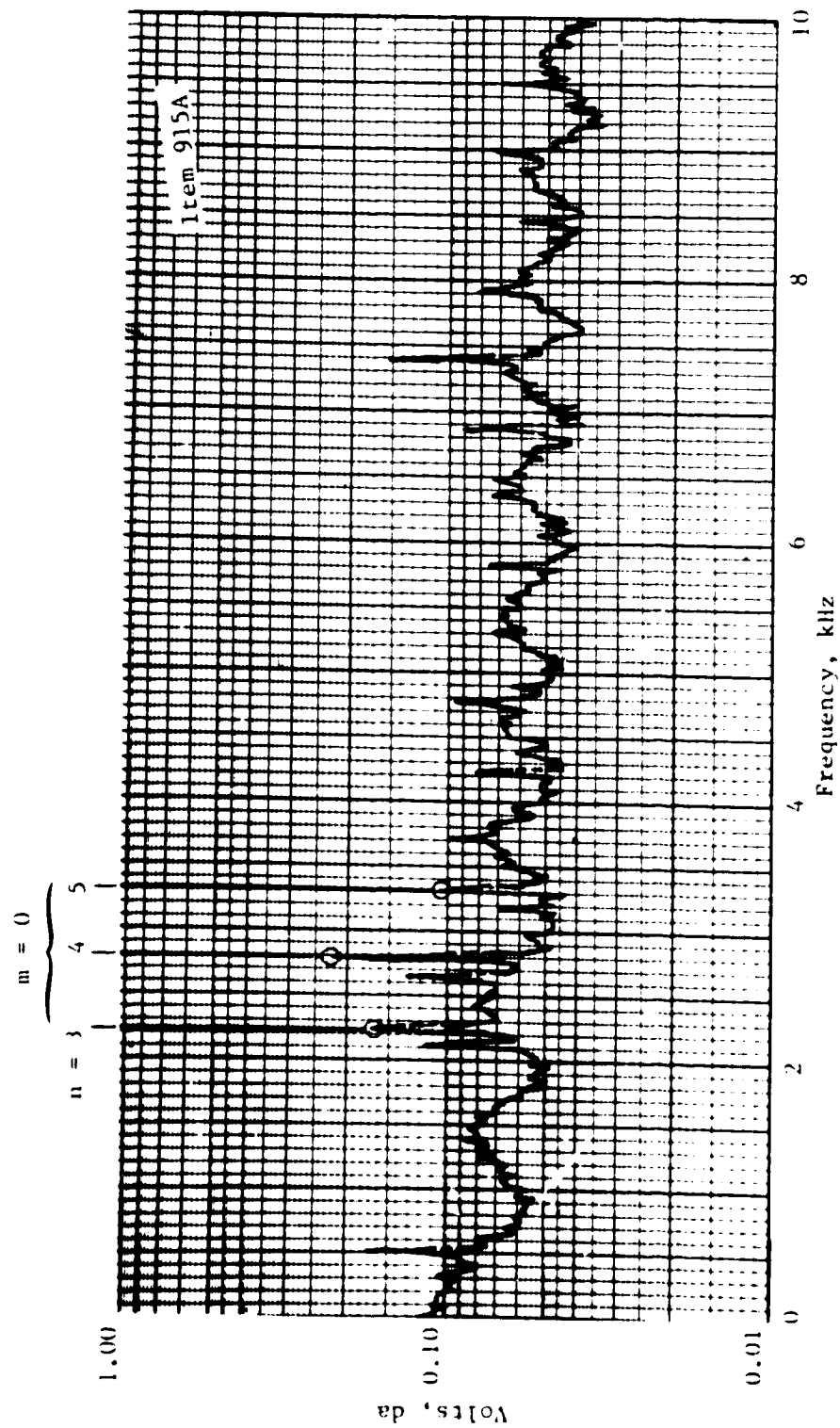


Figure 174. Exit Velocity Spectrum, 42.2 Percent Immersion, 95 Percent Speed Flutter.

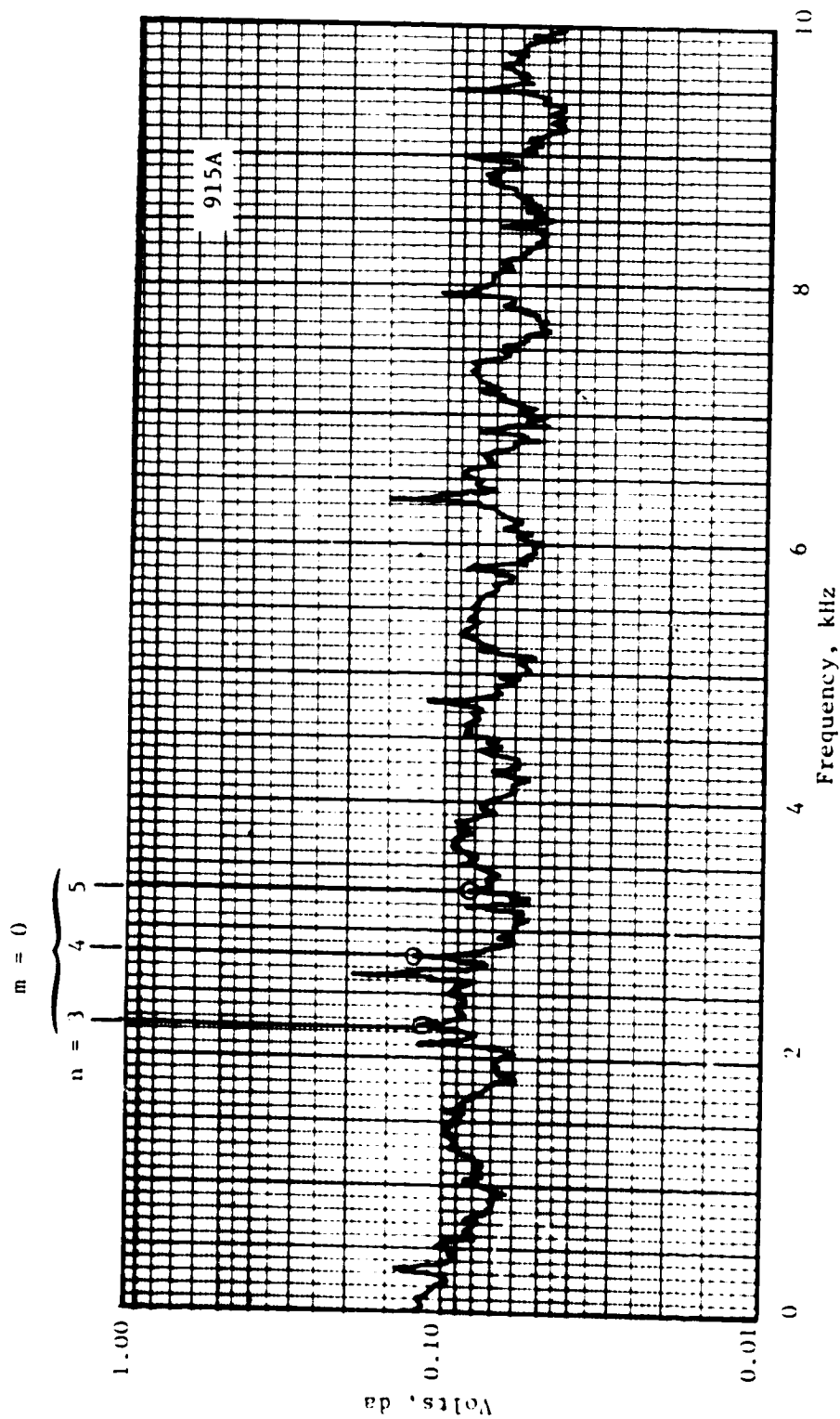


Figure 175. Exit Velocity Spectrum, 82 Percent Immersion, 95 Percent Speed Flutter.

ORIGINAL
OF POOR QUALITY

Table XXIII. Damping Data at 70 Percent Speed Torsional Flutter.

		Model Diameter	δ_{aero}	Pressure and phasing data used in calculations.																													
Kulite	Z Chord	n = 3																n = 4				n = 5				n = 6				n = 7			
		Pressure		Suction		Pressure		Suction		Pressure		Suction		Pressure		Suction		Pressure		Suction		Pressure		Suction		Pressure		Suction					
		p	ϕ	p	ϕ	p	ϕ	p	ϕ	p	ϕ	p	ϕ	p	ϕ	p	ϕ	p	ϕ	p	ϕ	p	ϕ	p	ϕ	p	ϕ	p	ϕ				
702	-13.1*	0.39	229	0.43	62	0.50	56	0.53	262	0.45	289	0.37	128	0.41	92	0.25	186	0.38	239	0.22	75												
704	22.9	0.64	54	0.47	20	1.00	239	0.50	241	0.64	115	0.55	125	0.50	340	0.56	59	0.39	337	0.64	302												
706	49.3	0.29	225	0.40	262	0.31	251	0.31	42	0.26	284	0.47	298	0.34	118	0.36	129	0.50	211	0.43	340												
708	74.7	0.33	276	0.33	277	0.50	91	0.49	101	0.43	323	0.40	332	0.33	148	0.31	149	0.39	347	0.47	353												
710	94.6	0.30	271	0.28	280	0.64	106	0.55	114	0.47	347	0.43	350	0.38	157	0.34	151	0.52	356	0.48	3												

Note: p = Pressure, normalized to 1.78 N/cm² (2.58 psi)

ϕ = Phase angle relative to S/C 828, degrees; positive ϕ means Kulite leads S/C

*CX 702 is forward of blade

Table XXIV. Damping Data at 95 Percent Speed Flexural Flutter.

		Nodal Diameter		δ_{aero}	
		2		+0.024	
		3		-0.047	
		4		+0.026	
		5		+0.022	

Pressure and phasing data used in calculations.																	
Kulite	Z Chord	n = 2				n = 3				n = 4				n = 5			
		Pressure		Suction		Pressure		Suction		Pressure		Suction		Pressure		Suction	
		P	ϕ	P	ϕ	P	ϕ	P	ϕ	P	ϕ	P	ϕ	P	ϕ	P	ϕ
702	-11.8*	0.60	303	0.57	158	0.93	176	0.91	39	0.99	45	1.00	288	0.54	326	0.52	206
704	20.6	0.43	158	0.16	94	0.57	29	0.14	291	0.53	283	0.17	141	0.30	200	0.13	30
706	44.0	0.36	271	0.31	106	0.45	129	0.47	306	0.41	336	0.39	173	0.25	238	0.26	90
708	65.8	0.13	217	0.23	174	0.12	50	0.24	22	0.18	232	0.25	243	0.15	139	0.15	149
712	103.5	0.20	181	0.14	159	0.26	23	0.24	358	0.25	236	0.23	213	0.17	144	0.15	123

Note: p = pressure, normalized to 2.41 N/cm^2 (3.50 psi)

ϕ = phase angle relative to S/G 822, degrees; positive ϕ means Kulite leads S/G

*CK 702 is forward of blade

instability. For 70 percent speed torsional flutter, Table XXIII, the fourth and sixth nodal diameters are seen to be unstable, the fifth nodal diameter is marginally stable, and the third and seventh are stable. For 95 percent speed flexural flutter, Table XXIV, the third nodal diameter is shown to be unstable while the others ($n = 2, 4, \text{ and } 5$) are stable. Also shown in Tables XXIII and XXIV are the blade tip pressure and suction surface pressure and phase data from the casing Kulites.

These results agree with the phase data obtained from the strain gage and light probe sensors as shown in Figures 66 and 67. However, the torsional flutter phase plot, Figure 66, does not indicate the sixth nodal diameter to be the principal flutter mode as does Table XXIII. These results also suggest that mistuning may serve to couple more than one nodal diameter mode in flutter, at least in torsional flutter. Since no effort was made to systematically arrange the blades in the rotor, this fan had 2 percent random mistuning as can be seen in Figure 31. The strain gage response showed the high response region for torsional flutter to be circumferentially different from that for flexural flutter, with no correlation to high or low frequency blades.

The presence of multiple nodal diameters in the instability suggests that a practical flutter prediction analysis should have the capability to consider multiple spatial harmonics.

7.0 SUMMARY, CONCLUSIONS, AND RECOMMENDATIONS

7.1 SUMMARY

The purpose of this program was to obtain detailed quantitative measurements of both the steady and unsteady flowfields surrounding the rotor, and to determine the mechanical state of the rotor while it was operating in both the steady and flutter modes.

The measured data needed to calculate the overall fan performance and blade element data were successfully obtained from both the fixed and the traversable instrumentation. Comparing the scale model rotor performance with that of the full scale fan verified that similar performance characteristics were achieved. The scale model rotor exhibited the same type of rotating stall and stall flutter as Fan C at similar aerodynamic conditions.

The vibratory response of the fan blades was obtained from strain gage signals in terms of stress amplitude, frequency, and interblade phase angle. Each rotor blade was instrumented with one strain gage located so it would respond to the blade's first three vibratory modes.

The strain gage data showed that there was virtually no separated flow vibration on this fan even at conditions near the flutter boundary. At the flutter boundary, there was a sharp increase in blade stress, with some blades responding at their established fatigue limits. A large variation in the blade stresses around the rotor was observed, by a factor of 8 in flexure and over 3 in torsion, with different maximum stress regions on the rotor depending upon whether the flutter mode was flexure or torsion. Also, aerodynamic coupling forced all the blades to respond at the same flutter frequency, which was the same as the blade's natural frequency. At flutter, the strain gage based interblade phase angles showed that while there may be more than one traveling wave present, they are all forward traveling waves: $n = 2$ or 3 in flexural flutter and $n = 4$ or 6 in torsional flutter. Moreover, the interblade phase angles were found to be constant in time.

The primary objective of the blade deformation measurements made during this program was to obtain the steady and unsteady tangential deflections of each blade of the test stage while it operated at the onset of instability and while it was in instability. These measurements were used to determine the changes in blade stagger (untwist) and camber (chordwise bending) and to determine the vibratory interblade phase angles. These measurements were successfully made with casing-mounted light probes. Axial deformation measurements were also desired, but were not obtained due to light probe misalignment.

The measured blade tip steady deflections agreed well with predictions. However, at the two spanwise locations the measured deflections showed only fair qualitative agreement with predictions due to reflectivity problems. The data showed that the steady untwist increased about 2° as the rotor speed was

increased from 65 to 95 percent of design. At all speeds, the untwist increased as the fan was throttled to the flutter boundary as would be expected with the increased loading. As calculated from the measured data, the chordwise bending was shown to be largest at the flutter boundary, being greatest at the torsional flutter boundary. The measured unsteady deflections showed a circumferential variation in the blade deflections similar to that of the strain gage data, with the maximum deflection occurring at about the same point on the rotor as the maximum stress. The light probe based interblade phase angles also agreed well with those from the strain gages by also indicating the existence of forward traveling waves of different nodal diameters: $n = 2$ or 3 in flexural flutter and $n = 4$ or 6 in torsional flutter.

Quantitative and qualitative measurements of the flowfield within a blade passage were made with two kinds of blade-mounted sensors: Kulites and hot-film sensors. Operational problems were encountered with both sensors: the mounting technique for the Kulites, the temperature compensation for the hot-films, and the induced strain sensitivity for both. A new installation technique was developed for blade-mounted Kulite sensors which successfully reduced their sensitivity to mechanical strain. The limited qualitative data obtained from the blade-mounted Kulites showed the front portion of the blade to be more highly loaded than the aft portion.

Casing-mounted Kulites were successfully used to investigate the shock structure within the blade passage. The casing-mounted Kulite data provided the circumferential variation of the unsteady component of the static pressure, contour plots of the total static pressure distribution over the rotor blade tips, unsteady pressure relative amplitude and phasing, analysis of the traveling wave content present during flutter, and the unsteady pressure information on each side of the blade for the blade work/mode/cycle calculations.

Static pressure distributions at the blade tip indicated that the pressure contours were well defined only through the forward half of the blade passage. Similarly, the pressure gradients associated with the presence of the blade were well defined only in the leading edge region. The location of the leading edge bow shock in the blade passage was accurately defined and its forward movement in the blade passage was observed as the rotor was throttled toward the stall flutter boundary. Analysis also showed that the flutter related unsteady pressure amplitude did not repeat itself from blade passage to blade passage. Linear spectra of the casing Kulite data showed the flutter signals to be composed of several forward traveling waves and their harmonics. The amplitudes of these traveling wave components increase as a function of chordwise position from the blade leading edge, peaking at about 75 percent chord in torsional flutter and at about 45 percent chord in flexural flutter. The traveling wave information was used to generate the total unsteady pressure signal that would be perceived in the rotating reference system. Strong variations in the unsteady pressure magnitude were shown over an equivalent blade passage in both the circumferential and the axial directions. The corresponding absolute phase angle data show a significant phase shift (about 180°) over the front portion of the blade.

Traversable probes were successfully used to measure the radial distributions of the free stream total pressure at the rotor's exit plane and of the two-dimensional flowfield data (absolute flow velocity and flow angle) forward and aft of the rotor. The data from these probes was used to obtain ensemble average time histories, circumferentially averaged radial distributions, contour plots of the radial distributions, circumferential amplitude variation and phasing relative to a reference strain gage, and traveling wave content.

The radial distribution of the exit total pressure showed that the flow near the casing always had the largest total pressure due to fan compression and that the total pressure increases at all immersions when the fan was throttled to the flutter boundary. The exit total pressure contour plots showed the blade wakes and areas of boundary layer buildup near the outer wall and at the splitter when the rotor was in torsional flutter. At the flexural flutter points and at the non-flutter points there was little or no evidence of the blade wakes. At the 70 percent speed flutter point, the unsteady pressure decreased as the blade approached the probe. Radially, the unsteady pressure was higher at the outer portion of the blade passage. Linear spectra of the unsteady exit total pressure showed evidence of forward traveling waves only near the outer wall.

The measured inlet and exit absolute flow velocity and flow angle data agreed reasonably well with theoretical results except in the exit plane at 95 percent speed. The flow velocities were generally larger at the inlet than at the exit. The unsteady inlet and exit flow velocities indicate flutter traveling wave contents similar to those indicated by the casing Kulite unsteady static pressure data.

The rotor blade data obtained during this program permitted the evaluation of the rotor system's stability by means of the aerodynamic logarithmic decrement. This was done for the predominant traveling wave components. The results of these calculations corroborate the strain gage and light probe data: the 4- and 6-nodal diameter forward traveling waves are unstable at the 70 percent speed torsional flutter point, and the 3-nodal diameter forward traveling wave is unstable at the 95 percent speed flexural flutter point.

7.2 CONCLUSIONS

Extensive quantitative measurements were made for the relevant mechanical and aerodynamic parameters for the 31.3 percent scale model of the QEP Fan C rotor system at various operating conditions encompassing both flexural and torsional stall flutter as well as non-flutter points. The data suggests the following observations:

- The large circumferential variation in the blade stresses and deflections at flutter strongly discourages any engine flutter test with only a few blades instrumented, unless one is certain that there will be only one traveling wave in the flutter mode or the most active or flutter-prone blade is known beforehand.

- At high speeds (90 and 95 percent), strong bow shock waves intersecting the adjacent blade's suction surface suggest that the flexural flutter may have been caused by the forward movement of the shock wave structure when the fan was throttled to the flutter boundary.
- At low speeds (65 and 70 percent), the weak shock waves that were shown to exist in the steady flow field suggest that the torsional flutter was due to something other than shock waves.
- The large phase jump across the front portion of the blade tip implies that the unsteady pressure on the pressure and suction sides of the blade tend to act in the same direction rather than against each other. Consequently, one would expect that a major portion of the work done by the air on the blades is over the leading edge portion of the blade.
- The existence of many forward traveling waves of different nodal diameters in the flutter response suggests that blade mistuning may be important in determining the characteristics of flutter onset.
- Flutter response data obtained in this program are detailed enough to serve as standard test cases for existing flutter prediction techniques.

7.3 RECOMMENDATIONS

During initial component or engine tests, if all the blades cannot be instrumented, some type of non-contacting stress measurement system (e.g., light probes) should be used to insure safe operation. The argument for light probes is that they look at every blade at least part of the time (once per revolution), whereas strain gages monitor only a few blades all of the time.

Further development is needed to achieve reliable measurements with blade-mounted aerodynamic instrumentation.

A reliable system capable of non-integral order data sampling would be a major contribution to greater phasing accuracy.

Blade mistuning research will be important in obtaining a definitive characterization of this contributory aspect of cascade flutter.

A better understanding of the physics of stall flutter may be obtained by a more in-depth analysis of the voluminous flutter data obtained in this program.

The data obtained during this program should be used to validate existing flutter prediction codes and to provide insight for the development of new codes.

APPENDIX A

BLADE ELEMENT DATA NOMENCLATURE

PCT IMM		Percent immersion, 0% at casing wall
IN	Subscript 1	Value at rotor leading edge
OUT	Subscript 2	Value at rotor trailing edge
RADIUS	r	Radius from rotor centerline, cm (in.)
MERID ANGLE	ϕ	Meridional angle, measured between stream surface and cylindrical surface, deg.
STREAM FUNCT	ψ	Stream function, 0.0 to 1.0 from rotor tip to rotor hub
ABS ANGLE	α	Absolute flow angle, measured from axial direction, deg.
REL ANGLE	β'	Relative flow angle, measured from axial direction, deg.
ABS VEL	V	Absolute air velocity, m/sec (ft/sec)
REL VEL	V'	Air Velocity relative to rotor blade, m/sec (ft/sec)
MERID VEL	V_m	Meridional component of air velocity, m/sec (ft/sec)
TANG VEL	V_θ	Tangential component of air velocity, m/sec (ft/sec)
BLADE SPEED	U	Rotor speed, m/sec (ft/sec)
ABS MACH NO	M	Absolute Mach number
REL MACH NO	M'	Mach number relative to rotor blade
STATIC PRES	p	Static pressure, N/cm ² (psi)
TOTAL PRES	P	Total or stagnation pressure, N/cm ² (psi)
TOTAL TEMP	T	Total or stagnation temperature, ° K (° R)

INCIDENCE, ML	i	Meanline incidence angle, difference between flow angle and the blade camber line angle at the leading edge in the cascade projection, deg.
INCIDENCE, SS	i_{ss}	Suction surface incidence angle, difference between flow angle and the blade suction surface angle near the leading edge, deg.
DEV	$\bar{\delta}$	Deviation angle, difference between flow angle and blade camber line angle at trailing edge in the cascade projection, deg.
TURN	$\Delta\beta$	Change in the relative flow angle from rotor inlet to exit, deg.
D-FACT	D	Diffusion factor $D = 1 - \frac{V_2'}{V_1'} + \frac{(r V_\theta)_2 - (r V_\theta)_1}{2 \bar{r} \sigma V_1'}$
LOSS COEF	$\bar{\omega}$	Total pressure loss coefficient $\bar{\omega} = \frac{P_{2'id}' - P_2'}{P_1' - P_1}$
LOSS PARAM	$\bar{\omega}_p$	Loss parameter $\bar{\omega}_p = \frac{\bar{\omega} \cos \beta_2'}{2\sigma}$
EFFICIENCY, ADIA	η_{ad}	Adiabatic efficiency
EFFICIENCY, POLY	η_p	Polytropic efficiency
INLET CORR WTFLOW		Corrected inlet flow rate = $W\sqrt{\theta}/\delta$, kg/sec (lbm/sec)
PRESS RATIO		Stage pressure ratio = P_2/P_1
TEMP RATIO		Stage temperature ratio = T_2/T_1
ADIA EFF	η_{ad}	Mass-weighted average adiabatic efficiency
INLET CORR RPM		Corrected rotor speed = $N/\sqrt{\theta}$

ORIGINAL FILED
OF POOR QUALITY

Table A-1. Design Point (Predicted) Blade Element Data.

(a) Metric

Percent Immersion	Radius		Meridional Angle		Stream Function		Absolute Angle		Relative Angle	
	In	Out	In	Out	In	Out	In	Out	In	Out
5.0	26.152	25.453	-9.2	-8.3	0.064	0.067	0.	36.2	66.5	61.3
10.0	25.339	24.695	-7.6	-6.7	0.129	0.133	0.	37.5	65.3	59.5
15.0	24.509	23.954	-6.3	-5.7	0.195	0.197	0.	36.1	63.9	57.0
30.0	21.971	21.780	-1.7	-2.3	0.386	0.385	0.	35.4	60.0	53.7
50.0	18.612	18.856	3.9	3.3	0.610	0.611	0.	38.6	55.2	46.3
60.0	16.925	17.401	6.9	5.8	0.707	0.709	0.	40.7	52.7	40.6
70.0	15.222	15.963	10.4	8.1	0.795	0.797	0.	43.3	50.0	33.4
80.0	13.478	14.566	14.9	6.9	0.874	0.874	0.	43.7	47.3	23.4
85.0	12.581	13.892	17.6	7.2	0.909	0.910	0.	44.1	46.1	17.5
90.0	11.666	13.236	20.5	7.8	0.942	0.943	0.	45.1	45.1	11.5
95.0	10.735	12.596	23.3	8.4	0.973	0.973	0.	46.2	43.7	5.4

Percent Immersion	Absolute Velocity		Relative Velocity		Meridional Velocity		Tangential Velocity		Blade Speed	
	In	Out	In	Out	In	Out	In	Out	In	Out
5.0	199.9	216.7	496.4	353.4	199.9	171.1	0.	133.0	454.4	442.3
10.0	204.3	220.2	485.4	343.8	204.3	175.2	0.	133.3	440.3	429.1
15.0	209.9	224.2	474.8	337.4	209.9	181.4	0.	131.7	425.9	416.2
30.0	220.2	224.1	440.7	308.6	220.2	162.7	0.	129.8	381.8	378.5
50.0	225.0	227.6	394.0	257.3	225.0	176.1	0.	141.8	343.4	327.6
60.0	226.0	232.5	370.9	232.7	226.0	176.6	0.	151.2	294.1	302.4
70.0	225.7	239.2	347.7	209.0	225.7	175.0	0.	163.0	264.5	277.4
80.0	223.5	253.1	323.7	199.9	223.5	183.7	0.	174.1	234.2	253.1
85.0	220.6	262.7	310.6	196.4	220.6	189.3	0.	182.1	218.6	241.4
90.0	215.8	271.0	296.1	196.0	215.8	192.1	0.	191.0	202.7	230.0
95.0	212.3	279.9	282.6	195.9	212.3	195.0	0.	200.8	186.5	218.9

Percent Immersion	Absolute Mach No.		Relative Mach No.		Static Pressure		Total Pressure		Total Temperature	
	In	Out	In	Out	In	Out	In	Out	In	Out
5.0	0.608	0.601	1.511	0.980	7.89	12.61	10.14	16.10	288.2	346.6
10.0	0.623	0.613	1.480	0.957	7.80	12.67	10.14	16.33	288.2	345.2
15.0	0.641	0.627	1.451	0.944	7.68	12.73	10.14	16.59	288.2	345.4
30.0	0.676	0.633	1.352	0.871	7.46	12.79	10.14	16.75	288.2	337.1
50.0	0.692	0.646	1.211	0.730	7.36	12.55	10.14	16.62	288.2	334.5
60.0	0.695	0.662	1.141	0.663	7.34	12.36	10.14	16.59	288.2	333.7
70.0	0.694	0.683	1.069	0.597	7.34	12.14	10.14	16.60	288.2	333.2
80.0	0.687	0.728	0.995	0.575	7.33	11.62	10.14	16.55	288.2	332.2
85.0	0.677	0.759	0.953	0.574	7.45	11.24	10.14	16.47	288.2	332.0
90.0	0.661	0.786	0.907	0.569	7.57	10.82	10.14	16.26	288.2	332.0
95.0	0.649	0.815	0.864	0.571	7.63	10.36	10.14	16.01	288.2	332.0

Percent Immersion	Incidence		Deviation Angle	Turning Angle	D-Factor	Loss Coefficient	Loss Parameter	Efficiency	
	ML	SS						Adiabatic	Polytropic
5.0	0.8		3.6	5.2	0.382	0.220	0.038	0.695	0.715
10.0	1.0		3.8	7	0.388	0.191	0.034	0.736	0.755
15.0	1.1		3.3	6.2	0.387	0.168	0.028	0.796	0.811
30.0	0.3		3.1	6.3	0.404	0.066	0.014	0.911	0.917
50.0	0.3		5.9	8.9	0.472	0.044	0.011	0.946	0.949
60.0	-0.1		6.4	12.0	0.511	0.036	0.009	0.956	0.961
70.0	-0.1		7.6	16.3	0.552	0.029	0.008	0.969	0.971
80.0	1.0		12.3	23.8	0.544	0.011	0.003	0.989	0.990
85.0	1.4		13.3	28.5	0.525	0.020	0.005	0.982	0.983
90.0	1.2		13.5	33.5	0.510	0.052	0.013	0.956	0.959
95.0	0.4		14.4	38.3	0.490	0.099	0.023	0.922	0.927

Inlet Corrosion Weight Flow	Pressure Ratio	Temperature Ratio	Adiabatic Efficiency	Inlet Corrosion RPM
89.91	1.6311	1.1708	0.880	14,400

ORIGINAL PAGE IS
OF POOR QUALITY

Table A-1. Design Point (Predicted) Blade Element Data (Concluded).
(b) English

Percent Immersion	Radius		Meridional Angle		Stream Function		Absolute Angle		Relative Angle	
	In	Out	In	Out	In	Out	In	Out	In	Out
5.0	10.296	10.021	-9.2	-8.3	0.064	0.067	0.	38.2	66.5	61.3
10.0	9.976	9.723	-7.6	-6.7	0.129	0.133	0.	37.5	65.3	59.5
15.0	9.649	9.431	-6.3	-5.7	0.195	0.197	0.	36.1	63.9	57.6
30.0	8.650	8.575	-1.7	-2.3	0.386	0.385	0.	35.4	60.0	53.7
50.0	7.328	7.424	3.9	3.3	0.610	0.611	0.	38.6	55.2	46.3
60.0	6.664	6.851	6.9	5.8	0.707	0.709	0.	40.7	52.7	40.6
70.0	5.993	6.285	10.4	8.1	0.795	0.797	0.	43.3	50.0	33.4
80.0	5.306	5.735	14.9	6.9	0.874	0.874	0.	43.7	47.3	23.4
85.0	4.953	5.469	17.6	7.2	0.909	0.910	0.	44.1	46.1	17.5
90.0	4.593	5.211	20.5	7.8	0.942	0.943	0.	45.1	45.1	11.5
95.0	4.226	4.959	23.3	8.4	0.973	0.973	0.	46.2	43.7	5.4

Percent Immersion	Absolute Velocity		Relative Velocity		Meridional Velocity		Tangential Velocity		Blade Speed	
	In	Out	In	Out	In	Out	In	Out	In	Out
5.0	655.7	711.1	1628.6	1159.5	655.7	561.4	0.	436.4	1490.9	1451.0
10.0	670.3	722.3	1592.5	1128.0	670.3	574.7	0.	437.4	1444.5	1407.8
15.0	688.7	735.6	1557.7	1107.0	688.7	595.2	0.	432.2	1397.2	1365.6
30.0	722.3	735.1	1445.9	1012.4	722.3	599.3	0.	425.7	1252.5	1241.7
50.0	738.3	746.8	1292.6	844.0	738.3	584.3	0.	465.3	1061.0	1075.0
60.0	741.5	763.0	1216.9	763.6	741.5	579.4	0.	496.1	964.9	992.0
70.0	740.5	784.6	1140.8	685.8	740.5	574.0	0.	534.9	867.8	910.0
80.0	733.3	830.4	1062.1	655.9	733.3	602.7	0.	571.3	768.3	830.4
85.0	723.9	862.0	1019.1	651.0	723.9	621.2	0.	597.6	717.2	792.0
90.0	708.0	889.0	971.3	643.2	708.0	630.4	0.	626.7	665.0	754.6
95.0	696.5	918.2	927.3	642.6	696.5	639.7	0.	658.7	612.0	718.1

Percent Immersion	Absolute Mach No.		Relative Mach No.		Static Pressure		Total Pressure		Total Temperature	
	In	Out	In	Out	In	Out	In	Out	In	Out
5.0	0.608	0.601	1.511	0.980	11.46	18.29	14.70	23.35	518.7	624.2
10.0	0.623	0.613	1.480	0.957	11.31	18.37	14.70	23.68	518.7	621.3
15.0	0.641	0.627	1.451	0.944	11.14	18.46	14.70	24.06	518.7	617.0
30.0	0.676	0.633	1.352	0.871	10.82	18.55	14.70	24.29	518.7	606.8
50.0	0.692	0.646	1.211	0.730	10.67	18.20	14.70	24.10	518.7	602.1
60.0	0.695	0.662	1.141	0.663	10.64	17.92	14.70	24.06	518.7	600.6
70.0	0.694	0.683	1.069	0.597	10.65	17.61	14.70	24.07	518.7	599.8
80.0	0.687	0.728	0.995	0.575	10.72	16.86	14.70	24.01	518.7	598.0
85.0	0.677	0.759	0.953	0.574	10.81	16.30	14.70	23.89	518.7	597.6
90.0	0.661	0.786	0.907	0.569	10.98	15.70	14.70	23.58	518.7	597.6
95.0	0.649	0.815	0.864	0.571	11.06	15.02	14.70	23.22	518.7	597.6

Percent Immersion	Incidence		Deviation Angle	Turning Angle	D-Factor	Loss Coefficient	Loss Parameter	Efficiency	
	ML	SS						Adiabatic	Polytropic
5.0	0.8		3.6	5.2	0.382	0.220	0.038	0.695	0.715
10.0	1.0		3.8	5.7	0.388	0.191	0.034	0.738	0.755
15.0	1.1		3.3	6.2	0.387	0.148	0.028	0.798	0.811
30.0	0.3		3.1	6.3	0.404	0.066	0.014	0.911	0.917
50.0	0.3		5.9	8.9	0.472	0.044	0.011	0.946	0.949
60.0	-0.1		6.4	12.0	0.511	0.036	0.009	0.958	0.961
70.0	-0.1		7.6	16.5	0.552	0.029	0.008	0.969	0.971
80.0	1.0		12.3	23.8	0.544	0.011	0.003	0.989	0.990
85.0	1.4		13.3	28.5	0.525	0.020	0.005	0.982	0.983
90.0	1.2		13.5	33.5	0.510	0.052	0.013	0.956	0.959
95.0	0.4		14.4	38.3	0.490	0.099	0.023	0.922	0.927

Inlet Corrosion Weight Flow	Pressure Ratio	Temperature Ratio	Adiabatic Efficiency	Inlet Corrosion RPM
89.91	1.6311	1.1708	0.880	14,522.4

Table A-2. Blade-Element Data from Fixed Instrumentation, Intermediate O.L.,
65% Speed, Reading 158.

(a) Metric

PCT	IN	OUT	RADIUS	MERID ANGLE	STREAM FUNK	ABS ANGLE	REL ANGLE	PCT	IN	OUT	RADIUS	MERID ANGLE	STREAM FUNK	ABS ANGLE	REL ANGLE	PCT	IN	OUT	RADIUS	MERID ANGLE	STREAM FUNK	ABS ANGLE	REL ANGLE
5.0	26.152	25.451	5.3	-8.2	0.059	0.069	71.3	5.0	10.296	10.021	-5.3	-8.2	0.059	0.069	71.3	5.0	10.296	10.021	-5.3	-8.2	0.059	0.069	71.3
10.0	26.131	24.135	5.3	-8.2	0.122	0.136	71.3	10.0	9.976	9.723	-5.3	-8.2	0.122	0.136	71.3	10.0	9.976	9.723	-5.3	-8.2	0.122	0.136	71.3
15.0	24.903	21.904	13.7	-5.6	0.180	0.201	47.0	15.0	9.649	9.431	-1.7	-5.6	0.180	0.201	47.0	15.0	9.649	9.431	-1.7	-5.6	0.180	0.201	47.0
20.0	21.971	21.200	13.3	-2.9	0.180	0.174	45.3	20.0	9.650	0.576	1.3	-2.9	0.170	0.378	45.3	20.0	9.650	0.576	1.3	-2.9	0.170	0.378	45.3
25.0	21.971	21.200	13.3	-2.9	0.180	0.174	45.3	25.0	9.650	0.576	1.3	-2.9	0.170	0.378	45.3	25.0	9.650	0.576	1.3	-2.9	0.170	0.378	45.3
30.0	21.971	21.200	13.3	-2.9	0.180	0.174	45.3	30.0	9.650	0.576	1.3	-2.9	0.170	0.378	45.3	30.0	9.650	0.576	1.3	-2.9	0.170	0.378	45.3
35.0	21.971	21.200	13.3	-2.9	0.180	0.174	45.3	35.0	9.650	0.576	1.3	-2.9	0.170	0.378	45.3	35.0	9.650	0.576	1.3	-2.9	0.170	0.378	45.3
40.0	21.971	21.200	13.3	-2.9	0.180	0.174	45.3	40.0	9.650	0.576	1.3	-2.9	0.170	0.378	45.3	40.0	9.650	0.576	1.3	-2.9	0.170	0.378	45.3
45.0	21.971	21.200	13.3	-2.9	0.180	0.174	45.3	45.0	9.650	0.576	1.3	-2.9	0.170	0.378	45.3	45.0	9.650	0.576	1.3	-2.9	0.170	0.378	45.3
50.0	21.971	21.200	13.3	-2.9	0.180	0.174	45.3	50.0	9.650	0.576	1.3	-2.9	0.170	0.378	45.3	50.0	9.650	0.576	1.3	-2.9	0.170	0.378	45.3
55.0	21.971	21.200	13.3	-2.9	0.180	0.174	45.3	55.0	9.650	0.576	1.3	-2.9	0.170	0.378	45.3	55.0	9.650	0.576	1.3	-2.9	0.170	0.378	45.3
60.0	21.971	21.200	13.3	-2.9	0.180	0.174	45.3	60.0	9.650	0.576	1.3	-2.9	0.170	0.378	45.3	60.0	9.650	0.576	1.3	-2.9	0.170	0.378	45.3
65.0	21.971	21.200	13.3	-2.9	0.180	0.174	45.3	65.0	9.650	0.576	1.3	-2.9	0.170	0.378	45.3	65.0	9.650	0.576	1.3	-2.9	0.170	0.378	45.3
70.0	21.971	21.200	13.3	-2.9	0.180	0.174	45.3	70.0	9.650	0.576	1.3	-2.9	0.170	0.378	45.3	70.0	9.650	0.576	1.3	-2.9	0.170	0.378	45.3
75.0	21.971	21.200	13.3	-2.9	0.180	0.174	45.3	75.0	9.650	0.576	1.3	-2.9	0.170	0.378	45.3	75.0	9.650	0.576	1.3	-2.9	0.170	0.378	45.3
80.0	21.971	21.200	13.3	-2.9	0.180	0.174	45.3	80.0	9.650	0.576	1.3	-2.9	0.170	0.378	45.3	80.0	9.650	0.576	1.3	-2.9	0.170	0.378	45.3
85.0	21.971	21.200	13.3	-2.9	0.180	0.174	45.3	85.0	9.650	0.576	1.3	-2.9	0.170	0.378	45.3	85.0	9.650	0.576	1.3	-2.9	0.170	0.378	45.3
90.0	21.971	21.200	13.3	-2.9	0.180	0.174	45.3	90.0	9.650	0.576	1.3	-2.9	0.170	0.378	45.3	90.0	9.650	0.576	1.3	-2.9	0.170	0.378	45.3
95.0	21.971	21.200	13.3	-2.9	0.180	0.174	45.3	95.0	9.650	0.576	1.3	-2.9	0.170	0.378	45.3	95.0	9.650	0.576	1.3	-2.9	0.170	0.378	45.3

(b) English

PCT	IN	OUT	RADIUS	MERID ANGLE	STREAM FUNK	ABS ANGLE	REL ANGLE	PCT	IN	OUT	RADIUS	MERID ANGLE	STREAM FUNK	ABS ANGLE	REL ANGLE	PCT	IN	OUT	RADIUS	MERID ANGLE	STREAM FUNK	ABS ANGLE	REL ANGLE
5.0	10.296	10.021	5.0	-8.2	0.059	0.069	71.3	5.0	459.7	1810.3	5.0	-8.2	0.059	0.069	71.3	5.0	459.7	1810.3	5.0	-8.2	0.059	0.069	71.3
10.0	9.976	9.723	5.0	-8.2	0.122	0.136	71.3	10.0	297.9	450.0	5.0	-8.2	0.122	0.136	71.3	10.0	297.9	450.0	5.0	-8.2	0.122	0.136	71.3
15.0	9.649	9.431	15.0	-5.6	0.180	0.201	47.0	15.0	297.3	437.3	15.0	-5.6	0.180	0.201	47.0	15.0	297.3	437.3	15.0	-5.6	0.180	0.201	47.0
20.0	9.650	0.576	15.0	-5.6	0.180	0.201	47.0	20.0	297.3	437.3	15.0	-5.6	0.180	0.201	47.0	20.0	297.3	437.3	15.0	-5.6	0.180	0.201	47.0
25.0	9.650	0.576	15.0	-5.6	0.180	0.201	47.0	25.0	297.3	437.3	15.0	-5.6	0.180	0.201	47.0	25.0	297.3	437.3	15.0	-5.6	0.180	0.201	47.0
30.0	9.650	0.576	15.0	-5.6	0.180	0.201	47.0	30.0	297.3	437.3	15.0	-5.6	0.180	0.201	47.0	30.0	297.3	437.3	15.0	-5.6	0.180	0.201	47.0
35.0	9.650	0.576	15.0	-5.6	0.180	0.201	47.0	35.0	297.3	437.3	15.0	-5.6	0.180	0.201	47.0	35.0	297.3	437.3	15.0	-5.6	0.180	0.201	47.0
40.0	9.650	0.576	15.0	-5.6	0.180	0.201	47.0	40.0	297.3	437.3	15.0	-5.6	0.180	0.201	47.0	40.0	297.3	437.3	15.0	-5.6	0.180	0.201	47.0
45.0	9.650	0.576	15.0	-5.6	0.180	0.201	47.0	45.0	297.3	437.3	15.0	-5.6	0.180	0.201	47.0	45.0	297.3	437.3	15.0	-5.6	0.180	0.201	47.0
50.0	9.650	0.576	15.0	-5.6	0.180	0.201	47.0	50.0	297.3	437.3	15.0	-5.6	0.180	0.201	47.0	50.0	297.3	437.3	15.0	-5.6	0.180	0.201	47.0
55.0	9.650	0.576	15.0	-5.6	0.180	0.201	47.0	55.0	297.3	437.3	15.0	-5.6	0.180	0.201	47.0	55.0	297.3	437.3	15.0	-5.6	0.180	0.201	47.0
60.0	9.650	0.576	15.0	-5.6	0.180	0.201	47.0	60.0	297.3	437.3	15.0	-5.6	0.180	0.201	47.0	60.0	297.3	437.3	15.0	-5.6	0.180	0.201	47.0
65.0	9.650	0.576	15.0	-5.6	0.180	0.201	47.0	65.0	297.3	437.3	15.0	-5.6	0.180	0.201	47.0	65.0	297.3	437.3	15.0	-5.6	0.180	0.201	47.0
70.0	9.650	0.576	15.0	-5.6	0.180	0.201	47.0	70.0	297.3	437.3	15.0	-5.6	0.180	0.201	47.0	70.0	297.3	437.3	15.0	-5.6	0.180	0.201	47.0
75.0	9.650	0.576	15.0	-5.6	0.180	0.201	47.0	75.0	297.3	437.3	15.0	-5.6	0.180	0.201	47.0	75.0	297.3	437.3	15.0	-5.6	0.180	0.201	47.0
80.0	9.650	0.576	15.0	-5.6	0.180	0.201	47.0	80.0	297.3	437.3	15.0	-5.6	0.180	0.201	47.0	80.0	297.3	437.3	15.0	-5.6	0.180	0.201	47.0
85.0	9.650	0.576	15.0	-5.6	0.180	0.201	47.0	85.0	297.3	437.3	15.0	-5.6	0.180	0.201	47.0	85.0	297.3	437.3	15.0	-5.6	0.180	0.201	47.0
90.0	9.650	0.576	15.0	-5.6	0.180	0.201	47.0	90.0	297.3	437.3	15.0	-5.6	0.180	0.201	47.0	90.0	297.3	437.3	15.0	-5.6	0.180	0.201	47.0
95.0	9.650	0.576	15.0	-5.6	0.180	0.201	47.0	95.0	297.3	437.3	15.0	-5.6	0.180	0.201	47.0	95.0	297.3	437.3	15.0	-5.6	0.180	0.201	47.0

Table A-3. Blade-Element Data from Fixed Instrumentation, Near Stall Flutter, 65% Speed, Reading 54.

[illegible]

Table A-4. Blade-Element Data from Fixed Instrumentation, Stall Flutter, 65% Speed, Reading 79.

(a) Metric

PCT	RADIUS	MERID ANGLE	STREAM FUNCT	ABS ANGLE	REL ANGLE	PCT	RADIUS	MERID ANGLE	STREAM FUNCT	ABS ANGLE	REL ANGLE	PCT	RADIUS	MERID ANGLE	STREAM FUNCT	ABS ANGLE	REL ANGLE
INM	IN	OUT	IN	OUT	IN	OUT	IN	OUT	IN	OUT	IN	OUT	IN	OUT	IN	OUT	IN
5.0	26.152	25.013	0.059	0.064	0.496	74.0	67.5	5.0	10.296	10.021	-5.0	-0.4	0.059	0.069	0.496	74.0	67.5
10.0	25.337	24.095	0.123	0.136	0.487	72.6	61.0	10.0	9.976	9.723	-1.0	-0.9	0.123	0.136	0.487	72.6	61.0
15.0	24.509	23.294	0.189	0.201	0.480	70.1	54.4	15.0	9.649	9.431	-1.0	-0.8	0.189	0.201	0.480	70.1	54.4
20.0	23.671	22.480	0.254	0.277	0.473	67.3	47.4	20.0	9.320	9.075	-1.0	-0.7	0.254	0.277	0.473	67.3	47.4
25.0	22.823	21.666	0.319	0.352	0.466	64.6	40.4	25.0	9.000	8.724	-1.0	-0.6	0.319	0.352	0.466	64.6	40.4
30.0	21.975	20.852	0.384	0.427	0.459	61.9	33.4	30.0	8.679	8.372	-1.0	-0.5	0.384	0.427	0.459	61.9	33.4
35.0	21.127	20.038	0.449	0.502	0.452	59.2	26.4	35.0	8.358	7.999	-1.0	-0.4	0.449	0.502	0.452	59.2	26.4
40.0	20.279	19.224	0.514	0.577	0.445	56.5	19.4	40.0	8.037	7.629	-1.0	-0.3	0.514	0.577	0.445	56.5	19.4
45.0	19.431	18.410	0.579	0.640	0.438	53.8	12.4	45.0	7.716	7.259	-1.0	-0.2	0.579	0.640	0.438	53.8	12.4
50.0	18.583	17.596	0.644	0.701	0.431	51.1	5.4	50.0	7.395	6.889	-1.0	-0.1	0.644	0.701	0.431	51.1	5.4
55.0	17.735	16.782	0.709	0.762	0.424	48.4	-2.6	55.0	7.074	6.519	-1.0	0.0	0.709	0.762	0.424	48.4	-2.6
60.0	16.887	15.968	0.774	0.813	0.417	45.7	-9.6	60.0	6.753	6.149	-1.0	0.1	0.774	0.813	0.417	45.7	-9.6
65.0	16.039	15.154	0.839	0.864	0.410	43.0	-16.6	65.0	6.432	5.779	-1.0	0.2	0.839	0.864	0.410	43.0	-16.6
70.0	15.191	14.340	0.904	0.919	0.403	40.3	-23.6	70.0	6.111	5.408	-1.0	0.3	0.904	0.919	0.403	40.3	-23.6
75.0	14.343	13.530	0.969	0.974	0.396	37.6	-30.6	75.0	5.790	5.105	-1.0	0.4	0.969	0.974	0.396	37.6	-30.6
80.0	13.495	12.716	1.034	1.029	0.389	34.9	-37.6	80.0	5.469	4.740	-1.0	0.5	1.034	1.029	0.389	34.9	-37.6
85.0	12.647	11.902	1.099	1.084	0.382	32.2	-44.6	85.0	5.148	4.379	-1.0	0.6	1.099	1.084	0.382	32.2	-44.6
90.0	11.799	11.097	1.164	1.139	0.375	29.5	-51.6	90.0	4.827	4.018	-1.0	0.7	1.164	1.139	0.375	29.5	-51.6
95.0	10.951	10.294	1.229	1.194	0.368	26.8	-58.6	95.0	4.506	3.659	-1.0	0.8	1.229	1.194	0.368	26.8	-58.6

(b) English

PCT	RADIUS	MERID ANGLE	STREAM FUNCT	ABS ANGLE	REL ANGLE	PCT	RADIUS	MERID ANGLE	STREAM FUNCT	ABS ANGLE	REL ANGLE	PCT	RADIUS	MERID ANGLE	STREAM FUNCT	ABS ANGLE	REL ANGLE
INM	IN	OUT	IN	OUT	IN	OUT	IN	OUT	IN	OUT	IN	OUT	IN	OUT	IN	OUT	IN
5.0	10.296	10.021	0.059	0.069	0.496	74.0	67.5	5.0	10.296	10.021	-5.0	-0.4	0.059	0.069	0.496	74.0	67.5
10.0	9.976	9.723	0.123	0.136	0.487	72.6	61.0	10.0	9.976	9.723	-1.0	-0.9	0.123	0.136	0.487	72.6	61.0
15.0	9.649	9.431	0.189	0.201	0.480	70.1	54.4	15.0	9.649	9.431	-1.0	-0.8	0.189	0.201	0.480	70.1	54.4
20.0	9.320	9.075	0.254	0.277	0.473	67.3	47.4	20.0	9.320	9.075	-1.0	-0.7	0.254	0.277	0.473	67.3	47.4
25.0	9.000	8.724	0.319	0.352	0.466	64.6	40.4	25.0	9.000	8.724	-1.0	-0.6	0.319	0.352	0.466	64.6	40.4
30.0	8.679	8.372	0.384	0.427	0.459	61.9	33.4	30.0	8.679	8.372	-1.0	-0.5	0.384	0.427	0.459	61.9	33.4
35.0	8.358	7.999	0.449	0.502	0.452	59.2	26.4	35.0	8.358	7.999	-1.0	-0.4	0.449	0.502	0.452	59.2	26.4
40.0	8.037	7.629	0.514	0.577	0.445	56.5	19.4	40.0	8.037	7.629	-1.0	-0.3	0.514	0.577	0.445	56.5	19.4
45.0	7.716	7.259	0.579	0.640	0.438	53.8	12.4	45.0	7.716	7.259	-1.0	-0.2	0.579	0.640	0.438	53.8	12.4
50.0	7.395	6.889	0.644	0.701	0.431	51.1	5.4	50.0	7.395	6.889	-1.0	-0.1	0.644	0.701	0.431	51.1	5.4
55.0	7.074	6.519	0.709	0.762	0.424	48.4	-2.6	55.0	7.074	6.519	-1.0	0.0	0.709	0.762	0.424	48.4	-2.6
60.0	6.753	6.149	0.774	0.813	0.417	45.7	-9.6	60.0	6.753	6.149	-1.0	0.1	0.774	0.813	0.417	45.7	-9.6
65.0	6.432	5.779	0.839	0.864	0.410	43.0	-16.6	65.0	6.432	5.779	-1.0	0.2	0.839	0.864	0.410	43.0	-16.6
70.0	6.111	5.408	0.904	0.919	0.403	40.3	-23.6	70.0	6.111	5.408	-1.0	0.3	0.904	0.919	0.403	40.3	-23.6
75.0	5.790	5.105	0.969	0.974	0.396	37.6	-30.6	75.0	5.790	5.105	-1.0	0.4	0.969	0.974	0.396	37.6	-30.6
80.0	5.469	4.740	1.034	1.029	0.389	34.9	-37.6	80.0	5.469	4.740	-1.0	0.5	1.034	1.029	0.389	34.9	-37.6
85.0	5.148	4.379	1.099	1.084	0.382	32.2	-44.6	85.0	5.148	4.379	-1.0	0.6	1.099	1.084	0.382	32.2	-44.6
90.0	4.827	4.018	1.164	1.139	0.375	29.5	-51.6	90.0	4.827	4.018	-1.0	0.7	1.164	1.139	0.375	29.5	-51.6
95.0	4.506	3.659	1.229	1.194	0.368	26.8	-58.6	95.0	4.506	3.659	-1.0	0.8	1.229	1.194	0.368	26.8	-58.6

Table A-6. Blade-Element Data from Fixed Instrumentation, Low Operating Line, 75% Speed, Reading 154.

(a) Metric									
PCT	RADIUS	REL ANGLE	STREAM FUNCT	ABS ANGLE	REL ANGLE	PCT	RADIUS	REL ANGLE	STREAM FUNCT
INM	IN	OUT	IN	OUT	IN	INM	IN	OUT	IN
5.0	20.152	23.473	0.000	0.000	0.000	5.0	10.296	10.021	0.000
10.0	20.319	24.099	0.124	0.139	0.139	10.0	9.916	9.723	0.124
15.0	20.471	24.954	0.190	0.205	0.205	15.0	9.619	9.431	0.190
20.0	21.011	21.704	0.210	0.225	0.225	20.0	9.322	9.130	0.210
25.0	21.551	21.006	0.230	0.245	0.245	25.0	9.025	8.833	0.230
30.0	22.091	20.308	0.250	0.265	0.265	30.0	8.728	8.536	0.250
35.0	22.631	19.610	0.270	0.285	0.285	35.0	8.431	8.239	0.270
40.0	23.171	18.912	0.290	0.305	0.305	40.0	8.134	7.942	0.290
45.0	23.711	18.214	0.310	0.325	0.325	45.0	7.837	7.645	0.310
50.0	24.251	17.516	0.330	0.345	0.345	50.0	7.540	7.348	0.330
55.0	24.791	16.818	0.350	0.365	0.365	55.0	7.243	7.051	0.350
60.0	25.331	16.120	0.370	0.385	0.385	60.0	6.946	6.754	0.370
65.0	25.871	15.422	0.390	0.405	0.405	65.0	6.649	6.457	0.390
70.0	26.411	14.724	0.410	0.425	0.425	70.0	6.352	6.160	0.410
75.0	26.951	14.026	0.430	0.445	0.445	75.0	6.055	5.863	0.430
80.0	27.491	13.328	0.450	0.465	0.465	80.0	5.758	5.566	0.450
85.0	28.031	12.630	0.470	0.485	0.485	85.0	5.461	5.269	0.470
90.0	28.571	11.932	0.490	0.505	0.505	90.0	5.164	4.972	0.490
95.0	29.111	11.234	0.510	0.525	0.525	95.0	4.867	4.675	0.510
PCT	ABS VEL	REL VEL	MERID VEL	TANG VEL	BLADE SPEED	PCT	ABS VEL	REL VEL	MERID VEL
INM	IN	OUT	IN	OUT	IN	INM	IN	OUT	IN
5.0	99.6	150.4	311.3	234.8	311.3	5.0	326.7	493.5	1093.6
10.0	104.8	148.1	311.3	229.1	311.3	10.0	343.8	485.8	1057.6
15.0	109.9	145.4	311.3	223.4	311.3	15.0	360.9	478.1	1021.6
20.0	115.0	142.7	311.3	217.7	311.3	20.0	378.0	470.4	985.6
25.0	120.1	140.0	311.3	212.0	311.3	25.0	395.1	462.7	949.6
30.0	125.2	137.3	311.3	206.3	311.3	30.0	412.2	455.0	913.6
35.0	130.3	134.6	311.3	200.6	311.3	35.0	429.3	447.3	877.6
40.0	135.4	131.9	311.3	194.9	311.3	40.0	446.4	439.6	841.6
45.0	140.5	129.2	311.3	189.2	311.3	45.0	463.5	431.9	805.6
50.0	145.6	126.5	311.3	183.5	311.3	50.0	480.6	424.2	769.6
55.0	150.7	123.8	311.3	177.8	311.3	55.0	497.7	416.5	733.6
60.0	155.8	121.1	311.3	172.1	311.3	60.0	514.8	408.8	697.6
65.0	160.9	118.4	311.3	166.4	311.3	65.0	531.9	401.1	661.6
70.0	166.0	115.7	311.3	160.7	311.3	70.0	549.0	393.4	625.6
75.0	171.1	113.0	311.3	155.0	311.3	75.0	566.1	385.7	589.6
80.0	176.2	110.3	311.3	149.3	311.3	80.0	583.2	378.0	553.6
85.0	181.3	107.6	311.3	143.6	311.3	85.0	600.3	370.3	517.6
90.0	186.4	104.9	311.3	137.9	311.3	90.0	617.4	362.6	481.6
95.0	191.5	102.2	311.3	132.2	311.3	95.0	634.5	354.9	445.6
PCT	ABS MACH NO	REL MACH NO	STATIC PRES	TOTAL PRES	TOTAL TEMP	PCT	ABS MACH NO	REL MACH NO	STATIC PRES
INM	IN	OUT	IN	OUT	IN	INM	IN	OUT	IN
5.0	0.295	0.427	0.488	0.667	9.44	5.0	0.295	0.427	0.488
10.0	0.311	0.411	0.465	0.653	9.45	10.0	0.311	0.411	0.465
15.0	0.327	0.395	0.441	0.639	9.46	15.0	0.327	0.395	0.441
20.0	0.343	0.379	0.417	0.625	9.47	20.0	0.343	0.379	0.417
25.0	0.359	0.363	0.393	0.611	9.48	25.0	0.359	0.363	0.393
30.0	0.375	0.347	0.369	0.597	9.49	30.0	0.375	0.347	0.369
35.0	0.391	0.331	0.345	0.583	9.50	35.0	0.391	0.331	0.345
40.0	0.407	0.315	0.321	0.569	9.51	40.0	0.407	0.315	0.321
45.0	0.423	0.299	0.297	0.555	9.52	45.0	0.423	0.299	0.297
50.0	0.439	0.283	0.273	0.541	9.53	50.0	0.439	0.283	0.273
55.0	0.455	0.267	0.249	0.527	9.54	55.0	0.455	0.267	0.249
60.0	0.471	0.251	0.225	0.513	9.55	60.0	0.471	0.251	0.225
65.0	0.487	0.235	0.201	0.499	9.56	65.0	0.487	0.235	0.201
70.0	0.503	0.219	0.177	0.485	9.57	70.0	0.503	0.219	0.177
75.0	0.519	0.203	0.153	0.471	9.58	75.0	0.519	0.203	0.153
80.0	0.535	0.187	0.129	0.457	9.59	80.0	0.535	0.187	0.129
85.0	0.551	0.171	0.105	0.443	9.60	85.0	0.551	0.171	0.105
90.0	0.567	0.155	0.081	0.429	9.61	90.0	0.567	0.155	0.081
95.0	0.583	0.139	0.057	0.415	9.62	95.0	0.583	0.139	0.057
PCT	INCIDENCE	DEV	TURN D-FACT	LOSS	EFFICIENCY	PCT	INCIDENCE	DEV	TURN D-FACT
INM	IN	OUT	IN	OUT	IN	INM	IN	OUT	IN
5.0	6.9	6.6	4.5	10.2	0.402	5.0	6.9	6.6	4.5
10.0	7.4	6.2	5.7	9.7	0.399	10.0	7.4	6.2	5.7
15.0	7.9	6.0	7.0	9.2	0.396	15.0	7.9	6.0	7.0
20.0	8.4	5.8	7.4	8.7	0.393	20.0	8.4	5.8	7.4
25.0	8.9	5.6	7.8	8.2	0.390	25.0	8.9	5.6	7.8
30.0	9.4	5.4	8.2	7.7	0.387	30.0	9.4	5.4	8.2
35.0	9.9	5.2	8.6	7.2	0.384	35.0	9.9	5.2	8.6
40.0	10.4	5.0	9.0	6.7	0.381	40.0	10.4	5.0	9.0
45.0	10.9	4.8	9.4	6.2	0.378	45.0	10.9	4.8	9.4
50.0	11.4	4.6	9.8	5.7	0.375	50.0	11.4	4.6	9.8
55.0	11.9	4.4	10.2	5.2	0.372	55.0	11.9	4.4	10.2
60.0	12.4	4.2	10.6	4.7	0.369	60.0	12.4	4.2	10.6
65.0	12.9	4.0	11.0	4.2	0.366	65.0	12.9	4.0	11.0
70.0	13.4	3.8	11.4	3.7	0.363	70.0	13.4	3.8	11.4
75.0	13.9	3.6	11.8	3.2	0.360	75.0	13.9	3.6	11.8
80.0	14.4	3.4	12.2	2.7	0.357	80.0	14.4	3.4	12.2
85.0	14.9	3.2	12.6	2.2	0.354	85.0	14.9	3.2	12.6
90.0	15.4	3.0	13.0	1.7	0.351	90.0	15.4	3.0	13.0
95.0	15.9	2.8	13.4	1.2	0.348	95.0	15.9	2.8	13.4
PCT	INLET CORR	PRESS	TEMP	INLET CORR	ADIA	PCT	INLET CORR	PRESS	TEMP
INM	IN	OUT	IN	OUT	IN	INM	IN	OUT	IN
5.0	1.000	1.000	1.000	1.000	1.000	5.0	1.000	1.000	1.000
10.0	1.000	1.000	1.000	1.000	1.000	10.0	1.000	1.000	1.000
15.0	1.000	1.000	1.000	1.000	1.000	15.0	1.000	1.000	1.000
20.0	1.000	1.000	1.000	1.000	1.000	20.0	1.000	1.000	1.000
25.0	1.000	1.000	1.000	1.000	1.000	25.0	1.000	1.000	1.000
30.0	1.000	1.000	1.000	1.000	1.000	30.0	1.000	1.000	1.000
35.0	1.000	1.000	1.000	1.000	1.000	35.0	1.000	1.000	1.000
40.0	1.000	1.000	1.000	1.000	1.000	40.0	1.000	1.000	1.000
45.0	1.000	1.000	1.000	1.000	1.000	45.0	1.000	1.000	1.000
50.0	1.000	1.000	1.000	1.000	1.000	50.0	1.000	1.000	1.000
55.0	1.000	1.000	1.000	1.000	1.000	55.0	1.000	1.000	1.000
60.0	1.000	1.000	1.000	1.000	1.000	60.0	1.000	1.000	1.000
65.0	1.000	1.000	1.000	1.000	1.000	65.0	1.000	1.000	1.000
70.0	1.000	1.000	1.000	1.000	1.000	70.0	1.000	1.000	1.000
75.0	1.000	1.000	1.000	1.000	1.000	75.0	1.000	1.000	1.000
80.0	1.000	1.000	1.000	1.000	1.000	80.0	1.000	1.000	1.000
85.0	1.000	1.000	1.000	1.000	1.000	85.0	1.000	1.000	1.000
90.0	1.000	1.000	1.000	1.000	1.000	90.0	1.000	1.000	1.000
95.0	1.000	1.000	1.000	1.000	1.000	95.0	1.000	1.000	1.000

Table A-7. Blade-Element Data from Fixed Instrumentation, Intermediate O.L.,
70% Speed, Reading 179.

236

(a) Metric

(b) English

PCT INM	RADIUS IN	INLET ANGLE IN	STREAM FUNKT IN	MERID ANGLE IN	REL ANGLE IN	PCT INM	RADIUS IN	INLET ANGLE IN	STREAM FUNKT IN	MERID ANGLE IN	REL ANGLE IN	PCT INM	RADIUS IN	INLET ANGLE IN	STREAM FUNKT IN	MERID ANGLE IN	REL ANGLE IN	PCT INM	RADIUS IN	INLET ANGLE IN	STREAM FUNKT IN	MERID ANGLE IN	REL ANGLE IN
5.0	10.150	151.8	0.074	0.074	0.074	5.0	10.296	151.821	0.074	0.074	0.074	5.0	10.296	151.821	0.074	0.074	0.074	5.0	10.296	151.821	0.074	0.074	0.074
10.0	10.150	151.8	0.074	0.074	0.074	10.0	10.296	151.821	0.074	0.074	0.074	10.0	10.296	151.821	0.074	0.074	0.074	10.0	10.296	151.821	0.074	0.074	0.074
15.0	10.150	151.8	0.074	0.074	0.074	15.0	10.296	151.821	0.074	0.074	0.074	15.0	10.296	151.821	0.074	0.074	0.074	15.0	10.296	151.821	0.074	0.074	0.074
20.0	10.150	151.8	0.074	0.074	0.074	20.0	10.296	151.821	0.074	0.074	0.074	20.0	10.296	151.821	0.074	0.074	0.074	20.0	10.296	151.821	0.074	0.074	0.074
25.0	10.150	151.8	0.074	0.074	0.074	25.0	10.296	151.821	0.074	0.074	0.074	25.0	10.296	151.821	0.074	0.074	0.074	25.0	10.296	151.821	0.074	0.074	0.074
30.0	10.150	151.8	0.074	0.074	0.074	30.0	10.296	151.821	0.074	0.074	0.074	30.0	10.296	151.821	0.074	0.074	0.074	30.0	10.296	151.821	0.074	0.074	0.074
35.0	10.150	151.8	0.074	0.074	0.074	35.0	10.296	151.821	0.074	0.074	0.074	35.0	10.296	151.821	0.074	0.074	0.074	35.0	10.296	151.821	0.074	0.074	0.074
40.0	10.150	151.8	0.074	0.074	0.074	40.0	10.296	151.821	0.074	0.074	0.074	40.0	10.296	151.821	0.074	0.074	0.074	40.0	10.296	151.821	0.074	0.074	0.074
45.0	10.150	151.8	0.074	0.074	0.074	45.0	10.296	151.821	0.074	0.074	0.074	45.0	10.296	151.821	0.074	0.074	0.074	45.0	10.296	151.821	0.074	0.074	0.074
50.0	10.150	151.8	0.074	0.074	0.074	50.0	10.296	151.821	0.074	0.074	0.074	50.0	10.296	151.821	0.074	0.074	0.074	50.0	10.296	151.821	0.074	0.074	0.074
55.0	10.150	151.8	0.074	0.074	0.074	55.0	10.296	151.821	0.074	0.074	0.074	55.0	10.296	151.821	0.074	0.074	0.074	55.0	10.296	151.821	0.074	0.074	0.074
60.0	10.150	151.8	0.074	0.074	0.074	60.0	10.296	151.821	0.074	0.074	0.074	60.0	10.296	151.821	0.074	0.074	0.074	60.0	10.296	151.821	0.074	0.074	0.074
65.0	10.150	151.8	0.074	0.074	0.074	65.0	10.296	151.821	0.074	0.074	0.074	65.0	10.296	151.821	0.074	0.074	0.074	65.0	10.296	151.821	0.074	0.074	0.074
70.0	10.150	151.8	0.074	0.074	0.074	70.0	10.296	151.821	0.074	0.074	0.074	70.0	10.296	151.821	0.074	0.074	0.074	70.0	10.296	151.821	0.074	0.074	0.074
75.0	10.150	151.8	0.074	0.074	0.074	75.0	10.296	151.821	0.074	0.074	0.074	75.0	10.296	151.821	0.074	0.074	0.074	75.0	10.296	151.821	0.074	0.074	0.074
80.0	10.150	151.8	0.074	0.074	0.074	80.0	10.296	151.821	0.074	0.074	0.074	80.0	10.296	151.821	0.074	0.074	0.074	80.0	10.296	151.821	0.074	0.074	0.074
85.0	10.150	151.8	0.074	0.074	0.074	85.0	10.296	151.821	0.074	0.074	0.074	85.0	10.296	151.821	0.074	0.074	0.074	85.0	10.296	151.821	0.074	0.074	0.074
90.0	10.150	151.8	0.074	0.074	0.074	90.0	10.296	151.821	0.074	0.074	0.074	90.0	10.296	151.821	0.074	0.074	0.074	90.0	10.296	151.821	0.074	0.074	0.074
95.0	10.150	151.8	0.074	0.074	0.074	95.0	10.296	151.821	0.074	0.074	0.074	95.0	10.296	151.821	0.074	0.074	0.074	95.0	10.296	151.821	0.074	0.074	0.074

Table A-8. Blade-Element Data from Fixed Instrumentation, Near Stall Flutter, 70% Speed, Reading 56.

(1) Metric:

[illegible]

(1) **Notic**

(b) English

[illegible]

75% Speed, Reading 57.

[illegible]

Table A-11. Blade-Element Data from Fixed Instrumentation, Near Stall Flutter, 85% Speed, Reading 61.

(a) Metric

(b) English

PCT	RADIUS	MERID ANGLE	STREAM FUNCT	ABS ANGLE	REL ANGLE	PCT	RADIUS	MERID ANGLE	STREAM FUNCT	ABS ANGLE	REL ANGLE	PCT	RADIUS	MERID ANGLE	STREAM FUNCT	ABS ANGLE	REL ANGLE	PCT	RADIUS	MERID ANGLE	STREAM FUNCT	ABS ANGLE	REL ANGLE	
IN	OUT	IN	OUT	IN	OUT	IN	OUT	IN	OUT	IN	OUT	IN	OUT	IN	OUT	IN	OUT	IN	OUT	IN	OUT	IN	OUT	
5.0	26.15	25.13	0.061	0.070	71.4	68.5	5.0	10.296	10.021	-6.9	-7.9	0.061	0.070	71.4	68.5	5.0	10.296	10.021	-6.9	-7.9	0.061	0.070	71.4	68.5
10.0	26.11	24.95	0.126	0.141	46.9	45.0	10.0	9.976	9.723	-4.0	-5.9	0.126	0.141	46.9	45.0	10.0	9.976	9.723	-4.0	-5.9	0.126	0.141	46.9	45.0
15.0	26.08	24.92	0.194	0.211	45.0	43.0	15.0	9.649	9.431	-2.1	-4.0	0.194	0.211	45.0	43.0	15.0	9.649	9.431	-2.1	-4.0	0.194	0.211	45.0	43.0
20.0	26.05	24.89	0.262	0.280	43.0	41.0	20.0	9.322	9.104	0.0	1.9	0.262	0.280	43.0	41.0	20.0	9.322	9.104	0.0	1.9	0.262	0.280	43.0	41.0
25.0	26.02	24.86	0.330	0.348	41.0	39.0	25.0	8.995	8.777	2.1	4.0	0.330	0.348	41.0	39.0	25.0	8.995	8.777	2.1	4.0	0.330	0.348	41.0	39.0
30.0	25.99	24.83	0.398	0.416	39.0	37.0	30.0	8.668	8.450	4.2	6.1	0.398	0.416	39.0	37.0	30.0	8.668	8.450	4.2	6.1	0.398	0.416	39.0	37.0
35.0	25.96	24.80	0.466	0.484	37.0	35.0	35.0	8.337	8.119	6.3	8.2	0.466	0.484	37.0	35.0	35.0	8.337	8.119	6.3	8.2	0.466	0.484	37.0	35.0
40.0	25.93	24.77	0.534	0.552	35.0	33.0	40.0	8.006	7.788	8.4	10.3	0.534	0.552	35.0	33.0	40.0	8.006	7.788	8.4	10.3	0.534	0.552	35.0	33.0
45.0	25.90	24.74	0.602	0.620	33.0	31.0	45.0	7.675	7.457	10.5	12.4	0.602	0.620	33.0	31.0	45.0	7.675	7.457	10.5	12.4	0.602	0.620	33.0	31.0
50.0	25.87	24.71	0.670	0.688	31.0	29.0	50.0	7.344	7.126	12.6	14.5	0.670	0.688	31.0	29.0	50.0	7.344	7.126	12.6	14.5	0.670	0.688	31.0	29.0
55.0	25.84	24.68	0.738	0.756	29.0	27.0	55.0	7.013	6.795	14.7	16.6	0.738	0.756	29.0	27.0	55.0	7.013	6.795	14.7	16.6	0.738	0.756	29.0	27.0
60.0	25.81	24.65	0.806	0.824	27.0	25.0	60.0	6.682	6.464	16.8	18.7	0.806	0.824	27.0	25.0	60.0	6.682	6.464	16.8	18.7	0.806	0.824	27.0	25.0
65.0	25.78	24.62	0.874	0.892	25.0	23.0	65.0	6.351	6.133	18.9	20.8	0.874	0.892	25.0	23.0	65.0	6.351	6.133	18.9	20.8	0.874	0.892	25.0	23.0
70.0	25.75	24.59	0.942	0.960	23.0	21.0	70.0	6.020	5.802	21.0	22.9	0.942	0.960	23.0	21.0	70.0	6.020	5.802	21.0	22.9	0.942	0.960	23.0	21.0
75.0	25.72	24.56	1.010	1.028	21.0	19.0	75.0	5.689	5.471	23.1	25.0	1.010	1.028	21.0	19.0	75.0	5.689	5.471	23.1	25.0	1.010	1.028	21.0	19.0
80.0	25.69	24.53	1.078	1.096	19.0	17.0	80.0	5.358	5.140	25.2	27.1	1.078	1.096	19.0	17.0	80.0	5.358	5.140	25.2	27.1	1.078	1.096	19.0	17.0
85.0	25.66	24.50	1.146	1.164	17.0	15.0	85.0	5.027	4.809	27.3	29.2	1.146	1.164	17.0	15.0	85.0	5.027	4.809	27.3	29.2	1.146	1.164	17.0	15.0
90.0	25.63	24.47	1.214	1.232	15.0	13.0	90.0	4.696	4.478	29.4	31.3	1.214	1.232	15.0	13.0	90.0	4.696	4.478	29.4	31.3	1.214	1.232	15.0	13.0
95.0	25.60	24.44	1.282	1.300	13.0	11.0	95.0	4.365	4.147	31.5	33.4	1.282	1.300	13.0	11.0	95.0	4.365	4.147	31.5	33.4	1.282	1.300	13.0	11.0
100.0	25.57	24.41	1.350	1.368	11.0	9.0	100.0	4.034	3.816	33.6	35.5	1.350	1.368	11.0	9.0	100.0	4.034	3.816	33.6	35.5	1.350	1.368	11.0	9.0
105.0	25.54	24.38	1.418	1.436	9.0	7.0	105.0	3.703	3.485	35.7	37.6	1.418	1.436	9.0	7.0	105.0	3.703	3.485	35.7	37.6	1.418	1.436	9.0	7.0
110.0	25.51	24.35	1.486	1.504	7.0	5.0	110.0	3.372	3.154	37.8	39.7	1.486	1.504	7.0	5.0	110.0	3.372	3.154	37.8	39.7	1.486	1.504	7.0	5.0
115.0	25.48	24.32	1.554	1.572	5.0	3.0	115.0	3.041	2.823	39.9	41.8	1.554	1.572	5.0	3.0	115.0	3.041	2.823	39.9	41.8	1.554	1.572	5.0	3.0
120.0	25.45	24.29	1.622	1.640	3.0	1.0	120.0	2.710	2.492	42.0	43.9	1.622	1.640	3.0	1.0	120.0	2.710	2.492	42.0	43.9	1.622	1.640	3.0	1.0
125.0	25.42	24.26	1.690	1.708	1.0	-1.0	125.0	2.379	2.161	44.1	46.0	1.690	1.708	1.0	-1.0	125.0	2.379	2.161	44.1	46.0	1.690	1.708	1.0	-1.0
130.0	25.39	24.23	1.758	1.776	-1.0	-3.0	130.0	2.048	1.830	46.2	48.1	1.758	1.776	-1.0	-3.0	130.0	2.048	1.830	46.2	48.1	1.758	1.776	-1.0	-3.0
135.0	25.36	24.20	1.826	1.844	-3.0	-5.0	135.0	1.717	1.499	48.3	50.2	1.826	1.844	-3.0	-5.0	135.0	1.717	1.499	48.3	50.2	1.826	1.844	-3.0	-5.0
140.0	25.33	24.17	1.894	1.912	-5.0	-7.0	140.0	1.386	1.168	50.4	52.3	1.894	1.912	-5.0	-7.0	140.0	1.386	1.168	50.4	52.3	1.894	1.912	-5.0	-7.0
145.0	25.30	24.14	1.962	1.980	-7.0	-9.0	145.0	1.055	0.837	52.5	54.4	1.962	1.980	-7.0	-9.0	145.0	1.055	0.837	52.5	54.4	1.962	1.980	-7.0	-9.0
150.0	25.27	24.11	2.030	2.048	-9.0	-11.0	150.0	0.724	0.506	54.6	56.5	2.030	2.048	-9.0	-11.0	150.0	0.724	0.506	54.6	56.5	2.030	2.048	-9.0	-11.0
155.0	25.24	24.08	2.098	2.116	-11.0	-13.0	155.0	0.393	0.175	56.7	58.6	2.098	2.116	-11.0	-13.0	155.0	0.393	0.175	56.7	58.6	2.098	2.116	-11.0	-13.0
160.0	25.21	24.05	2.166	2.184	-13.0	-15.0	160.0	0.062	-0.156	58.8	60.7	2.166	2.184	-13.0	-15.0	160.0	0.062	-0.156	58.8	60.7	2.166	2.184	-13.0	-15.0
165.0	25.18	24.02	2.234	2.252	-15.0	-17.0	165.0	-0.269	-0.487	60.9	62.8	2.234	2.252	-15.0	-17.0	165.0	-0.269	-0.487	60.9	62.8	2.234	2.252	-15.0	-17.0
170.0	25.15	23.99	2.302	2.320	-17.0	-19.0	170.0	-0.538	-0.756	63.0	64.9	2.302	2.320	-17.0	-19.0	170.0	-0.538	-0.756	63.0	64.9	2.302	2.320	-17.0	-19.0
175.0	25.12	23.96	2.370	2.388	-19.0	-21.0	175.0	-0.807	-1.025	65.1	67.0	2.370	2.388	-19.0	-21.0	175.0	-0.807	-1.025	65.1	67.0	2.370	2.388	-19.0	-21.0
180.0	25.09	23.93	2.438	2.456	-21.0	-23.0	180.0	-1.076	-1.294	67.2	69.1	2.438	2.456	-21.0	-23.0	180.0	-1.076	-1.294	67.2	69.1	2.438	2.456	-21.0	-23.0
185.0	25.06	23.90	2.506	2.524	-23.0	-25.0	185.0	-1.345	-1.562	69.3	71.2	2.506	2.524	-23.0	-25.0	185.0	-1.345	-1.562	69.3	71.2	2.506	2.524	-23.0	-25.0
190.0	25.03	23.87	2.574	2.592	-25.0	-27.0	190.0	-1.614	-1.832	71.4	73.3	2.574	2.592	-25.0	-27.0	190.0	-1.614	-1.832	71.4	73.3	2.574	2.592	-25.0	-27.0
195.0	25.00	23.84	2.642	2.660	-27.0	-29.0	195.0	-1.883	-2.101	73.5	75.4	2.642	2.660	-27.0	-29.0	195.0	-1.883	-2.101	73.5	75.4	2.642	2.660	-27.0	-29.0
200.0	24.97	23.81	2.710	2.728	-29.0	-31.0	200.0	-2.152	-2.370	75.6	77.5	2.710	2.728	-29.0	-31.0	200.0	-2.152	-2.370	75.6	77.5	2.710	2.728	-29.0	-31.0
205.0	24.94	23.78	2.778	2.796	-31.0	-33.0	205.0	-2.421	-2.639	77.7	79.6	2.778	2.796	-31.0	-33.0	205.0	-2.421	-2.639	77.7	79.6	2.778	2.796	-31.0	-33.0
210.0	24.91	23.75	2.846	2.864	-33.0	-35.0	210.0	-2.690	-2.908	79.8	81.7	2.846	2.864	-33.0	-35.0	210.0	-2.690	-2.908	79.8	81.7	2.846	2.864	-33.0	-35.0
215.0	24.88	23.72	2.914	2.932	-35.0	-37.0	215.0	-2.959	-3.177	81.9	83.8	2.914	2.932	-35.0	-37.0	215.0	-2.959	-3.177	81.9	83.8	2.914	2.932	-35.0	-37.0
220.0	24.85	23.69	2.982	3.000	-37.0	-39.0	220.0	-3.228	-3.446	84.0	85.9	2.982	3.000	-37.0	-39.0	220.0	-3.228	-3.446	84.0	85.9	2.982	3.000	-37.0	-39.0
225.0	24.82	23.66	3.050	3.068	-39.0	-41.0	225.0	-3.497	-3.715	86.1	88.0	3.050	3.068	-39.0	-41.0	225.0	-3.497	-3.715	86.1	88.0	3.050	3.068	-39.0	-41.0
230.0	24.79	23.63	3.118	3.136	-41.0	-43.0	230.0	-3.766	-3.984	88.2	90.1	3.118	3.136	-41.0	-43.0	230.0	-3.766	-3.984	88.2	90.1	3.118	3.136	-41.0	-43.0
235.0	24.76	23.60	3.186	3.204	-43.0	-45.0	235.0	-4.035	-4.253	90.3	92.2	3.186	3.204	-43.0	-45.0	235.0	-4.035	-4.253	90.3	92.2	3.186	3.204	-43.0	-45.0
240.0	24.73	23.57	3.254	3.272	-45.0	-47.0	240.0	-4.304	-4.522	92.4	94.3	3.254	3.272	-45.0	-47.0	240.0	-4.304	-4.522	92.4	94.3	3.254	3.272	-45.0	-47.0
245.0	24.70	23.54	3.322	3.340	-47.0	-49.0	245.0	-4.573	-4.791	94.5	96.4	3.322	3.340	-47.0	-49.0	245.0								

Table A-13. Blade-Element Data from Fixed Instrumentation, Intermediate O.L., 90° Speed, Reading 176.

(a) Metric

PCT INM	RADIUS		MERID ANGLE	STREAM FUNC		ABS ANGLE	REL ANGLE		PCT INM
	IN	OUT		IN	OUT		IN	OUT	
5.0	16.15	25.453	-5.7	0.061	0.071	0.	44.3	61.2	5.0
10.0	16.33	24.695	-7.8	0.127	0.147	0.	44.3	54.9	10.0
15.0	24.507	23.954	-1.7	0.195	0.211	0.	42.7	59.0	15.0
20.0	21.971	21.788	4.1	0.260	0.401	0.	44.1	55.6	20.0
25.0	18.615	18.850	7.1	0.311	0.620	0.	47.3	62.5	25.0
30.0	16.925	17.401	9.2	0.367	0.713	0.	48.7	68.3	30.0
35.0	15.227	15.963	11.9	0.424	0.794	0.	49.6	74.6	35.0
40.0	13.474	14.500	16.3	0.472	0.877	0.	49.7	81.3	40.0
45.0	12.581	13.892	19.4	0.508	0.913	0.	49.3	87.4	45.0
50.0	11.666	13.236	21.8	0.541	0.945	0.	51.0	93.1	50.0
55.0	10.735	12.536	24.2	0.572	0.974	0.	53.6	98.6	55.0

PCT INM	ABS VEL		REL VEL	TANG VEL	BLADE SPEED	TANG VEL	REL VEL		PCT INM
	IN	OUT					IN	OUT	
5.0	18.1	20.13	414.2	208.6	143.1	139.9	0.	144.7	5.0
10.0	55.5	194.2	412.7	284.8	155.5	143.3	0.	139.1	10.0
15.0	154.7	196.0	412.4	280.6	154.7	144.0	0.	133.3	15.0
20.0	152.3	191.2	327.8	241.4	154.7	129.9	0.	140.3	20.0
25.0	152.9	194.3	195.1	182.2	152.8	129.9	0.	144.4	25.0
30.0	154.3	201.8	163.2	166.5	154.3	134.5	0.	150.6	30.0
35.0	154.7	213.9	161.0	155.2	154.7	140.5	0.	161.3	35.0
40.0	154.8	218.9	249.4	152.2	154.8	143.4	0.	165.4	40.0
45.0	151.6	224.9	235.8	145.8	151.6	142.3	0.	174.2	45.0
50.0	151.6	233.1	225.5	139.9	151.6	139.3	0.	186.8	50.0

PCT INM	ABS MACH NO		REL MACH NO	TOTAL PRES	TOTAL TEMP	TOTAL PRES	TOTAL TEMP		PCT INM
	IN	OUT					IN	OUT	
5.0	0.444	0.557	1.308	0.798	12.57	18.99	14.48	518.7	5.0
10.0	0.466	0.555	1.274	0.782	12.62	18.99	14.64	518.7	10.0
15.0	0.464	0.558	1.237	0.784	12.63	18.98	14.68	518.7	15.0
20.0	0.456	0.541	0.983	0.569	12.75	18.29	14.71	518.7	20.0
25.0	0.458	0.552	0.915	0.517	12.75	18.00	14.73	518.7	25.0
30.0	0.463	0.576	0.849	0.475	12.73	17.72	14.75	518.7	30.0
35.0	0.464	0.614	0.793	0.445	12.74	17.25	14.77	518.7	35.0
40.0	0.467	0.638	0.748	0.430	12.78	16.88	14.79	518.7	40.0
45.0	0.454	0.649	0.710	0.421	12.85	16.48	14.81	518.7	45.0
50.0	0.452	0.674	0.676	0.404	12.90	16.02	14.85	518.7	50.0

PCT INM	INCIDENCE		DEV	TURN D-FACT	LOSS COEFF	LOSS PARAM	EFFICIENCY	ADIA POLY	PCT INM
	ML	SS							
5.0	4.1	4.0	3.5	8.6	0.452	0.212	0.716	0.734	5.0
10.0	4.1	3.5	4.2	8.4	0.443	0.189	0.764	0.779	10.0
15.0	5.1	3.9	4.7	8.8	0.429	0.142	0.816	0.828	15.0
20.0	6.0	4.9	4.9	10.0	0.464	0.117	0.862	0.870	20.0
25.0	7.6	6.2	9.5	12.3	0.531	0.110	0.888	0.894	25.0
30.0	7.5	6.4	10.2	15.5	0.501	0.083	0.917	0.922	30.0
35.0	7.4	7.0	10.8	20.7	0.505	0.013	0.963	0.965	35.0
40.0	8.5	8.0	14.2	24.0	0.509	0.029	0.993	0.994	40.0
45.0	8.4	8.1	15.7	33.1	0.573	0.029	0.993	0.995	45.0
50.0	8.4	7.9	14.8	38.7	0.577	0.071	0.971	0.973	50.0
55.0	7.3	6.7	13.0	45.9	0.591	0.146	0.934	0.937	55.0

INLET CORR WTFLOW	PRESS RATIO	TEMP RATIO	ADIA EFF	INLET CORR RPM	ADIA EFF
0.733	1.5469	1.1549	0.858	14896.1	0.858

(b) English

PCT INM	RADIUS		MERID ANGLE	STREAM FUNC		ABS ANGLE	REL ANGLE		PCT INM
	IN	OUT		IN	OUT		IN	OUT	
5.0	18.296	18.021	-5.7	0.81	0.861	0.	45.3	70.2	5.0
10.0	9.976	9.723	-2.8	6.3	0.127	0.	45.3	68.5	10.0
15.0	9.649	9.431	-1.7	5.0	0.195	0.	42.7	68.0	15.0
20.0	8.658	8.575	3.1	3.3	0.399	0.	44.1	65.7	20.0
25.0	7.328	7.424	7.1	3.6	0.611	0.	47.3	62.5	25.0
30.0	6.664	6.851	9.2	6.8	0.787	0.	48.2	68.3	30.0
35.0	5.993	6.285	11.9	8.5	0.794	0.	48.6	74.6	35.0
40.0	5.386	5.735	16.3	7.2	0.872	0.	49.2	81.3	40.0
45.0	4.953	5.469	19.4	7.4	0.908	0.	49.3	87.4	45.0
50.0	4.593	5.211	21.8	7.9	0.941	0.	51.0	93.1	50.0
55.0	4.226	4.959	24.2	8.5	0.972	0.	53.6	98.6	55.0

PCT INM	ABS VEL		REL VEL	TANG VEL	BLADE SPEED	TANG VEL	REL VEL		PCT INM
	IN	OUT					IN	OUT	
5.0	485.8	660.4	1424.4	946.7	485.8	459.1	0.	474.8	5.0
10.0	510.1	655.3	1393.3	934.5	510.1	478.2	0.	456.2	10.0
15.0	507.6	645.8	1353.7	920.7	507.6	475.2	0.	437.4	15.0
20.0	507.5	639.7	1233.7	811.7	507.5	459.2	0.	445.3	20.0
25.0	499.6	627.3	1875.5	668.2	499.6	426.3	0.	468.2	25.0
30.0	501.2	637.3	1800.9	597.6	501.2	426.3	0.	473.9	30.0
35.0	506.1	662.0	929.1	546.4	506.1	448.6	0.	494.0	35.0
40.0	507.6	701.6	856.4	509.2	507.6	468.9	0.	525.0	40.0
45.0	505.1	710.0	810.4	499.5	505.1	470.4	0.	542.5	45.0
50.0	497.4	737.9	776.9	478.5	497.4	466.9	0.	571.5	50.0
55.0	495.2	764.8	739.8	459.8	495.2	457.1	0.	613.0	55.0

PCT INM	ABS MACH NO		REL MACH NO	TOTAL PRES	TOTAL TEMP	TOTAL PRES	TOTAL TEMP		PCT INM
	IN	OUT					IN	OUT	
5.0	0.444	0.557	1.308	0.798	12.57	18.99	14.48	518.7	5.0
10.0	0.466	0.555	1.274	0.782	12.62	18.99	14.64	518.7	10.0
15.0	0.464	0.558	1.237	0.784	12.63	18.98	14.68	518.7	15.0
20.0	0.456	0.541	0.983	0.569	12.75	18.29	14.71	518.7	20.0
25.0	0.458	0.552	0.915	0.517	12.75	18.00	14.73	518.7	25.0
30.0	0.463	0.576	0.849	0.475	12.73	17.72	14.75	518.7	30.0
35.0	0.464	0.614	0.793	0.445	12.74	17.25	14.77	518.7	35.0
40.0	0.467	0.638	0.748	0.430	12.78	16.88	14.79	518.7	40.0
45.0	0.454	0.649	0.710	0.421	12.85	16.48	14.81	518.7	45.0
50.0	0.452	0.674	0.676	0.404	12.90	16.02	14.85	518.7	50.0

PCT INM	INCIDENCE		DEV	TURN D-FACT	LOSS COEFF	LOSS PARAM	EFFICIENCY	ADIA POLY	PCT INM
	ML	SS							
5.0	4.1	4.0	3.5	8.6	0.452	0.212	0.716	0.734	5.0
10.0	4.1	3.5	4.2	8.4	0.443	0.189	0.764	0.779	10.0
15.0	5.1	3.9	4.7	8.8	0.429	0.142	0.816	0.828	15.0
20.0	6.0	4.9	4.9	10.0	0.464	0.117	0.862	0.870	20.0
25.0	7.6	6.2	9.5	12.3	0.531	0.110	0.888	0.894	25.0
30.0	7.5	6.4	10.2	15.5	0.501	0.083	0.917	0.922	30.0
35.0	7.4	7.0	10.8	20.7	0.505	0.013	0.963	0.965	35.0
40.0	8.5	8.0	14.2	24.0	0.509	0.029	0.993	0.994	40.0
45.0	8.4	8.1	15.7	33.1	0.573	0.029	0.993	0.995	45.0
50.0	8.4	7.9	14.8	38.7	0.577	0.071	0.971	0.973	50.0
55.0	7.3	6.7	13.0	45.9	0.591	0.146	0.934	0.937	55.0

INLET CORR WTFLOW	PRESS RATIO	TEMP RATIO	ADIA EFF	INLET CORR RPM	ADIA EFF
0.733	1.5469	1.1549	0.858	14896.1	0.858

Table A-14. Blade-Element Data from Fixed Instrumentation, At Stall Flutter, 90% Speed, Reading 169.

(a) Metric

PCT INM	RADIUS		MERID ANGLE		STREAM FUNCT		REL ANGLE		PCT OUTM
	IN	OUT	IN	OUT	IN	OUT	IN	OUT	
5.0	26.15	25.45	0.5	-0.3	0.401	0.867	71.8	72.4	5.0
10.0	25.13	24.69	4.0	-0.5	0.116	3.135	70.1	70.8	10.0
15.0	24.98	24.94	-1.0	-0.5	0.193	3.204	69.7	69.9	15.0
20.0	21.91	21.760	-2.1	-1.7	0.100	0.39	67.1	67.2	20.0
25.0	18.615	18.856	7.4	2.9	0.617	0.620	63.7	63.2	25.0
30.0	14.925	17.441	10.1	5.1	0.710	0.715	61.6	61.3	30.0
35.0	15.222	15.963	11.5	7.1	0.797	0.801	59.1	59.1	35.0
40.0	12.548	14.566	10.6	5.9	0.675	0.681	57.0	57.0	40.0
45.0	12.541	13.892	21.2	6.5	0.910	0.916	55.4	55.4	45.0
50.0	11.656	13.766	23.5	7.3	0.943	0.948	54.4	54.4	50.0
55.0	11.735	13.570	26.2	8.2	0.972	0.976	53.5	53.5	55.0

(b) English

PCT INM	RADIUS		MERID ANGLE		STREAM FUNCT		REL ANGLE		PCT OUTM
	IN	OUT	IN	OUT	IN	OUT	IN	OUT	
5.0	18.296	18.021	-6.5	-0.3	0.861	0.867	51.5	51.5	5.0
10.0	9.976	9.723	-4.0	-0.5	0.126	0.135	49.3	49.3	10.0
15.0	9.649	9.431	-3.0	-0.5	0.193	0.204	47.9	47.9	15.0
20.0	8.650	8.575	2.1	-1.7	0.300	0.307	46.2	46.2	20.0
25.0	7.328	7.424	7.4	2.9	0.612	0.620	44.9	44.9	25.0
30.0	6.664	6.851	10.1	5.1	0.710	0.715	43.7	43.7	30.0
35.0	5.993	6.285	13.5	7.1	0.797	0.801	42.8	42.8	35.0
40.0	5.366	5.735	16.6	5.9	0.675	0.681	41.4	41.4	40.0
45.0	4.953	5.459	21.2	6.5	0.910	0.916	40.1	40.1	45.0
50.0	4.593	5.211	23.5	7.3	0.943	0.948	38.8	38.8	50.0
55.0	4.226	4.959	25.2	8.2	0.972	0.976	37.6	37.6	55.0

PCT INM	REL VEL		TANG VEL		BLADE SPEED		ABS ANGLE		PCT OUTM
	IN	OUT	IN	OUT	IN	OUT	IN	OUT	
5.0	443.3	662.6	1410.3	898.2	443.3	415.6	515.0	1338.4	5.0
10.0	464.3	659.2	1377.3	878.7	464.3	431.5	515.0	1296.8	10.0
15.0	464.2	646.5	1337.5	864.7	464.2	434.7	478.5	1254.4	15.0
20.0	474.6	643.6	1220.5	788.5	474.6	445.7	464.2	1224.5	20.0
25.0	473.7	628.7	1063.8	631.0	473.7	405.2	480.6	952.6	25.0
30.0	476.3	640.7	908.7	567.4	476.3	405.1	495.5	866.2	30.0
35.0	479.6	664.4	914.9	517.6	479.6	420.1	514.7	779.1	35.0
40.0	472.8	690.3	836.3	481.0	472.8	437.3	545.1	689.8	40.0
45.0	465.5	714.6	794.5	468.8	465.5	437.1	565.3	643.9	45.0
50.0	453.1	737.3	749.5	437.9	453.1	431.2	598.2	597.1	50.0
55.0	449.3	768.8	709.9	414.6	449.3	412.6	645.6	549.4	55.0

PCT INM	ABS MACH NO		REL MACH NO		STATIC PRES		TOTAL PRES		PCT OUTM
	IN	OUT	IN	OUT	IN	OUT	IN	OUT	
5.0	0.483	0.555	1.283	0.745	12.98	19.44	14.44	23.96	5.0
10.0	0.423	0.555	1.255	0.739	12.95	19.39	14.55	23.91	10.0
15.0	0.423	0.547	1.219	0.731	12.95	19.35	14.65	23.72	15.0
20.0	0.433	0.550	1.113	0.673	12.98	19.12	14.68	23.48	20.0
25.0	0.434	0.553	0.970	0.542	12.94	18.95	14.71	22.67	25.0
30.0	0.438	0.577	0.835	0.490	12.92	18.23	14.72	22.43	30.0
35.0	0.431	0.610	0.762	0.428	12.92	17.98	14.74	22.42	35.0
40.0	0.424	0.625	0.724	0.403	13.06	17.35	14.77	22.31	40.0
45.0	0.412	0.646	0.682	0.384	13.16	16.56	14.78	22.10	45.0
50.0	0.409	0.673	0.646	0.364	13.22	16.09	14.83	21.94	50.0

PCT INM	INCIDENCE		DEV		TURN D-FACT		LOSS		PCT OUTM
	ML	SS	ML	SS	ML	SS	ML	SS	
5.0	6.4	5.6	4.7	9.2	0.497	0.497	0.252	0.252	5.0
10.0	6.1	5.3	5.0	9.4	0.489	0.489	0.229	0.229	10.0
15.0	6.9	5.6	5.6	9.7	0.478	0.478	0.198	0.198	15.0
20.0	7.4	6.3	4.9	11.4	0.466	0.466	0.123	0.123	20.0
25.0	8.0	7.4	9.7	13.3	0.501	0.501	0.027	0.027	25.0
30.0	8.0	7.7	10.1	17.0	0.594	0.594	0.184	0.184	30.0
35.0	9.0	8.5	10.2	22.9	0.618	0.618	0.067	0.067	35.0
40.0	10.7	10.2	11.7	31.7	0.618	0.618	0.052	0.052	40.0
45.0	11.1	10.7	14.4	36.7	0.615	0.615	0.078	0.078	45.0
50.0	11.3	10.6	12.5	43.5	0.673	0.673	0.129	0.129	50.0
55.0	10.2	9.7	8.7	52.7	0.646	0.646	0.220	0.220	55.0

PCT INM	EFFICIENCY		ADIA		POLY		LOSS		PCT OUTM
	ML	SS	ML	SS	ML	SS	ML	SS	
5.0	0.693	0.713	0.693	0.713	0.693	0.713	0.693	0.713	5.0
10.0	0.735	0.753	0.735	0.753	0.735	0.753	0.735	0.753	10.0
15.0	0.776	0.791	0.776	0.791	0.776	0.791	0.776	0.791	15.0
20.0	0.801	0.808	0.801	0.808	0.801	0.808	0.801	0.808	20.0
25.0	0.807	0.812	0.807	0.812	0.807	0.812	0.807	0.812	25.0
30.0	0.808	0.808	0.808	0.808	0.808	0.808	0.808	0.808	30.0
35.0	0.808	0.808	0.808	0.808	0.808	0.808	0.808	0.808	35.0
40.0	0.808	0.808	0.808	0.808	0.808	0.808	0.808	0.808	40.0
45.0	0.808	0.808	0.808	0.808	0.808	0.808	0.808	0.808	45.0
50.0	0.808	0.808	0.808	0.808	0.808	0.808	0.808	0.808	50.0
55.0	0.808	0.808	0.808	0.808	0.808	0.808	0.808	0.808	55.0

PCT INM	INLET CORR		PRESS		TEMP		INLET CORR		PCT OUTM
	W/FLOW	RPM	W/FLOW	RPM	W/FLOW	RPM	W/FLOW	RPM	
5.0	10.48	1.087	1.087	1.087	1.087	1.087	1.087	1.087	5.0
10.0	10.48	1.087	1.087	1.087	1.087	1.087	1.087	1.087	10.0
15.0	10.48	1.087	1.087	1.087	1.087	1.087	1.087	1.087	15.0
20.0	10.48	1.087	1.087	1.087	1.087	1.087	1.087	1.087	20.0
25.0	10.48	1.087	1.087	1.087	1.087	1.087	1.087	1.087	25.0
30.0	10.48	1.087	1.087	1.087	1.087	1.087	1.087	1.087	30.0
35.0	10.48	1.087	1.087	1.087	1.087	1.087	1.087	1.087	35.0
40.0	10.48	1.087	1.087	1.087	1.087	1.087	1.087	1.087	40.0
45.0	10.48	1.087	1.087	1.087	1.087	1.087	1.087	1.087	45.0
50.0	10.48	1.087	1.087	1.087	1.087	1.087	1.087	1.087	50.0
55.0	10.48	1.087	1.087	1.087	1.087	1.087	1.087	1.087	55.0

Table A-15. Blade-Element Data from Fixed Instrumentation, Below Peak Efficiency, 95% Speed, Reading 110.

(a) Metric

PCT INM	RADIUS		MERID ANGLE		STREAM FUNCT		ABS ANGLE		REL ANGLE		PCT		TANG VEL		BLADE SPEED		REL VEL		MERID VEL		STREAM FUNCT		ABS ANGLE		REL ANGLE	
	IN	OUT	IN	OUT	IN	OUT	IN	OUT	IN	OUT	INM	OUT	IN	OUT	IN	OUT	IN	OUT	IN	OUT	IN	OUT	IN	OUT	IN	OUT
5.0	26.152	25.453	-8.6	-7.5	0.054	0.062	0	0	69.9	61.3	5.0	5.0	10.296	10.021	-0.6	-7.5	0.054	0.062	0	0	69.9	61.3	0	0	69.9	61.3
10.0	25.319	24.695	-7.0	-5.3	0.113	0.125	0	0	33.7	61.7	10.0	10.0	9.976	9.723	-7.0	-5.3	0.113	0.125	0	0	33.7	61.7	0	0	33.7	61.7
15.0	24.509	23.954	-6.1	-4.0	0.176	0.187	0	0	33.7	61.7	15.0	15.0	9.649	9.431	-6.1	-4.0	0.176	0.187	0	0	33.7	61.7	0	0	33.7	61.7
20.0	23.721	23.200	-5.3	-3.3	0.235	0.246	0	0	33.7	61.7	20.0	20.0	9.350	9.155	-5.3	-3.3	0.235	0.246	0	0	33.7	61.7	0	0	33.7	61.7
25.0	22.971	22.486	-4.6	-2.6	0.292	0.303	0	0	33.7	61.7	25.0	25.0	9.080	8.900	-4.6	-2.6	0.292	0.303	0	0	33.7	61.7	0	0	33.7	61.7
30.0	22.251	21.799	-3.9	-1.9	0.348	0.359	0	0	33.7	61.7	30.0	30.0	8.830	8.660	-3.9	-1.9	0.348	0.359	0	0	33.7	61.7	0	0	33.7	61.7
35.0	21.561	21.136	-3.2	-1.2	0.401	0.412	0	0	33.7	61.7	35.0	35.0	8.590	8.430	-3.2	-1.2	0.401	0.412	0	0	33.7	61.7	0	0	33.7	61.7
40.0	20.901	20.499	-2.6	-0.6	0.454	0.465	0	0	33.7	61.7	40.0	40.0	8.360	8.210	-2.6	-0.6	0.454	0.465	0	0	33.7	61.7	0	0	33.7	61.7
45.0	20.271	19.889	-2.0	0.0	0.507	0.518	0	0	33.7	61.7	45.0	45.0	8.140	8.000	-2.0	0.0	0.507	0.518	0	0	33.7	61.7	0	0	33.7	61.7
50.0	19.681	19.319	-1.4	0.6	0.559	0.570	0	0	33.7	61.7	50.0	50.0	7.930	7.800	-1.4	0.6	0.559	0.570	0	0	33.7	61.7	0	0	33.7	61.7
55.0	19.131	18.789	-0.8	1.2	0.611	0.622	0	0	33.7	61.7	55.0	55.0	7.730	7.610	-0.8	1.2	0.611	0.622	0	0	33.7	61.7	0	0	33.7	61.7
60.0	18.621	18.299	-0.2	1.8	0.663	0.674	0	0	33.7	61.7	60.0	60.0	7.540	7.430	-0.2	1.8	0.663	0.674	0	0	33.7	61.7	0	0	33.7	61.7
65.0	18.151	17.839	0.4	2.4	0.715	0.726	0	0	33.7	61.7	65.0	65.0	7.360	7.260	0.4	2.4	0.715	0.726	0	0	33.7	61.7	0	0	33.7	61.7
70.0	17.721	17.429	1.0	3.0	0.767	0.778	0	0	33.7	61.7	70.0	70.0	7.190	7.100	1.0	3.0	0.767	0.778	0	0	33.7	61.7	0	0	33.7	61.7
75.0	17.331	17.059	1.6	3.6	0.819	0.830	0	0	33.7	61.7	75.0	75.0	7.030	6.950	1.6	3.6	0.819	0.830	0	0	33.7	61.7	0	0	33.7	61.7
80.0	16.981	16.729	2.2	4.2	0.871	0.882	0	0	33.7	61.7	80.0	80.0	6.880	6.810	2.2	4.2	0.871	0.882	0	0	33.7	61.7	0	0	33.7	61.7
85.0	16.671	16.439	2.8	4.8	0.923	0.934	0	0	33.7	61.7	85.0	85.0	6.740	6.680	2.8	4.8	0.923	0.934	0	0	33.7	61.7	0	0	33.7	61.7
90.0	16.401	16.179	3.4	5.4	0.975	0.986	0	0	33.7	61.7	90.0	90.0	6.610	6.560	3.4	5.4	0.975	0.986	0	0	33.7	61.7	0	0	33.7	61.7
95.0	16.171	15.959	4.0	6.0	1.027	1.038	0	0	33.7	61.7	95.0	95.0	6.490	6.450	4.0	6.0	1.027	1.038	0	0	33.7	61.7	0	0	33.7	61.7
100.0	16.000	15.800	4.6	6.6	1.079	1.090	0	0	33.7	61.7	100.0	100.0	6.380	6.350	4.6	6.6	1.079	1.090	0	0	33.7	61.7	0	0	33.7	61.7
105.0	15.870	15.680	5.2	7.2	1.131	1.142	0	0	33.7	61.7	105.0	105.0	6.280	6.260	5.2	7.2	1.131	1.142	0	0	33.7	61.7	0	0	33.7	61.7
110.0	15.780	15.600	5.8	7.8	1.183	1.194	0	0	33.7	61.7	110.0	110.0	6.190	6.180	5.8	7.8	1.183	1.194	0	0	33.7	61.7	0	0	33.7	61.7
115.0	15.730	15.560	6.4	8.4	1.235	1.246	0	0	33.7	61.7	115.0	115.0	6.110	6.110	6.4	8.4	1.235	1.246	0	0	33.7	61.7	0	0	33.7	61.7
120.0	15.700	15.540	7.0	9.0	1.287	1.298	0	0	33.7	61.7	120.0	120.0	6.040	6.050	7.0	9.0	1.287	1.298	0	0	33.7	61.7	0	0	33.7	61.7
125.0	15.690	15.540	7.6	9.6	1.339	1.350	0	0	33.7	61.7	125.0	125.0	5.980	6.000	7.6	9.6	1.339	1.350	0	0	33.7	61.7	0	0	33.7	61.7
130.0	15.700	15.560	8.2	10.2	1.391	1.402	0	0	33.7	61.7	130.0	130.0	5.930	6.000	8.2	10.2	1.391	1.402	0	0	33.7	61.7	0	0	33.7	61.7
135.0	15.730	15.600	8.8	10.8	1.443	1.454	0	0	33.7	61.7	135.0	135.0	5.890	6.000	8.8	10.8	1.443	1.454	0	0	33.7	61.7	0	0	33.7	61.7
140.0	15.780	15.660	9.4	11.4	1.495	1.506	0	0	33.7	61.7	140.0	140.0	5.860	6.000	9.4	11.4	1.495	1.506	0	0	33.7	61.7	0	0	33.7	61.7
145.0	15.850	15.740	10.0	12.0	1.547	1.558	0	0	33.7	61.7	145.0	145.0	5.840	6.000	10.0	12.0	1.547	1.558	0	0	33.7	61.7	0	0	33.7	61.7
150.0	15.940	15.840	10.6	12.6	1.599	1.610	0	0	33.7	61.7	150.0	150.0	5.830	6.000	10.6	12.6	1.599	1.610	0	0	33.7	61.7	0	0	33.7	61.7
155.0	16.050	15.960	11.2	13.2	1.651	1.662	0	0	33.7	61.7	155.0	155.0	5.830	6.000	11.2	13.2	1.651	1.662	0	0	33.7	61.7	0	0	33.7	61.7
160.0	16.180	16.100	11.8	13.8	1.693	1.704	0	0	33.7	61.7	160.0	160.0	5.840	6.000	11.8	13.8	1.693	1.704	0	0	33.7	61.7	0	0	33.7	61.7
165.0	16.330	16.260	12.4	14.4	1.735	1.746	0	0	33.7	61.7	165.0	165.0	5.860	6.000	12.4	14.4	1.735	1.746	0	0	33.7	61.7	0	0	33.7	61.7
170.0	16.500	16.440	13.0	15.0	1.777	1.788	0	0	33.7	61.7	170.0	170.0	5.890	6.000	13.0	15.0	1.777	1.788	0	0	33.7	61.7	0	0	33.7	61.7
175.0	16.690	16.640	13.6	15.6	1.819	1.830	0	0	33.7	61.7	175.0	175.0	5.930	6.000	13.6	15.6	1.819	1.830	0	0	33.7	61.7	0	0	33.7	61.7
180.0	16.900	16.860	14.2	16.2	1.861	1.872	0	0	33.7	61.7	180.0	180.0	5.980	6.000	14.2	16.2	1.861	1.872	0	0	33.7	61.7	0	0	33.7	61.7
185.0	17.130	17.100	14.8	16.8	1.893	1.904	0	0	33.7	61.7	185.0	185.0	6.040	6.000	14.8	16.8	1.893	1.904	0	0	33.7	61.7	0	0	33.7	61.7
190.0	17.380	17.360	15.4	17.4	1.925	1.936	0	0	33.7	61.7	190.0	190.0	6.110	6.000	15.4	17.4	1.925	1.936	0	0	33.7	61.7	0	0	33.7	61.7
195.0	17.650	17.640	16.0	18.0	1.957	1.968	0	0	33.7	61.7	195.0	195.0	6.190	6.000	16.0	18.0	1.957	1.968	0	0	33.7	61.7	0	0	33.7	61.7
200.0	17.940	17.940	16.6	18.6	1.989	1.999	0	0	33.7	61.7	200.0	200.0	6.280	6.000	16.6	18.6	1.989	1.999	0	0	33.7	61.7	0	0	33.7	61.7
205.0	18.250	18.260	17.2	19.2	2.021	2.032	0	0	33.7	61.7	205.0	205.0	6.380	6.000	17.2	19.2	2.021	2.032	0	0	33.7	61.7	0	0	33.7	61.7
210.0	18.580	18.600	17.8	19.8	2.053	2.064	0	0	33.7	61.7	210.0	210.0	6.490	6.000	17.8	19.8	2.053	2.064	0	0	33.7	61.7	0	0	33.7	61.7
215.0	18.930	18.960	18.4	20.4	2.085	2.096	0	0	33.7	61.7	215.0	215.0	6.610	6.000	18.4	20.4	2.085	2.096	0	0	33.7	61.7	0	0	33.7	61.7
220.0	19.300	19.340	19.0	21.0	2.117	2.12																				

Table A-16. Blade-Element Data from Fixed Instrumentation, Below Peak Efficiency, 95% Speed, Reading 117.

(b) English

(a) Metric

PCT	INM	RADIUS		MERID ANGLE	STREAM FUNCT		ABS ANGLE	REL ANGLE		PCT	INM	PCT	INM	RADIUS		MERID ANGLE	STREAM FUNCT		ABS ANGLE	REL ANGLE		PCT	INM
		IN	OUT		IN	OUT		IN	OUT					IN	OUT		IN	OUT		IN	OUT		
5.0	26.157	25.453	26.157	4.1	0.057	0.067	0.0	38.1	69.2	5.0	26.157	5.0	26.157	10.296	10.021	-0.1	-7.3	0.057	0.067	0.0	38.1	69.2	
10.0	25.114	24.645	25.114	4.9	0.110	0.134	0.0	38.1	69.2	10.0	25.114	10.0	25.114	9.976	9.723	-0.1	-4.9	0.110	0.134	0.0	38.1	69.2	
15.0	24.549	23.954	24.549	5.0	0.110	0.134	0.0	35.0	66.0	15.0	24.549	15.0	24.549	9.649	9.431	-0.1	-3.6	0.102	0.134	0.0	35.0	66.0	
30.0	21.971	21.788	21.971	1.5	0.172	0.381	0.0	35.0	66.0	30.0	21.971	30.0	21.971	8.658	8.575	-1.5	-0.2	0.172	0.381	0.0	35.0	66.0	
50.0	18.612	18.056	18.612	4.0	0.594	0.681	0.0	35.0	66.0	50.0	18.612	50.0	18.612	7.328	7.424	4.0	3.6	0.599	0.681	0.0	35.0	66.0	
60.0	16.925	17.401	16.925	4.0	0.594	0.681	0.0	35.0	66.0	60.0	16.925	60.0	16.925	6.664	6.051	7.2	5.6	0.599	0.681	0.0	35.0	66.0	
70.0	15.473	15.963	15.473	7.7	0.789	0.791	0.0	39.7	52.1	70.0	15.473	70.0	15.473	5.993	6.205	10.0	7.7	0.789	0.791	0.0	39.7	52.1	
80.0	13.473	14.566	13.473	6.4	0.869	0.871	0.0	41.2	49.4	80.0	13.473	80.0	13.473	5.306	5.735	10.0	6.4	0.865	0.873	0.0	41.2	49.4	
95.0	12.501	13.092	12.501	6.4	0.946	0.949	0.0	42.0	48.2	95.0	12.501	95.0	12.501	4.953	5.211	21.3	7.5	0.946	0.949	0.0	42.0	48.2	
98.0	11.606	12.216	11.606	21.3	0.946	0.949	0.0	43.4	47.1	98.0	11.606	98.0	11.606	4.593	5.211	21.3	7.5	0.946	0.949	0.0	43.4	47.1	
99.0	10.735	12.596	10.735	23.0	0.971	0.973	0.0	45.3	45.5	99.0	10.735	99.0	10.735	4.226	4.959	23.0	8.3	0.971	0.973	0.0	45.3	45.5	
PCT	INM	RADIUS		MERID ANGLE	STREAM FUNCT		ABS ANGLE	REL ANGLE		PCT	INM	PCT	INM	RADIUS		MERID ANGLE	STREAM FUNCT		ABS ANGLE	REL ANGLE		PCT	INM
IN	OUT	IN	OUT		IN	OUT		IN	OUT					IN	OUT		IN	OUT		IN	OUT		
5.0	166.1	242.1	166.1	464.9	338.4	166.1	159.6	124.8	434.8	427.4	5.0	166.1	166.1	545.1	663.2	1525.3	1110.1	545.1	523.6	407.8	1423.8	1385.7	
10.0	170.1	241.3	456.6	331.6	178.1	161.5	161.5	118.2	406.7	397.5	10.0	170.1	170.1	584.3	663.2	1525.3	1110.1	584.3	523.6	407.8	1423.8	1385.7	
15.0	182.1	199.9	445.5	324.4	187.1	163.9	163.9	114.9	364.6	361.4	15.0	182.1	182.1	625.7	654.4	1349.9	969.6	625.7	534.0	377.1	1196.2	1105.0	
30.0	190.7	199.5	411.5	295.5	190.7	163.9	163.9	114.9	364.6	361.4	30.0	190.7	190.7	658.2	676.4	1204.0	910.9	658.2	534.0	407.8	1196.2	1105.0	
50.0	198.7	208.2	367.0	249.6	190.2	164.2	164.2	111.1	280.9	248.0	50.0	198.7	198.7	655.9	674.6	1131.1	751.2	655.9	544.1	430.1	921.5	947.4	
60.0	199.9	211.4	344.0	220.4	194.9	165.0	165.0	110.3	252.6	248.0	60.0	199.9	199.9	657.4	674.6	1057.7	690.4	657.4	551.2	453.8	820.7	869.1	
70.0	200.4	217.6	322.4	248.4	200.4	166.0	166.0	109.1	223.7	241.7	70.0	200.4	200.4	657.4	674.6	981.0	640.6	657.4	565.9	492.6	733.0	793.0	
80.0	198.9	220.7	299.3	195.3	198.0	172.5	172.5	107.1	200.0	214.5	80.0	198.9	198.9	655.0	674.6	911.4	625.7	655.9	577.1	515.7	684.9	751.1	
95.0	193.1	241.1	273.4	184.2	193.1	175.9	175.9	104.9	193.6	219.6	95.0	193.1	193.1	643.6	674.6	841.0	604.3	643.6	577.1	541.2	635.1	720.4	
98.0	191.5	245.1	261.6	177.0	191.5	173.3	173.3	103.3	178.1	209.0	98.0	191.5	191.5	620.2	684.1	860.2	580.7	620.2	580.7	568.6	603.5	685.0	
PCT	INM	RADIUS		MERID ANGLE	STREAM FUNCT		ABS ANGLE	REL ANGLE		PCT	INM	PCT	INM	RADIUS		MERID ANGLE	STREAM FUNCT		ABS ANGLE	REL ANGLE		PCT	INM
IN	OUT	IN	OUT		IN	OUT		IN	OUT					IN	OUT		IN	OUT		IN	OUT		
5.0	0.500	0.504	0.500	1.399	0.943	0.29	12.54	9.86	15.56	200.2	349.4	5.0	0.500	0.504	1.399	0.943	12.93	10.19	14.30	22.87	510.7	612.6	
10.0	0.510	0.504	0.510	1.379	0.929	0.26	12.55	10.06	15.57	200.2	347.2	10.0	0.510	0.504	1.379	0.929	11.90	10.20	14.59	22.89	510.7	607.0	
15.0	0.551	0.505	0.510	1.340	0.912	0.20	12.56	10.04	15.53	200.2	334.2	15.0	0.551	0.505	1.340	0.912	11.50	10.21	14.59	22.93	510.7	601.6	
30.0	0.579	0.505	0.510	1.240	0.937	0.05	12.40	10.11	15.50	200.2	329.6	30.0	0.579	0.505	1.240	0.937	11.60	10.10	14.66	22.40	510.7	593.2	
50.0	0.603	0.500	0.510	1.116	0.712	7.94	12.24	10.15	15.46	200.2	327.1	50.0	0.603	0.500	1.116	0.712	11.61	17.76	14.73	22.43	510.7	580.7	
60.0	0.609	0.495	0.500	1.049	0.655	7.92	12.11	10.17	15.51	200.2	325.9	60.0	0.609	0.500	1.049	0.655	11.40	17.58	14.78	22.49	510.7	586.6	
70.0	0.610	0.525	0.500	0.982	0.685	7.97	11.99	10.10	15.61	200.2	324.7	70.0	0.610	0.525	0.982	0.685	11.40	17.58	14.78	22.49	510.7	584.4	
80.0	0.605	0.504	0.500	0.911	0.504	7.97	11.62	10.21	15.57	200.2	324.3	80.0	0.605	0.504	0.911	0.504	11.56	16.05	14.81	22.58	510.7	583.0	
95.0	0.599	0.493	0.500	0.873	0.582	8.02	11.33	10.23	15.49	200.2	324.3	95.0	0.599	0.493	0.873	0.582	11.64	16.43	14.83	22.46	510.7	583.7	
98.0	0.586	0.700	0.500	0.830	0.534	8.11	11.01	10.25	15.24	200.2	324.3	98.0	0.586	0.700	0.830	0.534	11.77	15.97	14.86	22.15	510.7	583.7	
99.0	0.581	0.712	0.500	0.794	0.514	8.10	10.67	10.25	15.24	200.2	324.3	99.0	0.581	0.712	0.794	0.514	11.06	15.40	14.92	21.72	510.7	583.7	
PCT	INM	RADIUS		MERID ANGLE	STREAM FUNCT		ABS ANGLE	REL ANGLE		PCT	INM	PCT	INM	RADIUS		MERID ANGLE	STREAM FUNCT		ABS ANGLE	REL ANGLE		PCT	INM
IN	OUT	IN	OUT		IN	OUT		IN	OUT					IN	OUT		IN	OUT		IN	OUT		
5.0	3.5	3.1	3.5	4.3	0.365	0.173	0.029	0.716	0.733	6.9	0.365	5.0	3.5	3.1	3.5	4.3	0.365	0.173	0.029	0.716	0.733		
10.0	2.9	2.1	2.9	5.2	0.384	0.159	0.018	0.762	0.776	6.2	0.384	10.0	2.9	2.1	2.9	5.2	0.384	0.159	0.029	0.762	0.776		
15.0	3.2	1.9	3.2	5.9	0.360	0.126	0.022	0.808	0.819	5.9	0.360	15.0	3.2	1.9	3.2	5.9	0.360	0.126	0.022	0.808	0.819		
30.0	2.7	1.6	2.7	5.9	0.378	0.088	0.013	0.808	0.844	5.7	0.378	30.0	2.7	1.6	2.7	5.9	0.378	0.088	0.013	0.808	0.844		
50.0	2.4	1.1	2.4	8.5	0.437	0.041	0.004	0.852	0.955	8.3	0.437	50.0	2.4	1.1	2.4	8.5	0.437	0.041	0.004	0.852	0.955		
60.0	2.1	0.9	2.1	9.5	0.461	0.016	0.004	0.909	0.989	9.5	0.461	60.0	2.1	0.9	2.1	9.5	0.461	0.016	0.004	0.909	0.989		
70.0	1.9	1.5	1.9	11.5	0.496	-0.022	-0.006	1.017	1.075	11.5	0.496	70.0	1.9	1.5	1.9	11.5	0.496	-0.022	-0.006	1.017	1.075		
80.0	3.1	2.7	3.1	21.0	0.496	-0.022	-0.006	1.042	1.040	21.0	0.496	80.0	3.1	2.7	3.1	21.0	0.496	-0.022	-0.006	1.042	1.040		
95.0	3.5	2.9	3.5	25.0	0.407	-0.007	-0.002	1.011	1.079	25.0	0.407	95.0	3.5	2.9	3.5	25.0	0.407	-0.007	-0.002	1.011	1.079		
98.0	3.2	2.7	3.2	29.3	0.484	0.016	0.009	0.998	0.998	29.3	0.484	98.0	3.2	2.7	3.2	29.3	0.484	0.016	0.009	0.998	0.998		
99.0	2.7	1.6	2.7	20.0	0.492	0.016	0.006	0.946	0.949	20.0	0.492	99.0	2.7	1.6	2.7	20.0	0.492	0.016	0.006	0.946	0.949		
PCT	INM	RADIUS		MERID ANGLE	STREAM FUNCT		ABS ANGLE	REL ANGLE		PCT	INM	PCT	INM	RADIUS		MERID ANGLE	STREAM FUNCT		ABS ANGLE	REL ANGLE		PCT	INM
IN	OUT	IN	OUT		IN	OUT		IN	OUT					IN	OUT		IN	OUT		IN	OUT		
5.0	15046.4	15046.4	15046.4	15046.4	15046.4	15046.4	15046.4	15046.4	15046.4	15046.4	15046.4	5.0	15046.4	15046.4	15046.4	15046.4	15046.4	15046.4	15046.4	15046.4	15046.4	15046.4	
10.0	15046.4	15046.4	15046.4	15046.4	15046.4	15046.4	15046.4	15046.4	15046.4	15046.4	15046.4	10.0	15046.4	15046.4	15046.4	15046.4	15046.4	15046.4	15046.4	15046.4	15046.46		

Table A-17. Blade-Element Data from Fixed Instrumentation, Intermediate O.L.,
95% Speed, Reading 151.

(a) Metric

PCT INM	RADIUS		MERID ANGLE	STREAM FUNCT		ABS ANGLE	REL ANGLE		PCT INM	RADIUS		MERID ANGLE	STREAM FUNCT		ABS ANGLE	REL ANGLE		PCT INM
	IN	OUT		IN	OUT		IN	OUT		IN	OUT		IN	OUT		IN	OUT	
5.0	26.15	25.453	-6.7	-0.1	0.063	0.471	0	69.9	61.4	10.296	10.021	-6.7	-0.1	0.063	0.471	0	69.9	61.4
10.0	25.319	24.695	-3.7	-6.2	0.130	0.143	0	64.4	54.9	9.976	9.723	-3.7	-6.2	0.130	0.143	0	64.4	54.9
15.0	24.509	23.954	-1.9	-4.9	0.199	0.214	0	67.7	58.9	9.649	9.413	-1.9	-4.9	0.199	0.214	0	67.7	58.9
20.0	23.709	23.200	-0.7	-0.7	0.268	0.283	0	65.5	55.0	9.328	9.075	-0.7	-0.7	0.268	0.283	0	65.5	55.0
25.0	22.912	22.456	0.5	4.5	0.337	0.352	0	63.7	53.4	9.008	8.755	0.5	4.5	0.337	0.352	0	63.7	53.4
30.0	22.120	21.701	1.8	7.8	0.406	0.421	0	62.0	51.7	8.688	8.435	1.8	7.8	0.406	0.421	0	62.0	51.7
35.0	21.332	20.943	3.1	10.9	0.475	0.490	0	60.3	49.9	8.368	8.115	3.1	10.9	0.475	0.490	0	60.3	49.9
40.0	20.548	20.190	4.4	14.0	0.544	0.559	0	58.6	48.1	8.048	7.795	4.4	14.0	0.544	0.559	0	58.6	48.1
45.0	19.768	19.440	5.7	17.1	0.613	0.628	0	56.9	46.4	7.728	7.475	5.7	17.1	0.613	0.628	0	56.9	46.4
50.0	18.992	18.693	7.0	20.2	0.682	0.697	0	55.2	44.7	7.408	7.155	7.0	20.2	0.682	0.697	0	55.2	44.7
55.0	18.220	17.941	8.3	23.3	0.751	0.766	0	53.5	43.0	7.088	6.835	8.3	23.3	0.751	0.766	0	53.5	43.0
60.0	17.452	17.193	9.6	26.4	0.820	0.835	0	51.8	41.3	6.768	6.515	9.6	26.4	0.820	0.835	0	51.8	41.3
65.0	16.688	16.449	10.9	29.5	0.889	0.904	0	50.1	39.6	6.448	6.195	10.9	29.5	0.889	0.904	0	50.1	39.6
70.0	15.928	15.699	12.2	32.6	0.958	0.973	0	48.4	37.9	6.128	5.875	12.2	32.6	0.958	0.973	0	48.4	37.9
75.0	15.172	14.953	13.5	35.7	1.027	1.042	0	46.7	36.2	5.808	5.555	13.5	35.7	1.027	1.042	0	46.7	36.2
80.0	14.420	14.211	14.8	38.8	1.096	1.111	0	45.0	34.5	5.488	5.235	14.8	38.8	1.096	1.111	0	45.0	34.5
85.0	13.672	13.473	16.1	41.9	1.165	1.180	0	43.3	32.8	5.168	4.915	16.1	41.9	1.165	1.180	0	43.3	32.8
90.0	12.928	12.739	17.4	45.0	1.234	1.249	0	41.6	31.1	4.848	4.595	17.4	45.0	1.234	1.249	0	41.6	31.1
95.0	12.188	12.009	18.7	48.1	1.303	1.318	0	39.9	29.4	4.528	4.275	18.7	48.1	1.303	1.318	0	39.9	29.4

(b) English

PCT INM	RADIUS		MERID ANGLE	STREAM FUNCT		ABS ANGLE	REL ANGLE		PCT INM	RADIUS		MERID ANGLE	STREAM FUNCT		ABS ANGLE	REL ANGLE		PCT INM
	IN	OUT		IN	OUT		IN	OUT		IN	OUT		IN	OUT		IN	OUT	
5.0	106.15	104.53	-6.7	-0.1	0.063	0.471	0	69.9	61.4	10.296	10.021	-6.7	-0.1	0.063	0.471	0	69.9	61.4
10.0	104.319	102.695	-3.7	-6.2	0.130	0.143	0	64.4	54.9	9.976	9.723	-3.7	-6.2	0.130	0.143	0	64.4	54.9
15.0	102.489	100.954	-1.9	-4.9	0.199	0.214	0	67.7	58.9	9.649	9.413	-1.9	-4.9	0.199	0.214	0	67.7	58.9
20.0	100.659	99.200	-0.7	-0.7	0.268	0.283	0	65.5	55.0	9.328	9.075	-0.7	-0.7	0.268	0.283	0	65.5	55.0
25.0	98.820	97.456	0.5	4.5	0.337	0.352	0	63.7	53.4	9.008	8.755	0.5	4.5	0.337	0.352	0	63.7	53.4
30.0	96.972	95.701	1.8	7.8	0.406	0.421	0	62.0	51.7	8.688	8.435	1.8	7.8	0.406	0.421	0	62.0	51.7
35.0	95.120	93.943	3.1	10.9	0.475	0.490	0	60.3	49.9	8.368	8.115	3.1	10.9	0.475	0.490	0	60.3	49.9
40.0	93.268	92.140	4.4	14.0	0.544	0.559	0	58.6	48.1	8.048	7.795	4.4	14.0	0.544	0.559	0	58.6	48.1
45.0	91.412	90.335	5.7	17.1	0.613	0.628	0	56.9	46.4	7.728	7.475	5.7	17.1	0.613	0.628	0	56.9	46.4
50.0	89.552	88.528	7.0	20.2	0.682	0.697	0	55.2	44.7	7.408	7.155	7.0	20.2	0.682	0.697	0	55.2	44.7
55.0	87.688	86.715	8.3	23.3	0.751	0.766	0	53.5	43.0	7.088	6.835	8.3	23.3	0.751	0.766	0	53.5	43.0
60.0	85.828	84.905	9.6	26.4	0.820	0.835	0	51.8	41.3	6.768	6.515	9.6	26.4	0.820	0.835	0	51.8	41.3
65.0	83.968	83.095	10.9	29.5	0.889	0.904	0	50.1	39.6	6.448	6.195	10.9	29.5	0.889	0.904	0	50.1	39.6
70.0	82.108	81.285	12.2	32.6	0.958	0.973	0	48.4	37.9	6.128	5.875	12.2	32.6	0.958	0.973	0	48.4	37.9
75.0	80.248	79.475	13.5	35.7	1.027	1.042	0	46.7	36.2	5.808	5.555	13.5	35.7	1.027	1.042	0	46.7	36.2
80.0	78.388	77.665	14.8	38.8	1.096	1.111	0	45.0	34.5	5.488	5.235	14.8	38.8	1.096	1.111	0	45.0	34.5
85.0	76.528	75.855	16.1	41.9	1.165	1.180	0	43.3	32.8	5.168	4.915	16.1	41.9	1.165	1.180	0	43.3	32.8
90.0	74.668	74.045	17.4	45.0	1.234	1.249	0	41.6	31.1	4.848	4.595	17.4	45.0	1.234	1.249	0	41.6	31.1
95.0	72.808	72.235	18.7	48.1	1.303	1.318	0	39.9	29.4	4.528	4.275	18.7	48.1	1.303	1.318	0	39.9	29.4

INLET CORR
RPM
15746.5

ADIA
EFF
0.062

TEMP
RATIO
1.1000

PRESS
RATIO
1.6558

INLET CORR
W/FLOW
74.59

DEV
TURN
0.393

LOSS
PARAM
0.037

ADIA
EFF
0.062

TEMP
RATIO
1.1000

INLET CORR
W/FLOW
74.59

DEV
TURN
0.393

LOSS
PARAM
0.037

ADIA
EFF
0.062

Table A-18. Blade-Element Data from Fixed Instrumentation, Near Stall Flutter, 95% Speed, Reading 63.

(a) Metric

PCT INM	RADIUS		MERID ANGLE		STREAM FUNCT		ABS ANGLE		REL ANGLE		PCT INM	RADIUS		MERID ANGLE		STREAM FUNCT		ABS ANGLE		REL ANGLE	
	IN	OUT	IN	OUT	IN	OUT	IN	OUT	IN	OUT		IN	OUT	IN	OUT	IN	OUT	IN	OUT	IN	OUT
5.0	26.15	25.453	-7.3	-0.0	0.067	0.073	0	52.1	70.5	58.5	5.0	10.296	10.021	-7.3	-0.0	0.067	0.073	0	52.1	70.5	58.5
10.0	5.31	24.645	-4.0	-6.1	0.134	0.140	0	50.0	69.7	57.5	10.0	9.949	9.723	-4.0	-6.1	0.134	0.140	0	50.0	69.7	57.5
15.0	4.30	23.954	-1.3	-4.0	0.202	0.221	0	50.0	69.1	57.5	15.0	9.646	9.431	-1.3	-4.0	0.202	0.221	0	50.0	69.1	57.5
30.0	21.971	21.780	3.6	-1.5	0.394	0.408	0	51.7	63.9	49.3	30.0	0.650	0.578	3.6	-1.5	0.394	0.408	0	51.7	63.9	49.3
50.0	6.1	10.856	7.3	2.5	0.613	0.618	0	51.4	63.9	49.3	50.0	7.328	7.424	7.3	2.5	0.613	0.618	0	51.4	63.9	49.3
60.0	16.55	17.401	9.6	4.4	0.789	0.797	0	52.7	61.5	43.5	60.0	6.664	6.081	9.6	4.4	0.789	0.797	0	52.7	61.5	43.5
70.0	15.22	15.962	12.4	6.0	0.789	0.797	0	54.2	58.9	36.2	70.0	5.993	5.205	12.4	6.0	0.789	0.797	0	54.2	58.9	36.2
80.0	13.478	14.566	16.9	4.7	0.873	0.869	0	51.0	56.2	34.0	80.0	5.306	5.735	16.9	4.7	0.873	0.869	0	51.0	56.2	34.0
90.0	12.501	13.492	19.7	5.4	0.909	0.905	0	50.5	55.0	32.4	90.0	4.953	5.469	19.7	5.4	0.909	0.905	0	50.5	55.0	32.4
95.0	11.663	13.116	22.3	6.3	0.941	0.940	0	51.5	54.0	31.6	95.0	4.593	5.211	22.3	6.3	0.941	0.940	0	51.5	54.0	31.6
95.0	10.735	12.596	24.4	7.6	0.972	0.971	0	52.9	52.2	31.5	95.0	4.226	4.959	24.4	7.6	0.972	0.971	0	52.9	52.2	31.5
PCT INM	RADIUS		MERID ANGLE		STREAM FUNCT		ABS ANGLE		REL ANGLE		PCT INM	RADIUS		MERID ANGLE		STREAM FUNCT		ABS ANGLE		REL ANGLE	
	IN	OUT	IN	OUT	IN	OUT	IN	OUT	IN	OUT		IN	OUT	IN	OUT	IN	OUT	IN	OUT	IN	OUT
5.0	134.3	230.3	459.6	277.4	154.3	146.0	0	185.6	432.9	471.4	5.0	506.3	775.4	1500.0	918.2	505.3	479.1	0	600.9	1420.4	1302.5
10.0	155.4	230.9	447.5	275.9	155.0	146.9	0	176.5	419.5	460.0	10.0	511.3	757.6	1460.1	905.2	511.3	408.7	0	579.2	1376.2	1341.2
15.0	155.1	221.5	424.5	267.7	155.1	144.0	0	170.9	405.7	376.6	15.0	508.0	733.3	1425.1	898.2	508.0	472.5	0	560.0	1331.2	1301.8
30.0	152.1	208.6	394.2	235.5	152.1	129.3	0	163.7	363.7	309.6	30.0	499.0	684.4	129.4	772.6	499.0	424.2	0	537.1	1193.3	1103.0
50.0	153.9	209.9	319.7	176.1	153.9	128.3	0	163.6	308.1	312.2	50.0	500.0	682.1	112.7	633.7	500.0	421.0	0	536.0	1010.9	1024.1
70.0	155.7	211.3	296.2	155.4	155.7	125.3	0	172.6	252.0	240.3	70.0	505.0	680.4	1049.0	577.9	505.0	417.0	0	547.1	919.3	945.1
80.0	156.1	228.4	272.3	137.5	156.1	144.0	0	177.3	223.1	241.1	80.0	510.7	699.9	971.0	509.0	510.7	411.3	0	566.3	826.0	867.0
90.0	154.9	234.0	259.5	157.2	154.9	149.2	0	180.3	200.3	230.0	90.0	512.1	749.4	893.4	516.0	512.1	472.4	0	591.6	732.0	791.1
95.0	151.9	238.1	245.6	152.3	151.9	149.2	0	186.0	193.1	219.1	95.0	500.0	767.9	851.5	515.9	500.0	409.6	0	630.1	633.6	710.9
95.0	151.4	244.7	233.3	149.2	151.4	140.4	0	194.6	177.7	208.5	95.0	495.0	802.0	785.5	489.5	495.0	407.0	0	630.3	503.1	604.1
PCT INM	RADIUS		MERID ANGLE		STREAM FUNCT		ABS ANGLE		REL ANGLE		PCT INM	RADIUS		MERID ANGLE		STREAM FUNCT		ABS ANGLE		REL ANGLE	
	IN	OUT	IN	OUT	IN	OUT	IN	OUT	IN	OUT		IN	OUT	IN	OUT	IN	OUT	IN	OUT	IN	OUT
5.0	0.487	0.941	1.379	0.753	0.64	14.14	10.00	18.64	208.2	306.0	5.0	0.463	0.641	1.379	0.753	12.52	20.51	14.51	27.04	510.7	650.0
10.0	0.401	0.811	1.343	0.754	0.60	14.00	10.00	18.40	208.2	306.0	10.0	0.468	0.631	1.343	0.754	12.59	20.42	14.62	26.69	510.7	648.0
15.0	0.405	0.813	1.303	0.734	0.60	14.01	10.00	18.00	208.2	305.7	15.0	0.465	0.613	1.303	0.734	12.51	20.32	14.63	26.19	510.7	648.0
30.0	0.457	0.577	1.102	0.651	0.78	13.71	10.12	17.17	208.2	339.1	30.0	0.456	0.577	1.102	0.651	12.73	19.00	14.68	24.91	510.7	624.5
50.0	0.457	0.582	1.030	0.549	0.79	13.17	10.14	16.57	208.2	339.1	50.0	0.457	0.582	1.030	0.549	12.75	19.10	14.71	24.03	510.7	610.3
60.0	0.462	0.591	0.959	0.496	0.77	12.09	10.16	16.32	208.2	336.0	60.0	0.462	0.591	0.959	0.496	12.73	18.70	14.73	23.67	510.7	610.3
70.0	0.467	0.603	0.889	0.439	0.76	12.62	10.17	16.14	208.2	333.6	70.0	0.467	0.603	0.889	0.439	12.70	18.30	14.75	23.41	510.7	600.5
80.0	0.469	0.602	0.817	0.450	0.77	12.21	10.14	16.14	208.2	330.8	80.0	0.468	0.602	0.817	0.450	12.72	17.71	14.78	23.57	510.7	595.4
90.0	0.463	0.611	0.779	0.451	0.80	11.94	10.20	16.15	208.2	329.5	90.0	0.465	0.611	0.779	0.451	12.76	17.31	14.80	23.42	510.7	593.1
95.0	0.453	0.605	0.736	0.430	0.86	11.64	10.21	15.93	208.2	320.0	95.0	0.455	0.605	0.736	0.430	12.65	16.80	14.82	23.11	510.7	591.0
95.0	0.453	0.706	0.699	0.430	0.89	11.30	10.22	15.76	208.2	320.6	95.0	0.453	0.706	0.699	0.430	12.90	16.30	14.85	23.11	510.7	591.5
PCT INM	RADIUS		MERID ANGLE		STREAM FUNCT		ABS ANGLE		REL ANGLE		PCT INM	RADIUS		MERID ANGLE		STREAM FUNCT		ABS ANGLE		REL ANGLE	
	IN	OUT	IN	OUT	IN	OUT	IN	OUT	IN	OUT		IN	OUT	IN	OUT	IN	OUT	IN	OUT	IN	OUT
5.0	4.4	4.4	9.0	11.9	0.539	0.539	0	11.9	0.539	0.539	5.0	4.4	4.4	0.0	11.9	0.539	0.539	0	11.9	0.539	0.539
10.0	5.4	4.6	1.7	12.1	0.521	0.521	0	12.1	0.521	0.521	10.0	5.4	4.6	1.7	12.1	0.521	0.521	0	12.1	0.521	0.521
15.0	6.1	5.0	3.2	11.5	0.510	0.510	0	11.5	0.510	0.510	15.0	6.1	5.0	3.2	11.5	0.510	0.510	0	11.5	0.510	0.510
30.0	7.0	7.6	6.1	10.4	0.545	0.545	0	10.4	0.545	0.545	30.0	7.0	7.6	6.1	10.4	0.545	0.545	0	10.4	0.545	0.545
50.0	8.4	7.7	9.4	14.0	0.592	0.592	0	14.0	0.592	0.592	50.0	8.4	7.7	9.4	14.0	0.592	0.592	0	14.0	0.592	0.592
60.0	9.3	10.5	22.9	32.9	0.669	0.669	0	32.9	0.669	0.669	60.0	9.3	10.5	22.9	32.9	0.669	0.669	0	32.9	0.669	0.669
70.0	9.9	9.4	12.9	32.7	0.617	0.617	0	32.7	0.617	0.617	70.0	9.9	9.4	12.9	32.7	0.617	0.617	0	32.7	0.617	0.617
80.0	10.3	14.3	36.9	35.9	0.590	0.590	0	35.9	0.590	0.590	80.0	10.3	14.3	36.9	35.9	0.590	0.590	0	35.9	0.590	0.590
90.0	10.1	9.6	14.5	41.6	0.503	0.503	0	41.6	0.503	0.503	90.0	10.1	9.6	14.5	41.6	0.503	0.503	0	41.6	0.503	0.503
95.0	9.4	8.4	14.5	46.0	0.575	0.575	0	46.0	0.575	0.575	95.0	9.4	8.4	14.5	46.0	0.575	0.575	0	46.0	0.575	0.575
PCT INM	RADIUS		MERID ANGLE		STREAM FUNCT		ABS ANGLE		REL ANGLE		PCT INM	RADIUS		MERID ANGLE		STREAM FUNCT		ABS ANGLE		REL ANGLE	
	IN	OUT	IN	OUT	IN	OUT	IN	OUT	IN	OUT		IN	OUT	IN	OUT	IN	OUT	IN	OUT	IN	OUT
5.0	0.817	0.817	1.6095	1.1902	0.817	0.817	0	1.6095	1.1902	1.1902	5.0	0.817	0.817	1.6095	1.1902	0.817	0.817	0	1.6095	1.1902	1.1902
10.0	0.817	0.817	1.6095	1.1902	0.817	0.817	0	1.6095	1.1902	1.1902	10.0	0.817	0.817	1.6095	1.1902	0.817	0.817	0	1.6095	1.1902	1.1902
15.0	0.817	0.817	1.6095	1.1902	0.817	0.817	0	1.6095	1.1902	1.1902	15.0	0.817	0.817	1.6095	1.1902	0.817	0.817	0	1.6095	1.1902	1.1902
30.0	0.817	0.817	1.6095	1.1902	0.817	0.817	0	1.6095	1.1902	1.1902	30.0	0.817	0.817	1.6095	1.1902	0.817	0.817	0	1.6095	1.1902	1.1902
50.0	0.817	0.817	1.6095	1.1902	0.817	0.817	0	1.6095	1.1902	1.1902	50.0	0.817	0.817	1.6095	1.1902	0.817	0.817	0	1.6095	1.1902	1.1902
60.0	0.817	0.817	1.6095	1.1902	0.817	0.817	0	1.6095	1.1902	1.1902	60.0	0.817	0.817	1.6095	1.1902	0.817	0.817	0	1.6095	1.1902	1.1902
70.0	0.817	0.817	1.6095	1.1902	0.817	0.817	0	1.6095	1.1902	1.1902	70.0	0.817	0.817	1.6095	1.1902	0.817	0.817	0	1.6095	1.1902	1.1902
80.0	0.817	0.817	1.6095	1.1902	0.817	0.817	0	1.6095	1.1902	1.1902	80.0	0.817	0.817	1.6095	1.1902	0.817	0.817	0	1.6095	1.1902	1.1902
90.0	0.817	0.817	1.6095	1.1902	0.817	0.817	0	1.6095	1.1902	1.1902	90.0	0.817	0.817	1.6095	1.1902	0.817	0.817	0	1.6095	1.1902	1.1902
95.0	0.817	0.817	1.6095	1.1902	0.817	0.817	0	1.6095	1.1902	1.1902	95.0	0.817	0.817	1.6095	1.1902	0.817	0.817	0			

Table A-19.

(b) English

(a) Metric

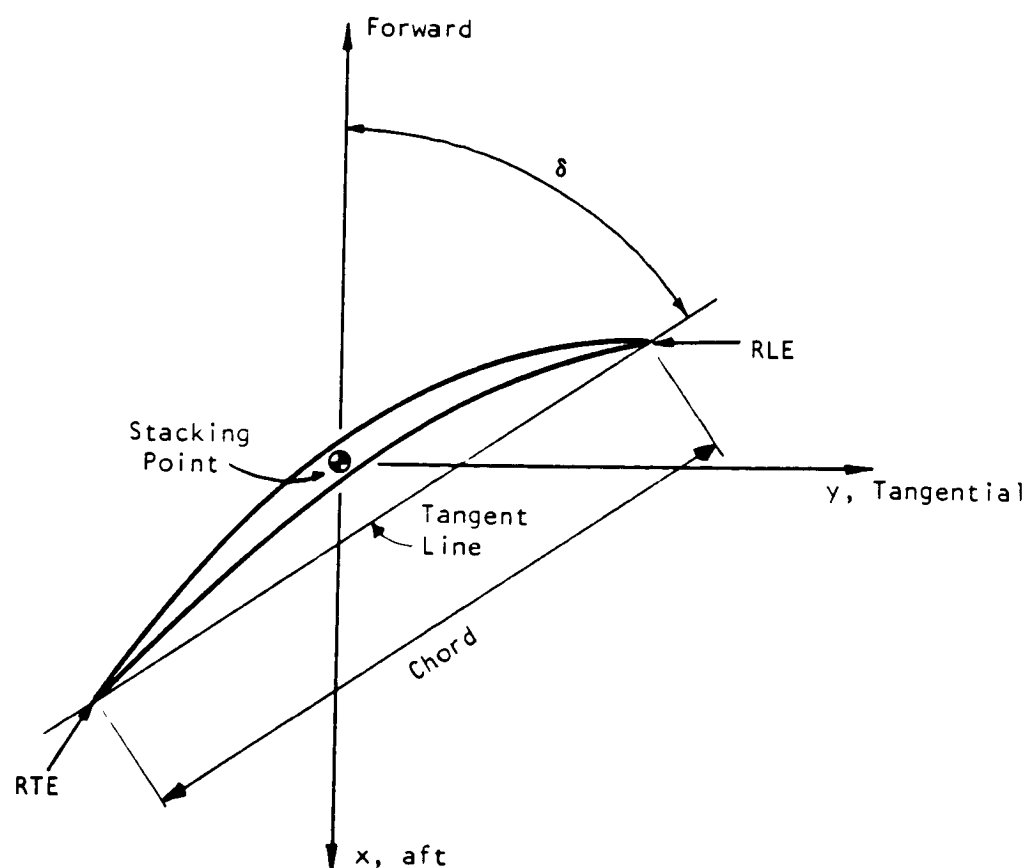
PCT IMM	RADIUS		MERID ANGLE		STREAM FUNCT		ARS ANGLE		REL ANGLE	
	IN	OUT	IN	OUT	IN	OUT	IN	OUT	IN	OUT
5.0	26.152	25.453	-7.9	-8.6	0.063	0.065	0	54.4	71.0	62.0
10.0	25.3	24.695	-5.4	-6.0	0.129	0.133	0	51.3	70.5	60.4
15.0	24.509	23.954	-3.5	-5.5	0.196	0.204	0	49.0	69.7	59.3
30.0	21.911	21.708	2.0	-1.6	0.392	0.403	0	48.1	67.2	55.3
50.0	18.612	18.956	0.3	3.2	0.615	0.626	0	52.0	64.1	51.5
60.0	16.975	17.481	18.0	5.4	0.712	0.720	0	52.9	62.1	46.0
70.0	15.222	15.963	13.0	7.1	0.798	0.803	0	53.1	59.7	37.6
80.0	13.478	14.566	10.6	5.9	0.875	0.881	0	52.5	57.4	35.4
90.0	12.501	13.092	21.5	6.6	0.910	0.917	0	52.9	56.3	19.7
95.0	11.060	13.236	23.5	7.4	0.942	0.949	0	55.0	55.4	11.9
95.0	10.735	12.596	25.2	8.3	0.972	0.977	0	60.6	53.6	0.7

PCT IMM	RADIUS		MERID ANGLE		MERID VEL		TANG VEL		BLADE SPEED	
IN	OUT	IN	OUT	IN	OUT	IN	OUT	IN	OUT	
5.0	143.5	217.0	454.0	275.4	143.5	127.0	0	176.2	431.5	414.0
10.0	140.4	213.2	443.6	274.5	140.4	136.4	0	169.2	418.1	407.4
15.0	149.5	217.0	431.1	270.4	149.5	130.4	0	162.9	404.4	395.2
30.0	152.7	210.3	393.3	246.6	152.7	140.3	0	156.6	362.5	359.4
50.0	150.4	199.5	341.9	190.0	150.4	122.9	0	157.2	307.1	311.1
60.0	150.6	201.5	317.3	176.2	150.6	121.0	0	160.6	279.3	287.1
70.0	151.4	209.2	293.2	150.9	151.4	126.2	0	160.0	251.2	263.4
80.0	150.1	222.5	268.3	150.1	150.1	135.9	0	176.2	222.4	240.3
90.0	148.2	226.7	255.1	145.7	148.2	137.3	0	180.4	207.6	229.2
95.0	144.7	233.2	240.7	137.3	144.7	136.6	0	190.5	192.5	210.4
95.0	140.2	241.7	220.5	127.4	140.2	126.6	0	205.6	177.1	207.0
PCT IMM	RADIUS		MERID ANGLE		STATIC PRES		REL MACH NO		TOTAL TEMP	
IN	OUT	IN	OUT	IN	OUT	IN	OUT	IN	OUT	
5.0	0.429	0.591	1.360	0.747	0.70	14.15	9.97	17.92	280.2	361.0
10.0	0.440	0.594	1.320	0.750	0.81	14.09	10.09	17.09	280.2	356.0
15.0	0.448	0.587	1.291	0.743	0.79	14.05	10.09	17.45	280.2	352.3
30.0	0.458	0.584	1.179	0.685	0.76	13.02	10.12	17.42	280.2	344.2
50.0	0.451	0.559	1.025	0.551	0.83	13.31	10.15	16.46	280.2	336.9
60.0	0.451	0.567	0.951	0.490	0.83	13.03	10.16	16.22	280.2	334.1
70.0	0.454	0.592	0.879	0.450	0.83	12.75	10.18	16.17	280.2	331.9
80.0	0.450	0.635	0.809	0.429	0.86	12.33	10.16	16.17	280.2	330.4
90.0	0.444	0.648	0.764	0.417	0.91	12.03	10.20	15.97	280.2	329.4
95.0	0.433	0.668	0.720	0.393	0.90	11.72	10.21	15.81	280.2	329.6
95.0	0.431	0.694	0.683	0.366	0.92	11.36	10.25	15.67	280.2	330.7
PCT IMM	INCIDENCE		DEV	TURN	D-FACT	LOSS COEFF	EFFICIENCY			
ML	SS	ADIA	POLY							
5.0	6.0	5.6	4.9	9.1	0.531	0.274	0.715			
10.0	6.3	5.5	4.6	10.1	0.515	0.238	0.759			
15.0	7.0	5.7	5.0	10.3	0.505	0.200	0.779			
30.0	7.5	6.4	4.7	11.7	0.510	0.132	0.807			
50.0	9.2	7.0	4.7	12.3	0.579	0.087	0.879			
60.0	9.4	8.2	11.9	15.6	0.613	0.112	0.926			
70.0	9.5	9.1	11.9	21.6	0.643	0.078	0.944			
80.0	11.1	10.6	14.3	31.4	0.636	0.048	0.976			
90.0	11.7	11.0	15.5	35.0	0.622	0.060	0.975			
95.0	11.5	11.1	13.0	42.1	0.603	0.112	0.948			
95.0	10.3	9.0	9.7	51.4	0.607	0.213	0.906			

ORIGINAL FILED
OF POOR QUALITY

EMP	OUT
51.3	42.3
34.1	19.6
86.4	91.3
97.5	

APPENDIX B - BLADE COORDINATES



Note: Manufacturing coordinates for blade sections are in cylindrical coordinates.

Figure B-1. Airfoil Geometry Definitions for Manufacturing Coordinates.

Table B-2.

SECTION B

CENTIMETERS		INCHES	
X	Y	X	Y
-0.01290	0.01189	-0.01689	0.00468
-0.01757	0.11666	-0.25495	0.04593
-1.3746	0.28542	-0.48719	0.11237
-1.6558	0.50696	-0.69511	0.19959
-2.1694	0.74752	-0.87281	0.29430
-2.58216	0.97389	-1.01660	0.38342
-2.83459	1.14851	-1.11598	0.45217
-2.98917	1.26423	-1.17681	0.49773
-3.07556	1.32718	-1.21085	0.52251
-3.12341	1.32083	-1.22969	0.52001
-3.14041	1.29004	-1.23638	0.50789
-3.11076	1.22984	-1.22471	0.48419
-3.01320	1.12260	-1.18630	0.44197
-2.84422	0.94508	-1.11977	0.37208
-2.57330	0.68534	-1.01311	0.26982
-2.19258	0.36058	-0.86322	0.14196
-1.72481	0.02824	-0.67906	0.01112
-1.15921	-0.27059	-0.45638	-0.10653
-0.53200	-0.48136	-0.24945	-0.18951
0.12069	-0.59009	0.04756	-0.23232
0.78235	-0.59190	0.30801	-0.23303
1.42243	-0.45956	0.56003	-0.18093
1.96365	-0.22499	0.77553	-0.08858
2.43365	0.03129	0.95813	0.01232
2.80269	0.23076	1.10342	0.09005
3.05599	0.36594	1.20311	0.14007
3.20332	0.46040	1.26115	0.18125
3.27132	0.51831	1.28792	0.20406
3.27058	0.56040	1.28763	0.22003
3.13642	0.58034	1.27416	0.22878
3.15765	0.55550	1.24317	0.21870
3.09571	0.49827	1.18335	0.19617
2.75107	0.42177	1.08310	0.16605
2.37635	0.31841	0.93557	0.12536
1.90947	0.16594	0.75176	0.06533
1.37627	0.02233	0.54184	0.00879
0.77330	-0.04039	0.30445	-0.01590
0.16043	-0.01115	0.06316	-0.00439

RADIUS = 10.89152 CM
CHORD = 6.46176 CM
RLE = 0.04318 CM
RTE = 0.04826 CM
DELTA = 0.11839 RAD.
= 4.28000 INCHES
= 2.54400 INCHES
= 0.01700 INCHES
= 0.01900 INCHES
= 6.78333 DEG.

Table B-1.

SECTION A

CENTIMETERS		INCHES	
X	Y	X	Y
0.07922	0.01321	0.03119	0.00520
-0.55697	-0.02939	-0.21928	-0.01157
-1.18435	0.06731	-0.46628	0.02650
-1.72824	0.30795	-0.68041	0.12124
-2.20248	0.54775	-0.86712	0.21565
-2.69515	0.74044	-1.02565	0.29151
-2.83920	0.88519	-1.13748	0.34850
-3.00045	0.98946	-1.20490	0.38955
-3.15427	1.04899	-1.24184	0.41299
-3.20479	1.04115	-1.26173	0.40990
-3.22593	1.00990	-1.27005	0.39760
-3.20114	0.94242	-1.26029	0.37103
-3.09618	0.82715	-1.21897	0.32565
-2.90604	0.64478	-1.14411	0.25385
-2.59900	0.38290	-1.02323	0.15075
-2.18577	0.03825	-0.86054	0.01506
-1.69075	-0.34059	-0.66880	-0.13409
-1.08742	-0.65248	-0.42812	-0.25688
-0.33529	-0.75319	-0.15169	-0.29653
0.32426	-0.69535	0.12766	-0.27376
1.02418	-0.56749	0.40322	-0.22342
1.64752	-0.24808	0.64863	-0.09767
2.09878	0.20559	0.82629	0.08094
2.45604	0.64877	0.96726	0.25542
2.78785	0.95245	1.09758	0.37498
3.04792	1.12606	1.19800	0.44333
3.16089	1.25365	1.25232	0.49364
3.23779	1.33157	1.27472	0.52424
3.22938	1.37648	1.27141	0.54192
3.19174	1.39334	1.25659	0.54856
3.11424	1.35611	1.22608	0.53390
2.96800	1.27112	1.16874	0.50044
2.71412	1.16408	1.06867	0.45830
2.34635	1.00178	0.92376	0.39440
1.95219	0.67818	0.76058	0.26700
1.50533	0.31834	0.59267	0.12533
0.97661	0.08024	0.38482	0.03159
0.29129	0.02802	0.11468	0.01103

RADIUS = 9.54024 CM
CHORD = 6.47700 CM
RLE = 0.05842 CM
RTE = 0.04572 CM
DELTA = -0.05381 RAD.
= 3.75600 INCHES
= 2.55000 INCHES
= 0.02300 INCHES
= 0.01800 INCHES
= -3.08333 DEG.

Table B-3.

SECTION C

CENTIMETERS		INCHES	
X	Y	X	Y
-0.09119	0.03759	-0.03359	0.01480
-0.06678	0.21151	-0.26251	0.08327
-1.22499	0.43497	-0.48228	0.17125
-1.72695	0.68600	-0.67990	0.27008
-2.15806	0.94150	-0.84963	0.37067
-2.50762	1.17579	-0.98733	0.46291
-2.74993	1.35412	-1.08265	0.53312
-2.89883	1.47071	-1.14127	0.57902
-2.98117	1.53571	-1.17369	0.60461
-3.02037	1.54577	-1.19227	0.60857
-3.04757	1.51892	-1.19983	0.59000
-3.02298	1.45806	-1.19015	0.57404
-2.92832	1.35616	-1.15288	0.53392
-2.76344	1.18852	-1.08797	0.46792
-2.50254	0.94036	-0.98525	0.37022
-2.13860	0.62728	-0.84197	0.24696
-1.69649	0.29906	-0.66791	0.11774
-1.17117	-0.01882	-0.46109	-0.00741
-0.59309	-0.28186	-0.23350	-0.11097
0.01384	-0.46881	0.00545	-0.18457
0.64028	-0.57287	0.25208	-0.22554
1.26804	-0.58821	0.49923	-0.23158
1.83647	-0.52786	0.72302	-0.20782
2.33276	-0.41859	0.91841	-0.16480
2.71602	-0.29616	1.06930	-0.11060
2.97307	-0.19736	1.17050	-0.07770
3.12804	-0.13241	1.23151	-0.05213
3.20378	-0.09213	1.26133	-0.03627
3.20893	-0.05184	1.26336	-0.02941
3.17790	-0.02873	1.25114	-0.01131
3.09756	-0.04221	1.21951	-0.01662
2.94193	-0.07501	1.15824	-0.02953
2.63575	-0.12276	1.05738	-0.04833
2.30774	-0.16944	0.90856	-0.06671
1.82733	-0.19403	0.71942	-0.07639
1.28631	-0.18115	0.50642	-0.07132
0.69492	-0.11928	0.27359	-0.04696
0.10378	-0.00914	0.04086	-0.00360

RADIUS = 12.00104 CM
 CHORD = 6.45922 CM
 RLE = 0.03556 CM
 RTE = 0.03810 CM
 DELTA = 0.24950 RAD.
 = 4.72600 INCHES
 = 2.54300 INCHES
 = 0.01400 INCHES
 = 0.01500 INCHES
 = 14.30000 DEG.

Table B-4.

SECTION D

CENTIMETERS		INCHES	
X	Y	X	Y
-0.11480	0.06955	-0.04523	0.02738
-0.15936	0.30734	-0.25963	0.12100
-1.08693	0.58087	-0.46732	0.22869
-1.6266	0.86614	-0.65459	0.34100
-2.07327	1.14300	-0.81625	0.45000
-2.40736	1.39085	-0.94778	0.54758
-2.63969	1.57612	-1.09579	0.66760
-2.78331	1.69570	-1.2714	0.69374
-2.86294	1.76210	-1.12714	0.69374
-2.90792	1.77932	-1.14485	0.70052
-2.92395	1.75296	-1.15116	0.69014
-2.93865	1.69367	-1.14120	0.66680
-2.94927	1.59278	-1.10601	0.62708
-2.95079	1.42878	-1.04362	0.56251
-2.90132	1.18435	-0.94540	0.46628
-2.85562	0.87234	-0.80930	0.34344
-1.64938	0.53642	-0.64582	0.21119
-1.15204	0.19538	-0.45356	0.07692
-0.61849	-0.11280	-0.24350	-0.04441
-0.05740	-0.36736	-0.02260	-0.14463
0.52700	-0.56238	0.20740	-0.22141
1.12278	-0.68969	0.44204	-0.27153
1.67422	-0.74844	0.65914	-0.29466
2.16708	-0.75717	0.85318	-0.29810
2.55666	-0.73363	1.00656	-0.28083
2.82194	-0.70274	1.11100	-0.26767
2.98341	-0.68052	1.17457	-0.26792
3.05502	-0.66317	1.20670	-0.26109
3.03326	-0.62845	1.21380	-0.24742
3.01123	-0.59751	1.20521	-0.23524
2.98105	-0.59134	1.17364	-0.23281
2.82397	-0.58598	1.11180	-0.23076
2.56669	-0.57269	1.01055	-0.22547
2.19250	-0.53322	0.86319	-0.20993
1.72311	-0.45789	0.67839	-0.18027
1.25015	-0.34569	0.47250	-0.13610
0.63315	-0.19129	0.24927	-0.07531
0.07003	-0.00150	0.02757	-0.00059

RADIUS = 13.03782 CM
 CHORD = 6.46604 CM
 RLE = 0.25400 CM
 RTE = 0.03210 CM
 DELTA = 0.38019 RAD.
 = 5.13300 INCHES
 = 2.54600 INCHES
 = 0.01000 INCHES
 = 0.01500 INCHES
 = 21.78333 DEG.

Table B-5.

SECTION E

CENTIMETERS		INCHES	
X	Y	X	Y
-0.12286	0.10196	-0.04837	0.04014
-0.63716	0.39400	-0.25085	0.15517
-1.13624	0.71140	-0.44734	0.28008
-1.58059	1.02786	-0.62543	0.40467
-1.93064	1.32631	-0.77986	0.52217
-2.29977	1.59034	-0.90542	0.62612
-2.52131	1.78625	-0.99264	0.70325
-2.65892	1.91140	-1.04682	0.75252
-2.73502	1.98110	-1.07678	0.77990
-2.77686	2.00571	-1.09325	0.78965
-2.79436	1.98252	-1.10014	0.78052
-2.77033	1.92354	-1.09068	0.75720
-2.66717	1.81978	-1.05794	0.71645
-2.53528	1.65377	-0.99814	0.65109
-2.29781	1.40406	-0.90465	0.55270
-1.96840	1.08377	-0.77496	0.42608
-1.57442	0.73373	-0.61985	0.28807
-1.11498	0.36711	-0.43897	0.14453
-0.61659	0.01885	-0.24275	0.00742
-0.09378	-0.29154	-0.03692	-0.11478
0.45260	-0.55819	0.17819	-0.21976
1.01463	-0.77155	0.39946	-0.30376
1.54160	-0.91895	0.60693	-0.36170
2.01872	-1.01364	0.79477	-0.39907
2.40066	-1.06263	0.94514	-0.41850
2.66339	-1.08301	1.04858	-0.42658
2.82395	-1.09205	1.11179	-0.42994
2.90619	-1.09088	1.14417	-0.42948
2.92882	-1.05979	1.15306	-0.41724
2.90967	-1.02735	1.14554	-0.40447
2.83187	-1.00002	1.11491	-0.39686
2.67880	-0.97561	1.05467	-0.38410
2.42946	-0.91648	0.95648	-0.36087
2.05919	-0.81394	0.81464	-0.32045
1.63011	-0.66479	0.63784	-0.26173
1.12204	-0.47694	0.44175	-0.18777
0.58115	-0.24727	0.22998	-0.09735
0.05166	0.01021	0.02034	-0.00402

RADIUS = 13.9 280 CM
 CHORD = 0.49224 CM
 RLE = 0.01778 CM
 RTE = 0.03010 CM
 DELTA = 0.49073 RAD.
 = 5.50900 INCHES
 = 2.55600 INCHES
 = 0.00700 INCHES
 = 0.01500 INCHES
 = 28.11667 DEG.

Table B-6.

SECTION F

CENTIMETERS		INCHES	
X	Y	X	Y
-0.04064	0.13071	-0.002781	0.05146
-0.04261	0.51862	-0.20725	0.20418
-0.04703	0.91999	-0.38204	0.36220
-1.17018	1.31016	-0.53944	0.51591
-1.72237	1.66332	-0.67810	0.65405
-2.01648	1.96172	-0.79389	0.77233
-2.24494	2.17640	-0.87596	0.85005
-2.35227	2.31498	-0.92609	0.91141
-2.42296	2.39184	-0.95392	0.94167
-2.46319	2.41910	-0.96976	0.95240
-2.43559	2.39718	-0.97058	0.94377
-2.47274	2.33520	-0.97352	0.91937
-2.39669	2.22573	-0.94350	0.87627
-2.26001	2.04648	-0.88978	0.80570
-2.04389	1.77731	-0.80468	0.69973
-1.74655	1.42596	-0.68762	0.56140
-1.39916	1.02834	-0.55086	0.40486
-0.99825	0.59703	-0.39301	0.23505
-0.56639	0.16736	-0.22299	0.06509
-0.11013	-0.23619	-0.04336	-0.00299
0.36655	-0.61549	0.14431	-0.24232
0.85717	-0.96487	0.33747	-0.37987
1.32382	-1.25263	0.52119	-0.49316
1.75511	-1.47937	0.69099	-0.58243
2.13603	-1.63792	0.82946	-0.64495
2.43128	-1.73759	0.92570	-0.68409
2.63134	-1.79619	0.98478	-0.70716
2.79999	-1.82080	1.01571	-0.71665
2.91501	-1.80414	1.02953	-0.71079
2.95429	-1.76736	1.02575	-0.69561
2.91279	-1.71656	1.00110	-0.67581
2.47782	-1.63391	0.94790	-0.61327
2.13570	-1.50000	0.86051	-0.52905
1.86374	-1.30071	0.73356	-0.51209
1.46444	-1.03579	0.57655	-0.40779
1.03766	-0.72052	0.40459	-0.28367
0.55220	-0.36807	0.21740	-0.14191
0.08237	0.00264	0.00243	0.00104

RADIUS = 15.60164 CM
 CHORD = 6.61416 CM
 RLE = 0.02540 CM
 RTE = 0.03302 CM
 DELTA = 0.69115 RAD.
 = 6.16600 INCHES
 = 2.60400 INCHES
 = 0.01000 INCHES
 = 0.01300 INCHES
 = 39.60000 DEG.

Table B-7.

SECTION G

CENTIMETERS		INCHES	
X	Y	X	Y
-0.03172	0.21674	-0.01249	1.08533
-0.43642	0.68626	-0.17182	1.27016
-0.83165	1.16380	-0.32742	0.55819
-1.20363	1.60693	-0.47387	0.13265
-1.53930	2.00706	-0.60248	0.79016
-1.80327	2.34437	-0.70995	0.92296
-1.99761	2.58580	-0.78646	1.01803
-2.11905	2.73827	-0.83427	1.07806
-2.18646	2.82280	-0.86081	1.11134
-2.22529	2.85511	-0.87610	1.12466
-2.24879	2.83307	-0.88535	1.11538
-2.23406	2.76972	-0.87955	1.09044
-2.16162	2.65356	-0.85103	1.04471
-2.03299	2.46121	-0.80039	0.96898
-1.83492	2.16731	-0.72241	0.85327
-1.56385	1.78024	-0.61569	0.70068
-1.24785	1.33985	-0.49128	0.52750
-0.88773	0.85423	-0.34950	0.33631
-0.50025	0.35707	-0.20010	0.14058
-0.11704	-0.13089	-0.04608	-0.05153
0.28245	-0.61209	0.11120	-0.24090
0.69164	-1.07582	0.27230	-0.42355
1.03473	-1.47861	0.42706	-0.58213
1.45929	-1.82021	0.57098	-0.71602
1.71310	-2.08140	0.68823	-0.81945
1.96014	-2.25014	0.77171	-0.89508
2.09012	-2.35240	0.82288	-0.92614
2.16927	-2.39972	0.85050	-0.94477
2.19355	-2.39039	0.86557	-0.94110
2.19936	-2.35133	0.86589	-0.92572
2.14714	-2.28570	0.84533	-0.89980
2.03652	-2.16471	0.80178	-0.85225
1.85478	-1.96693	0.73023	-0.77438
1.59220	-1.67500	0.62605	-0.65948
1.26413	-1.30325	0.49769	-0.51309
0.91011	-0.87970	0.35473	-0.34634
0.50367	-0.41361	0.19796	-0.16284
0.10079	0.05819	0.03968	0.02291

RADIUS = 18.28546 CM
 CHORD = 6.86816 CM
 RLE = 0.02286 CM
 RLE = 0.03302 CM
 DELTA = 0.86830 RAD.
 = 7.19900 INCHES
 = 2.70400 INCHES
 = 0.00900 INCHES
 = 0.01300 INCHES
 = 49.75000 DEG.

Table B-8.

SECTION H

CENTIMETERS		INCHES	
X	Y	X	Y
-0.12500	0.25207	-0.01017	0.05974
-0.37001	0.83713	-0.14599	0.32958
-0.71242	1.42418	-0.28048	0.56070
-1.03500	1.97528	-0.40381	0.77767
-1.30813	2.46576	-0.51501	0.97077
-1.51449	2.87833	-0.60003	1.13329
-1.71445	3.17228	-0.67498	1.24093
-1.87904	3.35008	-0.71643	1.32248
-1.97857	3.46062	-0.73978	1.36245
-1.94395	3.49049	-0.75546	1.37736
-1.92634	3.47558	-0.76534	1.36834
-1.86329	3.40637	-0.75600	1.34109
-1.75445	3.27127	-0.73358	1.28790
-1.58427	3.04355	-0.69073	1.19875
-1.35677	2.69649	-0.62373	1.05161
-1.09539	2.23406	-0.53416	0.87955
-0.79703	1.70386	-0.43122	0.67001
-0.48916	1.11580	-0.31379	0.43929
-0.14907	0.51176	-0.18904	0.29148
0.19139	-0.08461	-0.05869	-0.03331
0.54704	-0.67567	0.07535	-0.26601
0.88963	-1.24879	0.21537	-0.49165
1.20754	-1.75857	0.35001	-0.69235
1.47018	-2.20165	0.47541	-0.86679
1.65423	-2.54462	0.57881	-1.00182
1.76713	-2.77589	0.65129	-1.09287
1.82768	-2.91655	0.69574	-1.14625
1.86921	-2.98640	0.73591	-1.17575
1.87769	-2.99430	0.71950	-1.17886
1.83530	-2.95300	0.73925	-1.16262
1.74400	-2.87142	0.72256	-1.13048
1.59413	-2.71623	0.60697	-1.06918
1.37384	-2.46344	0.62761	-0.96906
1.09653	-2.09398	0.54080	-0.82440
0.73506	-1.62672	0.43170	-0.64034
0.43642	-1.10073	0.30908	-0.43300
0.03931	-0.52667	0.17182	-0.20775
	0.05712	0.03516	0.02249

RADIUS = 21.78304 CM
 CHORD = 7.52348 CM
 RLE = 0.02286 CM
 RLE = 0.02794 CM
 DELTA = 1.04196 RAD.
 = 8.57600 INCHES
 = 2.96200 INCHES
 = 0.00900 INCHES
 = 0.01100 INCHES
 = 59.70000 DEG.

Table B-9.

SECTION J

CENTIMETERS		INCHES	
X	Y	X	Y
-0.00892	0.22888	-0.00351	0.09011
-0.00591	0.91204	-0.11654	0.35907
-0.00469	1.59144	-0.23295	0.62655
-0.00330	2.22308	-0.34382	0.87523
-1.13449	2.78262	-0.44665	1.09552
-1.35870	3.25036	-0.53492	1.27967
-1.51950	3.58414	-0.59823	1.41108
-1.62243	3.79319	-0.63875	1.49338
-1.67899	3.90942	-0.66102	1.53914
-1.71552	3.95790	-0.67540	1.55823
-1.74495	3.93758	-0.68699	1.55023
-1.77326	3.86077	-0.68216	1.51999
-1.80077	3.71051	-0.65739	1.46083
-1.82411	3.45623	-0.61579	1.36072
-1.84531	3.06555	-0.55327	1.20691
-1.86493	2.54556	-0.46901	1.00219
-0.94943	1.94762	-0.37381	0.76678
-0.68516	1.27051	-0.26975	0.50335
-0.49914	0.58737	-0.16108	0.23125
-0.33005	-0.10251	-0.05120	-0.04036
0.16261	-0.78674	0.06402	-0.30974
0.46400	-1.44079	0.19055	-0.57039
0.80933	-2.03916	0.31509	-0.80282
1.09268	-2.55778	0.43019	-1.00700
1.33533	-2.96187	0.52572	-1.16009
1.50759	-3.23449	0.59354	-1.27342
1.61567	-3.39898	0.63609	-1.33318
1.67559	-3.47990	0.65968	-1.37004
1.71094	-3.49433	0.67714	-1.37572
1.72654	-3.44876	0.67974	-1.35778
1.63666	-3.35658	0.66404	-1.32149
1.60043	-3.18066	0.63009	-1.25223
1.45639	-2.89367	0.57338	-1.13924
1.24983	-2.47228	0.49206	-0.97334
0.99243	-1.93830	0.39072	-0.76311
0.70165	-1.32670	0.27742	-0.52626
0.33948	-0.67516	0.15334	-0.26581
0.00753	0.00150	0.03446	0.00059

RADIUS = 24.24684 CM
 CHORD = 8.21436 CM
 RLE = 0.02286 CM
 RTE = 0.02286 CM
 DELTA = 1.13737 RAD.

= 9.54600 INCHES
 = 3.23400 INCHES
 = 0.00900 INCHES
 = 0.00900 INCHES
 = 65.16667 DEG.

Table B-10.

SECTION K

CENTIMETERS		INCHES	
X	Y	X	Y
0.00052	0.27302	0.00414	0.10749
-0.00275	1.02354	-0.09557	0.40297
-0.01707	1.76657	-0.20357	0.69550
-0.03862	2.45412	-0.31040	0.96619
-1.01369	3.06294	-0.41090	1.20588
-1.25829	3.57416	-0.49539	1.40715
-1.41234	3.93901	-0.55604	1.55079
-1.51028	4.16801	-0.59460	1.64095
-1.56281	4.29583	-0.61528	1.69127
-1.59662	4.35176	-0.62859	1.71329
-1.62278	4.33032	-0.63889	1.70405
-1.60762	4.24823	-0.63292	1.67253
-1.55481	4.08275	-0.61213	1.60738
-1.45542	3.80634	-0.57300	1.49856
-1.30305	3.38310	-0.51301	1.33193
-1.10211	2.81795	-0.43390	1.10943
-0.86759	2.17114	-0.34157	0.85476
-0.61521	1.44645	-0.24221	0.56947
-0.36954	0.69159	-0.14549	0.27228
-0.12393	-0.06330	-0.04079	-0.02492
0.11136	-0.81732	0.04896	-0.32178
0.40317	-1.55108	0.15869	-0.61066
0.66052	-2.20944	0.26792	-0.86986
0.94889	-2.78498	0.37358	-1.09645
1.17574	-3.14223	0.46289	-1.23710
1.35126	-3.35896	0.52530	-1.39329
1.47253	-3.72448	0.56399	-1.46033
1.48387	-3.81904	0.58420	-1.50356
1.41420	-3.84528	0.60008	-1.51389
1.31215	-3.79067	0.60321	-1.49554
1.16003	-3.69755	0.58901	-1.45573
1.02268	-3.50136	0.56011	-1.37849
1.30104	-3.18041	0.51222	-1.25213
1.12151	-2.71198	0.44154	-1.06771
0.86280	-2.12501	0.34756	-0.83662
0.62682	-1.45971	0.24678	-0.57469
0.35022	-0.72692	0.13738	-0.28619
0.09461	0.02276	0.03725	0.00896

RADIUS = 26.00452 CM
 CHORD = 8.73078 CM
 RLE = 0.01524 CM
 RTE = 0.02286 CM
 DELTA = 1.20573 RAD.

= 10.23800 INCHES
 = 3.45700 INCHES
 = 0.00600 INCHES
 = 0.00900 INCHES
 = 69.08333 DEG.

ORIGINAL
 OF P.O.

Table B-11.

SECTION L

CENTIMETERS		INCHES	
X	Y	X	Y
0.03858	0.35621	0.01519	0.14024
-0.19728	1.15654	-0.07767	0.45533
-0.47297	1.94401	-0.18621	0.75530
-0.74691	2.67302	-0.29405	1.05237
-1.00528	3.31859	-0.39578	1.30653
-1.21610	3.86331	-0.47878	1.52099
-1.36515	4.25300	-0.53746	1.67441
-1.45603	4.49913	-0.57324	1.77131
-1.50419	4.63649	-0.59220	1.82539
-1.53660	4.69740	-0.60496	1.84937
-1.55592	4.67093	-0.61296	1.83395
-1.53850	4.58483	-0.60571	1.80505
-1.49344	4.40781	-0.58797	1.73536
-1.40231	4.11284	-0.55209	1.61923
-1.25291	3.66420	-0.49327	1.44260
-1.05783	3.06464	-0.41647	1.20655
-0.82822	2.37884	-0.32607	0.93655
-0.57335	1.61351	-0.22573	0.63524
-0.34099	0.81209	-0.13425	0.31972
-0.12497	0.00607	-0.04920	0.00239
0.06395	-0.30051	0.00502	-0.31516
0.32738	-1.59047	0.12889	-0.62617
0.56482	-2.30297	0.22237	-0.90668
0.79045	-2.93124	0.31120	-1.15403
0.90629	-3.42209	0.38830	-1.34728
1.12867	-3.75448	0.44436	-1.47814
1.21925	-3.95572	0.48002	-1.55737
1.26685	-4.05831	0.49876	-1.59776
1.30428	-4.09049	0.51377	-1.61043
1.31168	-4.04114	0.51641	-1.59100
1.23359	-3.93156	0.50535	-1.54786
1.22852	-3.71790	0.48367	-1.46374
1.13716	-3.36804	0.44770	-1.32600
0.93093	-2.86027	0.39013	-1.12609
0.77031	-2.22007	0.30347	-0.87793
0.54493	-1.51404	0.21454	-0.59608
0.31830	-0.72050	0.12551	-0.28366
0.10937	0.08722	0.04306	0.03434

RADIUS = 27.26944 CM = 10.73600 INCHES
 CHORD = 9.24560 CM = 3.64000 INCHES
 RLE = 0.01524 CM = 0.00600 INCHES
 RTE = 0.02286 CM = 0.00900 INCHES
 DELTA = 1.25780 RAD. = 72.06667 DEG.

ORIGINAL COPY
OF POOR QUALITY

APPENDIX C - BLADE/MOUNTED-KULITE TIME HISTORIES

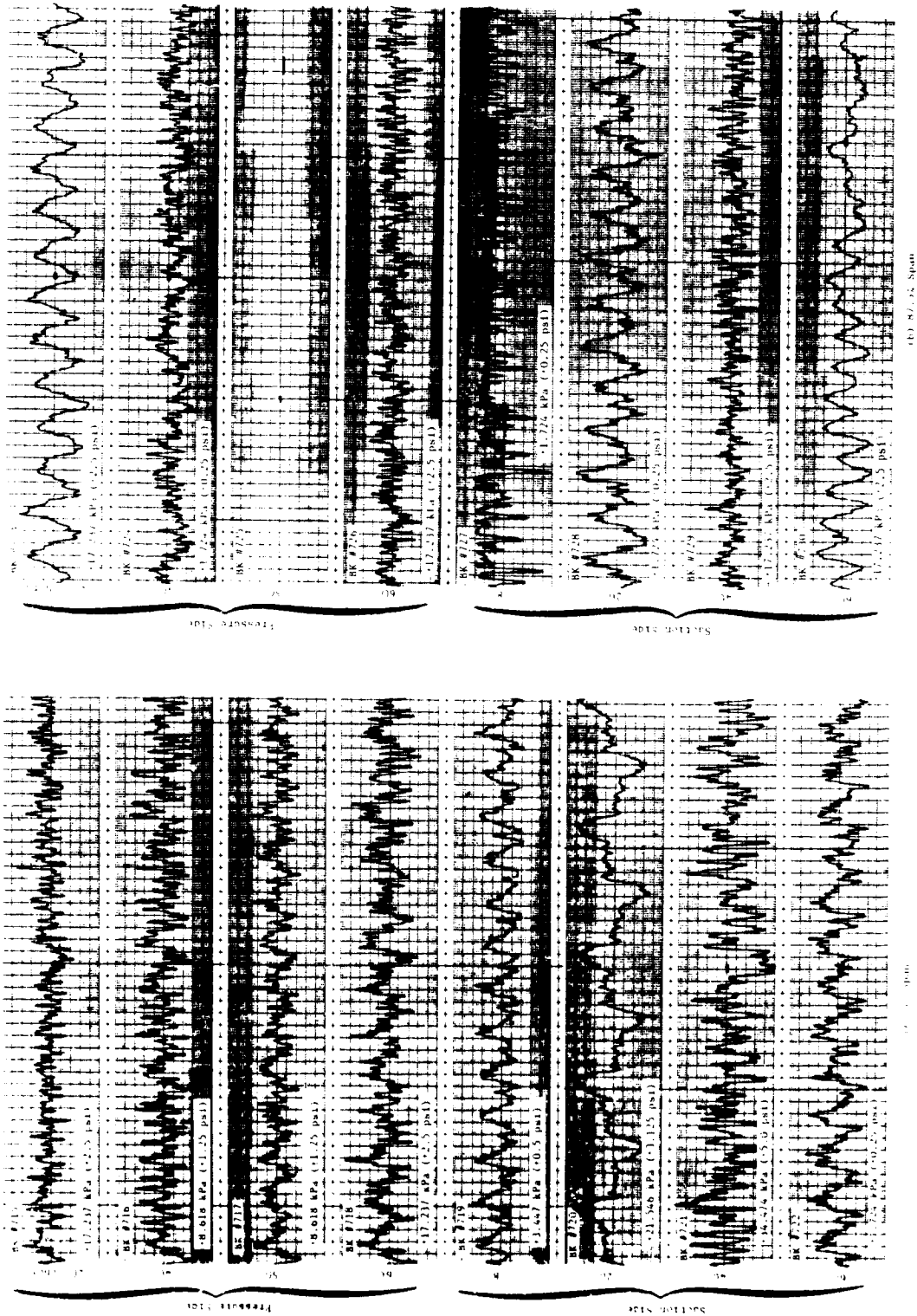


Figure C-1. Blade-Mounted Kulite Time Histories, 65 Percent Speed Intermediate Operating Line.

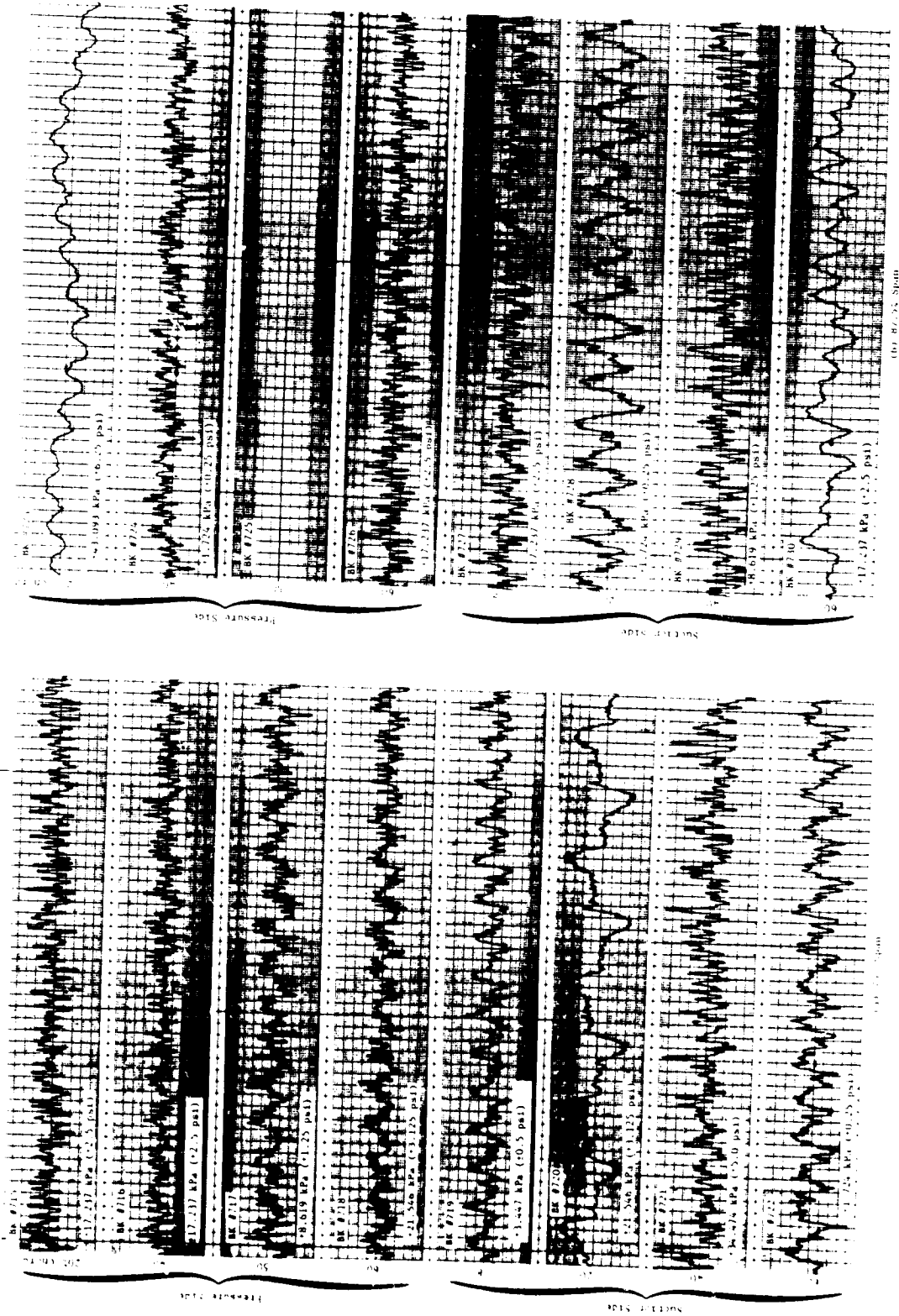


Figure C-2. Blade-Mounted Kulite Time Histories, 70 Percent Speed Nominal Operating Line.

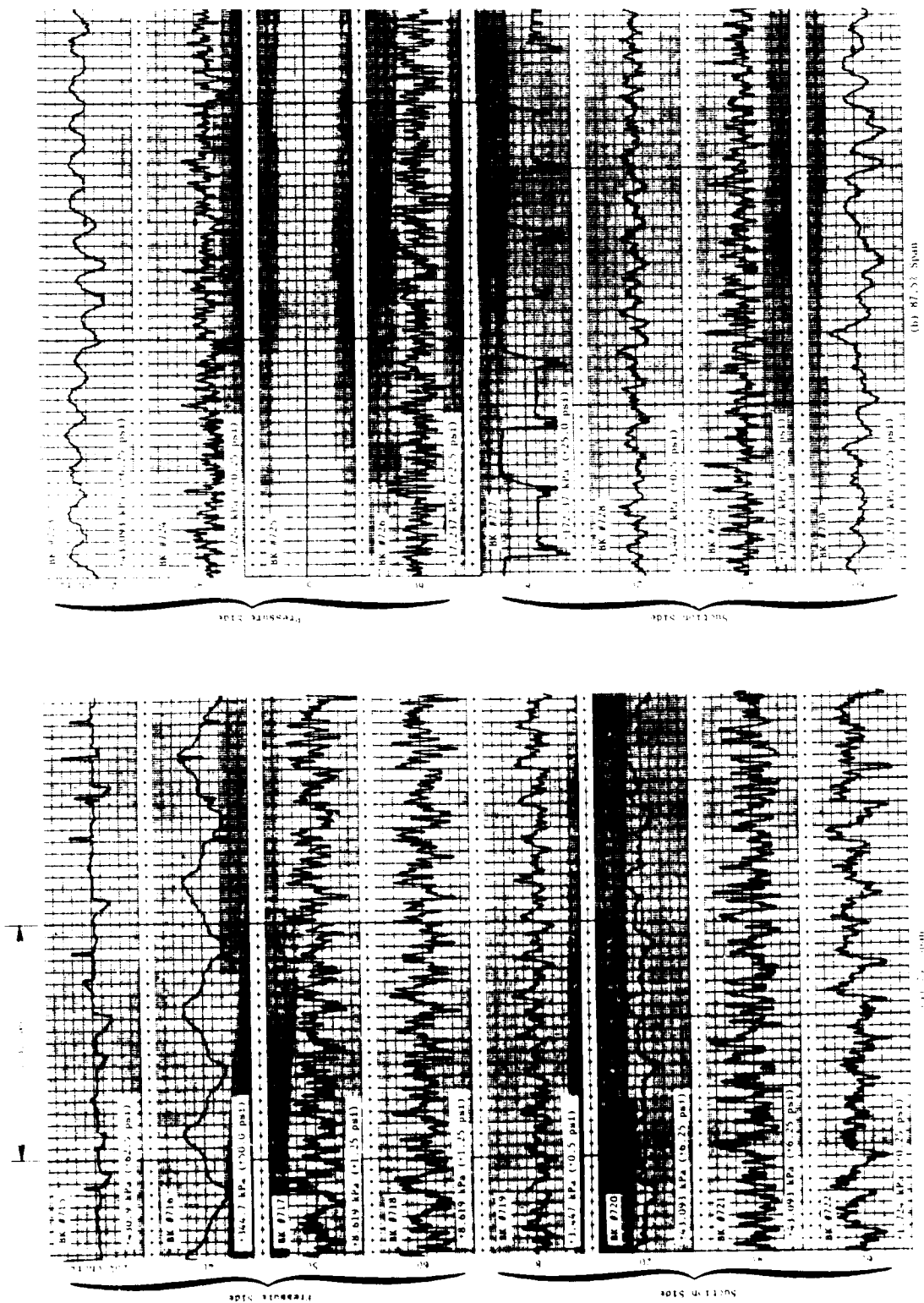


Figure C-3. Blade-Mounted Kulite Time Histories, 70 Percent Speed Intermediate Operating Line.

ORIGINAL
OF POOR QUALITY

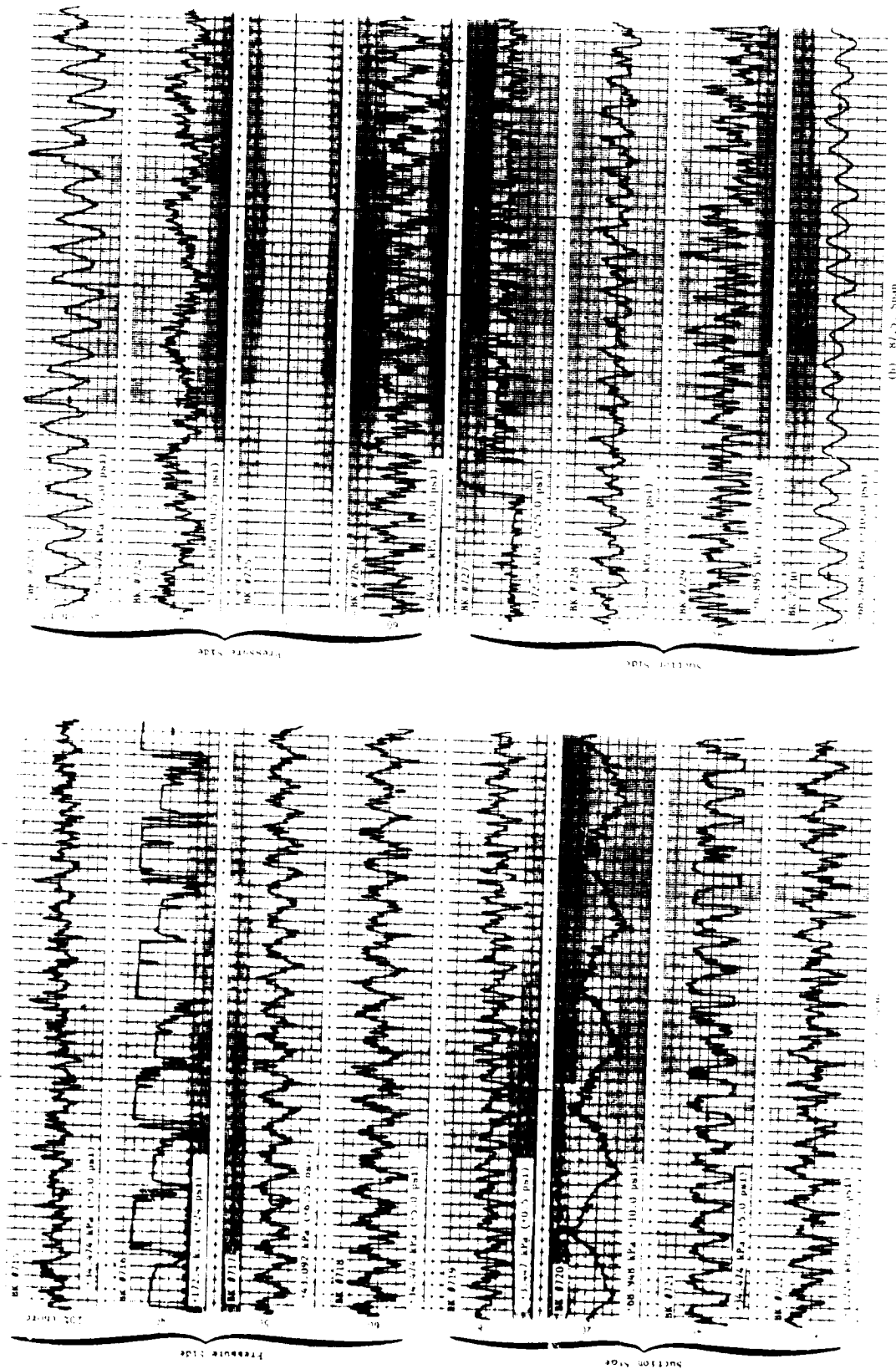


Figure C-5. Blade-Mounted Kulite Time Histories, 90 Percent Speed Intermediate Operating Line.

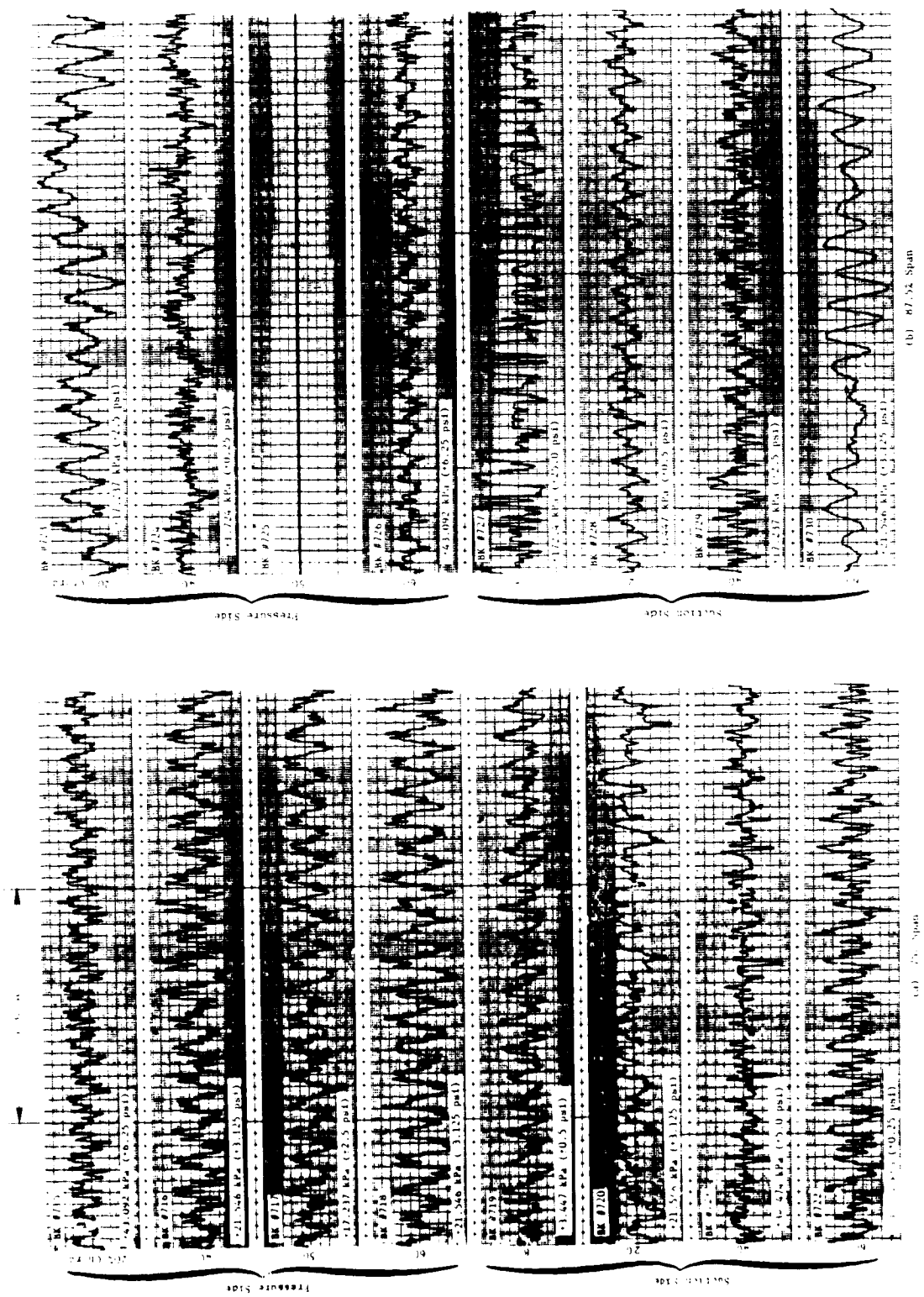


Figure C-6. Blade-Mounted Kulite Time Histories, 95 Percent Speed Intermediate Operating Line.

APPENDIX D - EXAMPLES OF UNSTEADY DATA COMPUTER PROCESSING

Table D-1. Casing Kulite Ensemble Average for 200 Points.

NUMBER OF FRAMES IN THE AVERAGE = 64
 AVERAGE SPEED = 11680
 NUMBER OF SAMPLE POINTS = 200
 MACH NUMBER = 0.500
 SAMPLE RATE = 320000. HZ
 RADIAL POSITION = 10.500

INDEX	DISTANCE (INCHES)	CK # 705 (PSI)	INDEX	DISTANCE (INCHES)	CK # 705 (PSI)
1	0.0000E+00	0.1108E+01	101	0.4013E+01	-0.9193E+00
2	0.4013E-01	0.1040E+01	102	0.4054E+01	-0.6864E+00
3	0.8027E-01	0.9446E+00	103	0.4094E+01	-0.5304E+00
4	0.1204E+00	0.9135E+00	104	0.4134E+01	-0.4425E+00
5	0.1605E+00	0.8921E+00	105	0.4174E+01	-0.2165E+00
6	0.2007E+00	0.8680E+00	106	0.4214E+01	-0.1624E+00
7	0.2408E+00	0.8253E+00	107	0.4254E+01	-0.1654E+00
8	0.2809E+00	0.7874E+00	108	0.4294E+01	-0.1525E+00
9	0.3211E+00	0.7375E+00	109	0.4334E+01	-0.1615E+00
10	0.3612E+00	0.7482E+00	110	0.4375E+01	-0.1811E+00
11	0.4013E+00	0.7090E+00	111	0.4415E+01	-0.2067E+00
12	0.4415E+00	0.6616E+00	112	0.4455E+01	-0.1912E+00
13	0.4816E+00	0.6164E+00	113	0.4495E+01	-0.8870E-01
14	0.5217E+00	0.5650E+00	114	0.4535E+01	0.2221E-01
15	0.5619E+00	0.5791E+00	115	0.4575E+01	0.1119E+00
16	0.6020E+00	0.6237E+00	116	0.4615E+01	0.3304E+00
17	0.6421E+00	0.4816E+00	117	0.4656E+01	0.4424E+00
18	0.6823E+00	0.4141E+00	118	0.4696E+01	0.4861E+00
19	0.7224E+00	0.6337E+00	119	0.4736E+01	0.6710E+00
20	0.7625E+00	0.5663E+00	120	0.4776E+01	0.7373E+00
21	0.8027E+00	0.3491E+00	121	0.4816E+01	0.7496E+00
22	0.8428E+00	0.3939E+00	122	0.4856E+01	0.8080E+00
23	0.8829E+00	0.3278E+00	123	0.4896E+01	0.8393E+00
24	0.9231E+00	0.1958E+00	124	0.4936E+01	0.8542E+00
25	0.9632E+00	0.1166E+00	125	0.4977E+01	0.8795E+00
26	0.1003E+01	-0.7633E-02	126	0.5017E+01	0.9543E+00
27	0.1043E+01	-0.1044E+00	127	0.5057E+01	0.9774E+00
28	0.1084E+01	-0.3163E+00	128	0.5097E+01	0.9159E+00
29	0.1124E+01	-0.6961E+00	129	0.5137E+01	0.9223E+00
30	0.1164E+01	-0.1023E+01	130	0.5177E+01	0.1013E+01
31	0.1204E+01	-0.1415E+01	131	0.5217E+01	0.1045E+01
32	0.1244E+01	-0.1668E+01	132	0.5257E+01	0.9045E+00
33	0.1284E+01	-0.1783E+01	133	0.5297E+01	0.7980E+00
34	0.1324E+01	-0.1957E+01	134	0.5338E+01	0.8109E+00
35	0.1365E+01	-0.1891E+01	135	0.5378E+01	0.6295E+00
36	0.1405E+01	-0.1667E+01	136	0.5418E+01	0.4601E+00
37	0.1445E+01	-0.1408E+01	137	0.5458E+01	0.4249E+00
38	0.1485E+01	-0.1110E+01	138	0.5498E+01	0.3301E+00
39	0.1525E+01	-0.9404E+00	139	0.5538E+01	0.3739E+00
40	0.1565E+01	-0.7666E+00	140	0.5579E+01	0.5023E+00
41	0.1605E+01	-0.5994E+00	141	0.5619E+01	0.4643E+00
42	0.1645E+01	-0.6190E+00	142	0.5659E+01	0.3293E+00
43	0.1686E+01	-0.5832E+00	143	0.5699E+01	0.3399E+00
44	0.1726E+01	-0.5721E+00	144	0.5739E+01	0.3500E+00
45	0.1766E+01	-0.5167E+00	145	0.5779E+01	0.2172E+00
46	0.1806E+01	-0.2778E+00	146	0.5819E+01	0.2169E+00
47	0.1846E+01	-0.2322E+00	147	0.5859E+01	0.2328E+00
48	0.1886E+01	-0.2779E+00	148	0.5900E+01	0.2117E+00
49	0.1926E+01	-0.2458E+00	149	0.5940E+01	0.2084E+00
50	0.1967E+01	-0.2385E+00	150	0.5980E+01	0.1878E+00
51	0.2007E+01	-0.1630E+00	151	0.6020E+01	0.2771E-01
52	0.2047E+01	-0.6895E-01	152	0.6060E+01	-0.1914E+00
53	0.2087E+01	0.6862E-01	153	0.6100E+01	-0.2882E+00
54	0.2127E+01	0.2373E+00	154	0.6140E+01	-0.4425E+00
55	0.2167E+01	0.3050E+00	155	0.6181E+01	-0.6487E+00
56	0.2207E+01	0.4559E+00	156	0.6221E+01	-0.9564E+00
57	0.2247E+01	0.6682E+00	157	0.6261E+01	-0.1319E+01
58	0.2288E+01	0.7205E+00	158	0.6301E+01	-0.1440E+01
59	0.2328E+01	0.7907E+00	159	0.6341E+01	-0.1646E+01
60	0.2368E+01	0.9165E+00	160	0.6381E+01	-0.1879E+01
61	0.2408E+01	0.9951E+00	161	0.6421E+01	-0.1932E+01
62	0.2448E+01	0.9195E+00	162	0.6462E+01	-0.1802E+01
63	0.2488E+01	0.7939E+00	163	0.6502E+01	-0.1633E+01
64	0.2528E+01	0.8493E+00	164	0.6542E+01	-0.1350E+01
65	0.2569E+01	0.9686E+00	165	0.6582E+01	-0.1338E+01
66	0.2609E+01	0.8601E+00	166	0.6622E+01	-0.7972E+00
67	0.2649E+01	0.6722E+00	167	0.6662E+01	-0.6330E+00
68	0.2689E+01	0.6643E+00	168	0.6702E+01	-0.5105E+00
69	0.2729E+01	0.7353E+00	169	0.6742E+01	-0.3895E+00
70	0.2769E+01	0.8044E+00	170	0.6783E+01	-0.2965E+00
71	0.2809E+01	0.6727E+00	171	0.6823E+01	-0.3108E+00
72	0.2850E+01	0.6562E+00	172	0.6863E+01	-0.2914E+00
73	0.2890E+01	0.6504E+00	173	0.6903E+01	-0.1937E+00
74	0.2930E+01	0.5627E+00	174	0.6943E+01	-0.1235E+00
75	0.2970E+01	0.5403E+00	175	0.6983E+01	-0.1104E+00
76	0.3010E+01	0.6132E+00	176	0.7023E+01	-0.1054E+00
77	0.3050E+01	0.6583E+00	177	0.7064E+01	-0.1221E-02
78	0.3090E+01	0.6158E+00	178	0.7104E+01	0.1299E+00
79	0.3130E+01	0.6007E+00	179	0.7144E+01	0.2272E+00
80	0.3171E+01	0.6230E+00	180	0.7184E+01	0.3417E+00
81	0.3211E+01	0.6994E+00	181	0.7224E+01	0.4485E+00
82	0.3251E+01	0.7358E+00	182	0.7264E+01	0.5541E+00
83	0.3291E+01	0.6303E+00	183	0.7304E+01	0.6164E+00
84	0.3331E+01	0.7362E+00	184	0.7344E+01	0.6787E+00
85	0.3371E+01	0.8892E+00	185	0.7385E+01	0.8017E+00
86	0.3411E+01	0.6985E+00	186	0.7425E+01	0.8438E+00
87	0.3452E+01	0.5707E+00	187	0.7465E+01	0.8310E+00
88	0.3492E+01	0.5639E+00	188	0.7505E+01	0.7656E+00
89	0.3532E+01	0.3865E+00	189	0.7545E+01	0.7415E+00
90	0.3572E+01	0.1517E+00	190	0.7585E+01	0.8107E+00
91	0.3612E+01	-0.6282E-01	191	0.7625E+01	0.8138E+00
92	0.3652E+01	-0.3711E+00	192	0.7665E+01	0.7657E+00
93	0.3692E+01	-0.6931E+00	193	0.7705E+01	0.8345E+00
94	0.3732E+01	-0.9573E+00	194	0.7745E+01	0.8767E+00
95	0.3772E+01	-0.1251E+01	195	0.7785E+01	0.7434E+00
96	0.3813E+01	-0.1417E+01	196	0.7825E+01	0.6749E+00
97	0.3853E+01	-0.1436E+01	197	0.7865E+01	0.6446E+00
98	0.3893E+01	-0.1434E+01	198	0.7905E+01	0.5144E+00
99	0.3933E+01	-0.1288E+01	199	0.7945E+01	0.4762E+00
100	0.3973E+01	-0.1113E+01	200	0.7985E+01	0.5338E+00

Table D-2. Cross Spectral Analysis of Casing Kulite and Reference Strain Gage for Phasing.

AVERAGE SPEED = 11680 CIRCUMFERENTIAL LOCATION = 0.21271E+01 CHANNEL A = SG # 828						
MACH NUMBER = 0.500 RADIAL POSITION = 10.500 CHANNEL B = CK # 705						
INDEX	FREQUENCY HZ	CROSS-SPECTRUM MAGNITUDE	PHASE ANGLE DEGREES	AUTO-CH A	AUTO-CH B	COHERENCE
1	0.00	0.6610E+01	-180.00	0.4377E+01	0.1507E+01	1.000
2	1.52	0.2444E+00	-84.38	0.7425E+00	0.3542E+00	0.863
3	3.04	0.8553E-01	-39.37	0.1368E+00	0.5740E+00	1.000
4	4.56	0.2444E+00	78.75	0.2736E+00	0.2598E+00	1.000
5	6.08	0.2810E+00	-30.94	0.3517E+00	0.8574E+00	0.869
6	7.60	0.6476E+00	45.00	0.9380E+00	0.7963E+00	0.752
7	9.12	0.2322E+00	22.50	0.4299E+00	0.6106E+00	0.782
8	10.65	0.9286E+00	61.87	0.8598E+00	0.1158E+01	0.870
9	12.17	0.3666E-01	135.00	0.5862E-01	0.5740E+00	1.000
10	13.69	0.1711E+00	56.25	0.5765E+00	0.2956E+00	1.000
11	15.21	0.2933E+00	-144.84	0.3908E+00	0.7132E+00	1.000
12	16.73	0.7820E+00	-14.06	0.8989E+00	0.8964E+00	0.942
13	18.25	0.1173E+01	60.47	0.9770E+00	0.1312E+01	0.838
14	19.77	0.4154E+00	-105.47	0.4983E+00	0.7865E+00	1.000
15	21.29	0.4032E+00	-161.72	0.1065E+01	0.3908E+00	0.939
16	22.81	0.2444E-01	135.00	0.2052E+00	0.9038E-01	1.000
17	24.33	0.1955E+00	129.37	0.2931E+00	0.6546E+00	1.000
18	25.85	0.1344E+00	123.75	0.3517E+00	0.3835E+00	0.993
19	27.37	0.5865E+00	-59.06	0.6448E+00	0.9331E+00	0.950
20	28.89	0.3177E+00	160.31	0.4006E+00	0.8123E+00	0.939
21	30.42	0.5254E+00	-43.59	0.7621E+00	0.7474E+00	0.851
22	31.94	0.1466E+00	146.25	0.3810E+00	0.3859E+00	0.994
23	33.46	0.4888E-01	-78.75	0.2247E+00	0.1954E+00	1.000
24	34.98	0.6476E+00	50.62	0.1045E+01	0.7157E+00	0.749
25	36.50	0.7331E-01	33.75	0.4885E-01	0.1331E+01	1.000
26	38.02	0.1833E+00	149.06	0.2931E+00	0.5789E+00	1.000
27	39.54	0.2566E+00	-106.87	0.4494E+00	0.5960E+00	0.918
28	41.06	0.3177E+00	137.81	0.6155E+00	0.5056E+00	1.000
29	42.58	0.1833E+00	-123.75	0.4104E+00	0.4446E+00	1.000
30	44.10	0.1833E+00	-33.75	0.4885E+00	0.4006E+00	0.877
31	45.62	0.3421E+00	125.16	0.3615E+00	0.1058E+01	0.801
32	47.15	0.1222E+00	28.13	0.5091E+00	0.2614E+00	0.847
33	48.67	0.2810E+00	-78.75	0.2345E+00	0.1212E+01	0.979
34	50.19	0.1222E+00	-73.12	0.3029E+00	0.3615E+00	1.000
35	51.71	0.1344E+00	-123.75	0.3713E+00	0.3078E+00	1.000
36	53.23	0.3666E+00	3.44	0.1192E+01	0.3346E+00	0.845
37	54.75	0.1955E+00	-132.19	0.4104E+00	0.4177E+00	1.000
38	56.27	0.1955E+00	129.37	0.5276E+00	0.3444E+00	1.000
39	57.79	0.1344E+00	163.75	0.4104E+00	0.2882E+00	1.000
40	59.31	0.2810E+00	46.41	0.4592E+00	0.6571E+00	0.868
41	60.83	0.1026E+01	-5.63	0.8012E+00	0.1343E+01	0.909
42	62.35	0.4521E+00	-99.84	0.8793E+00	0.5423E+00	0.899
43	63.87	0.1466E+00	0.00	0.2247E+00	0.6766E+00	0.930
44	65.40	0.7331E+00	81.56	0.8109E+00	0.9990E+00	0.819
45	66.92	0.7576E+00	33.75	0.5862E+00	0.1473E+01	0.770
46	68.44	0.6354E+00	-123.75	0.6351E+00	0.1077E+01	0.863
47	69.96	0.3910E+00	40.78	0.5667E+00	0.7425E+00	0.863
48	71.48	0.6476E+00	-119.53	0.1524E+01	0.4421E+00	0.924
49	73.00	0.8553E-01	-67.50	0.1348E+01	0.6595E-01	0.925
50	74.52	0.6354E+00	-160.31	0.2198E+01	0.3102E+00	0.868
51	76.04	0.1124E+01	-39.37	0.1348E+01	0.9551E+00	0.762
52	77.56	0.1454E+01	-1.41	0.9966E+00	0.1536E+01	0.902
53	79.08	0.1067E+02	-5.63	0.3683E+01	0.2995E+01	0.935
54	80.60	0.3374E+02	43.59	0.6615E+01	0.5957E+01	0.733
55	82.12	0.1735E+01	140.65	0.1266E+01	0.1050E+01	0.784
56	83.64	0.1062E+01	50.03	0.1593E+01	0.7181E+00	0.768
57	85.17	0.2370E+01	42.19	0.1983E+01	0.1304E+01	0.840
58	86.69	0.7576E+00	105.47	0.1094E+01	0.7621E+00	0.825
59	88.21	0.1711E+00	-30.94	0.1075E+01	0.1563E+00	1.000
60	89.73	0.2332E+00	70.31	0.9477E+00	0.2638E+00	0.862
61	91.25	0.2077E+00	67.50	0.1563E+00	0.1466E+01	0.822
62	92.77	0.4643E+00	130.78	0.7035E+00	0.6693E+00	0.973
63	94.29	0.3543E+00	2.81	0.3127E+00	0.1252E+01	0.812
64	95.81	0.1466E+00	26.31	0.1759E+00	0.8036E+00	1.000

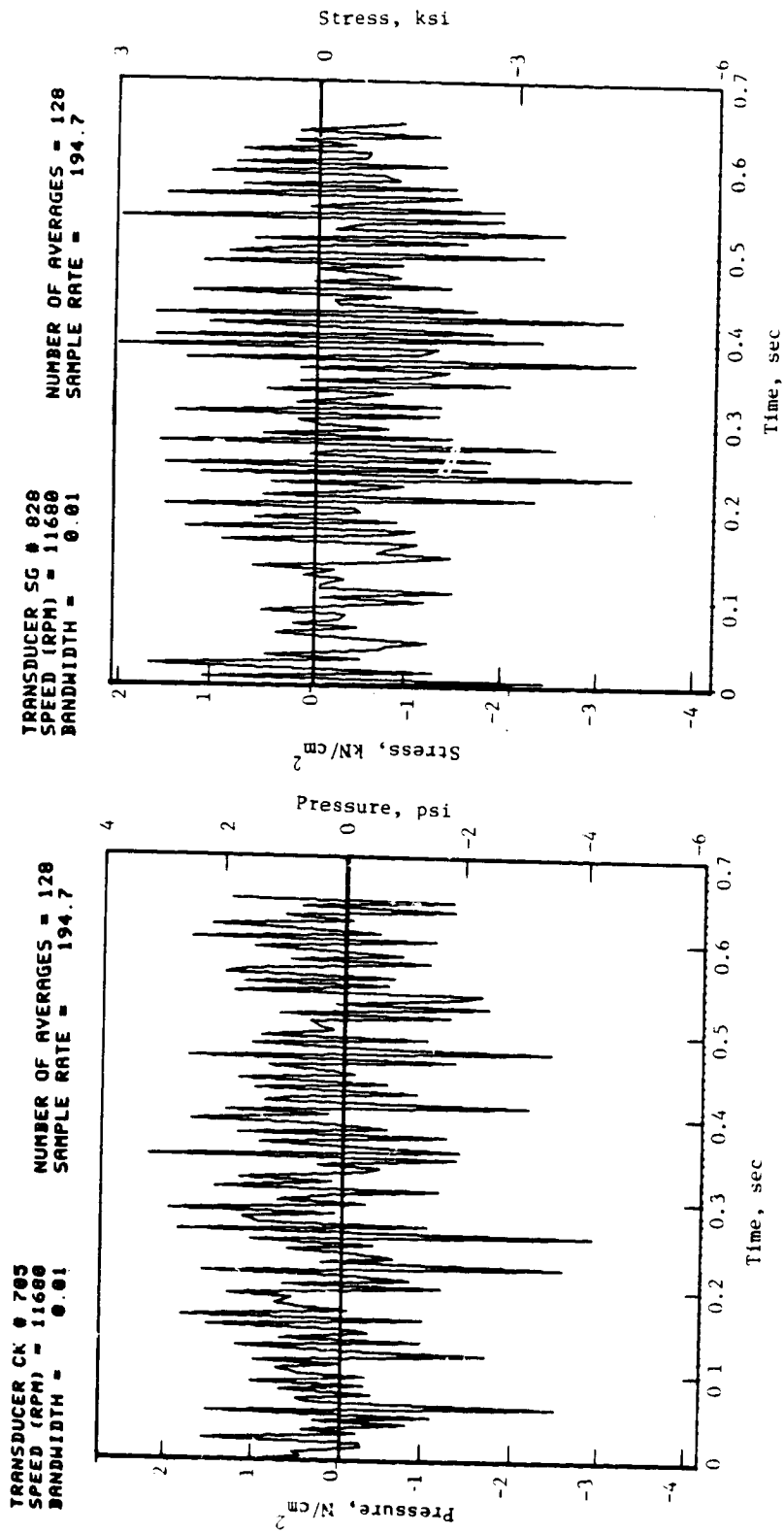


Figure D-1. Once Per Revolution Sampling of Casing Kulite.

Figure D-2. Once Per Revolution Sampling of Strain Gage.

Table D-3. P_T Yaw Probe Ensemble Average for 200 Points.

NUMBER OF FRAMES IN THE AVERAGE = 64
NUMBER OF SAMPLE POINTS = 200
SAMPLE RATE = 380000 Hz

AVERAGE SPEED = 11680
MACH NUMBER = 0.500
RADIAL POSITION = 9.968

INDEX	DISTANCE (INCHES)	TOTAL PRESSURE (PSI)	YAW ANGLE (DEGREES)	INDEX	DISTANCE (INCHES)	TOTAL PRESSURE (PSI)	YAW ANGLE (DEGREES)
1	0.0000E+00	0.1847E+02	81.70	2	0.3806E-01	0.1851E+02	81.70
3	0.7612E-01	0.1844E+02	81.70	4	0.1142E+00	0.1840E+02	81.70
5	0.1522E+00	0.1847E+02	81.70	6	0.1903E+00	0.1843E+02	81.70
7	0.2284E+00	0.1847E+02	81.70	8	0.2664E+00	0.1850E+02	81.70
9	0.3045E+00	0.1845E+02	81.70	10	0.3426E+00	0.1847E+02	81.70
11	0.3806E+00	0.1848E+02	81.70	12	0.4187E+00	0.1846E+02	81.70
13	0.4567E+00	0.1844E+02	81.70	14	0.4948E+00	0.1848E+02	81.70
15	0.5328E+00	0.1843E+02	81.70	16	0.5709E+00	0.1834E+02	81.70
17	0.6090E+00	0.1840E+02	81.70	18	0.6471E+00	0.1845E+02	81.70
19	0.6851E+00	0.1848E+02	81.70	20	0.7232E+00	0.1856E+02	81.70
21	0.7612E+00	0.1863E+02	81.70	22	0.7993E+00	0.1856E+02	81.70
23	0.8374E+00	0.1855E+02	81.70	24	0.8754E+00	0.1856E+02	81.70
25	0.9135E+00	0.1851E+02	81.70	26	0.9515E+00	0.1852E+02	81.70
27	0.9896E+00	0.1850E+02	81.70	28	0.1028E+01	0.1852E+02	81.70
29	0.1066E+01	0.1857E+02	81.70	30	0.1104E+01	0.1855E+02	81.70
31	0.1142E+01	0.1861E+02	81.70	32	0.1180E+01	0.1871E+02	81.70
33	0.1218E+01	0.1881E+02	81.70	34	0.1256E+01	0.1891E+02	81.70
35	0.1294E+01	0.1897E+02	81.70	36	0.1332E+01	0.1884E+02	81.70
37	0.1370E+01	0.1890E+02	81.70	38	0.1408E+01	0.1887E+02	81.70
39	0.1446E+01	0.1892E+02	81.70	40	0.1484E+01	0.1877E+02	81.70
41	0.1522E+01	0.1875E+02	81.70	42	0.1561E+01	0.1872E+02	81.70
43	0.1598E+01	0.1873E+02	81.70	44	0.1637E+01	0.1862E+02	81.70
45	0.1675E+01	0.1867E+02	81.70	46	0.1713E+01	0.1882E+02	81.70
47	0.1751E+01	0.1878E+02	81.70	48	0.1789E+01	0.1883E+02	81.70
49	0.1827E+01	0.1886E+02	81.70	50	0.1865E+01	0.1884E+02	81.70
51	0.1903E+01	0.1901E+02	81.70	52	0.1941E+01	0.1907E+02	81.70
53	0.1979E+01	0.1900E+02	81.70	54	0.2017E+01	0.1913E+02	81.70
55	0.2055E+01	0.1921E+02	81.70	56	0.2093E+01	0.1920E+02	81.70
57	0.2131E+01	0.1920E+02	81.70	58	0.2170E+01	0.1916E+02	81.70
59	0.2208E+01	0.1925E+02	81.70	60	0.2246E+01	0.1926E+02	81.70
61	0.2284E+01	0.1927E+02	81.70	62	0.2322E+01	0.1940E+02	81.70
63	0.2360E+01	0.1944E+02	81.70	64	0.2398E+01	0.1943E+02	81.70
65	0.2436E+01	0.1945E+02	81.70	66	0.2474E+01	0.1954E+02	81.70
67	0.2512E+01	0.1950E+02	81.70	68	0.2550E+01	0.1945E+02	81.70
69	0.2588E+01	0.1953E+02	81.70	70	0.2626E+01	0.1949E+02	81.70
71	0.2664E+01	0.1943E+02	81.70	72	0.2702E+01	0.1940E+02	81.70
73	0.2740E+01	0.1934E+02	81.70	74	0.2778E+01	0.1939E+02	81.70
75	0.2817E+01	0.1941E+02	81.70	76	0.2855E+01	0.1929E+02	81.70
77	0.2893E+01	0.1930E+02	81.70	78	0.2931E+01	0.1934E+02	81.70
79	0.2969E+01	0.1925E+02	81.70	80	0.3007E+01	0.1926E+02	81.70
81	0.3045E+01	0.1922E+02	81.70	82	0.3083E+01	0.1907E+02	81.70
83	0.3121E+01	0.1901E+02	81.70	84	0.3159E+01	0.1902E+02	81.70
85	0.3197E+01	0.1901E+02	81.70	86	0.3235E+01	0.1909E+02	81.70
87	0.3273E+01	0.1909E+02	81.70	88	0.3311E+01	0.1906E+02	81.70
89	0.3349E+01	0.1905E+02	81.70	90	0.3388E+01	0.1897E+02	81.70
91	0.3425E+01	0.1903E+02	81.70	92	0.3464E+01	0.1907E+02	81.70
93	0.3501E+01	0.1902E+02	81.70	94	0.3540E+01	0.1904E+02	81.70
95	0.3578E+01	0.1908E+02	81.70	96	0.3616E+01	0.1906E+02	81.70
97	0.3654E+01	0.1902E+02	81.70	98	0.3692E+01	0.1911E+02	81.70
99	0.3730E+01	0.1919E+02	81.70	100	0.3768E+01	0.1918E+02	81.70
101	0.3806E+01	0.1923E+02	81.70	102	0.3844E+01	0.1921E+02	81.70
103	0.3882E+01	0.1923E+02	81.70	104	0.3920E+01	0.1922E+02	81.70
105	0.3958E+01	0.1918E+02	81.70	106	0.3997E+01	0.1921E+02	81.70
107	0.4035E+01	0.1923E+02	81.70	108	0.4073E+01	0.1926E+02	81.70
109	0.4111E+01	0.1918E+02	81.70	110	0.4149E+01	0.1922E+02	81.70
111	0.4187E+01	0.1930E+02	81.70	112	0.4225E+01	0.1929E+02	81.70
113	0.4263E+01	0.1935E+02	81.70	114	0.4301E+01	0.1938E+02	81.70
115	0.4339E+01	0.1930E+02	81.70	116	0.4377E+01	0.1926E+02	81.70
117	0.4415E+01	0.1932E+02	81.70	118	0.4453E+01	0.1929E+02	81.70
119	0.4491E+01	0.1917E+02	81.70	120	0.4529E+01	0.1918E+02	81.70
121	0.4567E+01	0.1920E+02	81.70	122	0.4605E+01	0.1926E+02	81.70
123	0.4644E+01	0.1923E+02	81.70	124	0.4682E+01	0.1922E+02	81.70
125	0.4720E+01	0.1934E+02	81.70	126	0.4758E+01	0.1925E+02	81.70
127	0.4796E+01	0.1915E+02	81.70	128	0.4834E+01	0.1919E+02	81.70
129	0.4872E+01	0.1919E+02	81.70	130	0.4910E+01	0.1923E+02	81.70
131	0.4948E+01	0.1918E+02	81.70	132	0.4986E+01	0.1916E+02	81.70
133	0.5024E+01	0.1928E+02	81.70	134	0.5062E+01	0.1933E+02	81.70
135	0.5100E+01	0.1931E+02	81.70	136	0.5138E+01	0.1931E+02	81.70
137	0.5176E+01	0.1931E+02	81.70	138	0.5215E+01	0.1924E+02	81.70
139	0.5252E+01	0.1918E+02	81.70	140	0.5291E+01	0.1915E+02	81.70
141	0.5328E+01	0.1917E+02	81.70	142	0.5367E+01	0.1920E+02	81.70
143	0.5404E+01	0.1916E+02	81.70	144	0.5443E+01	0.1923E+02	81.70
145	0.5480E+01	0.1936E+02	81.70	146	0.5519E+01	0.1924E+02	81.70
147	0.5556E+01	0.1923E+02	81.70	148	0.5595E+01	0.1915E+02	81.70
149	0.5632E+01	0.1913E+02	81.70	150	0.5671E+01	0.1913E+02	81.70
151	0.5708E+01	0.1912E+02	81.70	152	0.5747E+01	0.1917E+02	81.70
153	0.5784E+01	0.1927E+02	81.70	154	0.5824E+01	0.1944E+02	81.70
155	0.5860E+01	0.1947E+02	81.70	156	0.5900E+01	0.1934E+02	81.70
157	0.5936E+01	0.1927E+02	81.70	158	0.5976E+01	0.1927E+02	81.70
159	0.6012E+01	0.1922E+02	81.70	160	0.6052E+01	0.1919E+02	81.70
161	0.6088E+01	0.1924E+02	81.70	162	0.6128E+01	0.1916E+02	81.70
163	0.6164E+01	0.1921E+02	81.70	164	0.6204E+01	0.1937E+02	81.70
165	0.6240E+01	0.1923E+02	81.70	166	0.6280E+01	0.1916E+02	81.70
167	0.6316E+01	0.1918E+02	81.70	168	0.6356E+01	0.1910E+02	81.70
169	0.6392E+01	0.1913E+02	81.70	170	0.6432E+01	0.1913E+02	81.70
171	0.6471E+01	0.1905E+02	81.70	172	0.6508E+01	0.1905E+02	81.70
173	0.6547E+01	0.1905E+02	81.70	174	0.6584E+01	0.1912E+02	81.70
175	0.6623E+01	0.1901E+02	81.70	176	0.6661E+01	0.1899E+02	81.70
177	0.6699E+01	0.1916E+02	81.70	178	0.6737E+01	0.1917E+02	81.70
179	0.6775E+01	0.1918E+02	81.70	180	0.6813E+01	0.1921E+02	81.70
181	0.6851E+01	0.1930E+02	81.70	182	0.6889E+01	0.1942E+02	81.70
183	0.6927E+01	0.1925E+02	81.70	184	0.6965E+01	0.1929E+02	81.70
185	0.7003E+01	0.1939E+02	81.70	186	0.7041E+01	0.1927E+02	81.70
187	0.7079E+01	0.1930E+02	81.70	188	0.7118E+01	0.1943E+02	81.70
189	0.7155E+01	0.1948E+02	81.70	190	0.7194E+01	0.1955E+02	81.70
191	0.7231E+01	0.1954E+02	81.70	192	0.7270E+01	0.1958E+02	81.70
193	0.7307E+01	0.1968E+02	81.70	194	0.7346E+01	0.1963E+02	81.70
195	0.7383E+01	0.1963E+02	81.70	196	0.7422E+01	0.1962E+02	81.70
197	0.7459E+01	0.1978E+02	81.70	198	0.7498E+01	0.1980E+02	81.70
199	0.7535E+01	0.1983E+02	81.70	200	0.7574E+01	0.1980E+02	81.70

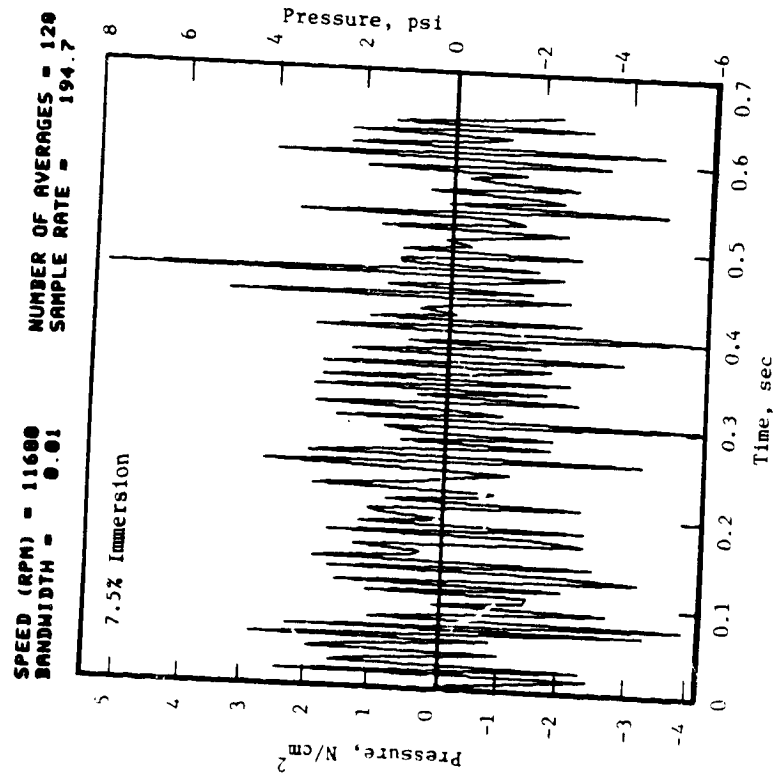


Figure D-3. Once Per Revolution Sampling of P_T Yaw Probe.

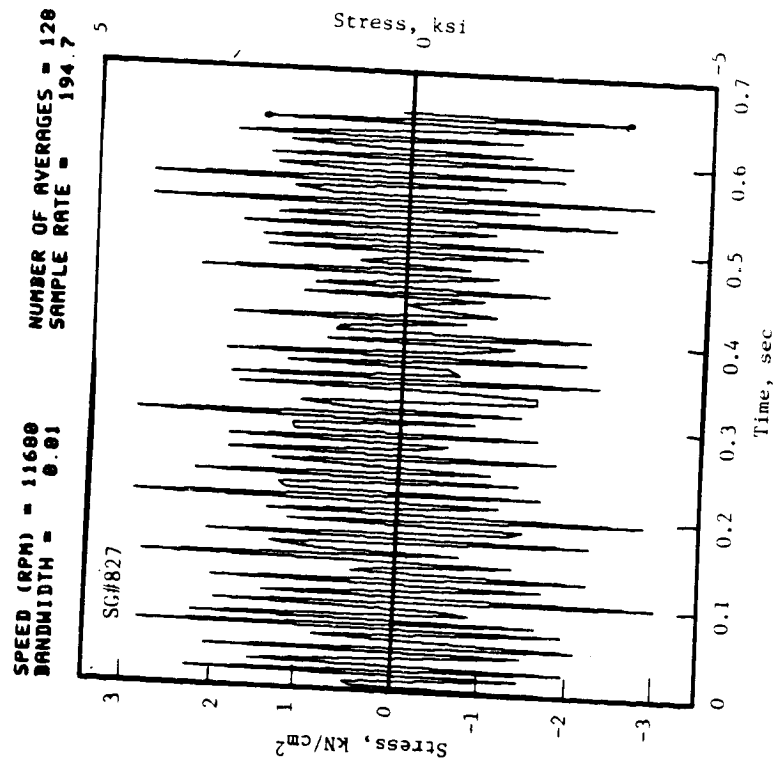


Figure D-4. Once Per Revolution Sampling of Strain Gage.

GENERAL ANALYSIS OF POWER SPECTRA

Table D-4. Cross Spectral Analysis of P_T Yaw Probe and Reference Strain Gage for Phasing.

AVERAGE SPEED = 11680 CIRCUMFERENTIAL LOCATION = 0.15225E+00 CHANNEL A = S/G # 827				MACH NUMBER = 0.500 RADIAL POSITION = 9.958 CHANNEL B = Xp/YC		
INDEX	FREQUENCY HZ	CROSS-SPECTRUM MAGNITUDE	PHASE ANGLE DEGREES	AUTO-CH A	AUTO-CH B	COHERENCE
1	0.00	0.4154E+00	-180.00	0.1856E+00	0.2074E+01	1.000
2	1.52	0.2322E+00	-8.44	0.3322E+00	0.7425E+00	0.886
3	3.04	0.2199E+00	98.44	0.8109E+00	0.2833E+00	0.916
4	4.56	0.9775E+00	91.41	0.6937E+00	0.1571E+01	0.805
5	6.08	0.2810E+00	-172.97	0.7035E+00	0.4079E+00	0.959
6	7.60	0.4277E+00	-61.87	0.4201E+00	0.1031E+01	0.975
7	9.12	0.6965E+00	12.66	0.6351E+00	0.1172E+01	0.875
8	10.65	0.5010E+00	-59.06	0.4006E+00	0.1346E+01	0.863
9	12.17	0.3543E+00	92.81	0.5765E+00	0.6351E+00	0.937
10	13.69	0.5805E+00	-154.69	0.8989E+00	0.6883E+00	0.897
11	15.21	0.1833E+00	0.00	0.1524E+01	0.1368E+00	0.773
12	16.73	0.7331E-01	-123.75	0.2345E+00	0.2394E+00	1.000
13	18.25	0.9653E+00	-75.94	0.9477E+00	0.1060E+01	0.923
14	19.77	0.2199E+00	8.44	0.1036E+01	0.2198E+00	0.933
15	21.29	0.3299E+00	106.87	0.5178E+00	0.6424E+00	0.924
16	22.81	0.4888E-01	-157.25	0.9770E-01	0.5496E+00	0.829
17	24.33	0.9775E-01	-157.50	0.1075E+00	0.8012E+00	1.000
18	25.85	0.7087E+00	-8.44	0.8305E+00	0.8623E+00	0.980
19	27.37	0.1466E+00	-39.37	0.2638E+00	0.5569E+00	0.996
20	28.90	0.1955E+00	-165.94	0.3322E+00	0.5447E+00	1.000
21	30.42	0.6232E+00	-56.25	0.7914E+00	0.8183E+00	0.926
22	31.94	0.5376E+00	-19.69	0.6546E+00	0.8598E+00	0.912
23	33.46	0.7209E+00	18.28	0.5374E+00	0.1448E+01	0.858
24	34.98	0.3666E-01	-112.50	0.2247E+00	0.1295E+00	1.000
25	36.50	0.3543E+00	91.41	0.4885E+00	0.7987E+00	0.825
26	38.02	0.1955E+00	160.31	0.3127E+00	0.6302E+00	0.985
27	39.54	0.7331E-01	-168.75	0.3908E+00	0.1734E+00	1.000
28	41.06	0.4888E-01	-45.00	0.5569E+00	0.9770E-01	0.807
29	42.58	0.1466E+00	-101.25	0.3224E+00	0.3957E+00	1.000
30	44.10	0.4643E+00	63.28	0.4104E+00	0.1155E+01	0.959
31	45.62	0.3421E+00	92.03	0.2833E+00	0.1336E+01	0.817
32	47.15	0.2810E+00	-54.84	0.4006E+00	0.7450E+00	0.887
33	48.67	0.1100E+00	-168.75	0.6742E+00	0.1612E+00	1.000
34	50.19	0.1955E+00	-112.50	0.3615E+00	0.5081E+00	1.000
35	51.71	0.8675E+00	153.28	0.4003E+00	0.2247E+01	0.929
36	53.23	0.7209E+00	-94.22	0.9770E+00	0.7767E+00	0.902
37	54.75	0.4888E-01	11.25	0.6839E-01	0.6815E+00	1.000
38	56.27	0.7087E+00	19.69	0.7914E+00	0.9697E+00	0.853
39	57.79	0.1466E+00	-112.50	0.4885E+00	0.2907E+00	1.000
40	59.31	0.9531E+00	71.72	0.6058E+00	0.1688E+01	0.869
41	60.83	0.3421E+00	5.63	0.9380E+00	0.4152E+00	0.772
42	62.35	0.5499E+00	-90.00	0.6155E+00	0.1026E+01	0.758
43	63.87	0.6720E+00	-101.25	0.7621E+00	0.9795E+00	0.811
44	65.39	0.1234E+01	-43.59	0.1378E+01	0.9209E+00	0.946
45	66.91	0.1711E+00	-19.69	0.4201E+00	0.4250E+00	0.918
46	68.43	0.3531E+01	-21.09	0.1309E+01	0.2951E+01	0.836
47	69.95	0.2444E+00	22.50	0.4787E+00	0.5520E+00	0.855
48	71.47	0.3751E+01	-5.63	0.2247E+01	0.1742E+01	0.919
49	72.99	0.2468E+01	-122.34	0.2785E+01	0.1011E+01	0.768
50	74.51	0.1603E+02	-49.22	0.4231E+01	0.4314E+01	0.772
51	76.03	0.1136E+01	-19.69	0.2198E+01	0.5520E+00	0.877
52	77.55	0.6232E+00	-79.77	0.9663E+01	0.6778E+01	0.929
53	79.07	0.3715E+01	11.25	0.2687E+01	0.1549E+01	0.797
54	80.59	0.5951E+01	-43.59	0.1944E+01	0.3173E+01	0.930
55	82.11	0.3666E+00	73.12	0.5067E+00	0.6961E+00	0.853
56	83.63	0.1051E+01	-8.44	0.1827E+01	0.6424E+00	0.802
57	85.15	0.3421E+00	-30.37	0.6546E+00	0.5300E+00	0.972
58	86.67	0.7820E+00	-5.63	0.7132E+00	0.1180E+01	0.864
59	88.19	0.9775E+00	-19.69	0.8012E+00	0.1365E+01	0.798
60	89.71	0.3421E+00	123.75	0.7425E+00	0.5129E+00	0.807
61	91.23	0.1039E+01	28.13	0.8403E+00	0.1426E+01	0.751
62	92.75	0.1197E+01	-25.31	0.6448E+00	0.2040E+01	0.829
63	94.27	0.4888E+00	-29.53	0.4963E+00	0.1019E+01	0.927
64	95.79	0.9164E+00	-40.78	0.6644E+00	0.1492E+01	0.854

ORIGINAL COPY OF POOR QUALITY

Table D-5. X-Array Probe Ensemble Average for 200 Points.

AVERAGE SPEED = 11680

NUMBER OF FRAMES IN THE AVERAGE = 64

NUMBER OF SAMPLE POINTS = 200

SAMPLE RATE = 320000. HZ

MACH NUMBER = 0.300

RADIAL POSITION = 10.168

INLET

DENSITY = 0.072400

LOCATION	AXIAL VELOCITY	AXIAL MASS FLOW	TANGENTIAL VELOCITY	TANGENTIAL MASS FLOW	ABSOLUTE VELOCITY	ABSOLUTE MASS FLOW	FLOW DIRECTION (AXIAL-REF)
0.0000E+00	0.3372E+03	0.2442E+02	0.5771E+02	0.4178E+01	0.3421E+03	0.2477E+02	0.9711E+01
0.3886E-01	0.3370E+03	0.2440E+02	0.5970E+02	0.4323E+01	0.3423E+03	0.2478E+02	0.1005E+02
0.7773E-01	0.3343E+03	0.2420E+02	0.5716E+02	0.4139E+01	0.3391E+03	0.2455E+02	0.9703E+01
0.1166E+00	0.3282E+03	0.2376E+02	0.5018E+02	0.3633E+01	0.3320E+03	0.2404E+02	0.3692E+01
0.1555E+00	0.3232E+03	0.2340E+02	0.4224E+02	0.3058E+01	0.3260E+03	0.2360E+02	0.7444E+01
0.1943E+00	0.3204E+03	0.2320E+02	0.3652E+02	0.2644E+01	0.3225E+03	0.2335E+02	0.6502E+01
0.2332E+00	0.3189E+03	0.2300E+02	0.3432E+02	0.2485E+01	0.3207E+03	0.2322E+02	0.6144E+01
0.2721E+00	0.3182E+03	0.2304E+02	0.3483E+02	0.2521E+01	0.3195E+03	0.2318E+02	0.6313E+01
0.3109E+00	0.3176E+03	0.2300E+02	0.3240E+02	0.2549E+01	0.3201E+03	0.2322E+02	0.6144E+01
0.3498E+00	0.3161E+03	0.2288E+02	0.2743E+02	0.2158E+01	0.3195E+03	0.2314E+02	0.6257E+01
0.3886E+00	0.3147E+03	0.2279E+02	0.2580E+02	0.1986E+01	0.3155E+03	0.2289E+02	0.5403E+01
0.4275E+00	0.3143E+03	0.2275E+02	0.2770E+02	0.2006E+01	0.3160E+03	0.2288E+02	0.4988E+01
0.4664E+00	0.3148E+03	0.2279E+02	0.2923E+02	0.2116E+01	0.3172E+03	0.2297E+02	0.5287E+01
0.5052E+00	0.3159E+03	0.2287E+02	0.2855E+02	0.2067E+01	0.3195E+03	0.2313E+02	0.5126E+01
0.5441E+00	0.3183E+03	0.2304E+02	0.2628E+02	0.1903E+01	0.3208E+03	0.2323E+02	0.4699E+01
0.5830E+00	0.3197E+03	0.2315E+02	0.1938E+02	0.1662E+01	0.3201E+03	0.2318E+02	0.4112E+01
0.6218E+00	0.3184E+03	0.2305E+02	0.1725E+02	0.1403E+01	0.3190E+03	0.2309E+02	0.3484E+01
0.6607E+00	0.3168E+03	0.2293E+02	0.1537E+02	0.1249E+01	0.3195E+03	0.2313E+02	0.3095E+01
0.6996E+00	0.3147E+03	0.2278E+02	0.1275E+02	0.1113E+01	0.3171E+03	0.2296E+02	0.2778E+01
0.7384E+00	0.3068E+03	0.2221E+02	0.7908E+01	0.9228E+00	0.3150E+03	0.2280E+02	0.2319E+01
0.7773E+00	0.2982E+03	0.2159E+02	0.3414E+01	0.5728E+00	0.3069E+03	0.2222E+02	0.1477E+01
0.8162E+00	0.2933E+03	0.2123E+02	0.2044E+01	0.3414E+01	0.2983E+03	0.2159E+02	0.6555E+00
0.8550E+00	0.2956E+03	0.2140E+02	0.2709E+01	0.2209E+00	0.2933E+03	0.2123E+02	0.3993E+00
0.8939E+00	0.2948E+03	0.2134E+02	0.2889E+01	0.2164E+00	0.2956E+03	0.2140E+02	0.5913E+00
0.9328E+00	0.2918E+03	0.2113E+02	0.1178E+01	0.8526E-01	0.2948E+03	0.2134E+02	0.5810E+00
0.9716E+00	0.2927E+03	0.2106E+02	0.1587E+01	0.1149E+00	0.2927E+03	0.2119E+02	0.2405E+00
0.1010E+01	0.2936E+03	0.2106E+02	0.4689E+01	0.3395E+00	0.2918E+03	0.2113E+02	0.3116E+00
0.1049E+01	0.2950E+03	0.2136E+02	0.6521E+01	0.4721E+00	0.2936E+03	0.2126E+02	0.9151E+00
0.1088E+01	0.2946E+03	0.2133E+02	0.4961E+01	0.3592E+00	0.2951E+03	0.2136E+02	0.1266E+01
0.1127E+01	0.2927E+03	0.2119E+02	0.2042E+01	0.1478E+00	0.2927E+03	0.2134E+02	0.9646E+00
0.1166E+01	0.2917E+03	0.2109E+02	0.3969E+00	0.2873E-01	0.2917E+03	0.2119E+02	0.3998E+00
0.1205E+01	0.2891E+03	0.2093E+02	0.3294E+00	0.2385E-01	0.2913E+03	0.2112E+02	0.7796E-01
0.1244E+01	0.2893E+03	0.2095E+02	0.4529E+01	0.1634E+00	0.2891E+03	0.2109E+02	0.6478E-01
0.1283E+01	0.2900E+03	0.2100E+02	0.3847E+01	0.3062E+00	0.2893E+03	0.2093E+02	0.4474E+00
0.1321E+01	0.2908E+03	0.2106E+02	0.2316E+01	0.2785E+00	0.2900E+03	0.2095E+02	0.8376E+00
0.1360E+01	0.2908E+03	0.2105E+02	0.2283E+01	0.1677E+00	0.2908E+03	0.2106E+02	0.7600E+00
0.1399E+01	0.2923E+03	0.2116E+02	0.2635E+01	0.1653E+00	0.2908E+03	0.2106E+02	0.4563E+00
0.1438E+01	0.2950E+03	0.2120E+02	0.2425E+01	0.1908E+00	0.2923E+03	0.2116E+02	0.4497E+00
0.1477E+01	0.3015E+03	0.2136E+02	0.3373E+00	0.2442E-01	0.2950E+03	0.2120E+02	0.5166E+00
0.1516E+01	0.3091E+03	0.2183E+02	0.4557E+01	0.3300E+00	0.2950E+03	0.2136E+02	0.4744E+00
0.1555E+01	0.3145E+03	0.2238E+02	0.1034E+02	0.7486E+00	0.3015E+03	0.2183E+02	0.6551E-01
0.1593E+01	0.3173E+03	0.2277E+02	0.1402E+02	0.1015E+01	0.3091E+03	0.2238E+02	0.8660E+00
0.1632E+01	0.3198E+03	0.2297E+02	0.1479E+02	0.1071E+01	0.3145E+03	0.2277E+02	0.1916E+01
0.1671E+01	0.3200E+03	0.2317E+02	0.1498E+02	0.1085E+01	0.3173E+03	0.2300E+02	0.2553E+01
0.1710E+01	0.3213E+03	0.2335E+02	0.1590E+02	0.1152E+01	0.3198E+03	0.2318E+02	0.2669E+01
0.1749E+01	0.3225E+03	0.2349E+02	0.1854E+02	0.1343E+01	0.3200E+03	0.2320E+02	0.2845E+01
0.1788E+01	0.3245E+03	0.2361E+02	0.2066E+02	0.1597E+01	0.3213E+03	0.2330E+02	0.3303E+01
0.1827E+01	0.3262E+03	0.2361E+02	0.2425E+02	0.1755E+01	0.3225E+03	0.2341E+02	0.3913E+01
0.1866E+01	0.3279E+03	0.2374E+02	0.2533E+02	0.1848E+01	0.3245E+03	0.2356E+02	0.4273E+01
0.1904E+01	0.3291E+03	0.2382E+02	0.2797E+02	0.2025E+01	0.3262E+03	0.2369E+02	0.4475E+01
0.1943E+01	0.3294E+03	0.2395E+02	0.3141E+02	0.2274E+01	0.3279E+03	0.2383E+02	0.4875E+01
0.1982E+01	0.3301E+03	0.2390E+02	0.3431E+02	0.2484E+01	0.3291E+03	0.2393E+02	0.5452E+01
0.2021E+01	0.3305E+03	0.2393E+02	0.3670E+02	0.2657E+01	0.3301E+03	0.2398E+02	0.5947E+01
0.2060E+01	0.3308E+03	0.2395E+02	0.3727E+02	0.2699E+01	0.3305E+03	0.2404E+02	0.6345E+01
0.2099E+01	0.3301E+03	0.2390E+02	0.3545E+02	0.2567E+01	0.3308E+03	0.2408E+02	0.6434E+01
0.2138E+01	0.3301E+03	0.2390E+02	0.3279E+02	0.2453E+01	0.3305E+03	0.2403E+02	0.6118E+01
0.2176E+01	0.3301E+03	0.2390E+02	0.3279E+02	0.2374E+01	0.3308E+03	0.2403E+02	0.5860E+01
0.2215E+01	0.3301E+03	0.2390E+02	0.3165E+02	0.2291E+01	0.3301E+03	0.2382E+02	0.5719E+01
0.2254E+01	0.3301E+03	0.2390E+02	0.3071E+02	0.2223E+01	0.3301E+03	0.2365E+02	0.5560E+01
0.2293E+01	0.3301E+03	0.2390E+02	0.2897E+02	0.2098E+01	0.3301E+03	0.2354E+02	0.5419E+01
0.2332E+01	0.3301E+03	0.2390E+02	0.2734E+02	0.1975E+01	0.3301E+03	0.2344E+02	0.5149E+01
0.2371E+01	0.3301E+03	0.2390E+02	0.2678E+02	0.1939E+01	0.3301E+03	0.2328E+02	0.4881E+01
0.2410E+01	0.3301E+03	0.2390E+02	0.2678E+02	0.2002E+01	0.3301E+03	0.2319E+02	0.4796E+01
0.2448E+01	0.3301E+03	0.2390E+02	0.2678E+02	0.2068E+01	0.3301E+03	0.2309E+02	0.4973E+01
0.2487E+01	0.3301E+03	0.2390E+02	0.2678E+02	0.2136E+01	0.3301E+03	0.2300E+02	0.5133E+01
0.2526E+01	0.3301E+03	0.2390E+02	0.2678E+02	0.2199E+01	0.3301E+03	0.2293E+02	0.4849E+01
0.2565E+01	0.3301E+03	0.2390E+02	0.2678E+02	0.2265E+01	0.3301E+03	0.2285E+02	0.4499E+01
0.2604E+01	0.3301E+03	0.2390E+02	0.2678E+02	0.2330E+01	0.3301E+03	0.2277E+02	0.4309E+01
0.2643E+01	0.3301E+03	0.2390E+02	0.2678E+02	0.2395E+01	0.3301E+03	0.2266E+02	0.4164E+01
0.2682E+01	0.3301E+03	0.2390E+02	0.2678E+02	0.2460E+01	0.3301E+03	0.2259E+02	0.3819E+01
0.2721E+01	0.3301E+03	0.2390E+02	0.2678E+02	0.2525E+01	0.3301E+03	0.2252E+02	0.3494E+01
0.2760E+01	0.3301E+03	0.2390E+02	0.2678E+02	0.2590E+01	0.3301E+03	0.2248E+02	0.3143E+01
0.2799E+01	0.3301E+03	0.2390E+02	0.2678E+02	0.2655E+01	0.3301E+03	0.2246E+02	0.2878E+01
0.2837E+01	0.3301E+03	0.2390E+02	0.2678E+02	0.2720E+01	0.3301E+03	0.2246E+02	0.2759E+01
0.2876E+01	0.3301E+03	0.2390E+02	0.2678E+02	0.2785E+01	0.3301E+03	0.2246E+02	0.2464E+01
0.2915E+01	0.3301E+03	0.2390E+02	0.2678E+02	0.2850E+01	0.3301E+03	0.2246E+02	0.2065E+01
0.2954E+01	0.3301E+03	0.2390E+02	0.2678E+02	0.2915E+01	0.3301E+03	0.2246E+02	0.1485E+01
0.2993E+01	0.3301E+03	0.2390E+02	0.2678E+02	0.2980E+01	0.3301E+03	0.2246E+02	0.8801E+00
0.3031E+01	0.3301E+03	0.2390E+02	0.2678E+02	0.3045E+01	0.3301E+03	0.2246E+02	0.4726E+00
0.3070E+01	0.3301E+03	0.2390E+02	0.2678E+02	0.3110E+01	0.3301E+03	0.2246E+02	0.8907E-01
0.3109E+01	0.3301E+03	0.2390E+02	0.2678E+02	0.3175E+01	0.3301E+03	0.2246E+02	0.2657E+00
0.3148E+01	0.3301E+03	0.2390E+02	0.2678E+02	0.3240E+01	0.3301E+03	0.2246E+02	0.4619E+00
0.3187E+01	0.3301E+03	0.2390E+02	0.2678E+02	0.3305E+01	0.3301E+03	0.2246E+02	0.6647E+00
0.3226E+01	0.3301E+03	0.2390E+02	0.2678E+02	0.3370E+01	0.3301E+03	0.2246E+02	0.7302E+00
0.3265E+01	0.3301E+03	0.2390E+02	0.2678E+02	0.3435E+01	0.3301E+03	0.2246E+02	0.6981E+00
0.3304E+01	0.3301E+03	0.2390E+02	0.2678E+02	0.3500E+01	0.3301E+03	0.2246E+02	0.7228E+00
0.3343E+01	0.3301E+03	0.2390E+02	0.2678E+02	0.3565E+01	0.3301E+03	0.2246E+02	0.6719E+00
0.3382E+01	0.3301E+03	0.2390E+02	0.2678E+02	0.3630E+01	0.3301E+03	0.2246E+02	0.7193E+00
0.3421E+01	0.3301E+03	0.2390E+02	0.2678E+02	0.3695E+01	0.3301E+03	0.2246E+02	0.9285E+00
0.3460E+01	0.3301E+03	0.2390E+02	0.2678E+02	0.3760E+01	0.3301E+03	0.2246E+02	0.9285E+00
0.3499E+01	0.3301E+03	0.2390E+02	0.2678E+02	0.3825E+01	0.3301E+03	0.2246E+02	0.9285E+00
0.3538E+01	0.3301E+03	0.2390E+02	0.2678E+02	0.3890E+01	0.3301E+03	0.2246E+02	0.9285E+00
0.3577E+01	0.3301E+03	0.2390E+02	0.2678E+02	0.3955E+01	0.3301E+03	0.2246E+02	0.9285E+00

Table D-5. X-Array Probe Ensemble Average for 200 Points (Concluded).

INLET HOT WIRE PROBE				RADIAL POSITION * 10.168			
LOCATION	AXIAL VELOCITY	AXIAL MASS FLOW	TANGENTIAL VELOCITY	TANGENTIAL MASS FLOW	ABSOLUTE VELOCITY	ABSOLUTE MASS FLOW	DIRECTION (AXIAL-REF)
0.3576E+01	0.2840E+03	0.2056E+02	-0.4957E+01	-0.3589E+00	0.2841E+03	0.2057E+02	-0.9698E+00
0.3614E+01	0.2841E+03	0.2057E+02	-0.4666E+01	-0.3379E+00	0.2841E+03	0.2057E+02	-0.9410E+00
0.3653E+01	0.2829E+03	0.2048E+02	-0.5438E+01	-0.3937E+00	0.2839E+03	0.2049E+02	-0.1101E+01
0.3692E+01	0.2820E+03	0.2042E+02	-0.6175E+01	-0.4471E+00	0.2821E+03	0.2042E+02	-0.1254E+01
0.3731E+01	0.2818E+03	0.2040E+02	-0.6177E+01	-0.4472E+00	0.2819E+03	0.2041E+02	-0.1256E+01
0.3770E+01	0.2822E+03	0.2043E+02	-0.6157E+01	-0.4438E+00	0.2823E+03	0.2044E+02	-0.1250E+01
0.3809E+01	0.2821E+03	0.2043E+02	-0.5561E+01	-0.4030E+00	0.2821E+03	0.2043E+02	-0.1130E+01
0.3848E+01	0.2820E+03	0.2042E+02	-0.4018E+01	-0.2909E+00	0.2820E+03	0.2043E+02	-0.8162E+00
0.3887E+01	0.2825E+03	0.2046E+02	-0.2918E+01	-0.2107E+00	0.2825E+03	0.2046E+02	-0.5901E+00
0.3926E+01	0.2835E+03	0.2053E+02	-0.2253E+01	-0.1635E+00	0.2836E+03	0.2053E+02	-0.4564E+00
0.3965E+01	0.2848E+03	0.2062E+02	-0.1433E+01	-0.1038E+00	0.2848E+03	0.2062E+02	-0.2884E+00
0.4004E+01	0.2855E+03	0.2067E+02	-0.1091E+01	-0.7898E-01	0.2856E+03	0.2064E+02	-0.2193E+00
0.4043E+01	0.2855E+03	0.2067E+02	0.3111E+00	0.2252E-01	0.2855E+03	0.2067E+02	0.6242E-01
0.4082E+01	0.2892E+03	0.2094E+02	0.2557E+01	0.1852E+00	0.2892E+03	0.2094E+02	0.5067E+00
0.4121E+01	0.2900E+03	0.2100E+02	0.3591E+01	0.2600E+00	0.2900E+03	0.2100E+02	0.7095E+00
0.4160E+01	0.2910E+03	0.2107E+02	0.4500E+01	0.3258E+00	0.2911E+03	0.2107E+02	0.8857E+00
0.4199E+01	0.3021E+03	0.2187E+02	0.7886E+01	0.5709E+00	0.3022E+03	0.2188E+02	0.1495E+01
0.4238E+01	0.3070E+03	0.2222E+02	0.1068E+02	0.7731E+00	0.3072E+03	0.2224E+02	0.1992E+01
0.4277E+01	0.3122E+03	0.2261E+02	0.1337E+02	0.9680E+00	0.3125E+03	0.2263E+02	0.2452E+01
0.4316E+01	0.3161E+03	0.2288E+02	0.1720E+02	0.1245E+01	0.3165E+03	0.2292E+02	0.3114E+01
0.4355E+01	0.3189E+03	0.2309E+02	0.2013E+02	0.1458E+01	0.3195E+03	0.2313E+02	0.3613E+01
0.4394E+01	0.3200E+03	0.2317E+02	0.2218E+02	0.1606E+01	0.3208E+03	0.2323E+02	0.3965E+01
0.4433E+01	0.3234E+03	0.2342E+02	0.2507E+02	0.1815E+01	0.3244E+03	0.2361E+02	0.4431E+01
0.4472E+01	0.3250E+03	0.2353E+02	0.2810E+02	0.2035E+01	0.3262E+03	0.2376E+02	0.4943E+01
0.4511E+01	0.3255E+03	0.2357E+02	0.3063E+02	0.2218E+01	0.3270E+03	0.2380E+02	0.5376E+01
0.4550E+01	0.3269E+03	0.2367E+02	0.3580E+02	0.2534E+01	0.3278E+03	0.2373E+02	0.5827E+01
0.4589E+01	0.3272E+03	0.2369E+02	0.3732E+02	0.2592E+01	0.3291E+03	0.2382E+02	0.6111E+01
0.4628E+01	0.3277E+03	0.2372E+02	0.3781E+02	0.2702E+01	0.3298E+03	0.2386E+02	0.6245E+01
0.4667E+01	0.3282E+03	0.2375E+02	0.3844E+02	0.2738E+01	0.3304E+03	0.2392E+02	0.6498E+01
0.4706E+01	0.3285E+03	0.2376E+02	0.3677E+02	0.2754E+01	0.3298E+03	0.2388E+02	0.6572E+01
0.4745E+01	0.3282E+03	0.2375E+02	0.3511E+02	0.2662E+01	0.3298E+03	0.2388E+02	0.6624E+01
0.4784E+01	0.3282E+03	0.2375E+02	0.3373E+02	0.2442E+01	0.3273E+03	0.2370E+02	0.6449E+01
0.4823E+01	0.3286E+03	0.2381E+02	0.3251E+02	0.2353E+01	0.3273E+03	0.2370E+02	0.5972E+01
0.4862E+01	0.3124E+03	0.2313E+02	0.3248E+02	0.2352E+01	0.3211E+03	0.2325E+02	0.5789E+01
0.4901E+01	0.3187E+03	0.2307E+02	0.3321E+02	0.2405E+01	0.3204E+03	0.2320E+02	0.5806E+01
0.4940E+01	0.3181E+03	0.2303E+02	0.3395E+02	0.2458E+01	0.3199E+03	0.2316E+02	0.5950E+01
0.4979E+01	0.3171E+03	0.2296E+02	0.3390E+02	0.2454E+01	0.3189E+03	0.2309E+02	0.6092E+01
0.5018E+01	0.3155E+03	0.2284E+02	0.3383E+02	0.2449E+01	0.3173E+03	0.2297E+02	0.6102E+01
0.5057E+01	0.3146E+03	0.2278E+02	0.3396E+02	0.2458E+01	0.3164E+03	0.2291E+02	0.6151E+01
0.5096E+01	0.3138E+03	0.2272E+02	0.3359E+02	0.2432E+01	0.3155E+03	0.2285E+02	0.6110E+01
0.5135E+01	0.3127E+03	0.2264E+02	0.3332E+02	0.2412E+01	0.3145E+03	0.2277E+02	0.6081E+01
0.5174E+01	0.3128E+03	0.2265E+02	0.3320E+02	0.2404E+01	0.3146E+03	0.2277E+02	0.6059E+01
0.5213E+01	0.3126E+03	0.2263E+02	0.3293E+02	0.2384E+01	0.3144E+03	0.2276E+02	0.6014E+01
0.5252E+01	0.3126E+03	0.2263E+02	0.3280E+02	0.2331E+01	0.3143E+03	0.2275E+02	0.5881E+01
0.5291E+01	0.3132E+03	0.2267E+02	0.3147E+02	0.2279E+01	0.3147E+03	0.2279E+02	0.5739E+01
0.5330E+01	0.3130E+03	0.2266E+02	0.3052E+02	0.2210E+01	0.3145E+03	0.2277E+02	0.5569E+01
0.5369E+01	0.3130E+03	0.2266E+02	0.2899E+02	0.2095E+01	0.3144E+03	0.2276E+02	0.5291E+01
0.5408E+01	0.3137E+03	0.2271E+02	0.2717E+02	0.1967E+01	0.3148E+03	0.2279E+02	0.4950E+01
0.5447E+01	0.3142E+03	0.2275E+02	0.2471E+02	0.1789E+01	0.3151E+03	0.2282E+02	0.4496E+01
0.5486E+01	0.3141E+03	0.2274E+02	0.2263E+02	0.1638E+01	0.3149E+03	0.2280E+02	0.4120E+01
0.5525E+01	0.3148E+03	0.2279E+02	0.2050E+02	0.1484E+01	0.3155E+03	0.2284E+02	0.3725E+01
0.5564E+01	0.3137E+03	0.2271E+02	0.1799E+02	0.1302E+01	0.3142E+03	0.2275E+02	0.3282E+01
0.5603E+01	0.3107E+03	0.2250E+02	0.1621E+02	0.1173E+01	0.3111E+03	0.2253E+02	0.2986E+01
0.5642E+01	0.3071E+03	0.2224E+02	0.1423E+02	0.1030E+01	0.3075E+03	0.2226E+02	0.2653E+01
0.5681E+01	0.3041E+03	0.2202E+02	0.1184E+02	0.8570E+00	0.3044E+03	0.2204E+02	0.2225E+01
0.5720E+01	0.3032E+03	0.2195E+02	0.1033E+02	0.7479E+00	0.3034E+03	0.2197E+02	0.1951E+01
0.5759E+01	0.3028E+03	0.2193E+02	0.9878E+01	0.7151E+00	0.3030E+03	0.2194E+02	0.1868E+01
0.5798E+01	0.3032E+03	0.2195E+02	0.9855E+01	0.7135E+00	0.3034E+03	0.2196E+02	0.1868E+01
0.5837E+01	0.3033E+03	0.2196E+02	0.9172E+01	0.6641E+00	0.3035E+03	0.2197E+02	0.1733E+01
0.5876E+01	0.3030E+03	0.2194E+02	0.7923E+01	0.5736E+00	0.3031E+03	0.2194E+02	0.1498E+01
0.5915E+01	0.3017E+03	0.2184E+02	0.7855E+01	0.5687E+00	0.3018E+03	0.2185E+02	0.1492E+01
0.5954E+01	0.2981E+03	0.2158E+02	0.7037E+01	0.5085E+00	0.2982E+03	0.2159E+02	0.1352E+01
0.5993E+01	0.2957E+03	0.2141E+02	0.5789E+01	0.4191E+00	0.2958E+03	0.2142E+02	0.1121E+01
0.6032E+01	0.2945E+03	0.2132E+02	0.5143E+01	0.3723E+00	0.2946E+03	0.2133E+02	0.1000E+01
0.6071E+01	0.2917E+03	0.2112E+02	0.3966E+01	0.2799E+00	0.2917E+03	0.2112E+02	0.7392E+00
0.6110E+01	0.2917E+03	0.2112E+02	0.2546E+01	0.2133E+00	0.2918E+03	0.2112E+02	0.5786E+00
0.6149E+01	0.2925E+03	0.2118E+02	0.1966E+01	0.2280E+00	0.2925E+03	0.2118E+02	0.6169E+00
0.6188E+01	0.2911E+03	0.2108E+02	0.3508E+01	0.2540E+00	0.2911E+03	0.2108E+02	0.6905E+00
0.6227E+01	0.2902E+03	0.2101E+02	0.3440E+01	0.2497E+00	0.2902E+03	0.2101E+02	0.6809E+00
0.6266E+01	0.2906E+03	0.2104E+02	0.3715E+01	0.2690E+00	0.2906E+03	0.2104E+02	0.7325E+00
0.6305E+01	0.2944E+03	0.2131E+02	0.4582E+01	0.3317E+00	0.2944E+03	0.2131E+02	0.8918E+00
0.6344E+01	0.2966E+03	0.2147E+02	0.5899E+01	0.4271E+00	0.2966E+03	0.2148E+02	0.1140E+01
0.6383E+01	0.3000E+03	0.2172E+02	0.8338E+01	0.6036E+00	0.3001E+03	0.2173E+02	0.1592E+01
0.6422E+01	0.3027E+03	0.2192E+02	0.1080E+02	0.7818E+00	0.3029E+03	0.2193E+02	0.2043E+01
0.6461E+01	0.3046E+03	0.2205E+02	0.1223E+02	0.8857E+00	0.3048E+03	0.2207E+02	0.2300E+01
0.6500E+01	0.3073E+03	0.2225E+02	0.1271E+02	0.9159E+00	0.3075E+03	0.2227E+02	0.2368E+01
0.6539E+01	0.3090E+03	0.2237E+02	0.1346E+02	0.9746E+00	0.3092E+03	0.2239E+02	0.2495E+01
0.6578E+01	0.3106E+03	0.2240E+02	0.1424E+02	0.1031E+01	0.3109E+03	0.2251E+02	0.2626E+01
0.6617E+01	0.3140E+03	0.2273E+02	0.1569E+02	0.1136E+01	0.3144E+03	0.2276E+02	0.2861E+01
0.6656E+01	0.3156E+03	0.2285E+02	0.1807E+02	0.1309E+01	0.3161E+03	0.2288E+02	0.3278E+01
0.6695E+01	0.3175E+03	0.2299E+02	0.2053E+02	0.1486E+01	0.3182E+03	0.2303E+02	0.3700E+01
0.6734E+01	0.3195E+03	0.2313E+02	0.2330E+02	0.1687E+01	0.3203E+03	0.2319E+02	0.4172E+01
0.6773E+01	0.3210E+03	0.2324E+02	0.2622E+02	0.1899E+01	0.3220E+03	0.2332E+02	0.4671E+01
0.6812E+01	0.3242E+03	0.2347E+02	0.2919E+02	0.2113E+01	0.3237E+03	0.2344E+02	0.5173E+01
0.6851E+01	0.3242E+03	0.2347E+02	0.3236E+02	0.2343E+01	0.3258E+03	0.2359E+02	0.5700E+01
0.6890E+01	0.3260E+03	0.2365E+02	0.3477E+02	0.2518E+01	0.3279E+03	0.2374E+02	0.6089E+01
0.6929E+01	0.3269E+03	0.2367E+02	0.3639E+02	0.2668E+01	0.3289E+03	0.2381E+02	0.6432E+01
0.6968E+01	0.3277E+03	0.2372E+02	0.3876E+02	0.2844E+01	0.3300E+03	0.2392E+02	0.6745E+01
0.7007E+01	0.3284E+03	0.2377E+02	0.3997E+02	0.2894E+01	0.3308E+03	0.2395E+02	0.6941E+01
0.7046E+01	0.3286E+03	0.2379E+02	0.4070E+02	0.2947E+01	0.3311E+03	0.2398E+02	0.7069E+01
0.7085E+01	0.3276E+03	0.2372E+02	0.4076E+02	0.2951E+01	0.3301E+03	0.2390E+02	0.7093E+01
0.7124E+01	0.3265E+03	0.2364E+02	0.3969E+02	0.2874E+01	0.3289E+03	0.2382E+02	0.6930E+01
0.7163E+01	0.3259E+03	0.2359E+02	0.3875E+02	0.2806E+01	0.3281E+03	0.2376E+02	0.6783E+01
0.7202E+01	0.3246E+03	0.2350E+02	0.3879E+02	0.2779E+01	0.3269E+03	0.2364E+02	0.6744E+01
0.7241E+01	0.3241E+03	0.2347E+02	0.3920E+02	0.2838E+01	0.3263E+03	0.2363E+02	0.6896E+01
0.7280E+01	0.3238E+03	0.2344E+02	0.4050E+02	0.2912E+01	0.3259E+03	0.2360E+02	0.7128E+01
0.7319E+01	0.3235E+03	0.2342E+02	0.4056E+02	0.2914E+01	0.3259E+03	0.2360E+02	0.7094E+01

Table D-6. Once Per Revolution Sampling of X-Array Probe.

AVERAGE SPEED = 11680
 NUMBER OF FRAMES IN THE AVERAGE = 128
 NUMBER OF SAMPLE POINTS = 128
 SAMPLE RATE = 320000 HZ
 CIRCUMFERENTIAL DISTANCE = 0.1555E+00

MACH NUMBER = 0.300
 RADIAL POSITION = 10.168
 INLET
 DENSITY = 0.072400

TIME	AXIAL VELOCITY	AXIAL MASS FLOW	TANGENTIAL VELOCITY	TANGENTIAL MASS FLOW	ABSOLUTE VELOCITY	ABSOLUTE MASS FLOW	FLOW DIRECTION (AXIAL-REF)
0.0000E+00	0.3145E+03	0.2277E+02	0.3274E+02	0.2371E+01	0.3163E+03	0.2290E+02	0.5943E+01
0.5137E-02	0.3252E+03	0.2354E+02	0.4770E+02	0.3454E+01	0.7287E+03	0.2379E+02	0.8346E+01
0.1027E-01	0.3215E+03	0.2328E+02	0.4570E+02	0.3309E+01	0.3247E+03	0.2351E+02	0.8091E+01
0.1541E-01	0.3242E+03	0.2347E+02	0.4957E+02	0.3539E+01	0.3279E+03	0.2374E+02	0.8694E+01
0.2055E-01	0.3219E+03	0.2331E+02	0.4607E+02	0.2901E+01	0.3244E+03	0.2349E+02	0.7095E+01
0.2568E-01	0.3246E+03	0.2350E+02	0.4547E+02	0.3232E+01	0.3278E+03	0.2373E+02	0.7973E+01
0.3082E-01	0.3248E+03	0.2352E+02	0.3450E+02	0.2409E+01	0.3266E+03	0.2365E+02	0.6063E+01
0.3596E-01	0.3272E+03	0.2369E+02	0.4614E+02	0.3341E+01	0.3305E+03	0.2393E+02	0.8026E+01
0.4110E-01	0.3212E+03	0.2325E+02	0.2723E+02	0.1971E+01	0.3223E+03	0.2333E+02	0.4846E+01
0.4623E-01	0.3246E+03	0.2350E+02	0.4438E+02	0.3213E+01	0.3277E+03	0.2372E+02	0.7784E+01
0.5137E-01	0.3304E+03	0.2390E+02	0.4298E+02	0.3107E+01	0.3326E+03	0.2390E+02	0.7401E+01
0.5651E-01	0.3163E+03	0.2290E+02	0.2986E+02	0.2162E+01	0.3177E+03	0.2323E+02	0.5393E+01
0.6164E-01	0.3188E+03	0.2308E+02	0.3713E+02	0.2688E+01	0.3209E+03	0.2323E+02	0.6643E+01
0.6678E-01	0.3241E+03	0.2346E+02	0.4843E+02	0.3506E+01	0.3277E+03	0.2372E+02	0.8500E+01
0.7192E-01	0.3312E+03	0.2398E+02	0.4848E+02	0.3510E+01	0.3347E+03	0.2423E+02	0.8328E+01
0.7706E-01	0.3149E+03	0.2280E+02	0.3877E+02	0.2807E+01	0.3173E+03	0.2297E+02	0.7018E+01
0.8219E-01	0.3235E+03	0.2342E+02	0.5489E+02	0.3974E+01	0.3282E+03	0.2376E+02	0.9620E+01
0.8733E-01	0.3222E+03	0.2337E+02	0.2817E+02	0.2039E+01	0.3234E+03	0.2341E+02	0.4997E+01
0.9247E-01	0.3244E+03	0.2348E+02	0.4194E+02	0.3036E+01	0.3271E+03	0.2368E+02	0.7367E+01
0.9760E-01	0.3373E+03	0.2442E+02	0.5785E+02	0.4188E+01	0.3422E+03	0.2477E+02	0.9730E+01
0.1027E+00	0.3182E+03	0.2246E+02	0.3867E+02	0.2890E+01	0.3126E+03	0.2263E+02	0.7107E+01
0.1079E+00	0.3240E+03	0.2403E+02	0.4774E+02	0.3457E+01	0.3354E+03	0.2428E+02	0.8184E+01
0.1130E+00	0.3126E+03	0.2263E+02	0.3808E+02	0.2757E+01	0.3149E+03	0.2280E+02	0.6945E+01
0.1182E+00	0.3256E+03	0.2359E+02	0.4632E+02	0.3353E+01	0.3289E+03	0.2381E+02	0.8095E+01
0.1233E+00	0.3312E+03	0.2393E+02	0.4007E+02	0.2911E+01	0.3336E+03	0.2415E+02	0.6898E+01
0.1284E+00	0.3257E+03	0.2358E+02	0.5177E+02	0.2749E+01	0.3299E+03	0.2388E+02	0.9031E+01
0.1336E+00	0.3378E+03	0.2417E+02	0.4726E+02	0.3422E+01	0.3371E+03	0.2441E+02	0.8958E+01
0.1387E+00	0.3189E+03	0.2308E+02	0.3659E+02	0.2643E+01	0.3209E+03	0.2325E+02	0.6548E+01
0.1439E+00	0.3244E+03	0.2349E+02	0.4491E+02	0.3251E+01	0.3275E+03	0.2371E+02	0.7581E+01
0.1490E+00	0.3254E+03	0.2356E+02	0.3834E+02	0.2776E+01	0.3276E+03	0.2372E+02	0.6721E+01
0.1541E+00	0.3179E+03	0.2315E+02	0.3756E+02	0.2710E+01	0.3229E+03	0.2331E+02	0.6698E+01
0.1593E+00	0.3241E+03	0.2347E+02	0.4109E+02	0.2975E+01	0.3267E+03	0.2366E+02	0.7252E+01
0.1644E+00	0.3165E+03	0.2292E+02	0.3412E+02	0.2470E+01	0.3184E+03	0.2306E+02	0.6153E+01
0.1695E+00	0.3207E+03	0.2318E+02	0.4177E+02	0.3243E+01	0.3233E+03	0.2341E+02	0.7042E+01
0.1747E+00	0.3284E+03	0.2378E+02	0.4177E+02	0.3024E+01	0.3310E+03	0.2397E+02	0.7249E+01
0.1798E+00	0.3112E+03	0.2253E+02	0.3432E+02	0.2497E+01	0.3131E+03	0.2267E+02	0.6292E+01
0.1849E+00	0.3389E+03	0.2453E+02	0.6417E+02	0.4646E+01	0.3449E+03	0.2497E+02	0.1072E+02
0.1901E+00	0.3239E+03	0.2331E+02	0.3973E+02	0.2877E+01	0.3244E+03	0.2349E+02	0.7035E+01
0.1952E+00	0.3243E+03	0.2347E+02	0.4568E+02	0.3589E+01	0.3279E+03	0.2374E+02	0.8694E+01
0.2003E+00	0.3219E+03	0.2330E+02	0.4568E+02	0.3298E+01	0.3251E+03	0.2354E+02	0.8056E+01
0.2055E+00	0.3277E+03	0.2377E+02	0.4248E+02	0.3076E+01	0.3305E+03	0.2393E+02	0.7386E+01
0.2106E+00	0.3271E+03	0.2368E+02	0.4129E+02	0.2989E+01	0.3303E+03	0.2392E+02	0.7180E+01
0.2158E+00	0.3287E+03	0.2377E+02	0.5597E+02	0.4052E+01	0.3319E+03	0.2403E+02	0.9708E+01
0.2209E+00	0.3249E+03	0.2352E+02	0.4754E+02	0.3443E+01	0.3283E+03	0.2376E+02	0.8257E+01
0.2260E+00	0.3249E+03	0.2352E+02	0.4647E+02	0.3365E+01	0.3283E+03	0.2376E+02	0.8141E+01
0.2312E+00	0.3303E+03	0.2391E+02	0.3828E+02	0.2771E+01	0.3325E+03	0.2407E+02	0.6611E+01
0.2363E+00	0.3190E+03	0.2316E+02	0.3450E+02	0.2498E+01	0.3218E+03	0.2300E+02	0.6155E+01
0.2414E+00	0.3360E+03	0.2433E+02	0.5684E+02	0.4115E+01	0.3409E+03	0.2467E+02	0.1550E+02
0.2466E+00	0.3229E+03	0.2338E+02	0.3410E+02	0.2469E+01	0.3247E+03	0.2351E+02	0.6082E+01
0.2517E+00	0.3188E+03	0.2308E+02	0.4248E+02	0.3075E+01	0.3216E+03	0.2329E+02	0.5894E+01
0.2568E+00	0.3396E+03	0.2458E+02	0.5321E+02	0.3852E+01	0.3437E+03	0.2488E+02	0.8906E+01
0.2620E+00	0.3120E+03	0.2259E+02	0.2739E+02	0.1983E+01	0.3132E+03	0.2268E+02	0.5017E+01
0.2671E+00	0.3209E+03	0.2322E+02	0.3117E+02	0.2257E+01	0.3223E+03	0.2333E+02	0.5551E+01
0.2723E+00	0.3140E+03	0.2277E+02	0.4190E+02	0.3034E+01	0.3168E+03	0.2297E+02	0.7602E+01
0.2774E+00	0.3132E+03	0.2311E+02	0.3885E+02	0.2813E+01	0.3216E+03	0.2328E+02	0.6939E+01
0.2825E+00	0.3208E+03	0.2323E+02	0.4273E+02	0.3094E+01	0.3237E+03	0.2344E+02	0.7586E+01
0.2877E+00	0.3210E+03	0.2324E+02	0.4930E+02	0.3569E+01	0.3247E+03	0.2351E+02	0.8733E+01
0.2928E+00	0.3209E+03	0.2324E+02	0.5293E+02	0.3931E+01	0.3340E+03	0.2418E+02	0.9115E+01
0.2979E+00	0.3181E+03	0.2297E+02	0.3267E+02	0.2362E+01	0.3197E+03	0.2315E+02	0.5855E+01
0.3030E+00	0.3120E+03	0.2287E+02	0.3970E+02	0.2902E+01	0.3183E+03	0.2304E+02	0.6985E+01
0.3082E+00	0.3239E+03	0.2345E+02	0.4932E+02	0.2257E+01	0.3223E+03	0.2333E+02	0.5551E+01
0.3133E+00	0.3201E+03	0.2318E+02	0.4617E+02	0.3571E+01	0.3276E+03	0.2372E+02	0.8659E+01
0.3185E+00	0.3109E+03	0.2250E+02	0.3072E+02	0.2224E+01	0.3235E+03	0.2342E+02	0.8296E+01
0.3236E+00	0.3215E+03	0.2328E+02	0.2979E+02	0.2150E+01	0.3233E+03	0.2342E+02	0.8296E+01
0.3288E+00	0.3142E+03	0.2275E+02	0.3678E+02	0.2667E+01	0.3163E+03	0.2300E+02	0.5278E+01
0.3339E+00	0.3244E+03	0.2349E+02	0.4297E+02	0.3111E+01	0.3270E+03	0.2369E+02	0.7545E+01
0.3390E+00	0.3262E+03	0.2362E+02	0.4666E+02	0.3378E+01	0.3295E+03	0.2386E+02	0.8173E+01
0.3442E+00	0.3177E+03	0.2300E+02	0.3421E+02	0.2477E+01	0.3195E+03	0.2313E+02	0.6147E+01
0.3493E+00	0.3318E+03	0.2402E+02	0.5887E+02	0.4262E+01	0.3379E+03	0.2440E+02	0.1006E+02
0.3545E+00	0.3203E+03	0.2318E+02	0.4463E+02	0.3231E+01	0.3234E+03	0.2342E+02	0.7332E+01
0.3596E+00	0.3235E+03	0.2342E+02	0.5181E+02	0.3751E+01	0.3276E+03	0.2372E+02	0.9100E+01
0.3647E+00	0.3282E+03	0.2376E+02	0.3740E+02	0.2714E+01	0.3304E+03	0.2392E+02	0.6516E+01
0.3699E+00	0.3177E+03	0.2297E+02	0.3846E+02	0.2785E+01	0.3196E+03	0.2314E+02	0.6912E+01
0.3750E+00	0.3231E+03	0.2375E+02	0.3890E+02	0.2758E+01	0.3302E+03	0.2391E+02	0.6624E+01
0.3802E+00	0.3231E+03	0.2340E+02	0.3815E+02	0.2762E+01	0.3255E+03	0.2357E+02	0.6731E+01
0.3853E+00	0.3236E+03	0.2346E+02	0.4207E+02	0.3046E+01	0.3267E+03	0.2366E+02	0.7398E+01
0.3905E+00	0.3240E+03	0.2351E+02	0.3950E+02	0.2857E+01	0.3291E+03	0.2383E+02	0.6893E+01
0.3956E+00	0.3174E+03	0.2296E+02	0.3770E+02	0.2874E+01	0.3196E+03	0.2314E+02	0.7134E+01
0.4008E+00	0.3171E+03	0.2294E+02	0.2770E+02	0.1967E+01	0.3155E+03	0.2284E+02	0.4945E+01
0.4059E+00	0.3147E+03	0.2276E+02	0.2730E+02	0.1977E+01	0.3103E+03	0.2284E+02	0.4964E+01
0.4110E+00	0.3147E+03	0.2276E+02	0.2730E+02	0.1977E+01	0.3103E+03	0.2284E+02	0.4964E+01
0.4162E+00	0.3270E+03	0.2309E+02	0.3941E+02	0.2953E+01	0.3213E+03	0.2391E+02	0.8026E+01
0.4213E+00	0.3129E+03	0.2277E+02	0.4211E+02	0.2940E+01	0.3255E+03	0.2375E+02	0.7434E+01
0.4264E+00	0.3129E+03	0.2277E+02	0.3654E+02	0.2645E+01	0.3200E+03	0.2324E+02	0.6537E+01
0.4315E+00	0.3275E+03	0.2349E+02	0.5090E+02	0.2540E+01	0.3298E+03	0.2397E+02	0.6119E+01
0.4367E+00	0.3173E+03	0.2247E+02	0.4574E+02	0.3124E+01	0.3252E+03	0.2346E+02	0.8091E+01
0.4418E+00	0.3173E+03	0.2247E+02	0.4574E+02	0.3124E+01	0.3252E+03	0.2346E+02	0.8091E+01
0.4469E+00	0.3173E+03	0.2247E+02	0.4574E+02	0.3124E+01	0.3252E+03	0.2346E+02	0.8091E+01
0.4520E+00	0.3173E+03	0.2247E+02	0.4574E+02	0.3124E+01	0.3252E+03	0.2346E+02	0.8091E+01
0.4571E+00	0.3173E+03	0.2247E+02	0.4574E+02	0.3124E+01	0.3252E+03	0.2346E+02	0.8091E+01
0.4622E+00	0.3173E+03	0.2247E+02	0.4574E+02	0.3124E+01	0.3252E+03	0.2346E+02	0.8091E+01

C - 4/

ORIGINAL
OF 1

Table D-6. Once Per Revolution Sampling of X-Array Probe (Concluded).

INLET HOT WIRE PROBE				RADIAL POSITION = 10.168			
TIME	AXIAL VELOCITY	AXIAL MASS FLOW	TANGENTIAL VELOCITY	TANGENTIAL MASS FLOW	ABSOLUTE VELOCITY	ABSOLUTE MASS FLOW	FLOW DIRECTION (AXIAL-REF)
0.4675E+00	0.3163E+03	0.2290E+02	0.3301E+02	0.2390E+01	0.3180E+03	0.2303E+02	0.5957E+01
0.4726E+00	0.3175E+03	0.2299E+02	0.4638E+02	0.3358E+01	0.3209E+03	0.2323E+02	0.8312E+01
0.4777E+00	0.3242E+03	0.2347E+02	0.3689E+02	0.2671E+01	0.3263E+03	0.2362E+02	0.6492E+01
0.4828E+00	0.3334E+03	0.2414E+02	0.5484E+02	0.3971E+01	0.3379E+03	0.2447E+02	0.9340E+01
0.4880E+00	0.3146E+03	0.2278E+02	0.3252E+02	0.2354E+01	0.3163E+03	0.2290E+02	0.5901E+01
0.4932E+00	0.3218E+03	0.2330E+02	0.3916E+02	0.2835E+01	0.3242E+03	0.2347E+02	0.6937E+01
0.4983E+00	0.3130E+03	0.2266E+02	0.3481E+02	0.2520E+01	0.3150E+03	0.2280E+02	0.6346E+01
0.5034E+00	0.3188E+03	0.2308E+02	0.2975E+02	0.2154E+01	0.3203E+03	0.2318E+02	0.5331E+01
0.5086E+00	0.3318E+03	0.2402E+02	0.4322E+02	0.3125E+01	0.3346E+03	0.2423E+02	0.7420E+01
0.5137E+00	0.3216E+03	0.2329E+02	0.4245E+02	0.3073E+01	0.3243E+03	0.2348E+02	0.7520E+01
0.5188E+00	0.3224E+03	0.2334E+02	0.3819E+02	0.2765E+01	0.3247E+03	0.2351E+02	0.6755E+01
0.5240E+00	0.3252E+03	0.2354E+02	0.3717E+02	0.2691E+01	0.3273E+03	0.2369E+02	0.6521E+01
0.5291E+00	0.3239E+03	0.2345E+02	0.4951E+02	0.3584E+01	0.3276E+03	0.2372E+02	0.8691E+01
0.5342E+00	0.3288E+03	0.2380E+02	0.3988E+02	0.2887E+01	0.3312E+03	0.2398E+02	0.6915E+01
0.5394E+00	0.3217E+03	0.2327E+02	0.3767E+02	0.2727E+01	0.3239E+03	0.2345E+02	0.6670E+01
0.5445E+00	0.3154E+03	0.2284E+02	0.4764E+02	0.3449E+01	0.3190E+03	0.2309E+02	0.8590E+01
0.5497E+00	0.3274E+03	0.2370E+02	0.3922E+02	0.2837E+01	0.3298E+03	0.2387E+02	0.6830E+01
0.5548E+00	0.3259E+03	0.2360E+02	0.4695E+02	0.3399E+01	0.3293E+03	0.2384E+02	0.8197E+01
0.5599E+00	0.3245E+03	0.2353E+02	0.3853E+02	0.2789E+01	0.3272E+03	0.2369E+02	0.6762E+01
0.5651E+00	0.3234E+03	0.2341E+02	0.3348E+02	0.2424E+01	0.3251E+03	0.2354E+02	0.5911E+01
0.5702E+00	0.3244E+03	0.2349E+02	0.4774E+02	0.3456E+01	0.3279E+03	0.2374E+02	0.8371E+01
0.5753E+00	0.3216E+03	0.2328E+02	0.3123E+02	0.2261E+01	0.3231E+03	0.2339E+02	0.5546E+01
0.5805E+00	0.3109E+03	0.2251E+02	0.2748E+02	0.1999E+01	0.3121E+03	0.2259E+02	0.5051E+01
0.5856E+00	0.3286E+03	0.2379E+02	0.4590E+02	0.3540E+01	0.3322E+03	0.2405E+02	0.8466E+01
0.5908E+00	0.3196E+03	0.2314E+02	0.4306E+02	0.3139E+01	0.3225E+03	0.2335E+02	0.7726E+01
0.5959E+00	0.3336E+03	0.2411E+02	0.3485E+02	0.2523E+01	0.3348E+03	0.2424E+02	0.5975E+01
0.6010E+00	0.3117E+03	0.2257E+02	0.3123E+02	0.2261E+01	0.3133E+03	0.2268E+02	0.5722E+01
0.6062E+00	0.3149E+03	0.2280E+02	0.3134E+02	0.2269E+01	0.3165E+03	0.2291E+02	0.5684E+01
0.6113E+00	0.3293E+03	0.2384E+02	0.3908E+02	0.2829E+01	0.3316E+03	0.2401E+02	0.6768E+01
0.6164E+00	0.3219E+03	0.2331E+02	0.4221E+02	0.3056E+01	0.3247E+03	0.2351E+02	0.7469E+01
0.6216E+00	0.3252E+03	0.2355E+02	0.5722E+02	0.3999E+01	0.3299E+03	0.2383E+02	0.9630E+01
0.6267E+00	0.3233E+03	0.2340E+02	0.3081E+02	0.2231E+01	0.3247E+03	0.2351E+02	0.5445E+01
0.6318E+00	0.3129E+03	0.2266E+02	0.3294E+02	0.2385E+01	0.3147E+03	0.2278E+02	0.6008E+01
0.6370E+00	0.3402E+03	0.2463E+02	0.6023E+02	0.4361E+01	0.3455E+03	0.2501E+02	0.1004E+02
0.6421E+00	0.3259E+03	0.2359E+02	0.4529E+02	0.3279E+01	0.3290E+03	0.2382E+02	0.7911E+01
0.6473E+00	0.3294E+03	0.2385E+02	0.5773E+02	0.4180E+01	0.3345E+03	0.2422E+02	0.9940E+01
0.6524E+00	0.3213E+03	0.2326E+02	0.3604E+02	0.2610E+01	0.3233E+03	0.2340E+02	0.6402E+01

ORIGINAL PAGE IS
OF POOR QUALITY

Table D-7. Cross Spectral Analysis of X-Array Probe and Reference Strain Gage for Phasing.

AVERAGE SPEED = 11680 CIRCUMFERENTIAL LOCATION = 0.15546E+00				MACH NUMBER = 0.300 RADIAL POSITION = 10.168	
CHANNEL A = SG # 828				CHANNEL B = X-ARRAY	
INDEX	FREQUENCY K2	CROSS-SPECTRUM MAGNITUDE	PHASE ANGLE DEGREES	AUTO-CH A	AUTO-CH B
1	0.00	0.5873E+01	-67.50	0.2722E+01	0.9718E+02
2	1.52	0.2875E+01	109.69	0.4639E+00	0.6978E+01
3	3.04	0.1899E+01	-56.25	0.4435E+00	0.2750E+01
4	4.56	0.2367E+00	-168.75	0.8666E-01	0.2867E+01
5	6.08	0.1809E+01	-5.63	0.4112E+00	0.4966E+01
6	7.60	0.2587E+01	-52.83	0.4741E+00	0.6229E+01
7	9.12	0.3534E+01	-67.50	0.7935E+00	0.4869E+01
8	10.65	0.5073E+00	-156.89	0.3313E+00	0.1555E+01
9	12.17	0.1522E+01	177.19	0.3059E+00	0.5637E+01
10	13.69	0.1776E+01	154.69	0.7952E+00	0.2459E+01
11	15.21	0.1403E+01	15.47	0.4146E+00	0.3557E+01
12	16.73	0.1437E+01	174.37	0.1014E+01	0.1574E+01
13	18.25	0.5479E+01	-109.69	0.1293E+01	0.4655E+01
14	19.77	0.1843E+01	160.31	0.3704E+00	0.5316E+01
15	21.29	0.1167E+01	16.87	0.1006E+01	0.1273E+01
16	22.81	0.4921E+01	-70.31	0.1195E+01	0.4577E+01
17	24.33	0.4312E+01	40.78	0.1305E+01	0.3518E+01
18	25.85	0.7948E+00	-174.37	0.2022E+00	0.4451E+01
19	27.37	0.5073E+00	-82.37	0.5675E+00	0.8746E+00
20	28.90	0.9131E+00	0.00	0.4520E+00	0.2391E+01
21	30.42	0.2063E+01	-56.25	0.3942E+00	0.5812E+01
22	31.94	0.9806E+00	80.16	0.5030E+00	0.2128E+01
23	33.46	0.2249E+01	50.62	0.8904E+00	0.2524E+01
24	34.98	0.2739E+01	135.00	0.6066E+00	0.5160E+01
25	36.50	0.7203E+01	7.93	0.7833E+00	0.1034E+02
26	38.02	0.7948E+00	-22.50	0.5624E+00	0.1565E+01
27	39.54	0.1471E+01	-109.69	0.3127E+00	0.5170E+01
28	41.06	0.1353E+01	0.00	0.4044E+00	0.3703E+01
29	42.58	0.8117E+00	12.66	0.2454E+00	0.3431E+01
30	44.10	0.2536E+01	153.28	0.3670E+00	0.7629E+01
31	45.62	0.2232E+01	75.94	0.3874E+00	0.6142E+01
32	47.15	0.1877E+01	158.91	0.7884E+00	0.2585E+01
33	48.67	0.1623E+01	115.31	0.4401E+00	0.4121E+01
34	50.19	0.1082E+01	-64.69	0.3687E+00	0.3217E+01
35	51.71	0.2080E+01	63.28	0.4265E+00	0.5306E+01
36	53.23	0.9131E+00	-8.44	0.4027E+00	0.2294E+01
37	54.75	0.1268E+01	-74.53	0.2855E+00	0.4723E+01
38	56.27	0.3145E+01	-140.63	0.1229E+01	0.2905E+01
39	57.79	0.1201E+01	171.56	0.2464E+00	0.4840E+01
40	59.31	0.1522E+01	25.31	0.4877E+00	0.3411E+01
41	60.83	0.1217E+01	-101.25	0.7425E+00	0.1837E+01
42	62.35	0.2796E+00	-78.75	0.1495E+00	0.1788E+01
43	63.87	0.2486E+01	-61.87	0.1013E+01	0.2673E+01
44	65.40	0.9700E+00	-173.28	0.2974E+00	0.3343E+01
45	66.92	0.7779E+00	163.12	0.4231E+00	0.1967E+01
46	68.44	0.3788E+01	-97.09	0.7799E+00	0.5481E+01
47	69.96	0.7508E+01	122.34	0.1118E+01	0.7162E+01
48	71.48	0.1268E+02	-68.91	0.1609E+01	0.8727E+01
49	73.00	0.3549E+01	111.89	0.7629E+00	0.5199E+01
50	74.52	0.3855E+01	-160.31	0.1526E+01	0.2760E+01
51	76.04	0.2587E+01	-22.50	0.4605E+00	0.1739E+01
52	77.56	0.4593E+02	-139.22	0.3840E+01	0.1396E+02
53	79.08	0.2555E+02	177.19	0.4105E+01	0.7017E+01
54	80.60	0.1480E+02	-137.81	0.2279E+01	0.7192E+01
55	82.12	0.1559E+02	-153.28	0.1390E+01	0.1237E+02
56	83.65	0.3754E+01	-143.44	0.5913E+00	0.6871E+01
57	85.17	0.1776E+01	57.66	0.3891E+00	0.4830E+01
58	86.69	0.1217E+01	-146.25	0.3670E+00	0.3450E+01
59	88.21	0.2401E+01	-137.81	0.2736E+00	0.3572E+01
60	89.73	0.3906E+01	-78.75	0.1263E+01	0.3363E+01
61	91.25	0.2756E+01	113.91	0.9295E+00	0.3304E+01
62	92.77	0.3162E+01	84.38	0.1409E+01	0.2604E+01
63	94.29	0.2384E+01	115.31	0.4316E+00	0.6025E+01
64	95.81	0.2131E+01	137.81	0.1076E+01	0.2177E+01
					COHERENCE
					1.000
					0.789
					0.812
					0.908
					0.785
					0.767
					0.837
					0.969
					0.779
					0.825
					0.906
					0.810
					0.825
					0.876
					0.830
					0.810
					0.882
					0.780
					1.000
					0.714
					0.811
					0.839
					0.927
					0.766
					0.791
					0.816
					0.828
					0.816
					0.922
					0.821
					0.880
					0.848
					0.801
					0.832
					0.845
					0.977
					0.895
					0.766
					1.000
					0.837
					0.797
					1.000
					0.843
					0.875
					0.877
					0.785
					0.879
					0.816
					0.809
					0.838
					0.891
					0.734
					0.787
					0.815
					0.834
					0.854
					0.842
					0.841
					0.847
					0.895
					0.743
					0.841
					0.829

ORIGINAL FILED
OF POOR QUALITY

APPENDIX E - X-ARRAY - PROBE CONTOUR PLOTS AT NON-FLUTTER POINTS

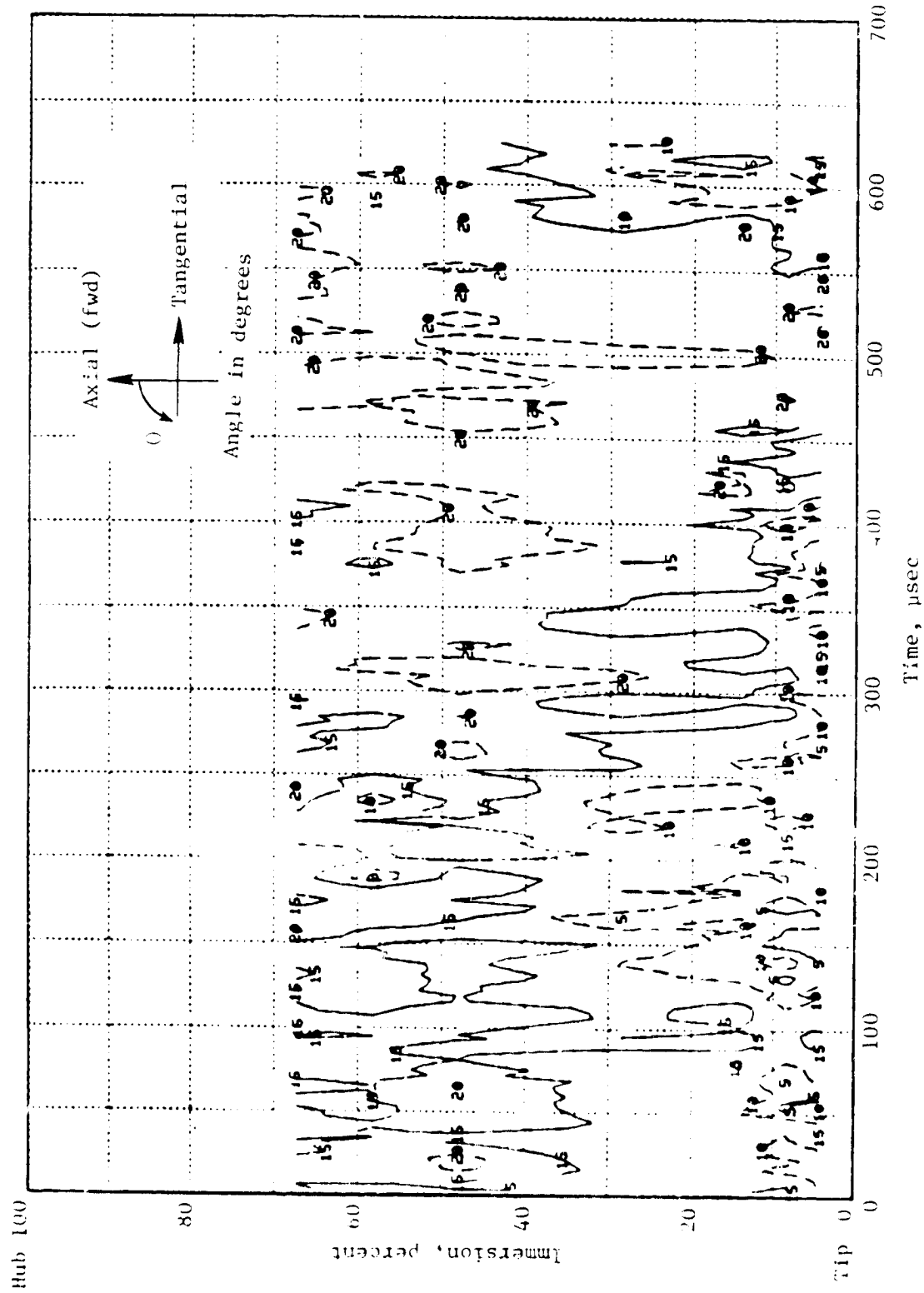


Figure E-1. Inlet Flow Angle Contour Plot, 65 Percent Speed Intermediate Operating Line.

ORIGINAL COPY
OF POOR QUALITY

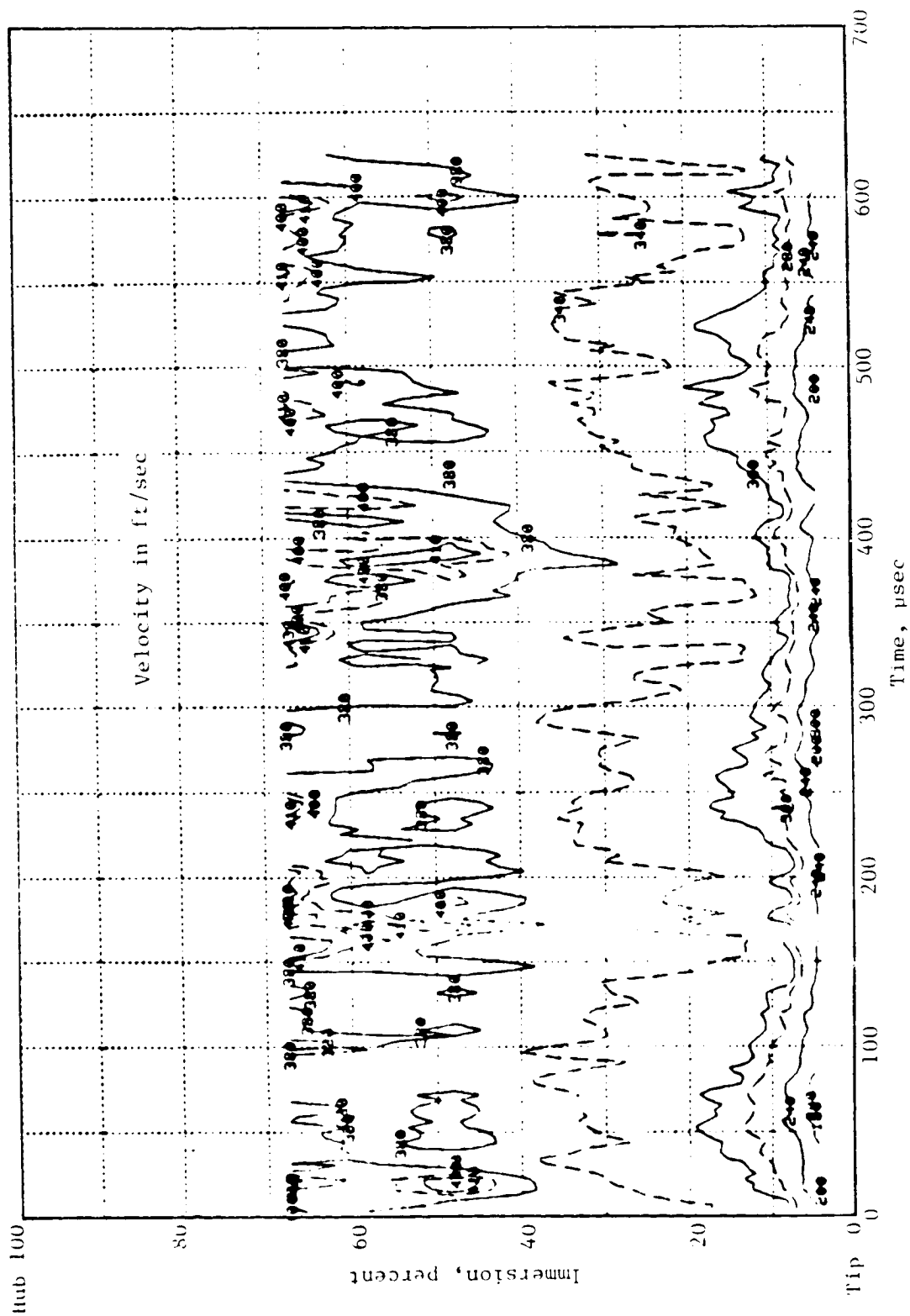


Figure E-2. Inlet Absolute Velocity Contour Plot, 65 Percent Speed Intermediate Operating Line.

ORIGINALLY
OF POOR QUALITY

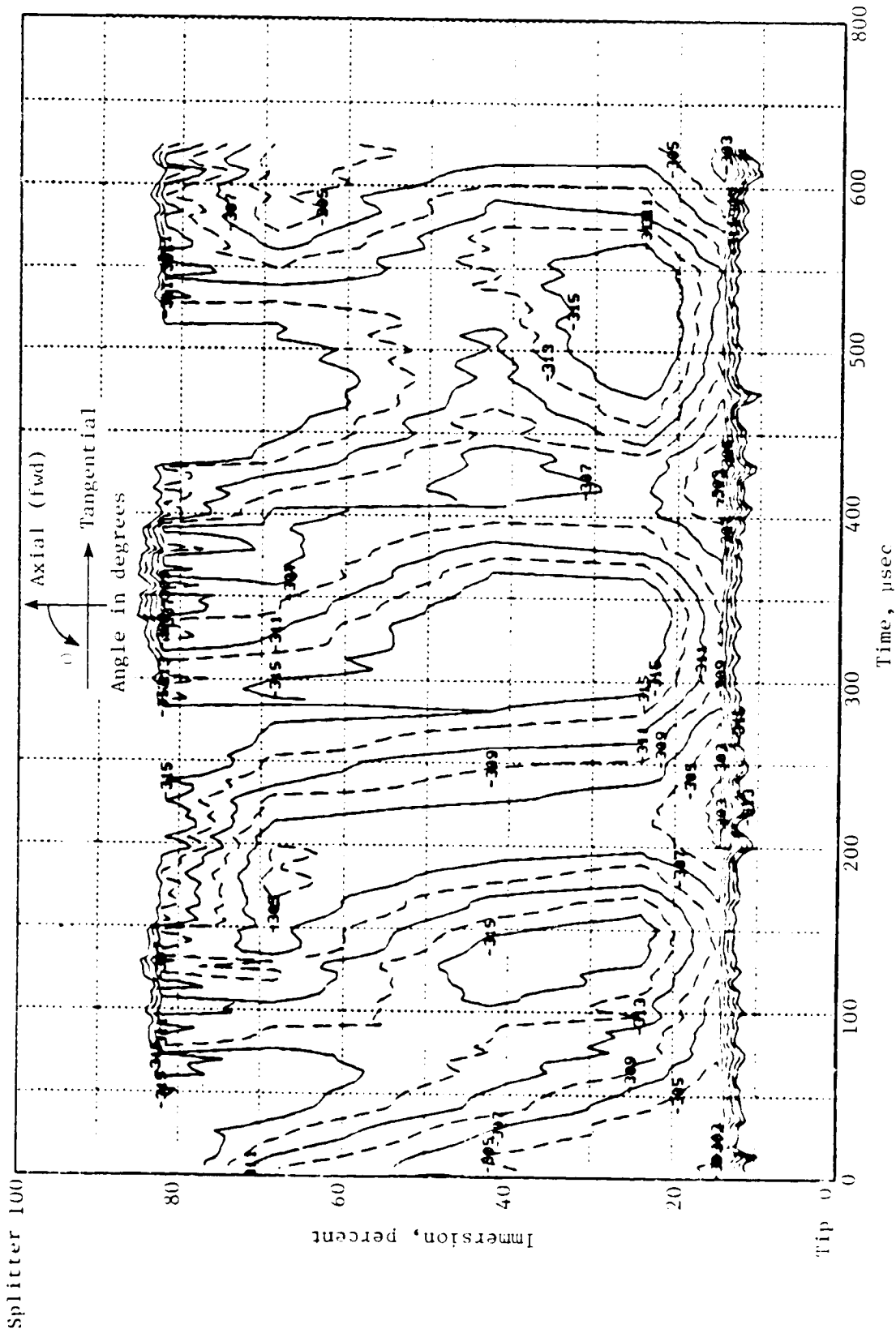


Figure E-3. Exit Flow Angle Contour Plot, 65 Percent Speed Intermediate Operating Line.

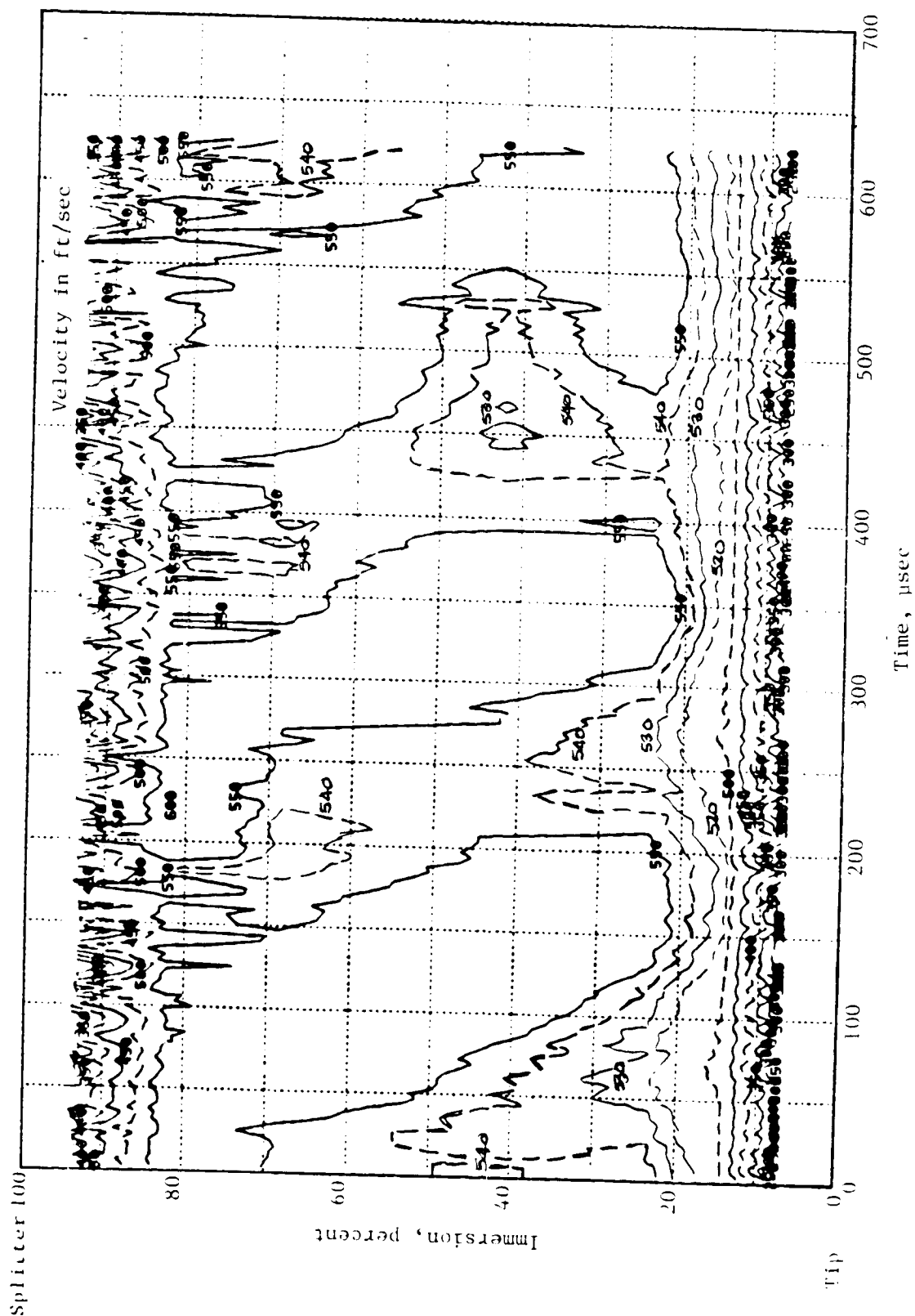


Figure E-4. Exit Absolute Velocity Contour Plot, 65 Percent Speed Intermediate Operating Line.

CONTINUOUS OF FLOW ANGLE

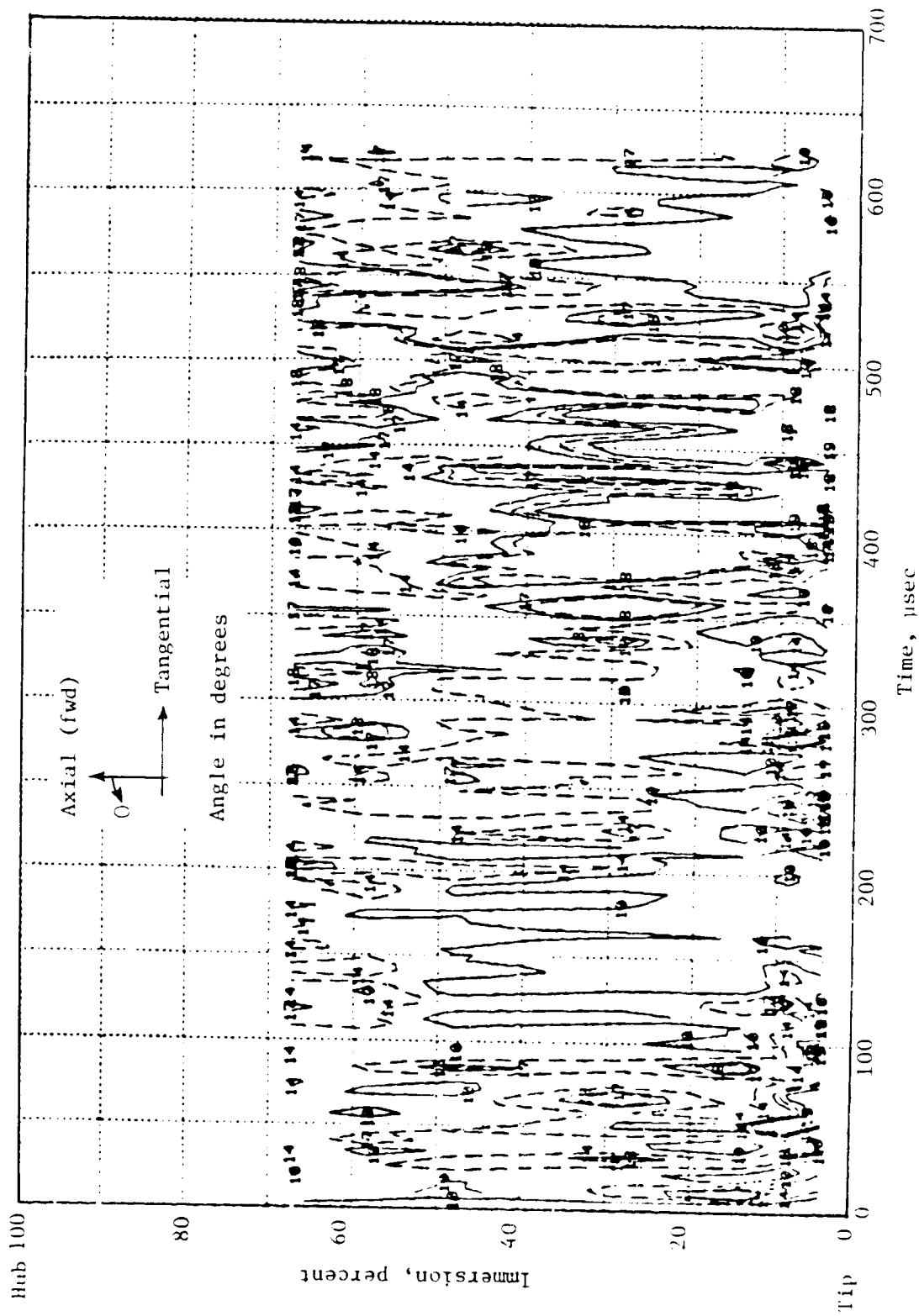


Figure E-5. Inlet Flow Angle Contour Plot, 70 Percent Speed Nominal Operating Line.

ORIGINAL OF POOR QUALITY

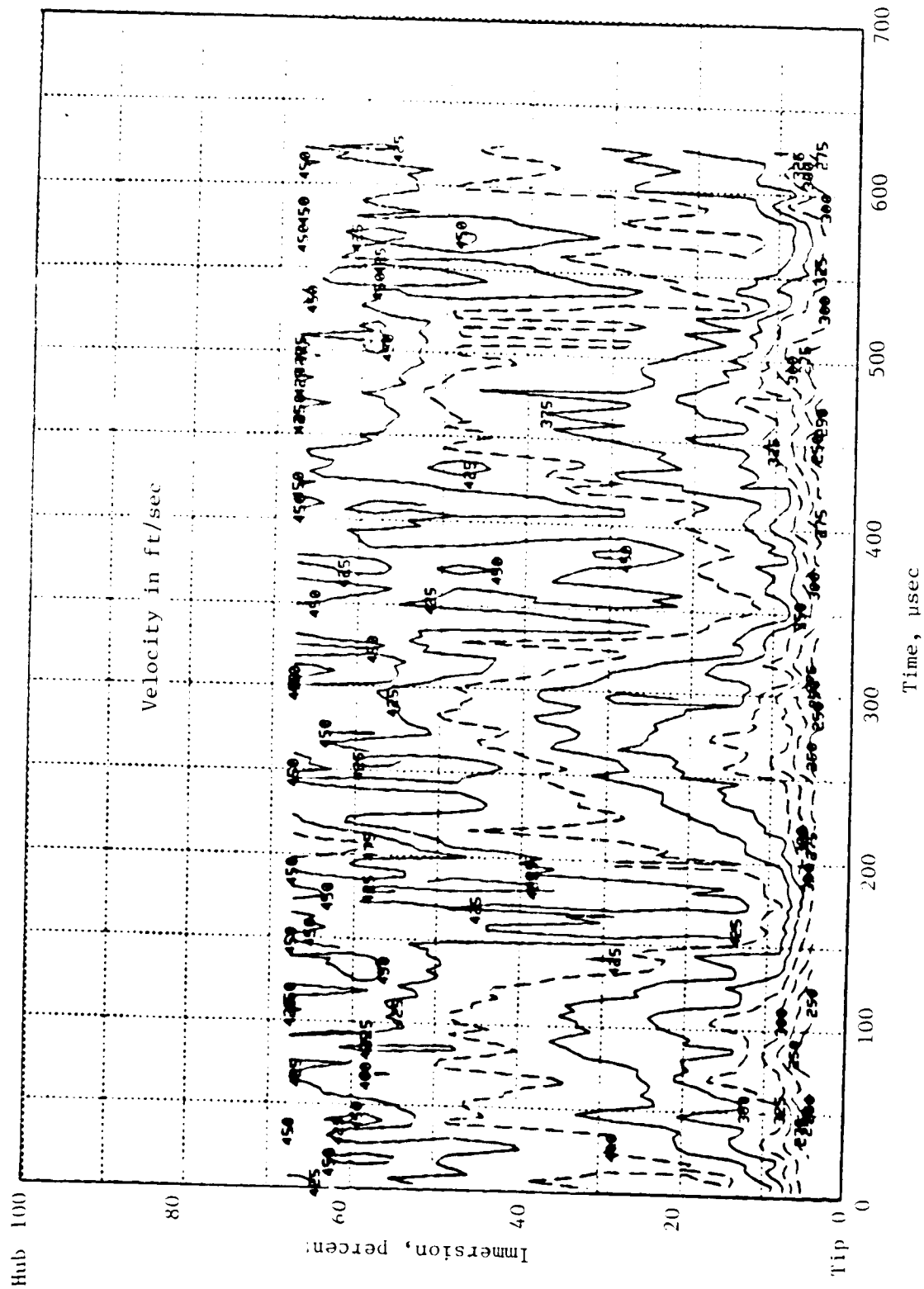


Figure E-6. Inlet Absolute Velocity Contour Plot, 70 Percent Speed Nominal Operating Line.

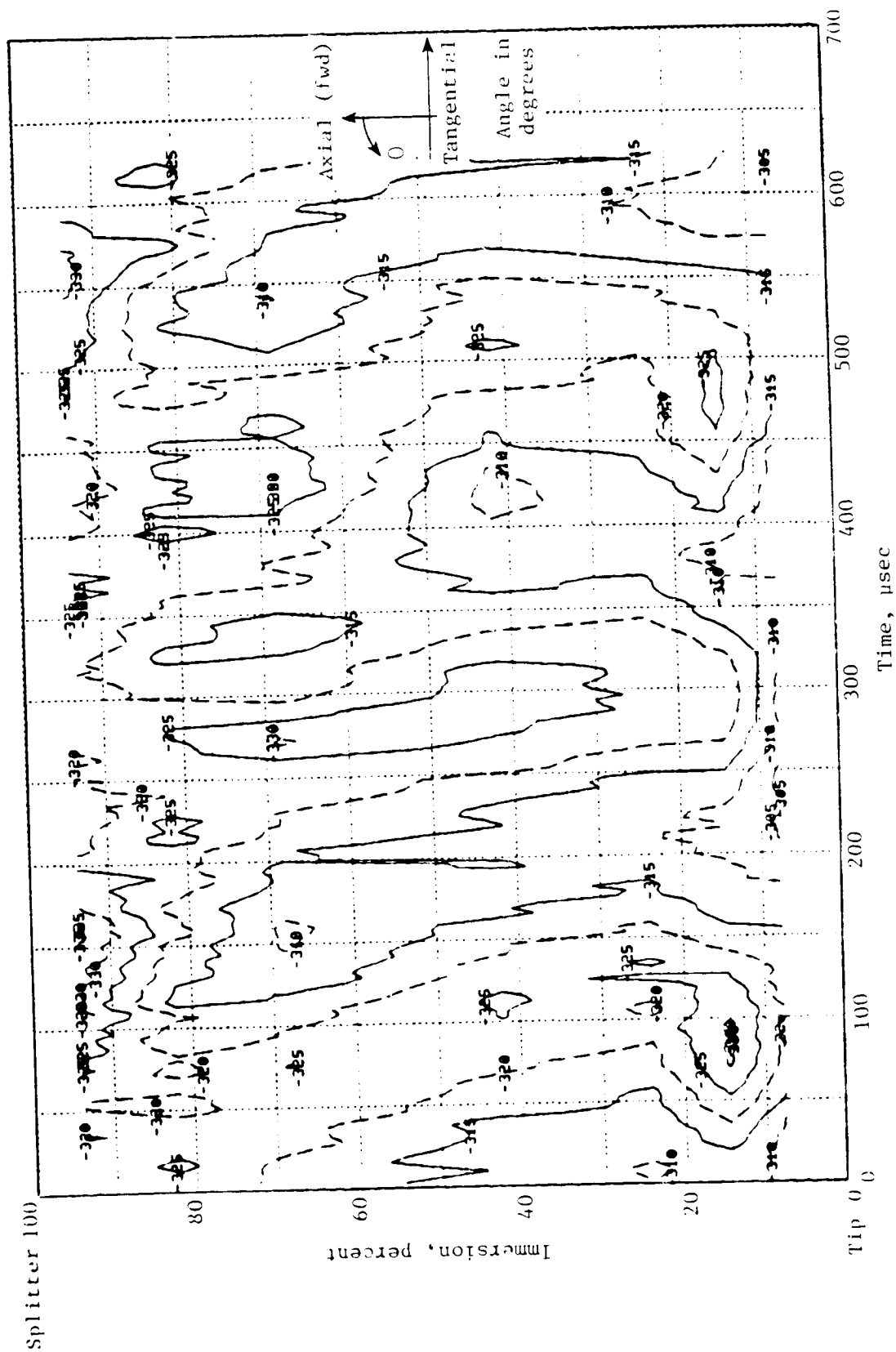


Figure E-7. Exit Flow Angle Contour Plot, 70 Percent Speed Nominal Operating Line.

ORIGINAL FILED IN
OF POOR QUALITY

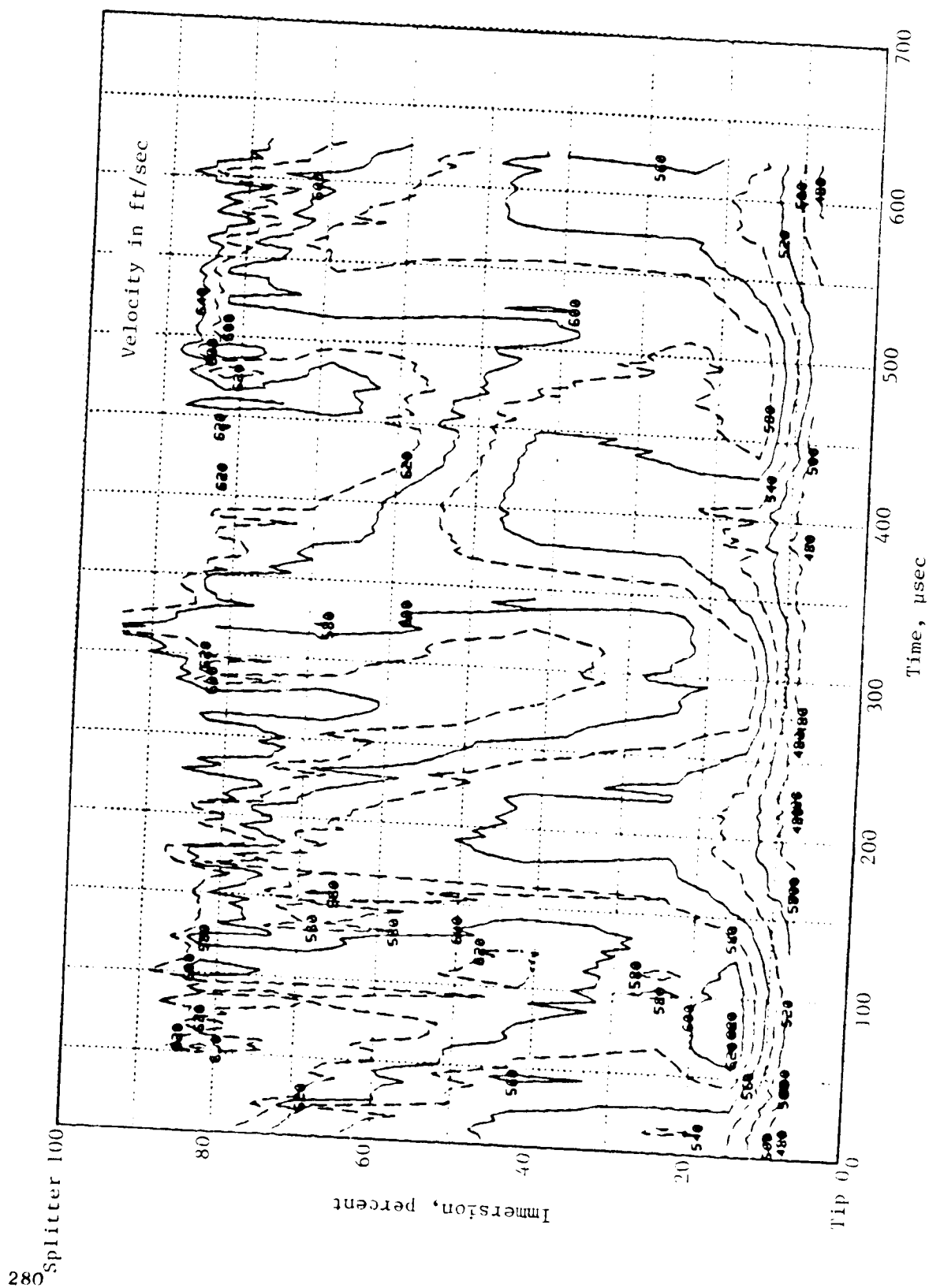


Figure E-8. Exit Absolute Velocity Contour Plot, 70 Percent Speed Nominal Operating Line.

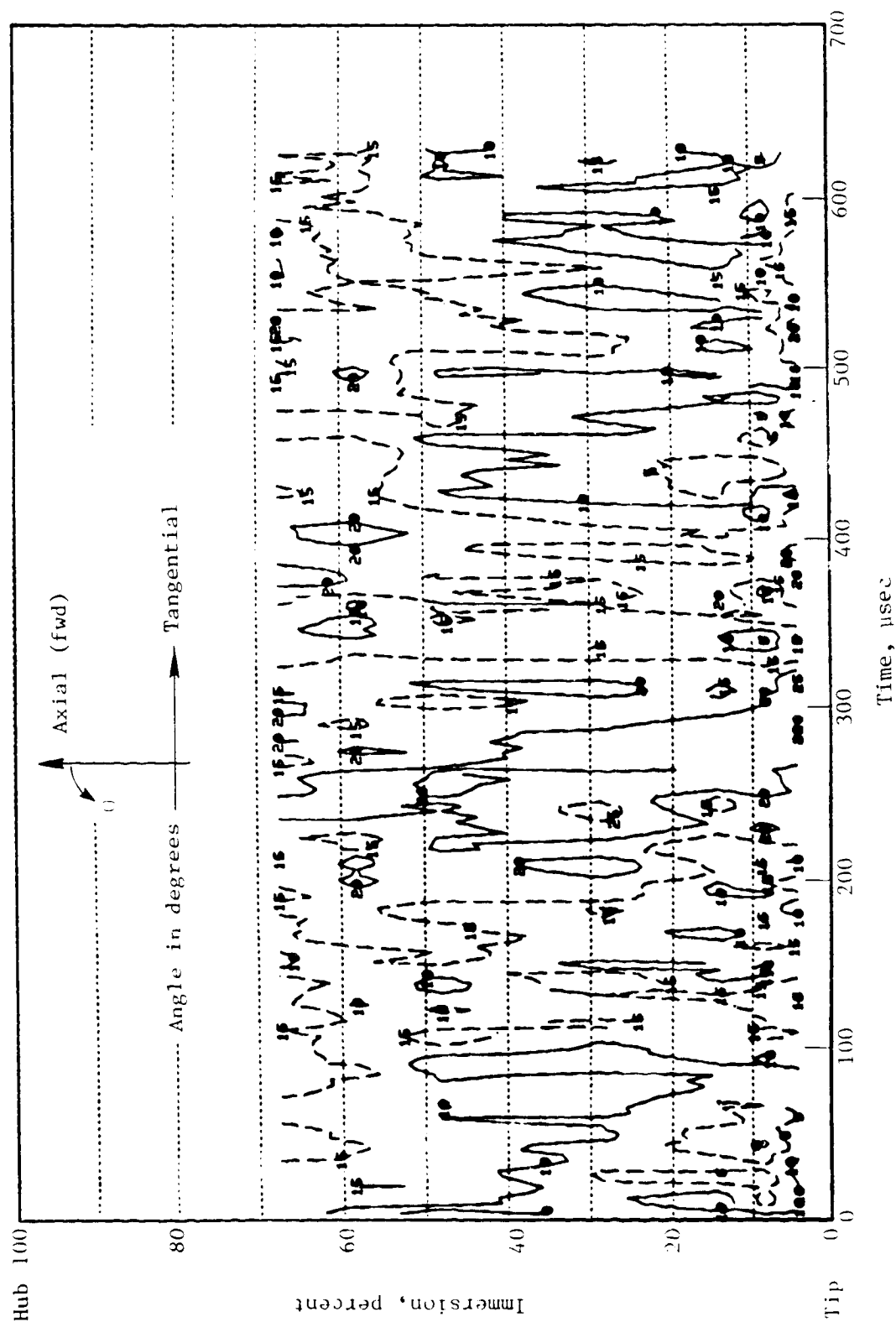


Figure E-9. Inlet Flow Angle Contour Plot, 70 Percent Speed Intermediate Operating Line.

OF POOR QUALITY

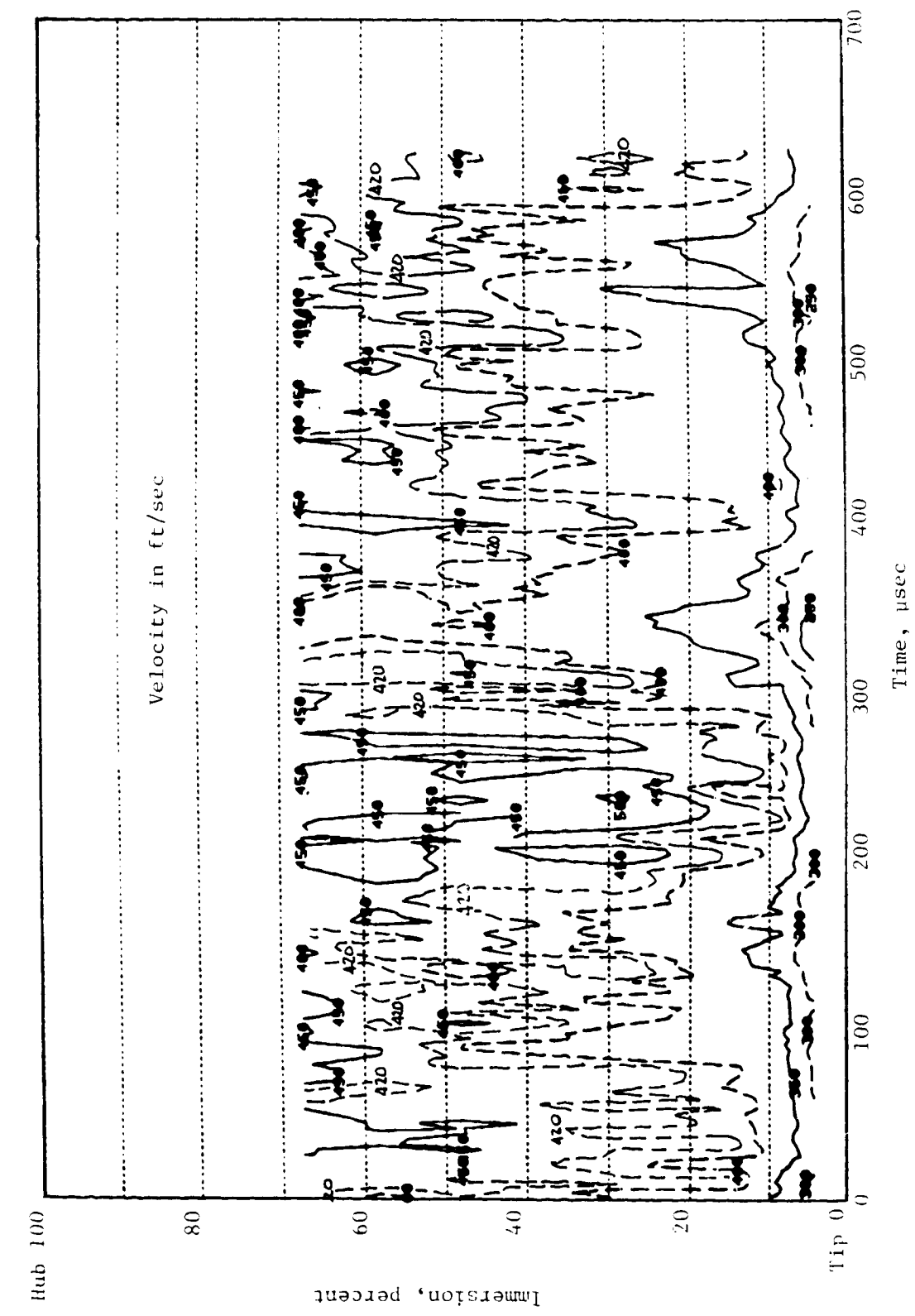


Figure E-10. Inlet Absolute Velocity Contour Plot, 70 Percent Speed Intermediate Operating Line.

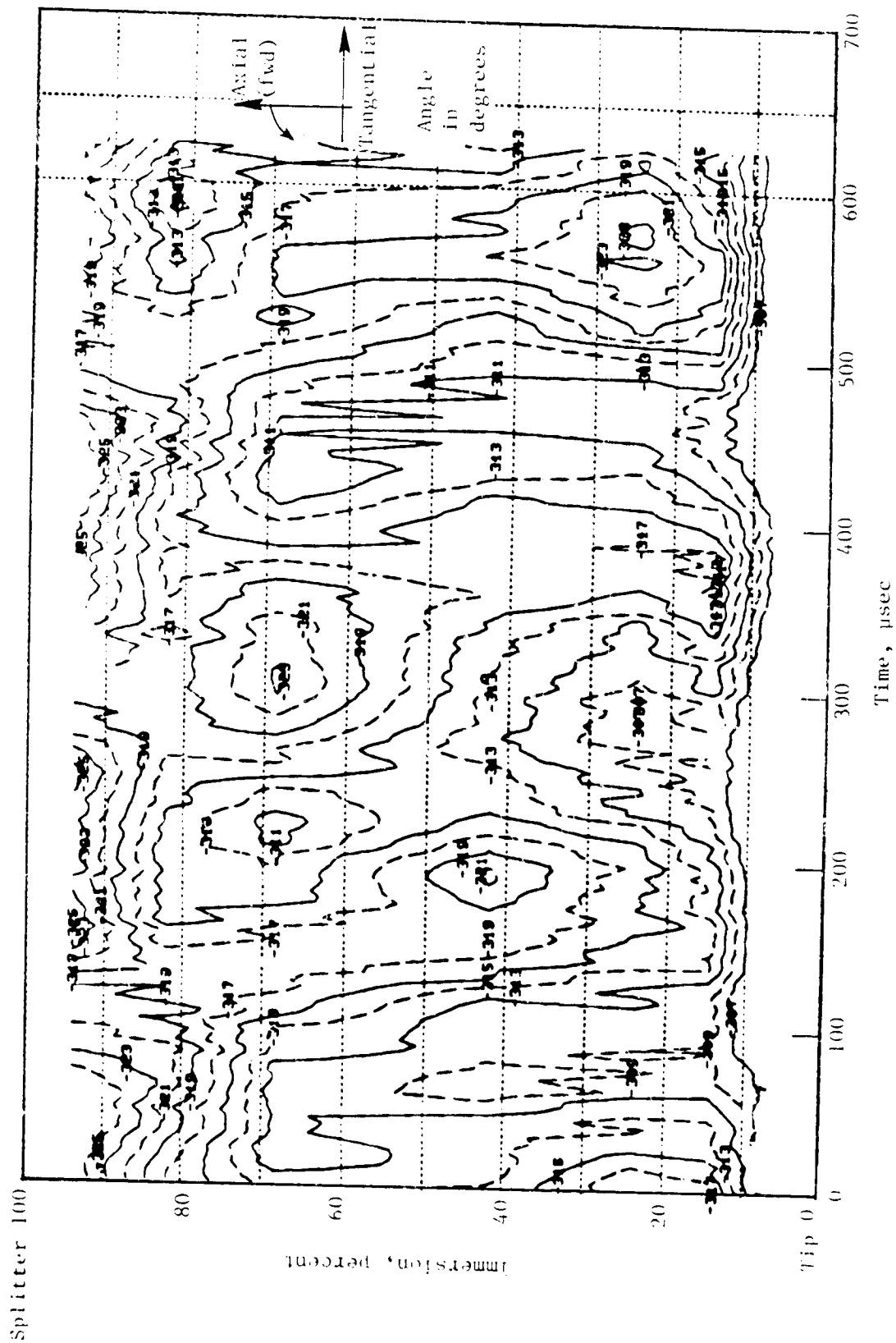


Figure E-11. Exit Flow Angle Contour Plot, 70 Percent Speed Intermediate Operating Line.

ORIGINAL COPY
OF RECORD COPY

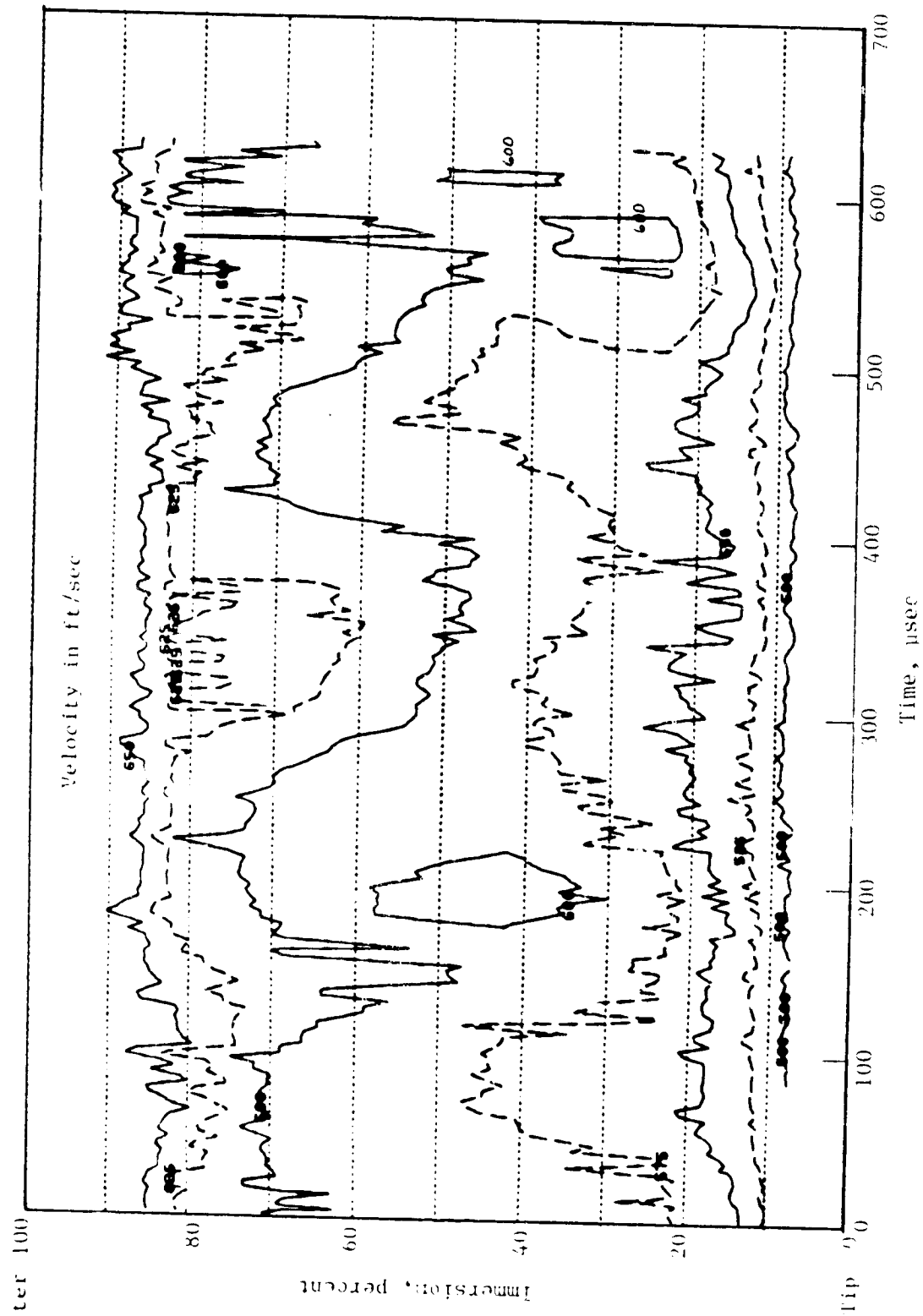


Figure E-12. Exit Absolute Velocity Contour Plot, 70 Percent Speed Intermediate Operating Line.

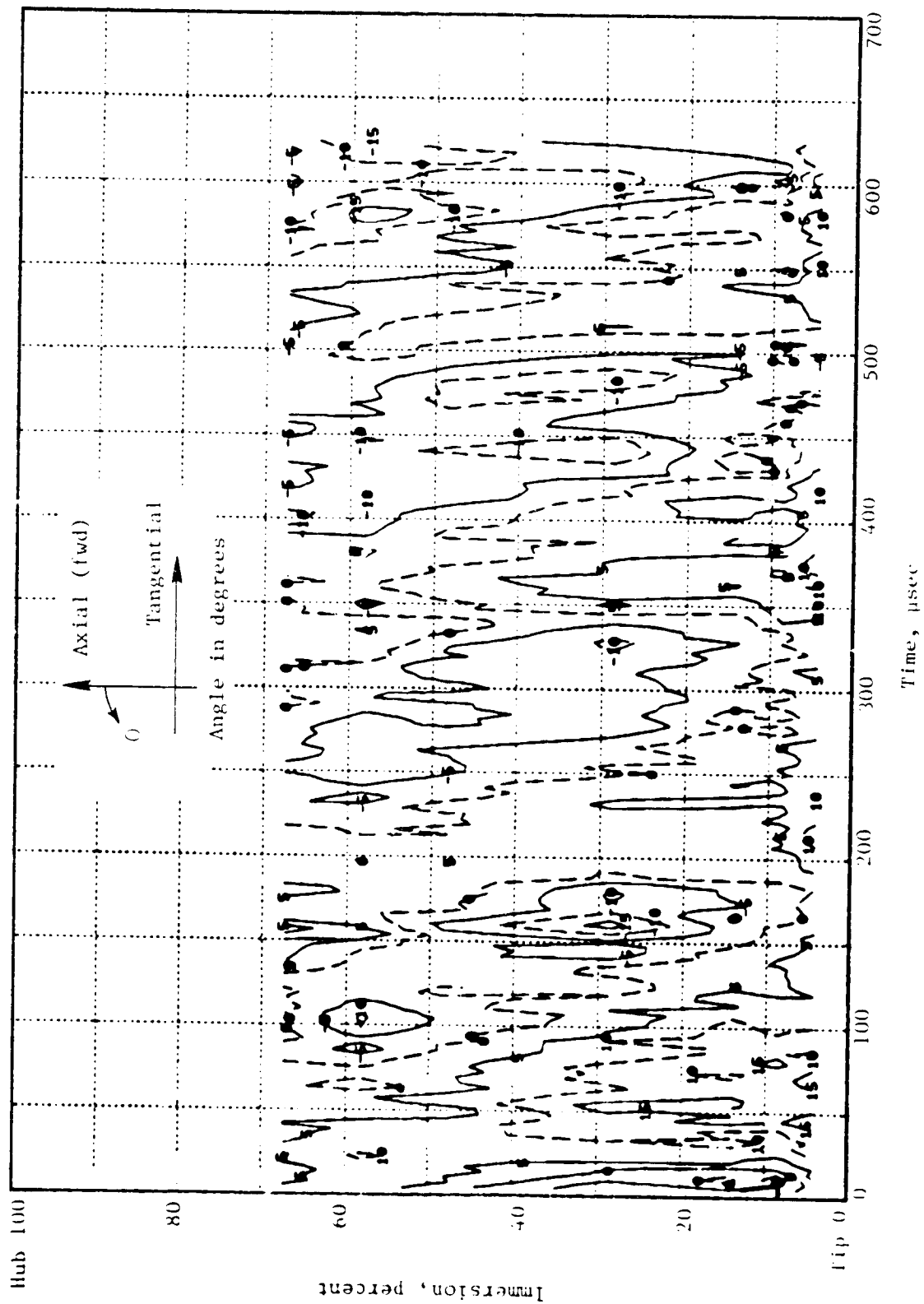


Figure E-13. Inlet Flow Angle Contour Plot, 90 Percent Speed Nominal Operating Line.

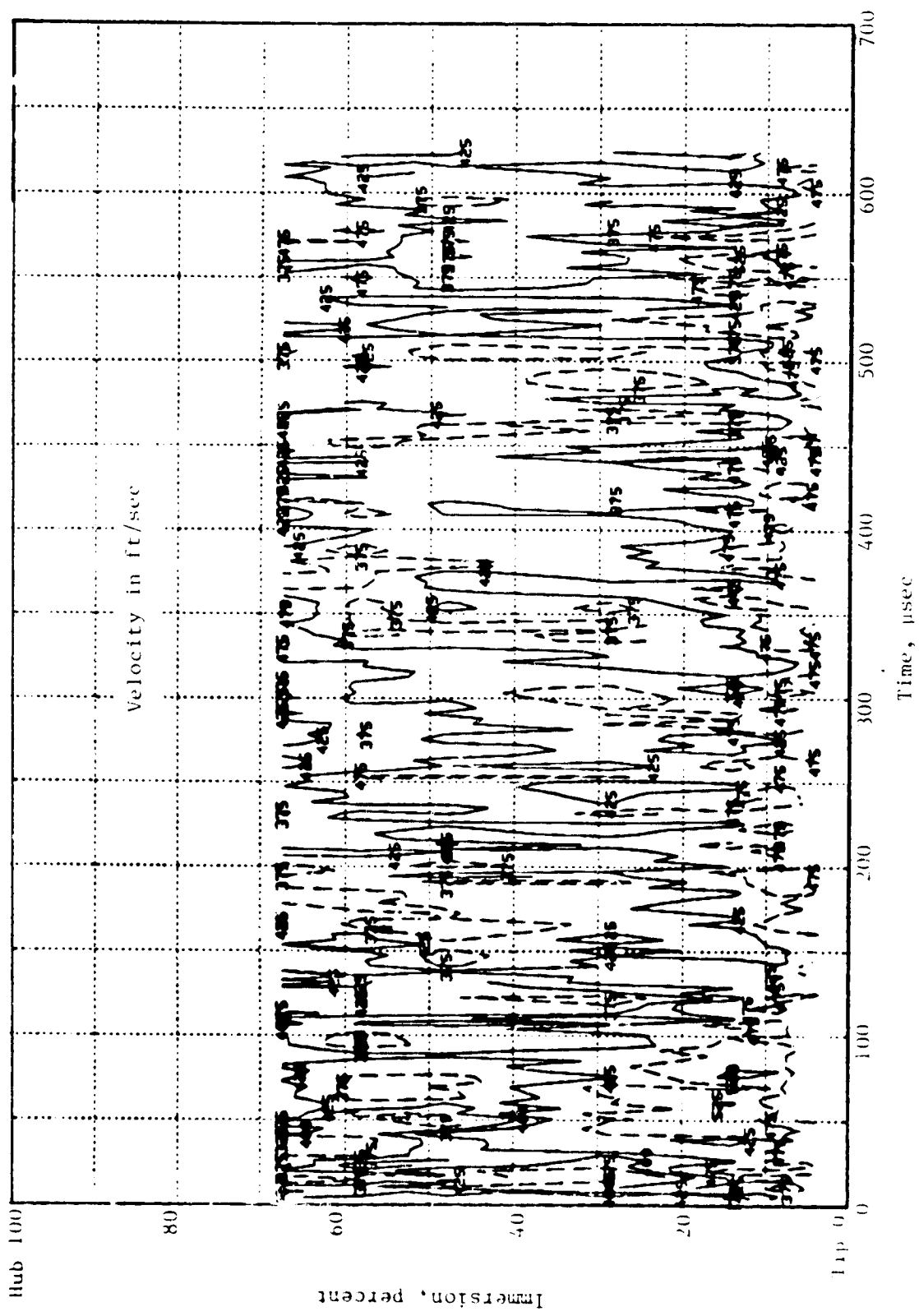


Figure E-14. Inlet Absolute Velocity Contour Plot, 90 Percent Speed Nominal Operating Line.

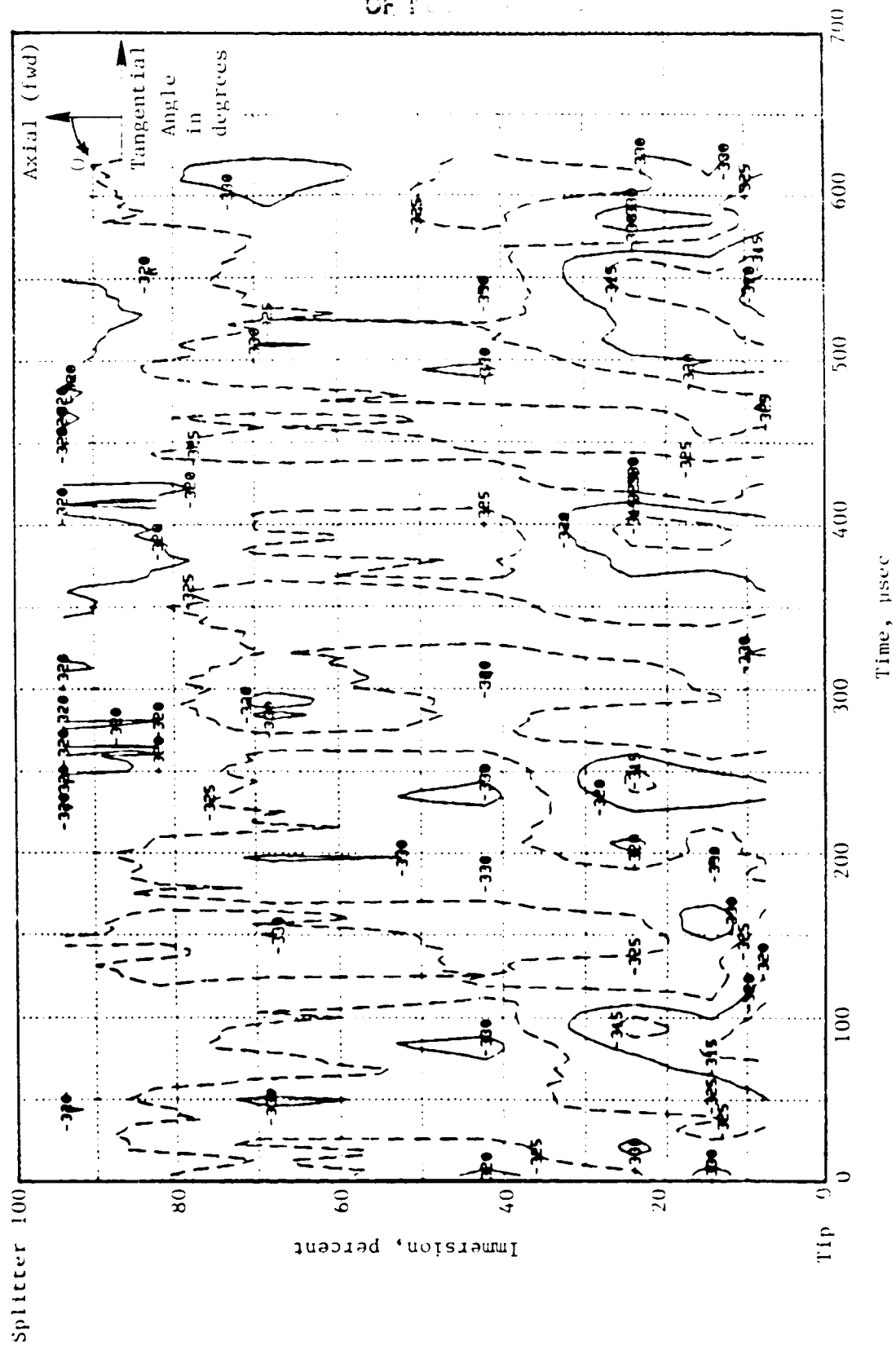


Figure E-15. Exit Flow Angle Contour Plot, 90 Percent Speed Nominal Operating Line.

ORIGINAL PLOT IS
OF POOR QUALITY

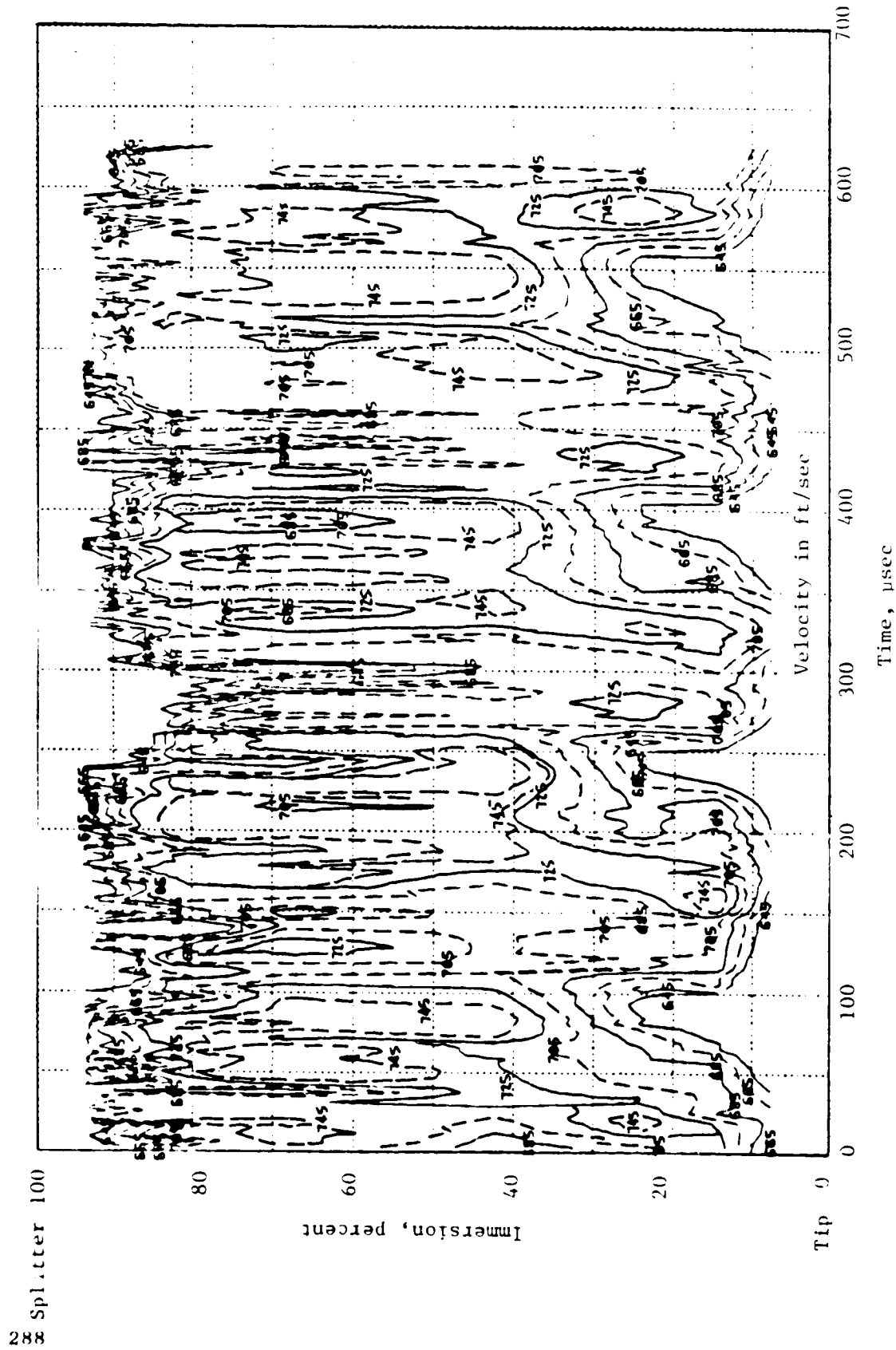


Figure E-16. Exit Absolute Velocity Contour Plot, 90 Percent Speed Nominal Operating Line.

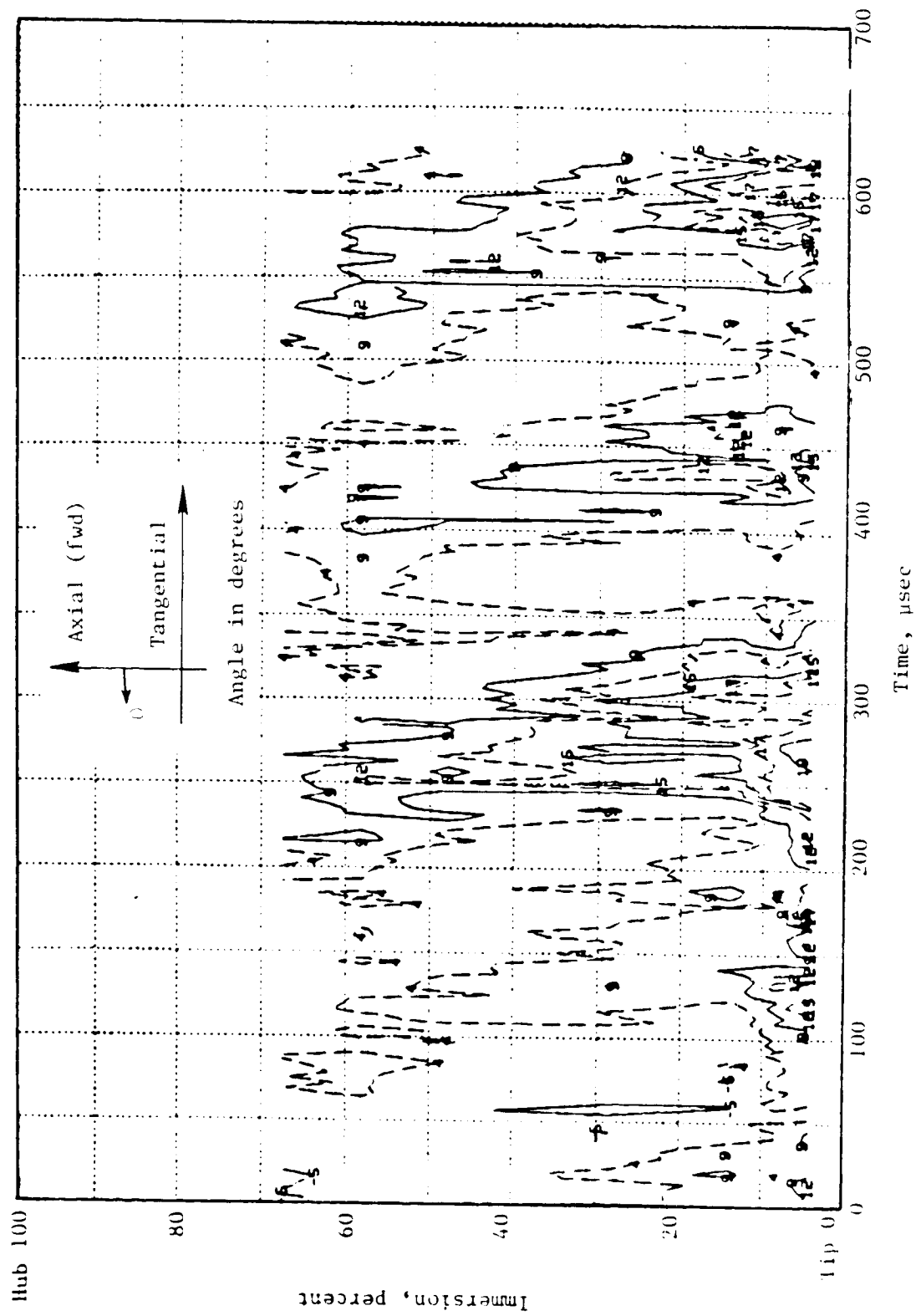


Figure E-17. Inlet Flow Angle Contour Plot, 90 Percent Speed Intermediate Operating Line.

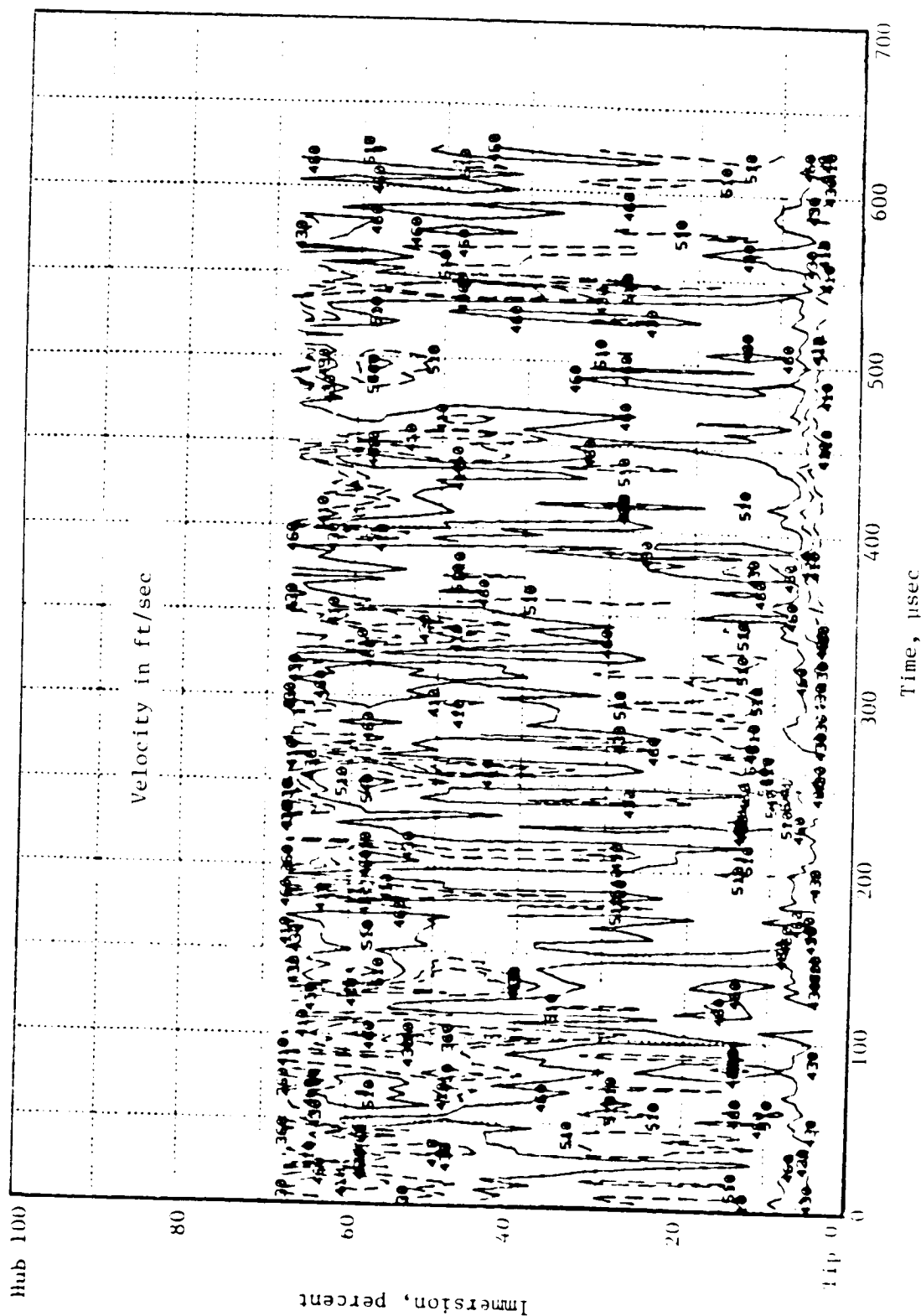
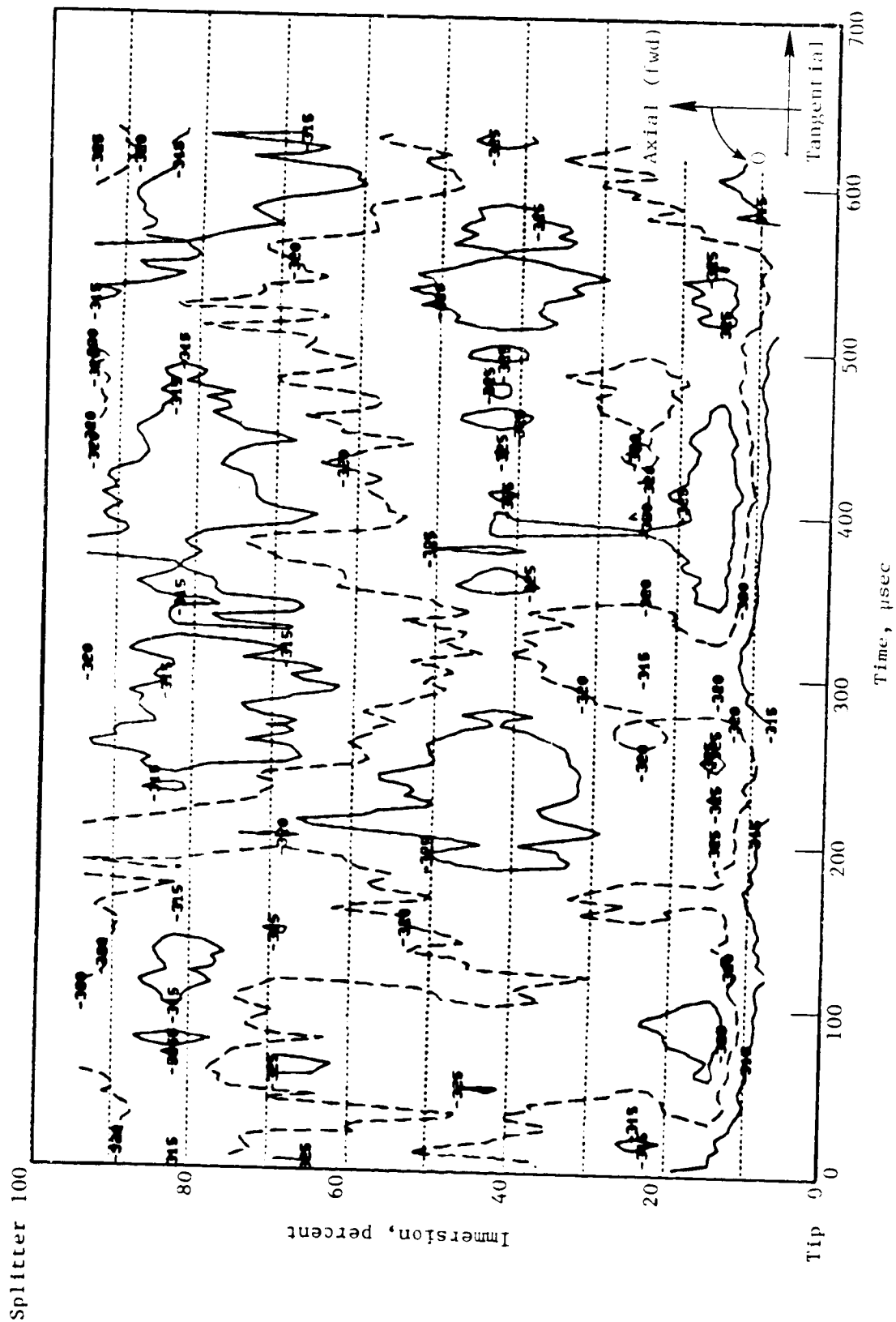


Figure E-18. Inlet Absolute Velocity Contour Plot, 90 Percent Speed Intermediate Operating Line.



CONTROL PLOTS OF POOR QUALITY

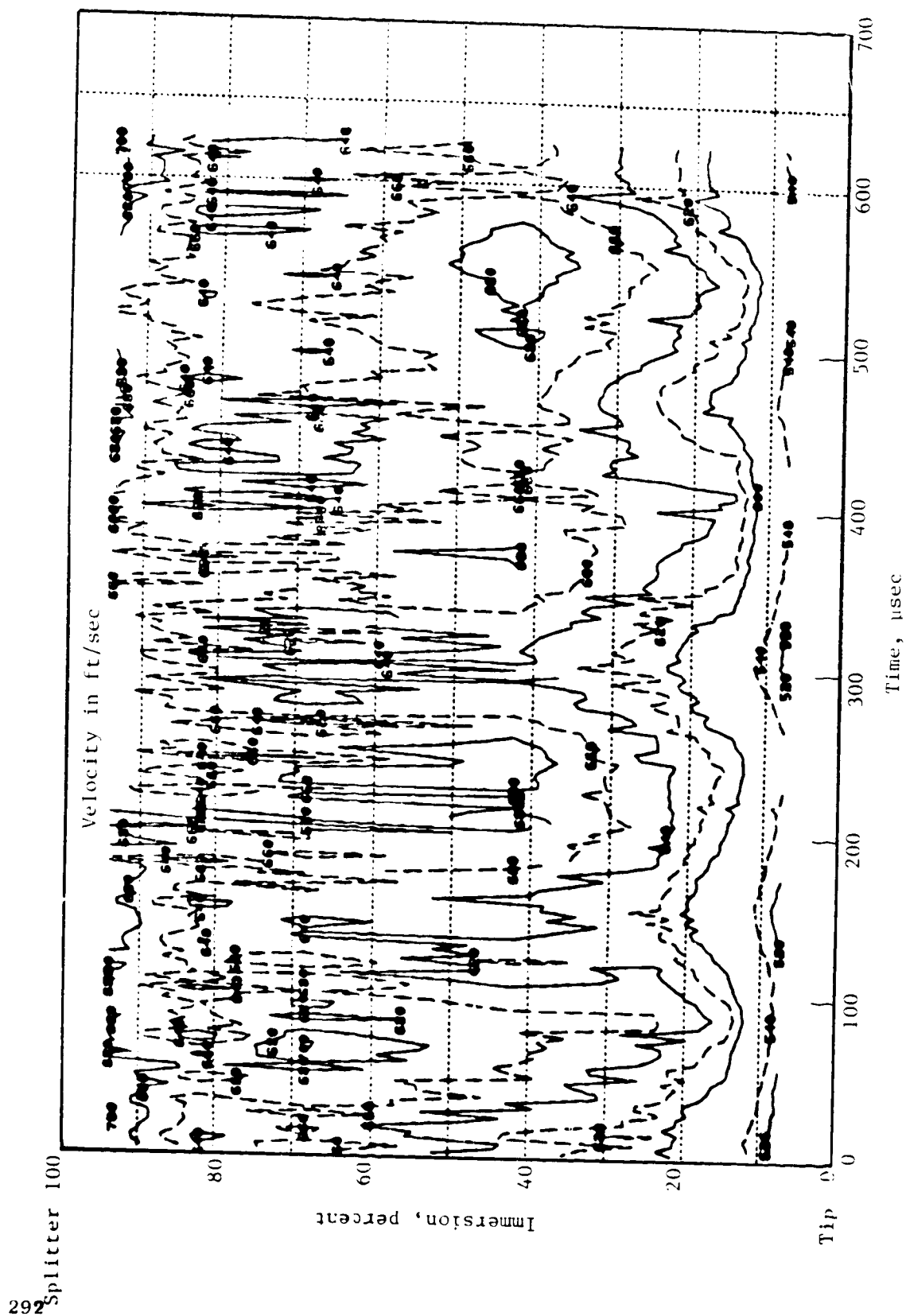


Figure E-20. Exit Absolute Velocity Contour Plot, 90 Percent Speed Intermediate Operating Line.

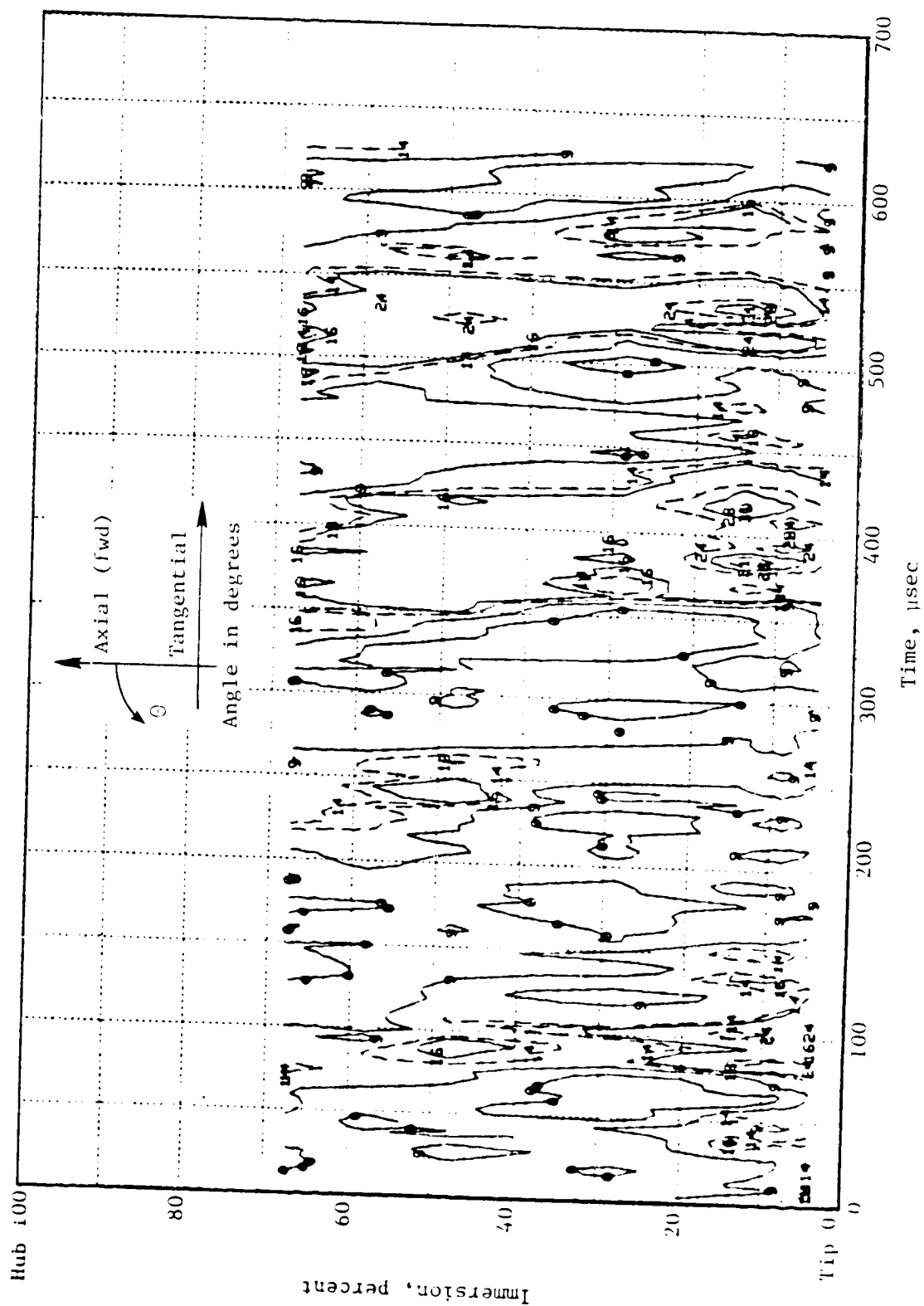


Figure E-21. Inlet Flow Angle Contour Plot, 95 Percent Speed Intermediate Operating Line.

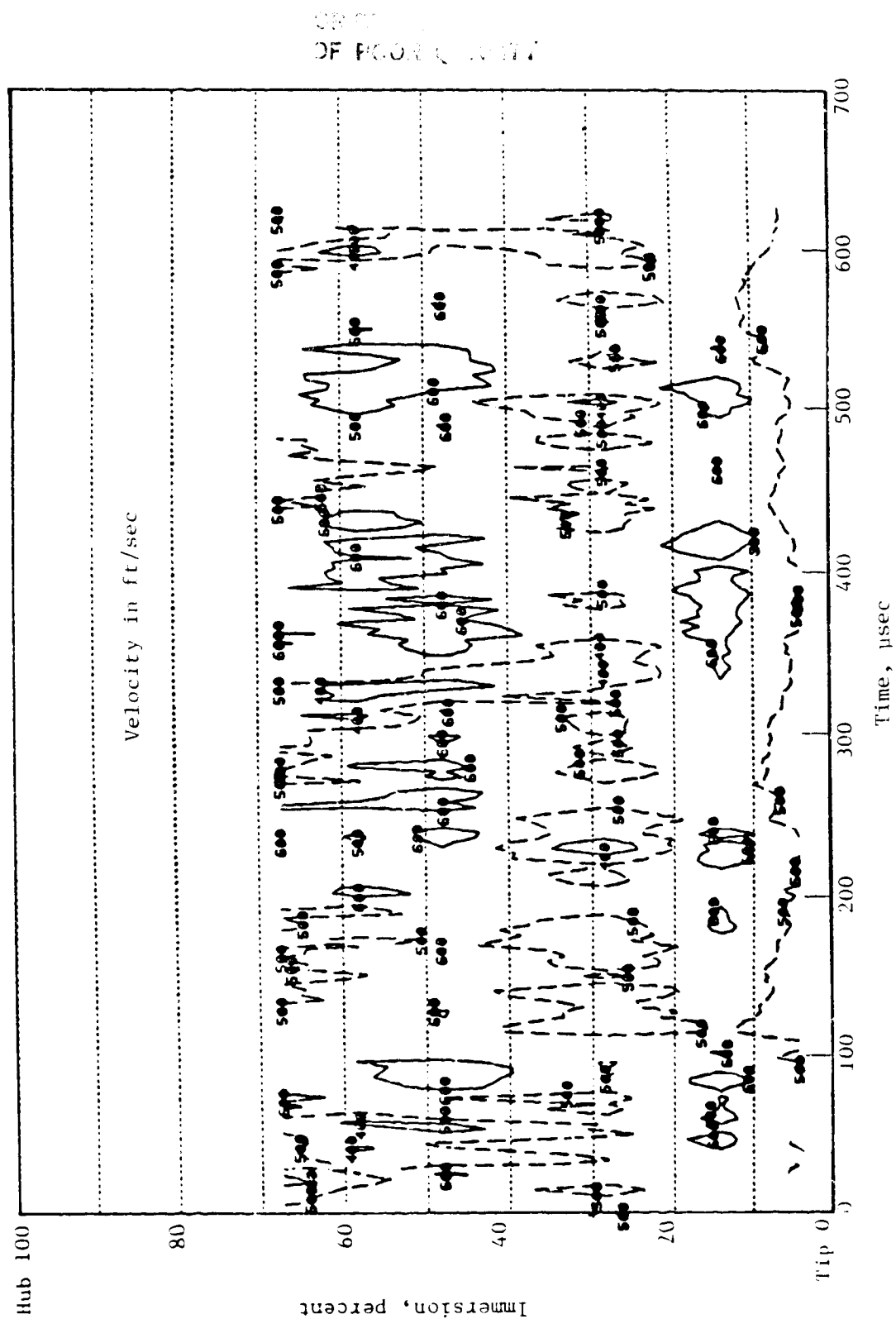


Figure E-22. Inlet Absolute Velocity Contour Plot, 95 Percent Speed Intermediate Operating Line.

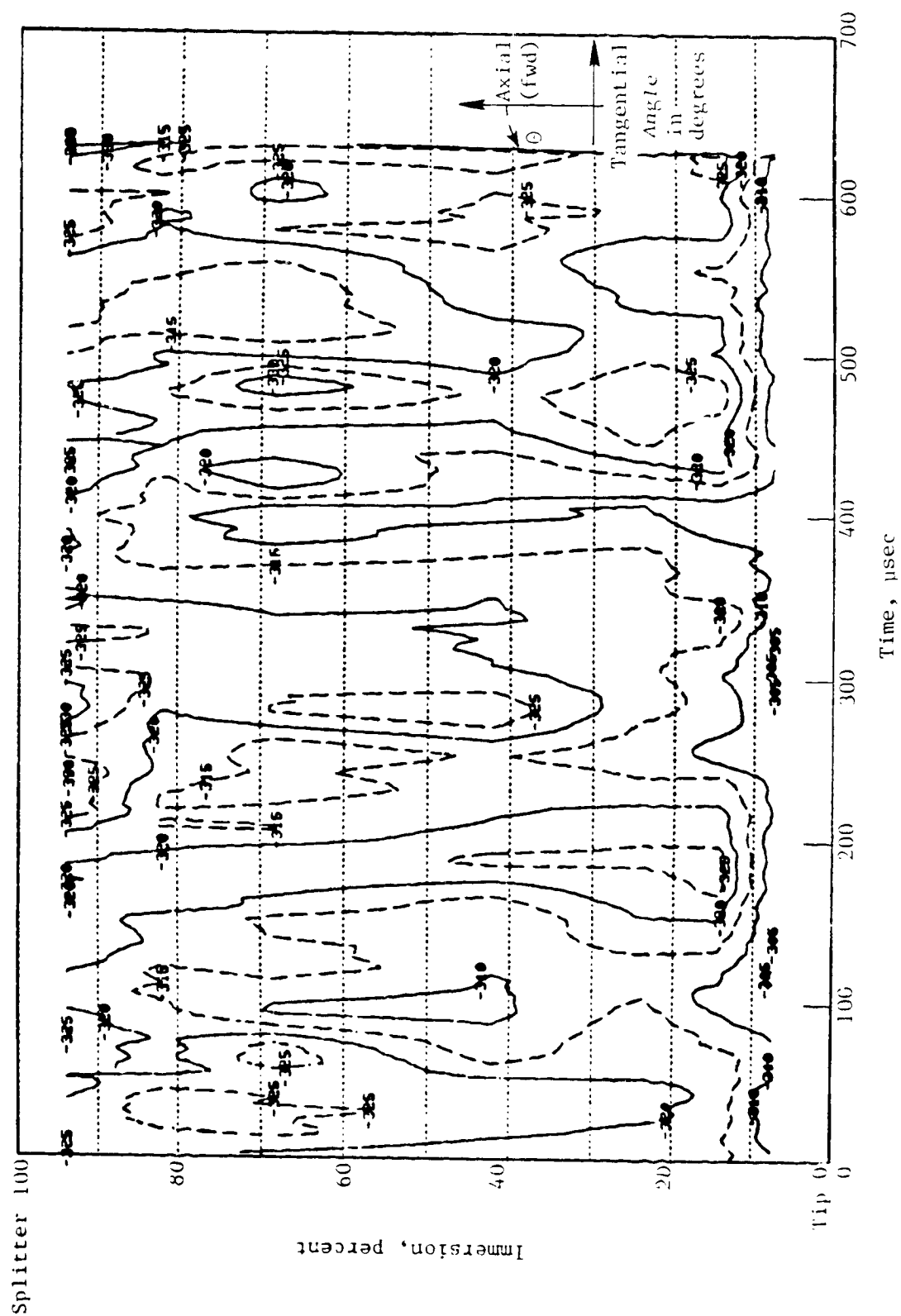


Figure E-23. Exit Flow Angle Contour Plot, 95 Percent Speed Intermediate Operating Line.

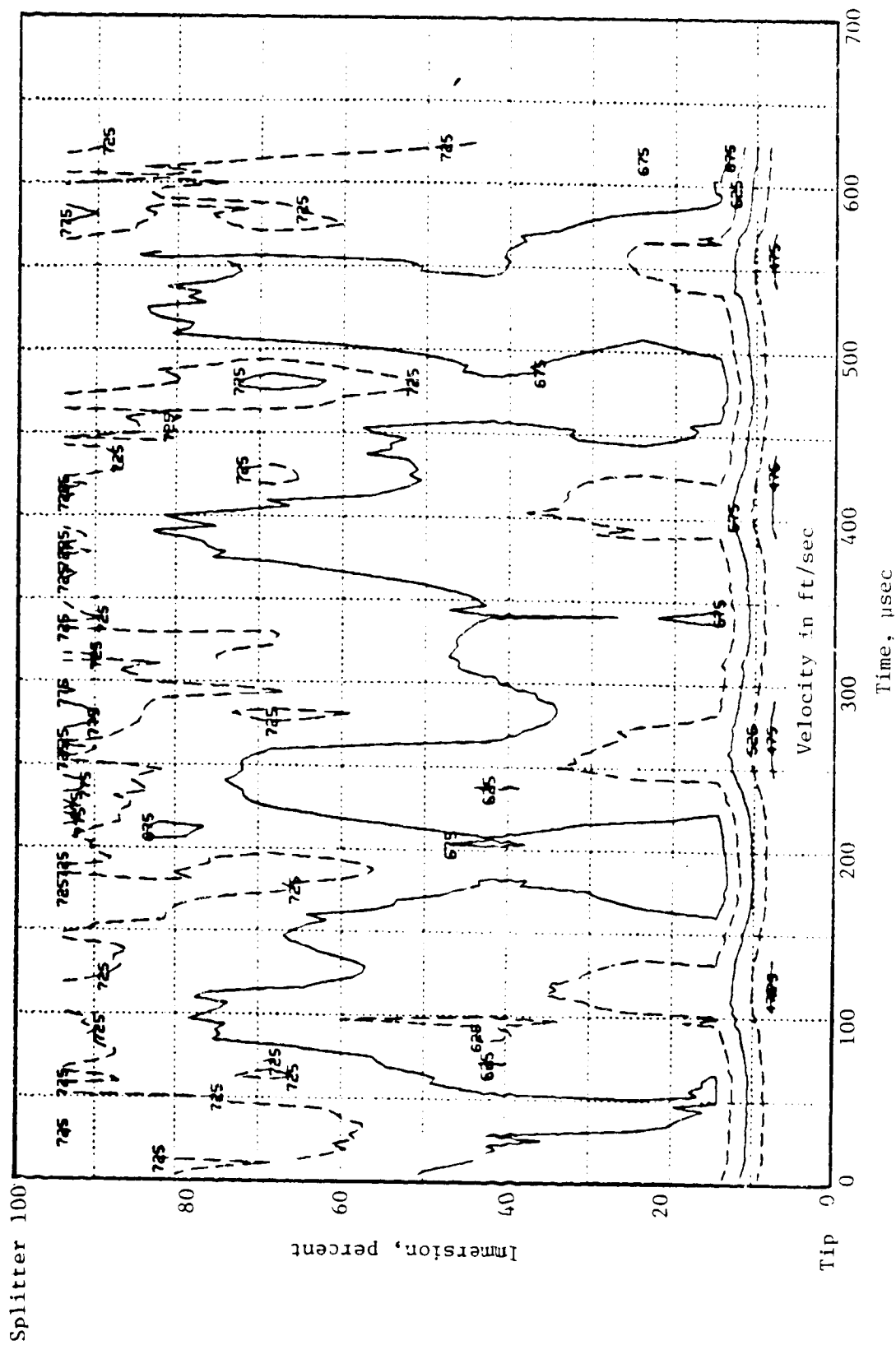


Figure E-24. Exit Absolute Velocity Contour Plot, 95 Percent Speed Intermediate Operating Line.

REFERENCES

1. Griffin, R.G., Parker, D.E., and Dunbar, L.W.; "Experimental Quiet Engine Program - Aerodynamic Performance of Fan C," NASA CR-120981, 1972.
2. Sullivan, T.J., Silverman, I., and Little, D.R., "Single-Stage, Low-Noise Advanced-Technology Fan, Volume IV - Fan Aerodynamics, Section 1 Results and Analysis," NASA CR-134892, 1976.
3. Kurkov, A.P., "Flutter Spectral Measurements Using Stationary Pressure Transducers," NASA TM 79293, also presented at Twenty-Fifth Annual International Gas Turbine Conference, New Orleans, Louisiana, March 9-13, 1980. (Don Braun's Formula)
4. Chi, M.R., "Unsteady Aerodynamics in Stalled Cascade and Stall Flutter Prediction," presented at the ASME Century 2 Aerospace Conference, San Francisco, California, ASME Paper No. 80-C2/Aero-1, August 13-15, 1980.
5. Adamczyk, J.J., Stevans, W., and Juoras, R.R., "Supersonic Stall Flutter of High Speed Fans," ASME Paper No. 81-GT-184.